

# Technical Sciences

**24/2021**

Wydawnictwo  
Uniwersytetu Warmińsko-Mazurskiego  
w Olsztynie

## **Editorial Board**

Ceslovas Aksamitauskas (Vilnius Gediminas Technical University, Lithuania), Olivier Bock (Institut National de L'Information Géographique et Forestière, France), Stefan Cenkowski (University of Manitoba, Canada), Adam Chrzanowski (University of New Brunswick, Canada), Davide Ciucci (University of Milan-Bicocca, Italy), Sakamon Devahastin (King Mongkut's University of Technology Thonburi in Bangkok, Thailand), German Efremov (Moscow Open State University, Russia), Mariusz Figurski (Military University of Technology, Poland), Maorong Ge (Helmholtz-Zentrum Potsdam Deutsches GeoForschungsZentrum, Germany), Dorota Grejner-Brzezinska (The Ohio State University, USA), Janusz Laskowski (University of Life Sciences in Lublin, Poland), Arnold Norkus (Vilnius Gediminas Technical University, Lithuania), Stanisław Pabis (Warsaw University of Life Sciences-SGGW, Poland), Lech Tadeusz Polkowski (Polish-Japanese Institute of Information Technology, Poland), Arris Tijsseling (Technische Universiteit Eindhoven, Netherlands), Alojzy Wasilewski (Koszalin University of Technology, Poland)

## **Editorial Committee**

Marek Markowski (Editor-in-Chief), Piotr Artiemjew, Kamil Kowalczyk, Wojciech Sobieski, Piotr Srokosz, Magdalena Zielińska (Assistant Editor), Marcin Zieliński

## **Features Editors**

Piotr Artiemjew (Information Technology), Marcin Dębowski (Environmental Engineering), Zdzisław Kaliniewicz (Biosystems Engineering), Grzegorz Królczyk (Materials Engineering), Marek Mróz (Geodesy and Cartography), Ryszard Myhan (Safety Engineering), Wojciech Sobieski (Mechanical Engineering), Piotr Srokosz (Civil Engineering), Jędrzej Trajer (Production Engineering)

## **Statistical Editor**

Paweł Drozda

## **Executive Editor**

Mariola Jezierska

The Technical Sciences is indexed and abstracted in BazTech (<http://baztech.icm.edu.pl>) and in IC Journal Master List (<http://journals.indexcopernicus.com>)

The Journal is available in electronic form on the web sites  
<http://www.uwm.edu.pl/techsci> (subpage Issues)  
<http://wydawnictwo.uwm.edu.pl> (subpage Czytelnia)

The electronic edition is the primary version of the Journal

PL ISSN 1505-4675  
e-ISSN 2083-4527

© Copyright by Wydawnictwo UWM • Olsztyn 2021

Address  
ul. Jana Heweliusza 14  
10-718 Olsztyn-Kortowo, Poland  
tel.: +48 89 523 36 61  
fax: +48 89 523 34 38  
e-mail: [wydawca@uwm.edu.pl](mailto:wydawca@uwm.edu.pl)

---

Ark. wyd. 27,45, ark. druk. 23,25, nakład 75 egz.  
Druk – Zakład Poligraficzny UWM, zam. 39



## CONTENTS

P. MAZUR, J. SZUSZKIEWICZ – <i>Impact of Microorganisms on Mechanical Properties Changes of Composite Materials with Sawdust as Organic Filler</i> .....	5
P. GORZELANCZYK, T. WIECZOREK – <i>Public Opinion Poll on the Parking System in Piła and the Possibility of Introducing the Smart Parking System in Piła</i> .....	13
Z. SYROKA – <i>Battery Supercharging System in Electrical Vehicles Using Photovoltaic Panels</i> .....	27
S. CELLMER, A. BOBOJC – <i>Optimization Method Based on Minimization M-order Central Moments Used in Surveying Engineering Problems</i> ..	39
Ł. MIAZIO – <i>The Influence of Layer Height on the Tensile Strength of Specimens Printed in the FDM Technology</i> .....	51
K. MATEJA, W. PANFIL – <i>Design of a Motion System for 3D Printed Snakebot</i> .....	57
D. WIŚNIEWSKI – <i>Analysis of a Method for Measuring Deposit Impedance Parameters Using Charge Amplifier and Lock-in Voltmeter</i> .....	67
W. SOBIESKI, <span style="border: 1px solid black; padding: 0 2px;">A. TRYKOZKO</span> – <i>The Use of the Inverse Problem Methodology in Analysis of Fluid flow Through Granular Beds with Non-Uniform Grain Sizes</i> .....	83
S. LIPIŃSKI, M. DUDA, D. GÓRSKI – <i>Waste Heat Recovery from Servers Using an Air to Water Heat Pump</i> .....	105
J. LITWIN, M. OLECH, A. SZYMUSIK – <i>Applying Python's Time Series Forecasting Method in Microsoft Excel – Integration as a Business Process Supporting Tool for Small Enterprises</i> .....	115
Ł. PAŚKO, A. KUŚ – <i>Bootstrap Aggregation Technique for Evaluating the Significance of Manufacturing Process Parameters in the Glass Industry</i> .....	135
P. STROJNY – <i>Modification of the Tooth Geometry of a Polymer Gear with a Straight Tooth Line to Adjust the Torque Transmission Capability in One Direction Only</i> .....	157
P. CHYŁA – <i>Study of the Process of Rolling Steel Balls in Skew Rolling Mill – Metallographic Analysis</i> .....	171
W. REJMER – <i>Influence of air Content on Thermal Degradation of Poly(Ethylene Terephthalate)</i> .....	183

---

Z. SYROKA – <i>Sniper Rifle Cartridge</i> .....	195
M. JASZTAL, M. KUNIKOWSKI – <i>Modelling and Simulation of Functioning of the GSh-23 Aviation Autocannon Mechanisms</i> .....	211
E. ŁADYŻYŃSKA-KOZDRAŚ, B. KOZŁOWSKA, D. POTOKA – <i>The Use of the Theory of Nonholonomic Constraints in the Process of Automatic Control of a Manipulating Machine</i> .....	221
A. PANUŚ – <i>Assessment of Wall Salinity in the Selection of Renovation Plaster Systems</i> .....	229
T. CHROSTEK – <i>Tribological Wear of Fe-Al Coatings Applied by Gas Detonation Spraying</i> .....	245
G. ŚWIACZNY – <i>Influence of Geometric Features Associativity of Cad Class Models on the Process of their Updating – Comparative Analysis</i> .....	257
T. ZADOROŻNY, M. KALINOWSKI, M. SZCZEPANIK – <i>Influence of Various Methods of Modelling the Welding Process in the CAE Environment on the Obtained Deformation Results</i> .....	273
M. KMIOTEK, A. KORDOS, T. IWAN – <i>Numerical Simulation of Flow Through Microchannels with Random Roughness</i> .....	283
S. RZYDZIK, M. ADAMIEC – <i>The Advanced CAD Model of a Cargo Bike</i> ....	301
P. ZENOWICZ – <i>Simulation Study of a Composite Landig Gear of Ultralight and Very Light Aircraft</i> .....	317
R. CYBULSKI – <i>Pseudo-Random Number Generator Based on Linear Congruence and Delayed Fibonacci Methode</i> .....	331
A. ORDON, P. KURNYTA-MAZUREK – <i>Test Rig Dedicated for Hardware Used in Wind Tunnels</i> .....	351
Reviewers of Years – book 2021 .....	366

## IMPACT OF MICROORGANISMS ON MECHANICAL PROPERTIES CHANGES OF COMPOSITE MATERIALS WITH SAWDUST AS ORGANIC FILLER

*Piotr Mazur<sup>1</sup>, Jarosław Szuszkiewicz<sup>2</sup>*

<sup>1</sup>ORCID: 0000-0002-5596-091X

<sup>2</sup>ORCID: 0000-0002-4490-3397

Institute of Fluid Flow Machinery

Faculty of Technical Sciences

University of Warmia and Mazury in Olsztyn

Received 10 September 2020, accepted 23 February 2021, available online 12 March 2021.

**Key words:** polymer, composite, organic filler, microorganisms, impact strength, polyethylene.

### Abstract

The beginning of the XXI<sup>st</sup> century is characterized by rapid development of polymer materials, including polymer composite materials, which consist of a natural organic filler (wood flour, sawdust, cellulose fiber, flax fiber, sisal fiber) and reinforcement carrier (polymer). In case of that kind of the fillers under the influence of weathering (humidity, temperature) they might be subject to biodegradation due to effect of microorganisms, including fungi, which are responsible for degradation of natural organic fillers. In case of the low melting temperature polymers (e.g. PE-LD) the processing temperature does not entirely eliminate some of the fungal spores. The paper has presented the research results of twelve months. The development of the microorganisms in the natural conditions was examined in a pure filler (sawdust) as well as in a composite. Simultaneously, change of one of the fundamental strength properties, which is the impact strength, was being tested. For the investigated composite the PE-LD as the matrix and a sawdust mixture of pine, larch and oak were used. The sawdust formed the composite in 30% vol. The research results confirmed that in the natural conditions the microorganisms development depends on weathering which varies in the time of the year. The value of the *V* notch impact strength changed from 12.5 kJ/m<sup>2</sup> for the composite in initial phase to the value of 6.7 kJ/m<sup>2</sup> after twelve months operation, which is close to 54%.

---

Correspondence: Jarosław Szuszkiewicz, Katedra Technologii Materiałów i Maszyn, Wydział Nauk Technicznych, Uniwersytet Warmińsko-Mazurski, ul. Oczapowskiego 11, 10-718 Olsztyn, phone: +48 89 523 36 64, e-mail: [jerry@uwm.edu.pl](mailto:jerry@uwm.edu.pl)

## Introduction

The dynamic research development on polymers can be noticed since the second half of the XX<sup>th</sup> century (BARTON 2014). One of the directions is creation of polymer composites with natural organic fillers. The thermoplastic polymers (usually of low melting temperature) are used as matrix and plant fibers or sawdust (byproduct of wood processing) might be applied as a filler (GARBARCZYK et al. 2009).

The paper discusses a problem of mechanic properties change on an example of V notch impact strength of mentioned above composites connected with their destruction while exploited in outer conditions under influence of microorganisms (MIEDZIANOWSKA et al. 2018).

## Materials and Methods

Low Density Polyethylene (PE-LD) was selected as the matrix because of common use and low temperature processing. Sawdust was the filler. It was composed of residue of processing of three tree species: pine, larch and oak. Sawdust share in polymer was equal to 30%. That type of composite can be applied for roofing of lightweight construction building, e.g. shed, garage, holiday cabin, deck, etc.

The composite has been produced as 4 mm plates by the extrusion method. The extruder was one screw type. The rotational speed of a screw was equal to 70 rpm. The working temperatures were as follows: feeding device – 125°C, charging barrel – 130°C, extruder head – 130°C, nozzle – 135°C. Sawdust prior to addition to the polymer was dried to the level of 0.1% (KOSZKUL 1999), which is the moisture limit value for PE-LD processing. Usually, no additional chemicals protecting against harmful effects of microorganisms during exploitation of a composite are used (POSTAWA et al. 2010).

The examined composite was kept in outer weather conditions (moisture, temperature) as the exploitation conditions are. The V notch strength research was done every 8 weeks for 12 months. Simultaneously, the presence and content of microorganisms in sawdust and the composite was investigated.

The maximum processing temperature (135°C) did not guarantee getting rid of all the microorganisms, primarily fungal spores, which are resistant to that level of that temperature. Regarding to the wood composition (cellulose 51%, hemicelluloses 23%, lignin 23% and other organic compounds 4%) and proper atmosphere conditions (moisture and temperature) the microorganisms

can freely grow. That state may lead to the sawdust decomposition and further partial biodegradation of the composite (MAŃKA 2011).

The V notch impact strength research has been carried out by the Charpy impact test method according to the standard procedure. The V notch impact strength samples were cut mechanically to the following dimensions:  $80(\pm 2)$  mm  $\times$   $10(\pm 0,5)$  mm  $\times$   $4(\pm 0,2)$  mm. The angle of the V notch equaled  $45^\circ \pm 1^\circ$ . The fillet radius was up to 0.2 mm. Each series of research consisted of 12 measurements. Two extreme results were rejected and on the basis of ten remaining measurements the mean value was calculated.

Out of the investigated sawdust and composites there were prepared series of 10-fold solutions by moving of 10 g of sawdust or shredded composite to a sterile bag. Subsequently, 90 cm<sup>3</sup> of the solution liquid was added to the bag and the content was homogenized in a stomacher (Seward, Great Britain) for one minute. Following this period the supernatant liquids were decanted to sterile Schott bottles and microbiological determinations were carried out in the sawdust and composite: raw sawdust (Fig. 1), after two weeks, after one month, after two months (Fig. 2) and composites just after production, after two weeks, after two months, after four months (Fig. 3) and after six months of storage (Fig. 4).

The Total Bacterial Count (TBC) was determined by transferring 1 cm<sup>3</sup> of selected solutions to the sterile Petri dishes with three replicates. The transfers were poured with the nutrient agar (Merck, Poland). They were mixed up and after solidifying they were incubated at the temperature of 30°C for 72 hours. Following the incubation all the grown colonies were counted and taking under consideration the solutions the result in cfu/g of the investigated sample was given.



Fig. 1. Raw sawdust after pick up from sawmill

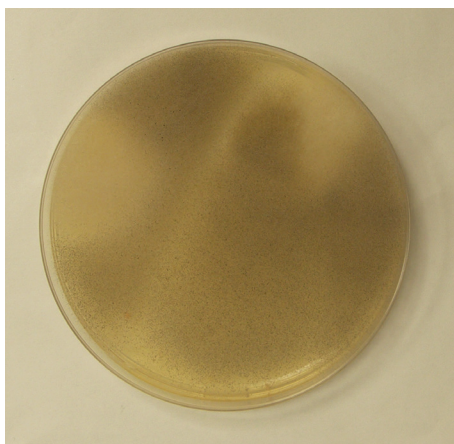


Fig. 2. Growth of fungi in sample of sawdust after two months



Fig. 3. Growth of fungi in composite after four months of storage in natural conditions

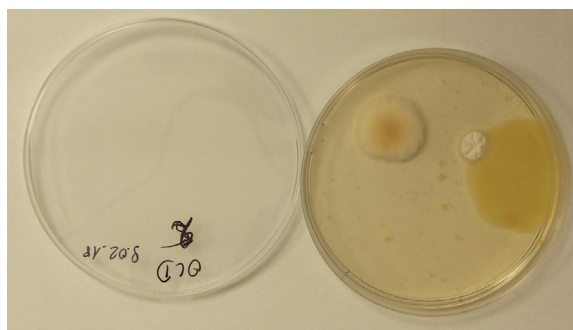


Fig. 4. Growth of fungi in composite after six months of storage in natural conditions

The number of fungi (yeasts and molds) were determined by transferring 1 cm<sup>3</sup> of selected solutions to the sterile Petri dishes with three replicates. The transfers were poured with YGC agar (Merck, Poland). They were mixed up and after solidifying they were incubated in the temperature of 25°C for 5 days. Following the incubation all the grown colonies of yeasts and/or molds were counted and taking under consideration solutions the result in cfu/g of the investigated sample was given (POSZYTEK 2016).

## Results Analysis and Conclusions

The results of the investigation of the V notch impact strength value was presented in the Table 1. The course change of the V notch impact strength was presented in the Figure 5. The Table 2 presents the results of the microbiological analysis of the sawdust and composite materials.

Table 1

V notch impact strength results

Time [months]	V notch impact strength [kJ/m <sup>2</sup> ]
0	12.51
2	11.39
4	9.3
6	10.88
8	8.01
10	7.36
12	6.7

In the raw sawdust the TBC number was high of about 10<sup>7</sup> cfu/g and during storage it was increasing which resulted in the growth of the fungi number. Directly after the production of the composite of the polymer and sawdust the TBC as well as the number of fungi were very low (about 10<sup>1</sup> cfu/g). This considerably significant decrease of the number of both groups of microorganisms relates to high temperature production procedure. During four months of storage, slowly but successively, the general number of microorganisms in the composite was increasing and number of fungi lingered at about the same number from the second month of storage.

The obtained results indicated that *Bacillus* sort dominated among the bacteria. These bacteria are capable of surviving in high temperatures applied during the composite production process. They owe this to the sporulation ability. Some of those bacteria, like *B. pumilus* and *B. circulans*, have cellulolytic



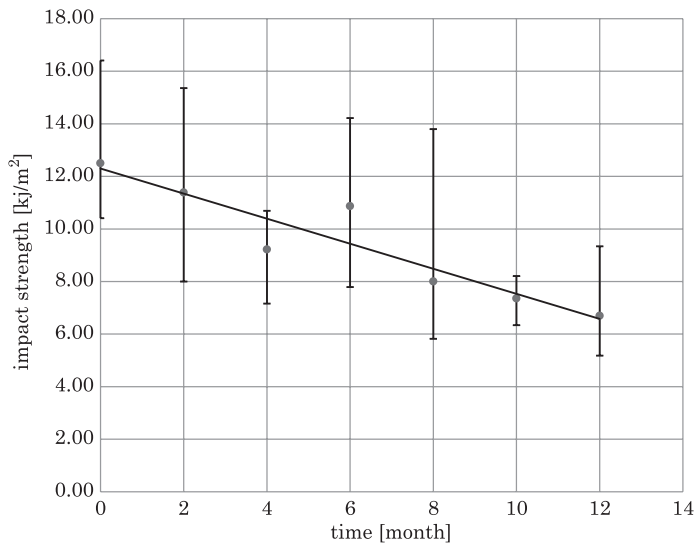


Fig. 5. Changes in the V notch impact strength for the composite

Table 2

Microbiological analysis of samples		
Sample	Number [cfu/g]	
	Total Bacterial Count (TBC)	Microscopic fungi
Sawdust (Raw)	$4.6 \cdot 10^7$	$4.2 \cdot 10^5$
Sawdust (2 weeks)	$7.25 \cdot 10^7$	$1.4 \cdot 10^7$
Sawdust (1 month)	$5.0 \cdot 10^5$ (Molds $7.1 \cdot 10^6$ )	$1.1 \cdot 10^7$
Sawdust (2 months)	$3.5 \cdot 10^5$ (Molds $1.5 \cdot 10^6$ )	$2.2 \cdot 10^6$
Composite material	$7.5 \cdot 10^1$ (spore-forming bacteria, e.g. <i>Bacillus</i> , that survive sterilization temperature even for several minutes) + white downy molds	$3.0 \cdot 10^1$ (white downy molds fouling all the plate)
Composite material after 2 months	$1.2 \cdot 10^3$ (mainly <i>Bacillus</i> bacteria type; single mold colonies)	$5.5 \cdot 10^1$ (flat colonies, low; grey or black colonies; other colonies are yellow, hyphae quite high, loose; <i>Zygomycetes</i> class – sporangium)
Composite materials after 4 months	$9.1 \cdot 10^3$ (including molds)	$4.8 \cdot 10^2$
Composite materials after 6 months	$1.08 \cdot 10^4$ (molds $4.0 \cdot 10^2$ ; mainly <i>Penicillium</i> )	$1.3 \cdot 10^2$
Composites after 8 months	$4.1 \cdot 10^2$	$2.1 \cdot 10^2$



properties thus they contribute to decomposition of the cellulose contained in sawdust. Yet, the microscopic fungi, especially *Trichoderma*, *Penicillium*, *Aspergillus*, *Fusarium*, etc., have greater cellulolytic capability (POSZYTEK 2016). So, their metabolic activity may become a reason of loss of lignocellulosic components contained in sawdust, and thus they weaken the composite structure.

The V notch impact strength changed from 12.5 kJ/m<sup>2</sup> in the initial phase to 6.7 kJ/m<sup>2</sup> after twelve months of exploitation, so by almost 54%. The rate of changes of V notch impact strength values depends on the rate of multiplication of microorganisms connected with weather conditions (according to the season of a year). Therefore, it is deliberate to apply additional means to avoid microbial growth in that sort of the composite materials.

## References

- BARTON J. 2014. *Polymer composites, biocomposites and nanocomposites. Obtaining, composition, properties and fields of application*. Chemik, 68(4): 280-287.
- GARBARCZYK J., PAUKSZTA D., BORYSIK S. 2009. *Thermoplastic polymer composites with lignocellulosic materials*. Mechanics, 106(1-M): 93-97.
- KOSZKUL J. 1999. *Polymer Materials*. Wydawnictwo Politechniki Częstochowskiej, Częstochowa.
- MAŃKA M. 2011. *Forest Trees Diseases*. Powszechne Wydawnictwo Rolnicze i Leśne, Warszawa.
- MIEDZIANOWSKA J., MASŁOWSKI M., STRZELEC K. 2018. *The natural fiber reinforced polymer composites - factors affecting the mechanical performance*. Technologia i Jakość Wytrobów, 63: 45-54.
- POSTAWA P., STACHOWIAK T., SZAREK A. 2010. *Research of properties of wood-polymer composite using DMTA method*. Kompozyty, 10(3): 266-269.
- POSZYTEK K. 2016. *Microbial cellulose utilization*. Postępy Mikrobiologii, 55(2): 132-146.



## PUBLIC OPINION POLL ON THE PARKING SYSTEM IN PIŁA AND THE POSSIBILITY OF INTRODUCING THE SMART PARKING SYSTEM IN PIŁA

*Piotr Gorzelanczyk<sup>1</sup>, Tymoteusz Wieczorek<sup>2</sup>*

<sup>1</sup>ORCID: 0000-0001-9662-400X

<sup>2</sup>ORCID: 0000-0002-4195-4893

Stanisław Staszic University of Applied Sciences in Piła

Received 06 February 2021, accepted 28 April 2021, available online 29 April 2021.

**Key words:** parking, Piła, smart parking, intelligent parking.

### Abstract

The aim of the article is to find out about the public opinion of the inhabitants of the city of Piła about the functioning of the parking system, in which residents have problems finding a parking space. The most important issues in this field were reviewed. On the basis of the survey, car parks were designated, where it was proposed to modify the existing parking system by introducing intelligent parking systems. The results of the research, after analysis and summary of observations in the form of conclusions, are presented in the table and in the form of graphs.

### Introduction

The technological development of the world causes the development of the automotive industry to a large extent. This is related to the constantly growing number of vehicles traveling on roads, which has more than doubled over the last 17 years (Fig. 1), and the number of parking spaces is not growing at such a pace. The problem of finding a parking space in urban areas has always been a problem for drivers living in developed countries.

---

Correspondence: Piotr Gorzelanczyk, Państwowa Uczelnia Stanisława Staszica w Piile, ul. Podchorążych 10, 64-920 Piła, e-mail: [piotr.gorzelanczyk@puss.pila.pl](mailto:piotr.gorzelanczyk@puss.pila.pl)

For years, solutions have been sought to ensure the largest possible number of parking spaces while using the minimum area of land, especially in large urban agglomerations, where there is no more space for additional parking spaces. A growing number of vehicles that go literally wherever possible. We can find cars not only on highways and streets, but also on well-worn roads and paths. Such a number of vehicles necessitates the creation and provision of a safe place to stop the vehicle. One of the main problems is that parking is possible not only in typical car parks, but also in non-urbanized areas.

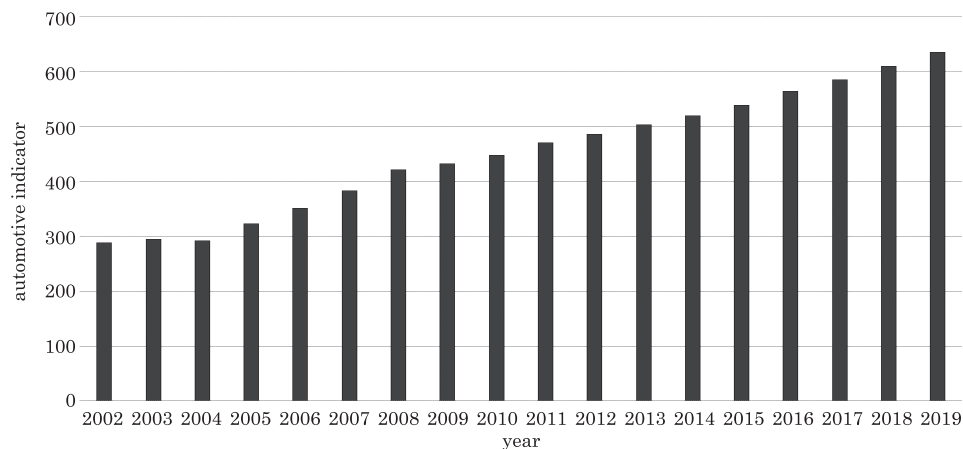


Fig. 1. Automotive index in 2002 ÷ 2019

Source: based on Statystyki CEPIK (2019), GORZELANCZYK (2020), Eurostat (2020).

Finding a parking space, especially in large urban agglomerations, is a time-consuming process. Some of the negative effects of the parking space search process include, for example, unplanned costs, harmful social interactions, and decreased employee productivity. An important factor is also the fact that many vehicles with “larger dimensions” cannot fit in most parking spaces.

In order to determine the dimensions of parking spaces for individual types of vehicles, the announcement of the Minister of Investment and Development of April 8, 2019 on the publication of the consolidated text of the ordinance of the Minister of Infrastructure on technical conditions to be met by buildings and their location (Obwieszczenie Ministra Inwestycji i Rozwoju z 8 kwietnia... 2019). The British Parking Association (BPA) (BPA 2020) analyzed the time spent by drivers looking for a free parking space. The BPA study also presents the driver’s feelings when looking for a parking space, as well as the criteria used by drivers looking for a parking space. Research shows that the average British driver spends almost 4 days (91 hours) a year finding a free parking space. In the United States, the situation is different. The average time it takes to find a parking space is 17 hours per year.

The research conducted by IRNIX was similar. The study analyzed not only the time needed to find a free parking space, but also the related costs. Two types of incurred costs were included in the analysis. Costs to drivers for wasting extra fuel looking for a parking space and overheads that take into account not only fuel costs but also factors such as environmental impact and driver time. According to an INRIX study (MCCOY 2020), searching for a free parking space costs \$ 345 per year per driver.

Based on the report of the European Automobile Manufacturers Association (ACEA), it can be concluded that 66.2% of households declared that they owned at least one car (OKUROWSKI 2020).

The report of the European Statistical Office (Eurostat 2020) was used to check the degree of motorization not only in Poland, but also in all European Union countries. The report shows that Poland is one of the most motorized countries in the European Union, next to such countries as: Liechtenstein, Luxembourg, Italy, Cyprus and Finland.

Many authors have addressed the subject of the limited number of parking spaces resulting in congestion, air pollution and frustration for drivers. The article (GONGJUN et al. 2008) presents how the time needed to find a parking space has changed before and after the introduction of an intelligent parking system and how this system influenced the use of the parking lot.

Intelligent parking is a system based on a special infrastructure that allows the driver to quickly and accurately locate a free parking space. This system allows for comprehensive management of parking lots and provides users with information about the availability of parking spaces in given parts of the city and within its territory. In a specially prepared application, users can check whether there is a free parking space at the airport, cinema or other popular city venues. There are two main factors in the intelligent parking system: a transport infrastructure using smart cameras, sensors and algorithms. systems and applications for mobile devices. The image from cameras installed in strategic places from the point of view of communication is analyzed using algorithms and sent to a database connected to a free mobile application. The application will not only indicate the free space, but also suggest which one is best for a specific vehicle, taking into account the free space and dimensions of the vehicle. Additionally, this system allows to increase the safety of parking lots by constant monitoring of the parking space (KIRCI et al. 2018).

Smart Parking is part of Intelligent Transportation Systems (ISP). This gives the opportunity to develop newer and newer parking improvements. This system not only controls the processes taking place in the car park, but also takes into account other aspects related to parking facilities (KIRCI et al. 2018). ISP includes several systems, the most popular are such systems as: expert and agent systems, system based on fuzzy logic, systems based on wireless sensors, systems based on GPS navigation, road communication systems and systems based on vision

The intelligent parking system should enable the driver to book the selected parking space and facilitate movement around it. The continuous “entry/exit” system is designed to automatically scan all vehicles entering and exiting the parking lot. These systems not only increase the protection of our car through its constant monitoring, but also allow for additional activities related to the parking process, such as, for example, the purchase of a parking ticket. The full automation of these systems means that the driver does not waste time looking for a parking space and does not care where he should pay for parking. As these systems monitor the traffic in the car park, this leads to a reduction in congestion and an overall improvement in road traffic (SZMIDT 2017). The benefits of implementing an intelligent system are described in (MUFAQIH et al. 2020).

The issues related to the systems used in intelligent parking systems are also described in the article (FAHEEM et al. 2013) which describes in detail: expert systems, systems based on fuzzy logic, wireless systems, road communication systems and vision systems.

The topic of using intelligent parking systems based on the use of intelligent real-time cameras was discussed in (ALAM et al. 2018). The work describes the principle of operation and construction of a system based on the use of intelligent cameras, examples of system applications and the correct arrangement of the entire infrastructure included in the system. The topic of intelligent parking lots was also included in (STANCZYK, PYREK 2013, SKRZYNIOWSKI et al. 2018, PARKITNY 2010).

Intelligent parking solutions have been implemented in Gdańsk, where parking spaces located on the streets in the city center are monitored, and the steering wheel in the application can check where there is a free parking space. Similar solutions exist in Warsaw, Gliwice and many other Polish cities.

## Materials and Methods

The main goal of the work is to find out the opinion of the inhabitants of the city of Piła on the functioning of the parking system, where residents have problems with finding a parking space. The study conducted a survey aimed at finding out the opinions of residents and people coming to the city of Piła about the transport infrastructure related to parking lots in Piła, and the city does not plan to improve the parking situation in the city of the future and there are currently no intelligent parking solutions in the city.

The first step in the study was to use a pilot study. The interviewers were assigned 10 questionnaires, the purpose of which was to express an opinion on the method of implementation and its clear image. Based on the conclusions reached through this procedure, the final version of the questionnaire was prepared. The next step in conducting the survey was to encourage the survey participants

to complete the final version of the survey in electronic form. The drivers survey asked, inter alia, o: the purpose of the trip, the time needed to find a parking space, whether they had previously encountered the Smart Parking concept and many other questions related to public transport. infrastructure. The research was conducted in the form of a questionnaire from March 2020 to the end of May 2020. The research involved randomly selected 286 people. The study was conducted on various social groups in order to thoroughly learn the opinions of the city's inhabitants.

The next step was to calculate the sample selection.

1. From a practical point of view, the maximum error is  $\delta = 2\%$ , based on surveys conducted within the city of Pila in most of them the maximum error was estimated  $\delta = 10\%$ .

2. The significance level assessed in most studies is 90%.

3. The standard variation of the population in Pila is 52% female and 48% male.

Then the sample was calculated using the following formula:

$$n = \frac{Z^2 \cdot p(1-p)}{\delta^2},$$

where:

$n$  – sample size number,

$Z$  – significance level dependent coefficient, 90% – 1.65,

$p$  – proportion in the population, (52% – 0.52, 48% – 0.48),

$\delta$  – estimation error, 5% – 0.05.

$$n = \frac{1.64^2 \cdot 0.52(1-0.52)}{0.05^2} = \frac{2.69 \cdot (0.52 \cdot 0.48)}{0.0025} = 268.57.$$

The minimum sample size took a value of approximately 269, but the number of people during the study increased to 286 people.

## Results

The highest percentage of respondents (39%) came from the age group of 18 to 25 years old, which is due to the fact that people in this age group have driving licenses and are active on the Internet. People in this age group are mostly students, who don't have many obligations and can afford to "waste" more time than other age groups. In the 26-50 age group the number of people taking part in the survey is 40%. The smallest percentage of respondents 21% are people over 50 years old.

Regarding their place of living 40% of the respondents stated that they live in the city of Pila, and a small number of people 13% live in areas between

5 and 10 km from the city center. A significant part of respondents (38%) live in places located more than 20 km from the city center (Fig. 2). Respondents mostly live in urban area (53%) and 47% live in rural areas. A vast majority of 73% of respondents states that they are the driver of the vehicle while driving. Only 27% of the respondents identify themselves as a passenger.

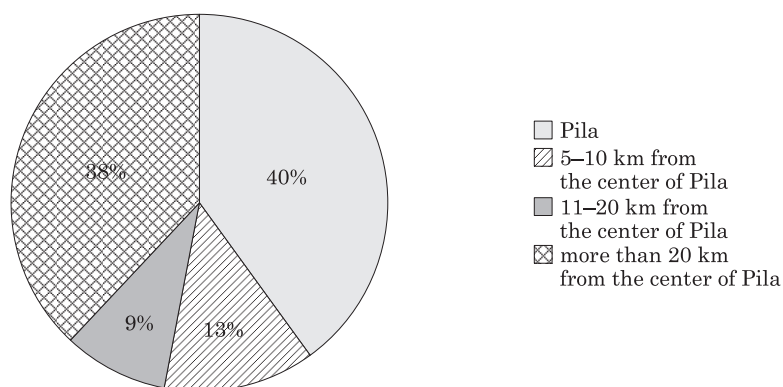


Fig. 2. Place of residence  
Source: own study.

Most of the respondents (over 50%) come to the city for education or work. 13% of respondents say they come to the city for shopping, 7% for a visit and only 3% of them choose the city as a leisure time destination (Fig. 3). Among other purposes of their visit, respondents most often cited visiting a specialist doctor or getting tests done in city health facilities as the reason.

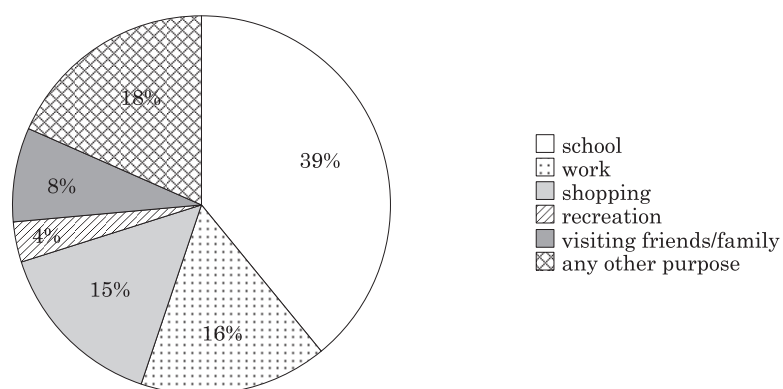


Fig. 3. Destination  
Source: own study.



The vast majority of respondents (61%) consider the city's transportation infrastructure to be at a good or very good level. Such a high result could be influenced mainly by renovations carried out over the years. 20% of respondents think that the city's infrastructure is at a neutral level, and only 15% see it as negative. 4% of respondents could not express their opinion on that (Fig. 4).

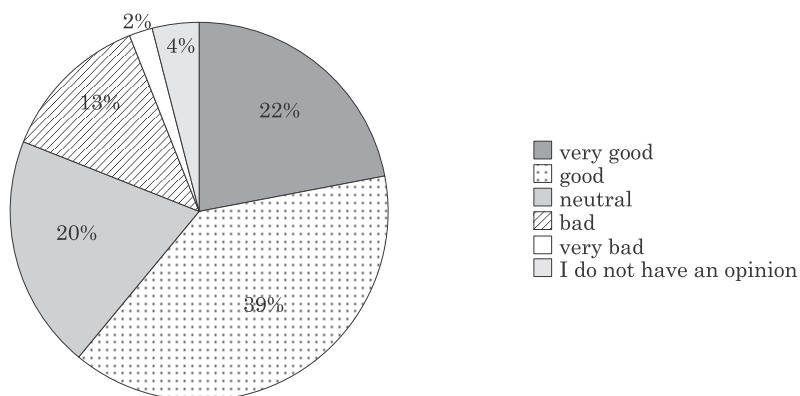


Fig. 4. Assessment of the city's transport infrastructure  
Source: own study.

38% of respondents state that the location of Pila's parking lots in relation to the places they visit is good, and 12% believe that parking availability is very good. 27% of respondents have a neutral approach to the subject. 16% of respondents think that the location of Pila's parking lots is bad and 7% think that the location is very bad (Fig. 5).

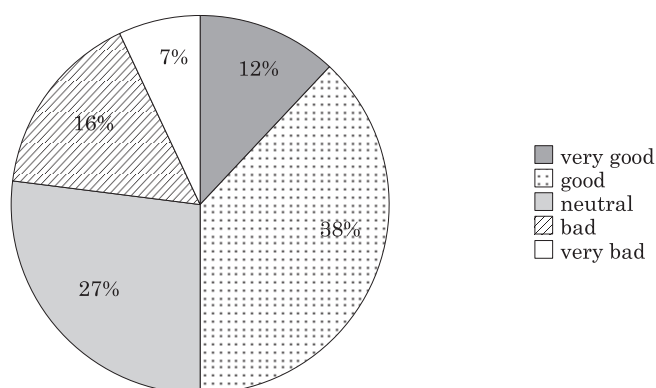


Fig. 5. Availability of parking in relation to places visited  
Source: own study.

The time spent finding an available parking space varies widely. This is most likely due to the different destinations and personal feelings of the respondents. Nevertheless, 44% of respondents find a parking space within a time range of up to 3 minutes. 24% of respondents need 4 to 6 minutes to find a free parking space and 32% of respondents spend 7 to even more than 10 minutes (Fig. 6). 64% of respondents admit that they have not encountered the concept of smart parking before. This may be due to the fact that the concept is relatively new and the technologies used in Smart City are rare. 36% of respondents state that they have encountered the concept before. The vast majority of 63% of respondents think that the introduction of smart parking is a good solution. 26% of respondents say they are indifferent to the idea and 11% are against it.

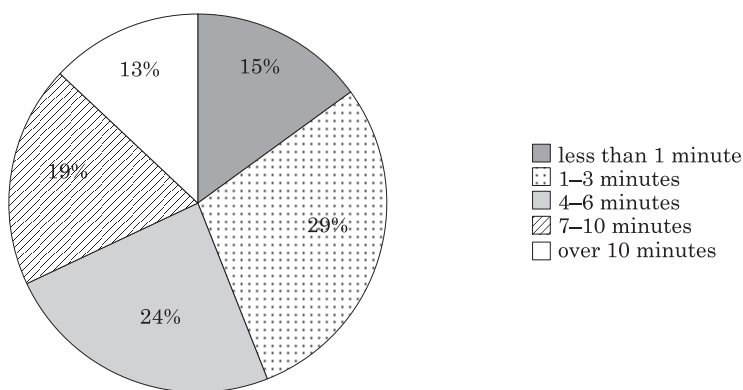


Fig. 6. The time it takes to find a free parking space  
Source: own study.

The vast majority of respondents state that they would use smart parking systems often 40% or very often 18%. 17% of respondents think they would use this solution from time to time, 11% of respondents think they would rather never use this solution and 5% of them declare they are not interested in such solution. 9% of respondents did not express their opinion (Fig. 7).

A significant number of respondents, as many as 37%, said that a smart parking system should appear at the Vivo shopping mall. 15% of respondents were in favor of Chestnut Gallery, 12% thought that a good place for a parking system would be a parking lot by the market square, and only 9% believe that the ideal place to introduce intelligent solutions is the Signify parking lot. A large number of respondents (27%) would choose other locations for such solutions (Fig. 8). The most frequent answers were: city center, Pila City Hall, Stanisław Staszic Specialist Hospital, Biedronka supermarkets and railway station.

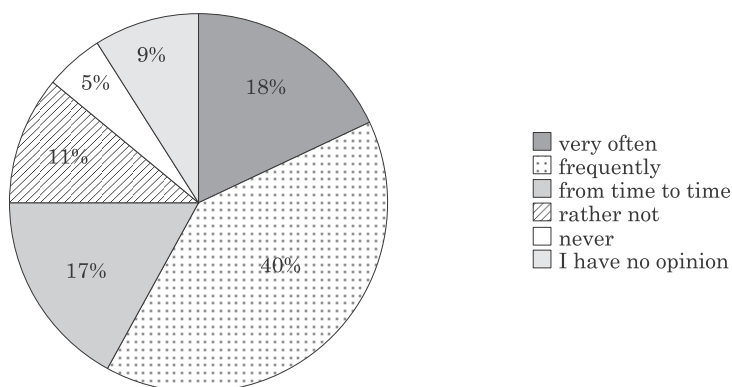


Fig. 7. How often would you use a smart parking system?  
Source: own study.

A significant number of respondents, as many as 37%, said that an intelligent parking system should appear by the Vivo shopping mall. 15% of respondents supported a parking lot next to a hospital, 12% said that a good place for a parking system would be a parking lot next to a pedestrian zone, and only 9% said that the ideal place for intelligent parking solutions is a parking lot next to a railway station. A large number of respondents (27%) would choose other places for such solutions (Fig. 8). Among respondents' answers there were: city center, Pila City Hall, Biedronka supermarkets and Galeria Kasztanowa.

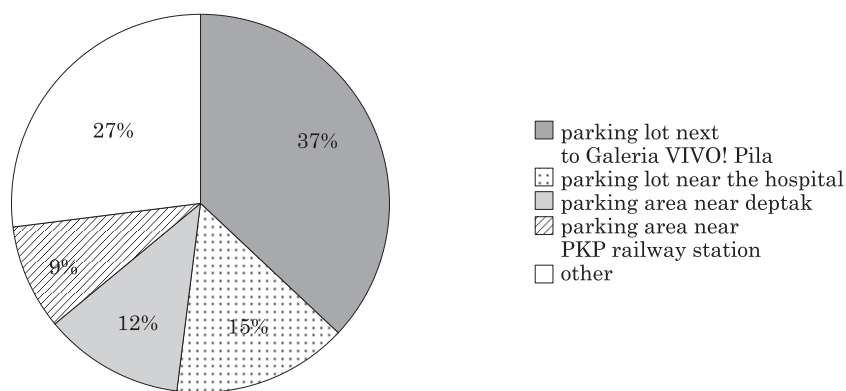


Fig. 8. Where do you propose to introduce Smart Parking  
Source: own study.

Almost all respondents, up to 98%, confirmed the use of payments with mobile devices such as smartphone and smartwatch. Only 2% of respondents said they do not use this form of payment. Poland is one of the leaders in mobile

payments in Europe, according to Visa Digital Payments research (PARKITNY 2010) as many as 86% of Poles expect to use mobile payments by the end of 2020.

For the last additional, open-ended question “How do you feel about the introduction of smart systems related to city management?” a significant number of respondents unanimously agreed that the introduction of smart systems to improve city management is needed and required. The respondents were unanimous in their willingness to support and use all the facilities provided to them by the smart systems in the Smart City project. A large number of respondents also pointed out that the urban environment should not have a significant impact on the natural environment, and the implemented solutions should be pro-ecological.

Based on the author's observations, confirmed by respondents' surveys (Fig. 8), places were selected where residents have a problem with finding a parking space:

- Parking lot next to Galeria VIVO! Pila;
- Parking lot near the Stanislaw Staszic Specialist Hospital;
- Parking area near Deptak (Pila Pedestrian Street);
- Parking area at the PKP railway station.

The technical data of the above-mentioned facilities are presented in Table 1.

Table 1

Technical data of selected car parks in the city of Pila

Car park parameter / Name of the car park	Parking lot next to Galeria VIVO! Pila	Parking lot near the Stanislaw Staszic Specialist Hospital	Parking area near Deptak (Pila Pedestrian Street)	Parking area at the PKP railway station
Total parking lot surface area	18,850 m <sup>2</sup>	7,250 m <sup>2</sup>	5,100 m <sup>2</sup>	1,600 m <sup>2</sup>
Total number of parking spaces	480	230	144	54
Number of parking spaces designated for passenger cars	434	224	134	50
Number of parking spaces designated for people with disabilities	20	10	10	4
Number of parking spaces designated for mothers with children	16	1	0	0

Source: own study.

In the analyzed car parks, the number of parked vehicles was examined during rush hours, and then the arithmetic mean was drawn. The research in all car parks was carried out from Monday to Friday from 5:00 p.m. to 7:00 p.m. and on weekends from 11:00 a.m. to 1:00 p.m. and from 3:00 p.m. to 6:00 p.m. in the period May – June 2020. The relevant data is presented in the Table 2.

Table 2  
Parkings lot utilization analysis

Car park parameter / Name of the car park	Parking lot next to Galeria VIVO! Pila	Parking lot near the Stanislaw Staszic Specialist Hospital	Parking area near Deptak (Pila Pedestrian Street)	Parking area at the PKP railway station
Occupancy rate of parking lot	$W_{orp} = \frac{363}{480} = 0.76$	$W_{orp} = \frac{149}{230} = 0.64$	$W_{orp} = \frac{102}{144} = 0.71$	$W_{orp} = \frac{38}{54} = 0.7$
Parking occupancy rate during peak hours	$W_{po} = \frac{417}{480} = 0.86$	$W_{po} = \frac{172}{230} = 0.74$	$W_{po} = \frac{129}{144} = 0.89$	$W_{powp} = \frac{47}{54} = 0.87$
Percentage of vehicles parked illegally	$P_{pvp} = \frac{39}{480} \cdot 100 = 8.1\%$	$P_{pvp} = \frac{9}{230} \cdot 100 = 3.9\%$	$P_{pvp} = \frac{39}{144} \cdot 100 = 27\%$	$P_{pvp} = \frac{6}{54} \cdot 100 = 11\%$

Source: own study.

Based on the layout of the first of the analyzed car parks, the car park at Vivo, it is proposed to install a system based on intelligent cameras. The solution with cameras is expensive, but taking into account the number of parking spaces, this solution seems to be a better solution than the use of individual sensors responsible for each individual parking space. An alternative solution that could be used to improve the functioning of the car park is the construction of a multi-storey car park.

The structure of the hospital car park resembles a square. The square structure of the car park suggests that the optimal way to improve the functioning of the car park would be to install a smart camera system. This system would not only have a navigation and protective function, but would also inform drivers about which zones the car park is divided into. The use of the intelligent camera system would allow assigning an individual number to each vehicle entering the hospital parking lot. Not only would this automate the ticket collection process, it would also automatically cause hospital patients to be charged.

Another of the discussed car parks are the Promenada car parks. This is a place frequented by many people. There are not only many shops and eateries here, but it is also the perfect place to spend time together with family or friends. Such a large number of frequently used facilities means that the number of people and vehicles in this area is large, and the number of parking spaces is limited. The key factor in finding a free parking space is that there is no single large parking lot in the area that can accommodate all vehicles. A large number of small parking lots and the presence of the main Piła roads in this area only increase the problems related to the effective flow of vehicles, which results in the formation of traffic jams in the city center.

The introduction of a system based on Smart Parking technologies would significantly relieve drivers, but would also have a positive impact on traffic in the city. As this area is characterized by a large number of small parking lots and high vehicle rotation in parking lots, the ideal solution would be to install an intelligent parking system based on the use of parking sensors connected to the application. The simple concept of the sensor operation makes it the most optimal solution. Each individual parking space is equipped with a sensor that is able to show us the current state of the parking space in real time.

The last of the considered car parks is the train station car park with a limited number of parking spaces. The solution to the problem of a small number of parking spaces seems to be the automatic modular car park (Car Towers). Car towers are ideal where a large number of parking spaces are required and parking is small. The car park is fully automated and does not need to be operated by any employee. The only person who takes an active part in using the car park is the driver of the vehicle.

## Conclusion

The article uses a questionnaire to conduct a public opinion poll on the parking system in Piła and the possibility of introducing the Smart Parking system in Piła. The research clearly shows that people take an active part in the life of the city and support the introduction of intelligent solutions. A large part of the respondents expressed their willingness to use modern technological solutions and stated that the systems that are elements of Smart City are the basis for a more comfortable life not only in large urban agglomerations.

In the comments provided in the survey, respondents indicated that the city is often impassable during rush hours and that the streets are often congested. Intelligent parking systems would enable some drivers to find a free parking space more efficiently, which would significantly reduce the number of vehicles in traffic.

The article also presents proposals for the implementation of the project of intelligent parking lots in the city of Piła and other modern parking solutions based on a study conducted on the inhabitants of Piła and the surrounding area. Proposals for the implementation of the project of intelligent parking lots in the city of Piła and other modern parking solutions based on a study conducted on the inhabitants of Piła and the surrounding area were also described. After talking to the city authorities, there is a chance to introduce the described solutions in the analyzed city.

## References

- ALAM M., MORONI D., PIERI G., TAMPUCCI M., GOMES M., FONSECA J., FERREIRA J., LEONE G.R. 2018. *Real-Time Smart Parking Systems Integration in Distributed ITS for Smart Cities*, Journal of Advanced Transportation, 2018, article ID 1485652. <https://doi.org/10.1155/2018/1485652>.
- BPA – British Parking Association. <https://www.britishparking.co.uk/News/motorists-spend-nearly-four-days-a-year-looking-for-a-parking-space> (access: 28.04.2020).
- Eurostat. [https://ec.europa.eu/eurostat/statistics-explained/index.php?title=File:Figure\\_2\\_Number\\_of\\_passenger\\_cars\\_per\\_thousand\\_ininhabitan\\_2018.png](https://ec.europa.eu/eurostat/statistics-explained/index.php?title=File:Figure_2_Number_of_passenger_cars_per_thousand_ininhabitan_2018.png) (access: 28.04.2020).
- FAHEEM Z., MAHMUD S.A., KHAN G.M., RAHMAN M., ZAFAR H. 2013. *A Survey of Intelligent Car Parking System*. Journal of Applied Research and Technology, 11(5): 714-726.
- GONGJUN Y., STEPHAN O., WEIGLE M.C., ABUELELA M. 2008. *SmartParking: A Secure of Intelligent Parking System Using NOTICE*. 11<sup>th</sup> International IEEE Conference on Intelligent Transportation Systems. DOI: 10.1109/ITSC.2008.4732702.
- GORZELANCZYK P. 2020. *Influence of selected aspects of the technical condition of means of transport operating in Greater Poland on road safety*. Technical Sciences, 23(3), 233–252. <https://doi.org/10.31648/ts.5935>.
- KIRCI P., SAGLAMAZ S., SENER M. 2018. *An intelligent vehicle detection management model for parking spaces*. Scientific Journal of Silesian University of Technology. Series Transport, 98: 35-43. Doi: <https://doi.org/10.20858/sjsutst.2018.98.4>.

- MCCOY K. 2020. *Drivers spend an average of 17 hours a year searching for parking spots*. USA Today Money. <https://eu.usatoday.com/story/money/2017/07/12/parking-pain-causes-financial-and-personal-strain/467637001/> (access: 28.04.2020).
- MUFAQIH M.S., KABURUAN E.R., WANG G. 2020. *Applying smart parking system with internet of things (IoT) design*. IOP Conference Series Materials Science and Engineering 725:012095. DOI:10.1088/1757-899X/725/1/012095.
- Obwieszczenie Ministra Inwestycji i Rozwoju z 8 kwietnia 2019 r. w sprawie ogłoszenia jednolitego tekstu rozporządzenia Ministra Infrastruktury w sprawie warunków technicznych, jakim powinny odpowiadać budynki i ich usytuowanie. Dz.U. z 2019 r., poz. 1065.
- OKUROWSKI T. 2020. *Poland compared to Europe in the number of owned cars*. Auto Świat. <https://www.auto-swiat.pl/wiadomosci/aktualnosc/polska-na-tle-europy-czyli-ile-mamy-samochodow/kf625hz> (access: 15.12.2020).
- PARKITNY W. 2010. *Logistyczne wskaniki parkingowe*. Przegląd Komunikacyjny, 11-12: 18-21. [http://www.transportation.overview.pwr.edu.pl/UPLOAD/BAZA-ARTYKULOW/PL/2010/11/A\\_PL\\_10\\_11\\_02.pdf](http://www.transportation.overview.pwr.edu.pl/UPLOAD/BAZA-ARTYKULOW/PL/2010/11/A_PL_10_11_02.pdf) (access: 26.07.2020).
- SKRZYŃOWSKI A., MRUK A., SKRZYŃOWSKA D. 2018. *Rotary Smart Car Parking System*. Technical Journal, 3.
- STAŃCZYK P., PYREK P. 2013. *Rotary car parks as an opportunity for crowded cities*. Scientific and Technical Journals of SITK RP, Branch in Krakow, p. 269-275.
- Statystyki CEPiK. Centralna Ewidencja Pojazdów i Kierowców. <http://www.cepik.gov.pl/statystyki> (access: 1.05.2019).
- SZMIDT E. 2017. *Overview of Types of Intelligent Parking Systems*. Motor Transport Institute. Road Transport, 4.



## BATTERY SUPERCHARGING SYSTEM IN ELECTRICAL VEHICLES USING PHOTOVOLTAIC PANELS

*Zenon Syroka*

ORCID: 0000-0003-3318-8495  
Technical Science Department  
University of Warmia & Mazury

Received 13 December 2020, accepted 19 May 2021, available online 30 May 2021.

**Key words:** digital control, motor controller, electric and hybrid vehicles, microcontroller.

### Abstract

In this project, a system was designed there was designed a system for charging batteries in electric vehicles using photovoltaic panels. Low cost of operation, cheap reliable construction and simple user interface were among the main criterias taken into account.

Each energy source was carefully selected and, modules were used so that they could in the way to power the microcontroller and charge the energy storage source.

This article is a part of a project related to the design of digital control devices with electric drives carried out at the UWM.

### Introduction

The solution was patented (SYROKA, JAKOCIUK 2020).

The core of this publication is to show elementary ideas of battery charging module with usage of PV panels in electric vehicles, patented by author. This kind of drive will become a primary type in nearest future.

Main goal in this work was to show block and idea scheme of module and to present its steering code. Symbols on electrical schemes were result of type of used design tools.

---

Correspondence: Zenon Syroka, Katedra Elektrotechniki, Energetyki, Elektroniki i Automatyki, Wydział Nauk Technicznych, Uniwersytet Warmińsko-Mazurski, ul. Oczapowskiego 11, 10-719 Olsztyn, e-mail: [zenon.syroka@uwm.edu.pl](mailto:zenon.syroka@uwm.edu.pl), [syrokaz@onet.eu](mailto:syrokaz@onet.eu).

The control system solutions developed at UWM have been published in the book (SYROKA 2019).

Presented bibliography is according to author, the core set of position treating about electric vehicles steering.

## Block scheme specification of battery charging

The photovoltaic supercharging system is simple, easy to use and cheap cost effective. It is also very efficient. Figure 1 shows a block diagram of the system for supercharging batteries in electric vehicles using photovoltaic panels. The system is switched on or off with buttons in manual mode. The system can be only switched on and off manually. When vehicle is switched off, the system draws power from external battery and, thanks to the photovoltaic panels, it can operate when the vehicle is not moving. The device can be reset by pressing the button which returns the microcontroller to its factory stock condition. The system uses an ATMEGA 328 PU microcontroller.

There are five modules in the system responsible for correct energy storage and control:

- control module 2;
- voltage measurement module (photovoltaic panels) 3;
- energy storage module (photovoltaic panels) 4;
- energy storage module (alternator) 5;
- voltage measuring module (alternator) 6.

The advantages includes:

- resistance to interference;
- small size of the control system which does not interfere with design of the vehicle;
- low cost and easy operation;
- support for two energy sources (battery and photovoltaic panels);
- clear interface.

In Figure 1, battery 1 of an in electric vehicle is connected to the control system 2 and voltage measurement module 3 of the photovoltaic panels. Control system 2 is connected to control module 4 collecting energy from photovoltaic panels, the control module 5 collecting energy from the alternator, control module 6 measuring alternator voltage, and control module 7 adjusting output signals from the microcontroller, which is connected on one side to LCD 8 screen, and on the other side is connected via microcontroller 9, system 10 adjusting the input signals, the control system 11 with module 6 for measuring voltage from the alternator and module 3 measuring the voltage of the photovoltaic panel.

System 2 controls the system for supercharging batteries of an electric vehicle. System 2 analyses signals from module 4 collecting energy from photovoltaic



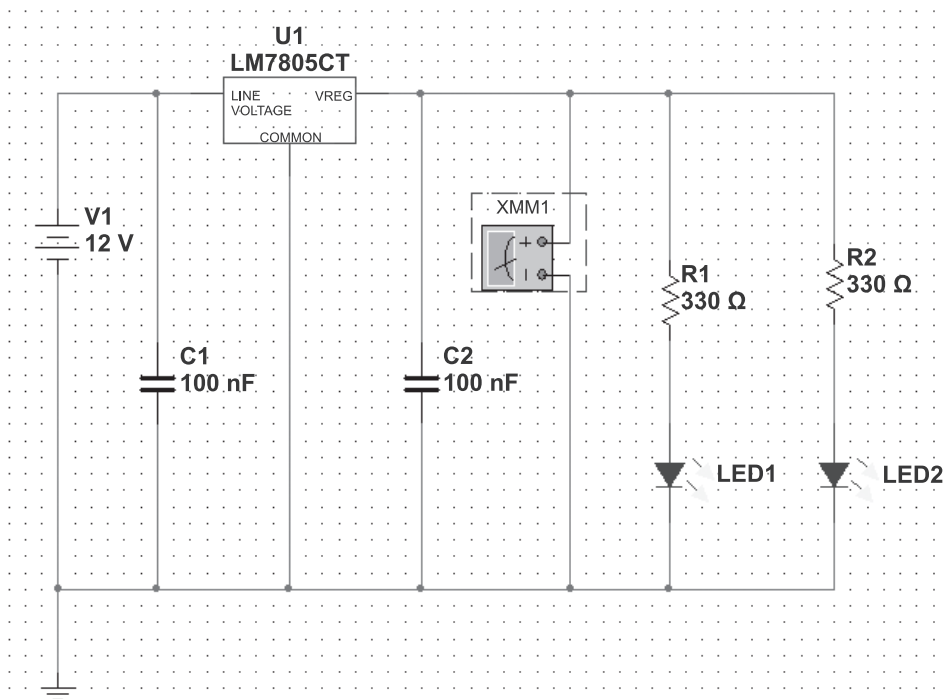


Fig. 2. System lowering and stabilizing voltage

## Control system

A block diagram of the system for charging batteries in electric vehicles using photovoltaic panels is presented in Figure 3 (BUSO, MATTAVELLI 2006, GREGORY 2006, MOUDGALYA 2007).

The control system consists of:

- a power supply system;
- 5 V relays with coil;
- SW buttons;
- LCD with I2 C converter;
- signalling LEDs with 330  $\Omega$  resistors;
- bypasses consisting of four 100 k $\Omega$  resistors;
- 16 MHz quartz oscillator;
- ATMEGA328P-PU system.

The system starts after the first voltage application. The system is then in the zero (neutral) state and a message is displayed (S1-enable supercharging, S2-disable supercharging).

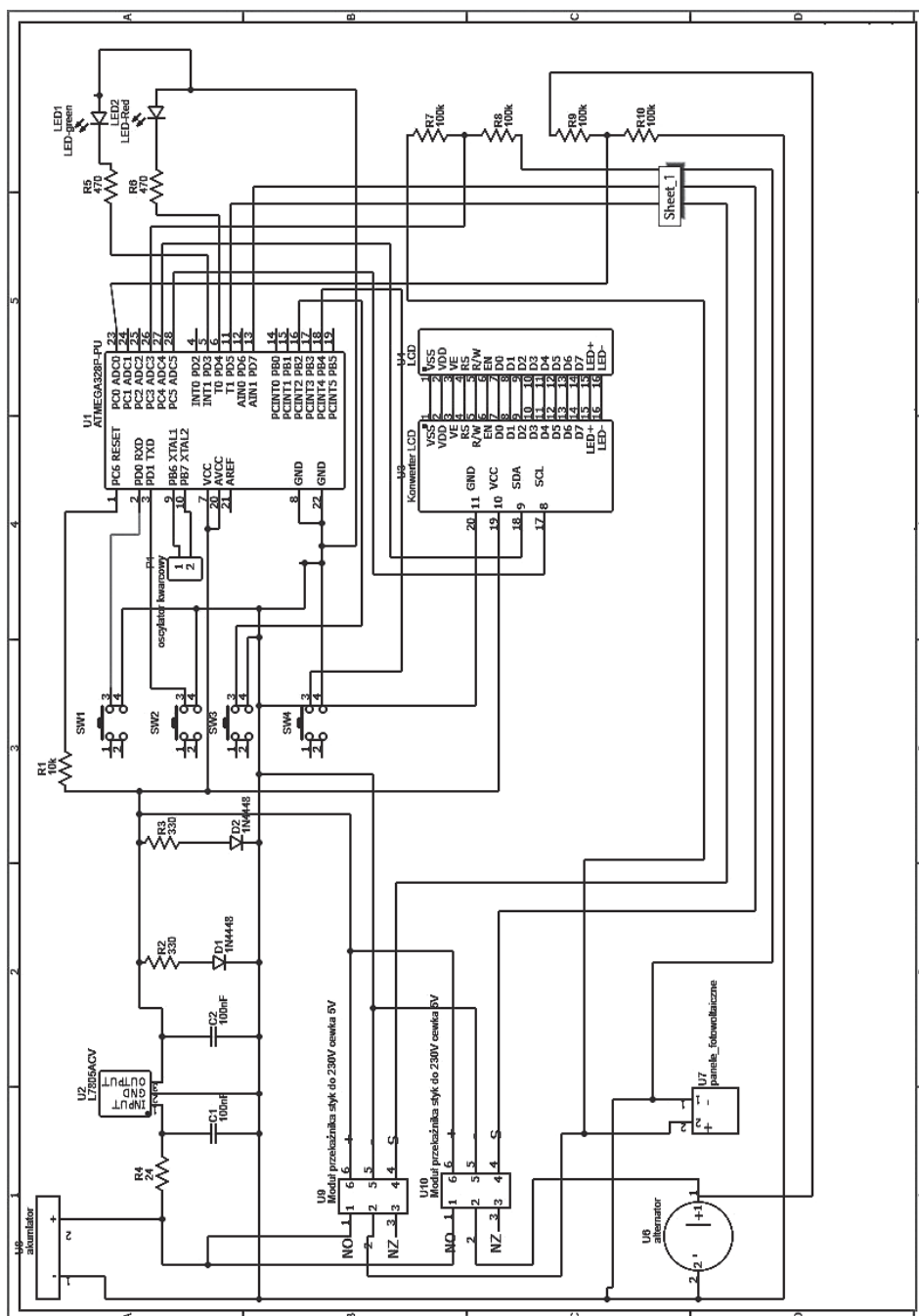


Fig. 3. Diagram of the control system for charging batteries in electric vehicles using photovoltaic panels

At this point, the user can perform four operations:

1. When the SW1 button is pressed, charging is activated (relay U9 and U10 are in high state), a message on the LCD is displayed (Charging on) and the green LED lights up.

2. When the SW2 button is pressed, charging is switched off (relay U9 and U10 are in the low state), a message on the LCD is displayed (Charging off), and the red LED lights up.

3. When the SW3 button is pressed, the voltage generated by the generators is measured, the information about the voltage is displayed on the LCD (Voltage= [measured voltage] V).

4. When the SW4 button is pressed, the voltage generated by the photovoltaic panels is measured, the information about the voltage is displayed on the LCD (Voltage= [measured voltage] V).

All of these operations can be performed at any time.

## **Control programme**

The programme is constantly being improved. One of the control program versions is shown in Figures 4-7.

```
#include <Wire.h>
#include <LiquidCrystal_I2C.h>
LiquidCrystal_I2C lcd(0x27, 16, 2);
void setup() {
  pinMode(3, OUTPUT);
  pinMode(4, OUTPUT);
  pinMode(5, OUTPUT);
  pinMode(7, OUTPUT);
  pinMode(10, OUTPUT);
  digitalWrite(10, HIGH);

  digitalWrite(7, LOW); //przełącznik prądnica
  digitalWrite(0, HIGH); //przycisk włączenie
  digitalWrite(1, HIGH); //przycisk wyłączenie
  digitalWrite(12, HIGH); // przycisk woltomierz na panelach
  digitalWrite(3, LOW); //lampka zielona
  digitalWrite(4, LOW); //lampka czerwona
  digitalWrite(5, LOW); //przełącznik panele fotowoltaiczne
  lcd.begin(16, 2);
  lcd.backlight();
  lcd.init();
  lcd.clear();
  lcd.setCursor(0, 0);
  lcd.print("S1=włącz doladowania");
  lcd.setCursor(0, 1);
  lcd.print("S2=wylłącz doladowania");

  for (int positionCounter = 0; positionCounter < 60; positionCounter++) {
    // scroll one position right:
    lcd.scrollDisplayRight();
    if (digitalRead(0) == LOW) {
      break;
    }
    if (digitalRead(1) == LOW) {
      break;
    }
    delay(150);

    for (int positionCounter = 0; positionCounter < 13; positionCounter++) {
      // scroll one position left:
      lcd.scrollDisplayLeft();
      if (digitalRead(0) == LOW) {
        break;
      }
      if (digitalRead(1) == LOW) {
        break;
      }
    }
  }
}
```

Fig. 4. Control programme code, part 1

```
        delay(400);

    }

}

}

void loop() {

    if (digitalRead(0) == LOW) {        // Włączenie układu doładowania
        digitalWrite(3, HIGH);
        digitalWrite(4, LOW);
        digitalWrite(5, HIGH);
        digitalWrite(7, HIGH);
        lcd.clear();
        lcd.setCursor(0, 0);
        lcd.print("Ładowanie włączone") ;

        for (int positionCounter = 0; positionCounter < 60; positionCounter++) {
            // scroll one position right:
            lcd.scrollDisplayRight();
            if (digitalRead(1) == LOW) {
                break;
            }
            if (digitalRead(12) == LOW) {
                break;
            }
            if (digitalRead(10) == LOW) {
                break;
            }
        }
        // wait a bit:
        delay(150);

        for (int positionCounter = 0; positionCounter < 13; positionCounter++) {
            // scroll one position left:
            lcd.scrollDisplayLeft();
            if (digitalRead(1) == LOW) {
                break;
            }
            if (digitalRead(12) == LOW) {
                break;
            }
            if (digitalRead(10) == LOW) {
                break;
            }
        }
    }
}
```

Fig. 5. Control programme code, part 2



```
    delay(400);
  }
}

}

if (digitalRead(1) == LOW) {      //Wyłączenie układu doładowania
  digitalWrite(4, HIGH);
  digitalWrite(3, LOW);
  digitalWrite(5, LOW);
  digitalWrite(7, LOW);
  lcd.clear();
  lcd.setCursor(0, 0);
  lcd.print("Ładowanie wyłączone");

  for (int positionCounter = 0; positionCounter < 60; positionCounter++) {
    // scroll one position right:
    lcd.scrollDisplayRight();
    // wait a bit:
    if (digitalRead(12) == LOW) {
      break;
    }
    if (digitalRead(0) == LOW) {
      break;
    }
    if (digitalRead(10) == LOW) {
      break;
    }
    delay(150);
  }

  for (int positionCounter = 0; positionCounter < 13; positionCounter++) {
    // scroll one position left:
    lcd.scrollDisplayLeft();
    if (digitalRead(12) == LOW) {
      break;
    }
    if (digitalRead(0) == LOW) {
      break;
    }
    if (digitalRead(10) == LOW) {
      break;
    }
    delay(400);
  }
}
```

Fig. 6. Control programme code, part 3

```
    }  
  
}  
  
    if (digitalRead(12) == LOW) {  
        digitalWrite(3, LOW);  
        digitalWrite(4, LOW);  
        digitalWrite(5, LOW);  
        lcd.clear();  
        lcd.setCursor(0, 0);  
        lcd.print("Napiecie:");  
        lcd.setCursor(0, 1);  
        lcd.print("U=    V");  
        int sensorValue = analogRead(A0);  
        float voltage = sensorValue / (90);  
        lcd.setCursor(2, 1);  
        lcd.print(voltage);  
        delay(10) ;  
    }  
  
    if (digitalRead(10) == LOW) {  
        digitalWrite(3, LOW);  
        digitalWrite(4, LOW);  
        digitalWrite(7, HIGH);  
        lcd.clear();  
        lcd.setCursor(0, 0);  
        lcd.print("Napiecie:");  
        lcd.setCursor(0, 1);  
        lcd.print("U=    V");  
        int sensorValue = analogRead(A3);  
        float voltage = sensorValue / (86.5);  
        lcd.setCursor(2, 1);  
        lcd.print(voltage);  
        delay(10) ;  
    }  
}
```

Fig. 7. Control programme code, part 4

## Summary

Under ideal weather conditions, it was concluded that the alternator is more efficient and generates more energy. Moreover, it can continue generating power when the photovoltaic panels are unable to do so, for example, at night.

It should still be noted that the alternator generates power when a vehicle is moving, whereas photovoltaic panels can draw energy when the car is immobile. Therefore, two energy sources were chosen to complement each other.

An industrial prototype was constructed to enable testing and improve the structure from both an electronic and mechanical perspective. The mechanical structure of the device posed quite a challenge due to the climate conditions in the car.

The software is being continuously improved, one version of which was presented in chapter Control system. Work results were patented SYROKA, JAKOCIUK (2020).

## References

- ALI E., KHALIGH A., NIE Z., LEE Y.J. 2009. *Integrated Power Electronic Converters and Digital Control*. CRC Press, Boca Raton.
- BOLTON W. 2006. *Programmable Logic Controllers*. Elsevier, Amsterdam, Boston.
- BUSO S., MATTAVELLI P. 2006. *Digital Control in Power Electronics*. Morgan & Claypool Publisher, San Rafael, CA.
- CHEN C.-T. 1991. *Analog and Digital Control system Design: Transfer Function, State Space, and Algebraic Methods*. Saunders College Publishing, Philadelphia, Pennsylvania.
- DENTON T. 2016. *Electric and Hybrid Vehicles*. Routledge, San Diego.
- DORF R.C., BISHOP R.H. 2008. *Modern Control System Solution Manual*. Prentice Hall, New Jersey.
- FADALI S. 2009. *Digital Control Engineering, Analysis and Design*. Elsevier, Burlington.
- FEUER A., GOODWIN G.C. 1996. *Sampling in Digital Signal Processing and Control*. Birkhauser, Boston.
- GABOR R., KOWOL M., KOŁODZIEJ J., KMIĘCIK S., MYNAREK P. 2019. *Switchable reluctance motor, especially for the bicycle*. Patent No. 231882.
- GREGORY P. 2006. *Starr Introduction to Applied Digital Control*. Gregory P. Starr, New Mexico.
- GLINKA T., FRĘCHOWICZ A. 2007. *Brushless DC motor speed control system*. Patent No. P.195447.
- HUSAIN I. 2003. *Electric and Hybrid Vehicles, Design Fundamentals*. CRC Press LLC, Boca Raton, London.
- JONGSEONG J., WONTAE J. 2019. *Method of controlling constant current of brushless dc motor and controller of brushless dc motor using the same*. United States Patent Application Publication, US2018323736 (A1).
- KHAJEPOUR A., FALLAH S., GOODARZI A. 2014. *Electric and Hybrid Vehicles Technologies, Modeling and Control: a Mechatronic Approach*. John Wiley & Sons Ltd, Chichester.
- KOLANO K. 2020. *Method for measuring the angular position of the shaft of a brushless DC motor with shaft position sensors*. Patent No. P.235653.
- KOJIMA N., ANNAKA T. 2019. *Motor control apparatus and motor unit*. United States Patent Application Publication, US2019047517 (A1).

- LANDAU I.D., ZITO G. 2006. *Digital Control Systems Design, Identification and Implementation*. Springer, London.
- LUECKE J. 2005. *Analog and Digital Circuits for Electronic Control System Applications Using the TI MSP430 Microcontroller*. Elsevier, Amsterdam, Boston.
- MI CH., MASRUR M.A., GAO D.W. 2011. *Hybrid Electric Vehicles Principles and Applications with Practical Perspectives*. John Wiley & Sons Ltd., Chichester.
- MOUDGALYA K.M. 2007. *Digital Control*. John Wiley & Sons Ltd., Chichester.
- MURRAY R.M., LI Z., SHANKAR SASTRY S. 1994. *A Mathematical Introduction to Robotic Manipulation*. CRC Press, Berkeley.
- OGATA K. 1995. *Discrete Time Control Systems*. Prentice-Hall, New Jersey.
- PISTOIA G. 2010. *Electric and Hybrid Vehicles Power Sources, Models, Sustainability, Infrastructure and the Market*. Elsevier, Amsterdam, Boston.
- SIKORA A., ZIELONKA A. 2011. *Power supply system for a BLDC motor*. Patent No. P.394971.
- SOYLU S. 2011. *Electric Vehicles – the Benefits and Barriers*. Edited by Seref Soylu, Rijeka.
- STEVIĆ Z. 2013. *New Generation of Electric Vehicles*. Edited by Zoran Stević, Rijeka.
- SYROKA Z.W., JAKOCIUK D. 2020. *Battery recharging system in electric vehicle*. Patent No. P.431380, filing date: 17 January 2020.
- SYROKA Z.W. 2019. *Electric Vehicles – Digital Control*. Scholars' Press, Mauritius.
- ŚLUSAREK B., PRZYBYLSKI M., GAWRYŚ P. 2014. *Hall effect sensor of the shaft position of the brushless DC motor*. Patent No. P.218476.
- WILLIAMSON S.S. 2013. *Energy Management Strategies for Electric and Plug-in Hybrid Electric Vehicles*. Springer, New York, London.



Yearbook peer-reviewed scientific journal

ISSN 1505-4675  
e-ISSN 2083-4527

**TECHNICAL SCIENCES**

Homepage: <https://czasopisma.uwm.edu.pl/index.php/ts/>



DOI: <https://doi.org/10.31648/ts.6555>

## OPTIMIZATION METHOD BASED ON MINIMIZATION M-ORDER CENTRAL MOMENTS USED IN SURVEYING ENGINEERING PROBLEMS

*Sławomir Cellmer<sup>1</sup>, Andrzej Bobojć<sup>2</sup>*

<sup>1</sup>ORCID: 0000-0002-2614-8017

<sup>2</sup>ORCID: 0000-0003-0228-5962

Department of Geodesy  
University of Warmia and Mazury in Olsztyn

Received 23 March 2021, accepted 26 May 2021, available online 31 May 2021.

**Key words:** the Least Squares method, the Newton method, objective function, *m*-estimation, surveying engineering.

### Abstract

A new optimization method presented in this work – the Least *m*-Order Central Moments method, is a generalization of the Least Squares method. It allows fitting a geometric object into a set of points in such a way that the maximum shift between the object and the points after fitting is smaller than in the Least Squares method. This property can be very useful in some engineering tasks, e.g. in the realignment of a railway track or gantry rails. The theoretical properties of the proposed optimization method are analyzed. The computational problems are discussed. The appropriate computational techniques are proposed to overcome these problems. The detailed computational algorithm and formulas of iterative processes have been derived. The numerical tests are presented, in order to illustrate the operation of proposed techniques. The results have been analyzed, and the conclusions were then formulated.

---

Correspondence: Sławomir Cellmer, Katedra Geodezji, Uniwersytet Warmińsko-Mazurski, ul. Oczapowskiego 1, 10-719 Olsztyn, e-mail: [slawomir.cellmer@uwm.edu.pl](mailto:slawomir.cellmer@uwm.edu.pl), [altair@uwm.edu.pl](mailto:altair@uwm.edu.pl)

## Introduction

Optimization techniques are sometimes applied in engineering tasks. In such applications, the problem is usually formulated as fitting a geometrical figure into a set of points in 2D or 3D space. In contrast to many estimation problems where the solution has to be free of outliers (CASPARY 1990, CHANG, GUO 2005, HAMPEL et al. 1986, HUBER 1981, KAMIŃSKI, WIŚNIEWSKI 1992, KOCH 1996, YANG 1999, YANG et al. 2002, XU 1989, ZHONG 1997, ZHU 1996), the opposite problem is presented here: an optimization method preferring outliers. This feature is beneficial in engineering applications, where constraints concerning maximum shifts appear. In some cases, the maximum shifts cannot exceed a critical value. Such constraints can appear e.g. during the realignment of a railway track (SKAŁA-SZYMAŃSKA et al. 2014). These constraints result from a limited structure gauge, i.e. the width of tunnels, bridges or distances to railway platforms, buildings or other objects. The constraints, mentioned above, have to be taken into account during the construction process when some elements of a structure are installed in a limited space. An example of such civil engineering task is to fit elevator guide rails inside the elevator shaft. One of the tools for solving the problem of limited shifts can be the min-max algorithm from game theory (VON NEUMANN 1947). Also, the Least Squares (LS) method with constraints can be applied (LIEW 1976, MEAD, RENAUT 2010, WERNER 1990). An alternative method is presented here. In the proposed method, the special form of the objective function is applied. This form is related to the  $m$ -order central moments (with  $m \geq 2$ ). Thus, the proposed method is a generalization of the LS method and the Least Fourth Powers (LFP) method (CELLMER 2014). Special attention must be paid to the optimization technique. So far, a lot of interesting optimization techniques were proposed e.g. (FLETCHER 1987, NOCEDAL, WRIGHT 1999, AVRIEL 2003). It was shown in (CELLMER 2014) that if an inappropriate technique of searching for the minimum of the objective function is applied, then the computational process is not convergent. In such a case, two alternate solutions are obtained in consecutive iterations like in the  $M$ -split estimation method (DUCHNOWSKI, WIŚNIEWSKI 2012, WIŚNIEWSKI 2009, 2010). In the  $M$ -split estimation method, this effect was obtained deliberately – it resulted from the theoretical foundations of this method. However, in the method considered here, a single, unique solution is required. The technique of searching for a solution should have the property of skipping local minima and pursue the global one. This property was described e.g. in (MARTINS, TSUZUKI 2009).

In the next section, the objective function of the Least  $m$ -Order Central Moments (LmOCM) method is presented. The justification for applying this form of the objective function was carried out using certain concepts of estimation theory and was illustrated using the plot of weight function for different values of the  $m$ -exponent. The third section contains the derivation of the formulas

of the computational process. Two different techniques of optimization of the LmOCM objective function have been discussed and two numerical examples were analyzed in the fourth section. The conclusions have been formulated on the basis of the results of tests.

## Objective function of the LmOCM method and its properties

The optimization method proposed in this article is based on minimizing the objective function  $\Psi(\mathbf{v})$ :

$$\min_{\mathbf{v}} \left( \Psi(\mathbf{v}) = \sum_{i=1}^n v_i^m \right) \quad (1)$$

where  $v_i$  are elements of the  $\mathbf{v}$  vector in the simple, linear model:

$$\mathbf{y} + \mathbf{v} = \mathbf{A}\mathbf{p} \quad (2)$$

where:

- $\mathbf{y}$  – vector of entries that are fitted into the  $\mathbf{A}$  model,
- $\mathbf{v}$  – vector of corrections (disclosures),
- $\mathbf{A}$  – design matrix,
- $\mathbf{p}$  – parameter vector.

The optimization method based on criterion (1), is a generalization of the LS or the LFP method (CELLMER 2014). In CELLMER (2014), the properties of the LFP method have been described using selected concepts of estimation theory. The considered estimation methods belong to the  $m$ -estimation class. These methods are based on the minimization:

$$\min_{\mathbf{v}} \left( \Psi_G(\mathbf{v}) = \sum_{i=1}^n \rho_i(\mathbf{v}) \right) \quad (3)$$

The  $\rho_i$  function is a component of the objective function  $\Psi_G(\mathbf{v})$ . The objective function  $\Psi(\mathbf{v})$  in the formula (1) is a special case of the the objective function  $\Psi_G(\mathbf{v})$ . The form of the component  $\rho_i$  determines the properties of the results. In the method proposed here, the  $\rho_i$  function takes the following form:

$$\rho_i(\mathbf{v}) = v_i^m \quad (4)$$

One of the properties of the optimization method can be described by the weight-function (KADAJ 1988). The form of this function is:

$$w(v) = \frac{\partial \rho(v)}{\partial v^2} \quad (5)$$

The plots of the weight function with the values of the  $m$ -parameter: 2, 4, 6, 8, 10 and 12 are depicted in Figure 1. The black line depicts the weight function of the LS method ( $m = 2$ ). As follows from the definition of the weight function (5), in the case of the LS method, it is constant. All observations are treated equally. In the case of large values of the  $m$ -parameter, there is a range around the zero value, where the trajectory of the plot of the function is almost horizontal. Outside this range, the function value rapidly increases. This means that if there are no outliers in the data set, this optimization method provides results similar to the results obtained with the LS method. However, if there are some outliers in the data set, they have more impact on the solution than other observations. The consequence of this is a smaller maximal value of the residuals in the optimization process.

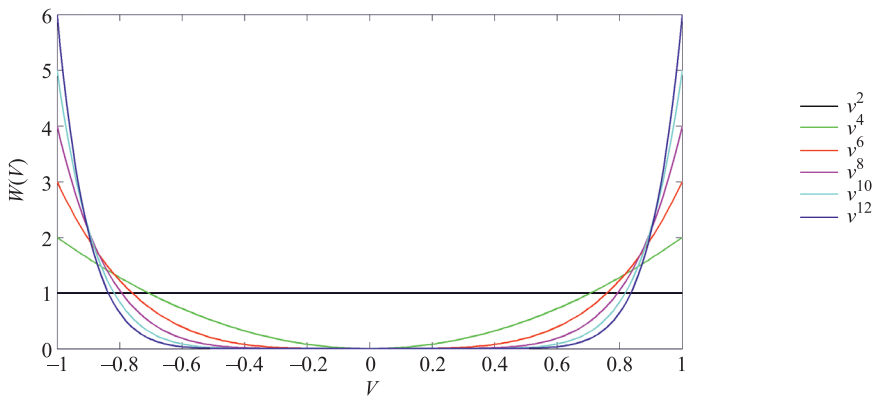


Fig. 1. Weight functions. The plots represent the weight functions of the objective functions, which are in the form of the central moments of various orders

## Optimization techniques

The objective function in minimization problem (1) can be presented in the following matrix notation:

$$\Psi(\mathbf{v}) = \mathbf{v}_r^T \mathbf{v}_r \quad (6)$$

where:

$$r = \frac{m}{2} \quad (7)$$

$$\mathbf{v}_r = [v_1^r, v_2^r, \dots, v_n^r]^T \quad (8)$$



The solution, which is at the point of a minimum of the objective function (6) can be found by zeroing the gradient of this function. As was shown in (CELLMER 2014), this technique cannot be employed in its simple, classic form. The gradient of the objective function (6) is derived, based on (2) and (7):

$$\frac{\partial \Psi}{\partial \mathbf{p}} = \frac{\partial \Psi}{\partial \mathbf{v}_r} \frac{\partial \mathbf{v}_r}{\partial \mathbf{p}} = 2\mathbf{v}_r^T \cdot r \cdot \text{diag}(\mathbf{v}_{r-1}) \cdot \mathbf{A} = 2r \cdot \mathbf{v}_{2r-1}^T \mathbf{A} = 2r \cdot \mathbf{v}^T \text{diag}(\mathbf{v}_{m-2}) \mathbf{A} \quad (9)$$

where  $\text{diag}(\mathbf{v}_{m-2})$  denotes a diagonal matrix, containing elements of the  $\mathbf{v}_{m-2}$  – vector on a diagonal. Thence the system of normal equations is obtained:

$$\mathbf{A}^T \mathbf{W} \mathbf{A} \mathbf{p} - \mathbf{A}^T \mathbf{W} \mathbf{y} = \mathbf{0} \quad (10)$$

where:

$$\mathbf{W} = \text{diag}(\mathbf{v}_{m-2}) \quad (11)$$

The solution can be obtained in an iterative process:

$$\begin{aligned} \mathbf{p}_{(i)} &= (\mathbf{A}^T \mathbf{W}_{(i-1)} \mathbf{A})^{-1} \mathbf{A}^T \mathbf{W}_{(i-1)} \mathbf{y} \\ \mathbf{v}_{(i)} &= \mathbf{A} \mathbf{p}_{(i)} - \mathbf{y}, \text{ for } i = 1, 2, \dots \text{ and } \mathbf{W}_{(0)} = \mathbf{I} \end{aligned} \quad (12)$$

The  $\mathbf{W}$  matrix is formed according to (11) in each iteration. However, as was shown in (CELLMER 2014), in the case of the objective function (6), process (12) does not work properly. This technique does not ensure proper convergence to the correct, unique solution. As a result of using formulas (12), two alternate solutions are obtained. They appear alternately in consecutive iterations. A similar effect is obtained when using the  $M$ -split estimation proposed by (WIŚNIEWSKI 2009, 2010). However, the unique solution of the minimization process of the objective function (6) exists. CELLMER (2014) proposed applying one of two optimization techniques for obtaining a unique solution in the considered problem. The first one is based on the modification of the process (12). The second is based on applying the Newton technique of optimization. In the first technique, the iterative process (12) is modified to the form:

$$\begin{aligned} \mathbf{d}\mathbf{y}_{(i)} &= \mathbf{y} - \mathbf{A} \mathbf{p}_{(i-1)} \\ \mathbf{d}\mathbf{p}_{(i)} &= k(\mathbf{A}^T \mathbf{W}_{(i-1)} \mathbf{A})^{-1} \mathbf{A}^T \mathbf{W}_{(i-1)} \mathbf{d}\mathbf{y}_{(i)} \\ \mathbf{p}_{(i)} &= \mathbf{p}_{(i-1)} + \mathbf{d}\mathbf{p}_{(i)} \\ \mathbf{v}_{(i)} &= \mathbf{A} \mathbf{d}\mathbf{p}_{(i)} - \mathbf{d}\mathbf{y}_{(i)} \\ \mathbf{W}_{(i)} &= \text{diag}(\mathbf{v}_{m-2(i)}) \text{ for } i = 1, 2, \dots \text{ and } \mathbf{p}_{(0)} = \mathbf{0}, \mathbf{W}_{(0)} = \mathbf{I} \end{aligned} \quad (13)$$

where the  $\mathbf{v}_{m-2(i)}$  vector in the last row is formed according to (8). In this technique, in contrast to process (12), the results obtained from consecutive iterations are accepted as the starting point (approximate value of the parameter) in the next iteration. This is performed by updating the  $\mathbf{dy}$  and  $\mathbf{p}$  vectors. Additionally, the reduction parameter  $k$  is introduced. This parameter reduces the length of every single step in the iterative process of searching for the solution. This was imposed to eliminate the effect of jumping over the global solution in consecutive iterations. The  $k$  parameter has to take the value from the range: (0; 1). Determination of the optimal value of this parameter is presented in the next section.

In the second technique, the Newton method of optimization is applied in its classic form:

$$\mathbf{p}_{(i)} = \mathbf{p}_{(i-1)} - \mathbf{H}^{-1}(\mathbf{p}_{(i-1)})\mathbf{G}(\mathbf{p}_{(i-1)}) \quad (14)$$

where  $\mathbf{G}$  and  $\mathbf{H}$  are, appropriately, the gradient and Hessian of the objective function  $\Psi$ . The gradient of the objective function (8) is expressed by formula (9). Let us denote the gradient  $\mathbf{G}$  as a transpose of (9):

$$\mathbf{G} = 2r \mathbf{A}^\top \mathbf{v}_{m-1} \quad (15)$$

or

$$\mathbf{G} = m \mathbf{A}^\top \mathbf{W} \mathbf{v} \quad (16)$$

The Hessian can then be formed as:

$$\begin{aligned} \mathbf{H} &= \frac{\partial \mathbf{G}}{\partial \mathbf{p}} = \frac{\partial \mathbf{G}}{\partial \mathbf{v}_{m-1}} \frac{\partial \mathbf{v}_{m-1}}{\partial \mathbf{v}} \frac{\partial \mathbf{v}}{\partial \mathbf{p}} = m \mathbf{A}^\top (m-1) \text{diag}(\mathbf{v}_{m-2}) \mathbf{A} = \\ &= m(m-1) \mathbf{A}^\top \mathbf{W} \mathbf{A} \end{aligned} \quad (17)$$

Thus, in this case the optimization process can be presented as follows:

$$\begin{aligned} \mathbf{p}_{(i)} &= \mathbf{p}_{(i-1)} - \frac{1}{m-1} (\mathbf{A}^\top \mathbf{W}_{(i-1)} \mathbf{A})^{-1} \mathbf{A}^\top \mathbf{W}_{(i-1)} \mathbf{v}_{(i-1)} \\ \mathbf{v}_{(i)} &= \mathbf{A} \mathbf{p}_{(i)} - \mathbf{y} \quad \text{for } i = 1, 2, \dots \text{ and } \mathbf{W}_{(0)} = \mathbf{I} \end{aligned} \quad (18)$$

The correction vector in the first iteration ( $\mathbf{v}_{(0)}$ ) is calculated using formula (12).

## Numerical examples

Table 1 contains the coordinates of the points. The axes are to be fitted into each set of these points using criterion (1). In the first example the formula of the fitted line is:

$$y = ax \quad (19)$$

whereas in the second example, it is:

$$y = ax + b \quad (20)$$

Table 1

Set of points for fitting the axes					
Example 1			Example 2		
No	$x$ [m]	$y$ [m]	No	$x$ [m]	$y$ [m]
1	1.000	0.102	1	1.000	0.507
2	2.000	0.196	2	2.000	0.603
3	3.000	0.302	3	3.000	0.699
4	4.000	0.405	4	4.000	0.801
5	5.000	0.501	5	5.000	0.897
6	6.000	0.603	6	6.000	1.006
7	7.000	0.727	7	7.000	1.128
8	8.000	0.799	8	8.000	1.202
9	9.000	0.914	9	9.000	1.310
10	10.000	0.998	10	10.000	1.401

The **A** matrix and the **y** vector in each example are formed based on the following observation equations:

$$y_i + v_i = ax_i \text{ (example 1)} \quad (21)$$

$$y_i + v_i = ax_i + b \text{ (example 2)} \quad (22)$$

Hence, in the first example, the **A** is the column vector of  $x$ -coordinates, whereas in the second example this is a two-column matrix: the first column contains  $x$ -coordinates and the second column is a vector of ones. At the start point of optimization, the **y**-vector contains the  $y$ -coordinates of the points listed in Table 1. The first test was performed in order to determine the optimal value of the  $k$ -factor in process (13). Therefore, this process was carried out for different values of  $k$ , and afterwards, the speed of convergence was analyzed for each of them. The results are listed in Table 2. It was shown in (CELLMER 2014) that if  $k = 1$ , the solution splits into two results, repeating alternately in consecutive iterations. Therefore, the  $k$ -factor values have been assumed here as:

$$k = \frac{1}{k_1}, \text{ for } k_1 = 2, 3, \dots, 14 \quad (23)$$

The first column contains the consecutive values of  $k_1$ . The next columns contain the number of iterations needed to stabilize the solution with a precision of 0.0001. An iterative process was terminated when the values of parameters in consecutive iterations have differed by less than 0.0001. Each column contains

results for a different  $m$ -value. The first part of Table 2 concerns the example of ' $y = ax$ ', and the second part the example of ' $y = ax + b$ '. Analyzing minima values, we can come to the conclusion that for most cases the fastest convergence is observed for  $k_1 = m - 1$ . The  $k$ -factor corresponding to such  $k_1$  value is identical to the factor in the formula of the Newton method (18). Tables 3 and 4 contain results of optimization using processes (13) and (18) for the case of ' $y = ax$ ' (Tab. 3) and for ' $y = ax + b$ ' (Tab. 4). For each ' $m$ ', the parameter values and maximum values of misclosures are given in consecutive iterations.

Determination of the optimal value of the  $k_1$ -factor

$k_1$	$y = ax$					$y = ax+b$				
	$m$					$m$				
	4	6	8	10	12	4	6	8	10	12
2	10	-	-	-	-	8	-	-	-	-
3	3	15	-	-	-	3	13	-	-	-
4	4	5	15	-	-	5	5	11	-	-
5	5	3	5	12	-	6	3	4	-	-
6	6	3	4	7	-	8	5	5	11	16
7	7	4	4	5	12	9	7	5	7	7
8	9	5	4	4	8	11	8	5	6	7
9	10	6	4	4	4	12	9	6	6	7
10	11	7	5	5	5	14	11	7	5	6
11	12	7	6	5	5	16	12	8	6	5
12	13	8	6	6	4	17	13	9	7	6
13	14	9	7	7	5	19	14	10	7	7
14	15	9	7	7	5	20	16	11	8	8
$v_{1\max}^*$ [mm]	21					22				
$v_{2\max}^{**}$ [mm]	18	18	17	17	17	17	16	16	15	15

\* maximal shift in the LS method ( $m = 2$ )  
\*\* maximal shift in the LmOCM method ( $m > 2$ )

Results of optimization ( $y = ax$ ). Table contains the value of the  $a$  parameter and maximum shift

$m$  after fitting axis into a set of points

Iter.	$m$									
	4		6		8		10		12	
	$a$	$v_{\max}$	$a$	$v_{\max}$	$a$	$v_{\max}$	$a$	$v_{\max}$	$a$	$v_{\max}$
1	0.1009	0.021	0.1009	0.021	0.1009	0.021	0.1009	0.021	0.1009	0.021
2	0.1013	0.018	0.1013	0.018	0.1013	0.018	0.1012	0.019	0.1011	0.019
3	<b>0.1012</b>	<b>0.018</b>	<b>0.1014</b>	<b>0.018</b>	<b>0.1014</b>	<b>0.017</b>	<b>0.1014</b>	<b>0.017</b>	0.1014	0.018
4	<b>0.1012</b>	<b>0.018</b>	<b>0.1014</b>	<b>0.018</b>	<b>0.1014</b>	<b>0.017</b>	<b>0.1014</b>	<b>0.017</b>	<b>0.1014</b>	<b>0.017</b>
5	<b>0.1012</b>	<b>0.018</b>	<b>0.1014</b>	<b>0.018</b>	<b>0.1014</b>	<b>0.017</b>	<b>0.1014</b>	<b>0.017</b>	<b>0.1014</b>	<b>0.017</b>



In process (13), the  $k$ -factor has been assumed as:

$$k = \frac{1}{m - 1} \quad (24)$$

In the case analyzed here, both methods (13) and (18) provided the same results in each iteration. The results with a stabilized solution (with a precision of 0.0001 for parameters, and 0.001 for maximum misclosure) are in bold. The result of the first iteration is merely the Least Squares (LS) solution. The maximal shift needed for the axis alignment according to the LS method ( $v_{\max}$ ) is above 2 cm in both examples. In the first example, it amounts to 21 mm and in the second example 22 mm. This value was reduced using the LmOCM method. In the first example this value amounts to 18 mm for  $m = 4$  or 6, and 17 mm for  $m = 8, 10$  or 12. In the second example, this value has been maximally reduced to 15 mm (for  $m = 12$ ). In some cases, this reduction can be of critical significance (e.g. in such engineering tasks where the values of shifts are limited to a range less than 20 mm). The  $v_{\max}$ -values for different 'm' differ by less than 1 mm in the first example, and by less than 2 mm in the second example. It is clearly seen, that for the lower required maximal shifts, the higher  $m$ -values should be taken in the adjustment process – the lowest shift values of 15 mm for the greater  $m$ -values (10 and 12) are visible in Table 4.

## Summary and Conclusions

In the paper, a generalization of the Least Squares optimization method is proposed. A new method is based on the criterion of minimization of a sum of misclosures raised to the power of ' $m$ '. This criterion allows one to reduce the maximum misclosure in the optimization problem in comparison to the LS method. A crucial problem in the use of this method is ensuring proper convergence of the computational process. Two techniques of finding the minimum of the objective function were tested: the simple gradient zeroing method and the Newton method. Both methods employ an iterative process. The formula of the computational process of the first technique contains the  $k$ -factor. This factor warrants the proper convergence of the computational process. It is proposed here, that the value of this factor is calculated as  $k = (m - 1)^{-1}$  if the sum of misclosures to the power of ' $m$ ' is the optimization criterion. In the case study considered here, the two optimization techniques provided the same results. The results of this case study confirmed the property of reducing the maximum shift in the task of the alignment of the axis into a set of points in comparison to the LS method.

## References

- AVRIEL M. 2003. *Nonlinear Programming: Analysis and Methods*. Dover Publishing.
- CASPARY W., HAEN W. 1990. *Simultaneous estimation of location and scale parameters in the context of robust M-estimation*. Manuscripta Geodaetica, 15: 273–282.
- CELLMER S. 2014. *Least fourth powers: optimisation method favouring outliers*. Survey Review, 47(345): 417. DOI: <https://doi.org/10.1179/1752270614Y.0000000142>.
- CHANG X.W., GUO Y. 2005. *Huber's M-estimation in relative GPS positioning: computational aspects*. Journal of Geodesy, 79: 351–362. DOI: <https://doi.org/10.1007/s00190-005-0473-y>.
- DUCHNOWSKI R., WIŚNIEWSKI Z. 2012. *Estimation of the shift between parameters of functional models of geodetic observations by applying M split estimation*. Journal of Surveying Engineering, 138: 1–8. DOI: 10.1061/(ASCE)SU.1943-5428.0000062.
- FLETCHER R. 1987. *Practical methods of optimization*. 2<sup>nd</sup> ed. John Wiley & Sons, New York.
- HAMPEL F.R., RONCHETTI E., ROUSSEUW P.J., STAHEL W.A. 1986. *Robust statistics: the approach based on influence function*. Wiley, New York.
- HUBER P.J. 1981. *Robust statistics*. Wiley, New York.
- KADAJ R. 1988. *Eine verallgemeinerte Klasse von Schätzverfahren mit praktischen Anwendungen*. Z Vermessungs-wesen, 113(4): 157–166.
- KAMIŃSKI W., WIŚNIEWSKI Z. 1992. *Analysis of some, robust, adjustment methods*. Geodezja i Kartografia, 41(3-4): 173-182.
- KOCH K.R. 1996. *Robuste Parameterschätzung*. Allgemeine Vermessungs-Nachrichten, 103(11): 1–18.
- LIEW C.K. 1976. *Inequality constrained least squares estimation*. Journal of the American Statistical Association, 71: 746–751.
- MARTINS T.C., TSUZUKI M.S.G. 2009. *Placement over containers with fixed dimensions solved with adaptive neighborhood simulated annealing*. Bulletin of the Polish Academy of Sciences. Technical Sciences, 57(3): 273-280.
- MEAD J.L., RENAUT R.A. 2010. *Least squares problems with inequality constraints as quadratic constraints*. Linear Algebra and its Applications, 432(8): 1936–1949.
- NEUMANN J. von, MORGENSTERN O. 1947. *Theory of games and economic behavior*. Princeton Univ. Press. Princeton, New Jersey.
- NOCEDAL J., WRIGHT S.J. 1999. *Numerical Optimization*. Springer-Verlag, Berlin.
- SKAŁA-SZYMAŃSKA M., CELLMER S., RAPIŃSKI J. 2014. *Use of Nelder-Mead simplex method to arc fitting for railway track realignment*. The 9<sup>th</sup> International Conference Environmental Engineering, selected papers. DOI: 10.3846/enviro.2014.244.
- WERNER H.J. 1990. *On inequality constrained generalized least-squares estimation*. Linear Algebra and its Applications, 27: 379–392. DOI: <http://dx.doi.org/10.1179/1752270614Y.0000000142>.
- WIŚNIEWSKI Z. 2009. *Estimation of parameters in a split functional model of geodetic observations (M split estimation)*. Journal of Geodesy, 83: 105–120. DOI: <https://doi.org/10.1007/s00190-008-0241-x>.
- WIŚNIEWSKI Z. 2010. *M split(q) estimation: estimation of parameters in a multi split functional model of geodetic observations*. Journal of Geodesy, 84: 355–372. DOI: <https://doi.org/10.1007/s00190-010-0373-7>.
- XU P. 1989. *On robust estimation with correlated observations*. Bulletin Géodésique, 63: 237–252.
- YANG Y. 1999. *Robust estimation of geodetic datum transformation*. Journal of Geodesy, 73: 268–274. DOI: <https://doi.org/10.1007/s001900050243>.
- YANG Y., SONG L., XU T. 2002. *Robust estimation for correlated observations based on bifactor equivalent weights*. Journal of Geodesy, 76: 353–358. DOI: <https://doi.org/10.1007/s00190-002-0256-7>.
- ZHONG D. 1997. *Robust estimation and optimal selection of polynomial parameters for the interpolation of GPS geoid heights*. Journal of Geodesy, 71: 552–561. DOI: <https://doi.org/10.1007/s001900050123>.
- ZHU J. 1996. *Robustness and the robust estimate*. Journal of Geodesy, 70: 586–590. DOI: <https://doi.org/10.1007/BF00867867>.







Yearbook peer-reviewed scientific journal

ISSN 1505-4675  
e-ISSN 2083-4527

**TECHNICAL SCIENCES**

Homepage: <https://czasopisma.uwm.edu.pl/index.php/ts/>



DOI: <https://doi.org/10.31648/ts.6297>

## THE INFLUENCE OF LAYER HEIGHT ON THE TENSILE STRENGTH OF SPECIMENS PRINTED IN THE FDM TECHNOLOGY

*Lukasz Miazio*

ORCID: 0000-0002-4693-4779

Faculty of Technical Sciences  
University of Warmia and Mazury in Olsztyn

Received 07 January 2021, accepted 19 July 2021, available online 30 July 2021.

**Key words:** rapid prototyping, 3D printing, PLA, FDM.

### Abstract

This article analyzes the influence of layer height on the tensile strength of PLA specimens printed in the Fused Deposition Modeling (FDM) technology. The maximum breaking force of specimens with 30% and 100% infill density was determined at layer height of 0.05 mm, 0.1 mm, 0.2 mm and 0.3 mm. In the case of 30% infill, the highest value of the force was obtained for a layer with a height of 0.05 mm (which corresponds to 22.7 MPa), and for a 100% infill for a layer of 0.2 (which corresponds to 40 MPa). Over this layer height of 0.2 mm is the most poly-optimal due to the time prints and strength (which corresponds to 19.7 MPa).

## Introduction

Rapid prototyping technologies, including 3D printing, enable the verification of CAD models in a short time and at a low cost. One of the most important parameters of 3D printing is the layer height. It affects the accuracy of the print as well as the printing time. On the other hand, this article analyzes the

---

Correspondence: Łukasz Miazio, Katedra Mechaniki i Podstaw Konstrukcji Maszyn, Wydział Nauk Technicznych, Uniwersytet Warmińsko-Mazurski, ul. M. Oczapowskiego 11, 10-957 Olsztyn, e-mail: lukasz.miazio@uwm.edu.pl.

influence of layer height on the tensile strength of specimens printed in the Fused Deposition Modeling (FDM) technology. The article will check whether increasing the layer height will have a negative impact on the strength of the printed samples. The paper is a continuation of the author's previous research into the strength of specimens printed in the FDM process. Previous studies (MIAZIO 2015, 2016, 2017, 2018) explored the tensile and bending strength of printed specimens with different infill density and different infill patterns. The effects exerted by printing speed (MIAZIO 2019) and the specimens' compressive strength (MIAZIO 2020) were also analyzed. These problems have also been investigated by other authors (LUZANIN et al. 2019, KIŃSKI, PIETKIEWICZ 2019). Moreover, they also dealt with the search for polyoptimal printing parameters in their research (RANEY et al. 2017, SATY, RAJEEV 2020, TORRES et al. 2015, WANKHEDE et al. 2020). The aim of the present study was to determine the influence of layer height on the tensile strength of the printed model and printing time. The filament material for 3D printing was polylactic acid (PLA).

## Materials and Methods

The specimen (Fig. 1) for the tensile test was modeled in the SolidWorks program. The model was saved in an STL file. The G-code file for executing the 3D printing program was generated based on the STL file in the Cura program (Ultimaker Cura, online).

The parameters and procedures for conducting tensile tests in plastics are described by standard PN-EN ISO 527:1998: *Plastics. Determination of mechanical properties during static tensile tests*. The dimensions of the analyzed specimen (type B1) are presented in Table 1.

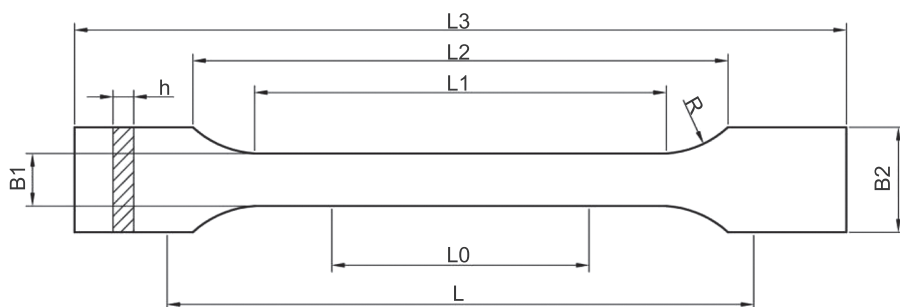


Fig. 1. Universal specimen

Table 1

Specimen dimensions	
Specimen dimensions	Type B1 [mm]
L3 – total length	150
L1 – length of the segment limited by lines	40
R – radius	60
L2 – distance between wide parallel segments located at both ends of the specimen	106
B2 – width of each wide segment	20
B1 – width of the narrow segment	10
h – recommended thickness	4
L0 – measured length	50
L – initial distance between holders	115

The specimens were printed with the use of PLA filament in the BIG Builder DUAL FEED printer (Builder 3D Printers HQ) with a 0.4 mm nozzle. All specimens were printed flat, along the Y-axis of the printer. They were printed in batches of five specimens each. The following printing parameters were applied:

- printing speed of the first layer: 20 mm/s,
- printing speed of successive layers: 60 mm/s,
- head temperature: 215°C,
- thickness of the top and bottom layer: 0.6 mm,



Fig. 2. Cross-section of a printed specimen with a grid infill pattern and 30% infill density

The printed specimens were subjected to a quasi-static uniaxial tensile test based on standard PN-EN ISO 527:1998, with a strain rate of 2 mm/min. The test was conducted in five replicates for each layer height and infill density.

## Results and Discussion

The results of tensile tests and the maximum breaking force values for each analyzed layer height in specimens with 30% and 100% infill density are presented in Tables 2 and 3, respectively. Curves representing the mean values

of the maximum breaking force vs. layer height are presented in Figure 3. The printing times of specimens with different layer height are presented in Table 4 and Figure 4.

The data in Figure 3 indicate that in specimens with 30% infill density, the highest tensile strength was achieved at 0.05 mm layer height. In these specimens, tensile strength decreased with an increase in layer height. In specimens with 100% infill density, tensile strength was highest at 0.2 mm layer height, and it decreased considerably at 0.3 mm layer height.

Table 2

Layer height [mm]	Breaking force values for specimens with 30% infill density					
	Breaking force [kN]					
	Specimen 1	Specimen 2	Specimen 3	Specimen 4	Specimen 5	Mean
0.05	0.9	0.91	0.91	0.92	0.9	0.9
0.1	0.84	0.83	0.84	0.83	0.82	0.84
0.2	0.8	0.81	0.76	0.77	0.8	0.8
0.3	0.71	0.71	0.73	0.74	0.71	0.71

Table 3

Layer height [mm]	Breaking force values for specimens with 100% infill density					
	Breaking force [kN]					
	Specimen 1	Specimen 2	Specimen 3	Specimen 4	Specimen 5	Specimen
0.05	1.44	1.45	1.43	1.45	1.43	1.44
0.1	1.55	1.56	1.58	1.57	1.58	1.55
0.2	1.62	1.59	1.61	1.6	1.63	1.62
0.3	1.27	1.3	1.25	1.25	1.24	1.27

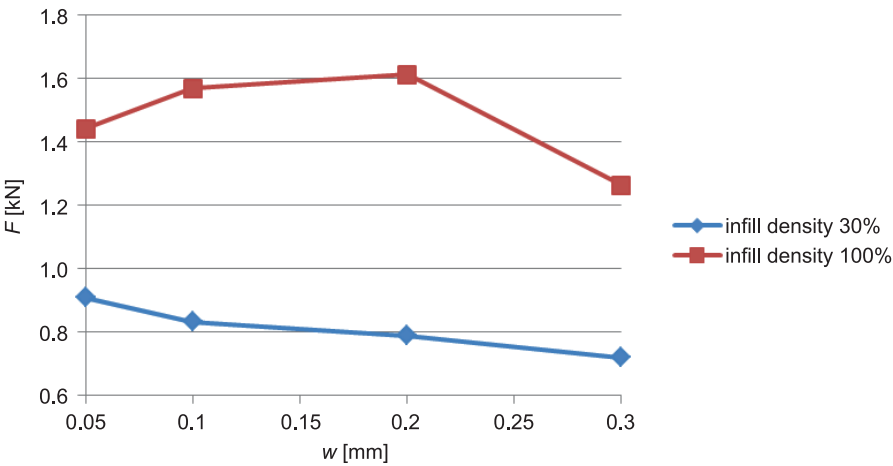


Fig. 3. Mean breaking force values vs. layer height

Table 4

Layer height [mm]	Printing time of a batch of five specimens	
	Printing time [min]	
	30% infill density	100% infill density
0.05	506	655
0.1	273	348
0.2	150	196
0.3	106	142

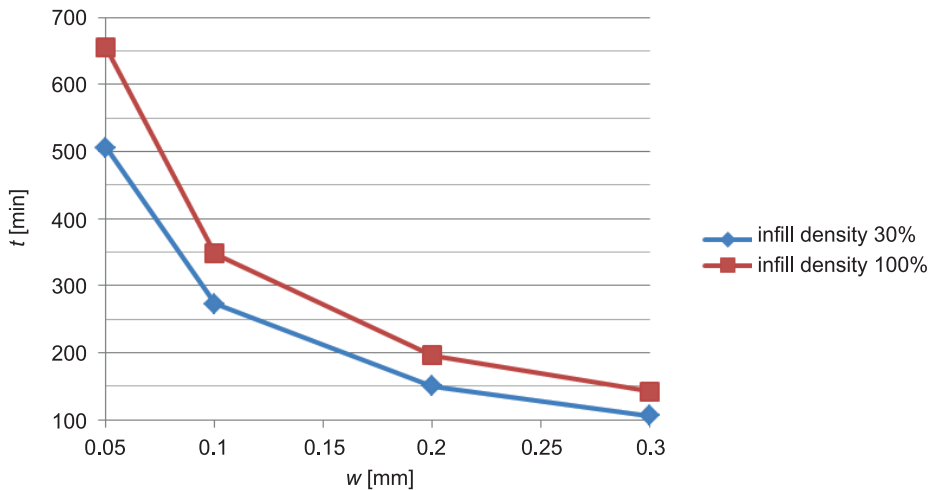


Fig. 4. Printing time of a batch of five specimens vs. layer height

An analysis of Figure 4 clearly indicates that printing time decreased significantly with an increase in layer height. Printing time was reduced by around 50% when layer height increased two-fold.

## Conclusions

The results of this experiment indicate that specimens with 0.2 mm layer height were characterized by the highest tensile strength and the shortest printing time. Taking into account the specimen cross-section 10×4 mm, the stress at break for 30% infill density was 19.7 MPa, and for 100% infill density it was 40.2 MPa. The printing time of the specimens with 0.2 mm layer height was more than three times shorter in comparison with specimens with 0.05 mm layer height. The tensile strength of the specimens with 0.2 mm layer height

and 100% infill density was higher, and it was only somewhat lower (by 11%) in specimens with 30% infill density. The decrease in strength at a layer height of 0.3 mm is caused by weaker plasticization of the filament and weaker gluing of the layers. Previous research by the author has shown problems with the plasticization of the filament at higher flow rates through the printer nozzle.

The present findings should be regarded as qualitative data. Quantitative data can differ considerably, depending on the type of filament material and the applied program for generating G-code files.

## References

- KIŃSKI W., PIETKIEWICZ P. 2019. *Influence of the print layer height in FDM technology on the rolling force value and the print time*. Agricultural Engineering, 23(4): 1-9.
- LUZANIN O., MOVRIN D., STATHOPOULOS V., PANDIS P., RADUSIN T., GUDURIC V. 2019. *Impact of processing parameters on tensile strength, in-process crystallinity and mesostructure in FDM-fabricated PLA specimens*. Rapid Prototyping Journal, 25(8): 1398-1410.
- MAZIO Ł. 2015. *Badanie wytrzymałości na rozciąganie próbek wydrukowanych w technologii FDM z różną gęstością wypełnienia*. Mechanik, 7: 533-538.
- MAZIO Ł. 2016. *Badanie wytrzymałości na zginanie próbek wydrukowanych w technologii FDM z różną gęstością wypełnienia*. Mechanik, 7: 758-759.
- MAZIO Ł. 2017. *Badanie wytrzymałości na rozciąganie próbek wydrukowanych w technologii FDM z różną gęstością wypełnienia – wypełnienie heksagonalne i koncentryczne*. Przegląd Mechaniczny, 6: 51-53.
- MAZIO Ł. 2018. *Badanie wytrzymałości na zginanie próbek wydrukowanych w technologii FDM z różną gęstością wypełnienia – wypełnienie heksagonalne, koncentryczne i trójkątne*. Mechanik, 7: 546-548.
- MAZIO Ł. 2019. *Impact of print speed on strength of samples printed in FDM technology*. Agricultural Engineering, 23(2): 33-38.
- MAZIO Ł. 2020. *Badanie wytrzymałości na ściskanie próbek wydrukowanych w technologii FDM z różnym stopniem wypełnienia*. In: *Komputerowe wspomaganie projektowania wytwarzania i eksploatacji*. Ed. R. Trębiński, Wojskowa Akademia Techniczna im. Jarosława Dąbrowskiego, Warszawa, p.155-160.
- RANEY K., LANI E., KALLA D.K. 2017. *Experimental characterization of the tensile strength of ABS parts manufactured by fused deposition modeling process*. Materials Today: Proceedings, 4: 7956-7961.
- SATY D., RAJEEV S. 2020. *Experimental investigation and optimization of FDM process parameters for material and mechanical strength*. Materials Today: Proceedings, 26(2): 1995-1999.
- TORRES J., COTELO J., KARL J., GORDON A. 2015. *Mechanical Property Optimization of FDM PLA in Shear with Multiple Objectives*. JOM, 67: 1183-1193.
- Ultimaker Cura. <https://ultimaker.com/en/products/ultimaker-cura-software> (access: 3.11.2020).
- WANKHEDE V., JAGETIYA D., JOSHI A., CHAUDHARI R. 2020. *Experimental investigation of FDM process parameters using Taguchi analysis*. Materials Today: Proceedings, 27: 2117-2120.

## DESIGN OF A MOTION SYSTEM FOR 3D PRINTED SNAKEBOT

*Krzysztof Mateja<sup>1</sup>, Wawrzyniec Panfil<sup>2</sup>*

<sup>1</sup>ORCID: 0000-0002-8882-8325

<sup>2</sup>ORCID: 0000-0001-7304-554X

Department of Fundamentals of Machinery Design  
Silesian University of Technology, Gliwice

Received 17 January 2021, accepted 19 July 2021, available online 30 July 2021.

**Key words:** snakebot, snake robot, drive system, rotate system, 3D print.

### Abstract

This article presents the results of work related to design, analysis and selection of the electric motors, servos and elements of motion system for 3D printed snakebot. Electric motors and servos had to meet a number of requirements like dimensions, torque, RPM. The drivetrain allowed to drive the snakebot and rotate system allowed to torsional movement between adjacent robot modules. CAD model and analysis allowed to select the proper elements of drivetrain and rotate system. We built test stands and after verification we built the prototype. Next step after building the robot was to carry out tests to verify the mobility of the snake robot. We checked, among others, movement of servos in different planes, snakebot speed, driving at angle (up and down).

## Introduction

Robotics is one of the industry sector that is developing exceptionally fast. One of the examples of robots that are gaining increasing recognition on the market are snakebots. The names serpentine, modular or chain robot are used interchangeably. The robots resemble a snake, thanks to them have many degrees of freedom, high maneuverability, and a modular structure. Modular construction allows to build snake robots from many similar segments. Individual

---

Correspondence: Krzysztof Mateja, Katedra Podstaw Budowy Maszyn, Politechnika Śląska, ul. Konarskiego 18a, 44-100 Gliwice, e-mail: [krzysztof.mateja@polsl.pl](mailto:krzysztof.mateja@polsl.pl).

segments are connected to each other by connections with two or three degrees of freedom. They allow to move the mechanism, transfer mechanical forces and torque. Additional elements like grippers, cameras, and sensors are attached to the segments (GILPIN, RUS 2010, p. 38-55, BUCHAN et al. 2012, p. 4347-4354, GRANOSIK et al. 2007).

Serpentine robots are used in urban search and rescue, medicine, and defense industries (REZAEI et al. 2008, p. 191-194, TRANSETH, PETTERSEN 2006, p. 1-8, MOATTARI, BAGHARZADEH 2013, BUCHAN et al. 2012, p. 4347-4354, GRANOSIK et al. 2007, p. 633-662, BORENSTEIN, HANSEN 2007, YIM et al. 2000, p. 514-520, VAN, SHIN 2017). Snakebots gained an advantage thanks to their design. They can easily cope with long and thin spaces, e.g., pipes, ventilation ducts. Their advantage is also the flexibility of connecting individual modules. The connection of each block has several degrees of freedom, thanks to which the snakebots have good maneuverability.

In recent years, 3D printing technology has enabled rapid technological development, especially in the R&D industry (ITUARTE et al. 2016, FIAZ et al. 2019). Additive manufacturing (AM) makes it possible to verify CAD models in a short time and low cost. If necessary, you can quickly make corrections and verify the next versions of the printed elements (ITUARTE et al. 2016, FIAZ et al. 2019, Cwikla et al. 2017, AYDIN, ESNAF 2019). In robotics, you can also use 3D printing to check the correct operation of mechanisms, connections, dimensional tolerances, and fits. However, the limitations of additive technology should be considered. While some elements can be made quickly and low-cost, their mechanical strength is much lower than in the case of metals or composites (FERNANDEZ-VICENTE et al. 2015, p. 116-128, TAKAGISHI, UMEZU 2017, p. 39852, BENIAK et al. 2017, SELVAM et al. 2021).

## **CAD model**

### **Concept model**

The design works began with the development of several concepts. We assumed that the criteria of the greatest importance would be mobility, so that the snakebot would not get stuck and the rescue operation would not stop. Additionally, we took into account the stability of the robot, easy control, and the possibility of technological manufacturing of the snakebot. Snakebot consist of 3 segments. They are responsible for moving the robot forward and backward. These segments include DC motors, transmission gears, DC motor controllers, and batteries. Each module is driven by eight tracks in pairs at 90 degrees. Between the modules are connectors. They are responsible for the rotation between adjacent modules. Servos and control units are mounted in the connectors. Each connector have



two servo drives that will allow for movement in two axes. Bumpers are placed on the front and rear of the robot. In the front bumper, there is a camera and LED diodes responsible for lighting to facilitate maneuvering the snake robot in working conditions and a better view from the camera. At this stage it was also decided to print the snakebot in FDM (FFF) method. We chose that snake robot will be printed with PLA. This filament is not durable, but it is easy in print. It can be useful in case of often corrections in 3D printed models. The designed concept model (Fig. 1) allowed to start next works related to analysis of drivetrain and rotate system.

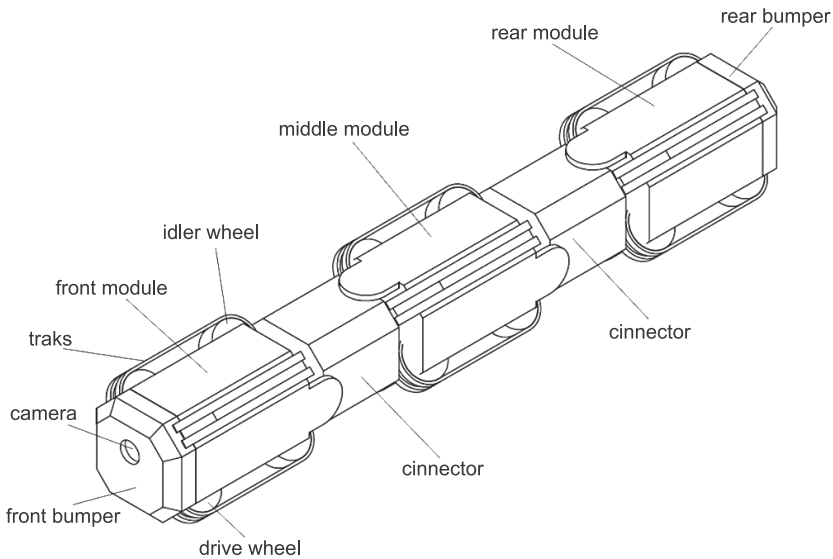


Fig. 1. Concept of snakebot construction

## Mechanical system – drive and rotate system

Drive transmission from the electric motor to the tracks is done by two gears – worm and toothed (Fig. 2). The worm gear is constructed in such a way that the torque is transmitted to all tracks thanks to the use of four worm wheels arranged perpendicular to each other (Fig. 3). The worm gear is a reducer and has a gear ratio 25: 1. Additionally, between the worm wheels and the next toothed wheels there is a ratio 1.25: 1. In total, the ratio of the gears themselves is 31.25: 1.

Servos transfer the torque to modules by 3D printed gears and shafts. Rotate system is located in two planes which are placed perpendicularly (Fig. 4). Servos should allow to lift and rotate the modules. This two types of movement ensure flexibility of snake robot and minimizes the robot getting stuck. If the robot overturns, it is still possible to maneuver it in the same way.

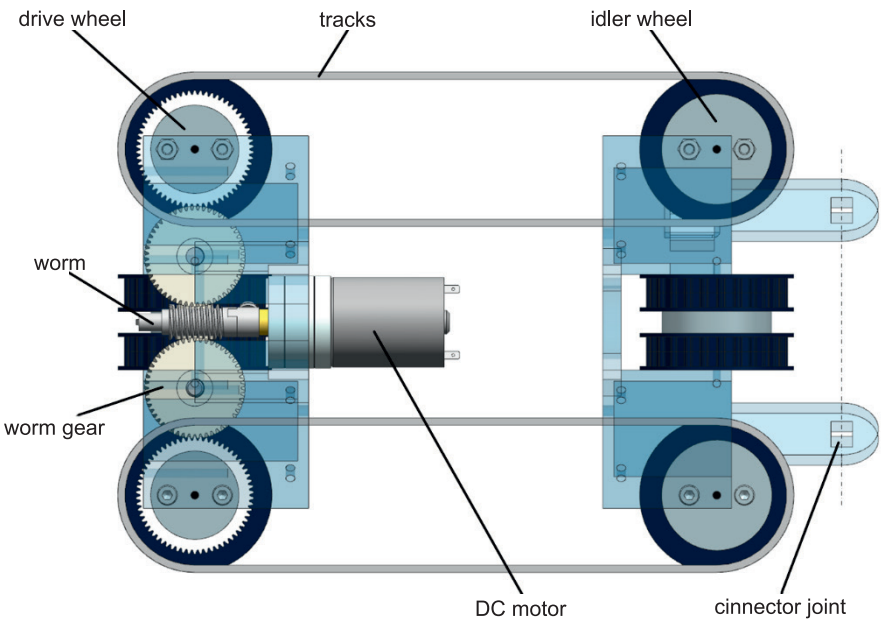


Fig. 2. Operating diagram of the drive system

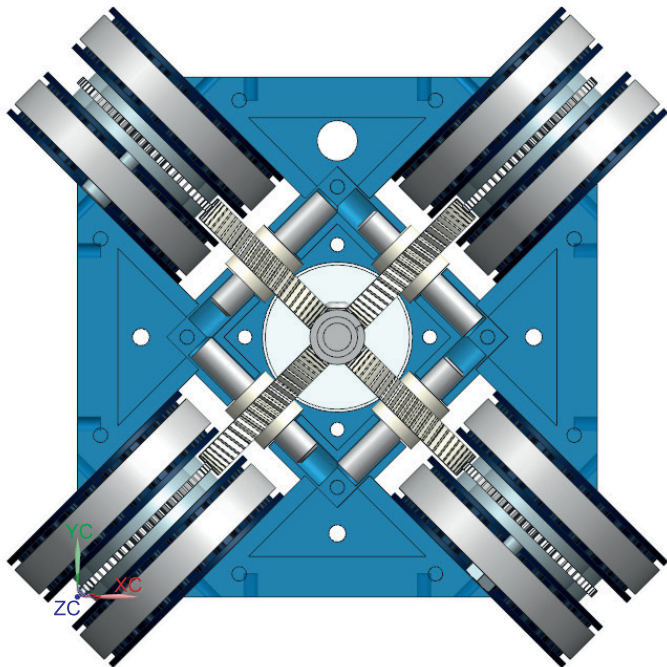


Fig. 3. Front view of the transmission gear

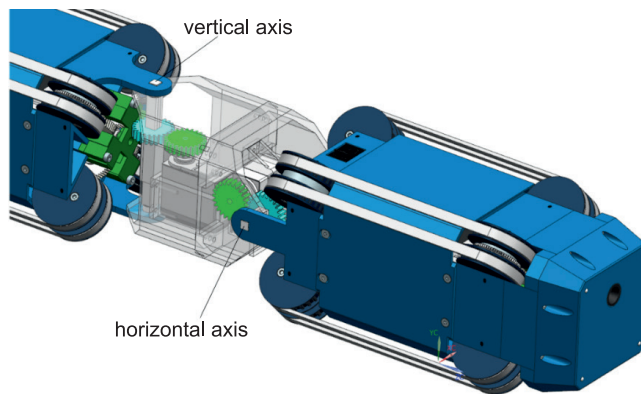


Fig. 4. CAD model of the relative rotation system of modules

## Simulation

Snakebot motion simulation allowed to select the electric motors. Dynamic analysis allowed to generate graphs (Fig. 5), so that it was possible to determine what torque must be supplied to the drive wheels. The plot is a sine wave due to the reciprocating movement determined in the dynamic analysis. Middle value that is equal 0.95 Nm is needed torque during start. Torque value decreases with increasing rotational speed and increases when the robot suddenly changes direction of drive (from forward to backward and vice versa). This change in the direction of rotation of the electric motor generates the highest torque of 1.21 Nm.

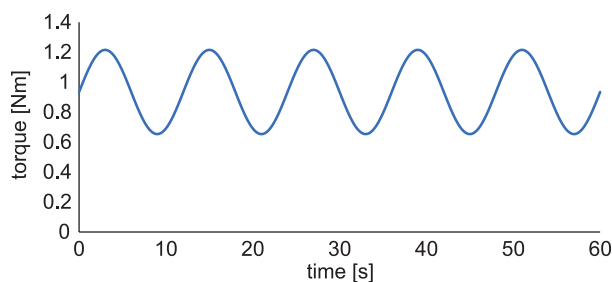


Fig. 5. Torque diagram of the longitudinal drive

After the simulation results, it was possible to select an electric motor that would provide the appropriate torque and rotational speed. We selected motors with a torque of 0.11 Nm and rotational speed 2,150 1/min. Taking into account the snakebot transmission gears, we received torque equal 3.6 Nm and RPM equal ~69 1/min. The 5 mm width tracks are driven by driving wheels with a diameter of 40 mm. It was calculated that the theoretical speed of snake robot will be 144 mm/s.

Dynamic simulation was also made to select the servos. It was necessary to carry out the analysis in two planes, because the system behaves differently in the horizontal axis (Fig. 6) and in the vertical axis. The amount of torque needed to lift the snakebot (horizontal axis) was greater than in the case of the twisting joint (vertical axis). The maximum value of the torque in the analysis was  $\sim 0.42$  Nm. We selected servo which generate torque 1 Nm and speed 0.14 s/60°.

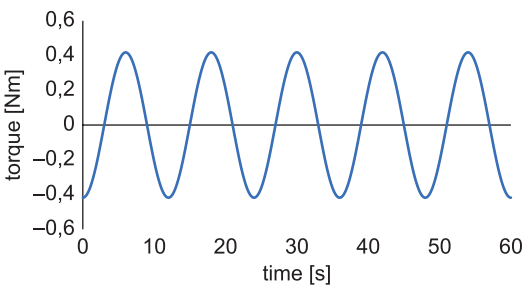


Fig. 6. Torque diagram on the horizontal axis

In the case of a snakebot built of three segments, it was enough to perform an analysis in which the servo lifts one module. Lift of the two segments would create such a torque that the snakebot would topple over.

Verification – mobility tests

Tests were divided into 3 categories. Their purpose was to check the behavior of the snake robot under the assumed operating conditions (Fig. 6). The first group of tasks was to verify how snakebot can cope with various types of ground (Tab. 1).

Table 1

The speed of the snakebot depends on the ground			
Type of surface	Rolling coefficient	Velocity [mm/s]	Remarks
Asphalt, Concrete	0.015 - 0.02	80	–
Gravel	0.05 – 0.14	$\sim 15$	the low ground clearance caused the robot to stop many times
Grass	0.06 – 0.11	–	the soft ground under the grass cause that snakebot stuck
Sand	0.15 – 0.30	–	in the sand, the robot stuck and is unable to move



Fig. 6. Snakebot tests

The second group of tasks checked the maneuverability of the robot and grip. In this test, it was checked whether the robot was able to rotate by a given angle in the vertical and horizontal axes. It was decided to build a test track, which primarily verified the operation of the joints. The developed track contained numerous obstacles that were aimed at verifying the operation of the snakebot connectors. These were, among others elements enabling the snakebot to pass in a slalom and elements verifying the lifting of the modules - small steps/stairs. The test results are presented below (Tabs. 2, 3).

Table 2

Operation of servos in the vertical axis

Angle	Turning radius [m]	Adhesion	Remarks
10°	$r = 1.78$	very good	–
20°	$r = 0.89$	very good	–
30°	$r = 0.6$	very good	–

Table 3

Operation of servos in the horizontal axis

Angle	Does the snakebot lift the main module?	Remarks
10°	–	Buckling of shafts, jump between teeth of gears
20°	–	
30°	–	

The last category of mobility tests was to verify how the snakebot will cope with the differentiation of the terrain, i.e., elevation, slope, depressions (Tab. 4). The test was carried out on a concrete surface.

Table 4

Drive system operation on an inclined surface			
Differentiation of the terrain	Does the snakebot drive?	Difficulties	Remarks
Slope 45°	–	–	one module is able to pull the other two
Slope 30°	–	–	–
Slope 15°	–	–	two modules are able to pull one additional module
Flat 0°	–	–	–
Rise 15°	–	heavy load on the drive system	–
Rise 30°	–	very heavy load on the drive system	–
Rise 45°	–	too much resistance prevented the snakebot move	–

Discussion and conclusions

Experiments related to the movement of the snakebot showed that in an environment such as rubble, the snakebot is enable to move and perform maneuvers. Tests performed in many environments have shown that the electric motors and servos were selected correctly. At the beginning of the test the only one problem was drive on the grass and sand. Snakebot was slipping on the grass and tearing out blades and was buried in the sand. The tracks performed well when had a large contact surface with the ground. The servos were able to move in the vertical axis but not in the horizontal. The reason was that resistance was so great that the teeth of the 3D printed gears jumped over each other and the shaft was bending. More problems started after using the robot for a longer time. Some 3D printed parts were more and more damaged, which resulted in dysregulation.

Additive manufacturing makes it easier to build prototypes. However, the design process should take into account the limitations of this method. For some elements, incl. bumpers, spacers, covers 3D printing is great. Other elements such as gears, shafts, wheels did not work that well especially after prolonged use. Continuous, multiple movement of these elements caused misaligned of them. The result was a backlash between the gears, damaged wheels or buckled shafts.



In subsequent prototypes we can change the design of 3D models by changing the cross-section or by using different material. PLA or ABS are much less durable than aluminum or steel. However, they gain an advantage thanks to their low density. In the urban search and rescue, replacing the metal or polymer elements with composite elements e.g., carbon or aramid fiber, can be a solution. Smooth move of snake robot we can increase by using wider tracks and by changing the material of the tracks. In the prototype we used neoprene tracks. It caused skidding and low coefficient of friction with the ground. We should try to reduce the weight of the snake robot by using lighter batteries and DC motors. However, we have to provide the right torque, RPM, voltage, and power.

## References

- ARACHCHIGE D., CHEN Y., GODAGE I. 2020. *Modeling and Validation of Soft Robotic Snake Locomotion*. Project: Soft Robotic Snakes, Lab: Robotics and Medical Engineering Laboratory, DePaul University.
- AYDIN H., ESNAF S. 2019. *Making Assembly Guides for Self-Assembly Products Three-Dimensional with Additive Manufacturing*. Conference: 10<sup>th</sup> International Symposium on Intelligent Manufacturing and Service Systems, IMSS 2019, Sakarya, Turkey.
- BENIAK J., KRIŽAN P., ŠOOŠ ŠOOŠ L.L., MATÚŠ M. 2017. *Roughness and compressive strength of FDM 3D printed specimens affected by acetone vapour treatment*. IOP Conference Series Materials Science and Engineering, 297(1): 012018.
- BORENSTEIN J., HANSEN M. 2007. *OmniTread OT-4serpentine robot: new features and experiments*. Defense and Security Symposium, Orlando, FL, 9–13 April.
- CWIKLA G., GRABOWIK C., KALINOWSKI K., PAPROCKA I., OCIEPKA P. 2017. *The influence of printing parameters on selected mechanical properties of FDM/FFF 3D-printed parts*. IOP Conference Series Materials Science and Engineering, 227(1): 012033. <http://doi.org/10.1088/1757-899X/227/1/012033>.
- FERNANDEZ-VICENTE M., CANYADA M., CONEJERO A. 2015. *Identifying limitations for design for manufacturing with desktop FFF 3D printers*. International Journal of Rapid Manufacturing, 5: 116–128.
- FAIZ M., IKRAM A., SALEEM A., ZAHRA A. 2019. *Role of 3D Printers Industry in Strengthening R&D Collaboration between Academia and Industry*. The Dialogue, XIV(3).
- FU Q., LI C. 2020. *Robotic modelling of snake traversing large, smooth obstacles reveals stability benefits of body compliance*. Royal Society Open Science, 7(2). <http://doi.org/10.1098/rsos.191192>.
- GILPIN K., RUS D. 2010. *Modular robot systems*. IEEE Robotics & Automation Magazine, 17(3): 38–55. <http://doi.org/10.1109/MRA.2010.937859>.
- GRANOSIK G., BORENSTEIN J., HANSEN M.G. 2007. *Serpentine Robots for Industrial Inspection and Surveillance*. Industrial Robotics – Programming, Simulation and Applications, February, p. 633–662.
- ITUARTE I.F., HUOTILAINEN E., MOHITE A., CHEKUROV S., SALMI M., HELLE J., WANG M., KUKKO K., BJÖRKSTRAND R., TUOMI J., PARTANEN J. 2016. *3D printing and applications: academic research through case studies in Finland*. Conference NordDesign - Engineering Design Society.
- MOATTARI M., BAGHARZADEH, M.A. 2013. *Flexible snake robot: Design and implementation*. AI & Robotics and 5<sup>th</sup> RoboCup Iran Open International Symposium (RIOS).
- REZAEI A., SHEKOFTEH Y., KAMRANI M. 2008. *Design and Control of a Snake Robot according to Snake Anatomy*. Proceedings of the International Conference on Computer and Communication Engineering, 2008 May 13–15, Kuala Lumpur, Malaysia, p. 191–194.

- SELVAM A., MAYILSWAMY S., WHENISH R., VELU R., SUBRAMANIAN B. 2021. *Preparation and Evaluation of the Tensile Characteristics of Carbon Fiber Rod Reinforced 3D Printed Thermoplastic Composites*. Journal of Composites Science, 5(1): 8.
- TAKAGISHI K., UMEZU S. 2017. *Development of the Improving Process for the 3D Printed Structure*. Scientific Reports, 7: 39852.
- TRANSETH A.A., PETTERSEN K.Y. 2006. *Developments in snake robot modeling and locomotion*. 9<sup>th</sup> International Conference on Control, Automation, Robotics and Vision, IEEE, p. 1–8.
- VAN L.T., SHIN S.Y. 2017. *Study on Snake Robot Design for Investigating Rough Terrain*. 7<sup>th</sup> International Workshop on Industrial IT Convergence (WIITC 2017).
- VIRGALA I., KELEMEN M., PRADA E., SUKOP M., KOT T., BOBOVSKÝ Z., VARGA M., FERENČÍK P. 2021. *A snake robot for locomotion in a pipe using trapezium-like travelling wave*. Mechanism and Machine Theory, 158(1): 104221.
- WRIGHT C., BUCHAN A., BROWN B., GEIST J., SCHWERIN M., ROLLINSON D., TESCH M., CHOSSET H. 2012. *Design and architecture of the unified modular snake robot*. IEEE International Conference on Robotics and Automation, p. 4347–4354.
- YIM M., DUFF D., ROUFAS K. 2000. *Polybot: a modular reconfigurable robot*. Millennium Conference, IEEE International Conference on Robotics and Automation. Symposia Proceedings, 1. IEEE, p. 514–520.





## ANALYSIS OF A METHOD FOR MEASURING DEPOSIT IMPEDANCE PARAMETERS USING CHARGE AMPLIFIER AND LOCK-IN VOLTMETER

*Dariusz Wiśniewski*

ORCID: 0000-0001-8909-3159

Department of Electrical Engineering, Power Engineering, Electronics and Automation  
University of Warmia and Mazury

Received 18 January 2021, accepted 10 August 2021, available online 13 August 2021.

**Key words:** impedance, conductivity, moisture content, deposit, charge amplifier, lock-in voltmeter.

### Abstract

Methods for measuring deposit parameters are often based on a capacitance or conductivity measurement aimed at estimating, e.g. deposit moisture content. In practice, these methods fail for materials with a low degree of homogeneity, a diverse porous structure or high conductivity, e.g. due to a high water content. This article demonstrates an approach that enables a more precise estimation of the parameters of any deposit. The presented method involves the use of a measuring system in a charge amplifier configuration and the application of a technique using lock-in detection or a lock-in voltmeter to determine resistance and capacitance parameters of a deposit based on signals received from the measuring system. This method can be successfully used wherever the test deposit material is highly heterogeneous and contains both dielectric and conductive materials. The article presents an example of a solution to a measuring system using two planar electrodes that can be dimensioned depending on the deposit dimensions. It is followed by a presentation of a method for converting the signal from the measuring system into impedance parameters of the deposit using a lock-in voltmeter. The analysis of the operation of the entire measuring system was modelled in Matlab/Simulink, and the operation results were presented.

## Method for measuring deposit parameters

In this paper, methods for measuring deposit parameters are to be understood as electrical quantities that characterise a deposit, such as conductivity and capacitance. These quantities are often used for indirect measurement of other parameters, e.g. deposit material moisture content or bulk density or for spatial imaging.

A study by (FUCHS et al. 2008, TAN et al. 2017) presents a measurement of solid material deposit capacitance parameters taken to determine the moisture content. The measuring element applied was a sensor in the form of two planar electrodes. The test materials were pellets, homogeneously structured powders and plant materials. A different approach is presented in a study by (TAN et al. 2017), which examined the possibility for the use of deposit capacitance parameters to approximately determine the bulk density of miscanthus. In addition, the effects of the moisture content and particle size on the measurement results were investigated. An interesting application of capacitance parameters of a deposit is presented in a study by (AULEN, SHIPLEY 2012), where deposit capacitance parameters within the nanofarad range were used to assess the root system of crop plants.

Methods for measuring the impedance parameters of a deposit are also used in imaging techniques, e.g. electrical capacitance tomography (ECT) or electrical impedance tomography (EIT). Work in this area was performed in a study by WEGLEITER (2006). Capacitance tomography is also used in medical sciences. AMBIKA et al. (2019) used capacitance tomography to analyse bone density.



Fig. 1. An example of a deposit with a porous, heterogeneous structure

Capacitance tomography systems using methods which also enable impedance measurements were also demonstrated in a study by SMOLIK (2017). The methods presented in the study is based on the application of a lock-in amplifier as a method for measuring very low capacitances of the fF fraction order as well as impedance through the application of an additional reference signal.

This paper will focus on deposit material in the form of a thick, porous layer with a heterogeneous structure characterised by a significant gradient of moisture content changes in space. An example of such a deposit is presented in Figure 1.

## Theoretical introduction

The method for measuring impedance parameters is based on the measurement of electrical conductivity and the capacitance of a deposit. It is assumed that the deposit will be placed in a reactor equipped with two parallelly arranged planar electrodes with a thin galvanic isolation layer. The system obtained in this way will be characterised by a certain capacitance of the order of single pF in the absence of a deposit and of the order of a maximum of several tens of pF in the presence of a very moist material. Conductivity between the electrodes will be strongly determined by the moisture content of the material placed between the electrodes. It was also assumed that the planar electrode surfaces had dimensions ensuring that electric field lines would penetrate through the largest possible cross-section of the deposit, which is aimed at ensuring the measurement of parameters for the largest possible volume of the test sample. Based on assumptions thus defined, the test system can be presented in the form of a planar loss capacitor with electrode surfaces  $S$  and the distance between them  $d$ . The system described in this way can be presented schematically, as in Figure 2.

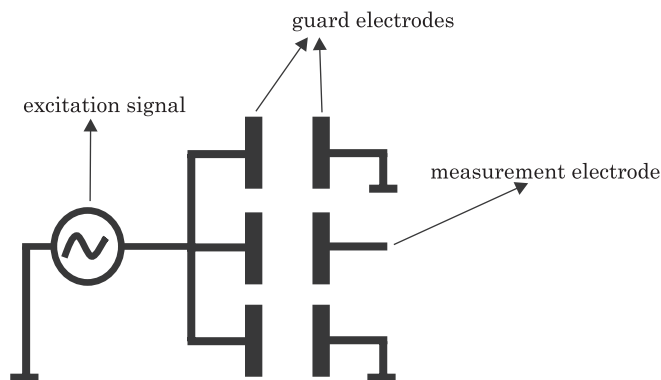


Fig. 2. A diagram of electrical connections of guard and measurement electrodes that neutralise field distortions

If there is air between the plates, the capacitor capacitance is described by the following relationship:

$$C = \frac{\varepsilon_o \varepsilon_r S}{d} = 8.854 \cdot 10^{-12} \frac{\varepsilon_r A}{d} \quad (1)$$

where:

$\varepsilon_o$  – vacuum dielectric constant of  $8.854 \cdot 10^{-12} \frac{\text{F}}{\text{m}}$ ,  
 $\varepsilon_r$  – relative dielectric constant,  
 $S$  – electrode surface [ $\text{m}^2$ ],  
 $d$  – distance between electrodes [m].

The relative dielectric constant for the air is 1.0006. Typical dielectric materials, e.g. plastic or oil, are characterised by a time-constant ranging from 3 to 10, while for polar fluids, e.g. water, the time-constant is 50 and more, depending on the temperature. Figure 3 presents the distribution of field force lines for a planar capacitor.

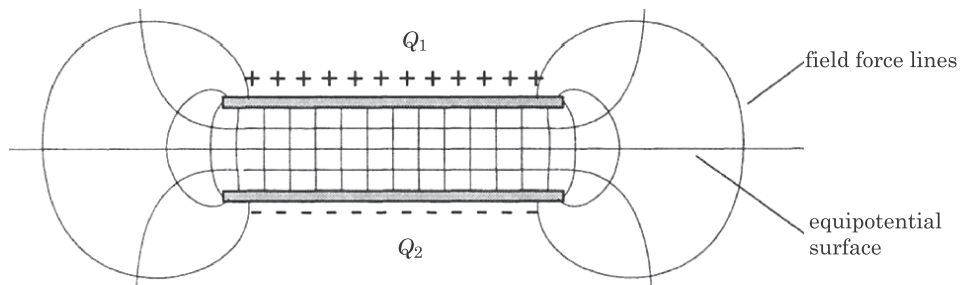


Fig. 3. Planar capacitor's field force lines  
 Source: based on BAXTER (1997).

Where the distances  $d$  for the electrodes are significant in relation to each other, in relation to plane A, the field lines at the planar capacitor electrode edges are arranged in semi-circles. This is such a strong phenomenon that formula (1) is only valid for small distances  $d$  between electrodes, such that the field lines are perpendicular to the electrode surfaces. For example, where the plates with a surface  $S = 1 \text{ m}^2$  are separated by a distance  $d = 1 \text{ mm}$ , the planar capacitor capacitance is 88.54 pF, and is consistent with expression (1). Where the distance between electrodes is considerable, the so-called edge fields (which are not perpendicular in relation to the electrodes' internal surface) are formed at the electrode edges. Therefore, the capacitance between the electrodes can be considerably greater than that determined using formula (1). Figure 4 presents a distorted arrangement of the field lines at the electrode edges and a way to counteract this phenomenon.

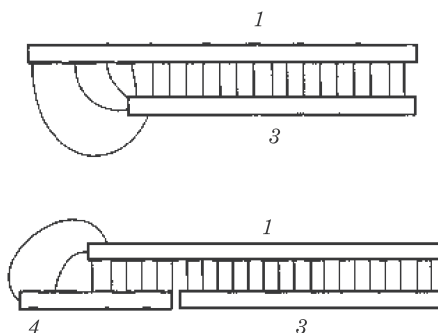


Fig. 4. The distribution of field lines at the electrode edges:

1, 3 – measurement electrode, 4 – guard electrode

Source: based on LARRY (1997).

The introduction of guard electrodes counteracts this phenomenon and brings the distorted field lines at the edges to the ground potential. Thanks to this solution, the distorted fields at the edges are insignificant for the measurement, and only the field lines that are perpendicular to the electrode plane play a role. Because of the application of guard electrodes, the distorted field lines generate a capacitance that is connected to the ground potential. Figure 2 presents an electrical diagram of connections that eliminates the impact of field distortions at the electrode edges on the measurement result.

The use of guard electrodes enables increasing the distance  $d$  of guard electrodes to a size allowing a porous deposit to be placed between the electrodes.

## Measuring system

The system for measuring impedance parameters of a deposit needs to exhibit characteristics that will ensure the measurement of small values of the physical parameters between the measurement electrodes. It should be stressed that parasitic capacitances of the measuring circuits can be greater than the capacitance between the electrodes by an order of magnitude. The study adopted an electrode model using a loss capacitor with capacitance  $C$  and parallel resistance  $R_p$ . The electrode circuit model is shown in Figure 5.

For dielectrics such as plastics or ceramics, the loss factor  $D$  is relatively constant with an increase in frequency. On the other hand, for water, the loss factor  $D$  changes 4-fold with a change in frequency from 100 kHz to 1 MHz at a constant temperature of 25°C. Measurement of parameters for water below 100 kHz is difficult as the loss angle  $\delta$  is almost 90°. At 100 kHz, the loss factor  $D$  amounts to 4, which means that the impedance angle is 76°, and the resistive element has a much lower impedance than that of the reactance element.

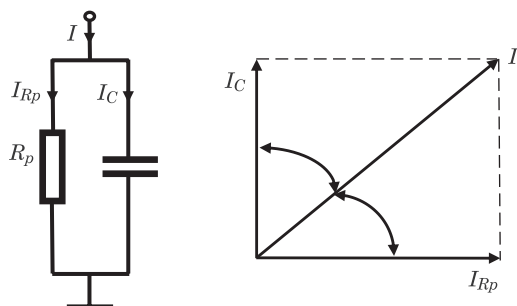


Fig. 5. A model of the measurement electrode circuit as a loss capacitor with capacitance  $C$  and loss resistance  $R_p$ . Phasor diagram of currents for the circuit

Figure 6 presents a diagram of changes in the relative permittivity  $\epsilon_r$  and the dielectric loss factor  $D$  for water as a function of temperature for a frequency of 1 MHz (LARRY 1997).

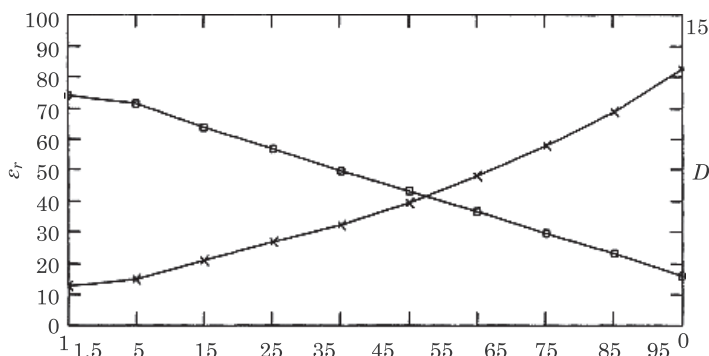


Fig. 6. A diagram of changes in the relative permittivity and the dielectric loss factor  $D$  for water as a function of temperature for a frequency of 1 MHz  
Source: based on LARRY (1997).

Figure 7 shows that for materials containing water, the loss factor  $D$  is a more sensitive indicator than the relative permittivity  $\epsilon_r$ . A change in water temperature from 15 to 75°C results in a 3-fold increase in the loss factor and a 2.5-fold decrease in the dielectric constant.

The design of the measuring system assumes the use of a two-electrode measuring element that will be subjected to sinusoidal excitations in order to obtain the best possible signal-to-noise ratio (ROFEE 1997). A basic diagram of the measuring transducer circuit is presented in Figure 8.

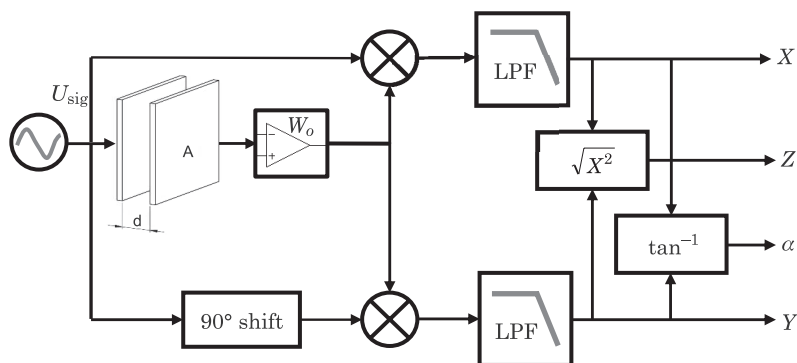


Fig. 7. Block diagram of the lock-in voltmeter circuit:  $X$  – real component,  $Y$  – imaginary component,  $Z$  – module,  $\alpha$  – phase shift

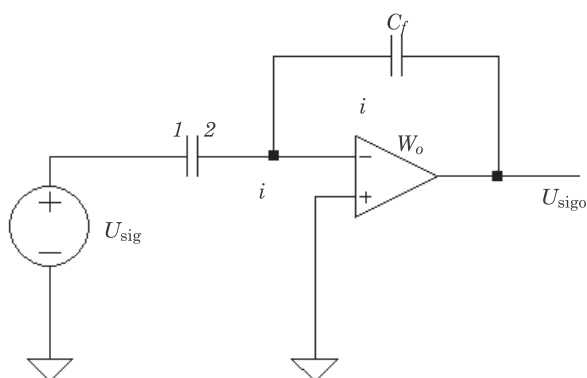


Fig. 8. Diagram of the measuring transducer circuit:  
1 – excitation electrode, 2 – detection electrode

The basis measuring system comprises two planar electrodes #1 and #2, a source of a sinusoidal signal with low impedance, and an operational amplifier operating in an inverting configuration with capacitive feedback  $C_f$ . An excitation signal in the form of a sinusoidal wave is delivered to electrode #1

$$U_{\text{sig}} = U_a \sin(\omega_{\text{sig}} t) \quad (2)$$

while electrode #2 serves as a detection electrode. The signal in the form of an electric charge  $Q$  will be received from the detection probe and converted into a value proportional to charge  $Q_x$  transferred between the electrodes. The presented configuration is known in the literature as a charge amplifier and is widely used in applications in which the output signal is proportional to the electric charge. The relationship between the excitation signal and the output signal from the charge amplifier is described by the following relationship:

$$U_{\text{signo}} = -\frac{C_x}{C_f} \cdot U_{\text{sig}} \quad (3)$$

where:

- $C_x$  – capacitance between the plates of electrodes #1 and #2 in [F],
- $C_f$  – capacitance of the charge amplifier feedback capacitor in [F],
- $U_{\text{sig}}$  – sinusoidal excitation signal,
- $U_{\text{signo}}$  – sinusoidal output signal of the measuring transducer.

It follows from expression (3) that it is possible to easily determine the unknown capacitance  $C_x$  based on the parameters of the input signal, output signal and the known feedback capacitance  $C_f$ . The solution presented above is suitable for materials for which the conductivity between electrodes is negligibly low, i.e. of the order of  $\mu\text{S}$ . For conductive material, e.g. contaminated water, the situation changes, and conductivity has a greater influence on changes in the deposit impedance. Thus, a measuring transducer circuit in the form presented in Figure 9 is obtained.

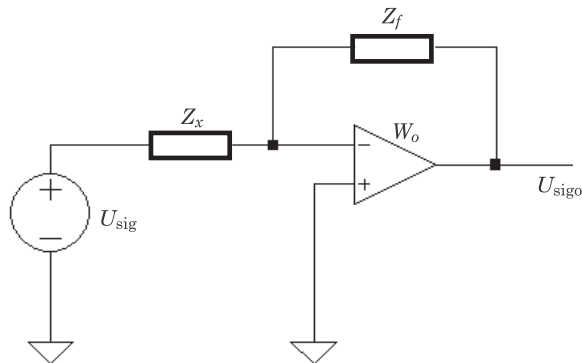


Fig. 9. A diagram of the measuring transducer circuit with a measurement electrode impedance model:  $Z_x$  – impedance of measurement electrodes, dependent on the deposit parameters,  $Z_f$  – feedback impedance of the operational amplifier

The transducer model shown in the figure can be described using equations in the complex form:

$$\underline{U}_{\text{signo}} = \frac{Z_x}{Z_f} \underline{U}_{\text{sig}} \quad (4)$$

where:

- $Z_f$  – feedback impedance,
- $Z_x$  – sought impedance of measurement electrodes,
- $U_{\text{sig}}$  – sinusoidal excitation signal,
- $U_{\text{signo}}$  – sinusoidal output signal of the measuring transducer.



It follows from equation (4) that the determination of unknown impedance  $Z_x$  requires knowledge of the parameters of the input signal, output signal, and the phase shift between these signals. The parameters of the input signal in relation to the output signal can be determined by the application of a lock-in voltmeter (SAIED 2016). The principle of operation of a lock-in voltmeter is shown in Figure 7. Excitation signal in the form of a sinusoidal wave:

$$U_{\text{sig}} = U_a \cdot \sin(\omega_{\text{sig}}t + \theta_{\text{sig}}) \quad (5)$$

where:

$U_a$  – excitation signal amplitude,  
 $\omega_{\text{sig}}$  – excitation signal angular frequency,  
 $\theta_{\text{sig}}$  – excitation signal phase shift,  
 is introduced onto excitation electrode #1.

In accordance with the linear system theory, a signal with the same frequency  $\omega_{\text{sig}}$  but with a changed amplitude  $U_{ao}$  and the angular shift of  $a$  will be obtained on detection electrode #2.

$$U_{\text{sigo}} = U_{ao} \cdot \sin(\omega_{\text{sig}}t + \theta_{\text{sig}} + a) \quad (6)$$

On the other hand, signals representing the real component  $X$ , imaginary component  $Y$ , module  $|Z|$ , and phase shift  $a$  will be obtained at the output of the lock-in voltmeter:

$$X = |Z|\cos(a) \quad (7)$$

$$Y = |Z|\sin(a) \quad (8)$$

$$|Z| = \frac{1}{2}U_a \cdot U_{ao} \quad (9)$$

$$a = \tan^{-1} \frac{Y}{X} \quad (10)$$

Based on the quantities obtained from the lock-in voltmeter and relationship (4), it is possible to determine the parameters of the sought impedance  $Z_x$ . Following the substitutions and conversions, the sought  $Z_x$  and its components are described with the following relationships:

$$\underline{Z}_x = \underline{Z}_f \frac{U_{\text{sig}}}{U_{\text{sigo}}} = |Z_f|e^{j\varphi_f} \cdot \left| \frac{U_a}{U_{ao}} \right| e^{-ja} \quad (11)$$

where:

$$U_{ao} = \frac{2 \cdot |Z|}{U_a} \quad (12)$$

$$\text{Re}\{Z_x\} = |Z_f| \cdot \left| \frac{U_a}{U_{ao}} \right| \cos(\varphi_f - a) = |Z| \cos(\varphi_f - a) \quad (13)$$

$$\text{Im}\{Z_x\} = |Z_f| \cdot \left| \frac{U_a}{U_{ao}} \right| \sin(\varphi_f - a) = |Z| \sin(\varphi_f - a) \quad (14)$$

$$X_{cx} = \sqrt{|Z|^2 \left( 1 + \frac{1}{\text{tg}(\varphi_f - a)^2} \right)} \quad (15)$$

$$R_x = X_{cx} \cdot \text{tg}(\varphi_f - a) \quad (16)$$

$$C_x = \frac{1}{\omega_{\text{sig}} X_{cx}} \quad (17)$$

## Simulation model

Based on the analysis of the measuring system using a charge amplifier, and the analysis of lock-in voltmeter operation, a simulation model was constructed. The simulation model of the system was realised assuming ideal properties of the operational amplifier, i.e. an infinitely high gain in an open feedback loop, infinitely high input impedance, and infinitely wide transfer band. With these assumptions, equations 4 are true. A diagram of the model realised in Matlab/Simulink is presented in Figure 10.

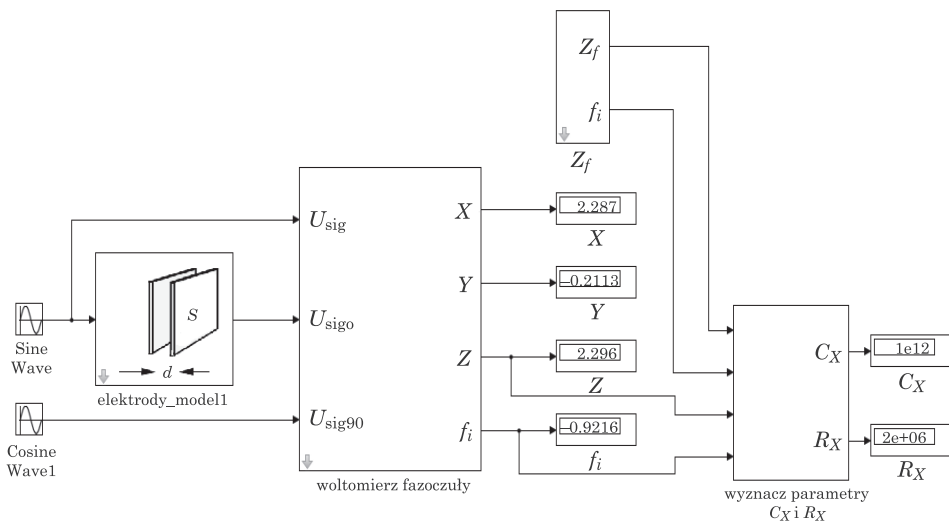


Fig. 10. A simulation model of the deposit impedance parameter measuring system

The simulation model comprises three independent blocks. The first block is responsible for simulations of the behaviour of measurement electrodes along with measuring transducer in accordance with equation (4) and the electrode model in the form of a loss capacitor with impedance  $Z_x$ . The second block simulates the operation of a lock-in voltmeter. In this block, synchronous detection and low-pass filtration occur, and the signal parameters in relation to the reference signal are then determined. The sinusoidal signal described by equation (5), which, at the same time, is the excitation signal of measurement electrode #1, was used as the reference signal. In a system with a single reference signal, it is possible to determine the amplitude  $U_{ao}$  of the test signal, which is received from measurement electrode #2. The determination of the phase shift between the reference signal and the test signal from detection electrode #2 requires the use of an additional reference signal phase-shifted by  $90^\circ$ . As a result of lock-in detection and the separation of the constant component using a third-order Butterworth low-pass filter with the corner frequency of 10 kHz, the parameters  $X$ ,  $Y$ ,  $|Z|$  and  $a$  are obtained. The third block is used to determine impedance parameters of the test deposit according to equations (12)-(16).

Simulation testing was conducted for feedback parameters  $C_f = 22$  pF and  $R_f = 220$  k $\Omega$ . In practice, the feedback parameters should be set to the expected variability of the deposit parameters in order to obtain flat amplification characteristics over a wide frequency range. Figure 11 shows an example of the characteristics of the shift of a measuring transducer with ideal WO for the parameters shown in Table 1. It follows from the characteristics provided in Figure 11 that for the assumed feedback parameters, it is possible to obtain 3 dB a transfer band from a frequency of 200 krad/s.

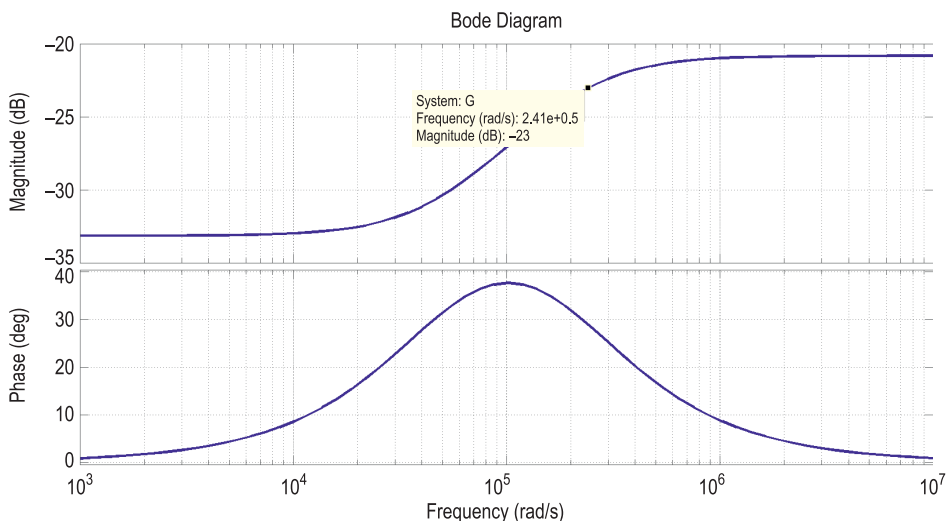


Fig. 11. Characteristics of the transfer of measuring transducer with ideal WO

Figure 12 shows a spectral analysis of the signal after the mixing of the signal received from the detection electrode with the reference signal. The spectrum has two characteristic peaks: the first one for the constant component, the second for the doubled frequency  $2 \cdot \omega_{\text{sig}}$  of the excitation signal  $U_{\text{sig}}$ .

Table 1

Examples of feedback parameters $Z_f$ of the operational amplifier		
Parameter	$R_f$ [M $\Omega$ ]	$C_f$ [pF]
Value	0.22	22

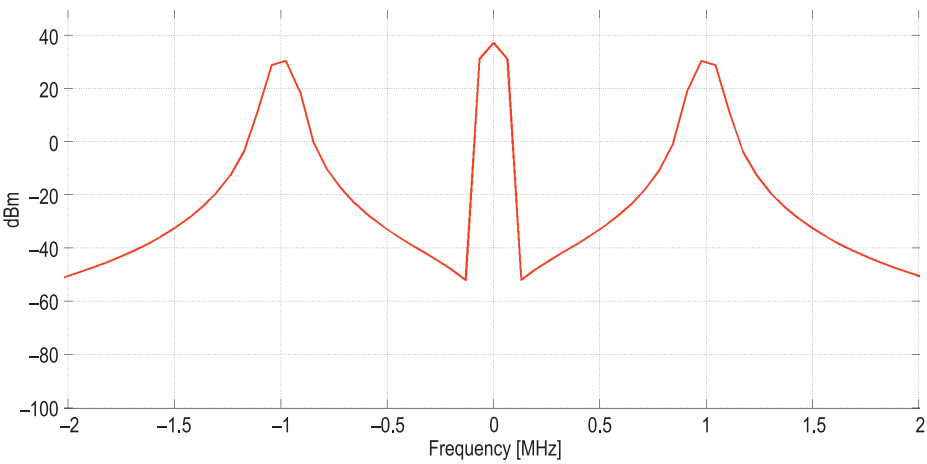


Fig. 12. The spectrum of the signal following the operation of multiplying the reference signal  $U_{\text{sig}}$  and the measurement signal  $U_{\text{sigo}}$

The results of simulation testing of the system for measuring deposit parameters are presented in Tables 2 and 3. The simulation testing was conducted by setting capacitance  $C_x$  and resistance  $R_x$  that model the measurement electrodes, followed by simulations of the system with the parameters set.

Table 2

Examples of simulation results for the deposit impedance parameter measuring system at constant $R_x=10$ M $\Omega$ and the values of feedback elements $C_f=22$ pF, $R_f=220$ K $\Omega$				
Set value $C_x$ [pF]	1	10	30	50
Determined value $C_x'$ [pF]	1	10	30	50

Table 3

Examples of simulation results for the deposit impedance parameter measuring system at constant  $C_x=1$  pF and the values of feedback elements  $C_f=22$  pF,  $R_f=220$  K $\Omega$

Set value $R_x$ [M $\Omega$ ]	0.1	1	100	1000
Determined value $R_x'$ [M $\Omega$ ]	0.1	1	99.92	991.7

The obtained simulation data presented for the feedback values  $C_f=22$  pF and  $R_f=220$  K $\Omega$  ensure full compliance with the parameters set. Sensitivity  $S_x$  to a change in the charge between the electrodes of the testes measuring transducer is determined by feedback capacitance  $C_f$ . This is due to the fact that charge  $Q_x$  accumulated on measurement electrodes #1 and #2 is presented by the following expression:

$$Q_x = C_x \cdot U_{\text{sig}} \quad (18)$$

and, from relationships (3) and (18), sensitivity  $S_x$  to a change in the charge on measurement electrodes #1 and #2 amounts to:

$$S_x = \frac{U_{\text{sigo}}}{Q_x} = \frac{1}{C_f} = \frac{1}{22 \cdot 10^{-12}} = 0.0455 \left[ \frac{\text{mV}}{\text{fC}} \right] \quad (19)$$

It is also possible to determine sensitivity  $S_c$  to a change in capacitance between the measuring transducer electrodes from equation (3). Assuming the excitation voltage amplitude  $U_a=10$  V, the following capacitance sensitivity is obtained:

$$S_c = \frac{U_{\text{sigo}}}{C_x} = \frac{U_{\text{sig}}}{C_f} = \frac{10 [\text{V}]}{22 \cdot 10^{-12} [\text{F}]} = 0.455 \left[ \frac{\text{mV}}{\text{fF}} \right] \quad (20)$$

Obviously, the signal from the measuring transducer requires further amplification in real measuring systems, although this is not required for simulation purposes

## Conclusions

The method for measuring impedance parameters of a deposit using a charge amplifier and a lock-in voltmeter allows very high accuracy to be achieved. The results of the simulation model testing lead to the conclusion that accuracy is limited only and exclusively by the accuracy of numerical methods of simulation programs. This is due to the fact that the process of determining impedance parameters in a numerical manner results directly from algebraic equations (7)-(17). A properly selected low-pass filter, which separates the constant component

from the variable component, which has a frequency twice as high as that of the excitation signal, guarantees accuracy arising directly from the numerical accuracy of algebraic transformations. The presented method ensures the certainty of the results obtained through simulation, but the situation is different as regards practical implementations. In practice, the process of detection from the detection electrode is affected by the influence of many interfering quantities, mainly in the form of parasitic capacitances of connections. These quantities are often higher by an order of magnitude than those being measured. Proper design of measuring circuits, shielding from external fields and proper design of guard electrodes will eliminate or significantly reduce their impact on the measurement process. As demonstrated using the examples of measuring transducer parameter values from relationship (20), it is possible to detect changes in capacitance on measurement electrodes of the femtofarad order. Methods using lock-in voltmeters are, due to their properties, often employed in many technical solutions, *inter alia* in capacitance tomography systems. The use of this method for measuring deposit impedance parameters will allow high accuracy to be achieved over a wide range of parameter changes. The practical implementation of a measuring system requires the preparation of measurement electrodes and their shielding and the selection of suitable electronic systems that ensure appropriate operation frequencies. The practical implementation can be carried out entirely using an analogue technique or partly using a digital technique.

## References

- AMBIKA M., MANIKANDAN K., PADMANABAN R. 2019. *Design and Fabrication of Electrical Capacitance Tomography Sensor with Signal Conditioning*. Biomed Research Journal BMRJ, 3(2): 79-85.
- BAXTER L. 1997. *Capacitive Sensors. Design and Applications*. IEEE Press Series on Electronics Technology. Robert J. Herrick, Series Editor.
- Characteristic and use charge amplifier. 2001. Technical information SD-37. Hamamatsu.
- FUCHS A., ZANGL H., HOLLER G. 2008. *Capacitance-Based Sensing of Material Moisture in Bulk Solids: Applications and Restrictions*. Lecture Notes in Electrical Engineering, 20: 235-248.
- KHOSHBAKHT M., LIN M. 2006. *Development of an electrical time domain reflectometry (ETDR) distributed moisture measurement technique for porous media*. Measurement Science and Technology, 17(11): 2989.
- KRASZEWSKI A., TRABELSI S., NELSON S. 1999. *Moisture content determination in grain by measuring microwave parameters*. Measurement Science and Technology, 8(8): 857. DOI:10.1088/0957-0233/8/8/004.
- MAURICE A., SHIPLEY B. 2012. *Non-destructive estimation of root mass using electrical capacitance on ten herbaceous species*. Plant and Soil, 355(1-2): 41-49. DOI:10.1007/s11104-011-1077-3.
- ROFFE J. 1997. *A high-sensitivity flexible – excitation electrical capacitance tomography system*. Institute of Science and Technology, Manchester.
- SAIED I., MERIBOUT M. 2016. *Electronic hardware design of electrical capacitance tomography systems*. In: *Philosophical Transactions of The Royal Society A Mathematical Physical and Engineering Sciences*. Royal Society. DOI: <https://doi.org/10.1098/rsta.2015.0331>.

- SMOLIK W., KRYSZYN J., OLSZEWSKI T., SZABATIN R. 2017. *Methods of small capacitance measurement in electrical capacitance tomography*. Informatyka, Automatyka, Pomiary w Gospodarce i Ochronie Środowiska, 7(1): 105-110.
- TAN Y., MIAO Z., ABDUL M., GRIFT T., TING K. 2017. *Electrical capacitance as a proxy measurement of miscanthus bulk density, and the influence of moisture content and particle size*. Computers and Electronics in Agriculture, 134: 102–108.
- TOMKIEWICZ D. 2009. *Budowa i działanie czujnika wilgotności ziarna zboża wykorzystującego promieniowanie w zakresie bliskiej podczerwieni*. Inżynieria Rolnicza, 6(115).
- WEGLEITER H. 2006. *Low-Z Carrier Frequency Front-End for Electrical Capacitance Tomography Applications*. Dissertation. Graz University of Technology, Austria.
- WOBSCHALL D., LAKSHMANAN D. 2005. *Wireless soil moisture sensor based on fringing capacitance*. Proc. of IEEE Sensors, p. 8–11.
- WYPYCH P. 2001. *Dilute-phase pneumatic conveying problems and solutions*. In: *Handbook of Conveying and Handling of Particulate Solids*. Eds. A. Levy, H. Kalman. Elsevier Science, Amsterdam, p. 303–318.
- YANG W.Q. 1996. *Hardware design of electrical capacitance tomography systems*. Meas. Sci. Technol., 7: 225–232.
- YANG W.Q., STOTT A.L., BECK M.S., XIE C.G. 1995. *Development of capacitance tomographic imaging systems for oil pipeline measurements*. Rev. Sci. Instrum., 66: 4326–4332.
- YANG W.Q., YORK T.A. 1999. *New AC – based capacitance tomography system*. IEE Proc-Sci. Measurement Technology, 146(1): 47–53.







## THE USE OF THE INVERSE PROBLEM METHODOLOGY IN ANALYSIS OF FLUID FLOW THROUGH GRANULAR BEDS WITH NON-UNIFORM GRAIN SIZES

*Wojciech Sobieski*<sup>1</sup>, *Anna Trykozko*<sup>2</sup>

<sup>1</sup>ORCID: 0000-0003-1434-5520

Department of Mechanical Engineering and Fundamentals of Machine Design  
University of Warmia and Mazury

<sup>2</sup>ORCID: 0000-0002-0674-7944

Interdisciplinary Center for Mathematical and Computational Modeling  
University of Warsaw

Received 19 May 2021, accepted 9 August 2021, available online 13 August 2021.

**Key words:** granular media, reverse problem, Darcy, Forchheimer.

### Abstract

The pressure drop during water flow through two gravel beds with 2-8 and 8-16 [mm] grain size was measured across a wide range of filtration velocities, and the optimal method for calculating the coefficients for Darcy's law and Forchheimer's law was selected. The laws and the experimental data were used to develop a computational program based on the Finite Element Method (FEM). The results were compared, and errors were analyzed to determine which law better describes flow data. Various methods of measuring porosity and average grain diameter, representative of the sample, were analyzed. The data were used to determine the limits of applicability of both laws. The study was motivated by the observation that computational formulas in the literature produce results that differ by several orders of magnitude, which significantly compromises their applicability. The present study is a continuation of our previous research into artificial granular materials with similarly sized particles. In our previous work, the results produced by analytical and numerical models were highly consistent with the experimental data. The aim of this study was to determine whether the inverse problem methodology can deliver equally reliable results in natural materials composed of large particles. The experimental data were presented in detail to facilitate the replication, reproduction and verification of all analyses and calculations.

Correspondence: Wojciech Sobieski, Katedra Mechaniki i Podstaw Konstrukcji Maszyn, Uniwersytet Warmińsko-Mazurski, 10-736 Olsztyn, ul. Oczapowskiego 11, e-mail: wojciech.sobieski@uwm.edu.pl; Anna Trykozko, Interdyscyplinarne Centrum Modelowania Matematycznego i Komputerowego Uniwersytetu Warszawskiego, 02-106 Warszawa, ul. Pawińskiego 5a (deceased author: 13 July, 2019).

## Introduction

Fluid flow through porous media can be described mathematically at two qualitatively different levels. The first level (historical) involves macroscopic measurements. In this approach, a porous medium is regarded as a homogeneous medium where flow resistance is generally averaged in space and time (ERGUN 1952, HELLSTRÖM, LUNDSTRÖM 2006, SIDIROPOULOU et al. 2007, SOBIESKI 2010). The structure of the material, channel shape and particle surface are not considered. Flow resistance is determined with the use of generalized parameters such as average particle diameter, porosity and tortuosity. The main disadvantage of this approach is that constant values, which usually differ for various types of porous media, have to be incorporated into mathematical models. As a result, a generally applicable mathematical model for measuring flow resistance in porous media has never been developed. Generalized Forchheimer's law appears to be the only relatively universal equation (SOBIESKI, TRYKOZKO 2011), but two coefficients have to be defined individually for every medium (SIDIROPOULOU et al. 2007). A dedicated methodology for calculating these coefficients has never been proposed, and dozens of formulas generating results that differ by many orders of magnitude have been described in the literature (SOBIESKI, TRYKOZKO 2011).

The second level involves microscopic measurements where the shape of channels and local factors are taken into consideration. This approach appears to be consistent with the laws of physics, but it requires highly complex numerical models and is very difficult to implement in practice. The main disadvantage of this approach is that microscopic observations cannot be expressed on the macroscopic scale. In practice, numerical grids can be generated to define a small fragment of space and calculate pressure fields and velocity with the use of CFD techniques. However, numerical grids describing geometrically complex pores are difficult to generate and require considerable computational power, which is why this approach cannot be used to develop full-size models of real objects. Numerous simplifications have been applied to overcome these problems. Problems are analyzed in 2D space, and pore space is modeled with simple geometric shapes, including circles (HELLSTRÖM, LUNDSTRÖM 2006, PESZYŃSKA et al. 2009a, 2009b) and rectangles (KOPONNEN et al. 1996, 1997, MATYKA et al. 2008). Pseudo-random methods are also used (NABOVATI, SOUSA 2007). Pore space is very rarely modeled in 3D space based on the actual structure of the porous medium. Such an attempt was made by CARMINATI (2007) who captured the real geometry of pore space by computed tomography and used the results to develop a classical CFD model. In other studies, the structure of porous space was described at the microscopic scale, but fluid flow was not modeled (MOTA et al. 1999, NEETHIRAJAN et al. 2006).

It should be noted that both levels can be combined by multiscale (hybrid) modeling. In this approach, flow is described with macroscale models, but the required parameters and coefficients, such as tortuosity, are determined analytically based on a simplified geometry of pore space. This approach has been rarely described in the literature, and notable examples include a study by WU et al. (2008) which presents a full mathematical model, or a study by YU and LI (2004) who proposed an analytical method for calculating tortuosity in geometrically simplified pore space. The multiscale approach can also be used in full CFD models (HELLSTRÖM, LUNDSTRÖM 2006, PESZYŃSKA et al. 2009a, 2009b) but significant progress in this area has not been made to date.

The current study relies on the macroscopic approach, but the existing empirical formulas for calculating the coefficients for Darcy's law and Forchheimer's law were not used. Empirical formulas produce highly varied results, which is why the proposed methodology was based on the inverse problem (VAN BATTENBURG, MILTON-TAYLER 2005, HUANG, AYOUB 2008, SOBIESKI, TRYKOZKO 2011, 2014a, 2014b). The method of processing experimental data plays an important role in this approach (SOBIESKI, TRYKOZKO 2011). The proposed methodology involves a simple laboratory experiment, but it guarantees high consistency of experimental data with the analytical or numerical model across a wide range of filtration velocities. In the work of SOBIESKI and TRYKOZKO (2011), data consistency was estimated at 1-3% across the tested range of filtration velocities. Similar results were reported by SOBIESKI and TRYKOZKO (2014b), but relative error was higher for several initial measurement points (with the lowest filtration velocity), and it reached 10.25% for the lowest filtration velocity (relative error decreased rapidly for successive filtration velocities). The greatest advantage of the inverse methodology is that pressure loss can be reliably predicted when the value of the permeability coefficient and/or the Forchheimer coefficient for a given porous medium is known. In a cross-validation procedure, an experiment involving the determination of the above coefficients can be regarded as an element of the training set, and a system where flow resistance is modeled can be regarded as the validation set. The training model is one-dimensional and simple to develop, whereas predictive models can be two- or three-dimensional, at least for isotropic media.

Porous media composed of glass beads with roughly identical diameters were investigated by SOBIESKI and TRYKOZKO (2011, 2014a, 2014b). Porosity and pressure loss during fluid flow were highly similar in the investigated media. These results could suggest that in less homogeneous media, experimental data will be less consistent with numerical data. To determine the magnitude of relative error in such cases, these experiments were replicated with the use of a different porous medium. The aim of this study was to determine whether the inverse problem method can produce equally reliable results in natural materials composed of large particles. The applied tools and methods are not new.

However, the presented results were obtained in a new medium, which contributes to the body of knowledge on the applicability of the inverse problem method for describing the properties of porous media with variable particle size.

## Experimental design

The test stand for analyzing the porous medium is presented in Figure 1. The stand is composed of a plexiglass tube filled with gravel (6). Water from a bottom tank (1) is supplied to the bottom of the plexiglass cylinder by a pump (2). The flow rate is controlled by a control valve (3) and an overflow valve (4). Water flows through gravel to the top tank (7), and it returns to the bottom tank via an overflow pipe (8). Volumetric flow rate was measured with a rotameter (5). Pressure was measured with U-tube manometers joined to pipe connectors (marked 1 to 4 in the diagram). Water temperature was measured with a thermometer (9). Measurement errors were as follows: volumetric flow rate  $0.000000056 \text{ m}^3/\text{s}$ , piezometric head  $1.0 \text{ mm H}_2\text{O}$ , temperature  $0.1 \text{ K}$ . The distance between extreme measurement points was  $0.9 \text{ m}$ , and the porous medium had a cross-sectional area of  $0.005 \text{ m}^2$ . Two porous media were tested: gravel with 8-16 mm grain size and gravel with 2-8 mm grain size.

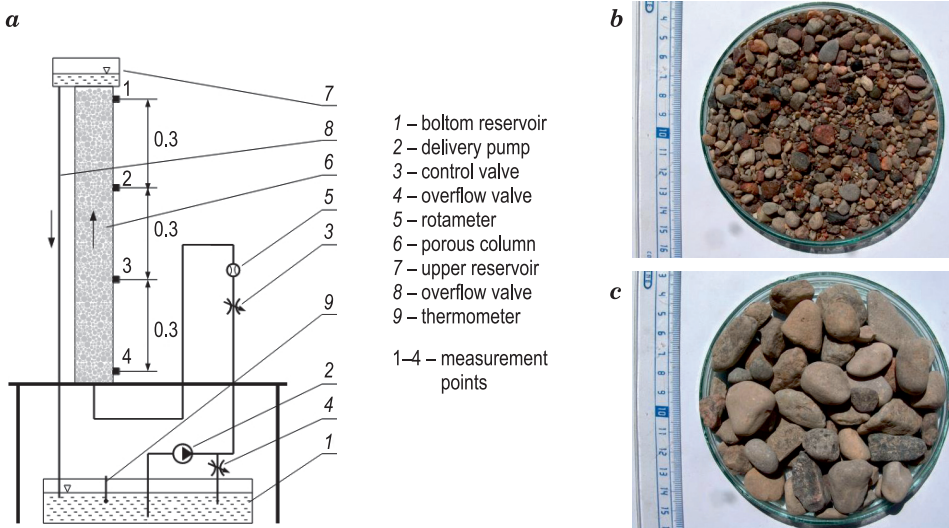


Fig. 1. Diagram of the test stand for analyzing a porous medium (a), gravel with 2-8 mm grain size (b), gravel with 8-16 mm grain size (c)

All measurements were conducted in the test site presented in Figure 1. The correlation between volumetric flow rate and piezometric head was determined between extreme measurement points (4-1). The drop in pressure was measured at different settings of the control valve (3). In the porous medium with 2-8 mm grain size, the control valve was set to 12 volumetric flow rates from  $1.9\text{E-}6 \text{ m}^3/\text{s}$  to  $52.2\text{E-}6 \text{ m}^3/\text{s}$ . In the porous medium with 8-16 mm grain size, the control valve was set to 7 volumetric flow rates from  $38.1\text{E-}6 \text{ m}^3/\text{s}$  to  $52.2\text{E-}6 \text{ m}^3/\text{s}$ . In the porous medium with 8-16 mm grain size, the range of valve settings was small because differences in the pressure of water flowing through the medium were negligible. Flow resistance was very low in the tested porous medium. The measurements were performed in triplicate for each medium. The cylinder was then emptied, gravel was stirred and poured back into the cylinder. This operation was repeated three times to calculate the average pressure difference  $\Delta h$ . The measurements were conducted at constant water temperature of 304 K, at which water density was  $\rho = 995,34 \text{ kg/m}^3$ , and water viscosity was  $\mu = 0.00078433 \text{ kg/(m}\cdot\text{s)}$ . The results of the measurements are presented in Tables 1 and 2. The measured values are presented graphically in Figure 2, where the average values for every cylinder refill are denoted by lines.

Table 1

Measurements performed in the medium with 2-8 mm grain size

Flow rate	Refill 1			Refill 2			Refill 3			Average
$\dot{V}$	$\Delta h$	$\Delta h$	$\Delta h$	$\Delta h$	$\Delta h$	$\Delta h$	$\Delta h$	$\Delta h$	$\Delta h$	$\overline{\Delta h}$
$\text{m}^3/\text{s}$	mm	mm	mm	mm	mm	mm	mm	mm	mm	mm
01.9E-6	9	9	9	8	7	6	9	8	8	8.11
06.1E-6	37	36	35	30	28	29	36	33	34	33.11
10.6E-6	70	71	68	55	54	54	67	67	66	63.56
12.5E-6	106	106	104	82	82	82	100	99	99	95.56
19.7E-6	142	144	144	114	116	110	138	135	135	130.89
24.4E-6	191	186	182	139	144	145	178	178	176	168.78
28.9E-6	231	230	226	176	180	180	219	218	216	208.44
33.3E-6	276	272	264	218	215	216	261	260	263	249.44
38.1E-6	329	325	323	257	255	257	310	311	311	297.56
42.8E-6	389	384	378	303	301	301	368	367	368	351.00
47.8E-6	448	444	444	353	351	351	427	428	425	407.89
52.2E-6	519	520	512	407	401	411	487	492	493	471.33

Table 2

Measurements performed in the medium with 8-16 mm grain size										
Refill 1			Refill 2			Refill 3				
$\dot{V}$	$\Delta h$	$\Delta h$	$\Delta h$	$\Delta h$	$\Delta h$	$\Delta h$	$\Delta h$	$\Delta h$	$\Delta h$	$\overline{\Delta h}$
m <sup>3</sup> /s	mm	mm	mm	mm	mm	mm	mm	mm	mm	mm
38.1E-6	11	12	12	10	11	10	12	11	11	11.11
40.3E-6	14	13	14	12	12	12	13	13	13	12.89
42.8E-6	16	15	16	14	14	14	14	15	15	14.78
45.0E-6	17	17	18	16	16	16	16	17	17	16.67
47.8E-6	19	19	20	17	18	18	19	19	19	18.67
49.7E-6	21	22	21	19	20	20	21	21	22	20.78
52.2E-6	23	24	24	22	22	23	24	24	24	23.33

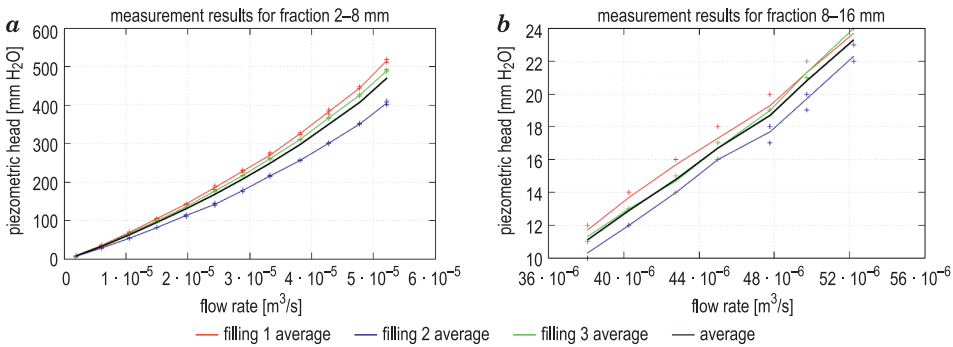


Fig. 2. The results of the measurements conducted in porous media with 2-8 mm grain size (a) and 8-16 mm grain size (b)

Mathematical model based on Darcy’s law

In the first stage of the study, a mathematical model was developed based on Darcy’s law (1856). Darcy’s law is an equation describing the flow of a fluid through a porous medium. The law can be expressed by the following equation (ANDERSON et al. 2004, HELLSTRÖM, LUNDSTRÖM 2006):

$$-\frac{dp}{dL} = -\frac{\rho g \overline{\Delta h}}{dL} = \frac{\mu}{\kappa} v_f \tag{1}$$

where:  
 $dL$  – distance [m] over which the pressure drop  $dp$  [Pa] takes place,  
 $\rho$  – fluid viscosity [kg/m<sup>3</sup>],  
 $g$  – gravity component [m/s<sup>2</sup>],  
 $\overline{\Delta h}$  – average piezometric head [m],

$\kappa$  – permeability coefficient [m<sup>2</sup>],  
 $\mu$  – dynamic viscosity coefficient [kg/(m·s)],  
 $v_f$  – filtration velocity [m/s].

Filtration velocity is calculated with the following continuity equation:

$$v_f = \frac{\dot{V}}{A} \quad (2)$$

where:

$\dot{V}$  – volumetric flow rate of water through the medium [m<sup>3</sup>/s],  
 $A$  – cross-sectional area of the medium [m<sup>2</sup>].

Darcy's law can also be expressed by the following formula:

$$v_f = -KJ = -K \frac{\overline{\Delta h}}{dL} \quad (3)$$

where:

$K$  – filtration coefficient [m/s],  
 $J$  – decrease in hydraulic head [-],  
 calculated as the piezometric gradient between two points (in this case, the average value from several measurements).

The filtration coefficient  $K$  and the permeability coefficient  $\kappa$  [m<sup>2</sup>] are bound by the following correlation:

$$K = \kappa \frac{\rho g}{\mu} \quad (4)$$

The results of the measurements in the model based on Darcy's law are presented in Tables 3 and 4. The average values of the permeability coefficient for porous media with 2-8 mm and 8-16 mm grain size were determined at 2.16E-09 and 3.9938E-08 [m<sup>2</sup>], respectively. The average values of the filtration coefficient for the above media were determined at 0.026892 m/s and 0.497196 m/s, respectively. The pressure drop in the compared media is presented in Figure 3.

Table 3

The results of measurements in the model based on Darcy's law  
for the medium with 2-8 mm grain size

$\dot{V}$	$\overline{\Delta h}$	$\Delta p$	$J$	$v_f$	$K$	$\kappa$
m <sup>3</sup> /s	m	a	[-]	m/s	m/s	m <sup>2</sup>
1	2	3	4	5	6	7
01.9E-6	0.0081	79.20	0.0090	0.0004	0.043151	3.466E-09
06.1E-6	0.0331	323.31	0.0368	0.0012	0.033221	2.669E-09

cont. Table 3

1	2	3	4	5	6	7
10.6E-6	0.0636	620.57	0.0706	0.0021	0.029895	2.401E-09
12.5E-6	0.0956	933.03	0.1062	0.0030	0.028256	2.27E-09
19.7E-6	0.1309	1278.04	0.1454	0.0039	0.027122	2.179E-09
24.4E-6	0.1688	1647.99	0.1875	0.0049	0.026070	2.094E-09
28.9E-6	0.2084	2035.31	0.2316	0.0058	0.024947	2.004E-09
33.3E-6	0.2494	2435.65	0.2772	0.0067	0.024053	1.932E-09
38.1E-6	0.2976	2905.42	0.3306	0.0076	0.023021	1.849E-09
42.8E-6	0.3510	3427.26	0.3900	0.0086	0.021937	1.762E-09
47.8E-6	0.4079	3982.74	0.4532	0.0096	0.021084	1.694E-09
52.2E-6	0.4713	4602.23	0.5237	0.0104	0.019943	1.602E-09

Table 4

The results of measurements in the model based on Darcy’s law  
for the medium with 8-16 mm grain size

$\dot{V}$	$\overline{\Delta h}$	$\Delta p$	$J$	$v_f$	$K$	$\kappa$
m <sup>3</sup> /s	m	Pa	[-]	m/s	m/s	m <sup>2</sup>
38.1E-6	0.0111	108.49	0.0123	0.0076	0.616500	4.952E-08
40.3E-6	0.0129	125.85	0.0143	0.0081	0.562500	4.518E-08
42.8E-6	0.0148	144.29	0.0164	0.0086	0.521053	4.185E-08
45.0E-6	0.0167	162.74	0.0185	0.0090	0.486000	3.904E-08
47.8E-6	0.0187	182.27	0.0207	0.0096	0.460714	3.701E-08
49.7E-6	0.0208	202.88	0.0231	0.0099	0.430749	3.460E-08
52.2E-6	0.0233	227.83	0.0259	0.0104	0.402857	3.236E-08

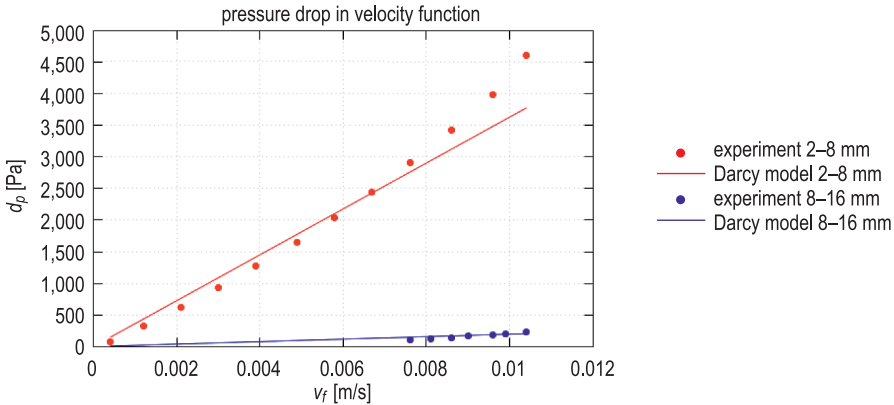


Fig. 3. Pressure drop as a function of velocity in the compared media (linear model)



## Mathematical model based on Forchheimer's law

Flow resistance in a porous medium is also described with Forchheimer's law (1901). The Forchheimer equation contains a non-linear term for adjusting the result in high-flow rate environments. The applicability limits of both laws are discussed in successive chapters of the study. The Forchheimer equation has the following form:

$$-\frac{dp}{dL} = \frac{1}{\kappa} \mu v_f + \beta \rho v_f^2 \quad (5)$$

where:

$\beta$  – Forchheimer coefficient (non-Darcy coefficient,  $\beta$  factor) [1/m].

If  $\beta = 0$ , the flow regime is described by Darcy's law.

To determine parameters  $\kappa$  and  $\beta$  based on the experimental data, equation (5) was transformed as follows (HUANG, AYOUB 2008):

$$-\frac{dp}{dL} \frac{1}{\mu v_f} = \frac{1}{\kappa} + \beta \left( \frac{\rho v_f}{\mu} \right) \quad (6)$$

The following expressions were introduced:

$$\begin{cases} Y = -\frac{dp}{dL} \frac{1}{\mu v_f} \\ X = \frac{\rho v_f}{\mu} \end{cases} \quad (7)$$

to produce a linear equation:

$$Y = \beta X + \frac{1}{\kappa} \quad (8)$$

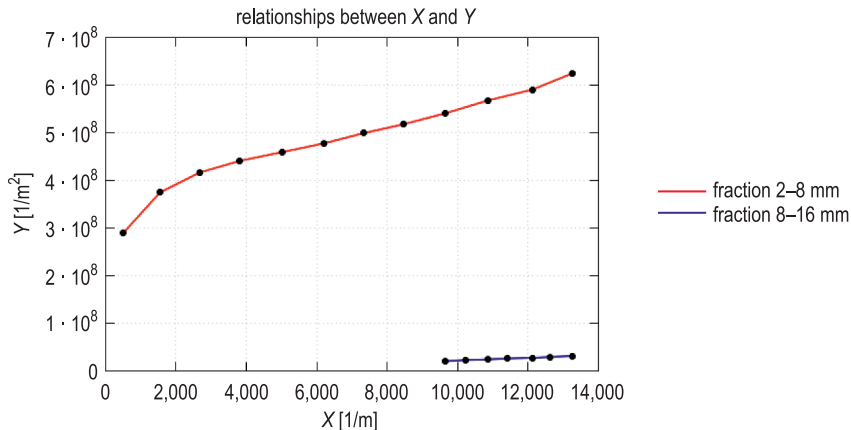


Fig. 4. The correlation between coefficients  $X$  and  $Y$  in the compared media

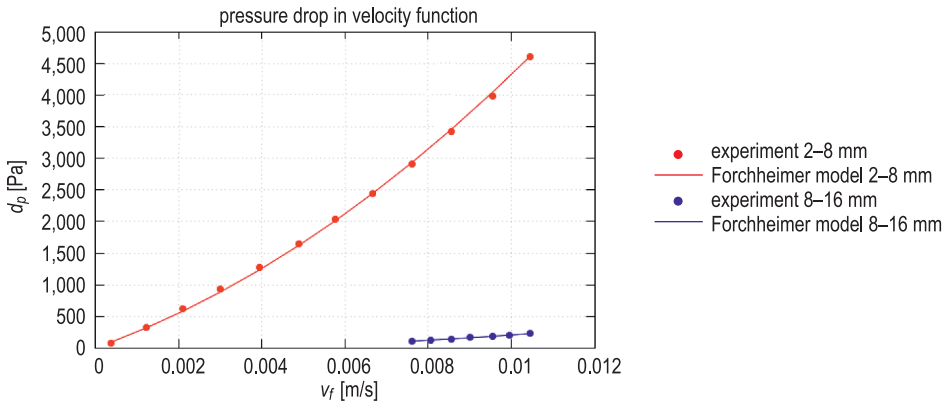


Fig. 5. Pressure drop as a function of velocity in the compared media (non-linear model)

Coefficients and were determined with the use of equation (7), and the coefficients in equation (8) were determined by least squares approximation. The results are shown in Figures 4 and 5. These coefficients are equivalent to the corresponding terms in equation (5). In the media with 2-8 mm and 8-16 mm grain size, the value of coefficient  $1/k$  was determined at  $0.33303\text{E}+09$  and  $-0.758964\text{E}+07$ , respectively, and the value of coefficient  $\beta$  was determined at  $0.221048\text{E}+05$  and  $0.578304\text{E}+04$ , respectively.

## Numerical model of fluid flow in a porous medium

Numerical calculations for replicating the experiment were performed in a self-designed computer program based on the steady-state flow equation:

$$\nabla \cdot K \nabla (\Delta h) = 0 \quad (9)$$

When the assumption of conservation of momentum modeled by Darcy's law is met:

$$v_f = -K \cdot K \nabla (\Delta h) \quad (10)$$

In equation (10), the filtration coefficient  $K$  is a generalized tensor (BREUGEM et al. 2004). Equation (10) is a generalization of formula (3) for multidimensional flow.

The following boundary conditions were imposed: the Neumann condition is zero along the cylinder, volumetric flow rate was imposed as the Neumann condition at the cylinder inlet, and piezometric head was imposed as the boundary condition at the cylinder outlet. It was assumed that the reference level  $z = 0$  corresponds to the cylinder inlet (bottom); therefore, piezometric head  $\Delta h$  at the

outlet was equal to the anticipated pressure, increased by the cylinder's total length. If pressure equals zero at the outlet, piezometric head at the outlet will be equal to the cylinder's length.

The flow equation (9) was solved with the Finite Element Method (FEM) with linear basis functions (LUCQUIN, PIRONNEAU 1998). A cross-section of the computational domain and its elements is presented in Figure 6. The model was build based on a discrete mesh that had been originally developed in GAMBIT (2004) and converted to the format used in the designed computational program.

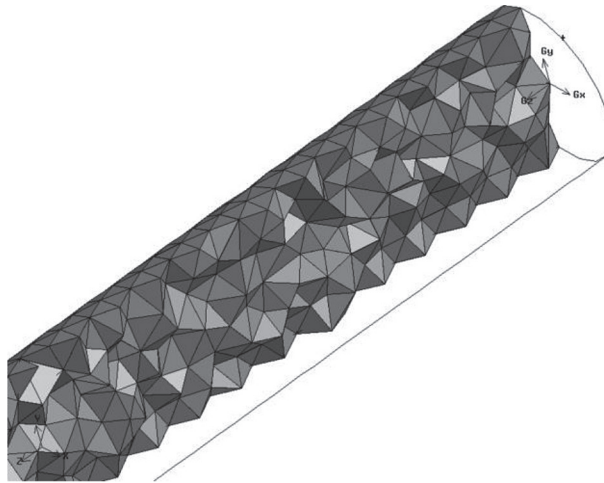


Fig. 6. Segment of the numerical mesh used in the designed computational program

A system of linear equations generated by the numerical mesh was solved with the conjugate gradient method and incomplete Cholesky preconditioning (KAASSCHIETER 1998).

The Forchheimer equation was modified for use in the designed program based on the solution presented by FOURAR et al. (2005). An iterative algorithm is based on the effective permeability coefficient. Successive approximations of the effective permeability coefficient were determined with the use of equation (5):

$$-\frac{dp}{dL} = \left( \frac{\mu}{\kappa} + \beta \rho v_f^{(i)} \right) v_f = \frac{1}{K_{eff}^{(i)}} v_f \quad (11)$$

where the upper index  $i$  denotes velocity fields in successive iterations.

Experimentally measured pressure was imposed as the boundary condition, and boundary conditions remained unchanged during iteration. The flow equation (11) was solved for  $K_{eff}^{(0)} = \frac{\kappa}{\mu}$  to approximate the velocity field  $v_f^{(i)}$ .

The iterative scheme was as follows: the following approximation of the permeability coefficient  $K_{eff}^{(i)}$  was derived with equation (11), and the corresponding velocity field was calculated. In each case, the calculated velocity field was compared with the field approximated in the previous iteration. Iterations were repeated until convergence was reached. This is not an optimal approach, but it offers an easy solution, including in non-linear models.

Results of numerical simulations

The results of the simulations conducted in the compared media are presented in Figure 7. The numbers in the diagram correspond to the measurements presented in Tables 1 and 2. In both cases, the pressure drops estimated with Darcy’s laws differ from the experimental data.

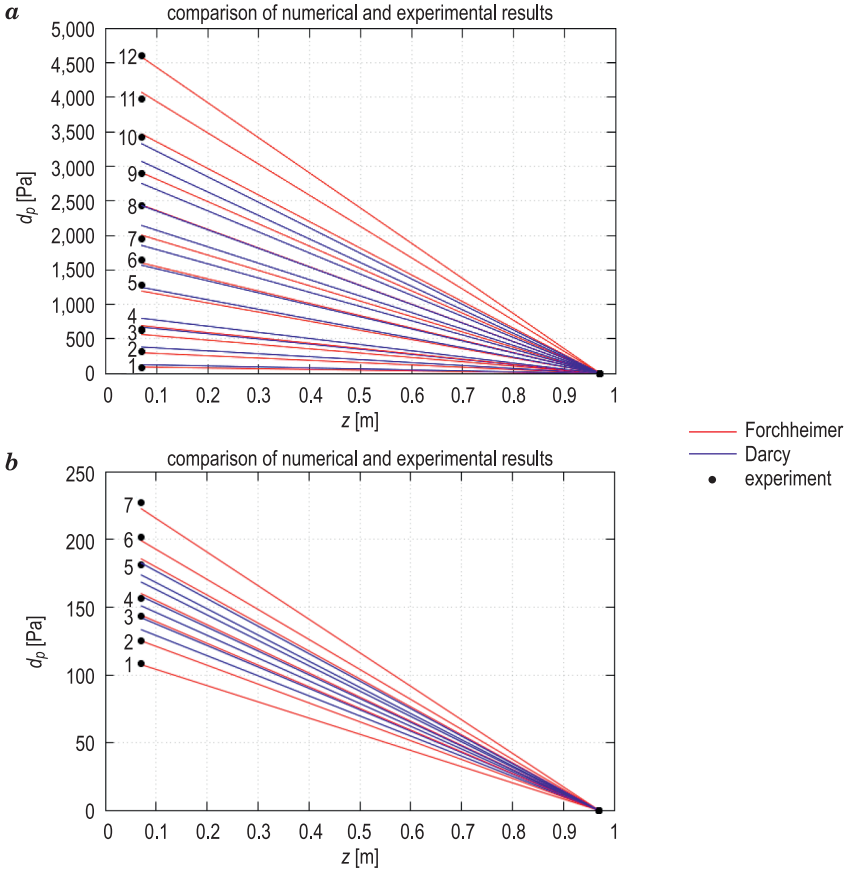


Fig. 7. Measurements conducted in porous media with 8-16 mm (a) and 2-8 mm (b) grain size

## Percentage errors

$$\delta = \left| \frac{x_i - x_0}{x_0} \right| \cdot 100\% \quad (12)$$

where  $x_i$  is the numerically determined value and  $x_0$  is the exact (measured) value, are presented in Tables 5 and 6 as well as in Figure 8.

Table 5

Percentage errors for the medium with 2-8 mm grain size

$v_f$	$dp_{\text{exp.}}$	$dp_{\text{Darcy}}$	$dp_{\text{Forchheimer}}$	$\delta_{\text{Darcy}}$	$\delta_{\text{Forchheimer}}$
m/s	Pa	Pa	Pa	%	%
0.0004	79.09	128.18	93.66	62.07	18.42
0.0012	323.2	384.54	300.86	18.98	6.91
0.0021	621.01	672.94	565.64	8.36	8.92
0.0025	640.54	801.12	694.09	25.07	8.36
0.0039	1 278.14	1 249.75	1 195.86	2.22	6.44
0.0049	1 648.21	1 570.2	1 603.97	4.73	2.68
0.0058	1 956.76	1 858.61	2 006.68	5.02	2.55
0.0067	2 435.21	2 147.01	2 442.9	11.83	0.32
0.0076	2 905.85	2 435.41	2 912.74	16.19	0.24
0.0086	3 427.26	2 755.84	3 474.09	19.59	1.37
0.0096	3 982.85	3 076.29	4 076.84	22.76	2.36
0.0104	4 601.91	3 332.65	4 589.00	27.58	0.28

Table 6

Percentage errors for the medium with 8-16 mm grain size

$v_f$	$dp_{\text{exp.}}$	$dp_{\text{Darcy}}$	$dp_{\text{Forchheimer}}$	$\delta_{\text{Darcy}}$	$\delta_{\text{Forchheimer}}$
[m/s]	[Pa]	[Pa]	[Pa]	[%]	[%]
0.0076	108.38	133.6	107.72	23.26	0.61
0.0081	124.98	142.39	125.32	13.92	0.27
0.0086	143.53	151.18	144.21	5.32	0.47
0.0090	156.81	158.21	160.27	0.89	2.20
0.0096	181.62	168.76	185.90	7.08	2.36
0.0099	202.12	174.03	199.42	13.9	1.34
0.0104	227.51	182.82	222.98	19.64	1.99

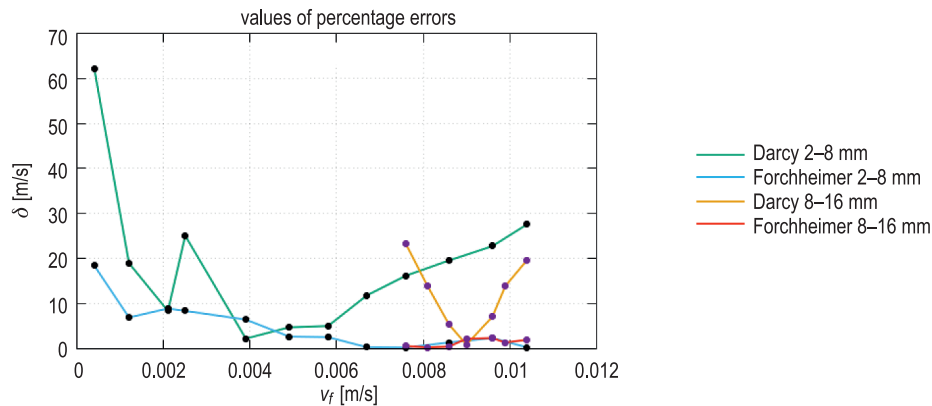


Fig. 8. Percentage errors for both numerical models

Determination of the porosity coefficient

The porosity coefficient was determined with the use of two graduated cylinders with 1 ml grading divisions. The first cylinder was filled with porous material with a known volume  $V_i$  and the second cylinder was filled with water. Total skeletal volume  $V_s$  can be determined when the volume of porous material and the volume of water required to completely fill the porous part  $V_p$  of the medium are known:  $V_s = V - V_p$ .

Table 7

Porosity measurements in the medium with 8-16 mm grain size					
$V$	$V_p$	$V_s$	$V_p$	$V_s$	$e_{8-16}$
m <sup>3</sup>	m <sup>3</sup>	m <sup>3</sup>	%	%	[-]
2E-03	816E-06	1.184E-03	40.8	59.2	0.408
2E-03	770E-06	1.230E-03	38.5	61.5	0.385
2E-03	854E-06	1.146E-03	42.7	57.3	0.427
2E-03	812E-06	1.188E-03	40.6	59.4	0.406
2E-03	820E-06	1.180E-03	41.0	59.0	0.410
2E-03	824E-06	1.176E-03	41.2	58.8	0.412
2E-03	838E-06	1.162E-03	41.9	58.1	0.419
2E-03	836E-06	1.164E-03	41.8	58.2	0.418
2E-03	820E-06	1.180E-03	41.0	59.0	0.410
2E-03	816E-06	1.184E-03	40.8	59.2	0.408
2E-03	814E-06	1.186E-03	40.7	59.3	0.407
2E-03	834E-06	1.166E-03	41.7	58.3	0.417

In the porous medium with 2-8 mm grain size, the material “settled” under the influence of water, which decreased its total volume. The medium’s volume decreased as flowing water transported the smallest grains which filled empty spaces between large grains. To account for the above observation, the porosity coefficient was measured twice. In the first measurement,  $0.0015 \text{ m}^3$  of gravel was loosely poured into the cylinder and covered with water, and pore volume was measured. In the second measurement,  $0.002 \text{ m}^3$  of gravel was lightly compacted in the cylinder, covered with water, and pore volume was measured. The “settling” of gravel particles was not observed in the medium with 8-16 mm grain size. Average porosity was determined at  $e_{8-16} = 0.411$ ,  $e_{2-8}^{\max} = 0.358$  and  $e_{2-8}^{\min} = 0.294$ . Results of measurements are available in Tables 7, 8 and 9.

Table 8

Porosity measurements in loosely arranged medium with 2-8 mm grain size

$V$	$V_p$	$V_s$	$V_p$	$V_s$	$e_{2-8}^{\max}$
$\text{m}^3$	$\text{m}^3$	$\text{m}^3$	%	%	[-]
1.5E-03	545E-06	955E-06	36.3	63.7	0.363
1.5E-03	538E-06	962E-06	35.9	64.1	0.359
1.5E-03	557E-06	943E-06	37.1	62.9	0.371
1.5E-03	530E-06	970E-06	35.3	64.7	0.353
1.5E-03	524E-06	976E-06	34.9	65.1	0.349
1.5E-03	548E-06	952E-06	36.5	63.5	0.365
1.5E-03	522E-06	978E-06	34.8	65.2	0.348
1.5E-03	532E-06	968E-06	35.5	64.5	0.355
1.5E-03	547E-06	953E-06	36.5	63.5	0.365
1.5E-03	532E-06	968E-06	35.5	64.5	0.355

Table 9

Porosity measurements in compacted medium with 2-8 mm grain size

$V$	$V_p$	$V_s$	$V_p$	$V_s$	$e_{2-8}^{\min}$
$\text{m}^3$	$\text{m}^3$	$\text{m}^3$	%	%	[-]
2E-03	602E-06	1.398E-03	30.1	69.9	0.301
2E-03	596E-06	1.404E-03	29.8	70.2	0.298
2E-03	580E-06	1.420E-03	29.0	71.0	0.290
2E-03	600E-06	1.400E-03	30.0	70.0	0.300
2E-03	556E-06	1.444E-03	27.8	72.2	0.278
2E-03	598E-06	1.402E-03	29.9	70.1	0.299
2E-03	578E-06	1.422E-03	28.9	71.1	0.289
2E-03	574E-06	1.426E-03	28.7	71.3	0.287
2E-03	595E-06	1.405E-03	29.8	70.2	0.298
2E-03	596E-06	1.404E-03	29.8	70.2	0.298

Determination of the equivalent diameter of gravel grains

The average diameter was determined by counting the number of grains  $n_s$  and measuring their total volume  $V_s$  in a control volume  $V$ . The average volume of one grain  $V_d$  was calculated by dividing total grain volume by the number of grains. The formula for calculating the volume of a sphere was used to determine the average grain diameter  $\delta$  [m]. The control volume was 6E-04 [m<sup>3</sup>] for the medium with 8-16 mm grain size and 15E-06 [m<sup>3</sup>] for the medium with 2-8 mm grain size.

The measured values of average grain diameter seem to be correct. This parameter was determined at 14.7 mm in the medium with 8-16 mm grain size, and 3.3 mm in the medium with 2-8 mm grain size. The obtained values were used in alternative calculations of the porosity coefficient. The results were highly similar to the previously obtained values. The results of the measurements and calculations performed for both media are presented in Tables 10 and 11. Grain “settlement” was negligible in the medium with 2-8 mm grain size due to small control volume, and this observation was not taken into consideration.

Table 10

Measurements of equivalent grain diameter in the medium with 8-16 mm grain size

$V$	$V_p$	$V_s$	$n_s$	$V_d$	$\delta_{8-16}$	$e'_{8-16}$
m <sup>3</sup>	m <sup>3</sup>	m <sup>3</sup>	[-]	m <sup>3</sup>	m	[-]
6E-04	255E-06	345E-06	194	1.78E-06	0.0150	0.425
6E-04	243E-06	357E-06	231	1.55E-06	0.0143	0.405
6E-04	240E-06	360E-06	227	1.59E-06	0.0145	0.400
6E-04	238E-06	362E-06	221	1.64E-06	0.0146	0.397
6E-04	235E-06	365E-06	219	1.67E-06	0.0147	0.392
–	–	–	–	<b>1.66E-06</b>	<b>0.0147</b>	<b>0.406</b>

Table 11

Measurements of equivalent grain diameter in the medium with 2-8 mm grain size

$V$	$V_p$	$V_s$	$n_s$	$V_d$	$\delta_{2-8}$	$e'_{2-8}$
m <sup>3</sup>	m <sup>3</sup>	m <sup>3</sup>	[-]	m <sup>3</sup>	m	[-]
15E-06	4.5E-06	10.5E-06	550	19.1E-09	0.00332	0.300
15E-06	5.0E-06	10.0E-06	490	20.4E-09	0.00339	0.333
15E-06	4.5E-06	10.5E-06	580	18.1E-09	0.00326	0.300
15E-06	4.0E-06	11.0E-06	600	18.3E-09	0.00327	0.267
15E-06	5.0E-06	10.0E-06	510	19.6E-09	0.00335	0.333
–	–	–	–	<b>19.1E-09</b>	<b>0.00332</b>	<b>0.307</b>



## Reynolds number

According to the literature, Darcy's law and Forchheimer's law have certain limits of applicability, as illustrated in Figure 9. The Reynolds number is the main criterion for determining the validity of both laws. The Reynolds number is defined as (NAŁĘCZ 1991, SAWICKI et al. 2004):

$$\text{Re} = \frac{\rho v_f \delta}{\mu} \quad (13)$$

where  $\delta$  is the grain diameter [m] in an ideally homogeneous medium composed of spherical particles that offer similar resistance as the real material.

In the literature, considerable variations are noted in the upper limit of applicability of Darcy's law and Forchheimer's law, for example:  $\text{Re} = 3-10$  (BEAR 1972),  $\text{Re} = 1-15$  (HASSANIZADEH, GRAY (1987); the suggested value is  $\text{Re} = 10$ ),  $\text{Re} = 1 \div 5$  (SAWICKI et al. 2004),  $\text{Re} = 10^{-5}-2.3$  (HANSEN 2007).

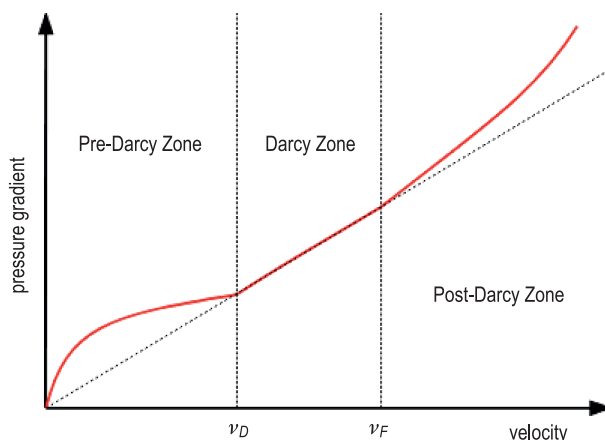


Fig. 9. Types of flow in porous media

Source: based on BLOSHANSKAYA et al. (2017) and HASSANIZADEH and GRAY (1987).

The Reynolds numbers calculated for equivalent diameters  $\delta_{2-8}$  and  $\delta_{8-16}$  are presented in Tables 12 and 13 and in Figure 10. Reynolds numbers were also calculated for extreme grain diameters in the compared media to present the full range of changes in the evaluated parameter. In the medium with 8-16 mm grain size, flow always occurred in a region that was separated by a considerable distance from the upper limit of applicability of Darcy's law and Forchheimer's law (regardless of the fact which limit value was adopted). In this medium, fluid flow should not be modeled with Darcy's law. This conclusion had been initially formulated in the error analysis, and it was further confirmed

by the above observations. In fine-grained gravel, measurements began at much lower filtration velocity, and based on literature data, the first two or three measurements could be classified as Darcy flow. However, high percentage error does not confirm the above observation. These findings suggest that in forced-flow systems, such as the presented test stand, flow should be generally modeled with the Forchheimer equation or similar non-linear equations.

Table 12

Values of the Reynolds number for the medium with 2-8 mm grain size and different values of the equivalent diameter

$v$	$Re_{\delta=0.002}$	$Re_{\delta=0.008}$	$Re_{\delta=0.00332}$
m/s	[-]	[-]	[-]
0.0004	0.99	3.95	1.64
0.0012	3.10	12.41	5.15
0.0021	5.36	21.43	8.89
0.0025	6.35	25.38	10.53
0.0039	10.01	40.05	16.62
0.0049	12.41	49.63	20.60
0.0058	14.66	58.66	24.34
0.0067	16.92	67.68	28.09
0.0076	19.32	77.27	32.07
0.0086	21.71	86.86	36.05
0.0096	24.25	97.01	40.26
0.0104	26.51	106.03	44.00

Table 13

Values of the Reynolds number for the medium with 8-16 mm grain size and different values of the equivalent diameter

$v$	$Re_{\delta=0.008}$	$Re_{\delta=0.0016}$	$Re_{\delta=0.0147}$
m/s	[-]	[-]	[-]
0.0076	77.27	154.54	141.98
0.0081	81.78	163.56	150.27
0.0086	86.86	173.72	159.60
0.0090	91.37	182.74	167.89
0.0096	97.01	194.02	178.26
0.0099	100.96	201.92	185.51
0.0104	106.03	212.07	194.84

The above conclusion confirms that the presented Reynolds numbers were calculated based on equivalent diameters, which does not guarantee that a given Reynolds number will describe all regions of a porous medium. Due to possible deviations, Forchheimer's law should be applied in this case because it applies to a wider range of velocities.

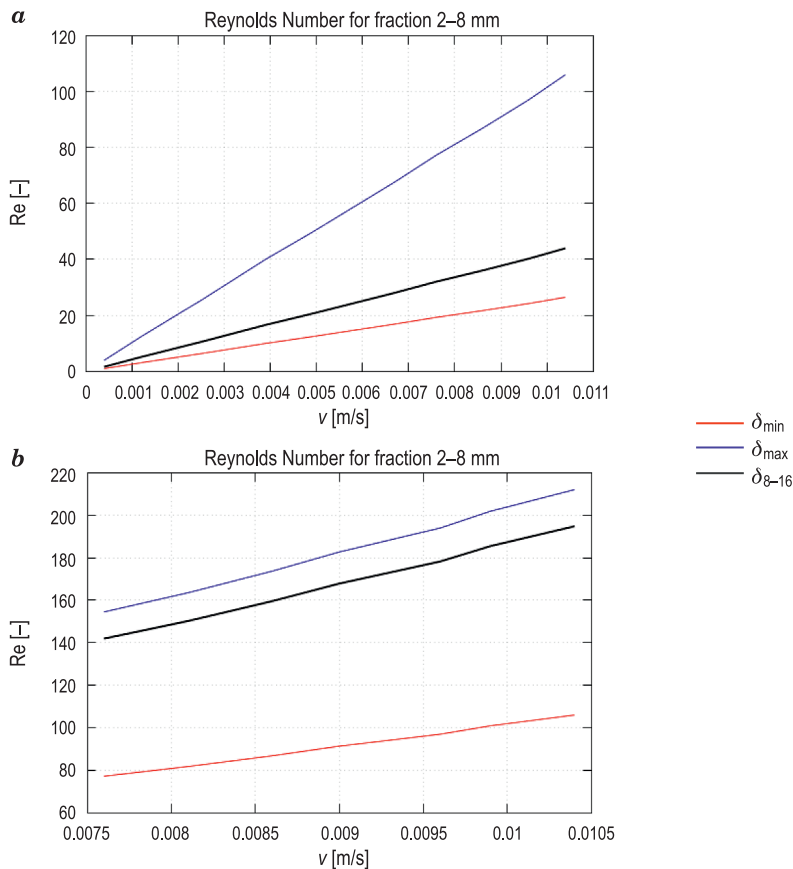


Fig. 10. Values of the Reynolds number for media with 2-8 mm (a) and 8-16 mm grain size (b) and different values of the equivalent diameter

## Conclusions

The results of the study supported the formulation of the following conclusions:

- Due to the absence of strict criteria for determining the validity of the basic laws for modeling flow in porous media, fluid flow in a gravel medium with 2-16 mm grain size should be generally described with the more universal

Forchheimer's law which applies to a wider range of velocities. Forchheimer's law can probably be also used to model flow in gravel and sand with different particle size fractions. The above is confirmed by Figure 7 which clearly indicate that unlike Darcy's law, Forchheimer's law guarantees high consistency of modeled data with experimental data across the entire range of filtration velocity values.

- The results of this study confirm that the upper limit of applicability of Darcy's law is  $Re \approx 8 \div 10$ .

- Forchheimer's law should be regarded as a broader version of Darcy's law, rather than its extension for flows with higher Reynolds numbers. Published sources (for example in Fig. 9) can be somewhat misleading by suggesting that Darcy's law should be applied to lower values of the Reynolds number, whereas Forchheimer's law should be applied to higher values of the Reynolds number. The results presented in Tables 5 and 6 and in Figure 8 indicate that Forchheimer's law can be used in all cases where Darcy's law could be applied. In these cases, the non-linear term of the Forchheimer equation will simply lose its significance.

- Flow resistance in porous media can be reliably modeled based on the results of a simple "training" experiment which produces accurate values of the coefficients for Forchheimer's law. These coefficients should be calculated by measuring pressure drops across the widest possible range of filtration velocities. The wider the velocity range and the more accurate the measurements, the smaller the discrepancy between simulation results and experimental data.

The presented findings indicate that flow resistance in sand and gravel (and probably many other porous media) should be modeled based on Forchheimer's law and the results of a preliminary "training" experiment. The application of the inverse problem methodology significantly increases the reliability of the modeled data.

## References

- ANDERSON B.A., SARKAR A., THOMPSON J.F., SINGH R.P. 2004. *Commercial-Scale Forced-Air Cooling Of Packaged Strawberries*. Transactions of the ASAE, 47(1): 183-190. American Society of Agricultural Engineers.
- BATTENBURG D. VAN, MILTON-TAYLER D. 2005. *Discussion of SPE 879325, Beyond Beta factors: a complete model for Darcy, Forchheimer, and Trans-Forchheimer flow in porous media*. Journal of Petroleum Technology, 57: 72-74.
- BEAR J. 1972. *Dynamics of Fluids in Porous Media*. Elsevier, Amsterdam.
- BLOSHANSKAYA L., IBRAGIMOV A., SIDDIQUI F., SOLIMAN M. 2016. *Productivity Index for Darcy and pre-/post-Darcy Flow (Analytical Approach)*. Journal of Porous Media, 20(9).
- BREUGEM W.P., BOERSMA B.J., UITTENBOGAARD R.E. 2004. *Direct numerical simulations of plane channel flow over a 3D Cartesian grid of cubes*. In: *Applications of porous media*. Eds. A.H. Reis, A.F. Miguel. Évora: Évora Geophysics Center, p. 27-35.

- CARMINATI A., KAESTNER A., IPPISCH O., KOLIJ A., LEHMANN P., HASSANEIN R., VONTOBEL P., LEHMANN E., LALOU L., VULLIET L. 2007. *Water flow between soil aggregates*. Transport in Porous Media, 68(2): 219-236.
- DARCY H. 1856. *Les Fontaines Publiques De La Ville De Dijon*. Victor Dalmont, Paris, France.
- ERGUN S. 1952. *Fluid flow through packed columns*. Chemical and Engineering Progress, 48: 89-94.
- FORCHHEIMER P. 1901. *Wasserbewegung durch boden*. Zeit. Ver. Deutsch. Ing., 45: 1781-1788.
- FOURAR M., LENORMAND R., KARIMI-FARD M. 2005. *Inertia Effects in High-Rate Flow Through Heterogeneous Porous Media*. Transport in Porous Media, 60: 353-370.
- GAMBIT 2.2 Tutorial Guide. 2004. Fluent, Incorporated.
- HANSEN T.E. 2007. *Flow in micro porous silicon carbide*. Master Thesis. Department of Micro and Nanotechnology, Technical University of Denmark, March 2nd.
- HASSANIZADEH S.M., GRAY W.G. 1987. *High Velocity Flow in Porous Media*. Transport in Porous Media, 2: 521-531.
- HELLSTRÖM J.G.I., LUNDSTRÖM T.S. 2006. *Flow through Porous Media at Moderate Reynolds Number*. International Scientific Colloquium, Modelling for Material Processing, Riga, June 8-9.
- HUANG H., AYOUB J. 2008. *Applicability of the Forchheimer Equation for Non-Darcy Flow in Porous Media*. SPE Journal, 13: 112-122.
- KAASSCHIETER E.F. 1988. *Preconditioned conjugate gradients for solving singular systems*. Journal of Computational and Applied Mathematics, 24: 265-275.
- KOPONEN A., KATAJA M., TIMONEN J. 1996. *Tortuous flow in porous media*. Physical Review E., 54(1): 406-410.
- KOPONEN A., KATAJA M., TIMONEN J. 1997. *Permeability and effective porosity of porous media*. Physical Review E., 56(3): 3319-3325.
- LUCQUIN B., PIRONNEAU O. 1998. *Introduction to Scientific Computing*. Wiley, New York.
- MATYKA M., KHALILI A., KOZA Z. 2008. *Tortuosity-porosity relation in the porous media flow*. Physical Review E, 78: 026306.
- MOTA M., TEIXEIRA J., YELSHIN A. 1999. *Image analysis of packed beds of spherical particles of different sizes*. Separation and Purification Technology, 15(1-4): 59-68.
- NABOVATI A., SOUSA C.M. 2007. *Fluid Flow Simulation In Random porous media at pore level using Lattice Boltzmann method*. Journal of Engineering Science and Technology, 2(3): 226- 237.
- NAŁĘCZ T. 1991. *Ćwiczenia laboratoryjne z mechaniki płynów*. Wydawnictwo ART, Olsztyn.
- NEETHIRAJAN S., KARUNAKARAN C., JAYAS D.S., WHITE N.D.G. 2006. *X-ray Computed Tomography Image Analysis to explain the Airflow Resistance Differences in Grain Bulks*. Biosystems Engineering, 94(4): 545-555.
- PESZYŃSKA M., TRYKOZKO A., AUGUSTSON K. 2009a. *Computational upscaling of inertia effects from porescale to mesoscale*. In: *ICCS 2009 Proceedings, LNCS 5544*. Part I. Eds. G. Allen, J. Nabrzyski, E. Seidel, D. van Albada, J. Dongarra, P. Sloot. Springer-Verlag, Berlin-Heidelberg, p. 695-704.
- PESZYŃSKA M., TRYKOZKO A., AUGUSTSON K., SOBIESKI W. 2009b. *Computational Upscaling of Inertia Effects from Porescale to Mesoscale*. Conference on Mathematical and Computational Issues in the Geosciences SIAM GS, Leipzig, 15-18 June.
- SAWICKI J., SZPAKOWSKI W., WEINEROWSKA K., WOŁOSZYN E., ZIMA P. 2004. *Laboratorium z mechaniki płynów i hydrauliki*. Politechnika Gdańska, Gdańsk.
- SIDIROPOULOU M.G., MOUTSOPOULOS K.N., TSIHRINTZIS V.A. 2007. *Determination of Forchheimer equation coefficients a and b*. Hydrological Processes, 21(4): 534-554.
- SOBIESKI W. 2010. *Examples of Using the Finite Volume Method for Modeling Fluid-Solid Systems*. Technical Sciences, 13: 256-265.
- SOBIESKI W., TRYKOZKO A. 2011. *Sensitivity aspects of Forchheimer's approximation*. Transport in Porous Media, 89(2): 155-164.
- SOBIESKI W., TRYKOZKO A. 2014a. *Darcy's and Forchheimer's laws in practice*. Part 1. *The experiment*. Technical Sciences, 17(4): 321-335.

- SOBIESKI W., TRYKOZKO A. 2014b. *Darcy's and Forchheimer's laws in practice. Part 2. The numerical model*. Technical Sciences, 17(4): 337-350.
- WU J., TU B., YUN M. 2008. *A resistance model for flow through porous media*. Transport in Porous Media, 71(3): 331-342.
- YU B.-M., LI J.-H. 2004. *A geometry model for tortuosity of flow path in porous media*. Chinese Physics Letters, 21(8): 1569-1571.



## WASTE HEAT RECOVERY FROM SERVERS USING AN AIR TO WATER HEAT PUMP

*Seweryn Lipiński<sup>1</sup>, Michał Duda<sup>2</sup>, Dominik Górski<sup>3</sup>*

<sup>1</sup>ORCID: 0000-0001-9771-6897

Faculty of Technical Sciences  
University of Warmia and Mazury in Olsztyn

<sup>2</sup>ORCID: 0000-0002-9174-3840

Faculty of Technical Sciences  
University of Warmia and Mazury in Olsztyn

<sup>3</sup>ORCID: 0000-0002-0812-9111

SKN EKO-ENERGIA  
Faculty of Technical Sciences  
University of Warmia and Mazury in Olsztyn

Received 14 April 2021, accepted 31 August 2021, available online 1 September 2021.

**Key words:** air-water heat pump, server cooling, waste heat, heat recovery, domestic hot water.

### Abstract

The analysis of advisability and profitability of using an air to water heat pump for the purpose of waste heat recovery from servers being used as cryptocurrency mining rigs, was performed. To carry out such an analysis, the cooling unit of the computing server was connected to the heat pump, and the entire system was adequately equipped with devices measuring parameters of the process. Performed experiments proves that the heat pump coefficient of performance (COP) reaches satisfactory values (i.e., an average of 4.21), what is the result of stable and high-temperature source of heat at the pump inlet (i.e., in the range of 29.9-34.1). Economic analysis shows a significant reduction in the cost of heating domestic hot water (by nearly 59-61%). The main conclusion which can be drawn from the paper, is that in a case of having a waste heat source in a form of a server or similar, it is advisable to consider the purchase of air-to-water heat pump for the purpose of domestic hot water heating.

---

Correspondence: Seweryn Lipiński, Katedra Elektrotechniki, Energetyki, Elektroniki i Automatyki, Wydział Nauk Technicznych, Uniwersytet Warmińsko-Mazurski, ul. Oczapowskiego 11, 10-719 Olsztyn, e-mail: [seweryn.lipinski@uwm.edu.pl](mailto:seweryn.lipinski@uwm.edu.pl)

## Introduction

Currently, heat pumps are usually associated with the heating of single-family houses (CARROLL et al. 2020, MARTINOPOULOS et al. 2018), what is not surprising, considering both ecological (no harmful emissions given off locally in the process) and exploitation (almost maintenance-free, compared to other heat sources, and a small area of the boiler room) aspects (LAKE et al. 2017, OCHSNER 2012, SELF et al. 2013). However, due to their high efficiency, as well as economical and ecological aspects, heat pumps are also increasingly used for other purposes, like e.g., supermarkets simultaneous heating and refrigeration (SALEHI, YARI 2019) or assisting in distillation process (YANG et al. 2016). SCHLOSSER et al. (2020) classifies 155 case studies of large-scale heat pumps to identify suitable characteristics that favour implementation. According to that review, utility water heating for cleaning purposes, process bath heating, drying, and thermal preservation processes, are identified as suitable processes that can be supplied with market-available heat pump technologies. Heat recovery, as stated above, is one of such applications, and quite big number of papers on the subject confirms that fact (HU et al. 2017, HUANG et al. 2017, JOUHARA et al. 2018, KOSMADAKIS 2019, SINGH et al. 2017, XU et al. 2018). However, above cited papers on waste heat recovery technologies and applications focus mainly on big, particularly industrial use (HUANG et al. 2017, JOUHARA et al. 2018), like district heating (HU et al. 2017, XU et al. 2018), paper and pulp industry (KOSMADAKIS 2019) or dairy industry (SINGH et al. 2017). Nevertheless, gradually falling prices of heat pumps, including low power ones, encourage attempts to use them also in non-standard and smaller-scale applications. For example, ADAMKIEWICZ and NIKOŃCZUK (2019) analyse waste heat recovery from the air preparation room in a paint shop while WANG et al. (2017) propose kitchen exhaust air waste heat recovery.

Other example is using heat pumps for waste heat recovery from computing servers, which are being used in many applications, like e.g., calculations for scientific purposes (as a computing cluster), processing of large data packages, rendering graphic designs, working as a company server 24/7, and for cryptocurrency mining.

That is why the aim of this study is to check how the air-to-water heat pump will perform in the recovery of waste heat from server being used for the last of the above-listed purposes, i.e., as cryptocurrency excavator (mining rig), but it should be underlined that conclusions drawn from performed analysis are valid for each computing server, of course after considering its characteristics and parameters.

Literature review shows that however waste heat recovery for data centres and big computing servers is more and more popular on an industrial scale (DEYMI-DASHTEBAYAZ, VALIPOUR-NAMANLO 2019, EBRAHIMI et al. 2014,



ORÓ et al. 2017), awareness of this topic and possibilities resulting from it for the individual user is small. That is why we aim to contribute to this knowledge gap and to show new opportunities in the field of waste heat recovery on a small scale, i.e., by an individual, not an industrial user. For individual user, often the economic aspect is the most important, that is why we supplemented the study on heating efficiency with economic analysis of an investment in low-power heat pump for the investigated purpose.

## Material and methods

As the waste heat source, the computing server Bitman Antminer D3 ver. 19.3 Gh with the cooling capacity of the server unit cooling system equal to 1.22 kW was used.

The analysis of the advisability of using a heat pump for waste heat recovery from server assumed that the heat is intended to be used for domestic hot water heating, because heating domestic hot water, unlike central heating systems, like computing servers, works all year round. That is why waste recovery was performed with the use of the heat pump intended for such purpose, i.e., 2 kW Basic 270 air-to-water heat pump, integrated with a 270-litre domestic hot water tank, produced by Galmet Sp. z o.o. This heat pump has total heating power (heat pump + 2 kW heater) equal to 4 kW and it allows to prepare domestic hot water for up to 4–5-person family (assuming the water consumption will amount to 50 l/person/day) with average power consumption equal to 0.49 kW and acoustic pressure at a distance of 2 meters equal to 46 dB.

The pump was installed according to the producer recommendations. Its air inlet was connected with the outlet of computing server cooling system using spiro pipe with the T-fitting allowing for compensating for the shortage of air for the heat pump resulting from the fact that the pump's air requirement is 313 m<sup>3</sup>/h, while the excavator's cooling system delivers about 200 m<sup>3</sup>/h. The second reason for using T-fitting is the fact that the heat input for heat pump should not and exceed 35°C, while the outlet temperature from the cooling system is about 40°C (value declared by the producer of the computing server, confirmed through measurement). Thanks to the use of a T-fitting, the temperature is reduced through mixing with cooler air from the room. It was confirmed experimentally that due to that mixing, the temperature supplied to the pump is within the operating temperature range specified by the manufacturer (i.e., it does not exceed 35°C).

Above-described configuration was equipped with measuring devices, allowing to measure temperatures on both air inlet and outlet (DS18B20 digital thermometers;  $\pm 0.5^\circ\text{C}$  accuracy), as well as temperature and humidity inside the laboratory (DHT11 temperature and humidity sensor; resolution:

8-bit ( $\pm 1\%$  relative humidity), accuracy  $\pm 4$  relative humidity (at  $25^{\circ}\text{C}$ )). Set up for the experiment and measurements is shown in Figure 1 while the scheme of the methodology used for the purpose of analysis presented in the article is shown in Figure 2.

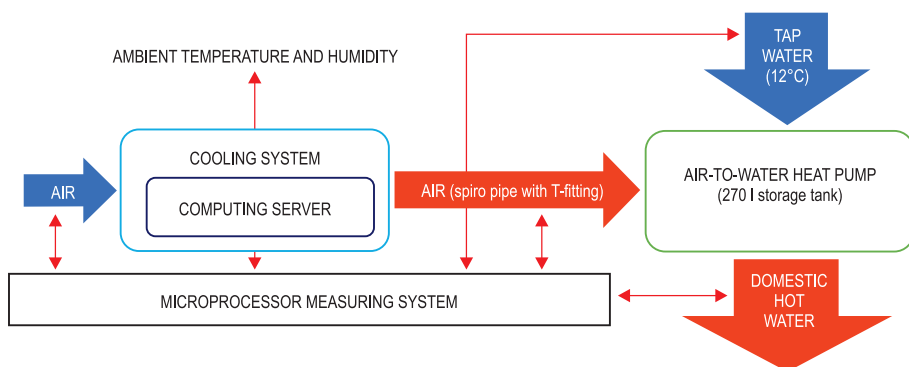


Fig. 1. Experiment/measurement set up

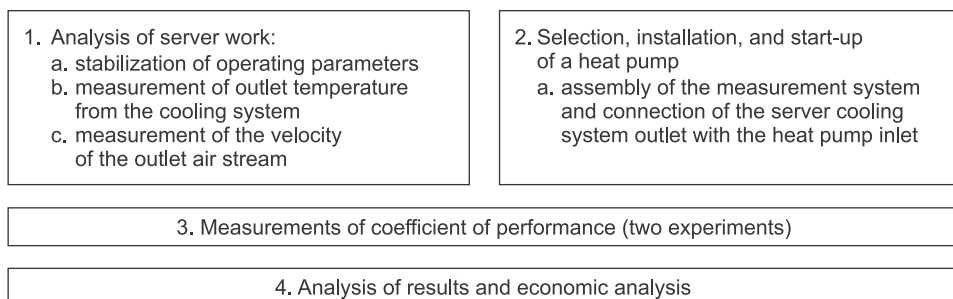


Fig. 2. Schematic of the methodology used for the analysis

## Results and discussion

### Heating efficiency

Crucial parameter that allows to evaluate heating efficiency for broadly understood cooling and heating devices (e.g., refrigerators, air conditioners, and of course heat pumps), is so-called COP (i.e., coefficient of performance) (HUNDY et al. 2016). COP is a ratio of useful heating or cooling provided to work (energy) required. To calculate heating efficiency, given as COP, we used measured air temperatures and velocities at the heat pump inlet/outlet to calculate power that is drawn out of the heat pump as heat  $Q$  [kW], and the amount of electricity consumed by the pump compressor  $P$  [kW],

obtained with the use of a universal electricity meter. Using these two values, we obtain  $COP = \frac{Q}{P} [-]$ . As it was mentioned above, the temperature of air obtained from server cooling thanks to the use of the T-fitting, was being decreased from about 40°C to the range of 29.9-34.1, i.e., proper temperature at the heat pump inlet. Based on that data, and on the assumption that domestic hot water is heated to the temperature of 50°C while its initial temperature (i.e., tap water temperature) is equal to 12°C, we performed an experiment of heating the tap water to the expected final temperature. The experiment was performed twice. All key input parameters in COP measurements are given in Table 1. Parameters of heat pump, as well as parameters of computing server, are given above, in “Material and methods” section.

Table 1

Key input parameters in COP measurements	
Ambient temperature/humidity	22.3°C/54%
Air temperature/humidity at the heat pump inlet	29.9-34.1°C/18.7%
Air velocity at the heat pump inlet	4.9 m s <sup>-1</sup>
Air duct diameter	0.12 m
Initial/final temperature of heated water	12°C/50°C

The results are shown in Figure 3, where COP is shown in a function of water temperature. Average COP for the entire heating cycle was equal to 4.21 which value in our opinion can be considered as satisfactory and in accordance with expected COP for air-to-water heat pump.

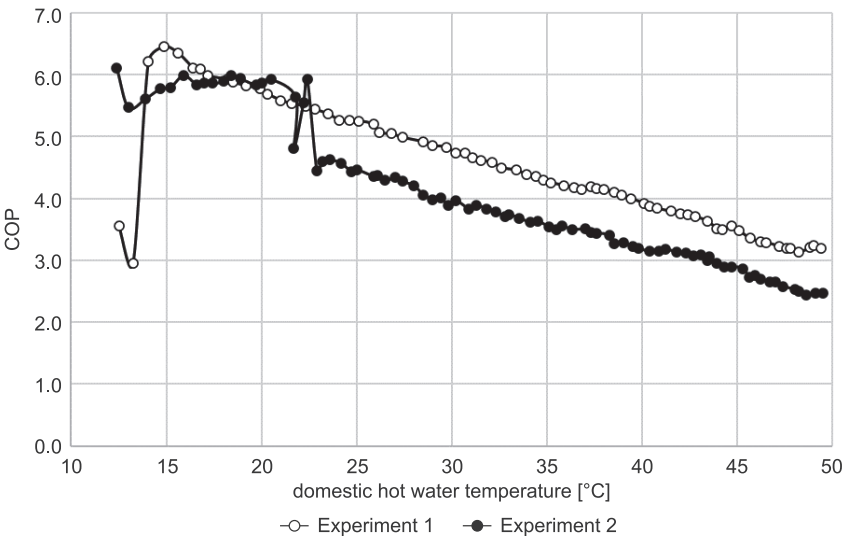


Fig. 3. The process of domestic hot water temperature heating obtained in two experiments shown as COP in a function of heated water temperature

Heating time obtained in both experiments was equal to 350 minutes, which is the result close to that given by the manufacturer of the pump (360 minutes).

Average energy consumption obtained in the heating cycle of 270 l of water was equal to 2.817 kWh, this result differs from the result obtained from the theoretical calculations (2.356 kWh), i.e., the difference is close to 20%.

## Economic analysis

To determine the profitability of the investment, which is the purchase of the heat pump, the key factor is the electricity costs. The calculations adopted the average price for electricity from 2020, which was equal to 0.62 PLN/kWh (cena-pradu.pl).

The analysis below is based on a comparison of two cases – the first case is a situation when the heat pump is used conventionally – using atmospheric air; the second case is the use of waste heat. In the case of conventional use of heat pump, following assumptions were made:

- the pump works only in periods when the air temperature outside the building is higher than 7°C;
- when the air temperature drops below 7°C, the heating role is then taken over by an electric heater built into the tank with a rated power of 2 kW;
- the analysis was carried out for Poland – average daily temperatures from the last four years were collected from the nationwide meteorological database (dane.imgw.pl). Based on that data, the average numbers of days of pump operation during the year in particular ranges were determined.

The results of the economic analysis are shown in Table 2 – it is clearly noticeable that the use of waste heat significantly improves the profitability of heat pump purchase. The annual electricity demand/cost drops by 59%-61.5%. Since annual savings are equal to about 1,000 PLN, while the cost of used heat pump is equal to about 7,500 PLN, an economic stimulus is easily noticeable for a potential heat pump buyer with a waste heat source in a form of a server or similar.

Table 2

The comparison of electricity demand/cost of heat pump with and without using waste heat

Specification	Electricity demand [kWh/year]	Electricity cost [PLN/year]
Heat pump using atmospheric air	2,644.21	1,639.41
Heat pump using waste heat	1,054.03	653.50
Difference	1,590.18	985.92

## Discussion and conclusions

Comparing the achieved results with those known from the literature on the subject, it should be stated that they are at least satisfactory. Obtained COP value, equal to 4.21, is close to 4.8 value obtained by HU et al. (2017) in the process of industrial waste heat recovery and much higher than value of 1.77 obtained by XU et al. (2018) in the process of waste heat recovery in power plant. KOSMADAKIS (2019) shows that if COP value is higher than 2.5, waste heat recovery is starting to make economic sense (case study of typical large-sized paper and pulp industry in Sweden). Considering small-scale applications, ADAMKIEWICZ and NIKOŃCZUK (2019) in the simulation study of waste heat recovery from the air preparation room in a paint shop obtained COP in the range of 3-3.5. The above examples, as well as the economic analysis performed, prove that the proposed solution for waste heat recovery from computing server at small scale makes practical and economic sense.

Summarizing, following conclusions can be drawn based on the performed experiment and analysis:

- the use of untypical heat sources for heat pumps, especially considering the declining prices of heat pumps, is advisable in terms of both economy and ecology;

- large and stable temperature difference between the heat source and tap water positively influences the value of the obtained COP – this difference results in the reduction of electricity consumption and so, quick return on investment in a heat pump (about 50% faster than in a case of using such pump in a conventional way);

- average COP in daily intended use would be obviously better in case of lowering expected domestic hot water temperature, which is a factor that can be influenced by the user;

- the recovered heat can also be used for other purposes (e.g., space heating), but the assumption of the analysis was to choose the method of its utilisation according to the source, i.e., as the computing server is assumed to operate all year round, then heat should also be used year-round as well;

- an additional positive aspect is the utilization of cooled air (pump outlet) at the inlet of the server cooling system – in this configuration, the temperature of the computing server is reduced by about 5°C, which is beneficial for the server's operation (LALL et al. 1997), and, thanks to the slower work of the fans, helps to reduce noise.

## Acknowledgements

The authors acknowledge support from Galmet Sp. z o.o. – one of the elements of the agreement on teaching and research cooperation is making its products available for research conducted by students and scientists.

The authors also want to thank Michał Stryjewski and Dominik Zwierzychowski for their help and support for the project, i.a. by providing the computing servers used in the experiment.

## References

- ADAMKIEWICZ A., NIKOŃCZUK P. 2019. *Waste heat recovery from the air preparation room in a paint shop*. Archives of Thermodynamics, 40(3): 229-241.
- CARROLL P., CHESSER M., LYONS P. 2020. *Air Source Heat Pumps field studies: A systematic literature review*. Renewable and Sustainable Energy Reviews, 134: 110275.
- Cena prądu. <http://www.cena-pradu.pl/> (access: 31.12.2020).
- DEYMI-DASHTEBAYAZ M., VALIPOUR-NAMANLO S. 2019. *Thermoeconomic and environmental feasibility of waste heat recovery of a data center using air source heat pump*. Journal of Cleaner Production, 219: 117-126.
- EBRAHIMI K., JONES G.F., FLEISCHER A.S. 2014. *A review of data center cooling technology, operating conditions and the corresponding low-grade waste heat recovery opportunities*. Renewable and Sustainable Energy Reviews, 31: 622-638.
- HU B., LIU H., WANG R.Z., LI H., ZHANG Z., WANG S. 2017. *A high-efficient centrifugal heat pump with industrial waste heat recovery for district heating*. Applied Thermal Engineering, 125: 359-365.
- HUANG F., ZHENG J., BALEYNAUD J.M., LU J. 2017. *Heat recovery potentials and technologies in industrial zones*. Journal of the Energy Institute, 90(6): 951-961.
- HUNDY G.F., TROTT A.R., WELCH T.C. 2016. *Refrigeration, Air Conditioning and Heat Pumps*. Butterworth-Heinemann, Oxford.
- Instytut Meteorologii i Gospodarki Wodnej. Dane publiczne IMGW-PIB. <https://dane.imgw.pl/> (access: 15.01.2021).
- JOUHARA H., KHORDEGHAN N., ALMAHMOUD S., DELPECH B., CHAUHAN A., TASSOU S.A. 2018. *Waste heat recovery technologies and applications*. Thermal Science and Engineering Progress, 6: 268-289.
- KOSMADAKIS G. 2019. *Estimating the potential of industrial (high-temperature) heat pumps for exploiting waste heat in EU industries*. Applied Thermal Engineering, 156: 287-298.
- LAKE A., REZAIE B., BEYERLEIN S. 2017. *Review of district heating and cooling systems for a sustainable future*. Renewable and Sustainable Energy Reviews, 67: 417-425.
- LALL P., PECHT M., HAKIM E.B. 1997. *Influence of Temperature on Microelectronics and System Reliability: A Physics of Failure Approach*. CRC Press, New York.
- MARTINOPOULOS G., PAPAPOSTAS K.T., PAPADOPOULOS A.M. 2018. *A comparative review of heating systems in EU countries, based on efficiency and fuel cost*. Renewable and Sustainable Energy Reviews, 90: 687-699.
- OCHSNER K. 2012. *Geothermal heat pumps: a guide for planning and installing*. Routledge, London.
- ORÓ E., TADDEO P., SALOM J. 2019. *Waste heat recovery from urban air cooled data centres to increase energy efficiency of district heating networks*. Sustainable Cities and Society, 45: 522-542.
- SALEHI S., YARI M. 2019. *Exergoeconomic assessment of two novel absorption-ejection heat pumps for the purposes of supermarkets simultaneous heating and refrigeration using NaSCN/NH<sub>3</sub>, LiNO<sub>3</sub>/NH<sub>3</sub> and H<sub>2</sub>O/NH<sub>3</sub> as working pairs*. International Journal of Refrigeration, 101: 178-195.

- SCHLOSSER F., JESPER M., VOGELSANG J., WALMSLEY T.G., ARPAGAU S. C., HESSELBACH J. 2020. *Large-scale heat pumps: Applications, performance, economic feasibility and industrial integration*. Renewable and Sustainable Energy Reviews, 133: 110219.
- SELF S.J., REDDY B.V., ROSEN M.A. 2013. *Geothermal heat pump systems: Status review and comparison with other heating options*. Applied Energy, 101: 341-348.
- SINGH S., DASGUPTA M.S. 2017. *CO<sub>2</sub> heat pump for waste heat recovery and utilization in dairy industry with ammonia based refrigeration*. International Journal of Refrigeration, 78: 108-120.
- WANG K., LI N., PENG J., WANG X., WANG C., WANG M. 2017. *A highly efficient solution for thermal compensation of ground-coupled heat pump systems and waste heat recovery of kitchen exhaust air*. Energy and Buildings, 138: 499-513.
- XU Z.Y., MAO H.C., LIU D.S., WANG R.Z. 2018. *Waste heat recovery of power plant with large scale serial absorption heat pumps*. Energy, 165: 1097-1105.
- YANG M., XIAO F., GUILIAN L. 2016. *Heat integration of heat pump assisted distillation into the overall process*. Applied Energy, 162: 1-10.







## APPLYING PYTHON'S TIME SERIES FORECASTING METHOD IN MICROSOFT EXCEL – INTEGRATION AS A BUSINESS PROCESS SUPPORTING TOOL FOR SMALL ENTERPRISES

*Jolanta Litwin<sup>1</sup>, Marcin Olech<sup>2</sup>, Anna Szymusik<sup>3</sup>*

<sup>1</sup>ORCID: 0000-0002-3650-1953

<sup>2</sup>ORCID: 0000-0002-8346-4673

<sup>3</sup>ORCID: 0000-0002-2472-851X

Department of Computer Science  
Rzeszow University of Technology

Received 27 August 2021, accepted 14 September 2021, available online 22 September 2021.

**Key words:** time series forecasting, python integration, excel integration.

### Abstract

The paper describes the current state of research, where integration of Microsoft Excel and Python interpreter, gives the business user the right tool to solve chosen business process analysis problems like: forecasting, classification or clustering. The integration is done by using Visual Basic for Application (VBA), as well as XLWings Python's library. Both mechanisms serve as an interfaces between MS Excel and Python to allow the data exchange between each other. Creating the suitable Graphical User Interface (GUI) in Microsoft Excel, gives the business user opportunity to select specific data analysis method available in Python's environment and set its parameters, without Python's programming. Running the method by Python's interpreter can bring the results, which are hard or even impossible to obtain by using Microsoft Excel only. However, the data analysis methods stored in the Python's script, which are available to the business user, as well as VBA source code, must be designed and implemented by the data scientist. Sample, basic integration between Microsoft Excel and Python's interpreter is presented in the paper. To present value-added of the proposed software solution, simple case study according to time series forecasting problem is described, where forecasting errors of different methods available in the Microsoft Excel and Python are presented and discussed. The paper ends with conclusions according to the results of the current researches and suggested directions of further research.

---

Correspondence: Jolanta Litwin, Zakład Informatyki, Wydział Budowy Maszyn i Lotnictwa, Politechnika Rzeszowska im. Ignacego Łukasiewicza, al. Powstańców Warszawy 12, 35-959 Rzeszów, e-mail: [j.litwin@prz.edu.pl](mailto:j.litwin@prz.edu.pl)

## Introduction

There is no doubt that business activity of the enterprise – conducted by business processes execution – is strictly connected to decision making. Nowadays enterprises have to adjust to ever changing market's condition. What is more, they must predict some phenomenon like consumer's requirements and apply the solution, which bring competitive advantage to them.

Successful and effective management of the enterprise is hardly based on the data the enterprise has. The data is used to plan activity of the organization in the daily routine, as well as in the future. Despite of the size of the organization or type of business activity the organization conducts (production, services, banking, commerce), the enterprises always try to predict future events and plan their development by using various prediction technique (WINKOWSKI 2019, KURZAK 2012).

The organizations can use whole palette of the prediction method. Some of them are simple enough that can be developed and implemented by using Microsoft Excel, which is very often used by business staff of the enterprise. What is worth to mention, despite of the fact the "Industry 4.0" conception comes into reality, analysis clearly show, that spreadsheets used for over 30 years, will be still in constant usage (BIRCH et al. 2018).

Of course many drawbacks can be seen when trying to apply Microsoft Excel to "Big Data" directly. However, by using additional data science software, which pre-process and aggregate raw data from "Big Data" repository into smaller and more suitable form, will bring possibility to still use spreadsheet as a simple analysis tool for aggregated data and as a dashboard for publish analysis results. Another way is to force business staff to learn and use rather complicated software and libraries like "BigQuery", "Redshift" or "PySpark", which allow direct access to "Big Data". However, is hard to imagine, the business user will interact with data by using programming-oriented source codes instead of familiar graphical user interface available in Microsoft Excel. It seems, that both worlds will have to integrate together and still co-exist.

The certain problem here is the fact, that sometimes – especially with "Industry 4.0" conception in mind – available data analysis method, which are available or can be implemented under spreadsheet environment are not as accurate as needed. This is mainly connected to the characteristics of the data source. In that case, enterprises can use more sophisticated analytical software e.g. Statistica with Automated Neural Networks mechanism or Online Analytical Processing (OLAP) available in Microsoft SQL Server or in Microsoft Dynamics. Those environments allow the organization to access to more complicated and suitable analysis method. The proposed solution however, has some drawbacks:

- the software license in many cases is expensive – especially when the license is commercial;

- dedicated software analytical solution has – in many cases – a lot of features and built-in tools, which are not necessary during normal business activity of small enterprises;
- the complicated software solution must be deployed in the organization, what is cost- and time-consuming, what is more, there are sometimes conflicts with legacy systems;
- business staff of the organization must be trained in order to be able to work with new software solution.

According to presented disadvantages it is worth to mention, that all of them generate expenses, so often deployment of “big” software supporting system is out of scope of small enterprises, which have to be cost-effective to have competitive advantage.

Potential solution according to data analysis and data visualization for small companies, can be found in “open-source” software projects, which can be successfully applied – under certain conditions – as an alternative to commercial software. One of the well-known environment, which can be used in the proposed area and which is “open-source” is Python. The main reason, the Python can be taken under consideration as an alternative to “paid” software, are connected to the fact, that proposed programming language is very popular nowadays (JANUSCHOWSKI et al. 2019). That popularity is connected mainly to the features of Python and its versatility (SAABITH et al. 2019). Another factor, which can motivate the organization to choose Python, is huge repository of additional libraries, which extend its scope of use widely. Some of the extensions are dedicated to data analysis and visualization area, e.g. “Pandas”, “Statsmodels” or “scikit-learn”. Proposed libraries give the user access i.a. to different forecasting method or machine learning tools (BROWNLEE 2020).

Of course making software solution in the area of data analysis and visualization in the form of Python's script(s) needs knowledge and ability according to business analytics, as well as Python's programming language. This is certainly, out of scope for typical business user of the enterprise. However, the data science labor's market is steadily growing (DONATI, WOOLSTON 2017), so hiring data scientist, who works as a freelancer, should not be a problem to create integration mechanism and to develop appropriate data analysis method. So, here is the point, where the researches briefly described in the current paper were started.

To sum, it seems that good data analytical solution for business people can be developed in form of Python's script(s), but those scripts have to be executable from “classical” tool, which is Microsoft Excel in the case. The possibility of performing integration between both proposed environments can be very attractive to business user and allows to perform sophisticated data analysis task with control mechanisms shared under traditional spreadsheet.

Researches performed so far were focused on basic integration of Microsoft Excel with Python environment. The main idea here, is to allow the business user to:

- prepare source data set under spreadsheet environment;
- perform initial transformation of the data by using traditional mechanism available under Microsoft Excel;
- send chosen data to the data analysis Python's script(s) by using developed graphical user interface (GUI) under spreadsheet;
- retrieve results generated by the Python's script(s) under Microsoft Excel and use them to support decision process.

In the current paper, the results of the researches and the developing process of integration mechanism between Microsoft Excel and Python interpreter are presented. To prove that kind of integration can be valuable to business user, the short and simple case study has been prepared. In the end of the paper, the pros and cons of current software solution are presented, as well as, further research are described.

## **Material and Methods**

The purpose of the studies is to develop a solution for integrating the Microsoft Excel environment and Python interpreter and to verify the validity of its use especially to business user. An important feature of the solution is its accessibility, ease of use and the possibility for unskilled programming workers to use through integration the analytical methods available in the Python package, such as: ARIMA (AutoRegressive Integrated Moving Average model) or Deep Neural Networks. Development of integrating solution according to data scientist point of view is presented in the "Solution development" section of the paper. Applying of proposed solution by the business user is presented in the same section as well.

An example of integration of both environments was presented by completing a case study that addresses the problem of time series prediction. In the presented case study a forecasting process based on data from two time series with different characteristics was conducted. The calculations for the selected, more traditional forecasting methods were performed in the Microsoft Excel, while the Python interpreter executed the ARIMA forecasting method by performing implemented script. After the forecasting results have been obtained, the forecast errors of the methods were calculated and a comparative analysis of the accuracy of used prediction methods was performed.

## Data characteristics

The data used in the case study were shared by a small production company, which manufacturing the range of products for the horticultural industry. The data are related to the value of demand determined on the basis of the purchasers' declarations and the unit costs incurred for the production of the selected product. Company name and details of the data provided were classified by the company.

The data provided by the company was recorded at the end of each month for a period of 5 years. Thus, a total of 60 values were obtained, as shown in the charts and analyzed to determine the characteristics of the time series. In the case of the demand, which was firstly considered, an upward trend was observed and there was a clear seasonal fluctuation (Fig. 1).

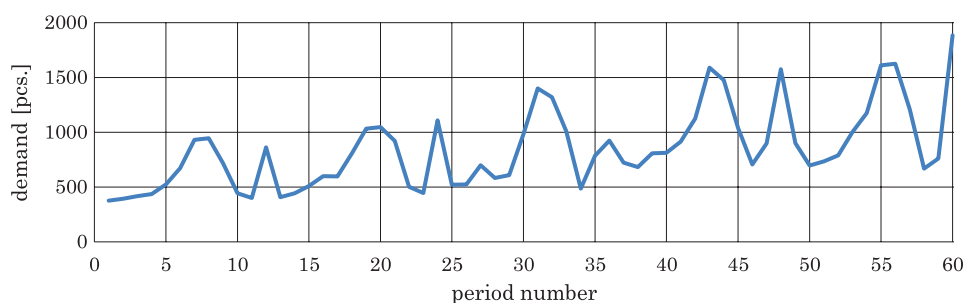


Fig. 1. Observed demand values  
Source: own study.

However, in the case of unit costs (Fig. 2) no periodic fluctuations were observed. The only characteristics according to this time series were random fluctuations and, as in the case of demand, upward trends.

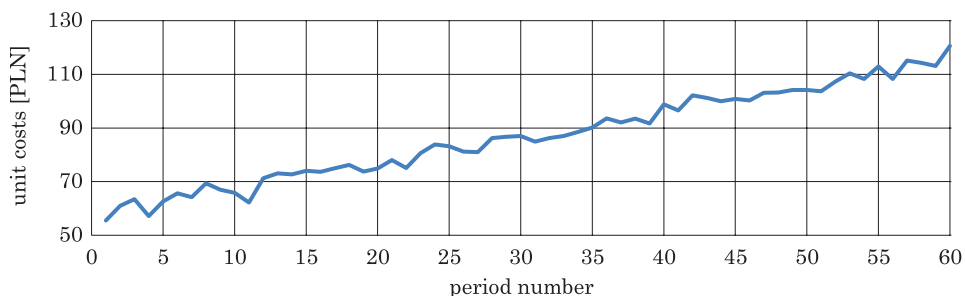


Fig. 2. Observed unit production costs values  
Source: own study.

## **Selection of forecasting methods and metrics**

The study uses the following methods of forecasting: naive, moving average, polynomial trend line, autoregression and ARIMA. The first four methods were implemented in a Microsoft Excel environment to illustrate, that some data forecasting methods can be developed by a business spreadsheet user itself. However, the ARIMA method was implemented by the business analyst by using the specific Python's libraries and workflow described by the script. All of the indicated forecast methods were applied and input data related to demand and product's unit costs were used in the prediction of time series.

The purpose of the ongoing case study was to make a forward-looking forecast for the next 12 periods (one year). Due to the fact that the chosen methods of forecasting are well known and described in the literature, their description has been omitted and only the parameters selected for them are indicated in the paper.

According to the naive method, it was assumed that the forecast value in the given period is equal to the value recorded in the time series by one period earlier (SHIM et al. 2012, HYNDMAN, ATHANASOPOULOS 2018). For example, the demand value from the first period is the forecast for the second period. In the moving average method, a lag equal to 6 periods was used, i.e. the arithmetic mean was calculated from the previous 6 parts of the time series (HANSUN, KRISTANDA 2017). In a forecasting using a trend line, a polynomial 6-degree trend line was used. The auto-regression method uses a delay parameter of 6 periods (PENA-SANCHEZ, RINGWOOD 2017). For the ARIMA method, the optimal choice of method parameters, i.e. co-efficients  $p$ ,  $d$  and  $q$  (SIAMI-NAMINI, NAMIN 2018) has been obtained by using a grid search (RASCHKA, MIRJALILI 2019).

The indicated parameter values for each forecast method were selected after a series of initial calculations using different values of parameters and comparing the accuracy of the generated forecast. The delay in the moving average method was verified for values of 3 and 6 periods (months), the degree of the polynomial trend line was verified for values between 2 and 6, and the delay in the autoregressive model was verified for values of 3 and 6 months. In the ARIMA method, models were tested by using the following parameters during grid search:  $p$  – from 0 to 20,  $d$  – from 0 to 2,  $q$  – from 0 to 5.

The final values of the parameters for both time series have provided forecasts with the highest accuracy. The accuracy of the methods was measured by calculating forecast error values. Among commonly used forecasting accuracy measures are: the mean square error (MSE), root mean square error (RMSE), mean absolute error (MAE) or mean absolute percentage error (MAPE). All mentioned metrics have a common disadvantage – their values can range between zero and +infinity. Despite, MAPE is one of the most popular measures of the forecast accuracy, especially among industry practitioners. What is more,

it is scale-independent, easy to interpret and intuitive (KIM, KIM 2016). In the presented case MAPE calculated according to formula 1 (CHICCO et al. 2021) was used:

$$\text{MAPE} = \frac{1}{m} \sum_{i=1}^m \left| \frac{y_i - y_i^P}{y_i} \right| \cdot 100 [\%] \quad (1)$$

where:

- $m$  – the number of periods available in the time series,
- $y_i$  – the actual value for period  $i$ ,
- $y_i^P$  – the forecast value for period  $i$ .

After determining the errors of each forecast method by using MAPE metric, a comparative analysis was performed and the most effective method was identified, in addition it was verified whether this method could be implemented directly by the business user in the Microsoft Excel environment, or whether it is necessary to integrate the spreadsheet with Python environment.

## The solution development

The preparation of the solution for environments integration, as part of the case study, was performed to provide the business user with easy and convenient access to more complex method of data analysis not available in the Microsoft Excel package. In this case this method was ARIMA that enables forecasting of time series data. The workflow of a data analyst in the process of preparing an environment integration solution included the following tasks:

- review and analysis of input data and business problem;
- selection of an advanced method of forecasting applicable in a Python environment but not available in the Microsoft Excel;
- development of a Python script with source code responsible for the executing the selected forecasting method;
- test and verification of the script operation;
- creation of sheet template for the data in an Excel workbook;
- development of a macro in VBA in the same Excel file;
- adjusting of fragments of Python's script and macro to ensure their correct cooperation.

The source code responsible for executing the ARIMA method (SWAMYNATHAN 2019), on the indicated and temporarily saved data in CSV file, is stored in the Python's script. The script also contains command from "XLWings" library (EHRHARDT et al. 2017). The library allows the developer to return the results of calculations to the Microsoft Excel environment. The detailed source code of the script is presented in the appendix of the current paper. The script itself



was developed under Anaconda environment with Visual Studio Code Editor. The Visual Studio Code Editor is an Integrated Development Environment (IDE) which supports the developer during implementation process of the script (SPEIGHT 2021).

The developed Python script, which realizes the ARIMA predication method is rather typical script, which consist of the following sections:

- load data section, where “Pandas” (NELLI 2018) library is imported and data stored in the “Input\_dataset.csv” temporary file are imported as a Python’s “DataFrame”;

- split data section, where the data stored in “DataFrame” are split into train and test set; at the current version of the script the size of the train is equal to 80% of data, other 20% of data creates test dataset; in the future version of the solution it is planned, that business user itself will use appropriate Graphical User Interface (GUI) elements to select desired size of train and test datasets;

- making ARIMA model section, here main part of the script is implemented; because the ARIMA method needs, that three parameters  $p$ ,  $d$  and  $q$  must be set, the grid search has been implemented to help the business user find most suitable parameters; the using “for” loop gives possibility to test whole range of parameters to determine the best ARIMA model; “best” here means the model with lowest mean absolute percentage error (MAPE) calculated between prediction of the chosen model and real data stored in the test set; in the current version of the script the tested parameters are as following:  $p$  – from 0 to 20,  $d$  – from 0 to 2,  $q$  – from 0 to 5, so during execution of the script 378 models were generated and tested against test data to find the optimal set of coefficients;

- generating final prediction results section, in the section the optimal ARIMA model found is used to generate prediction of the examined phenomenon and store the result in the chosen variable; generating the prediction is main goal of the business user;

- exporting prediction results, current section used the “XLWings” library to pass the prediction results stored in the chosen variable to the new sheet of Microsoft Excel named “Forecast”, to give the business user ability to check best ARIMA model prediction;

- cleaning section, the last section of the Python’s script consists of Python’s command, which goal is to remove temporary file “Input\_dataset.csv”.

The workbook designed in Microsoft Excel consist of a worksheet named “Data” which serves the business user to enter the input data for current issue. Moreover, the worksheet also includes a Graphical User Interface (GUI) element – a button (form control) that launches a developed VBA script enabling a business user to interact with prepared Python’s script. The Microsoft Excel software solution view is shown on the Figure 3.



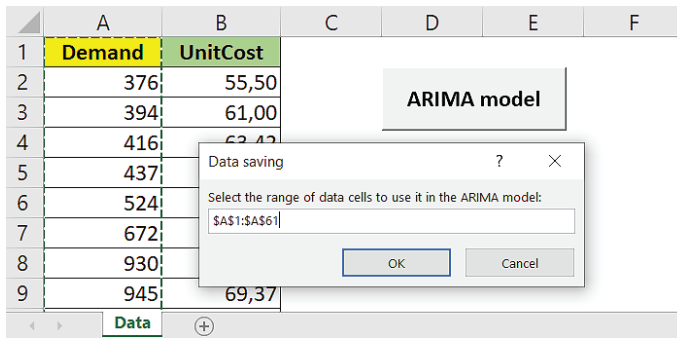


Fig. 3. Data saving in “Data” worksheet  
Source: own study.

The macro developed in the Visual Basic Editor (VBE) contains two sections:

- the first one is used for saving the selected data in “Data” worksheet in temporary file named “Input\_dataset.csv” as comma separated values (CSV); the business user selects the range of data cells by using specific dialog box (Fig. 3);

- the second one is responsible for proper launch of the Python’s interpreter and selection of the script that should be run by the interpreter; in this part of the VBA code, access paths to the interpreter and the script that executes the ARIMA method are assigned to individual variables.

The source code of the VBA macro is available in the appendix of the paper.

Finally, the workflow of the business user according to developed Excel and Python integration solution is shown in Figure 4.

The workflow of a business user while using the developed solution is rather straight-forward and include the following activities:

- open the Excel file with macro provided by business analyst;
- import, copy and paste or enter the data into “Data” sheet;
- run a macro using the button (the graphic element of the graphical user interface);
- indicate the range of cells with data to be used by the Python script in the prediction process;
- review and analysis of the results displayed in the “Forecast” sheet, when Python’s interpreter finishes script execution.

To sum, the developed Python’s script realizes the prediction, based on data selected in Microsoft Excel by using the best found ARIMA model and bring the results of the prediction process directly to business user in Microsoft Excel sheet by using proposed integration mechanism. All source code for an integration solution (VBA macro and Python script) are presented in the appendix.

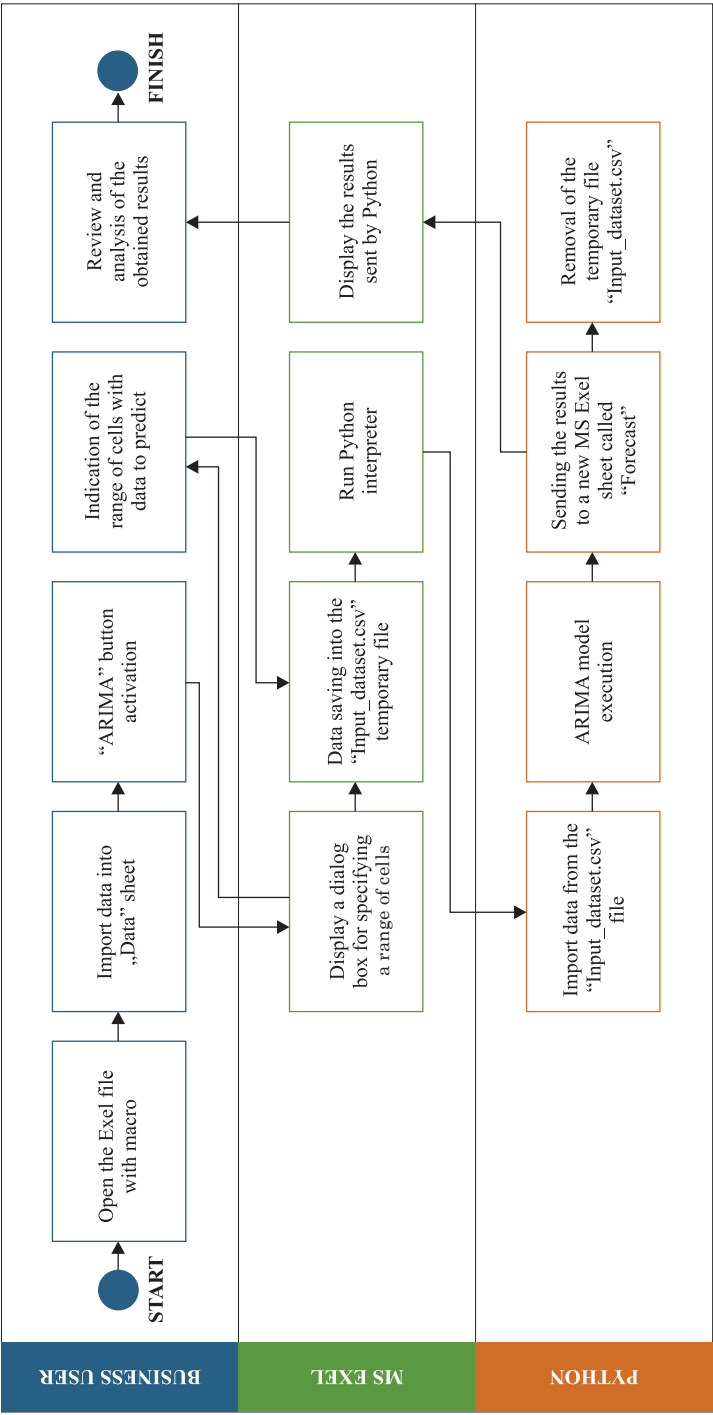


Fig. 4. Activity Diagram showing the business logic of the prepared solution  
Source: own study.

## Results and discussion

The execution process of developed software support for business user is very simple and intuitive. Business user needs to:

- put all developed files into one directory: the first file is Microsoft Excel's file with embedded VBA macro, which serves as a data input tool, as well as interface, which integrates spreadsheet environment with Python; the other file(s) are Python's script(s), which are developed as a chosen data analysis and/or visualization methods, which brings the final result of analysis back to Microsoft Excel, if all prepared methods are executed;
- open Microsoft Excel file and put all input data, which describes the problem into one column of the prepared "Data" sheet as shown on the Figure 3;
- set the parameters of the developed methods, if able, by using appropriate GUI elements and execute developed "Python" methods by using the button shown on the Figure 3;
- wait until all data analysis methods are executed by the Python's interpreter;
- review the results of the analysis by examining output data sheet called "Forecast" in that case in the Microsoft Excel.

In the following section of the paper, the results of analysis of case study are presented and discussed.

Forecast values for time series related to demand and unit production costs were determined with the use of selected methods and then their accuracy was assessed. The evaluation of a given method consisted of calculating the mean absolute percentage error (MAPE) and indicating the value of the standard deviation of error (SD). The data was divided into training set and test set. These sets consisted of 48 and 12 periods consecutively, regardless of the method chosen. The values of forecast errors for each of the sets and each analysed variable are presented in Table 1 and Table 2. Among the methods, only those were indicated, which business user can develop directly in the Microsoft Excel environment, ignoring the ARIMA method. The results of ARIMA method are presented later in this chapter.

Table 1

Demand and unit costs – training set [%]

Method	Demand		Unit costs	
	MAPE	SD	MAPE	SD
Naive	27.20	28.46	3.17	2.93
Moving average	29.80	24.52	3.72	2.59
Trend line	33.74	23.64	24.55	31.35
Autoregression	24.73	32.13	2.02	1.96

Source: own study.

Table 2

Method	Demand and unit costs – test set [%]			
	Demand		Unit costs	
	MAPE	SD	MAPE	SD
Naive	30.63	27.23	2.68	2.15
Moving average	36.50	21.92	7.42	4.20
Trend line	110.06	76.06	196.10	50.02
Autoregression	23.15	19.50	1.84	0.94

Source: own study.

After analysing the results presented in tables 1 and 2, it was found, that the most accurate of the forecasting methods was the autoregressive method. According to demand and unit production costs, this method is characterized by the lowest values of forecast errors and standard deviation. The standard deviation value calculated for the demand training set is an exception – in this case it is the largest. Forecasts determined by the autoregression method for each of the time series are shown on the Figures 5 and Figures 6. Due to the delay of six periods used, the method is calculated from period 7<sup>th</sup>.

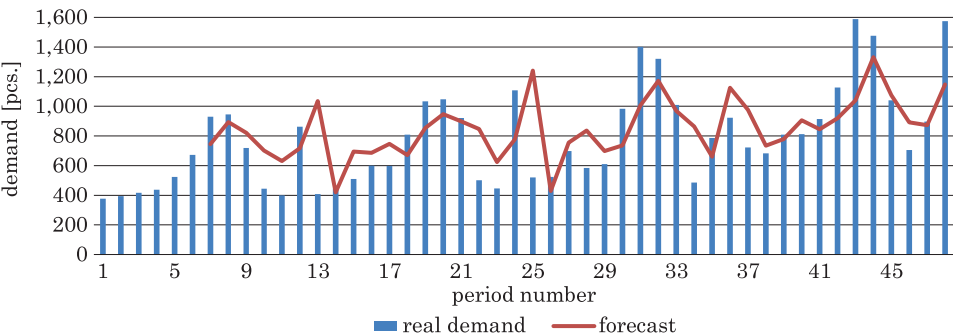


Fig. 5. Historical data and forecast of demand  
Source: own study.

The values of the forecasts generated by the autoregressive method were compared with the values returned as a result of running the script containing the ARIMA model. In this case, the forecast errors were calculated for the last 12 periods of the time series, because this part of data was used as a test set of the ARIMA model.

The mean absolute percentage error for the value of demand in the case of the autoregressive method was 23.15%, while in the case of the ARIMA model 10.39%. Thanks to the application of the ARIMA method it is possible

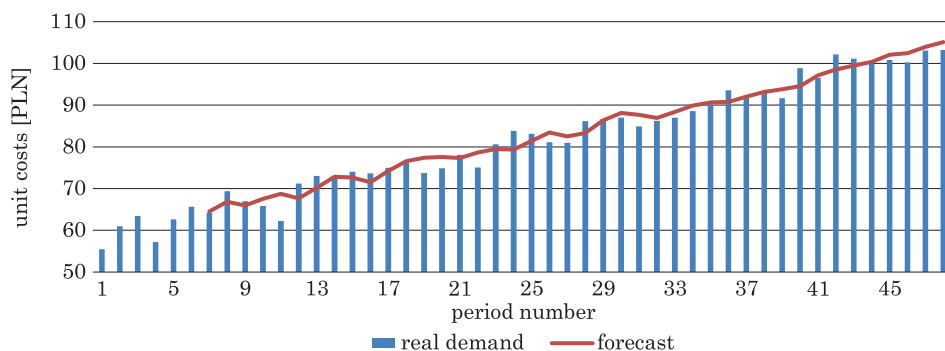


Fig. 6. Historical data and forecast of unit production costs

Source: own study.

to generate a forecast with nearly a half less error. In the case of the values of the unit production costs again the ARIMA model turned out to be more effective, the calculated MAPE was 1.30%, while in the autoregressive method its value was 1.84%. However, here the improvement in the effectiveness of the forecast as measured by the percentage error value is not so spectacular. The forecasts determined by the autoregression method and by the ARIMA model in the given period are shown in Figures 7 and 8 respectively.

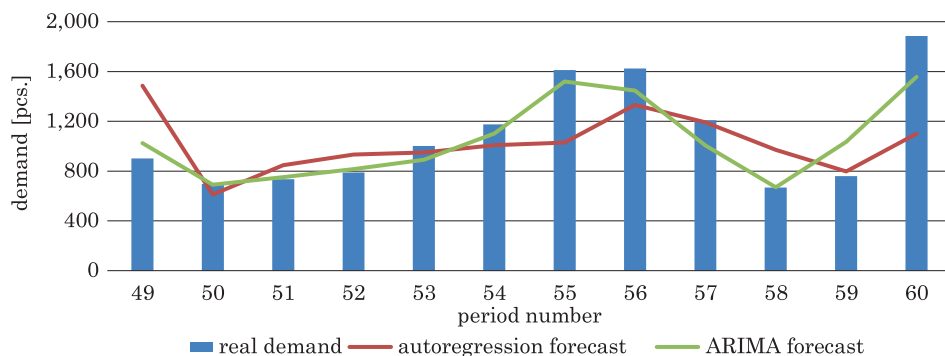


Fig. 7. Comparison of autoregressive and ARIMA forecasting methods for demand

Source: own study.

The analysis of the results carried out as part of the case study confirmed, that of all the prediction methods used, the ARIMA model provides the best results. However, the obtained average forecast error value equal to 10.39% is relatively high, which means that a business user should review other forecasting methods and try to select their parameters properly to achieve better accuracy.

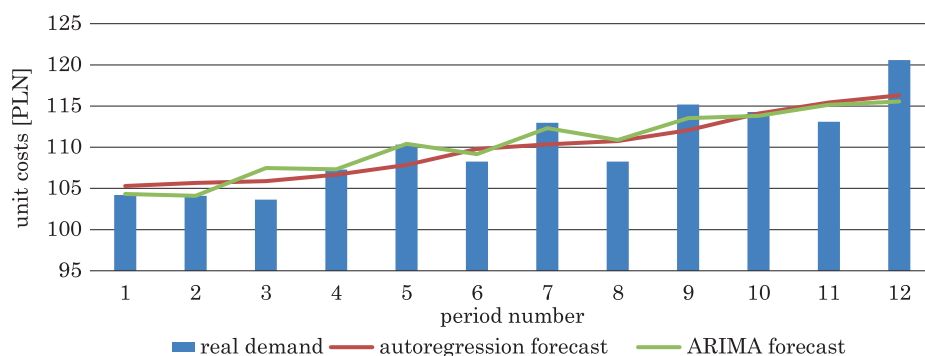


Fig. 8. Comparison of autoregressive and ARIMA forecasting methods for unit production costs  
Source: own study.

Summarizing the completed case study, the use of the integration mechanism of the Microsoft Excel and Python environments made it possible to obtain prognostic models more effective, than it is possible to achieve with the use of the Microsoft Excel alone. It is also important, that the many processes of data analysis methods developed in the form of Python's scripts are available in Python's repositories. The business user may applied selected data analysis workflows to any input data stored in a spreadsheet, which describe problem considered in the enterprise, by using proposed integration mechanism, without the need of knowledge the Python or VBA languages.

## Conclusions

Researches performed so far, clearly show that building software integration between Microsoft Excel and Python is possible. The result of the integration allows the business user to prepare input data set and then execute sophisticated data analysis method described in Python's script and see final result of the analysis, without Python's programming knowledge and skills. What is more, building appropriate graphical user interface in Microsoft Excel can give the business user possibility to control developed Python's scripts in easy way. The business user is able to select specific methods stored in the scripts or pass specific parameters of the chosen methods to change the way of execution. Moreover, developed integration mechanism can be offered to different business user as a business process analysis support tool using incorporated Python's data analysis and visualization methods.

It is worth to mention, that implementation of proposed solution still needs Python's developer, who will implement or adjust appropriate Python's script

to solve selected business problem. What is more, the developer will have to develop GUI under Microsoft Excel to give the business user ability to control the scripts, as well as, program VBA macros to connect spreadsheet's control elements to Python scripts and methods. So, the Python's developer is essential to create working efficient software tool, but if the development process is finished, the software tool can be used by typical business user, who is able to use Microsoft Excel. Another issue the research team had to face was incompatibility between specific versions of Python's libraries during integration mechanism development. For example, the problem still exists if developer uses newest "Pandas" and "XLWings" libraries. To resolve the problem, developer needs to downgrade problematic libraries to different version, what makes development process of integration solution harder to perform.

Further research according to presented integration mechanism will be oriented to implement different forecasting method e.g. by using neural networks, to improve forecasting results of product's demand prediction. In this case, it will also be necessary to introduce additional measures to ensure a more efficient assessment of the accuracy of forecasts, for example the coefficient of determination (also known as  $R$ -squared or  $R^2$ ) or the symmetric mean absolute percentage error (SMAPE). Another field of interest is building GUI in Microsoft Excel to give business user all control elements needed to fully control implemented Python's methods and their parameters. The more control mechanism the business user have, the developed Python's scripts will be more versatile and adjusted to specific business problem the business user wants to solve. Of course, the integration mechanism can be performed to solve different type of data analysis problems like: classification task, clustering or regression problems by using methods which are unavailable or hard to implement under Microsoft Excel environment. Because the problem described in the current case study was practically oriented, further research can be based on benchmark dataset published by UC Irvine Machine Learning Repository or Kaggle to compare results of proposed solution with some other methods or results presented by other authors in the literature, to obtain optimal business process supporting tool and to show value-added of the proposed solution.

To conclude, research in that field are consider as important, because the final goal of the current researches is to create and describe the whole development process of the integration between both environments. Performing specific activities described in the proposed development process, should result in software sharing most important and accurate data analysis and visualization methods available in Python to Microsoft Excel business user.

## References

- BIRCH D., LYFORD-SMITH D., GUO Y. 2018. *The Future of Spreadsheets in the Big Data Era*. Proceedings of the EuSpRIG 2017 Conference "Spreadsheet Risk Management". Imperial College, London, UK.
- BROWNLEE J. 2020. *Introduction to Time Series Forecasting with Python: How to Prepare Data and Develop Models to Predict the Future*. Machine Learning Mastery, San Francisco, p. 2-5.
- CHICCO D., WARRENS M.J., JURMAN G. 2021. *The coefficient of determination R-squared is more informative than SMAPE, MAE, MAPE, MSE and RMSE in regression analysis evaluation*. PeerJ Computer Science, 7: e623. DOI: <https://doi.org/10.7717/peerj-cs.623>.
- DONATI G., WOOLSTON C. 2017. *Information management: Data domination*. Nature 548: 613–614. DOI: <https://doi.org/10.1038/nj7669-613a>.
- EHRHARDT M., GÜNTHER M., TER MATEN E.J.W. 2017. *Novel Methods in Computational Finance*. Springer, Cham, p. 545.
- HANSUN S., KRISTANDA M.B. 2017. *Performance Analysis of Conventional Moving Average Methods in Forex Forecasting*. Proceedings of 2017 International Conference on Smart Cities, Automation & Intelligent Computing Systems. Yogyakarta, Indonesia.
- HYNDMAN R.J., ATHANASOPOULOS G. 2018. *Forecasting: Principles and Practice*. 2<sup>nd</sup> ed. OTexts, Melbourne, p. 57-58. <https://otexts.com/fpp2/> (access: 18.06.2021).
- JANUSCHOWSKI T., GASTHAUS J., WANG Y. 2019. *Open-Source Forecasting Tools in Python*. The International Journal of Applied Forecasting, 55: 20-26.
- KIM S., KIM H. 2016. *A new metric of absolute percentage error for intermittent demand forecasts*. International Journal of Forecasting, 32(3): 669-679.
- KOH L., ORZES G., JIA F. 2019. *The fourth industrial revolution (Industry 4.0): technologies disruption on operations and supply chain management*. International Journal of Operations & Production Management, 39(6/7/8): 817-828.
- KURZAK L. 2012. *Importance of forecasting in enterprise management*. Advanced Logistic Systems, 6(1): 173-182.
- NELLI F. 2018. *Python Data Analytics with Pandas, NumPy and Matplotlib*. 2<sup>nd</sup> ed. Apress, Rome, p. 143-145.
- PENA-SANCHEZ Y., RINGWOOD J. 2017. *A Critical Comparison of AR and ARMA Models for Short-term Wave Forecasting*. Proceedings of the 12<sup>th</sup> European Wave and Tidal Energy Conference, Kildare, Ireland.
- RASCHKA S., MIRJALILI V. 2019. *Python Machine Learning: Machine Learning and Deep Learning with Python, scikit-learn, and TensorFlow 2*. 3<sup>rd</sup> ed. Packt Publishing Ltd., Birmingham, p. 207-211.
- SAABITH A.L.S., FAREEZ M.M.M., VINOTHRAJ T. 2019. *Python Current Trend Applications – An Overview*. International Journal of Advance Engineering and Research Development, 6(10): 6-12.
- SHIM J.K., SIEGEL J.G., SHIM A.I. 2012. *Budgeting Basics and Beyond*. 4<sup>th</sup> ed. John Wiley & Sons, Inc., Hoboken, p. 277-279.
- SIAMI-NAMINI S., NAMIN A.S. 2018. *Forecasting economic and financial time series: ARIMA vs. LSTM*. <http://arxiv.org/abs/1803.06386> (access: 17.06.2021).
- SPEIGHT A. 2021. *Visual Studio Code for Python Programmers*. John Wiley & Sons, Inc., Hoboken, p. 3-49.
- SWAMYNATHAN M. 2019. *Mastering Machine Learning with Python in Six Steps. A Practical Implementation Guide to Predictive Data Analytics Using Python*. 2<sup>nd</sup> ed. Apress, Bangalore, p. 234-243.
- WINKOWSKI C. 2019. *Classification of forecasting methods in production engineering*. Engineering Management in Production and Services, 11(4): 23-33.



## Appendix

**VBA source code:**

```
Sub startPython()

Dim Rng As Range
Dim WorkRng As Range
Dim xFile As Variant
Dim xFileString As String
Dim newFile As Workbook

Dim objShell As Object
Dim PythonExe, PythonScript As String

'Data saving in csv
On Error Resume Next
xTitleId = "Data saving"
Set WorkRng = Application.Selection
Set WorkRng = Application.InputBox("Select the range of data cells to use
it in the ARIMA model:", xTitleId, WorkRng.Address, Type:=8)

If Err.Number = 424 Then
    Exit Sub
End If

Workbooks.Add
Set newFile = ActiveWorkbook
WorkRng.Copy Application.ActiveSheet.Range("A1")

newFile.SaveAs "D:\...\\" & "Input_dataset.csv", xlCSV
newFile.Close

'Running Python script
ActiveWorkbook.Save

Set objShell = VBA.CreateObject("Wscript.Shell")
PythonExe = """C:\...\python.exe"""
PythonScript = "D:\...\arima_model_1.py"
objShell.Run PythonExe & PythonScript

End Sub
```

**Python's source code:**

```

import pandas as pd

#data import
df = pd.read_csv('Input_dataset.csv')

#train and test set
a = df.size
train_data=round(0.8*a)
test_data = a - train_data

train = df.iloc[:-test_data]
test = df.iloc[-test_data:]

#ARIMA parameters test
import warnings
warnings.filterwarnings("ignore")
from statsmodels.tools.sm_exceptions import ConvergenceWarning
warnings.simplefilter('ignore', ConvergenceWarning)

from statsmodels.tsa.arima.model import ARIMA
best_error=1;
best_p=0;
best_d=0;
best_q=0;
for q in range(0,6):
    for d in range(0,3):
        for p in range(0,21):
            try:
                model=ARIMA(train,order=(p,d,q), trend='n',
enforce_invertibility=False, enforce_stationarity=False)
                model=model.fit()
                #prediction
                start=len(train)
                end=len(train)+len(test)-1
                forecast = model.predict(start=start,end=end)

                #scoring
                from sklearn.metrics import mean_absolute_percentage_error
                mape=mean_absolute_percentage_error(forecast,test)
                print("Current model: ",p,",",d,",",q," - error: ",mape)
                if (mape<best_error):
                    best_error=mape
                    best_p=p
                    best_d=d
                    best_q=q
            except:
                continue

```

---

```
print("Best ARIMA model p,d,q - error: ",best_p,"",best_d,"",best_q,"" -
      "\n,best_error")

model2=ARIMA(train,order=(best_p,best_d,best_q),trend='n',enforce_inverti-
bility=False, enforce_stationarity=False)
model2=model2.fit()

#prediction
start=len(train)
end=len(train)+len(test)-1
forecast2 = model2.predict(start=start,end=end)
print('Best ARIMA model: (\' ,best_p,\' ,\' ,best_d,\' ,\' ,best_q,\' )
      - predictions:')
print(forecast2)

#forecast export to Excel file
import xlwings as xw
wb = xw.Book('SWD1.xlsm')
ws2=wb.sheets.add('Forecast')
ws2['A1'].value = forecast2

#delete temporary data file
import os
os.remove('Input_dataset.csv')
```



## BOOTSTRAP AGGREGATION TECHNIQUE FOR EVALUATING THE SIGNIFICANCE OF MANUFACTURING PROCESS PARAMETERS IN THE GLASS INDUSTRY

*Łukasz Paśko<sup>1</sup>, Aneta Kuś<sup>2</sup>*

<sup>1</sup> ORCID: 0000-0001-8175-2295

<sup>2</sup> ORCID: 0000-0002-5028-0261

Department of Computer Science

Faculty of Mechanical Engineering and Aeronautics

Rzeszów University of Technology

Received 27 August 2021, accepted 14 September 2021, available online 22 September 2021.

**Key words:** manufacturing process, glassworks, neural networks, bagging, manufacturing parameters.

### Abstract

The article presents the application of the bootstrap aggregation technique to create a set of artificial neural networks (multilayer perceptron). The task of the set of neural networks is to predict the number of defective products on the basis of values of manufacturing process parameters, and to determine how the manufacturing process parameters affect the prediction result. For this purpose, four methods of determining the significance of the manufacturing process parameters have been proposed. These methods are based on the analysis of connection weights between neurons and the examination of prediction error generated by neural networks. The proposed methods take into account the fact that not a single neural network is used, but the set of networks. The article presents the research methodology as well as the results obtained for real data that come from a glassworks company and concern a production process of glass packaging. As a result of the research, it was found that it is justified to use a set of neural networks to predict the number of defective products in the glass industry, and besides, the significance of the manufacturing process parameters in the glassworks company was established using the developed set of neural networks.

---

Correspondence: Łukasz Paśko, Zakład Informatyki, Wydział Budowy Maszyn i Lotnictwa, Politechnika Rzeszowska im. Ignacego Łukasiewicza, al. Powstańców Warszawy 12, 35-959 Rzeszów, e-mail: [lpasko@prz.edu.pl](mailto:lpasko@prz.edu.pl)

## Introduction

Nowadays, it is difficult to find an industry that does not use artificial neural networks (ANNs). ANNs are even used in agriculture, to assess the degree of maturity of apples, as described by GÓRSKI et al. (2008), to assess the wheat damage, as presented by GOLKA et al. (2020) or to determine the hardness of wheat kernels, as discussed by HEBDA and FRANCIK (2006). Neural modelling in the agriculture field was also used by NIEDBAŁA et al. (2015) to predict starch content in potatoes. The methods of using ANN also vary. Staying on the topic of the non-obvious application of ANN in agriculture, but also in mechanical engineering, FRANCIK (2006) describes the use of the method of forecasting time series with the use of ANN to characterize agricultural machines. The use of ANNs in mechanical engineering has been discussed for many years; already LEFIK (2005) described the applications of ANNs in mechanics and engineering, but it can certainly be said that this application is still showing an upward trend and we are witnessing incredible developments in the field of ANNs.

The use of ANNs is also an indispensable element of the Big Data phenomenon. Collecting an enormous amount of data, including those that may seem to be useless, in combination with machine learning allows us to detect dependencies that may affect an entire process under study, and which were previously not taken into account. This combination is particularly useful in production processes, e.g. for the assessment of production parameters and detection of the causes of undesirable phenomena. As assessed by TADEUSIEWICZ and HADUCH (2015), ANNs are used, for example, for the examination of motor gasoline and constitute an excellent prognostic tool supporting the management of the production process. ANNs are also used in production quality control processes, as described by ROJEK (2015).

There are many types of ANNs and their applications, but one of the most popular types is the Multilayer Perceptron (MLP) network. This is confirmed by the scale of application of MLP-type neural networks in classification and regression, as discussed by KURT et al. (2014). MLP networks are used where there is a large number of input and output data, it is necessary to define the relationship between them and when the problem is very complex. The MLP network consists of layers: input, hidden and output neurons and is a type of unidirectional network, i.e. a signal that flows from the input neurons through the hidden layer to the output neurons no longer returns to “earlier” neurons. Various learning algorithms are used to train MLP neural networks. One of the most popular is the error backpropagation algorithm.

One of the concepts that has emerged in machine learning is ensemble machine learning. This concept implies the use of more than one model (e.g. ANN) to derive a classification or regression result. An example of ensemble machine learning is bootstrap aggregation—otherwise also known as bagging.

This is an aggregation method that uses the same training algorithm on different subsets of data created using cases from the original training dataset. These subsets of data are called “bags of data”. According to the described method, from a training dataset of size  $n$ ,  $m$  subsets of a dataset  $D$  ( $D_1, D_2, \dots, D_m$ ) of size  $n'$ , are created at random, using cases from the original dataset. Cases for subsets are selected randomly on the basis of replacement, which means that cases may repeat in one subset and this is not undesirable. The bagging method uses the  $n' < n$  rule. It means that each of the subsets of  $D$  contains fewer cases than the original dataset. Then each of the subsets is used as a training dataset, in effect creating  $m$  models of the same type – each of them trained on a different set of data. The results of each model are then averaged, resulting in the final classification or regression result.

The study described in this article is not the first use of bagging with ANNs. OPITZ and MACLIN (1997) assessed the possibility of using bagging in this field, ZHIBIN et al. (2018) described possibility of using bagging method in ANN for prediction of thermal comfort in buildings. Also, already in 1996, BREIMAN (1996) confirmed that the described method of data aggregation solves the problem of the lack of stability of classifiers. However, above-mentioned studies are related to the classifiers topic while in this research the bagging method was used in the regression problem. Another novelty introduced by this article is the use of the described method on a real-world data set obtained from a glassworks production process while OPITZ and MACLIN (1997) conduct research on a publicly available data set, very often used in this type of research. In addition, mentioned authors used cross validation method, while in the studies described in this article, the dataset is sufficient to divide it into three subsets: train, validation and test, without using cross validation method.

Having access to an enormous number of parameters that can be input variables using ANNs, it is extremely important and difficult to determine the significance of each of them. The methods of carrying out significance analysis are described by JASIŃSKI and BOCHENEK (2016), where the authors use ANN to forecast real estate prices. Examples of methods for determining the significance of parameters are: searching for the optimal set of parameters by building many models with a different set of explanatory variables or testing the sensitivity of the output variable to the input data. The result of carrying out such analyses is to remove those input parameters that have the least impact on the output variable. The results of tests carried out by the RODZIEWICZ and PERZYK (2016) who analysed the significance of the parameters of a continuous steel casting process, confirm the expediency of determining the significance of the input variables for the detection of defects in manufactured products.

This article presents the use of the previously described bagging (bootstrap aggregation) method and MLP-type ANNs to determine the significance of the manufacturing process parameters in a glassworks, which can be used

to determine the causes of defects in the glass products. The article is a continuation of previous research (PAŠKO 2020), which considers the possibility of using ANNs to determine the influence of production parameters on the number of defective products for a single ANN.

## Description of the Case Study

The aim of the research was to predict the number of defective products based on the values of selected manufacturing process parameters. Additionally, an attempt was made to determine the impact of the analyzed manufacturing process parameters on the number of defective products. Thanks to the conducted experiment, it is also possible to assess the usefulness of the bootstrap aggregation technique combined with ANNs.

The problem of product defectiveness discussed in the article is one of the most important problems for manufacturing companies. Product quality assurance is a key element of the strategy of manufacturing companies, because these companies are forced to constantly meet the needs of customers by offering them the highest quality products. For this reason, research on the quality of products and the search for the causes of product defects are still up-to-date and needed.

The research was based on a case study of a glassworks that produces glass packaging. In the glassworks, several dozen types of defects in products have been defined, but only one type of defect was considered in this study. The analyzed defect consists in the presence of small size air bubbles located inside the glass, which are visible in the finished products.

The more complicated the manufacturing process, the more various types of product defects may appear. It is particularly visible on the example of the manufacturing process in a glassworks, which consists of the following stages: preparation of an appropriate mixture of raw materials, melting of the prepared mixture, molding of liquid glass, hot refining of products, annealing of products to reduce internal stresses, and cold refining to increase the aesthetic value of the product. The occurrence of abnormalities in any of these stages can deteriorate the quality of the finished products.

The manufacturing process in a glassworks requires the maintenance of appropriate parameters, such as:

- temperature – determines the effectiveness of melting raw materials and the correctness of the annealing process of semi-finished products;
- atmospheric conditions – maintaining appropriate conditions affects the cleanliness of the glass;
- gas pressure – is responsible for the homogeneity of the glass mass.

It is necessary to establish appropriate values for the above parameters in order to avoid the production of defective products.



The experiment discussed in this paper concerns the problem of regression. In this type of problem, the value of the explained variable is predicted based on the values of the explanatory variables (predictors). The research was carried out on the basis of a dataset from the glassworks. The dataset consists of 70 explanatory variables and one explained variable. The explanatory variables concerned selected parameters of the manufacturing process. Their values were recorded every second, but for this study the dataset was transformed with an interval of ten minutes. The parameters of the manufacturing process that were taken into account in the research concern:

- the temperature of the glass measured in several places of the glass furnace (each measurement location was associated with a separate explanatory variable);
- the temperature of the glass measured in several places of the forehearth, which distributes the glass to the production line (each measurement place was associated with a separate explanatory variable);
- selected operating parameters of the glass furnace and the forehearth (e.g. the level of glass in the furnace, the speed of loading raw materials into the furnace, combustion air pressure in several dozen locations of the forehearth, and each operating parameter was associated with a separate explanatory variable);
- selected cooling parameters of glass molds.

The explained variable is the number of defective products in which the analyzed defect was identified. Data on the number of defective products was recorded every ten minutes. This means that each data point contains information on how many defective products have been identified at the quality control station in the last ten minutes. The dataset included the values of the above-mentioned manufacturing process parameters recorded during 27 days of continuous production.

Table 1 presents the basic statistics on selected predictors and the dependent variable. The table reveals the clear differences between the variables. These differences are also confirmed by the graphs shown in Figures 1-2. Figure 1 presents time series plots of three selected explanatory variables and the dependent variable. These types of graphs are used to assess the basic characteristics of variables, such as long-term trends, regular periodic fluctuations, the level of values, and the homogeneity of variance. For many predictors, it has been noted that their values fluctuate around more than one constant level, and the transition between levels occurs quickly. When observing the variance of the variables (differences in values around the average level of the variable), it is noticed that the variance is not homogeneous. For some variables, their variance increases over time. Focusing on observing periodic fluctuations, it can be stated that in some cases the periodic fluctuations are clearly visible. The best example is temperature variable, which contains data about the air temperature measured in the production hall. Its periodicity is related to the daily fluctuations in air temperature.

Table 1

Basic statistics of selected variables					
Variable	Min.	Mean	Median	Max.	Standard deviation
J2FFONTTPTCPV	1,271.3	1,300.2	1,299.9	1,321.2	8.9
J21BLCBPRPV	9.8	10.3	10.4	11.2	0.3
Pressure	987.9	1,015.7	1,016.7	1,028.1	7.7
No. of defects	1	36.7	30	255	28.4

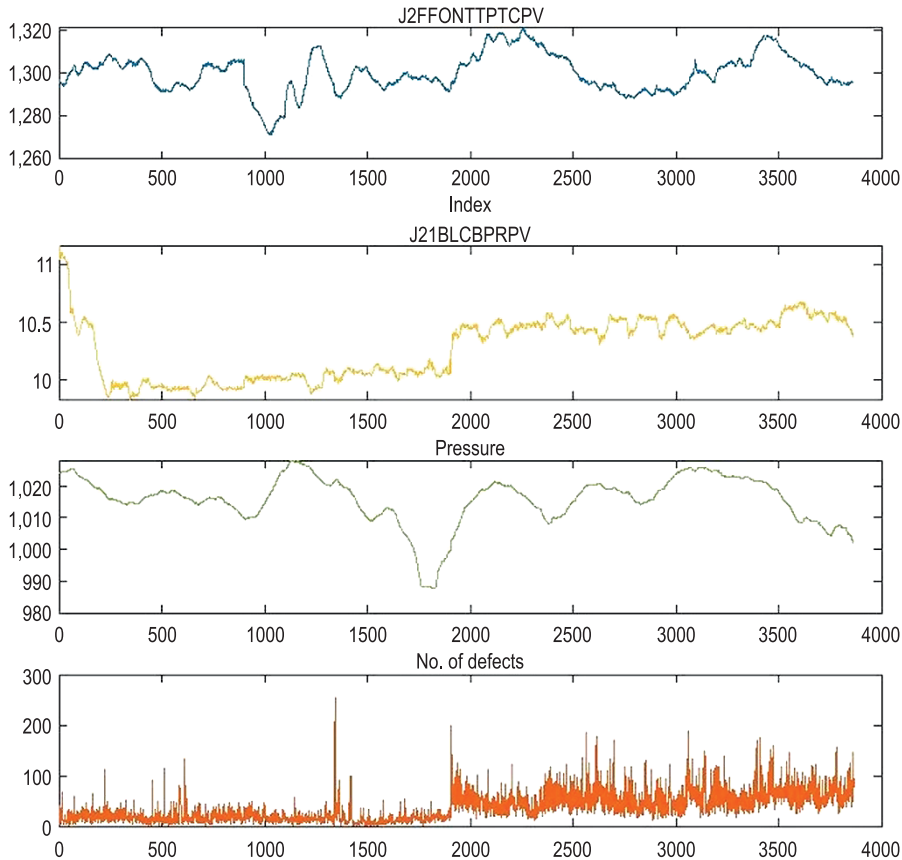


Fig. 1. Time series plots for selected variables

In turn, Figure 2 contains histograms of selected variables. The histograms show that distributions of the variables are diversified. In the case of many variables, bimodal distributions can be noticed, in which two histogram bars are clearly higher than the others. This arrangement of the histogram bars shows that most of the observations are concentrated around two levels of values.

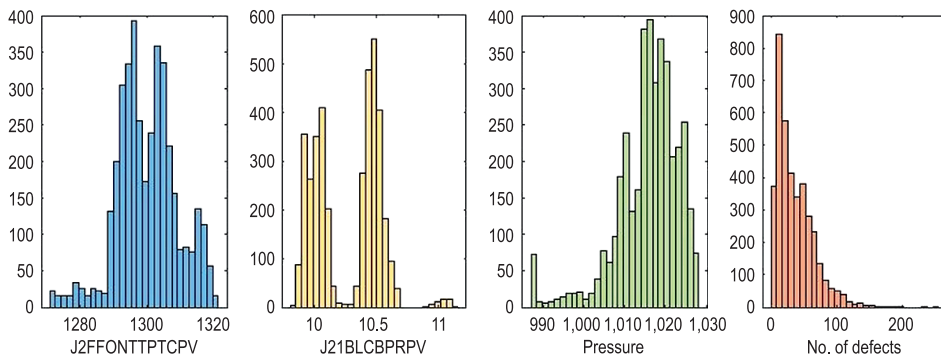


Fig. 2. Histograms for selected variables

Among the analyzed variables, there are also those that their histogram is characterized by a clear left-skewed (negative skewness), as in the case of the Pressure variable. In turn, a small part of the variables has a right-skewed distribution (positive asymmetry). Such a distribution applies to the dependent variable (no. of defects). The conducted exploratory data analysis showed that the methods of data analysis used during the research should be insensitive to heterogeneity of variance and to the distributions of the variables, as well as should be able to map the levels of the variables and their seasonal fluctuations.

## Research Methodology

The research was carried out according to the framework shown in Figure 3. MATLAB software was used to carry out all the activities in this experiment. The first stage was the exploratory data analysis. One of the explanatory variables was rejected at this stage because its values did not change over the period considered, so this variable could not affect the number of defective products in the analyzed period. Therefore, in the next stages, 69 explanatory variables were taken into account. Apart from the aforementioned rejection of one variable based on the time series graph, no other feature extraction techniques were used. This was because feature extraction techniques such as principal component analysis or independent component analysis transform the original variables into a set of new variables called components. A characteristic feature of the components is that they are artificial variables, the value of which is difficult to interpret in relation to the manufacturing process parameters. One of the goals of the conducted research was to establish the significance of the manufacturing process parameters, which would be difficult after the use of techniques that transform the original parameters.

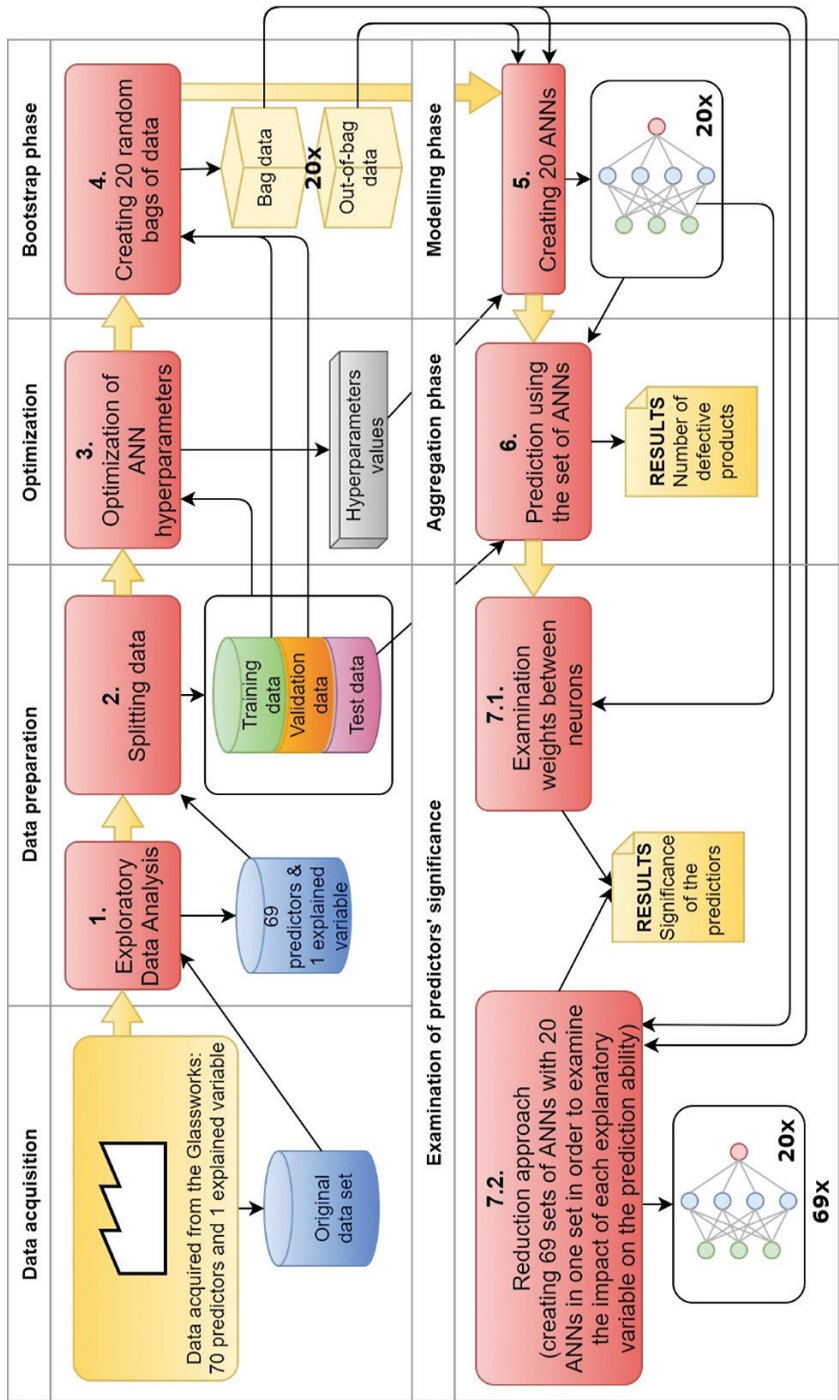


Fig. 3. Research framework

The second stage was to divide the dataset into training, validation and test subsets. The number of observations in each variable was 3,866. 3,094 cases were randomly selected for the training subset, which constitutes about 80% of all cases from the dataset (a “case” is a vector composed of the observations of all explanatory variables and the explained variable registered at a given time  $t$ ). The validation subset consisted of 386 randomly selected cases (approx. 10%). The remaining cases (386) were included in the test subset.

The third stage was to optimize the ANN hyperparameters. The aim of this stage was to determine the optimal values of the three MLP neural network hyperparameters: the number of neurons in the hidden layer, the activation function of hidden neurons, and regularization term strength (denoted as lambda). Table 2 shows the values of the hyperparameters that were taken into account during the optimization. 50 network sizes (the number of hidden neurons), 4 activation functions, and 51 lambda values were analyzed. Consequently, 10,200 ANNs were created. Such approach that involves generating all possible combinations of the analyzed hyperparameters would be computationally inefficient in the case of Big Data. However, the analyzed data does not have three basic features ascribed to Big Data, called 3V:

- Volume — a huge amount of data;
- Variety — various data formats and different degrees of data structuring;
- Velocity — high speed of generating new observations that need to be taken into account during the analysis and the need to generate analysis results as soon as possible.

Table 2

Hyperparameter values taken into account during optimization	
Hyperparameter	Considered values
Number of hidden neurons	2, 4, 6, ..., 100
Activation function of hidden neurons, $f$	<p>Rectified linear unit function (ReLU), which performs the following operation on each input element <math>x</math>:</p> $f(x) = \begin{cases} x, & x \geq 0 \\ 0, & x < 0 \end{cases}$ <p>Hyperbolic tangent function (tanh):</p> $f(x) = \tanh(x)$ <p>Sigmoid function:</p> $f(x) = \frac{1}{1 + e^{-x}}$ <p>Identity function:</p> $f(x) = x$
Regularization term strength (lambda)	$0.05 \cdot 10^{-4}, 1.0 \cdot 10^{-4}, \dots, 2.5 \cdot 10^{-3}$

Due to the fact that the analyzed data does not have the features of Big Data, it was decided to use the approach described below to optimize the hyperparameters.

Each of the created ANNs was trained with a different combination of hyperparameters. The learning algorithm called Limited-memory Broyden-Fletcher-Goldfarb-Shanno (LBFGS) was used to train the ANNs. The training subset was used to train the ANNs. The validation subset was used to control the end of ANN training. The ANN training process ended when the mean square error (MSE) calculated on the validation subset increased in ten consecutive iterations of the training algorithm. The MSE value is calculated according to the following formula:

$$\text{MSE} = \frac{1}{n} \sum_{i=1}^n (y_i - \hat{y}_i)^2 \quad (1)$$

where:

- $y_i$  – the observed value of the explained variable,
- $\hat{y}_i$  – the predicted value of the explained variable,
- $n$  – the number of cases in the dataset.

The role of the objective function was played by the root mean square error (RMSE =  $\sqrt{\text{MSE}}$ ) calculated on the test subset. Thanks to the use of RMSE, the error the ANNs is expressed in the same units as the original explained variable. The learning process of all ANNs was repeated ten times, each time assuming different initial values of the weights of connections between neurons. After ten iterations, the mean RMSE was calculated for each combination of the hyperparameters considered. Figure 4 shows three plots of averaged RMSE measure. The plots show that the RMSE value is most influenced by the number of hidden neurons – the more neurons, the smaller the RMSE (although over 50 neurons, the RMSE does not decrease significantly). There are also clear differences in the activation function. Relatively low RMSE values occur for the ReLU and sigmoid functions, while for the hyperbolic tangent the RMSE values are the highest. The lambda parameter has the least influence on the RMSE. For all tested values of the lambda parameter, the RMSE values calculated on the test subset do not differ significantly from each other.

Finally, the set of hyperparameters for which the average RMSE calculated on the test subset had the smallest value was selected. As a result of optimization, the following set of hyperparameters was established: 80 hidden neurons, ReLU activation function, lambda value of  $1.1 \cdot 10^{-3}$ . Such values of hyperparameters were adopted in the subsequent stages of the experiment.

The fourth stage of the research is the preparation of bags that are subsets of the original dataset. It was assumed that the number of bags  $m = 20$ , and the number of cases in each bag  $n' = 3400$ . Cases for each bag were drawn from among the cases included in the training and validation subsets. Those cases

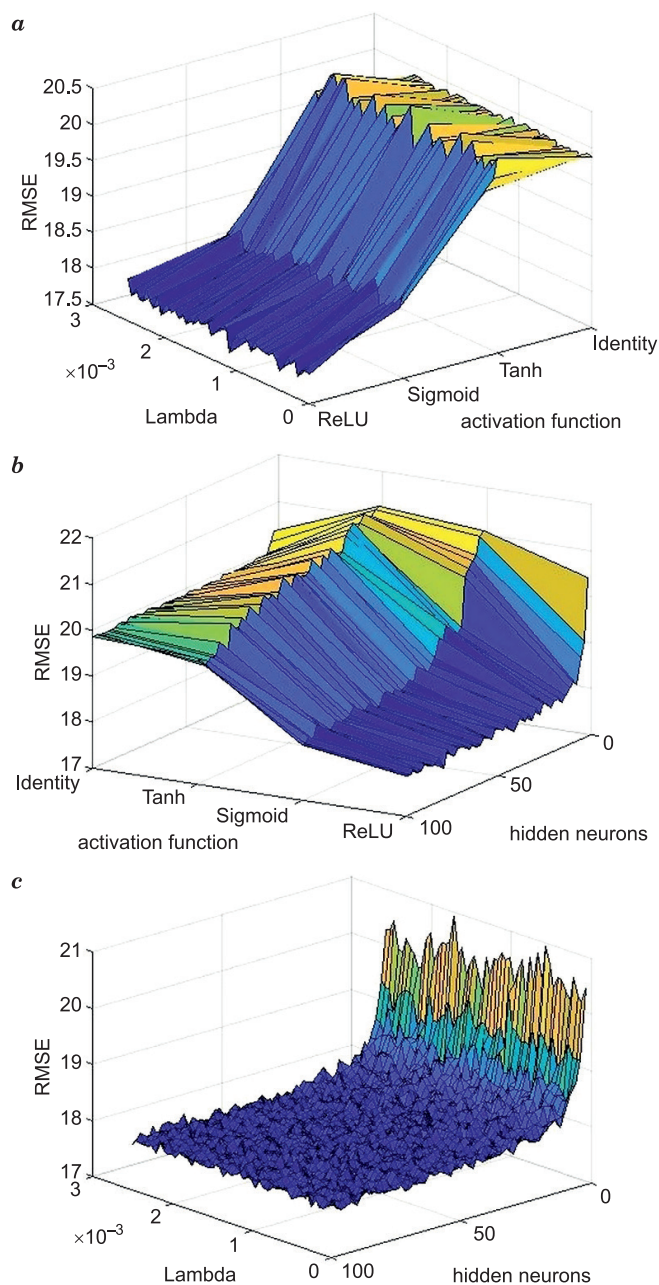


Fig. 4. Plots showing the influence of activation functions, number of hidden neurons, and lambda on RMSE obtained during optimization of hyperparameters: *a* – influence of lambda and activation function on RMSE (ANNs with 80 hidden neurons), *b* – influence of activation function and number of hidden neurons on RMSE (ANNs with lambda = 0.0011), *c* – influence of lambda and number of hidden neurons on RMSE (ANNs with ReLU activation function)



that were not selected for a given bag were placed in a set called out-of-bag. The cases included in the test subset were not used when creating bags.

In the fifth stage, a set of ANNs was created. The set consisted of  $m = 20$  ANNs. All ANNs were developed using the hyperparameters established in the third stage. Each ANN was trained on one of the bags created. The out-of-bag set, which was created from cases not included in the given bag, was used for validation. When the MSE value calculated for cases from the out-of-bag set increased in ten learning iterations, the ANN training process was completed. This situation can be seen in Figure 5. The graph shows the MSE values determined during the training of one of twenty ANNs. The lowest MSE value for the validation subset was achieved in iteration no. 109. From iteration no. 110, the MSE value was slightly higher than the lowest value. This caused the learning process to end in iteration 119.

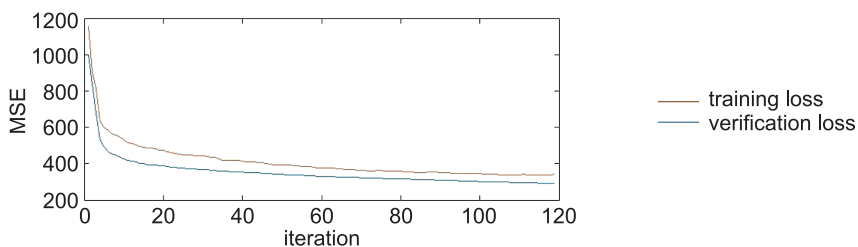


Fig. 5. MSE values calculated during training of one of the ANNs

The sixth stage is the prediction of the number of defective products using the twenty ANNs created. This stage can be called the aggregation phase in which the prediction results of each single ANN are aggregated by computing the arithmetic mean. The determined average number of defective products based on the results of twenty ANNs is treated as the final result of prediction by the set of ANNs. Prediction of the number of defective products was performed mainly for cases from the test subset. Based on the prediction results, the RMSE was calculated for each ANN separately and for the set of ANNs. For comparison, the RMSE on the training and validation subsets was also calculated.

In the last, seventh stage of the research, the significance of ANNs input variables, which are manufacturing process parameters, was examined. Two approaches were used to determine the significance of the input variables:

- Stage 7.1: examination of connections weights between input neurons and hidden neurons,
- Stage 7.2: reduction approach.

In step 7.1 it was assumed that for a given neural network  $v$  the significance of its input variable  $X_i$  is equal to the sum of the absolute values of connections



weights  $w_{I_i \rightarrow H_j}$  from the input neuron  $I_i$  which represents the variable  $X_i$  to each of the  $K$  hidden neurons (designation  $H$ ) in this ANN:

$$\text{ANN}_v \text{sig}_{X_i} = \sum_{j=1}^K |w_{I_i \rightarrow H_j}| \quad (2)$$

Having determined the significance of all input variables for each of twenty ANNs in the above manner, then three methods of calculating the significance of input variables were used, taking into account the entire set of ANNs:

– Method I: Significance of the variable  $X_i$  expressed as the sum of the significance of this variable for each of the ANNs:

$$\text{Sig}_{X_i}^I = \sum_{v=1}^m \text{ANN}_v \text{sig}_{X_i} \quad (3)$$

– Method II: Significance of the variable  $X_i$  expressed as the arithmetic mean of the significance of this variable for each of the ANNs:

$$\text{Sig}_{X_i}^{II} = \frac{1}{m} \sum_{v=1}^m \text{ANN}_v \text{sig}_{X_i} \quad (4)$$

– Method III: Significance of the variable  $X_i$  expressed as the median significance of this variable for each of the ANNs:

$$\text{Sig}_{X_i}^{III} = \text{median}_{v \in \{1, \dots, m\}} (\text{ANN}_v \text{sig}_{X_i}) \quad (5)$$

In turn, in step 7.2 a reduction approach was applied, thanks to which it was possible to use the fourth method of calculating the significance of input variables:

$$\text{Sig}_{X_i}^{IV} = \frac{\text{RMSE}_{X_i}}{\text{RMSE}} \quad (6)$$

The given set of ANNs, which is used to determine the significance of the variable  $\text{Sig}_{X_i}^{IV}$  is trained on a subset of data that is devoid of the variable  $X_i$ . After generating the set of ANNs, the  $\text{RMSE}_{X_i}$  error for that set is determined. Finally, the significance of the variable  $X_i$  is treated as the quotient of the prediction error of the ANNs trained on the dataset devoid of the variable  $X_i$  and the prediction error of the ANNs trained on the dataset containing all input variables. The rejection of the input variable usually results in the deterioration of the predictive ability of the model (the RMSE error value increases). Therefore, it is assumed that the greater the  $\text{RMSE}_{X_i}$ , the more significant the variable  $X_i$  is. It is also possible that removing a given variable  $X_i$  from the training set will improve the predictive ability of the model. Then the measure  $\text{Sig}_{X_i}^{IV}$  takes values

smaller than 1, and the variable  $X_i$  is treated as insignificant for the model. The reduction approach required the creation of  $N$  sets of ANNs, where  $N$  is the number of input variables. Each of the  $N$  sets was trained on a subset of data generated using the bagging technique.

## Results and Discussion

The plot in Figure 6 shows the RMSE values taking into account the prediction results of each of the twenty ANNs generated in the fifth stage. The RMSE was computed for the training, validation, and test subsets. In the case of most ANNs, the following relationship can be seen: the RMSE for the training subset has the lowest value (ranging from approx. 16.6 to 20.4), while the RMSE for the validation subset has the highest value (from approx. 18.6 to 21.5). Between these values is the RMSE calculated on the test subset (from about 18.2 to 20.5). In turn, the RMSE value calculated from the prediction results of the entire set of ANNs is 18.31 for the test subset. This result can be compared with the naive method of predicting the number of defective products. The naive method may consist, first of all, in determining the arithmetic mean of the number of defective products, taking into account all cases included in the training subset (36.74). Next, the computed score can be taken as the prediction score for each case in the test set. Prediction using the naive method has the RMSE error of 27.84. This value is much higher than the RMSE determined for the set of ANNs, which proves that prediction using developed ANNs is more effective.

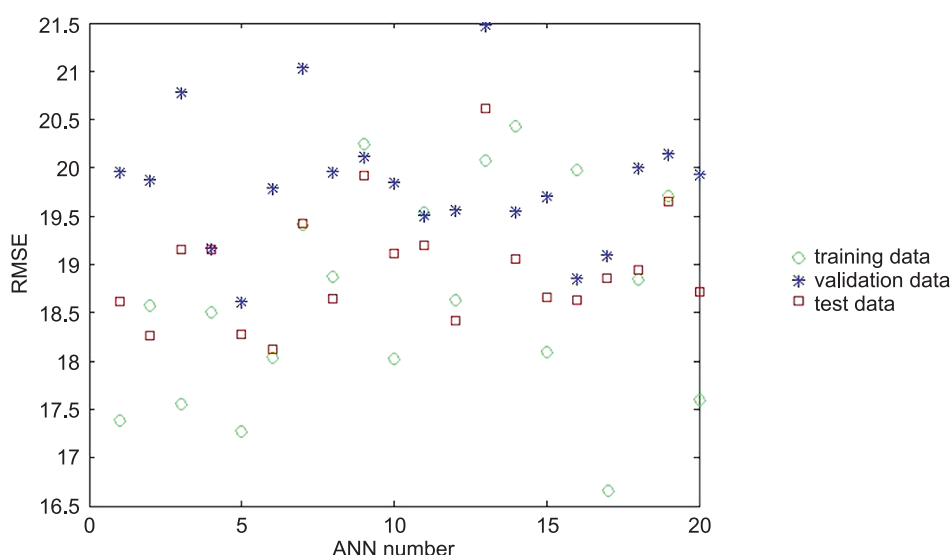


Fig. 6. RMSE values for each ANN belonging to the set of ANNs

Looking at the plot in Figure 7, it can be also concluded about the good quality of prediction using the set of ANNs. This plot shows the actual number of defective products for each case in the test subset along with the predicted number of defective products using the set of ANNs. The plot is in the form of a time series, but it should be noted that the time distances between adjacent cases may be different due to the fact that cases were assigned to the test subset randomly.

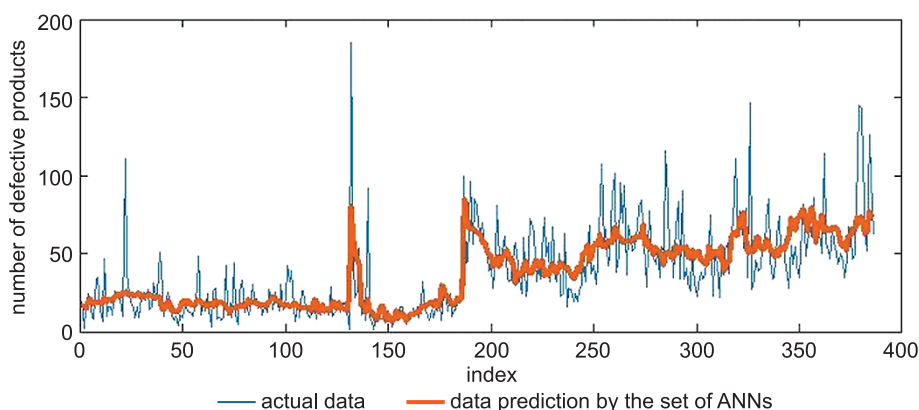


Fig. 7. Prediction results of the number of defective products compared to the actual number of defective products in the test subset

By comparing the actual number of defective products with the prediction results, it can be seen that for some cases there are large discrepancies (e.g. case no. 132: the actual value is 185 and the predicted value is 80.28). However, these single, large differences between the prediction result and the real value do not indicate a bad quality of prediction. The biggest differences are observed for the so-called outliers. The value of outliers is difficult to predict by any method. Moreover, predicting values for outliers is not the aim of this study. The purpose of the research was to create a model capable of capturing the most important properties of the explained variable for the analyzed period. The discussed plot shows that the set of ANNs is able to map the most important features of the explained variable in an appropriate way. In the left part of the plot (up to about 170 cases) it can be seen that the average number of defective products is less than the number of defects in the right part of the plot (above case no. 170). Similar dependencies can be observed for the predicted number of defective products. The set of ANNs is able to map not only the changing levels of the explained variable, but also correctly represent its variability understood as differences between the values in a given interval. For example, the variability in the number of defective products from 50 to 100 cases is less than the variability between 300 and 350 cases. This phenomenon can also be seen for prediction results generated by the set of ANNs.

Since it was found that the created set of ANNs can correctly map the most important phenomena occurring in the analyzed data, an attempt can be made to use the set of ANNs to determine the significance of the predictors. The significance of a given predictor is understood as the influence of this predictor on the prediction results, which is determined by the set of ANNs. The partial results of the predictor significance analysis are shown in Figure 8. This figure contains four column graphs corresponding to the four measures of significance described by Formulas 3, 4, 5, and 6. Each graph includes 10 most significant predictors of all 69 predictors analyzed.

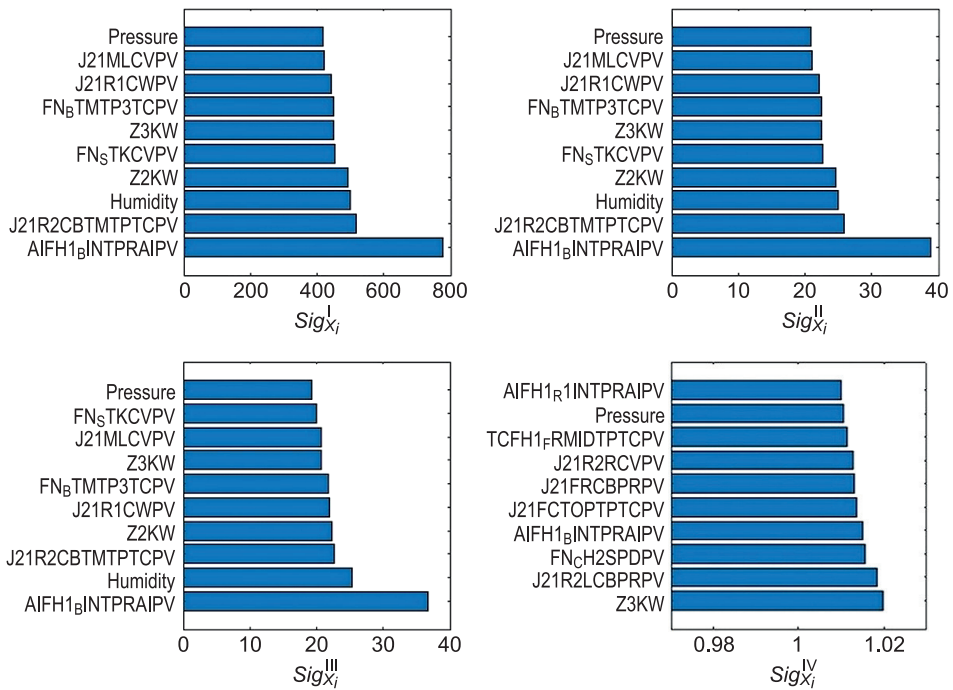


Fig. 8. Predictor significance rankings (included only 10 predictors with the highest value of a given measure of significance)

In the case of measures  $Sig_{x_i}^I$ ,  $Sig_{x_i}^{II}$  and  $Sig_{x_i}^{III}$  it can be seen a high similarity of the three significance rankings created. The top ten most important predictors are the same. Moreover, in the rankings created for the measures  $Sig_{x_i}^I$  and  $Sig_{x_i}^{II}$ , the predictors with the highest significance occupy the same positions. In the case of the ranking for  $Sig_{x_i}^{III}$ , the order of the variables is slightly different.

The first place in the three above-mentioned rankings is taken by the variable AIFH1<sub>B</sub>INTPRAIPV. The advantage of this variable over the other predictors is relatively large. This variable records the pressure values in one of zones

of the forehearth that supplies liquid glass to the production line. The time course of the  $\text{AIFH1}_B\text{INTPRAIPV}$  variable over the entire period under study is shown in Figure 9. The course of this variable is compared with the time series presenting the number of defective products. Comparing the course of both time series, it can be seen that the variability of these time series is similar. In the periods when the value of  $\text{AIFH1}_B\text{INTPRAIPV}$  remains approximately constant, the explained variable also shows relatively little variability (an example may be the period between cases no. 1500 and 1900). On the other hand, in periods of high variability of  $\text{AIFH1}_B\text{INTPRAIPV}$ , the number of defective products also fluctuates relatively strongly, which can be seen, for example, in the period from case no. 2000 to the last case. This observation may explain why the  $\text{AIFH1}_B\text{INTPRAIPV}$  is the most significant variable for the set of ANNs.

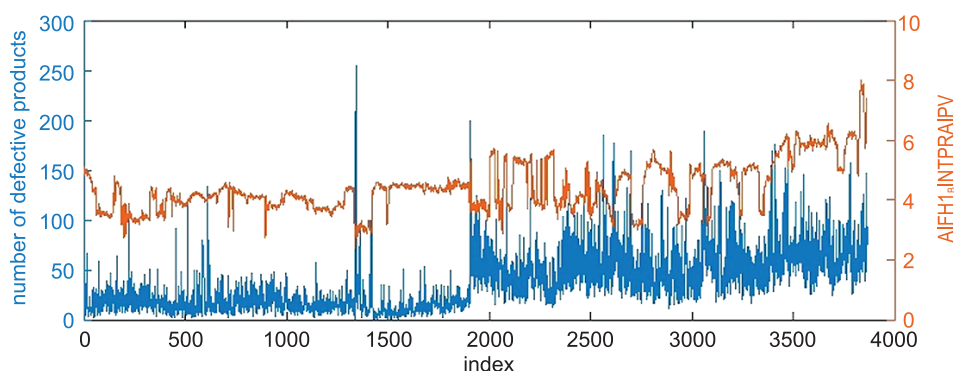


Fig. 9. Time series plots of the number of defective products and the predictor ranked highest in the three rankings

The differences in significance measures between the next variables in the rankings are much smaller. The following places are occupied by variables, which record: glass temperature in one of the forehearth zones, power of electric reheating, glass temperature in the lower part of the glass furnace, the degree of opening of valves that control cooling of some forehearth zones, humidity, and atmospheric pressure.

In the analysis of predictors significance in the stage 7.1, the values of bias of hidden neurons and weights of connections between hidden neurons and output neuron were also taken into account. However, the results obtained in that manner were similar to the results presented above.

The ranking for the measure  $\text{Sig}_{x_i}^{\text{IV}}$  looks slightly different. The differences between the obtained values are small and fall within the range from 0.98 to 1.02. Such small differences make it hard to draw unambiguous conclusions about the significance of the analyzed predictors. 13 out of 69 predictors have a value

of  $Sig_{x_i}^{IV}$  less than 1. As mentioned in the previous section, this value suggests that removing a given predictor from the training subset could improve the quality of the prediction. However, no such analyzes were carried out in the conducted experiment.

Looking at the top ten of the ranking for the significance measure  $Sig_{x_i}^{IV}$ , it can be seen that some variables also appear in the top ten of the remaining three rankings. Apart from these variables, the discussed ranking includes the following predictors: the degree of opening of valves that regulate the gas supply, the glass temperature in the upper part of one of the forehearth zones, and the speed of loading the raw materials into the furnace. The variable AIFH1<sub>B</sub>INTPRAIPV, which is the most significant in the other three rankings, occupies fourth place here.

It turns out that in the reduction approach the most important variable is Z3KW, which registers the power of electric reheating. This variable was also in the top positions in the three other rankings. Figure 10 shows the values of the variable Z3KW along with the number of defective products. Looking at the values of the Z3KW over time, one can notice clear, sudden changes in the levels of this variable. Comparing this with the time series of the explained variable, it can be seen that some changes in the levels of Z3KW are associated with relatively large increases or decreases in the number of defective products (for example, an increase in the value of Z3KW to the maximum level that begins in the case no. 1907 coexists with a sudden increase in the number of defects). Moreover, the minimum Z3KW value in the case no. 1339 coincides with the maximum number of defective products (255). These observations may explain why this predictor is important to the set of ANNs.

Of course, it is difficult to formulate an unequivocal conclusion that low or high values of a given predictor contribute to low or high values of the explained variable. The complexity of the glass packaging production process

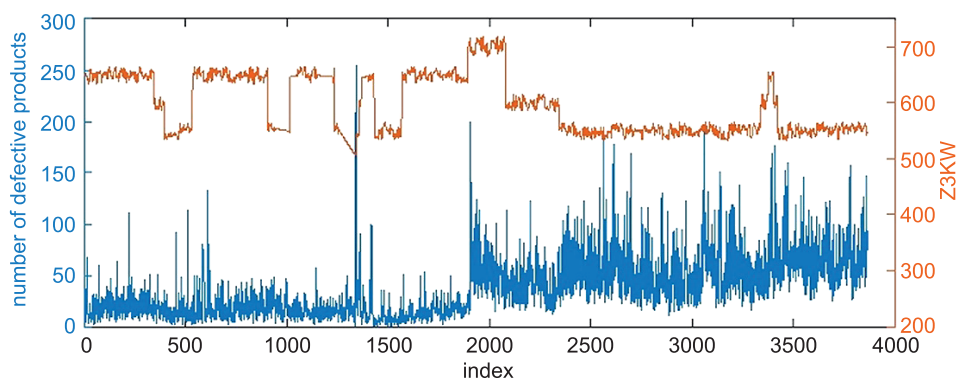


Fig. 10. Time series plots of the number of defective products and the predictor ranked highest in the fourth ranking

and the multitude of variables affecting the final quality of products make it difficult to formulate simple and unambiguous conclusions. However, the methods of predictor significance computation presented in this paper help to estimate which explanatory variables have the greatest impact on the results of prediction carried out using the set of ANNs and the bootstrap aggregation technique.

The presented research methodology has some limitations. The approach discussed in the paper takes into account only one type of products' defect. The applied techniques are aimed at predicting one type of defect, and the measures of significance of the predictors concern the influence of the predictors on the number of products with only a given type of defect. It should be borne in mind that glass products are characterized by the possibility of many types of defects, which are related to, among others, wrong shape of products, inadequate quality of a product's surface, or the occurrence of undesirable inclusions in the glass. In order to take into account more than one type of defect, the presented approach would have to be modified. There are also limitations to the applied method of ANNs hyperparameters optimization. For the considered dataset, the applied optimization method allowed for the selection of hyperparameters in a satisfactory time. However, in the case of a larger amount of data (in particular Big Data), the applied optimization method may be too time-consuming and computationally inefficient. In such a situation, other methods of selecting ANNs hyperparameters should be used, which were proposed by e.g. REN et al. (2021) and ELSKEN et al. (2019).

## Conclusions

The research described in this article were aimed at determining the significance of the manufacturing process parameters of the glass products in relation to the quality of these products, as well as the prediction of the number of defective products based on the values of the manufacturing process parameters. The fulfilment of the assumed goals was achieved with the use of the MLP-type ANNs. Moreover, the bagging (bootstrap aggregation) technique was used to create the ANNs. The research framework included seven stages: data acquisition, data preparation, optimization, bootstrap phase, modelling phase, aggregation phase, examination of predictors' significance. This article describes a data analysis model capable of predicting the number of defective products for real data obtained from a glassworks, and presents four ways of determining the significance of predictors. MATLAB software was used to carry out the experiment.

Despite the very high complexity of the production process and the enormous amount of data, the assumed goals were fulfilled. The validity of the use of the bagging technique with ANNs in predicting the number of defective products and



determining the significance of production parameters was confirmed. During the research, the development potential of the experiment was also identified. In subsequent iterations, it is planned to determine the optimal number of neural networks placed in the set of ANNs (20 ANNs were adopted in the described research) and to determine the optimal number of cases to be placed in one bag of data when using the bootstrap aggregation technique (a number of 3,400 cases was assumed) – the values were assumed intuitively; however, with appropriate optimization, it may be possible to obtain better prediction results. It is also planned to use other types of ANNs, e.g. networks with more than one hidden layer, which can model more complex relationships between predictors and the dependent variable. Continuing the research, other regression models can be applied, such as regression trees, random forests or support vector regression. Thanks to this, it will be possible to compare the predictive ability of these models in the task of predicting the number of defective products.

## References

- BREIMAN L. 1996. *Bias, variance and arcing classifiers*. Technical Report TR 460. Dept. of Statistics. University of California, Berkeley, CA, USA.
- ELSKEN T., METZEN J.H., HUTTER F. 2019. *Neural Architecture Search: A Survey*. Journal of Machine Learning Research, 20: 1-21.
- FRANCIK S. 2009. *Metoda prognozowania szeregów czasowych przy użyciu sztucznych sieci neuronowych*. Inżynieria Rolnicza, 13(6): 53-59.
- GOLKA W., ARSENIUK E., GOLKA A., GÓRAL T. 2020. *Sztuczne sieci neuronowe i teledetekcja w ocenie porażenia pszenicy jarej fuzariozą kłosów*. Biuletyn Instytutu Hodowli i Aklimatyzacji Roślin, 288: 67-75.
- GÓRSKI M., KALETA J., LANGMAN J. 2008. *Zastosowanie sztucznych sieci neuronowych do oceny stopnia dojrzałości jabłek*. Inżynieria Rolnicza, 12(7): 53-56.
- HEBDA T., FRANCIK S. 2006. *Model twardości ziarniaków pszenicy wykorzystujący sztuczne sieci neuronowe*. Inżynieria Rolnicza, 10(13): 139-146.
- JASIŃSKI T., BOCHENEK A. 2016. *Prognozowanie cen nieruchomości lokalowych za pomocą sztucznych sieci neuronowych*. Studia i Prace WNEiZ US, 45(1): 317-327.
- KURT I., TURE M., UNUBOL M., KATRANCI M., GUNEY E. 2014. *Comparing Performances of Logistic Regression, Classification & Regression Trees and Artificial Neural Networks for Predicting Albuminuria in Type 2 Diabetes Mellitus*. International Journal of Sciences: Basic and Applied Research (IJSBAR), 16(1): 173-187.
- LEFIK M. 2005. *Zastosowania sztucznych sieci neuronowych w mechanice i inżynierii*. Zeszyty Naukowe. Rozprawy Naukowe, 341: 3-258.
- NIEDBAŁA G., LENARTOWICZ T., KOZŁOWSKI J.R., ZABOROWICZ M. 2015. *Modelowanie neuronowe jako metoda prognozowania zawartości skrobi w ziemniakach na potrzeby Porejestrzowego Doświadczalnictwa Odmianowego i Rolniczego (PDOiR)*. Nauka Przyroda Technologie, 9(2): 1-7.
- OPITZ D.W., MACLIN R.F. 1997. *An empirical evaluation of bagging and boosting for artificial neural networks*. Proceedings of International Conference on Neural Networks (ICNN'97), 3: 1401-1405.
- PAŠKO Ł. 2020. *Significance of Manufacturing Process Parameters in a Glassworks*. Advances in Manufacturing Science and Technology, 44(2): 39-45.
- REN P., XIAO Y., CHANG X., HUANG P., LI Z., CHEN X., WANG X. 2021. *A Comprehensive Survey of Neural Architecture Search: Challenges and Solutions*. ACM Computing Surveys, 54(4): 1-34.



- RODZIEWICZ A., PERZYK M. 2016. *Application of significance analysis to finding root causes of product defects in continuous casting of steel*. Computer Methods in Materials Science, 16(4): 187-195.
- ROJEK I. 2015. *Sieci neuronowe w kontroli jakości procesu*. Studies & Proceedings Polish Association for Knowledge Management, 74: 91-100.
- TADEUSIEWICZ R., HADUCH B. 2015. *Wykorzystanie sieci neuronowych do analizy danych i pozyskiwania wiedzy w systemie ekspertowym do oceny parametrów benzyn silnikowych*. Nafta-Gaz, 71(10): 776-785.
- ZHIBIN W., NIANPING L., JINQUNG P., HAIJIAO C., PENGLONG L., HONGQIANG L., XIWANG L. 2018. *Using an ensemble machine learning methodology – Bagging to predict occupants' thermal comfort in buildings*. Energy and Buildings, 173: 117-127.



# MODIFICATION OF THE TOOTH GEOMETRY OF A POLYMER GEAR WITH A STRAIGHT TOOTH LINE TO ADJUST THE TORQUE TRANSMISSION CAPABILITY IN ONE DIRECTION ONLY

*Piotr Strojny*

ORCID: 0000-0001-8593-8548

Faculty of Mechanical Engineering and Aeronautics  
Rzeszow University of Technology

Received 6 July 2021, accepted 28 September 2021, available online 10 October 2021.

**Key words:** gears, tooth strength, tooth geometry modification, topological optimization, kinetic simulations.

## Abstract

This paper describes a methodology for modifying a tooth for the ability to transmit torque in one direction only. It presents two methods (analytical and numerical) of tooth mass reduction while maintaining functional features of the whole transmission. The results of the above mentioned methodology are presented on the example of a mass-produced transmission.

## Introduction

A significant percentage of devices incorporating gears are based on the principle of torque transmission in one direction only. Consequently, the gears in them use only one side of the tooth for direct torque transmission. This situation raises the important question of whether, and to what extent, the teeth of such gears can be modified in terms of the removal of unnecessary material, finishing treatments such as grinding, and heat treatments on the side of the tooth that

---

Correspondence: Piotr Strojny, Katedra Inżynierii Lotniczej i Kosmicznej, Politechnika Rzeszowska, al. Powstańców Warszawy 8. 35-959 Rzeszów, phone: 692 047 962, e-mail: pstrojny@prz.edu.pl

does not directly transmit torque. The paper mainly focuses on the first aspect of modification i.e. weight reduction, being the most measurable criterion in terms of numerical analysis.

After conducting a literature analysis of classic items (DZIAMA et al. 1995, HOMIK, POŁOWNIAK 2012, KURMAZ, KURMAZ 2016, MAZANEK 2012, OCHĘDUSZKO 1985), where the authors describe the modification of typical tooth geometries based on involutes and epicycloids as well as modern items (KOLLEK et al. 2015, OSIŃSKI et al. 2018, OSIŃSKI 2017) where the authors experiment with new contours, e.g. with polvolwent (OSIŃSKI 2017). It can be concluded that the subject matter discussed in the article is still valid and should be the subject of further research. It is worth to mention that the literature analysis did not come across any items that directly refer to the modification of the tooth geometry made of polymeric materials.

## Research object

In this paper, a polymer transmission of Zelmer Diana 886.8 MP mincer (Fig. 1) was used for analysis (Zelmer. 2021). Using reverse engineering (DZIUBEK 2018, KIŃSKI, SOBIESKI 2020, RATAJCZYK 2005, SHAH et al. 2019, SUN et al. 2019), the last gear speed was scanned from the output torque side – see Figure 1. Then, detailed measurements of the geometry of the scanned teeth were made, and on this basis the parameters of the mating pairs of gears were estimated. Some simplification was also made by replacing the angled teeth with straight teeth. DuPont™ company (Dupont. 2021), the supplier of polymers for Zelmer company, provided information about the material of which the above mentioned transmission is made. All information is summarized in Tables 1 and 2.

Table 1

Transmission parameters

Name	Modulus	Number of teeth	Width of rim	Pitch diameter	Pressure angle	Apical play	Lateral play	Tooth apex rounding	Output torque	Axial distance of mating gears	Tooth-form factor $y$	Tooth-form factor $x$
Unit	mm	–	mm	mm	deg	mm	mm	mm	Nm	mm	–	–
Pinion	2	9	20	18	20	0.5	0.08	0.3	3.575	48	1	0
Gear	2	39	18	78								

Source: based on Zelmer (2021).

Table 2

Material data for pairs of gears

Name	Young's modulus	Poisson number	Yield strength	Hardness H 358/30	Density
Unit	MPa	–	MPa	MPa	g/cm <sup>3</sup>
Derlin 500P NC010	300	0.37	70.5	192	1.42
Standard	ISO 179	ISO 527	ISO 527-2	ISO 2039-1	ISO 1183

Source: based on Dupont (2021).

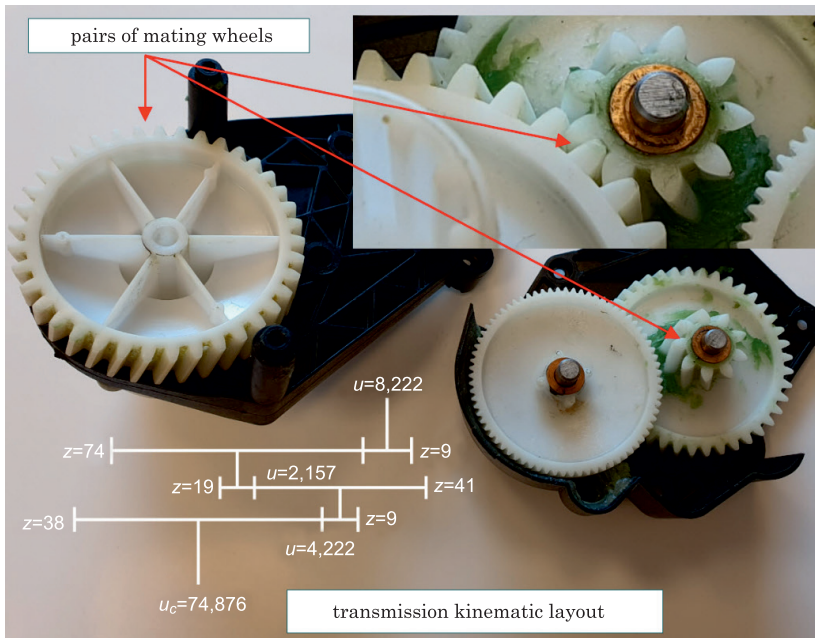


Fig. 1. Transmission from ZELMER Diana 886.8 MP mincer Transmission kinematic system  
Source: based on Zelmer (2021).

According to the kinematic diagram (Fig. 1) and the data from Tables 1 and 2 using the relationships (1) and (2) (DZIAMA et al. 1995, OCHEŁDUSZKO 1985), stress values at the tooth base and contact stresses (Hertz formula) were estimated:

$$\sigma_g \geq \frac{6 F h}{b s^2} \quad (1)$$

$$p_{\max.} \geq \sqrt{\frac{2}{\left(\frac{1}{E} + \frac{1}{E}\right) \pi (1 - \nu^2) \sin(\alpha) \cos(\alpha)}} \sqrt{\frac{F_{\text{calc}}}{b d_1} \left(1 + \frac{1}{u}\right)} \quad (2)$$

where:

- $\sigma_g$  – allowable bending stresses,
- $F$  – circumferential force from bending torque,
- $h$  – tooth height,
- $s$  – tooth thickness at the base, estimated on the basis of the numerical model (Fig. 3),
- $p_{\max.}$  – allowable stress under pressure,
- $E$  – Young's modulus of Derlin 500P NC010,
- $\nu$  – Poisson's ratio for Derlin 500P NC010,
- $a$  – pressure angle,
- $F_{\text{calc}}$  – resultant of circumferential force equal to  $F \cos(a)$ ,
- $u$  – gear ratio in the analysed part of the transmission.

The obtained values of stresses at the tooth base and at contact surfaces give safety factors of 2.1 and 3.9 respectively, which permits to assume that the analysed geometry of the transmission has been selected correctly.

## Tooth model

The numerical model of the transmission's teeth was developed based on the chiseling method (CHERNETS 2019, POŁOWNIAK et al. 2020, TWARDOCH 2014). See Figure 2 for a description of the individual diameters and curves 3 and 4.

The graphic interpretation of the above-mentioned one is described in more detail in DZIAMA et al. (1995, p. 26-30, 43-48) and OCHĘDUSZKO (1985, p. 61-63).

Ordinary involute equation – tooth side:

$$\begin{aligned} x_b &= r_b(\sin \phi - \hat{\phi} \cos \phi) \\ y_b &= r_b(\cos \phi + \hat{\phi} \sin \phi) \end{aligned} \quad (3)$$

Epicycloid equations – transition curve at tooth base:

$$\begin{aligned} x_p &= a \sin(\phi) - r_{a2} \sin\left(\left(1 + \frac{r_1}{r_2}\right)\phi\right) \\ y_p &= a \cos(\phi) - r_{a2} \cos\left(\left(1 + \frac{r_1}{r_2}\right)\phi\right) \end{aligned} \quad (4)$$

where:

- $x_b, y_b$  – coordinates of the points of the involute describing the side of the tooth,
- $x_p, y_p$  – coordinates of the epicycloid points describing the transition curve at the base,

- $\phi$  – angle of deflection of radial coordinate,  
 $\hat{\phi}$  – arc measure of the angle of deflection of the radial coordinate,  
 $r_b$  – basic radius,  
 $a$  – axial distance of mating gears,  
 $r_{a1,2}$  – radii of tooth heads,  
 $r_{1,2}$  – pitch radii of gears.

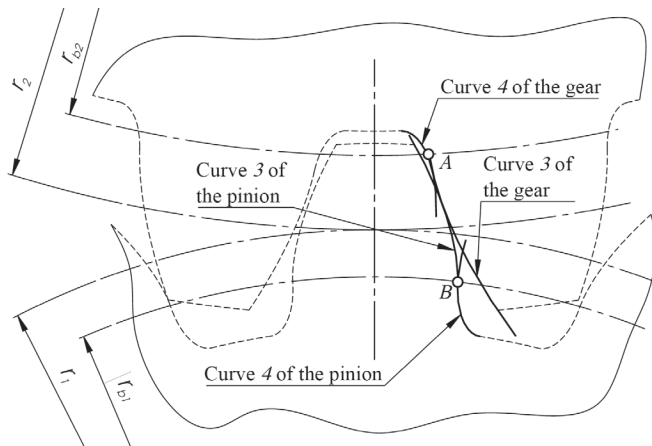


Fig. 2. Numerical model of curves describing transmission teeth geometry:

A – point connecting the base transition curve 4 with the curve describing the side of the tooth of the gear 3, B – point connecting the base transition curve 4 with the curve describing the side of the tooth of the pinion 3

An important factor in building a numerical model of a pinion tooth that will subsequently be subjected to loading is to correctly determine the pressure number and the areas in which the tooth is in single or double contact with the mating wheel. This allows to determine the tooth position that is least favourable in terms of the load to be transferred. Figure 3 shows two typical worst-case tooth positions. The first area is the variant in which the tooth is loaded with 1/2 of the peripheral force but on the longest arm ( $h_1$ ), while the second area is the variant in which the tooth is loaded with the total peripheral force but on the shorter arm ( $h_2$ ). Depending on the gear parameters, one of the above variants will result in higher stresses at the base of the tooth. Due to the large number of variables in a gear, the correct process of estimating the above mentioned areas must be done individually for each gear under consideration. Such an analysis can be carried out by means of modern CAD programs that allow kinetic simulations of gear mating (KROL, SOKOLOV 2021, PETR, DYNBYL 2014) and software dedicated to such tasks as KISSsoft (KISSsoft. 2021), KIMoS (KLINGELNBERG. 2021).

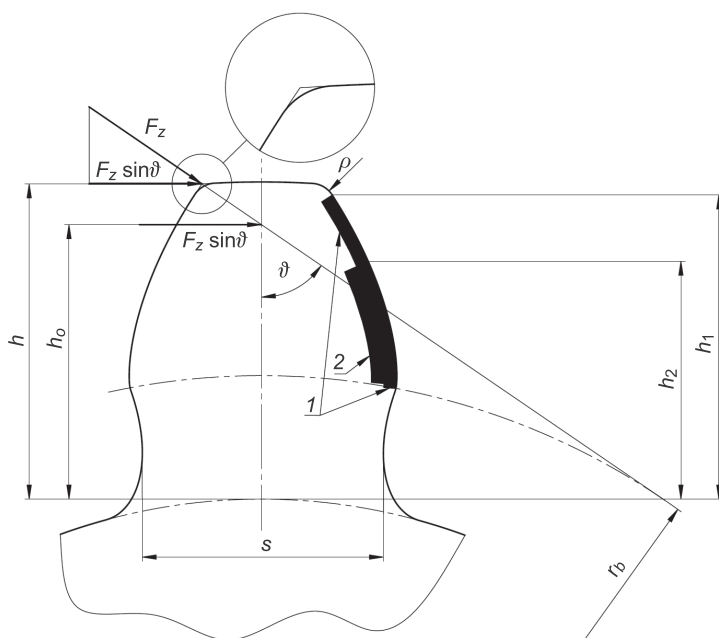


Fig. 3. Contact areas for one-pair (2) and two-pair (1) contact

The pressure number for the case under consideration was determined using CAD software in the dynamic simulation module. This allowed to determine how many pairs of teeth are in mesh for one complete cycle. For the analyzed transmission the pressure number was 1.31 for the test parameters: cycle 40 deg, number of transition steps 200/cycle.

According to OCHĘDUSZKO (1985, p. 354-356), the relationship (1) can also be presented in the form of equation (5). The author of the above-mentioned item states that the force  $F_z$  is distributed over one pair of teeth or into two pairs of teeth. For the calculations, however, it accepts only the second case, assuming the reduction of the force  $F_z$  by dividing it by  $\varepsilon_a$  (tooth contact ratio) (6) (DZIAMA et al. 1995, p. 63-65). At the same time stating that you are not making too much of a mistake:

$$\sigma_g \geq \frac{6 F_z \sin \vartheta h_o}{b s^2} \quad (5)$$

$$\varepsilon_a = \frac{\sqrt{r_{a1}^2 - r_{b1}^2} + \sqrt{r_{a2}^2 - r_{b2}^2} - a_w \sin \alpha}{\pi m \cos \alpha} \quad (6)$$

where:

$r_{b1,2}$  – basic radius,

$r_{a1,2}$  – radii of tooth heads,



- $a_w$  – axial distance of mating gears,
- $a$  – pressure angle,
- $m$  – modulus,
- $h_0$  – bending moment arm,
- $h$  – tooth depth.

For the analysed gear, in accordance with DZIAMA et al. (1995),  $\varepsilon_a$  was 1.36, which is a similar value to the result obtained from the numerical simulation (1.31). The obtained difference may result from the fact that in item DZIAMA et al. (1995) the rounding at the tooth apex was not taken into account (Fig. 3). However, with regard to the maximum bending stress at the tooth base, according to items OCHEŃDUSZKO (1985) and DZIAMA et al. (1995) formulas (5) and (6), the maximum bending stress was  $\sigma_g = 25.64$  MPa. This value differs from the values obtained from the numerical analysis, which for the arm  $h_1$  and 1/2 the value of the force  $F_z$  amounted to  $\sigma_g = 19.29$  MPa and for  $h_2$  and the full value of the force  $F_z$ ,  $\sigma_g = 29.62$  MPa. Taking into account the greater stresses, the obtained difference is slightly more than 13%. It may result mainly from the aforementioned rounding ( $\rho = 0.3$  mm) at the tooth apex, which occurs in the numerical analysis and is not included in the analytical formulas (5) and (6).

It is evident from the analyses presented above that the number of buttresses is of significant importance. Its growth reduces the stresses at the base. For the considered case, achieving  $\varepsilon_a$  equal to 2 would result in reaching  $\sigma_g = 25.64$  MPa, that is lowering the stresses at the base by almost 4 MPa.

## Tooth modification based on analytical calculations

After the numerical model of the tooth was made, the modification of its shape in terms of mass reduction due to the unidirectional nature of operation followed. A pinion tooth was used for the analysis due to the fact that it has a larger undercut at the base which leads to higher bending stresses. Based on relation (1) estimating the tooth thickness, graphs of tooth thickness minima versus its height  $\{1\}\{2\}$  (Fig. 4) were developed for two loading variants according to Figure 3. The effect of contact stresses is also considered in Figure 4. Based on Hertz's formula (7) (OCHEŃDUSZKO 1985, p. 369-371, 401-413) and Bielajew point (8) (BERCZYŃSKI et al. 2016), the minimum area to be preserved on the lateral tooth surface  $\{3\}$  was determined:

$$a = 1.52 \sqrt{\frac{F_{\text{calc}}}{b E} \frac{r_1 r_2}{r_1 + r_2}} \quad (7)$$

$$y = 0.78 a \quad (8)$$

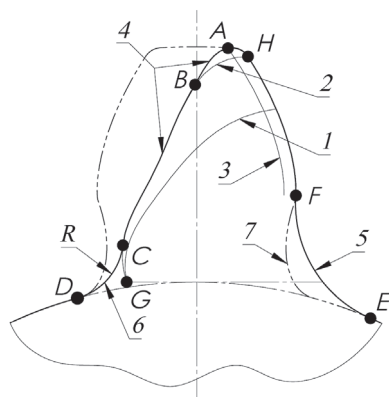


Fig. 4. Shape of the tooth after geometric modification; solid line – modified tooth shape, dashed line – base tooth shape

Due to the fact that the mating gear has undergone the same process of tooth shape modification, it was possible to replace the transition curve at the base of the pinion (epicycloid) by a classical arc tangent to the tooth working surface (involute) and the bottom of the tooth notch {5} arc  $|FE|$ . This resulted in a much smaller undercut and allowed us to model the side of the tooth responsible for the transmission of torque  $|HFE|$ . The side of the tooth on the side not carrying the torque {4} was determined from equation (1) taking into account the contact stresses (7) and (8). This allowed to obtain the tooth side based on equations (1), (3), (7) and (8), shown in Figure 4. In order to execute technologically the thus obtained tooth geometry it was necessary to replace the point G by the arc  $|CD|$  with radius  $\{R\}$  of the tool making the notch. A commercially available  $\phi 2$  cutter with a length of 20 mm was used due to the small tooth size relative to its width (Narzędzia profesjonalne EU. 2021). In addition, for reasons of the manufacturing process, the theoretical curve which should result from the resultant curves {2} and {3} should be replaced by curve  $|AB|$  tangent at point A to the rounding of the tooth apex. This allows to obtain the overall shape of the tooth  $\{a\}$ . The figure also shows the base shape of the tooth  $\{b\}$ .

## Tooth modification based on topology optimization

Due to the fact that modern FEM programs allow to perform numerical optimization (topology optimization) of structural elements, it has been decided, based on available examples from literature (DEPTULA, PARTYKA 2018, LARSSON 2016, MUMINOVIC et al. 2020, SHAH et al. 2019, SUN et al. 2019), to perform such optimization for the tooth of the gear described. Note that for the simulation,

the tooth was modified to remove the excessive undercut {7} and replaced with an arc {5}  $|FE|$  tangent to the side of the tooth at point  $F$  and the base arc (Fig. 4). The analysis was performed for simulation parameters Table 3. The results obtained are shown in Figure 5. Using granularity removal techniques (BRAUER 2002, BRECHER et al. 2009), the final pinion tooth shape obtained by topological optimization process of Figure 5c was developed.

Table 3

Boundary conditions		
Nazwa	Typ	Unit
Mesh type	solid mesh	–
Jacobian points	16	–
Element size	0.2	mm
Tolerance	0.01	mm
Total number of elements	299559	–
Solver type	Intel Direct Sparse	–
Total number of nodes	55528	–
Maximum aspect ratio	38.412	–
Percentage of elements with an aspect ratio <3	99.7	–
Percentage of elements with an aspect ratio >10	0.0945	–
Goal type	best stiffness to weight ratio	–
Reduction	reduce weight by 14%	–
Model type	Linear Flexible Isotropic	–

Source: based on LARSSON (2016).

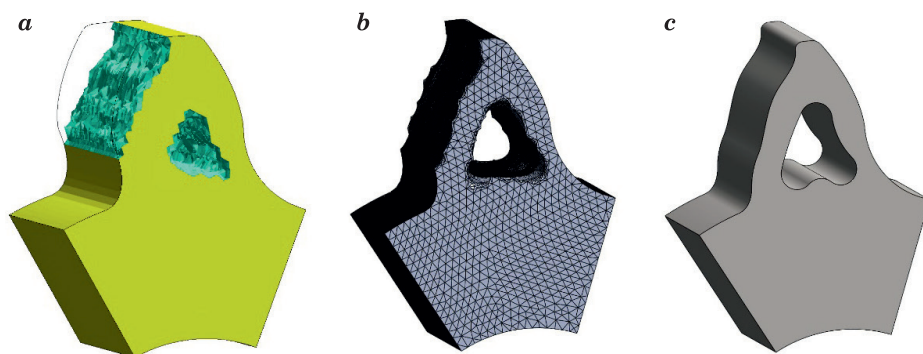


Fig. 5. Topological optimization results: *a* – view with areas to be removed, *b* – resulting model with granular structure, *c* – smoothed model

Source: based on LARSSON (2016).

## Analysis of results

The following section summarizes the results obtained by modification based on analytical relations and numerical optimization with the basic tooth geometry. The front surface of the tooth was chosen for comparison because the length of the tooth did not change in either method. Table 4 shows all the results obtained along with the percentage weight reduction assigned to each method relative to the original tooth geometry.

Table 4

Summary of tooth mass reduction results for different modification methods

Method	Tooth face area [mm <sup>2</sup> ]	Percentage weight reduction [%]
Basic tooth shape	4,135.391	–
Tooth shape after analytical modification	3,207.696	22.433
Tooth shape after topological optimization	2,383.496	42.3635

Note that the tooth mass is only a part of the mass of the entire gear. Therefore, in order to present the results more vividly, Table 5 additionally shows by how much the mass of the analyzed gear decreased for the proposed modification methods.

Table 5

Summary of the results of reducing the mass of a gear for different modification methods

Method	Pinion wheel mass [mm <sup>2</sup> ]	Percentage mass reduction [%]
Basic tooth shape	4,135.391	–
Tooth shape after analytical modification	3,207.696	9.966
Tooth shape after topological optimization	2,383.496	18.919

Figure 6 contains the superimposed tooth geometries obtained by the three methods. After obtaining the final tooth shapes for the two methods described above, kinetic analysis of the mating was performed to check for the occurrence of possible collisions and the pressure number was re-estimated. The results of the analyses did not reveal any irregularities in mating and the pressure number did not change. Figure 7 shows a visualization of the obtained pinions for all methods.

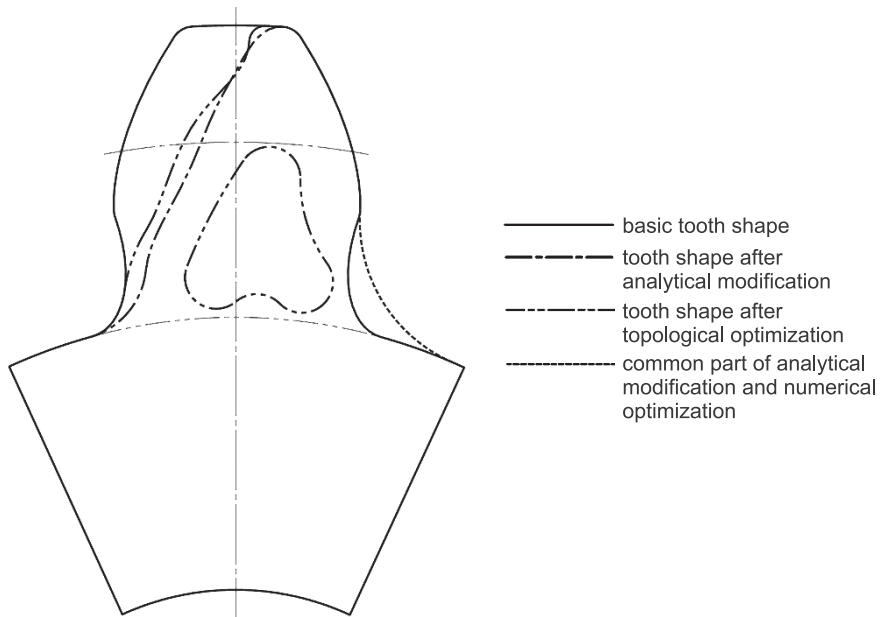


Fig. 6. Summary of the geometry of the obtained results

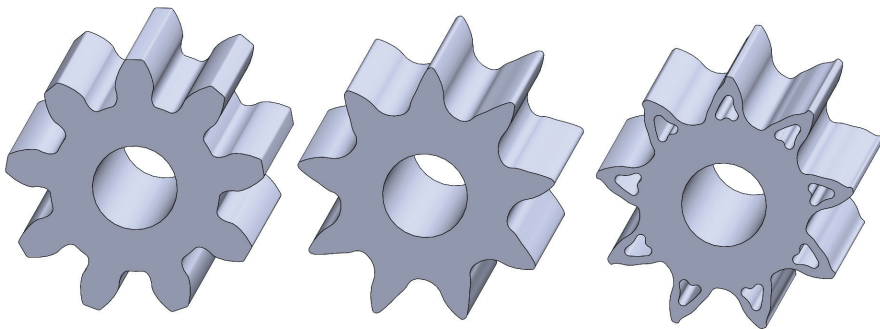


Fig. 7. Visualization of the obtained pinions

## Conclusions

On the basis of the obtained results it may be concluded that the proposed methods of tooth modification allow to decrease the tooth mass and thus of the whole transmission. The presented methodology can be used wherever torque transmission occurs in one direction only, both in steel and polymer transmissions. Percentage weight reduction of 10-19% shown in the paper is not a big amount,

but with polymeric gears used in appliances of the household sector, which are often produced in tens of millions, it may contribute to reduction of material purchase costs.

The methodology presented in the article allows for a more accurate estimate of the pressure  $\varepsilon_a$  (tooth contact ratio) for the analysed gears. Of course, only one gear was analysed, which does not allow for drawing general conclusions.

An interesting aspect is also the possibility of using a topological examination to reduce the mass of the tooth, described in chapter “Tooth modification based on topology optimization”. Which, however, entails certain difficulties of the technological implementation of the obtained shape. Especially when making gears from steel materials. This would result in longer production times and would be associated with higher costs.

The analytical methodology for determining the shape of the tooth flank, described in Chapter “Tooth modification based on analytical calculations”, which is not directly involved in the transmission of torque, allows for a relatively quick determination of the shape of the tooth flank. On the other hand, the disadvantage of the described methodology is the inability to derive universal dependencies for generating the shape of the tooth. In order to obtain the shape of the curves proposed in Figure 4, one should always use advanced computer systems (CAD), additionally supported by numerical calculations using, for example, Matlab software.

Another very important aspect of using the described methodology is creating solutions with lower weight while maintaining their original functionality. This can be used mainly in those designs where weight reduction is very important, such as: aircraft designs, racing cars and drone designs.

The proposed solution will also allow, in relation to steel gears, to reduce costs of finishing such as grinding or heat treatment. But in this matter the technology used in the above mentioned processes is very important, which sometimes determines the effect on both sides of the inter-tooth notch.

It should be emphasized that the proposed solution has not been experimentally verified, the proposed optimization should be read as a generally applied approach, and not as an appropriate solution for polymer gears. Nevertheless, the presented methodology is an introduction to further experimental studies, new geometries of gears made of polymer materials. The results of the above-mentioned research will be the subject of subsequent publications.

## References

- BERCZYŃSKI S., GRZADZIEL Z., RUKOWICZ S. 2016. *Analiza porównawcza naprężeń kontaktowych w zazębieniu przekładni zębatej napędu wału rozrządu silnika Sulzer RTA48T-B*. Zeszyty Naukowe Akademii Morskiej w Szczecinie, 10(82).
- BRAUER J. 2002. *Analytical geometry of straight conical involute gears*. Mechanism and Machine Theory, 37.
- BRECHER C., ROTHLINGSHOFER T., GORGELS C. 2009. *Manufacturing simulation of beveloid gears for the use in a general tooth contact analysis software*. Production Engineering, 3(1): 103-109.
- CHERNETS M. 2019. *Method of calculation of tribotechnical characteristics of the metal-polymer gear, reinforced with glass fiber, taking into account the correction of tooth*. Eksploatacja i Niezawodność, 21(4).
- DEPTULA A., PARTYKA M.A. 2018. *Application of complex game-tree structures for the Hsu graph in the analysis of automatic transmission gearboxes*. Journal of Machine Engineering, 18(4).
- Dupont. 2021. Delrin® 500P NC010 ACETAL RESIN POM. <https://dupont.materialdatacenter.com/en/products/datasheet/SI/Delrin%C2%AE%20500P%20NC010> (access: 20.09.2021).
- DZIAMA A., MICHNIEWICZ M., NIEDŹWIEDZKI A. 1995. *Przekładnie zębate*. Ed. 2. PWN, Warszawa.
- DZIUBEK T. 2018. *Application of coordination measuring methods for assessing the performance properties of polymer gears*. Polimery, 63(1).
- HOMIK W., POŁOWNIAK P. 2012. *Podstawy konstrukcji maszyn – wybrane zagadnienia*. Wydawnictwo Politechniki Rzeszowskiej, Rzeszów.
- KIŃSKI W., SOBIESKI W. 2020. *Geometry extraction from gcode files destined for 3d printers*. Technical Sciences, 23(2).
- KISSsoft. 2021. <https://www.kisssoft.com/en> (access: 20.09.2021).
- KLINGELNBERG. 2021. <https://www.klingelberg.de> (access: 20.09.2021).
- KOLLEK W., OSIŃSKI P., RUTAŃSKI J. 2015. *Wpływ zerowego luzu bocznego w zazębieniu na właściwości akustyczne pomp zębatych*. Napędy i Sterowanie, 1.
- KROL O., SOKOLOV V. 2021. *Selection of worm gearing optimal structure for machine rotary table*. Diagnostyka, 22(1).
- KURMAZ L.W., KURMAZ O.L. 2016. *Projektowanie węzłów i części maszyn*. Wydawnictwo Politechniki Świętokrzyskiej, Kielce.
- LARSSON R. 2016. *Methodology for Topology and Shape Optimization: Application to a Rear Lower Control Arm*. Chalmers University of Technology, Goeteborg.
- MAZANEK E. 2012. *Przykłady obliczeń z podstaw konstrukcji maszyn*. Część druga. Wydawnictwa Komunikacji i Łączności, Warszawa.
- MUMINOVIC A.J., COLIC M., MESIC E., SARIC I. 2020. *Innovative design of spur gear tooth with infill structure*. Bulletin of the Polish Academy of Sciences. Technical Sciences, 68(3).
- Narzędzia profesjonalne EU. 2021. <https://www.narzedziaprofesjonalne.eu/pl/p/Frez-monolityczny-LSM0202T-2%2C0-PAFANA-/2368> (access: 20.09.2021).
- OCHĘDUSZKO K. 1985. *Koła zębate*. Ed. 8. Wydawnictwo Naukowo-Techniczne, Warszawa.
- OSIŃSKI P. 2017. *Pompy zębate o obniżonym poziomie emisji hałasu*. Oficyna Wydawnicza Politechniki Wrocławskiej, Wrocław.
- OSIŃSKI P., BURY P., CIEŚLICKI R., LOREK L. 2018. *Badania trwałościowe niskopulsacyjnej pompy zębatej*. Napędy i Sterowanie, 11.
- PETR K., DYNBYL V. 2014. *Optimization of gear-mesh single-stage gearbox for regional trains by FEM*. Zeszyty Naukowe Politechniki Śląskiej. Transport, 84.
- POŁOWNIAK P., SOBOLAK M., MARCINIEC A. 2020. *Modelowanie wyjścia zwoju ślimaka globoidalnego z użyciem modyfikacji linii zęba*. Przegląd Mechaniczny, 12.
- RATAJCZYK E. 2005. *Współrzędnościowa technika pomiarowa*, Oficyna Wydawnicza Politechniki Warszawskiej, Warszawa.

- SHAH C., THIGALE S., SHAH R. 2019. *Optimizing weight of a Gear using Topology Optimization*. International Journal of Science, Engineering and Technology Research (IJSETR), 7(6).
- SUN K., WANG G., LU Y. 2019. *Optimization method of bevel gear reliability based on genetic algorithm and discrete element*. Eksploatacja i Niezawodność, 21(2).
- TAVČAR J., ČERNE B., DUHOVNIK J., ZORKO D. 2021. *A multicriteria function for polymer gear design optimization*. Journal of Computational Design and Engineering, 8(2): 581–599.
- TWARDOCH K. 2014. *Cyfrowe modelowanie geometryczne zarysu zębów z zastosowaniem metodologii CAD*. Zeszyty Naukowe Politechniki Śląskiej. Transport, 82.
- TYMCZYSZYN J. 2020. *The analysis of the gear's geometry measurement with various measuring systems*. Technologia i Automatyzacja Montażu, 3.
- WRÓBEL I., RYSIŃSKI J. 2012. *Analiza strukturalna koła zębatego o rzeczywistym kształcie*. Mechanik, 85(2), CD.
- Zelmer. 2021. ZMM4045B. <https://zelmer.pl/produkt/zmm4045b/> (access: 20.09.2021).





Yearbook peer-reviewed scientific journal

ISSN 1505-4675  
e-ISSN 2083-4527

**TECHNICAL SCIENCES**

Homepage: <https://czasopisma.uwm.edu.pl/index.php/ts/>



DOI: <https://doi.org/10.31648/ts.6814>

## STUDY OF THE PROCESS OF ROLLING STEEL BALLS IN SKEW ROLLING MILL – METALLOGRAPHIC ANALYSIS

*Piotr Chył*

ORCID: 0000-0001-5159-6746

Faculty of Mechanical Engineering and Robotics  
University of Science and Technology in Kraków

Received 15 June, accepted 13 October 2021, available online 28 October 2021.

**Key words:** skew rolling of balls, microstructure, 100Cr6, rail steel.

### Abstract

This paper presents the results of metallographic research studies carried out for stock materials as well as the samples collected from the balls formed in the rolling process in a skew rolling mill. The stock material was bearing steel 100Cr6 and the steel from rail scrap. The rolling process was carried out in parallel for the two assumptions: the conventional method (hereinafter referred to as conventional rolling) and the modified method (hereinafter referred to as modified rolling). After the rolling process, three cooling media were used: air, water and oil. The pictures below, which depict microstructures, were taken using the bright-field and the dark-field microscopy technique, the samples were etched with a 4% solution of picral.

### Introduction

Mass-scale production of steel balls, which are used as grinding media in various types of ball mills, forces producers to search for new technologies with greater efficiency and lower production costs. Currently, depending on the diameter, the balls for grinding media are manufactured worldwide in casting, closed-die forging and rolling processes (TOMCZAK et al. 2005).

---

Correspondence: Piotr Chył, Katedra Systemów Wytwarzania, Wydział Inżynierii Mechanicznej i Robotyki, Akademia Górniczo-Hutnicza, al. Mickiewicza 30, 30-059 Kraków, e-mail: [pchyla@agh.edu.pl](mailto:pchyla@agh.edu.pl).

Nowadays, they are manufactured mainly in the process of closed-die forging of semi-finished casting products or pre-cast cast steel. Unfortunately, such methods do not ensure the desired functional characteristics of the balls and the production costs are relatively high – mainly related to the price of the material and a relatively low level of its exploitation. For example, the concern KGHM Polska Miedź S.A. itself utilizes approximately 15 thousand tons of balls annually. Therefore, improving their performance is still a current issue.

In order to reduce the production costs, the stock material which is frequently used for their production are scrap rails (PATER et al. 2015). It is obvious that the life cycle of the balls depends on their performance characteristics, such as material strength, cracking and abrasion resistance. But an equally important factor is their correct shape, which depends on the production technique used to manufacture the balls (GRONOWSKIJ 1980, BŁAŻEWSKI et al. 1981, DOBRZAŃSKI 1993, ASHBT et al. 1996, Blicharki 2001, PRZYBYŁOWICZ 2007, XIAOZHONG et al. 2012, CHYŁA 2014).

The previous studies conducted to determine the properties of steel balls were rather focused on the possibility to shape these balls using rolling methods to obtain a product with the right shape (sphericity) (TOMCZAK et al. 2012a, 2012b, CHYŁA et al. 2016). However, there was no verification of the structure of the rolled balls or their mechanical properties (e.g. hardness), which resulted in carrying out the research studies presented in this article.

## Stock material

The skew rolling process of steel balls was carried out for the two different stock materials: bearing steel (100Cr6) and the steel obtained from rail heads and two different methods of tool calibration. Bearing steel 100Cr6 is characterized by exceptionally high quality due to particularly strict production conditions. This material is required to have a narrow and strictly maintained tolerance of alloying elements and impurities. Its chemical composition is as follows for 100Cr6: carbon 0.95-1.1%, manganese 0.25-0.45%, silicon 0.15-0.35%, chromium 1.3-1.65%, phosphorus 0.025%, and sulfur – up to 0.025%. Chemical composition for steel from rail scrap: carbon 0.62-0.8%, manganese 0.7-1.2%, silicon 0.15-0.58%, phosphorus max. 0.025%, and sulfur 0.008-0.025%.

The conventional method of tool calibration is based on the selection of such a contour of the groove and a pitch of the helical line, so as to maintain a constant volume of the metal captured by flanges throughout the entire process. The edges of the grooves – the flanges, projecting from the working surface of the rollers, are characterized by concave lateral surfaces, with the constant radius over the entire length of the helical impression and equal to the radius of the rolled ball. The extending flanges gradually narrow the connections between

the individual rolled balls, calibrating their diameter and separating them from each other. Such a method for tool calibration is difficult to implement and makes it necessary to continuously change the value of the pitch of the helical impression, which is calculated by dividing the stock material into the fixed volumes, equal to the volume of the rolled ball and the connecting bridge. A frequent result is the failure to fill or overfilling the helical impression, which adversely affects the accuracy of the rolled balls. Therefore, as part of the research work carried out at the Department of Computer Modelling and Metal Forming Technologies of the Lublin University of Technology, a new method of tool calibration for the skew rolling of balls was developed. A significant change, compared to the traditional method of calibration, is the introduction of a helical wedge surface in the grooving area, which then develops into the concave forming flanges. As in the case of traditional helical impressions, the basis for calculating the pitch and the shape of the groove outline is to keep a constant volume of the material between the flanges of the tools, as well as an equal volume of the rolled ball and the connector (CHYLA 2019).

Figure 1 demonstrates the working rolls used in the two rolling methods. The working impressions of each roller are formed by six tool segments (2), made of hot-work tool steel. The segments are attached to the shaft (1) of the rolling mill using two spindle nuts (3). On the surface of the segments, there are shaping grooves (5) separated by the flanges (6) having concave lateral surfaces. In the grooving area, there is a wedge-shaped helical ledge (4) with a wedge angle of  $2\beta$  and the inclination angle of the lateral walls of  $\alpha$ . A cutter (7) – denotations in Figure 1.

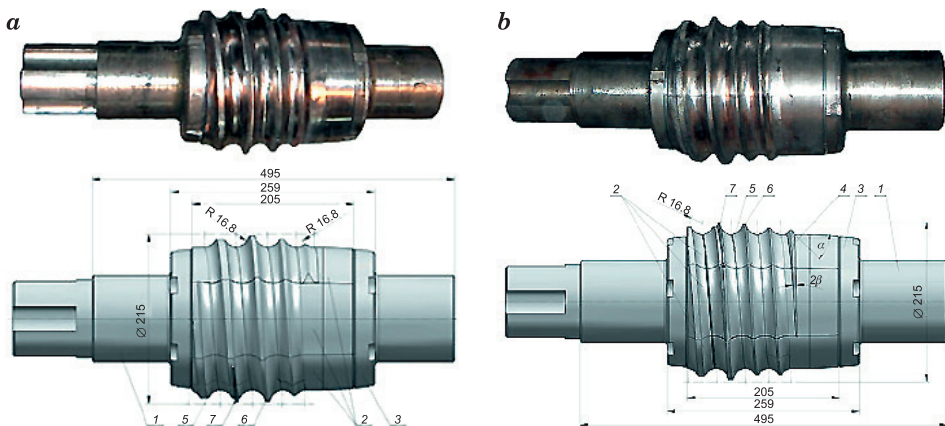


Fig. 1. Sets of screw segments tools for rolling the balls: *a* – conventional method, *b* – modified method; description in the text

Source: based on CHYLA (2019).

Immediately after rolling, the balls were cooled to room temperature using three media: water, oil and air. The balls for mechanical tests were cut from these samples (in this case, hardness tests were considered to be the most representative ones). The Vickers hardness test method was performed using a Zwick durometer according to the standard PN-EN ISO 6507-1:2007, owned by the Department of Metal Forming, Faculty of Metals Engineering and Industrial Computer Science of AGH University of Science and Technology in Krakow – as demonstrated in Figure 2*a*. The samples of the rolled balls were subjected to the measurements of hardness at 25 points. The first and last measurement points were located 2 mm from the edge of the sample, the remaining points at a distance of every 1 mm over the entire length. Figure 2*b* illustrates the scheme of the measurement points (CHYŁA 2019).

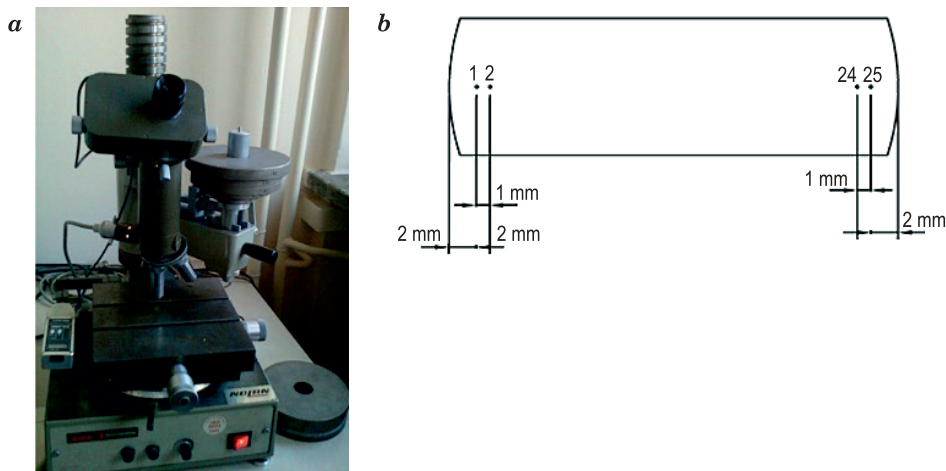


Fig. 2. Hardness measurements: *a* – hardness tester;  
*b* – scheme of points positioning on the length of the sample  
 Source: based on CHYŁA (2019).

From the images of microstructures of the bearing steel 100Cr6 (Fig. 3), it is visible in the stock material that it has been subjected to spheroidizing annealing. This is a typical condition of this type of stock material (high content of carbon and chromium) for further plastic working. There is abundant fine carbide precipitation (most probably  $M_3C$ ) of a spheroidal character, uniformly distributed throughout the volume of the material. Carbides are in the ferritic matrix, which is characteristic for long annealing used for this type of steel. In some places, the remains of pearlitic cementite platelets are noticeable, which did not coagulate completely. There are also areas where carbides are arranged

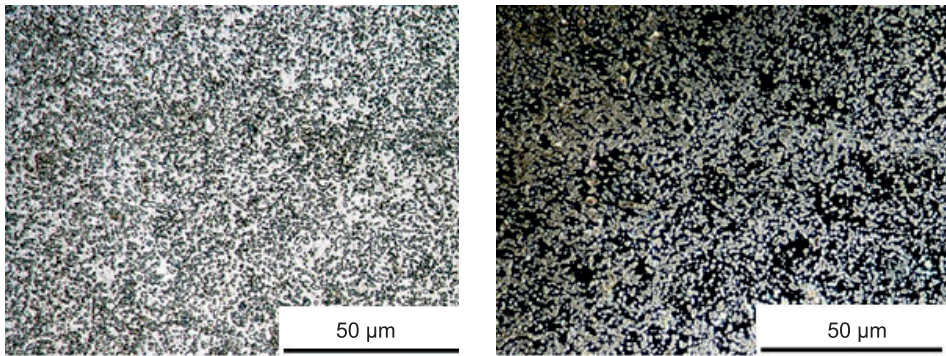


Fig. 3. Microstructure of the samples of the bearing steel 100Cr6 – stock material

linearly, resulting in the spheroidization of cementite present in pearlite (eutectoid cementite). However, these are small areas and they should not affect adversely material properties in the later stages.

Apparently, the microstructure of the steel from rail heads (Fig. 4) was delivered after spheroidizing (softening) annealing. If that was the case, the microstructure would look like in the first case (Fig. 3), ferrite + spheroidal  $\text{Fe}_3\text{C}$ . This is probably the microstructure after normalizing annealing, or immediately after rolling. In the picture there is a characteristic pearlitic microstructure with various thickness of platelets (mostly fine pearlite). Colonies of pearlite are visible, strongly deformed in some places. The average size of these colonies ranges from several to several tens of micrometers. This condition is typical for pearlitic steels without alloying elements and sufficient for further plastic working.

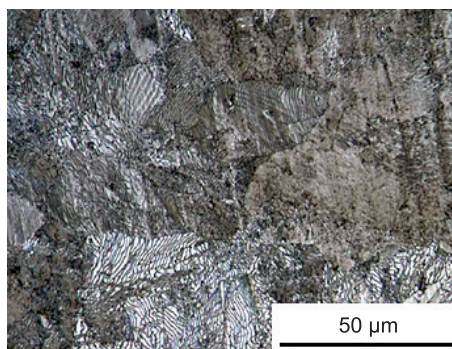


Fig. 4. Microstructure of the samples of the rail steel – stock material



## Microstructure of the rolled balls after cooling in different media

After the rolling process, the balls were directly subjected to cooling in three different cooling media: air, water and oil.

In the case of the air-cooled material, pearlitic microstructure was obtained (Fig. 5÷8). The microstructure of the bearing steel (approx. 1% C), in addition to pearlite, contains a characteristic cementite mesh at the grain boundaries (typical for the steel with such carbon content). In the picture depicting the sample of the bearing steel 100Cr6, obtained in the modified rolling process and cooled in air (Fig. 6), the mesh is not as visible as in the picture illustrating the sample from the same type of steel, obtained in the conventional rolling process, also cooled in air (Fig. 5). The microstructure of pearlite and cementite at the grain boundaries adversely affects both the mechanical and plastic properties. Cementite is a hard and brittle phase, and therefore, as a result of the applied stress (mesh), it is a place prone to cracks and their propagation at the grain boundaries.

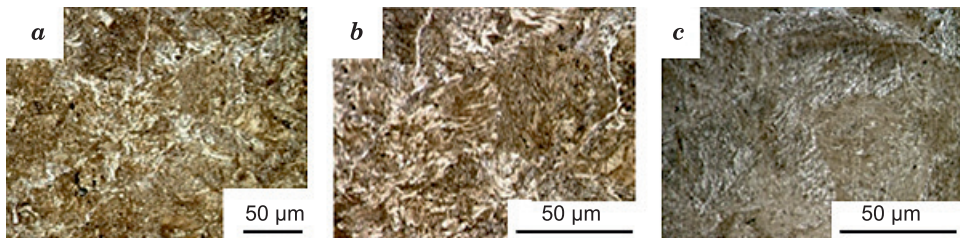


Fig. 5. Microstructure of the samples of the bearing steel 100Cr6 obtained in the conventional rolling process, cooled in air: *a* – left edge of the sample, *b* – the middle part of the sample, *c* – right edge of the sample

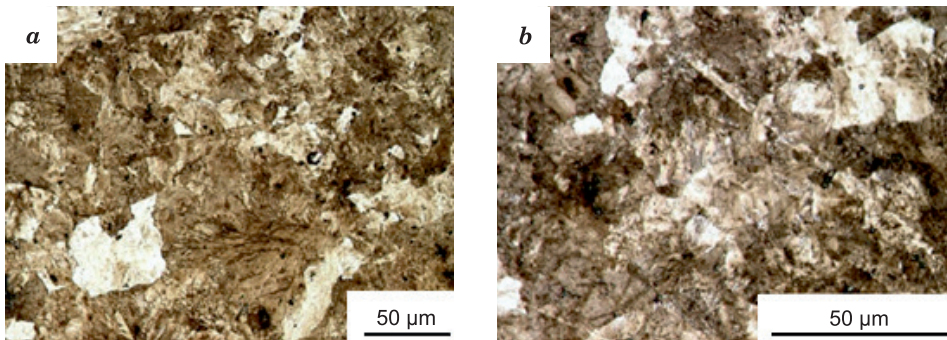


Fig. 6. Microstructure of the samples of the bearing steel 100Cr6 obtained in the modified rolling process, cooled in air: *a* – left edge of the sample, *b* – right edge of the sample

In the picture of the microstructure of the stock material, the most visible (distinguishable) alternately arranged platelets of ferrite and cementite are made of the rail steel (Fig. 4). In the case of both stock materials: the rail steel and the bearing steel (Fig. 7, 8), after deformation and cooling in air, individual platelets are not so distinguishable at specific magnification. Pearlite colony size for the individual analyzed cases varies in a wide range of several to tens of micrometers. The thickness of the platelets affects mechanical properties (of a given carbon content), e.g. the hardness of steel. On the other hand, it depends on the supercooling of austenite (above the temperature of bainite formation): the greater the supercooling, the smaller the thickness of the platelets. The lower the hardness of the balls, the more prone to wear they will become. Performance characteristics of the balls will be better with the smaller distance between the platelets.

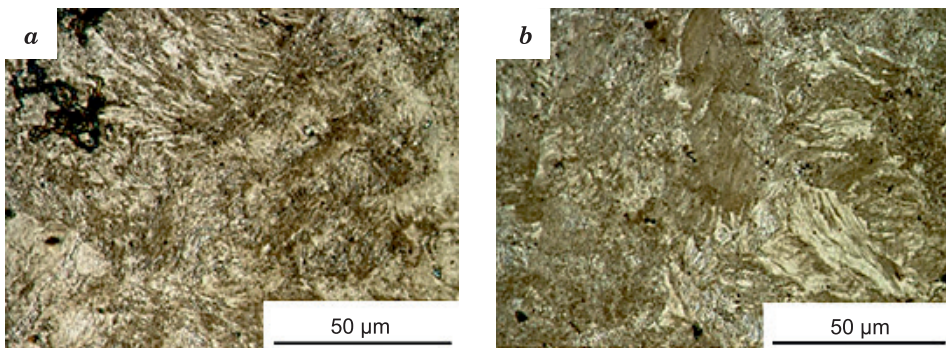


Fig. 7. Microstructure of the samples of the rail steel obtained in the conventional rolling process, cooled in air: *a* – left edge of the sample, *b* – right edge of the sample

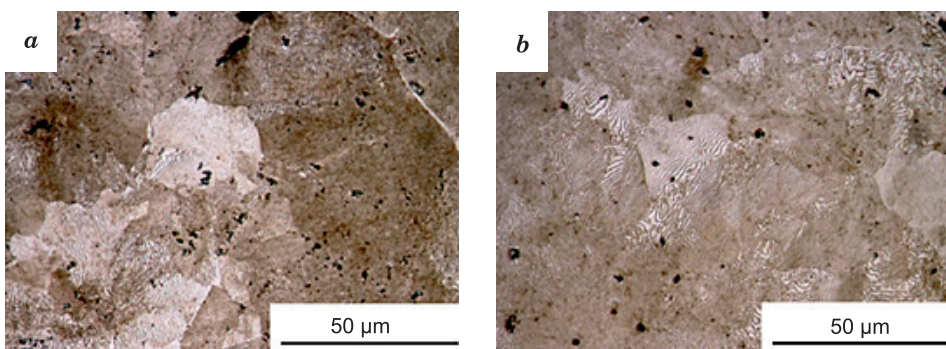


Fig. 8. Microstructure of the samples of the rail steel obtained in the modified rolling process, cooled in air: *a* – left edge of the sample, *b* – right edge of the sample



The microstructure of the steel both from the bearing steel (Fig. 9, 10) and from scrap rails (Fig. 11, 12), after cooling in water (quenching), is composed of martensite and retained austenite. In the case of the samples of the bearing steel 100Cr6 after the conventional rolling process (Fig. 9) and the modified rolling process (Fig. 10), there is a characteristic microstructure of (thick) plate martensite and retained austenite. The high content of retained austenite in the bearing steel 100Cr6 is associated with a high carbon and chromium contents,

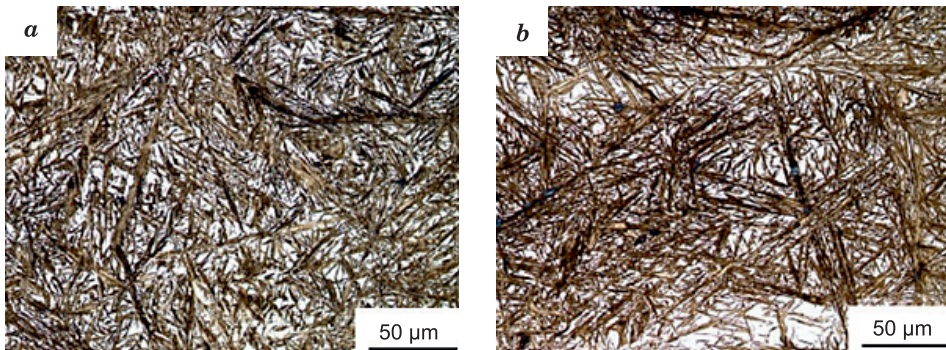


Fig. 9. Microstructure of the samples of the bearing steel 100Cr6 obtained in the conventional rolling process, cooled in water: *a* – left edge of the sample, *b* – right edge of the sample

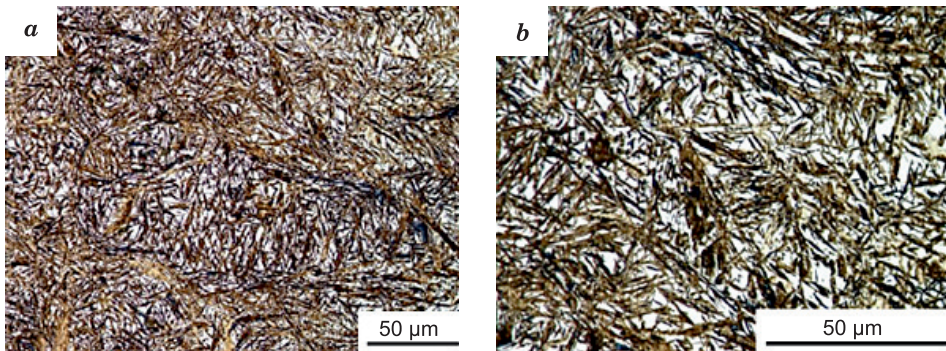


Fig. 10. Microstructure of the samples of the bearing steel 100Cr6 obtained in the modified rolling process, cooled in water: *a* – left edge of the sample, *b* – right edge of the sample

which lower the temperature  $M_s$  and  $M_f$ ; moreover, it is stabilized by chromium dissolved in austenite. Light-colored, non-etched stripes are visible (high content of retained austenite), which may be due to chromium dissolved in austenite.

In the case of the balls made of the rail steel (Fig. 11, 12), formed in the cross wedge rolling mills after the heat quenching treatment, the size (length) of the martensite platelets is smaller, which may indicate a finer austenite grain. The microstructure of the steel from scrap rails, after quenching in water,



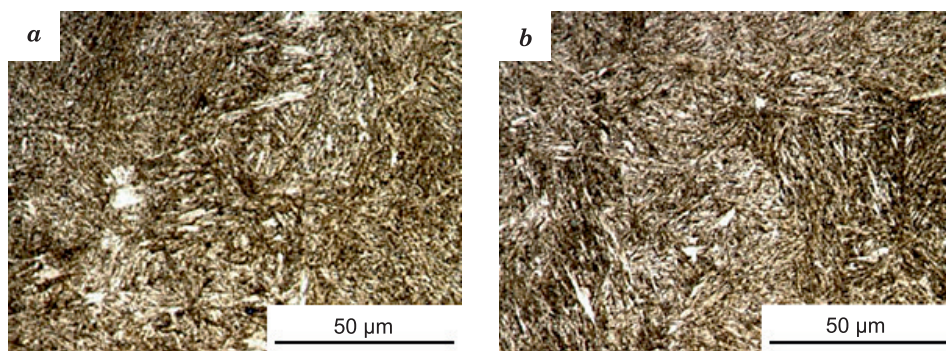


Fig. 11. Microstructure of the samples of the rail steel obtained in the conventional rolling process, cooled in water: *a* – left edge of the sample, *b* – right edge of the sample

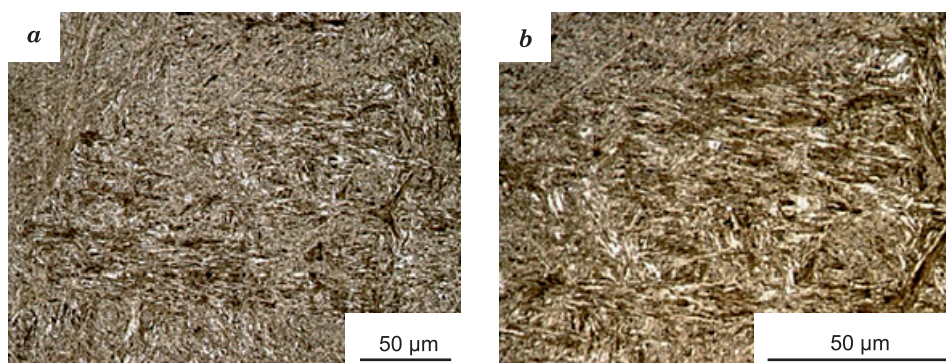


Fig. 12. Microstructure of the samples of the rail steel obtained in the modified rolling process, cooled in water: *a* – left edge of the sample, *b* – right edge of the sample

is composed of lath and plate martensite as well as retained austenite. Compared with the microstructure of hardened bearing steel, the content of austenite is much lower. Martensite with small-sized plates is better – there are smaller residual stresses. Retained austenite reduces the hardness but, on the other hand, it favorably affects the properties of steel such as wear resistance and fatigue strength, as well as reduces its tendency to brittle fracture. The hardness of the bearing steel should be slightly higher due to the carbon content. In the case of the steel from scrap rails, there are no major differences in the microstructure of the balls formed in the conventional and modified rolling processes.

As a result of the cooling process, after the deformation in oil, the martensitic transformation occurred (Fig. 13÷16). The microstructure of the balls formed from the bearing steel (Fig. 13, 14) consisted of: plate martensite and retained austenite (light-colored areas). In some places (light-colored spots), it could be associated with the segregation of chromium dissolved in austenite. The share of retained austenite is much higher than in the case of rail steel (higher carbon content).

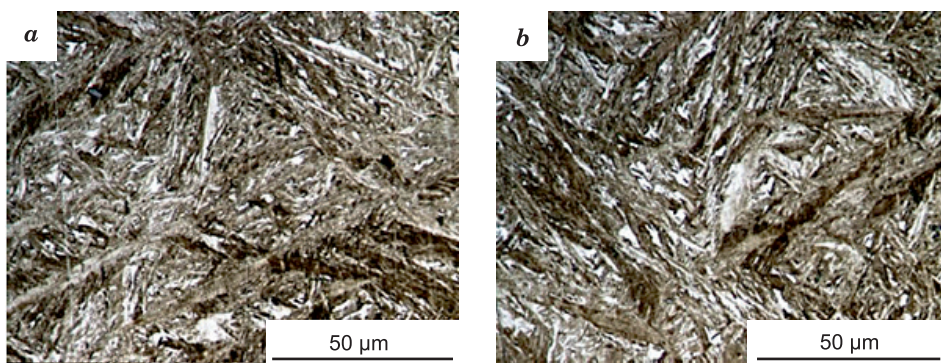


Fig. 13. Microstructure of the samples of the bearing steel 100Cr6 obtained in the conventional rolling process, cooled in oil: *a* – left edge of the sample, *b* – right edge of the sample

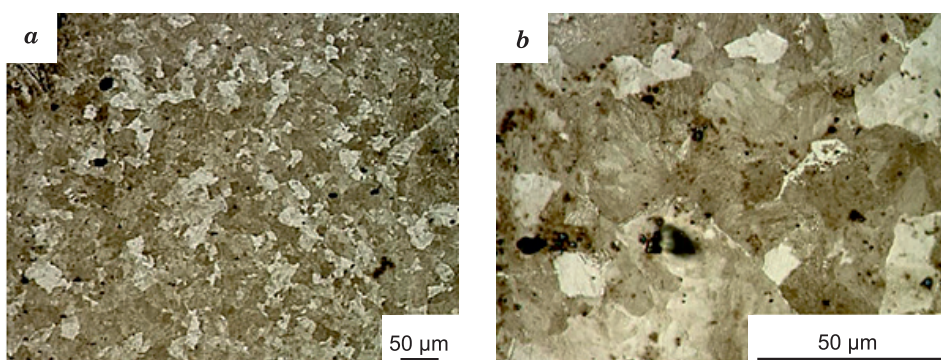


Fig. 14. Microstructure of the samples of the bearing steel 100Cr6 obtained in the modified rolling process, cooled in oil: *a* – left edge of the sample, *b* – right edge of the sample

In the case of rail steel (Fig. 15, 16), the microstructure is composed of lath and plate martensite (to a lesser extent) and retained austenite (light-colored areas).

Figure 17 illustrates a special case of the microstructure obtained by the conventional rolling process combined with the cooling in oil. Near the surface, it is composed of pearlite and cementite at the grain boundaries (as after the cooling in air), and farther from the surface, martensite (brown color) and dark areas – pearlite can be observed. This effect may be due to the fact that during the deformation, as a result of the contact with a tool, the temperature dropped (diffusional transformation), but inside the material, where the transformation did not occur (there was austenite in the structure), as a result of the cooling in oil, the martensitic transformation occurred where, in addition to pearlite, there is martensite.



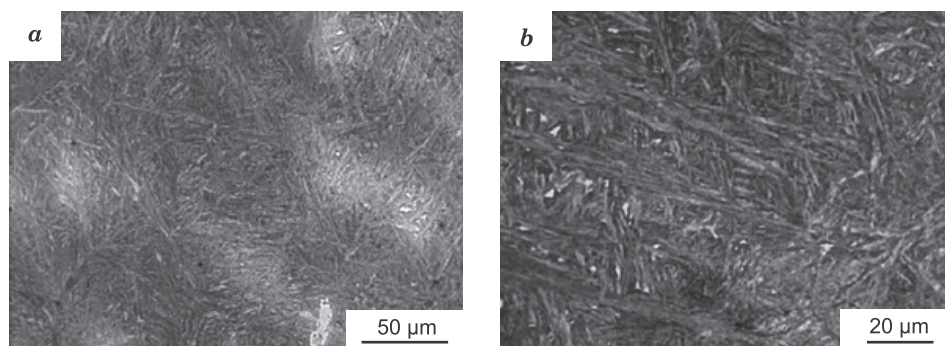


Fig. 15. Microstructure of the samples of the rail steel obtained in the conventional rolling process, cooled in oil: *a* – left edge of the sample, *b* – right edge of the sample

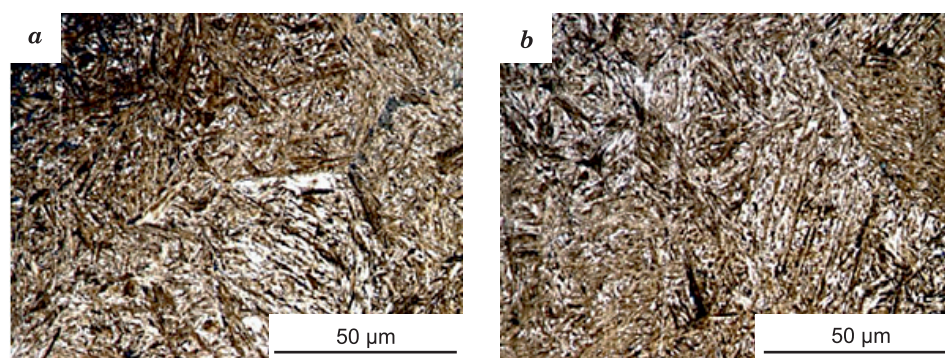


Fig. 16. Microstructure of the samples of the rail steel obtained in the modified rolling process, cooled in oil: *a* – left edge of the sample, *b* – right edge of the sample

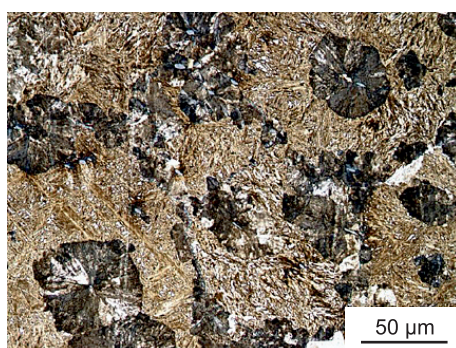


Fig. 17. Microstructure of the sample of the rail steel obtained in the conventional rolling process, cooled in oil (specific case)

## Summary and conclusions

Numerically analyzed processes of skew rolling of the balls (DOBRZAŃSKI 1993) were verified experimentally in the laboratory conditions of the Department of Metal Forming, Faculty of Metals Engineering and Industrial Computer Science of AGH University of Science and Technology in Krakow, using the skew rolling mill installed at this laboratory. The physical tests were performed on two stock materials: bearing steel 100Cr6 and rail steel.

After the rolling process, the balls were subjected to quenching treatment in three cooling media: they were placed in water, in oil and they were left in the air. The analyses of the physical test results allowed to formulate the following conclusions:

- despite a relatively long shaping time, the temperature of the material is maintained within the range appropriate for hot plastic working and it is sufficient to carry out the quenching process immediately after the rolling of the balls;
- the roll pass method of the working roller does not affect either the hardness or the microstructure of the obtained balls.

## References

- ASHBY M.F., JONES D.R.H. 1996. *Engineering materials*. Wydawnictwo Naukowo-Techniczne, Warszawa.
- BŁĄŻEWSKI S., MIKOSZEWSKI J. 1981. *Measurements of metal hardness*. Wydawnictwo Naukowo-Techniczne, Warszawa.
- BLICCHARSKI M. 2001. *Introduction to material engineering*. Wydawnictwo Naukowo-Techniczne, Warszawa.
- CHYLA P. 2014. *Study of the steel balls rolling process in the helical rolling mills*. Ph.D. AGH University of Science and Technology, Cracow.
- CHYLA P. 2019. *The influence of forming conditions on the hardness of balls formed in the skew rolling process*. Metallurgy and Foundry Engineering, 45: 7-17.
- CHYLA P., PATER Z., TOMCZAK J., CHYLA P. 2016. *Numerical analysis of a rolling process for producing steel balls using helical Rolls*. Archives of Metallurgy and Materials, 61: 485-491.
- DOBRZAŃSKI L. 1993. *Metallography and heat treatment of metal alloys*. Wydawnictwo Politechniki Śląskiej, Gliwice.
- GRONOWSKIJ S.P. 1980. *Nowyje processy i stany dla prokatki izdzielij w wintowych kalibrach*. Metalurgija, Moskwa.
- PATER Z., TOMCZAK J., BULZAK T. 2015. *A cross wedge rolling method for producing balls directly from rail heads*. Rudy i Metale Nieżelazne Recykling, 11: 555-559. doi:10.15199/67.2015.11.3.
- PRZYBYŁOWICZ K. 2012. *Metallography*. Wydawnictwo Naukowo-Techniczne, Kraków.
- TOMCZAK J., KAZANECKI J., PATER Z., BARTNICKI J., CHYLA P. 2012a. *Research on the process of shaping balls in screw rollers*. Mechanik, 11: 927-931.
- TOMCZAK J., PATER Z., BARTNICKI J., KAZANECKI J., CHYLA P. 2012b. *Influence of the method of calibrating helical blanks on the quality of rolled spheres in oblique mills*. Przegląd Mechaniczny, 11: 33-39.
- TOMCZAK J., PATER Z., BULZAK T. 2015. *Innovative process of shaping balls from heads of scrapped railway rails*. Hutnik – Wiadomości Hutnicze, 6: 387-392. doi:10.15199/24.2015.6.1.
- XIAOZHONG R., YONGQING L., YURONG J. 2012. *Optimization of Screw Rollin Ball Process Parameters Based on Orthogonal Test*, Applied Mechanics and Materials, 201-202: 1190-1193.



Yearbook peer-reviewed scientific journal

ISSN 1505-4675  
e-ISSN 2083-4527

**TECHNICAL SCIENCES**

Homepage: <https://czasopisma.uwm.edu.pl/index.php/ts/>



DOI: <https://doi.org/10.31648/ts.7069>

## INFLUENCE OF AIR CONTENT ON THERMAL DEGRADATION OF POLY(ETHYLENE TEREPHTHALATE)

*Wojciech Rejmer*

ORCID: 0000-0002-1955-1553

Faculty of Technical Sciences  
University of Warmia and Mazury in Olsztyn

Received 06 September 2021, accepted 28 October 2021, available online 20 November 2021.

**Key words:** poly(ethylene terephthalate), degradation, accelerated aging, air content, air pressure.

### Abstract

The aim of these research is to investigate the air content on aging of poly(ethylene terephthalate) (PET) preforms. Three air pressures were selected and in each pressure 5 samples were aged during 21 days in 80°C. Three samples were selected to be cut for determination of density with the use of hydrostatic method. Sample mass, Young modulus and surface roughness were measured for each sample before and after aging and differences between those parameters were presented as results. The changes of parameters may lead to a conclusion that mechanism of polymeric chain oxidation is dominant during thermal aging of PET. However aging process is not the fastest in atmospheric pressure but in lower air contents. This effect may be caused by greater evaporation of small molecule degradation products and shifting of reaction equilibrium in the direction of further decomposition.

---

Correspondence: Wojciech Rejmer, Katedra Technologii Materiałów i Maszyn, Wydział Nauk Technicznych, Uniwersytet Warmińsko-Mazurski, ul. Oczapowskiego 11, 10-719 Olsztyn, e-mail: [wojciech.rejmer@uwm.edu.pl](mailto:wojciech.rejmer@uwm.edu.pl)

## Introduction

The varied properties of polymers turned out to be extremely useful for industry, which resulted in large scale use. With time, however, irreversible and often negative changes in the properties of the material occur. Physical and chemical changes generated by usage are called aging. Natural aging proceeds under the influence of the surrounding natural environment during storage and use. Artificial aging of the material occurs under specially designed conditions and is used for research purposes. Several types of polymer aging can be observed based on physical conditions that cause structural change. This processes include: biological aging, electrical aging, mechanical aging, chemical aging and photochemical aging, thermal aging. Thermal degradation of polymers is called “molecular degradation resulting from overheating”. In high temperatures molecules of the polymer are defragmenting (molecular defragmentation) (SOBKÓW, CZAJA 2009). Products of this process can react with each other and with remaining polymer chains resulting in change of materials properties. During thermal degradation the molecular mass of polymer chains is impacted the most. Physical and optical properties that the process influences are: strain at break, maximum stress, rigidity, color change.

In this work poly(ethylene terephthalate) (PET) products are studied. PET is one of most common polymers used in industry. It is used for production of bottles, sprockets, and garments. The reason for PET popular use is that it retains its shape memory, i.e. after deformation it returns to the shape given before crystallization. The properties of PET depend on its degree of crystallinity. With the normal proportion of the crystalline phase (approx. 40%), it is characterized by high dimensional stability, good chemical resistance, and good sliding and dielectric properties. PET is not resistant to factors such as phenols, concentrated acids and solutions, alkalis and long-term exposure to hot water (hydrolysis). Sterilization of PET products is carried out in an atmosphere of ethylene oxide or by irradiation. It is mainly processed by injection molding at 260-290°C (injection shrinkage is 1.2-2%). With extrusion technique films, rods, plates and fibers are formed. Extrusion temperature is 260-280°C (LÓPEZ-FONSECA et al. 2011). Researchers have studied the degradation of recycled PET during processing and concluded that chain scission can occur and that formation of grafted copolymers and crystallization can be facilitated (ITIM, PHILIP 2015) and others concluded that during repetitive extrusion, chain scission is a dominant process and no chain branching or cross-linking were observed which decreased capabilities and crystallinity (BADÍA et al. 2009), whereas others concluded that cross-linking and chain branching occur during extrusion (NAIT-ALI et al. 2011). Researchers currently focus on the influence of physical ageing on the mechanical properties of semicrystalline PET, using several methods to characterize both the change in morphology and physical properties of PET:

Such as calorimetric analysis, FTIR, X-ray, NMR and other. These studies were carried out to enhance understanding of the structure–property relationships, which are important for materials that require stability and durability during their lifetime (ALJOUMAA, ABOUDI 2016). During the exposure to sunlight, many reactions in PET molecular chains may occur: chains scission reaction due to thermal degradation of vinylic and carboxylic chain ends, which may recombine by trans-esterification reaction (EL-TOUFAILI 2006), photo-degradation of methylene groups which will cause an irreversible rupture of the polymeric chain, and change in the color of the bottle to yellow due to many substances used in the process of synthesis and fabrication (YANG et al. 2010). Moreover, at outdoor ageing, the exposure to light and air will cause a photooxidation of PET (photochemical ageing). It is known that PET absorbs at the extreme limit of the UV band ( $300\text{ nm} < \lambda < 330\text{ nm}$ ). This phenomenon is superficial, thin layer may degrade by this reaction and is limited by the  $\text{O}_2$  diffusion and superficial light absorption. This material is also susceptible to physical aging below the glass transition temperature caused by the slow change of quenched material at a thermodynamically non-equilibrium state to equilibrium. This is related to the relaxation processes with characteristic, different time constants (SATO, SPRENGEL 2012). It results in a reduction in entropy, enthalpy and specific volume with an increase in yield stress and tensile and flexural module. Hay investigated the effect of the crystalline phase on the behavior and properties of PET (KONG, HAY 2003). It turned out that the crystalline phase limits mobility of the chain segments, influencing the macroscopic properties of the material (PANOWICZ et al. 2021). The aim of this paper is to investigate changes in PET surface structure and mechanical properties under thermally accelerated aging conditions and variable air content.

## Materials and methods

Research material consisted of 26 preforms made from PET (Fig. 1). Samples undergone the same heating cycle with variable air pressures. Samples from 1-5 were heated to  $80^\circ\text{C}$  under atmospheric pressure and kept for 21 days. Samples 7-12 were kept in a 6.8 l vacuum chamber under 5.7 Pa of air pressure. Aging conditions for samples 13, 14, 15, 17, 18, 19 were the same in terms of temperature and aging time but the vacuum chamber was depressurized to 2.8 Pa. The air pressure for aging process of samples 19, 21, 22, 23, 24 was 0.3 Pa. Mass and dimensions of samples were measured and presented in Table 1. Mass was determined with analytical scale RADWAG AS60/220.R2.

The samples roughness, Young modulus and mass were measured before and after aging process for all samples. Roughness was measured using SJ-210 Mitutoyo profilometer with elementary distance 0.8 mm and measuring



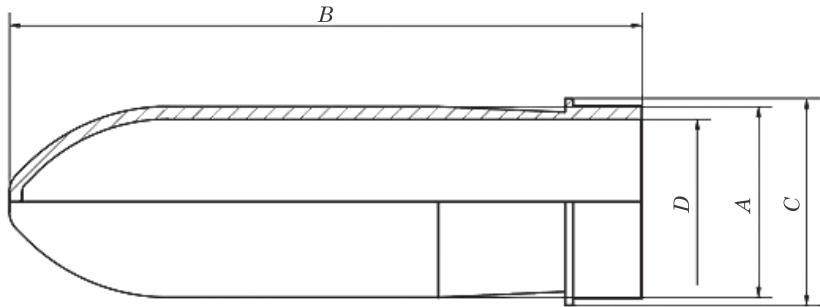


Fig. 1. Shape of investigated samples

Table 1

Dimensions and mass of samples

Sample no.	Dimension A [mm]	Dimension B [mm]	Dimension C [mm]	Dimension D [mm]	Mass [g]
1	47	159	51.54	41.1	98.1944
2	46.99	159.4	51.44	41.14	97.9173
3	46.97	159.6	51.55	41.11	98.2353
4	47.1	159	51.54	41.2	98.1148
5	47.4	159.4	51.5	41.19	98.0271
6	47.38	159.65	51.5	41.16	98.1842
7	47.37	159.6	51.45	41.13	98.0106
8	47.33	159.5	51.44	41.16	98.0271
9	47.43	159.6	51.51	41.19	97.9228
10	47.33	159.5	51.5	41.19	97.9176
11	47.36	159.4	51.48	41.13	97.8713
12	47.45	159.5	51.5	41.17	97.9062
13	47.36	159.6	51.57	41.2	98.2994
14	47.53	159.6	51.54	41.16	98.1164
15	47.54	159.6	51.45	41.14	98.0129
16	47.28	159.5	51.48	41.13	98.0319
17	47.43	159.5	51.5	41.18	98.1736
18	47.51	159.6	51.52	41.17	98.1608
19	47.6	159.5	51.55	41.19	98.2664
20	47.32	159.4	51.52	41.21	98.0329
21	47.36	159.5	51.49	41.1	97.9409
22	47.49	159.5	51.55	41.17	98.1704
23	47.4	159.5	51.59	41.19	98.1057
24	47.27	159.2	51.46	41.11	98.0223
25	47.48	159.5	51.58	41.19	98.3136
26	47.62	159.4	51.52	41.18	98.0894



distance 4 mm. Roughness was measured in 3 places inside of each sample (Tab. 2). Young modulus was determined using Impulse Excitation Technique (IET) with RFDA MF system by IMCE (Tab. 3).

Samples 6, 16 and 20 were chosen to measure non aged sample density by hydrostatic method with analytical scale RADWAG AS60/220.R2 equipped with density determination kit KIT-85 from Radwag. For density measurements distilled water was used as a submerging agent. With nondestructive tests (mass, roughness and Young modulus) difference between pre and post aging state were presented as results.

Table 2

Roughness of investigated samples

Sample no.	Ra 1 [ $\mu\text{m}$ ]	Ra 2 [ $\mu\text{m}$ ]	Ra 3 [ $\mu\text{m}$ ]	Average [ $\mu\text{m}$ ]
1	0.113	0.146	0.153	0.137
2	0.229	0.329	0.224	0.261
3	0.144	0.173	0.111	0.143
4	0.235	0.087	0.139	0.154
5	0.201	0.177	0.102	0.160
6	0.147	0.193	0.069	0.136
7	0.151	0.129	0.148	0.143
8	0.142	0.123	0.163	0.143
9	0.281	0.32	0.214	0.272
10	0.275	0.327	0.235	0.279
11	0.186	0.273	0.154	0.204
12	0.252	0.176	0.164	0.197
13	0.109	0.233	0.147	0.163
14	0.154	0.168	0.204	0.175
15	0.205	0.262	0.148	0.205
16	0.088	0.109	0.109	0.102
17	0.114	0.105	0.157	0.125
18	0.151	0.117	0.088	0.119
19	0.157	0.123	0.134	0.138
20	0.13	0.113	0.163	0.135
21	0.232	0.24	0.247	0.240
22	0.183	0.205	0.257	0.215
23	0.114	0.187	0.198	0.166
24	0.235	0.144	0.156	0.178
25	0.115	0.118	0.228	0.154
26	0.137	0.163	0.147	0.149

Table 3

Young modulus of pre aged material	
Sample no.	Young modulus [GPa]
1	2.92
2	2.97
3	2.96
4	2.92
5	2.81
6	2.81
7	2.8
8	2.84
9	2.81
10	2.85
11	2.81
12	2.78
13	2.85
14	2.76
15	2.75
16	2.84
17	2.8
18	2.76
19	2.75
20	2.84
21	2.82
22	2.78
23	2.83
24	2.83
25	2.8
26	2.69

## Results and discussion

The mass of all aged samples decreased. Mass decrease of samples kept under atmospheric pressure was between 0.099 to 0.10 g. The samples kept under 5.7 Pa decreased their mass by 0.25-0.27 g. Preforms kept under 2.8 Pa of pressure decreased their mass by 0.27-0.28 g. The lowest pressure samples decreased their mass by 0.2-0.21 g. Results of mass decrease were presented on Figure 2.

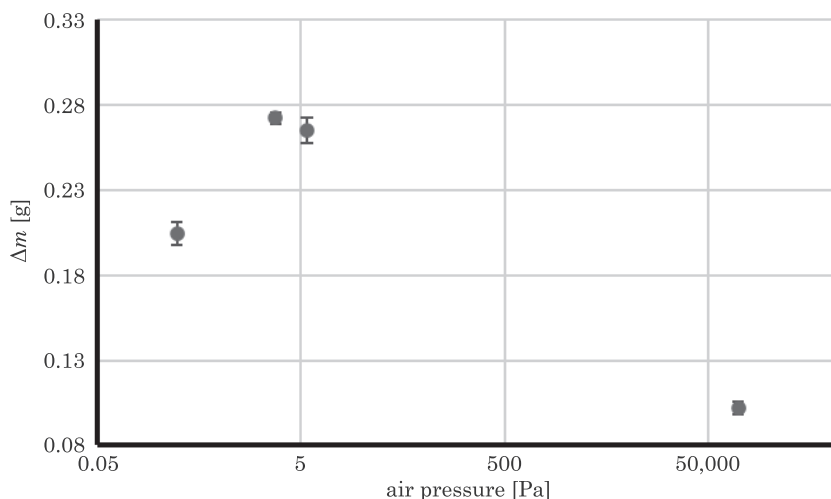


Fig. 2. Mass decrease versus air pressure during aging process

Samples aged with highest air content had lowest decrease of mass during the process this effect might be caused by oxidation of polymer chains which increases the molecular mass. The second processes that occurs during aging at increased temperatures is evaporation of small molecule additions to polymer such as plasticizers and thermostabilizers. In lower air pressures this effect is probably more predominant which causes higher mass decrease. In the lowest pressure the mass decrease is second lowest. Under such conditions both oxidation of polymer chains and conversion of addition compounds to vaporous oxides is least likely. This may give a value of mass loss caused only by terminal depolymerization of PET. The effect may also be caused by oxidation of polymeric chain it self predominantly to products such as carbon mono and di oxide, ethylene and ethyl aldehyde. Evaporation of these degradation products can also be the cause of mass decrease during aging time (VENKATACHALAM et al. 2012).

The decrease of mass is accompanied by change of mechanical properties. In this study this change was measured by calculation of Young modulus obtained with IET. The rigidity of the material decreased only in the samples aged under atmospheric pressure by 0.03-0.05 GPa. Samples aged under 5.7 Pa showed increased Young modulus by 0.4-0.6 GPa. Samples kept under 2.8 Pa of air showed the same effect in the magnitude of 0.4-0.5 GPa. Samples with least amount of air in their enviroment increased their rigidity by around 0.3 GPa. Results of Young modulus change were presented on Figure 3.

The Young modulus change of polymer material is largely dependant on degree of crystallinity (DONG et al. 2020). The decrease of rigidity in sample aged under atmospheric pressure may be cused by plastifying effect of some of decomposition products such as ethylene glycol (PIVSA-ART et al. 2016). In higher

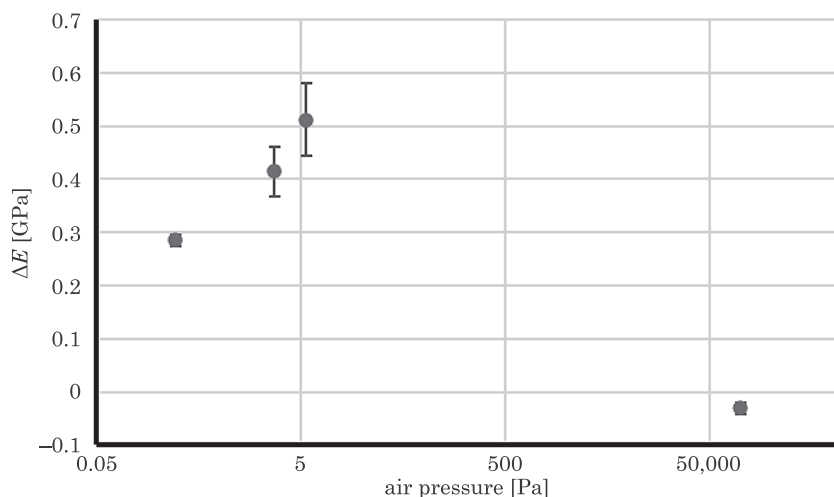


Fig. 3. Young modulus change versus air pressure

air pressures evaporation of those products is higher than in lower pressures under same temperatures. Higher oxygen contents provide also creation of more hydroxyl groups as well as cyclization reactions (KHEMANI 2000). Hydroxyl groups generally lead to increase of crystallization rates, and thus rigidity, due to formation of hydrogen bonds (SANG et al. 2020). In lowest pressure creation of hydrogen bonds can be assumed as minimal, but cyclization processes that cause the reduction of degrees of crystallinity still occur (CHANG et al. 2015). Therefore a lower rigidity of samples aged in 0.3 Pa in comparison to two kinds of samples kept under higher pressures can be observed.

Thermal aging caused increase of surface roughness. For samples aged under atmospheric pressure average roughness increased by 0.19-0.24  $\mu\text{m}$ . Material aged under 5.7 Pa of air pressure had roughness increased by 0.06-0.11  $\mu\text{m}$ . Polyester samples aged in presence of 2.8 Pa of air exhibited roughness increase of 0.15-0.21  $\mu\text{m}$ . Samples heated with the least amount of air showed roughness increase of 0.15-0.22  $\mu\text{m}$ . Figure 4 shows dependence of average roughness increase on air content.

The effect of greatest surface roughness increase in samples aged under atmospheric pressure may be caused by combined effect of oxidation and plastifying effect of decomposition products. The samples aged under 0.3 Pa and 2.8 Pa show similar increase of roughness which can imply similar sizes of crystal structures. Samples aged under 5.7 Pa of air pressure show lowest increase in surface roughness and highest increase of Young modulus, which implies creation of most new crystalline structures and their smaller sizes. Studies by ZABOROWSKA et al. (2021) have shown that significant changes of polymeric material roughness are present only with minimal changes

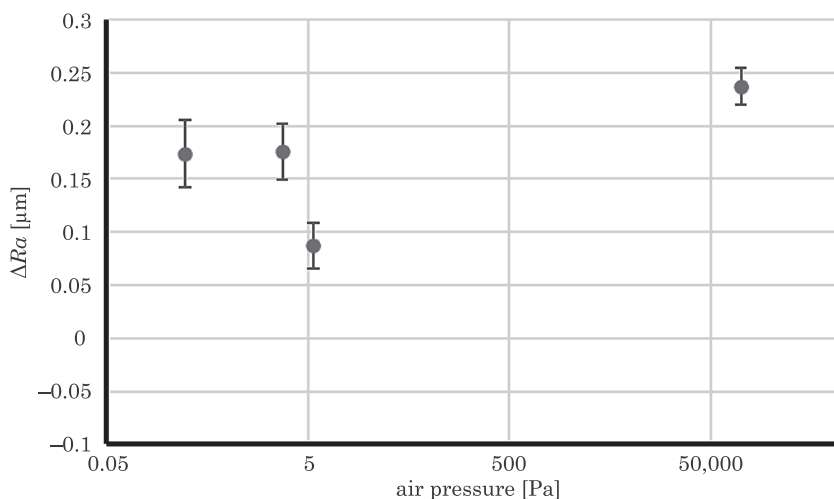


Fig. 4. Average roughness increase versus air pressure

to polymeric chains chemistry, with regard to methane production. However the significant changes in PET samples can be attributed mainly to changes occurring because of oxidation reactions.

Samples density was measured for every type of samples. The results of measured density for aged and non aged samples is presented on Figure 5. Nonaged samples had density of  $1.35 \pm 0.02 \text{ g/cm}^3$ . Samples aged at atmospheric pressure and at 0.3 Pa exhibited similar values of  $1.35 \pm 0.02 \text{ g/cm}^3$  and  $1.36 \pm 0.003 \text{ g/cm}^3$  respectively. PET preforms aged at 5.7 Pa and 2.8 Pa exhibited slight increase of density values being  $1.37 \pm 0.005 \text{ g/cm}^3$  and  $1.39 \pm 0.005 \text{ g/cm}^3$ .

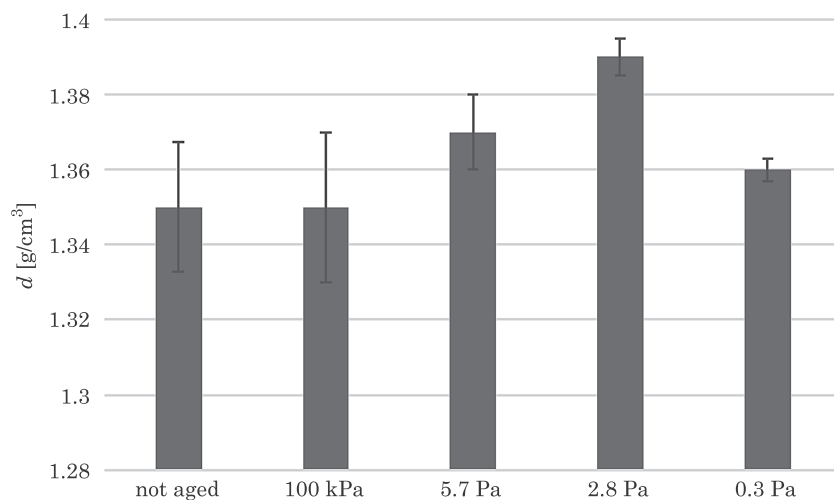


Fig. 5. Density of investigated samples

Density is usually correlated with rates of crystallinity. Higher crystallinity rate is associated with more polymer chains in a given space. Results of density change after aging are similar to mechanical properties results and show that greatest rates of crystallinity are to be expected in samples aged under 5.7 Pa and 2.8 Pa of air pressure (XU et al. 2016)

## Conclusions

The air content influences structural and mechanical properties of poly(ethylene terephthalate). Lower air pressure can lead to higher degrees of degradation than atmospheric pressure due to faster vaporization of degradation products. This effect can be used for faster degradation on PET products after reprocessing effects its utility properties to the point of non recyclability. Degradation in high temperatures (80°C) also provides additional increase of small molecule degradation products evaporation, causing accelerated degradation rate. Aging time in conjunction with increased temperature helps to assess PET degradation degree at around 1 year period. Minimal or small values of mechanical properties, density and mass loss at normal air pressure prove almost no degradation during annual periods. Changes of roughness can be attributed strictly to temperature process as it is characteristic only to surface regions and is probably caused by small heat conductivity of polymer.

## References

- ALJOUMAA K., ABOUDI M. 2016. *Physical ageing of polyethylene terephthalate under natural sunlight: correlation study between crystallinity and mechanical properties*. Applied Physics Letters A, 122(6): 1-10.
- BADÍA J.D., VILAPLANA F., KARLSSON S., RIBES-GREUS A. 2009. *Thermal analysis as a quality tool for assessing the influence of thermo-mechanical degradation on recycled polyethylene terephthalate*. Polymer Testing, 28(2): 169-175.
- DONG J., LIU J., LI X., LIANG Q., XU X. 2020. *Relationship between the Young's Modulus and the crystallinity of cross-linked poly( $\epsilon$ -caprolactone) as an immobilization membrane for cancer radiotherapy*. Global Challenges, 4: 2000008.
- EL-TOUFAILI F.A. 2006. *Catalytic and mechanistic studies of polyethylene terephthalate synthesis*. Ph.D. Dissertation, University of Berlin.
- ITIM B., PHILIP M. 2015. *Effect of multiple extrusions and influence of PP contamination on the thermal characteristics of bottle grade recycled PET*. Polymer Degradation and Stability, 117: 84-89.
- KHEMANI K.C. 2000. *A novel approach for studying the thermal degradation, and for estimating the rate of acetaldehyde generation by the chain scission mechanism in ethylene glycol based polyesters and copolyesters*. Polymer Degradation and Stability, 67: 91-99.
- KONG Y., HAY J.N. 2003 *Multiple melting behaviour of poly(ethylene terephthalate)*. Polymer, 44: 623-633.

- LIU CH., HU L., LU Y., ZHAO W. 2015. *Evolution of the crystalline structure and cyclization with changing tension during the stabilization of polyacrylonitrile fibers*. Journal of Applied Polymer Science, 132: 42182.
- LÓPEZ-FONSECA R., DUQUE-INGUNZA I., DE RIVAS B., FLORES-GIRALDO L., GUTIÉRREZ-ORTIZ J.I. 2011. *Kinetics of catalytic glycolysis of PET wastes with sodium carbonate*. Chemical Engineering Journal, 168: 312-320.
- NAIT-ALI L.K., COLIN X., BERGERET A. 2011. *Kinetic analysis and modelling of PET macromolecular changes during its mechanical recycling by extrusion*. Polymer Degradation and Stability, 96: 236-246.
- PANOWICZ R., KONARZEWSKI M., DUREJKO T., SZALA M., ŁAZIŃSKA M., CZERWIŃSKA M., PRASUŁA P. 2021. *Properties of polyethylene terephthalate (PET) after thermo-oxidative aging*, Materials, 14: 833.
- PIVSA-ART W., FUJII K., NOMURA K., ASO Y., OHARA H., YAMANE H. 2016. *The effect of poly(ethylene glycol) as plasticizer in blends of poly(lactic acid) and poly(butylene succinate)*. Journal of Applied Polymer Science, 133: 43044.
- SANG T., WALLIS C.J., HILL G., BRITOVSEK G.J.P. 2020. *Polyethylene terephthalate degradation under natural and accelerated weathering conditions*. European Polymer Journal, 136: 109873.
- SATO K., SPRENGEL W. 2012. *Element-specific study of local segmental dynamics of polyethylene terephthalate upon physical aging*. Journal of Chemical Physics, 137: 104906.
- SOBKÓW D., CZAJA K. 2009. *Badanie odporności materiałów na starzenie atmosferyczne*. Czasopismo Techniczne. Mechanika, 106: 429-430.
- VENKATACHALAM S., NAYAK S.G., LABDE J.V., GHARAL P.R., RAO K., KELKAR A.K. 2012. *Degradation and recyclability of poly (ethylene terephthalate)*. In: Polyester. Ed. H. Salach. InTech Open, London.
- XU M., HUANG G., FENG S., MCSHANE G.J., STRONGE W.J. 2016. *Static and dynamic properties of semi-crystalline polyethylene*. Polymers, 8: 77.
- YANG J., XIA Z., KONG F., MA X. 2010. *The effect of metal catalyst on the discoloration of poly(ethylene terephthalate) in thermo-oxidative degradation*. Polymer Degradation and Stability, 95: 53-58.
- ZABOROWSKA M., BERNAT K., PSZCZÓŁKOWSKI B., WOJNOWSKA-BARYŁA I., KULIKOWSKA D. 2021. *Challenges in sustainable degradability of bio-based and oxo-degradable packaging materials during anaerobic thermophilic treatment*. Energies, 14: 4775.





## SNIPER RIFLE CARTRIDGE

*Zenon Syroka*

ORCID: 0000-0003-3318-8495

Faculty of Technical Sciences

University of Warmia and Mazury in Olsztyn

Received 12 July 2021, accepted 15 November 2021, available online 20 November 2021.

**Key words:** cartridge, sniper rifle, firearm.

### Abstract

The paper proposes a modification of the 7.62 mm NATO rifle cartridge. The design and the results of a computer simulation were presented. The projectile's flight behavior under different weather conditions was simulated. A figure diagram and a digital model of the projectile were presented. Ballistic calculations were performed, and an animation showing the projectile's behavior under various weather conditions was developed. The results were patented.

## Introduction

This study describes a sniper rifle **cartridge**. The design was patented (SYROKA, SKŁODOWSKA 2020). A cartridge has two definitions in military terminology. In the basic definition, a cartridge is a unit of ammunition for a single shot – a gun cartridge (handgun, shotgun or rifle) or an artillery cartridge. A cartridge consists of:

- a projectile,
- propellant (such as gunpowder),
- and in fixed ammunition, also:
  - primer,
  - casing, such as a brass shell, that houses all projectile components.

---

Correspondence: Zenon Syroka, Katedra Elektrotechniki, Energetyki, Elektroniki i Automatyki, Wydział Nauk Technicznych, Uniwersytet Warmińsko-Mazurski, ul. Oczapowskiego 11, 10-719 Olsztyn, e-mail: [zenon.syroka@uwm.edu.pl](mailto:zenon.syroka@uwm.edu.pl), [syrokaz@onet.eu](mailto:syrokaz@onet.eu).

In the second definition, a cartridge is a propellant charge (such as a gunpowder cartridge) that is located behind the projectile in the firing chamber and leads to the explosion of gas in the barrel.

**The designed cartridge has several advantages.** It contains a lead core and penetrates hard targets at longer ranges. The projectile has an elongated shape, which increases its mass, reduces air resistance, and increases travel velocity, thus enabling the projectile to reach the intended target faster. The use of nitrocellulose powder as propellant slows down and stabilizes the burn rate in all types of weather, and it increases and stabilizes internal pressure which is always consistent with the specification.

Ammunition can be defined as cartridges that are intended for use in firearms. The main aim of sniper rifle ammunition is to neutralize a live enemy target.

## **Existing ammunition designs for sniper rifles**

### **7.62×51 mm NATO cartridge**

The cartridge was developed by the Institute of Armament Technology at the Faculty of Mechatronics and Aviation of the Military University of Technology in Warsaw and MESKO S.A. Metal Factory (presently MESKO S.A.) in Skarżysko-Kamienna. The cartridge contains a standard projectile with a lead core. Projectile tips are color-coded to indicate their type and designation. For example, projectiles with red tips are intended for live targets, whereas projectiles with black tips are light armor penetrators with a range of up to 500 m. Differently colored projectiles do not differ in size, but they contain different propellants or powders.

### **.300 Winchester Magnum**

.300 Winchester Magnum measures 7.62×67 mm, and it was developed by the US Army. It was initially used by hunters, and it is currently deployed in police sniper rifles. Similarly to the 7.62×51 mm NATO cartridge, .300 Win Mag has differently colored tips to identify various projectile types.

### **.338 Lapua Magnum**

.338 Lapua Magnum measures 8.6×70 mm or 8.58×70 mm. It has been designed for sniper rifles, but it is also used in hunting rifles. The cartridge was produced by the Finnish ammunition manufacturer Lapua, and it combines

the features of 7.62 mm and 12.7 mm NATO cartridges. .338 Lap Mag has a maximum effective range of 1,000 m, and it is not much heavier than NATO cartridges.

### Structural design of a patented cartridge for sniper rifles

The cartridge is presented in Figure 1, and the projectile is shown in Figure 2. The sniper rifle cartridge was designed as a long-range cartridge for penetrating hard targets. The cartridge (1) contains a lead projectile (2) in a brass jacket. The cartridge has a sharp tip (3), and the tungsten carbide core (4) weighs 1.62 g. Core height is equal to  $2/3$  of projectile length, and core width is equal to  $1/3$  of projectile width. The shell (5) was crimped to a length of 69.00 mm, and it contains N140 nitrocellulose powder (68.8%) (6). The shell is connected to a Large Rifle Magnum primer.

Projectile seating depth is 7.60 mm. The core material is protected against excess gas and friction by a solid brass jacket with a bridge. The cartridge has a boat tail base. Shell length is 69.00 mm. Shell volume is typical for projectiles of the type. The shell is filled with N140 nitrocellulose powder (6) with a weight of 4.760 g. A Large Rifle Magnum primer (5) is integrated into the base of the cartridge. This primer is characterized by higher explosive energy which facilitates the ignition of spherical powder propellant. Cartridge length is 81.42 mm.

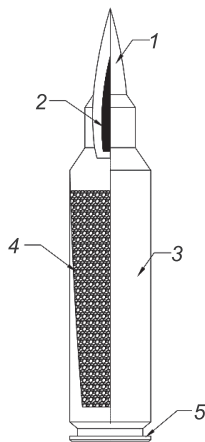


Fig. 1. Cartridge for a sniper rifle;  
description in the text

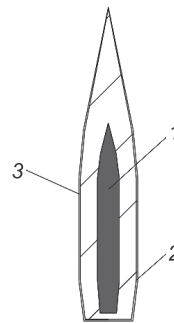


Fig. 2. Projectile in the sniper rifle cartridge;  
description in the text

## Projectile design and model

The trajectory of the designed projectile was calculated with Gordons Reloading Tool software. The program supports the selection of materials, primers and powders. All values are calculated automatically, the results are presented graphically in diagrams, and the optimal values are suggested. Trajectory calculations are presented in a diagram in Figure 3.

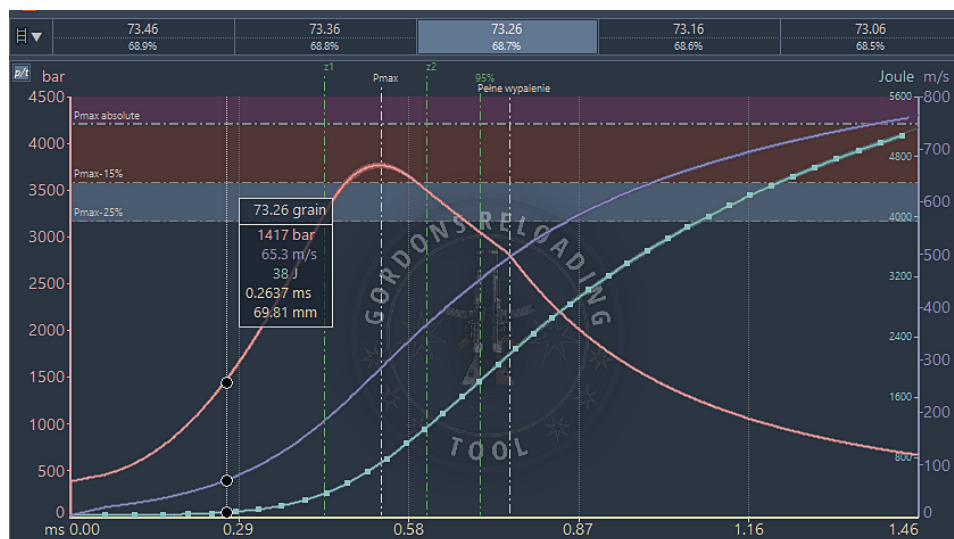


Fig. 3. Calculations of a projectile's trajectory parameters

## Cartridge model

The cartridge was modeled in Blender 2.8 software. The modeling process was divided into several stages. The projectile and its tip were modeled in the first stage. The carbide core was modeled in the second stage, and the shell and primer were modeled in the third stage.

### Model of the projectile and the projectile tip

In the first step, the projectile was modeled with the Circle tool. Cell layers were extruded and transformed to generate a grid object. The projectile tip was modeled separately because projectiles designed for various purposes have

differently colored tops. The Subdivision Surface modifier was added to smooth the edges of the modeled object. A model of a projectile without a tip is presented in Figure 4, and a model of the projectile tip is shown in Figure 5. The entire projectile is presented in Figure 6.

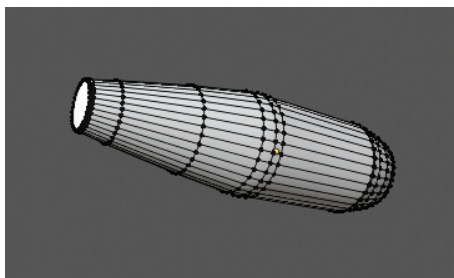


Fig. 4. Model of a projectile without a tip

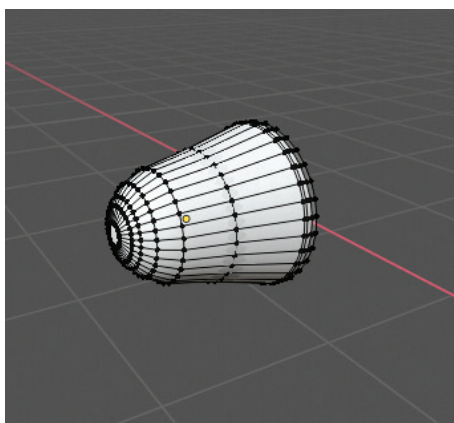


Fig. 5. Model of the projectile tip

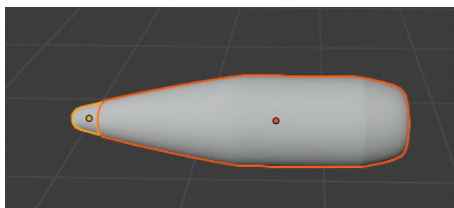


Fig. 6. Model of the entire projectile

## Core model

In the first step, the projectile core was modeled with the Circle tool. The resulting object was rescaled, and a modifier was added to smooth the edges. In the last step, the core was connected to the projectile based on the location and characteristics described in the patent. The core model is presented in Figure 7, and the model of the projectile with the core is shown in Figure 8.

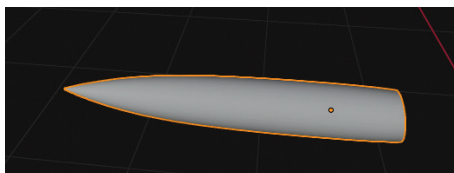


Fig. 7. Core model

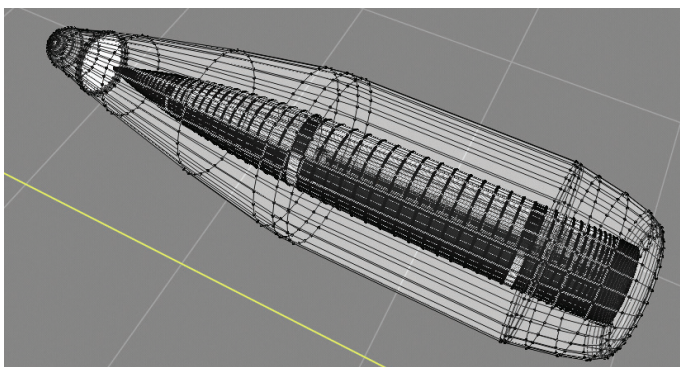


Fig. 8. Model of the projectile with the core

## Shell model

The projectile, the projectile tip and the core were modeled with the Circle tool, whereas the shell was modeled with the Cylinder tool. The object was opened, and several commands were used to model the shell. Wall thickness was modeled with the Solidify modifier. The same method was applied to model the primer and the shell. The front view of the shell model is presented in Figure 9, and the rear view is presented in Figure 10.

The materials for all cartridge components were selected. Nodes were not used. The selection of color was most problematic. Surface color and texture were modeled by the selecting the appropriate values of Specular and Roughness.

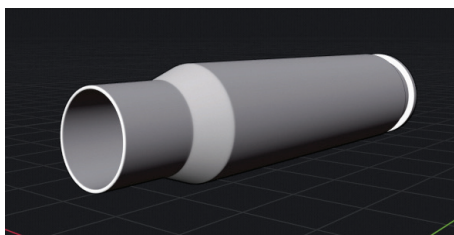


Fig. 9. Front view of the shell model

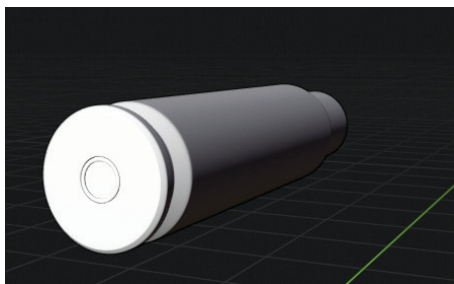


Fig. 10. Rear view of the shell model

## Basic calculations

### Ballistic resistance of armor against the designed projectile

Ballistic resistance is the protection offered by armor against projectiles that do not contain explosive materials. The ballistic resistance of armor is influenced by the projectile's kinetic energy which is calculated with the use of the following equation (SPERSKI 2009):

$$\frac{(m \cdot v_p^2)}{2} = k \cdot \pi \cdot d \cdot h \cdot h \quad (1)$$

where:

- $m$  – projectile's mass [kg],
- $v_p$  – projectile's velocity upon impact with target [m/s],
- $d$  – caliber [m],
- $h$  – shield thickness [m],
- $k$  – average shear stress on the lateral surface of a cylindrical shaft with base diameter  $d$  and height  $h$  (FLIS, SPERSKI 2012).

Shield thickness is calculated with the use of the following equation:

$$h = v_p \sqrt{\left(\frac{m}{K \cdot d}\right)} \quad (2)$$

where:

$$K = 2 \cdot k \cdot \pi \quad (3)$$

Coefficient  $K$  is determined experimentally for various types of steel and projectiles. Parameter  $K$  has to be computed, but a method where shield thickness is calculated based on the available data delivers better results. In this approach, the mass  $m_1$  of a cuboid that comes into contact with the shield is calculated. The volume of shield material that is displaced by the projectile upon impact is equal to the volume of a cylinder with diameter  $d$  and height  $h$  (SPERSKI 2009):

$$m_1 = \rho \cdot \left(\frac{\pi \cdot d^2}{4}\right) \cdot h \quad (3)$$

where:

$\rho$  – density of a shield made of steel with a density of 7,860 kg/m<sup>3</sup> (FLIS, SPERSKI 2011).

Projectile and shield parameters are presented in Figure 11 (SPERSKI 2009).

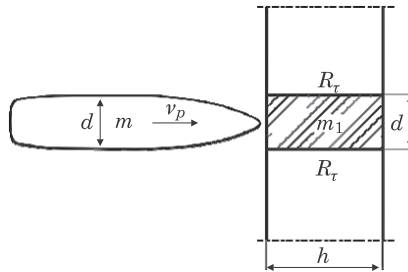


Fig. 11. Projectile upon impact with the shield

The initial velocity of the center of mass of a system composed of a projectile with mass  $m$  and a shield with mass  $m_1$  is calculated with the use of the following equation:

$$v_0 = \frac{m}{m + m_1} \cdot v_p \quad (4)$$

where:

$v_p$  – the projectile's velocity upon impact.

The distance that has to be traveled by the projectile to achieve a terminal velocity of 0 is referred to as the braking distance, and it is equivalent to the



thickness of the penetrated shield. A projectile's braking distance is calculated with the use of the below formula (SPERSKI 2009):

$$s = \frac{(m + m_1)}{2 \cdot \pi \cdot d \cdot h \cdot R_\tau} \quad (5)$$

where:

$R_\tau$  – the shear strength of the shield material, which is calculated with Huber's equation:

$$R_\tau = 0.577 \cdot R_m \quad (6)$$

where:

$R_m$  – the material's tensile strength which, in this case, equals 1,100 MPa.

The projectile's terminal velocity after shield penetration is calculated with the following equation (SPERSKI 2009):

$$v_k = \sqrt{v_0^2 - \frac{2 \cdot \pi \cdot d \cdot h^2}{m + m_1} \cdot R_\tau} \quad (7)$$

The following formula is applied to calculate shield penetration time (SPERSKI 2009):

$$t_k = \frac{m + m_1}{\pi \cdot d \cdot h \cdot R_\tau} \cdot (v_0 - v_k) \quad (8)$$

The above calculations were performed in Matlab.

The results of the calculations performed in Matlab for a projectile that travels in vacuum and does not penetrate the shield are presented in Table 1.

Table 1

Calculations for a projectile that does not penetrate the shield

Projectile's mass [kg]	0.019
Muzzle velocity [m/s]	736.2
Caliber [m]	0.00726
Shield thickness [m]	2.8
Shield density [kg/m <sup>3</sup> ]	7,860
Tensile strength [MPa]	1,100
Shear strength	634.7
Nose shape factor [°]	0.33
Acceleration of gravity	9.81
Height of the shooter [m]	1.72

cont. Table 1

Range [m]	2,532.5
Time of flight [s]	3.44
Velocity upon impact [m/s]	769.94
Volume of shield material displaced upon impact [m <sup>3</sup> ]	0.94
Initial velocity of the system's center of mass [m/s]	15.19
Distance traveled by projectile after impact [m]	2.64
Projectile's velocity after impact [m/s]	0
Shield penetration time [s]	0

The results of the calculations performed in Matlab for a projectile that travels in vacuum and penetrates the shield are presented in Table 2.

Table 2

Calculations for a projectile that penetrates the shield

Projectile's mass [kg]	0.019
Muzzle velocity [m/s]	736.2
Caliber [m]	0.00726
Shield thickness [m]	2.8
Shield density [kg/m <sup>3</sup> ]	7,860
Tensile strength [MPa]	1,100
Shear strength	634.7
Nose shape factor [°]	0.33
Acceleration of gravity	9.81
Height of the shooter [m]	1.72
Range [m]	2,532.5
Time of flight [s]	3.44
Velocity upon impact [m/s]	769.94
Volume of shield material displaced upon impact [m <sup>3</sup> ]	0.94
Initial velocity of the system's center of mass [m/s]	15.72
Distance traveled by projectile after impact [m]	2.83
Projectile's velocity after impact [m/s]	14.89
Shield penetration time [s]	0.0192

### Conclusions:

The results indicate that the projectile will not penetrate the shield if shield thickness exceeds the distance traveled by the projectile upon impact. The range and time of flight can be determined when the projectile penetrates the shield.

## Ballistic coefficient

The ballistic coefficient (BC) of a projectile is its ability to overcome air resistance, such as wind, during flight. This parameter is largely influenced by a projectile's geometric dimensions that affect aerodynamic drag. Aerodynamic drag, such as wind force, slows down a moving projectile. The ballistic coefficient is calculated with the use of the following equation:

$$BC = \frac{SD}{i} \quad (9)$$

where:

SD – sectional density determined with the GR calculator,

$i$  – form factor which, in this case, is given by the following formula:

$$i = \frac{2}{n} \cdot \sqrt{\frac{4 \cdot n - 1}{n}} \quad (10)$$

where:

$n$  – caliber of an ogive-tipped projectile.

The closer the value of BC is to one, the lower the aerodynamic drag and the more stable the projectile's flight. The designed projectile has a BC of 0.7798.

## Gyroscopic stability

A fired projectile is subjected to gyroscopic drift which is an interaction between the projectile's mass and aerodynamic forces. One of such forces is wind which exerts an adverse impact on a projectile's trajectory. A projectile has to be stabilized to ensure that it precisely hits the target. This is accomplished through gyroscopic stabilization. Projectiles for high-precision rifles are affected by gyroscopic precession when:

- a projectile rotates around its axis of symmetry with a certain speed – the higher the projectile's spin rate, the greater the gyroscopic motion,
- the direction of a projectile's rotation around its axis of symmetry does not change,
- the forces acting on a projectile can rotate the projectile by as much as 90°,
- a projectile is characterized by complex motion in three-dimensional space, which resembles that of a spinning top.

Gyroscopic stability is determined by the twist rate of the barrel. The twist rate should equal 1, and it should be higher than 1.2 for sporting projectiles and higher than 1.5 for military projectiles to guarantee stability (EJSMONT 2019).

This solution is not free of defects, and it can lead to the horizontal deflection of a projectile. The projectile can be stabilized or the twist rate can be decreased to minimize horizontal deflection. The gyroscopic spin of a projectile can be calculated with a formula developed by Bryan Litz (EJSMONT 2019):

$$Z = 1.25 \cdot (s_g + 1.2) \cdot t^{1.83} \quad (11)$$

where:

$S_g$  – gyroscopic stability factor calculated based on the Miller's twist rule,  
 $t$  – time of flight.

## Influence of wind on a projectile's trajectory

The presented examples apply to ideal conditions that are very difficult to achieve. Wind often influences a projectile's territory. A projectile can be deflected by crosswind that blows from right to left or from left to right, as well as by headwind that blows in the opposite direction of a projectile's flight path. These influences are very difficult to eliminate. Wind phenomena have been extensively studied, but their effect on a projectile's path is difficult to model. To compensate for this path deviation, the sighting components have to be adjusted based on the direction and speed of wind. The elevation angle at which the projectile leaves the muzzle has to be calculated. The Minute of Angle (MOA) adjustments to compensate for bullet drop at different wind speeds is given in Table 3. Wind angle was set at 90° and range at 500 m.

Table 3

Projectile's speed under different weather conditions

Wind speed [m/s]	Time of flight [s]	Velocity upon impact [m/s]	MOA
2	0.763	574	1.3
3	0.763	574	1.9
5	0.763	574	3.2

The time of flight and velocity upon impact with a target situated at a distance of 500 m are identical at different wind speeds, but the MOA ranges from 1.3 to 3.2. The MOA is critical for sighting the scope of a sniper rifle. The calculations were performed with the use of an online calculator, and they account for weather conditions such as temperature and barometric pressure. The parameters of a projectile influenced by a wind angle of 90° are presented in Table 4.

Table 4

Calculations for a projectile influenced by wind

Projectile's mass [kg]	0.019
Muzzle velocity [m/s]	736.2
Caliber [m]	0.00726
Shield thickness [m]	2.8
Shield density [kg/m <sup>3</sup> ]	7,860
Tensile strength [MPa]	1,100
Shear strength	634.7
Nose shape factor [°]	0.33
Acceleration of gravity	9.81
Height of the shooter [m]	1.72
Range [m]	2,532.5
Time of flight [s]	3.44
Velocity upon impact [m/s]	574
Volume of shield material displaced upon impact [m <sup>3</sup> ]	0.94
Initial velocity of the system's center of mass [m/s]	14.21
Distance traveled by projectile after impact [m]	2.32
Projectile's velocity after impact [m/s]	13.45
Shield penetration time [s]	0.0175

### Conclusions:

The projectile's parameters are influenced by the direction of wind. When the direction of wind changes, the projectile's velocity upon impact also changes, and shield thickness that can be effectively penetrated by the projectile decreases. Therefore, the MOA has to be optimized to guarantee that the projectile precisely hits the target.

## Animation of cartridge motion

When a round is fired, the cartridge is separated into two parts: the projectile and the shell. The spent shell is ejected from the chamber, and the projectile is fired from the muzzle (Fig. 12). The projectile travels towards the target and is flattened upon impact (Fig. 13). The projectile's trajectory was modeled in vacuum and under the influence of light wind with a speed of 2 m/s. The flattening of the projectile upon impact with the target was modeled in the animation. The tungsten carbide core is visible upon impact.



Fig. 12. Projectile leaving the muzzle

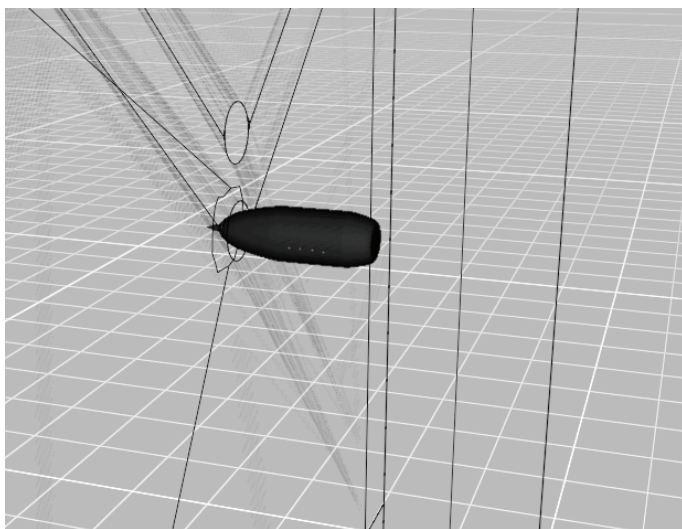


Fig. 13. Projectile upon impact with the target

## Summary

The structure of a cartridge for a sniper rifle was described. The design process and basic calculations were presented. The projectile's behavior under different weather conditions was simulated. The designed cartridge was patented (SYROKA, SKŁODOWSKA 2020).

## References

- Amunicja wojsk lądowych: podręcznik*. 1985. MON, Warszawa.
- BIAŁCZAK B. 1988. *Amunicja strzelecka*. Wydawnictwo Politechniki Świętokrzyskiej, Kielce.
- BRODACKI J. 1983. *Amunicja małokalibrowa*. Wydawnictwo Politechniki Warszawskiej, Warszawa.
- DINDL F. 2020. *Lightweight cartridge case and weapon system*. 2020-09-22, US10782107 (B1).
- DOBIECH I. 1982. *Balistyka doświadczalna*. Cz. I. *Metody i układy pomiarowe ciśnienia*. Wojskowa Akademia Techniczna, Warszawa.
- DOBIECH I., MAJEWSKI S., SIENKO S., TORECKI S. 1973. *Budowa i eksploatacja broni lufowej i amunicji*. Cz. 3. *Eksploatacja techniczna broni i amunicji*. Wojskowa Akademia Techniczna, Warszawa.
- EJSMONT J.A. 2007. *Celność broni strzeleckiej. Praktyczny poradnik*. Wydawnictwo Naukowo-Techniczne, Warszawa.
- EJSMONT J.A. 2018. *Amunicja i jej elaboracja*. Wydawnictwo Naukowo-Techniczne, Warszawa.
- EJSMONT J.A. 2019. *Balistyka dla snajperów*. Wydawnictwo Naukowo-Techniczne, Warszawa.
- FLIS L., SPERSKI M. 2011a. *Badanie odporności balistycznej pancerza ze stali 10GHMBA na ostrzał pociskiem 12,7 mm*. *Zeszyty Naukowe Akademii Marynarki Wojennej*, LII, 3(186): 27-42.
- FLIS L., SPERSKI M. 2011b. *Eksperymentalna weryfikacja wybranych modeli obliczeniowych balistyki końcowej*. *Zeszyty Naukowe Akademii Marynarki Wojennej*, 4(187): 35-44.
- FLIS L., SPERSKI M. 2012. *Ocena wpływu kształtu wierzchołka pocisku na proces przebijania pancerzy stalowych*. *Zeszyty Naukowe Akademii Marynarki Wojennej*, LIII, 2(189): 29-44.
- FURMANEK W., GACEK J., WOŹNIAK R. 2007. *Modelowanie i badanie charakterystyk balistycznych pocisków o ograniczonej podatności na rykoszetowanie*. *Modelowanie Inżynierskie*, 34: 23-28.
- FURMANEK W., WOŹNIAK R. 2009. *Zaprojektowanie, wykonanie oraz przeprowadzenie wstępnych badań modeli naboju karabinowych 7,62×51 mm z pociskiem zwykłym o zwiększonej przebijalności*. Wojskowa Akademia Techniczna, Warszawa.
- GACEK J. 1999. *Balistyka zewnętrzna*, Wojskowa Akademia Techniczna, Warszawa.
- GACEK J. 2007. *Opracowanie i wdrożenie do produkcji amunicji strzeleckiej o ograniczonym rykoszetowaniu kalibru 9×19 mm, 9×18 mm, 7,62×51 mm i 7,63×54 mm*. Sprawozdanie merytoryczne z realizacji projektu badawczego celowego nr 34/BO/B PC 013/WAT/2002. Wojskowa Akademia Techniczna, Warszawa.
- GACEK J. 2008. *Teoretyczno-doświadczalne badania konstrukcyjne, balistyczne, technologiczne i eksploatacyjne broni oraz amunicji strzeleckiej pod kątem realizacji przyszłościowego programu pn. "Zaawansowane wyposażenie żołnierza sił zbrojnych RP"*. Sprawozdanie z realizacji II etapu projektu badawczego PBS 777. Wojskowa Akademia Techniczna, Warszawa.
- HE W., GU P., LIANG Q., YANG G., LIN X., HUANG J. 2021 *Multi-stage buffer structure and large-caliber sniper rifle*. CN112833703 (A).
- HOGG I.V. 2001. *Amunicja strzelecka, artyleryjska i granaty*. Bellona, Warszawa.
- JĄŁOSZYŃSKI K. 1999. *Technika posługiwania się bronią*. Oficerska Szkoła Policji, Legionowo.
- KOCHAŃSKI S. 1986. *Wybrane zagadnienia z podstaw projektowania broni strzeleckiej*. Wydawnictwo Politechniki Warszawskiej, Warszawa.
- KOCHAŃSKI S. 1991. *Automatyczna broń strzelecka*. SIGMA-NOT, Warszawa.
- KYZIOŁ L. 2007. *Przestrzeliwanie materiałów w niemetalicznych stosowanych na konstrukcje okrętowe*. *Zeszyty Naukowe Akademii Marynarki Wojennej*, XLVIII, 2(169): 113-126.
- KYZIOŁ L., ŚWIĄTEK K. 2009. *Modelowanie i weryfikacja doświadczalna przebijalności tarczy pociskami*. *Zeszyty Naukowe Akademii Marynarki Wojennej*, 2(177): 71-90.
- LECIEJEWSKI Z., SOBČAK W., SURMA Z. 1997. *Balistyka wewnętrzna. Ćwiczenia laboratoryjne*. Wojskowa Akademia Techniczna, Warszawa.
- LI H. 2020. *Toy building block sniper rifle*. CN210773670 (U).
- ŁUKASZEWSKI T. 2019. *Amunicja karabinowa*. Wydawnictwo Napoleon V, Oświęcim.
- Podręcznik strzelca wyborowego*. 1972. Szkol. 444/71. Ministerstwo Obrony Narodowej, Warszawa.

- RADZISZEWSKI L. 2007. *Balistyka końcowa pocisków amunicji małokalibrowej przy strzelaniu do wybranych celów*. Wydawnictwo Politechniki Świętokrzyskiej, Kielce.
- SANNER M., CALDWELL E., PADGETT CH., WALL CH., HARDING G., PADGETT L. 2021. *Lightweight ammunition articles comprising a polymer cartridge case*. US2021231420.
- SOSZYŃSKI R. 2010. *Amunicja strzelecka i działowa*. Centrum Szkolenia Wojsk Lądowych, Poznań.
- SPERSKI M. 2009. *Model obliczeniowy do oszacowania odporności balistycznej pancerzy stalowych*, Zeszyty Naukowe Akademii Marynarki Wojennej, 4(179): 51-59.
- SYROKA Z., SKŁODOWSKA K. 2020 *Nabój do karabinów snajperskich*. Patent P.434026, data zgłoszenia 21.05.2020.
- SZADKOWSKI J. 2004. *Balistyka zewnętrzna, model balistyczny*. Wydawnictwo Politechniki Świętokrzyskiej, Kielce.
- SZULADZINSKI G. 2010. *Formulas for Mechanical and Structural Shock and Impact*. Taylor & Francis Group, New York.
- SZYRKOWIEC A. 2001. *Wszystko o broni myśliwskiej*. Bellona, Warszawa.
- TAN Y., DONG J., LIU J., TANG B., ZHOU W. 2021. *Micro-sound sniper rifle structure and working method thereof*. CN112665451 (A).
- TORECKI S. 1978. *Balistyka – wybrane zagadnienia balistyki wewnętrznej*. Wojskowa Akademia Techniczna, Warszawa.
- TORECKI S. 1980. *Balistyka wewnętrzna*. Wojskowa Akademia Techniczna, Warszawa.
- TORECKI S. 1982. *1000 słów o broni i balistyce*. Wydawnictwo MON, Warszawa.
- TORECKI S. 1985. *Broń i amunicja strzelecka*. MON, Warszawa.
- TRĘBIŃSKI R. 2003. *Amunicja strzelecka o zwiększonej zdolności do penetracji osłon obiektów opancerzonych*. Sprawozdanie z realizacji pracy badawczej nr 513/PBW. Wojskowa Akademia Techniczna, Warszawa.
- WAŻNY M., IDZIASZEK Z. 2005. *Model symulacyjny ruchu pocisku po jego wylocie z przewodu lufy*. Eksploatacja i Niezawodność, 3(30): 30-40.
- WIŚNIEWSKI A., ŻUROWSKI W. 2002. *Amunicja i pancerze*. Wydawnictwo Politechniki Radomskiej, Radom.
- WIŚNIEWSKI S., GACEK J. 1987. *Balistyka zewnętrzna. Cz. II. Uzbrojenie klasyczne*. Wojskowa Akademia Techniczna, Warszawa.
- WŁODARCZYK E. 2006. *Balistyka końcowa pocisków amunicji strzeleckiej*. Wojskowa Akademia Techniczna, Warszawa.
- WŁODARCZYK E., JACKOWSKI A. 2008. *Balistyka końcowa pocisków szybkich*. Wojskowa Akademia Techniczna, Warszawa.
- WOLSKY S.P., CZANDERNA A.W. 1980. *Ballistic materials and penetration mechanics*. Elsevier Scientific Publishing Company, New York.
- WOŹNIAK R., CIEPLIŃSKI A. 1994. *7,62 mm karabin wyborowy SWD*. Wydawnictwo Bellona, Warszawa.
- ZUKAS J.A. 1990. *High velocity impact dynamics*. John Wiley & Sons, New York.





## MODELLING AND SIMULATION OF FUNCTIONING OF THE GSH-23 AVIATION AUTOCANNON MECHANISMS

*Michał Jasztal<sup>1</sup>, Mateusz Kunikowski<sup>2</sup>*

<sup>1</sup>ORCID: 0000-0003-4133-2557

<sup>2</sup>ORCID: 0000-0003-4022-5047

Faculty of Mechatronics, Armament and Aviation  
Military University of Technology

Received 14 September, accepted 15 November 2021, available online 20 November 2021.

**Key words:** aviation autocannon, simulation model, multibody systems method.

### Abstract

Article presents the simulation model and the study of the basic mechanisms of the GSh-23 aviation autocannon. The research made use of Solid Edge ST9 software and the multibody systems method implemented in it. Simulation of functioning cannon mechanisms was carried out for two variants of forcing a piston mechanism movement by the gunpowder gases. The results obtained are time courses of a bolt and a cartridge belt drive mechanism elements movement. Assumed variants of a piston mechanism movement and elaborated simulation model will be verified in the next (planned) stage of studies basing on the results of the measurements of the experimental kinematic parameters utilising high-speed camera (Phantom) and TEMA software.

### Introduction

In the process of designing and developing the rules of operation of aviation weaponry assumptions regarding the period of device reliable operation and range of services are made, which is reflected in device expected lifespan provided by the producer (or prescribed way of tracking its current technical

---

Correspondence: Michał Jasztal, Wydział Mechatroniki, Uzbrojenia i Lotnictwa, Wojskowa Akademia Techniczna, ul. gen. Sylwestra Kaliskiego 2, 00-908 Warszawa 46, e-mail: [michal.jasztal@wat.edu.pl](mailto:michal.jasztal@wat.edu.pl).

condition). However, in the result of a long-term exploitation of the aviation armament there is sometimes a necessity to use equipment after the lifespan given by the manufacturer. In that scenario the need to define a new lifespan value or to change the way of exploitation to exploitation by technical condition arises (JASZTAL et al. 2007). Introduction of any changes in that aspect requires conducting range of studies related to the cognition of physical phenomena determining loss of durability of individual components, as well as identification of diagnostic parameters which allow tracking of device current technical condition. Unfortunately, there is often no possibility to use manufacturers full technical and test documentation, while only chosen statistical information from exploiting the device is available. Therefore there is a need to conduct such studies, of which inevitable is carrying out expensive and time-consuming experimental investigation. However, the number of planned experiments can be minimised by usage of modern modelling, calculation and simulation environment CAD/CAE (JASZTAL 2006, 2017). It is possible to simulate functioning of a selected mechanism or a whole device for different conditions of its work in such environments, registering values of selected parameters. Modelling wide range of exploiting situations makes identification of diagnostic parameters, determining device reliability condition, same as development of weapon malfunctions or mechanical failures models possible.

Following work discusses modelling and simulation of functioning mechanisms of the 23-mm twin-barreled GSh-23 aviation autocannon (Fig. 1), intended for being fired from the aircraft at both aerial and ground targets (*23 mm DZIAŁKO LOTNICZE GSz-23Ł* 1990). A GSh-23 cannon was an integral cannon armament of MiG-21 and MiG-23 fighters. It has also found its application in a SPPU-22-01 suspended gun pod, carried by Su-15TM, Su-17TM, Su-22M, Yak-28PM and Yak-38 aircraft. It was also mounted in tail gunner turret of bombers: Tu-95, Tu-22, transport aircraft: Il-78, Il-76 and patrol aircraft: Tu-142. Mi-24D/M attack helicopters carried UPK-23-250 gun pods armed with GSh-23 cannon. Another version, Mi-24VP had fixed NPPU-23 movable mounting with GSh-23 cannon (GRUSZCZYŃSKI 1993).

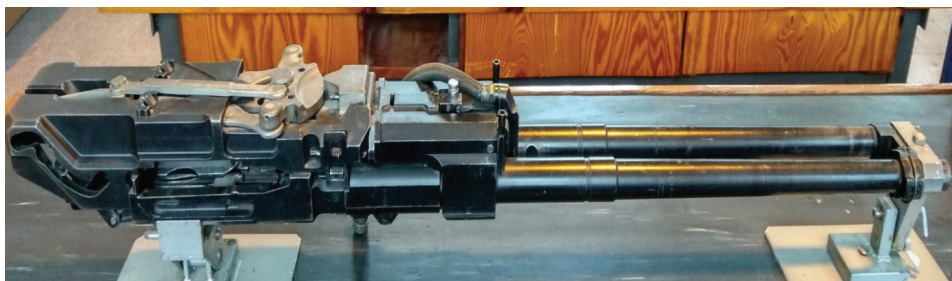
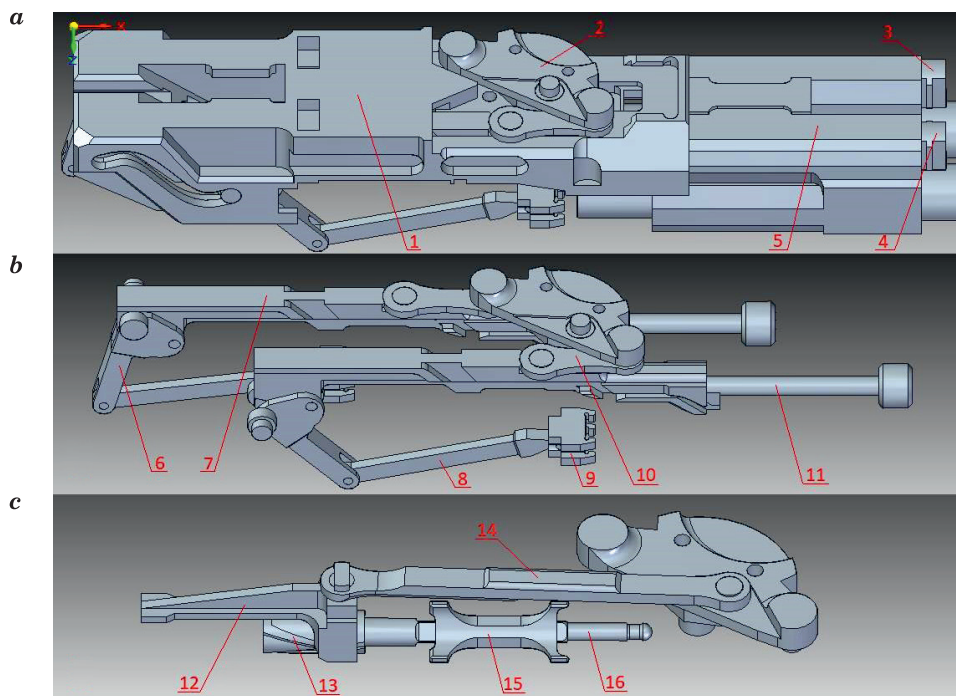


Fig. 1. GSh-23 autocannon  
Source: own elaboration.

The mechanism of the twin-barreled GSh-23 autocannon works on the principle of using gunpowder gases energy. The gases are discharged from barrels to the gas distributor. Reloading action of one of the cannon barrel is operated by the energy of expanding gases released by firing the other barrel. Driving link of the mechanism are sliders with gas shafts. Figure 2 presents a sliders scheme of operation. A cannon has two sliders (7, Fig. 2), kinematically joined with connectors (10, Fig. 2) and connecting lever (2, Fig. 2). During one full cycle of operation, every slider moves only in one direction (backward or forward). When the projectile passes the gas discharge holes in the barrel tube, the gunpowder gases are fed simultaneously into space in front of the piston of the retreating stem with slider and space behind the piston of the returning stem and slider. Due to the gunpowder gases, the stems begin to move: one backwards and the other forwards. When the movement of the stems with the slide occurs, the acceleration mechanisms, the so-called cam mechanisms, begin to work. One of them, by means of the bolt, feeds the cartridge into the



1 – base of the lift, 2 – connecting lever, 3 – left front plug, 4 – right front plug,  
5 – gas distributor, 6 – accelerator, 7 – slider, 8 – connecting rod, 9 – bolt, 10 – connector,  
11 – gas stem, 12 – feeder collector, 13 – feeder drum, 14 – feeder connecting rod,  
15 – feeder star, 16 – multi-spline shaft

Fig. 2. Diagram of the basic mechanism of the autocannon: *a* – body connecting the mechanisms, *b* – acceleration mechanism, *c* – feeding mechanism

Source: own elaboration.

chamber and ejects the previous cartridge case forward. The second, by means of the recoil, the bolt and the projections in the breech chamber, draws the cartridge case from the cartridge chamber and lowers it. This happens so that the case is ejected forward during the next cycle. The cartridge of the cannon is locked in the cartridge chamber by lateral displacement of the bolt (9, Fig. 2), which at the same time serves as a feeding element. The cannon has two bolts. Each of them is connected to its slider by a connecting rod (8, Fig. 2) and an accelerator (6, Fig. 2). The cam device is responsible for smooth acceleration and deceleration of the bolt (23 mm *DZIAŁKO LOTNICZE GSz-23Ł* 1990). To charge the cannon with cartridges one ammunition belt is used. The feeding mechanism is used here. The belt is moved by the feeder star (15, Fig. 2) which is connected kinematically through a connecting lever (2, Fig. 2) with the driving link of the mechanism (23 mm *DZIAŁKO LOTNICZE GSz-23Ł* 1990). During one cycle of the mechanism, the feeding unit moves the belt one stroke. Each cartridge is lowered by means of front and rear feeders to the feed line (i.e. to the bolt clamps). The feeders are kinematically connected to the sliders. Cartridges are inserted sequentially into each of the barrels by means of the bolts.

The accelerating and feeding mechanisms presented above are the basic mechanisms of the weapon and thus became the object of research within the framework of this work.

## Simulation model

The complex character of interactions of the elements of the weapon mechanism causes difficulties in description and analysis using the classical mathematical relationships. Hence, numerical simulations are commonly used in this type of applications (FLORIO 2011, HUAI-KU et al. 2007, 2009, SHIPLEY et al. 2006, PATHAK et al. 2006, URRIOLAGOITIA-SOSA et al. 2011, WEI WU et al. 2013). The use of computer methods for the analysis of kinematics and dynamics of weapon mechanisms is realised by two methods: the method of multibody systems (SCHABANA 2005, SCHIEHLEN 1997, TOMULIK et al. 2011) and the finite element method (ZIENKIEWICZ et al. 2005, LOGAN 2007). However, it should be noted that in the case of modelling various types of mechanisms, the method of multibody systems is more useful, as it assumes that all elements of the mechanism are rigid bodies connected to each other by means of various types of elements defining the degrees of freedom of a given connection (e.g. connections: linear, cylindrical, spherical, rotational etc.). Literature analysis of utilization of the multibody system indicates that it is successfully applied to solve the problem that is being researched in this work (SHIPLEY et al. 2006, HUAI-KU et al. 2007, 2009, Ni et al. 2011, PLATEK et al. 2015).

The first phase of building a simulation model of analysed mechanisms was to create CAD geometric model of those mechanisms parts and creation of an assembly model of the researched gun. For this purpose, Solid Edge ST9 software was used. Dimensions needed to create models of this gun were obtained from own measurements of that gun parts located in Aircraft Armaments Laboratory at the Military University of Technology, Warsaw, Poland. An assembly model prepared in this way was checked for geometric correctness using an automatic collision detection procedure and is shown in the Figure 3.

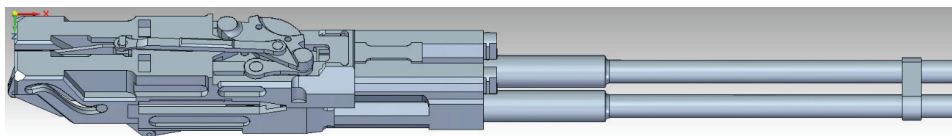


Fig. 3. CAD assembly model of the GSh-23 autocannon  
Source: own elaboration.

To prepare and simulate the movement of the researched mechanisms, DST (Design Simulation Technologies) module implemented in Solid Edge ST9 software was used. At this stage of preparation of the simulation a necessary relationships between particular CAD models of the cannon elements were introduced. The following relationships were used: revolute joint, planar joint, translational joint and cylindrical joint. Moreover, it was assumed that the value of the friction coefficient between individual elements of the mechanism is zero. After introduction of the necessary relationships for particular kinematic pairs, a model ready for analysing basic kinematic sequence was obtained.

In this work the functioning of the acceleration mechanism basic kinematic sequence was analysed: gas stem – slider – accelerator – connecting rod – bolt as well as ammunition belt pulling mechanism: gas stem – slider – connecting lever – feeder collector – feeder drum – feeder star. To predefine the forcing motion to simulate the movement of the mechanism, the tactical- technical information of the GSh-23 autocannon given by the producer were used. Rate of fire of 3000 rounds per minute was adopted, which translates to the time needed to fire one round being  $t = 0.02$  s. Dislocation of the gas stems due to the usage of part of the gunpowder gases energy is 110 mm, however during firing one shot the feeder drum rotates 90 degrees.

Considering the fact that on the realised stage of the research there was no available information regarding the time course of gunpowder gases pressure affecting the gas piston during the shot, in these tests it was assumed to conduct a simulation of the movement of the mechanisms for two adopted variants. In defining the first one preset displacement of the gas piston was used (eng. Displacement) and in the second one preset velocity of the gas piston was introduced (eng. Velocity).



First variant conventionally referred to as “Displacement” ( $D$ ) assumed that both slider and feeder drum move in uniformly accelerated motion in a timestamp from 0 to  $t = 0.01$  s and then uniformly decelerated motion from  $t = 0.01$  s to  $t = 0.02$  s. This variant assumption was made that the gunpowder gases pressure during the shot first increases in the gas cylinder and then decreases with the simultaneous action of the resistance forces of the cannon mechanism. Thus, the motion of the gas stem changes from uniformly accelerated to the half of its displacement, to uniformly decelerated to the end of its motion.

The second variant of calculations, conventionally referred to as “Velocity” ( $V$ ), assumed uniformly accelerated motion of the gas stem in the whole range of its displacement. This variant assumes that the gas stem is accelerated from the beginning to the end of the movement by the increasing pressure of the gunpowder gases. The assumed displacement and velocity of the gas stem as a function of time are shown in Figure 4.

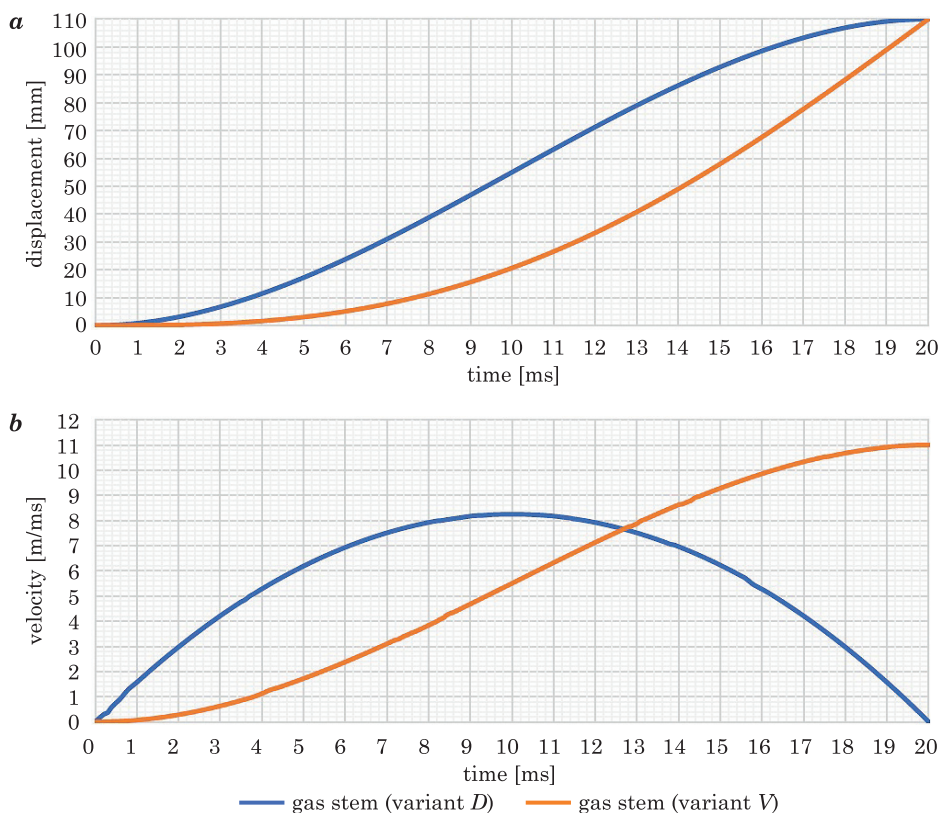


Fig. 4. The dependence of:  $a$  – displacement and  $b$  – velocity of the gas stem as a function of time for two forcing variants – Displacement ( $D$ ) and Velocity ( $V$ )

Source: own elaboration.

After defining the elements belonging to the basic kinematic sequence of the GSh-23 autocannon, assigning necessary relationships and introducing initial conditions, the simulation of the mechanism motion was carried out.

## **Research findings and their discussion**

The final element of the work was to make the calculations of the kinematic parameters of the examined mechanism selected elements and to generate graphs showing the kinematic dependencies between individual elements of the GSh-23 autocannon mechanism model during single shot. For this purpose, the Solid Edge ST9 software functions were used, enabling the desired kinematic parameters to be plotted against time. For comparing the kinematic parameters of selected elements of the mechanism, it was necessary to use the function of exporting numerical values of measured parameters to the Excel programme. This allowed creating any graphs facilitating comparison and drawing conclusions about mutual displacement of the elements of examined kinematic sequence.

The basic kinematic sequence of the cannon is responsible *inter alia* for transfer of the movement from the gas stem to the bolt using the acceleration mechanism. Therefore, it seems interesting to present the portrayal of the gas stem and bolt displacement on one graph (Fig. 5), which shows that the acceleration mechanism causes a much larger range of motion of the bolt than the gas piston. Namely, the bolt travels more than 1.8 times longer distance than the gas stem, which allows insertion of the relatively big cartridge into the bolt clamps and feeding it to the chamber despite a much smaller range of motion of the gas stem. Furthermore, determination of the bolt velocity during its movement shows that the acceleration mechanism causes an increase in the bolt movement velocity, which the maximum value is approximately 3.7 times bigger than the maximum velocity of the gas stem.

Another function of the basic kinematic sequence of the cannon is realisation of sending the cartridges to the bolt clamps. It is done *i.e.* through transmission of power from the gas stems, through sliders to the connecting lever, which drives feeder collector, feeder drum and feeder star which pulls the ammunition belt. Hence the values of the angular deflection of the connecting lever, feeder collector and feeder star were determined for the two assumed variants of gas stem displacement considered in this work (Fig. 6).

On their basis it was found that the angular deflection of aforementioned parts is directly proportional to the displacement of the gas piston.

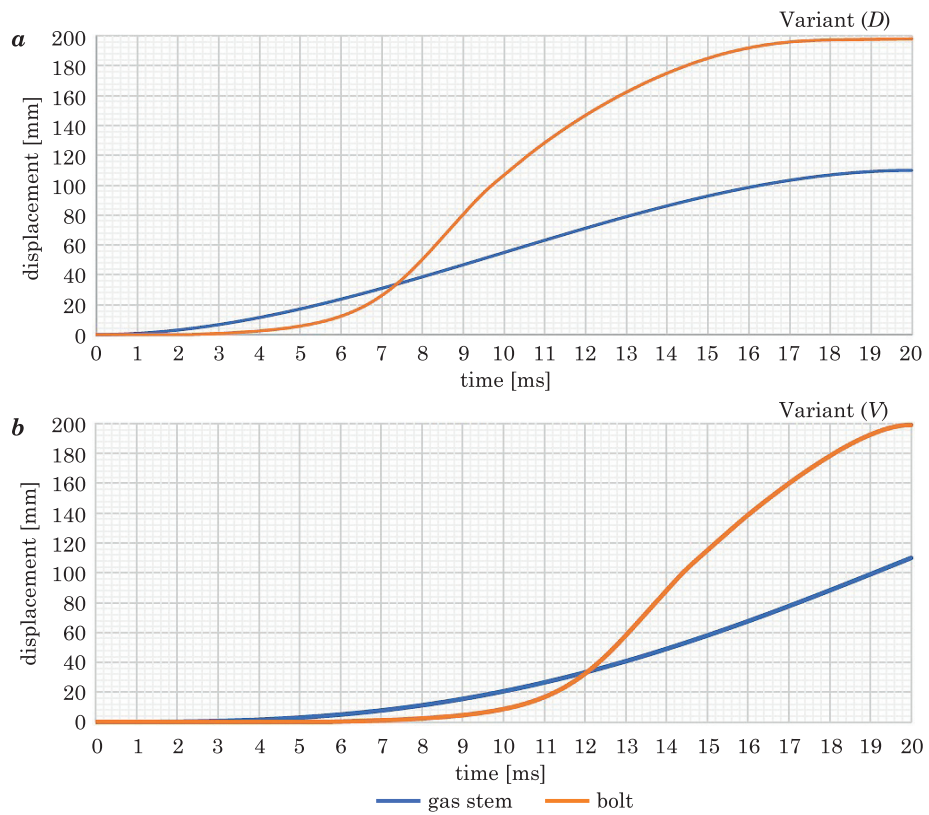


Fig. 5. The dependence of displacement of the gas stem and bolt as a function of time for two forcing variants: *a* – Displacement (*D*), *b* – Velocity (*V*)  
Source: own elaboration.

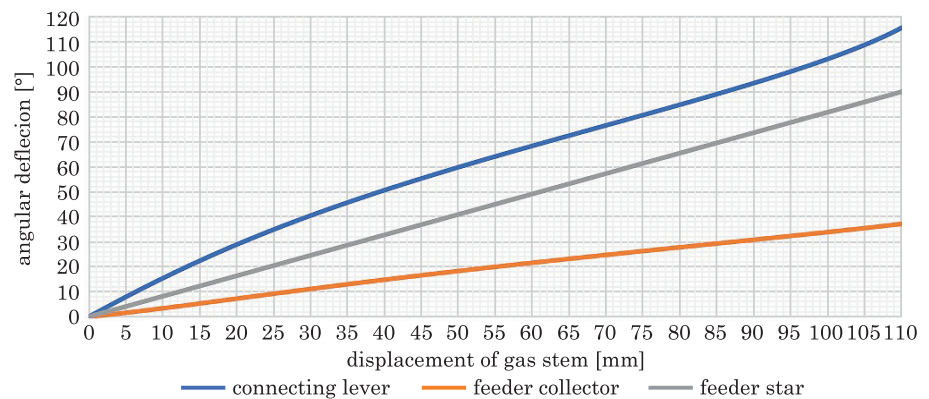


Fig. 6. Angular deflection of the connecting lever, feeder collector and feeder star as a function of the gas stem displacement  
Source: own elaboration.



## Conclusions

In this work graphs facilitating easier comparison of received parameters of the movement in two variants of forcing mechanism operation, called conventionally: Displacement ( $D$ ) and Velocity ( $V$ ) were presented. These variants can be treated as two limit means of displacement of the gas stem for various characteristics of the course of gunpowder gas pressure coming from the barrel tube. The differences in course of displacement and velocity for chosen variant of the simulation were plotted against the time for: gas stem, bolt, connecting lever, feeder collector and feeder star. The comparative graphs for two variants of forcing the movement were also developed as the graphs of displacement and velocity of the gas stem and the bolt plotted against the simulation time. On their basis, it can be seen that the “more beneficial” variant of the gunpowder-gases-based gas stem movement is the first variant called conventionally Displacement, because it allows more smooth joining the movement and decelerating of the cannon mechanisms parts, which achieve far lower speeds and hence the kinematic energy of said parts during collisions with other elements is lower, which results in slower wear of mechanisms. It should be noted that nevertheless, the first variant of driving the piston still provides a proper operation of the main kinematic sequence of the cannon. Assumed variants of the piston mechanism movement as well as elaborated simulation model will be verified in the next (planned) stage of studies basing on the results of the measurements of experimental kinetic parameters utilising high-speed camera (Phantom) and TEMA software.

It should also be noted that the created during the realisation 3D CAD models of the elements of the cannon paired with the assembly model and properly working simulation model have exceptional value as a didactic material for training of the Engineering and Aviation Service personnel operating this type of aviation weaponry.

Funding: This work was financed by Military University of Technology under research project UGB 897/2021.

## References

- 23 mm DZIAŁKO LOTNICZE GSz-23Ł *Opis techniczny i eksploatacja*. 1990. Dowództwo Wojsk Lotniczych, Poznań.
- FLORIO L.A. 2011. *Update on gas flow and heat transfer modeling in small arms systems*. US Army ARDEC conference publications.
- GRUSZCZYŃSKI J. 1993. *Uzbrojenie lotnicze Wschód*. Przegląd Konstrukcji Lotniczych, 15: 1-28.
- HUAI-KU S., CUN-GIN Ch., HUE-POE W. 2007. *Dynamic Analysis of rigid-body mechanisms mounted on flexible support structures – Spatial case*. J. Chinese Society Mech. Eng., 28(6): 585-591.
- HUAI-KU S., YUN-TIEN L., CUN-GIN CH. 2009a. *Dynamic analysis of a vehicular-mounted automatic weapon-planar case*. Defence Science Journal, 59(3): 265-272. doi: 10.14429/dsj.59.1520.

- HUAI-KU S., YUN-TIEN L., CUN-GIN Ch. 2009b. *Dynamic analysis of a vehicular-mounted automatic weapon-planar case*. Defence Science Journal, 59(3): 265-272. doi: 10.14429/dsj.59.1520.
- JASZTAL M. 2006. *Metoda modelowania i badania zespołów mechanicznych wybranych urządzeń uzbrojenia lotniczego*. Przegląd Mechaniczny, 4(6): 15-20.
- JASZTAL M. 2017. *Zastosowanie systemów CAD/CAE w badaniach elementów uzbrojenia lotniczego*. In: *Wybrane aspekty zastosowania bojowego lotnictwa*. Eds. A. Wetoszka, A. Truskowski. Wyższa Szkoła Oficerska Sił Powietrznych, Dęblin.
- JASZTAL M., TOMASZEK H., WAŻNY M. 2007. *Zarys modelu oceny niezawodności pracy działka lotniczego w aspekcie powstawania uszkodzeń katastroficznych w postaci zacięć*. Zagadnienia Eksploatacji Maszyn, 4(152): 129-140.
- LOGAN D.L. 2007. *A first course in finite element method*. Ed. 4. Thomas Learning, University of Wisconsin, Platteville.
- NI J., WANG X., XU Ch. 2011. *Virtual test technology study of automatic weapon*. World J. Modelling Simulation, 7: 155-160.
- PATHAK A., BREI D., LUNTZ J., LAVIGNA C. 2006. *A dynamic model for generating actuator specifications for small arms barrel active stabilisation*. The Proceedings of SPIE – the International Society for Optical Engineering.
- PLATEK P., DAMAZIAK K., MALACHOWSKI J., KUPIDURA P., WOZNIAK R., ZAHOR M. 2015. *Numerical Study of Modular 5.56 mm Standard Assault Rifle Referring to Dynamic Characteristics*. Defence Science Journal, 65(6): 431-437, doi: 10.14429/dsj.65.8259.
- SCHABANA A.A. 2005. *Dynamics of multibody systems*. Cambridge University Press, Cambridge.
- SCHIEHLEN W. 1997. *Multibody system dynamic: Roots and perspective*. Multibody Syst. Dyn., 1: 149-188.
- SHIPLEY P., MCCONVILLE J.B. 2006. *The creation of fully functional virtual prototype of an automatic weapon using MSC*. Adams, MSC, Software VPD Conference.
- TOMULIK P., FRACZEK J. 2011. *Simulation of multibody systems with the use of coupling techniques: A case study*. Multibody Syst. Dyn., 25(2): 145-165. doi: 10.1007/s11044-010-9206-y.
- URRIOLAGOITIA-SOSA G., MOLINA-BALLINAS A., VERDUZCO-CEDENO V.F., ROMERO-ANGELES B., URRIOLAGOITIA-CALDERÓN G., HERNÁNDEZ-GÓMEZ L.H., BELTRÁN-FERNÁNDEZ J.A. 2011. *Residual stress interaction against mechanical loading during the manufacturing process of an assault rifle component*. Appl. Mech. Mater., 70: 482-487. doi: 10.4028/www.scientific.net/AMM.70.482.
- WEI WU Ch., HAI WU Y., MAN FAN Q. 2013. *Analysis of temperature and stress of a thin-walled cylinder based on FEM*. Appl. Mech. Mater., 12: 373-375. doi:10.4028/www.scientific.net/AMM.373-375.12.
- ZIENKIEWICZ O.C., TAYLOR R.L. 2005. *The finite element method for solid and structural mechanics*. Ed. 6. Elsevier Ltd., Amsterdam.



Yearbook peer-reviewed scientific journal

ISSN 1505-4675  
e-ISSN 2083-4527

**TECHNICAL SCIENCES**

Homepage: <https://czasopisma.uwm.edu.pl/index.php/ts/>



DOI: <https://doi.org/10.31648/ts.7017>

## THE USE OF THE THEORY OF NONHOLONOMIC CONSTRAINTS IN THE PROCESS OF AUTOMATIC CONTROL OF A MANIPULATING MACHINE

*Edyta Ładyżyńska-Kozdraś<sup>1</sup>, Barbara Kozłowska<sup>2</sup>, Danyil Potoka<sup>3</sup>*

<sup>1</sup>ORCID: 0000-0002-4014-6982

<sup>2</sup>ORCID: 0000-0003-1869-340X

<sup>3</sup>ORCID: 0000-0002-1359-3509

Faculty of Mechatronics  
Warsaw University of Technology

Received 10 August 2021, accepted 12 November 2021, available online 15 November 2021.

**Key words:** automatic control, non-holonomic relations, control laws, manipulator.

### Abstract

The presented study contains a sample of utilization of the control laws treated as kinematic relations of parameter deviations and realized in the process of ordered automatic control of a manipulating machine. Movement of the grasping end is considered in an inertial reference standard rigidly joined with an immobile working environment of the manipulator. The specificity of the control's choice required creating program relations constituting the ordered parameters describing the movement of the manipulator's elements. During work, the ordered parameters are compared to the parameters realized in the process of the grasping end's work. This was deviations are determined, which thanks to properly prepared control laws are leveled by the manipulator's control executive system.

---

Correspondence: Edyta Ładyżyńska-Kozdraś, Instytut Mikromechaniki i Fotoniki, Wydział Mechatroniki, Politechnika Warszawska, ul. św. Andrzeja Boboli 8, 02-525 Warszawa, e-mail: [edyta.ladzynska@pw.edu.pl](mailto:edyta.ladzynska@pw.edu.pl).

## Introduction

Manipulating machines due to their accuracy and repetitive positioning properties are nowadays an essential part of different industries such as industrial processes, medical fields, and automotive industries. They are used to assist in dangerous, monotonous, and tedious work. Typical example applications of manipulating machines in industry include moving, arranging, packaging, cutting, welding, paint spraying and sanding. Task accomplishment is a consequence of movements of manipulator's joints in single or multiple directions following a certain systematic pattern. The control variables are mainly position, velocity, force/torque or a hybrid combination of all.

The literature on dynamics modeling, control, application and performance analysis of manipulating machines is extensive. Systematic overview can be found in (AJWAD et al. 2015, JANKOWSKI 2005, NIZIOŁ 2005, SINGH, KRISHNA 2015) and many others. However, as shown in the article (AJWAD et al. 2015), it is a myth that the area of manipulator control is already saturated. The continuous advancement of science and technology and the improvement of people's living standards promote the continuous development and improvement of autonomous robot and manipulators technology. In the design and research of the robotic arm, the design of the control system is often inseparably related to the overall dynamic performance, especially for the control of the robotic arm joint (CAI et al. 2021, IVANOV et al. 2020, JANKOWSKI 2005, WEN et al. 2015). Robust path-planning and control algorithms are sought that must ensure the stability of all intermediate configurations of the manipulator along the prescribed path (BI 2020, SINGH, KRISHNA 2015). The method of incorporating constraint equations, holonomic and nonholonomic, into the kinematics or dynamics of the system at the modeling level was presented in papers (BERTONCELLI et al. 2020, JARZĘBOWSKA, SANJUAN SZKLARZ 2017, KŁAK, JARZĘBOWSKA 2021, NEJMARK, FUFĄJEW 1971). However, the available literature does not mention the introduction of control laws as nonholonomic constraints and their coupling with the dynamic equations of the manipulator motion. This research gap is filled by this study.

The studied issue is an innovative approach stemming from the previous works of the author (ŁADYŻYŃSKA-KOZDRAŚ 2009, 2012, SIBILSKA-MROZIEWICZ, ŁADYŻYŃSKA-KOZDRAŚ 2018) regarding modeling of dynamics and automatic control of flying objects. The positive results achieved within these works allow assuming that an analogical model of a controlled mobile object may be adopted with automatic control of the manipulating machine. The developed algorithm of the object control makes use of the complete nonlinear model of the object's dynamics combining it with control rights treated as nonholonomic constraints.

Thus, the purpose of this topic is to compile control rights treated as non-holonomic relations imposed on the manipulator's arms' movement. Mobile objects, such as manipulators and mobile robots, have a limitation of degrees

of freedom through control. The imposed relations limiting free movement, which are non-holonomic relations, are considered control rights. It was assumed that a manipulator moves with program movement, thus the control rights were determined as geometric and kinematic relations of deviations between the ordered and actual trajectory of movement of the grasping end. This distinguishes the presented algorithm from among other control algorithms, which can be found in Polish and foreign literature.

### Kinematic model – realized parameters of the manipulator's movement

When modeling the movement of the manipulator frames of reference locating the object in space were assumed (Fig. 1). The primary frame of reference, in relation to which the manipulator's movements were considered, is the rigid inertial system related with its immobile foundation  $O_1x_1y_1z_1$ . The grasping end is related with the gravitational system  $O_Cx_gy_gz_g$  with axes parallel to appropriate axes of the immobile system  $O_1x_1y_1z_1$  as well as the grasping end's own system  $O_Cxyz$ . It is a dextrorotary system, with start in the  $C$  joint and axis  $O_Cx$  directed along the line connecting point  $C$  with the center of mass  $K$  of the grasping end along with the weight carried by it.

The study takes into account the example of a fictional manipulator, the model of which was selected in such a way, that it is possible to analyze a great variety of its kinematic pairs. And so (Fig. 1) two rotational parts were discriminated

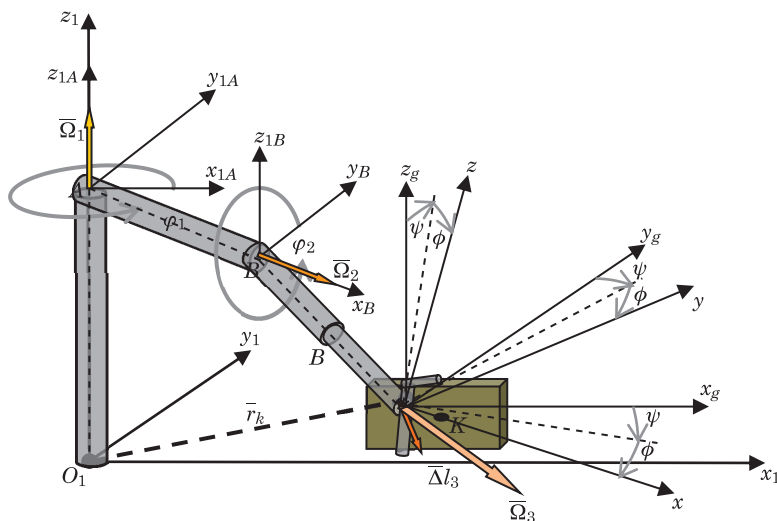


Fig. 1. Adopted frames of reference and locations as well as angular velocities of the elements manipulator

$O_1A$  and  $AB$   $|\overline{O_1A}| = r_1 = \text{const.}$ ,  $|\overline{AB}| = r_2 = \text{const.}$  rotations of which are described appropriately by angles  $\varphi_1$  and  $\varphi_2$  as well as angular velocities  $\Omega_1$  and  $\Omega_2$ . The third arm –  $BC$  – is the moved arm ( $|\overline{O_1A}| = r_1 = \text{const.}$ ,  $|\overline{AB}| = r_2 = \text{const.}$ ), which can extend itself with angular velocity of  $\Delta l_3$ . However, the manipulator's grasping end, the length of which  $r_C$  is treated as the distance from point  $C$  to the center of mass  $K$  of the grasping end along with the weight carried by it, may perform any spherical movements in relation to joint  $C$  with angular velocity  $\Omega_3$  (Fig. 1). Spherical movements of the grasping end were described with the use of quasi-Euler movements  $\varphi, \theta, \psi$  (NIZIOŁ 2005), combining the gravitational system  $O_C x_g y_g z_g$  with the grasping end's own system  $O_C xyz$ .

These angles create kinematic relations imposed on the end

$$\begin{aligned}\bar{\Omega}_3 &= \omega_x \bar{l}_1 + \omega_y \bar{j}_1 + \omega_z \bar{k}_1 \\ \omega_x &= \dot{\varphi} - \dot{\psi} \sin \theta \\ \omega_y &= \dot{\theta} \cos \varphi + \dot{\psi} \sin \varphi \cos \theta \\ \omega_z &= -\dot{\theta} \sin \varphi + \dot{\psi} \cos \varphi \cos \theta\end{aligned}\quad (1)$$

Components  $\omega_x, \omega_y, \omega_z$  of the temporary angular velocity of grasping end  $\Omega_3$  are linear relations of generalized velocities  $\frac{d\varphi}{dt}, \frac{d\theta}{dt}, \frac{d\psi}{dt}$  with coordinates depending on the generalized coordinates  $\varphi, \theta, \psi$ .

The kinematic relations imposed on the grasping end of the manipulator are described by dependencies formulated based on Figure 1.

The vector of temporary location of the working end in the system  $O_1 x_1 y_1 z_1$ :

$$\bar{r}_K = \bar{r}_1 + \bar{r}_2 + \bar{l}_3 + \bar{r}_C = x \bar{l}_1 + y \bar{j}_1 + z \bar{k}_1 \quad (2)$$

$$\begin{aligned}x &= r_2 \cos \phi_1 + (l_3 + \Delta l_3) \cos \phi_2 \sin \phi_1 + x_C \\ y &= r_2 \sin \phi_1 - (l_3 + \Delta l_3) \cos \phi_2 \cos \phi_1 + y_C \\ z &= r_2 + (l_3 + \Delta l_3) \sin \phi_2 + z_C\end{aligned}\quad (3)$$

The vector of temporary angular velocity of the end

$$\bar{\Omega}_K = \bar{\Omega}_1 + \bar{\Omega}_2 + \bar{\Omega}_3 = \Omega_x \bar{l}_1 + \Omega_y \bar{j}_1 + \Omega_z \bar{k}_1 \quad (4)$$

$$\begin{aligned}\Omega_x &= \Omega_2 \cos \phi_1 + \omega_x \\ \Omega_y &= \Omega_2 \sin \phi_1 + \omega_y \\ \Omega_z &= \Omega_1 + \omega_z\end{aligned}\quad (5)$$

The vector of temporary linear velocity of the end

$$\bar{V}_K = \frac{d\bar{r}_K}{dt} = \bar{\Omega}_1 \cdot \bar{r}_1 + \bar{\Omega}_2 \cdot \bar{r}_2 + \frac{\delta \bar{l}_3}{\delta t} + \bar{\Omega}_3 \cdot \bar{r}_C = V_x \bar{l}_1 + V_y \bar{j}_1 + V_z \bar{k}_1 \quad (6)$$

This way the kinematic relations, which provide information on the linear and angular location of the working end, realized during its work, were compiled. They were formulated in an inertial frame of reference  $O_1x_1y_1z_1$  rigidly related with an immobile foundation of the manipulator and they constitute parameters realized by the automatically controlled manipulator.

### Program relations – ordered parameters of the manipulator's movement

A necessary element of each control system is the targeting algorithm realized by it. Such an algorithm imposes boundaries on the object's movement. Thus, selection of the control method is very important.

In the case of a manipulator, in the situation, in which the grasping end is to perform a task specified in advance we assume, that the trajectory it should move along should be pre-ordered by the operator (Fig. 2). Thus it is a program movement, which is carried out along a spatial trajectory ordered in advance.

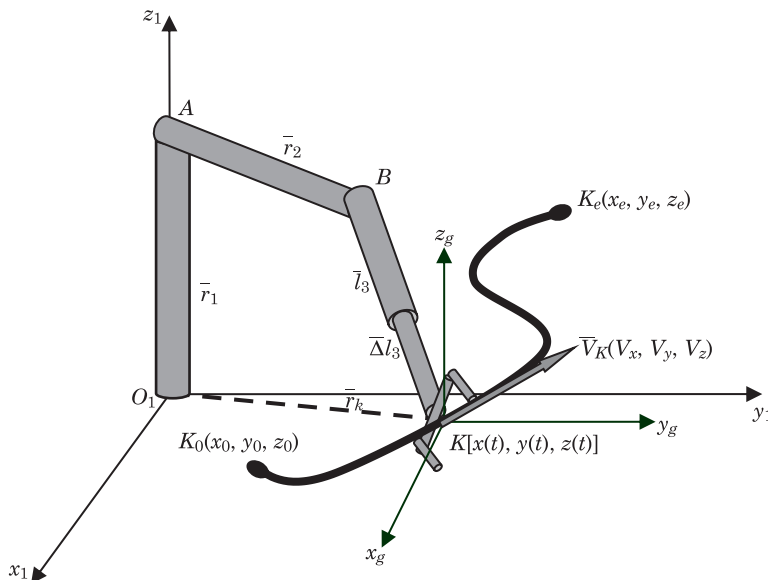


Fig. 2. Trajectory of the program movement of the manipulator's grasping end

### Ordered program relations

$$K_0 K_k = s(x_z, y_z, z_z, t) \quad (7)$$

$$V_k(t) = \dot{s}(x_z, y_z, z_z, t) \quad (8)$$

where:

$x_z, y_z, z_z$  – ordered parameters of the grasping end's movement.

In this case we are dealing, on one hand, with program geometrical relations (Eq. 7), which impose limitations on the spatial location of the manipulator's grasping end, and on the other hand with kinematic ties (Eq. 8), which impose limitations on its velocity vector – tangent to the ordered trajectory of movement. Thus the program ties constitute the ordered parameters of the manipulator's movement, which are compared to the parameters realized during targeting.

## Control rights of the working end

Automatic control systems perform numerous types of tasks, which include: improvement of the dynamic properties of the controlled object, stabilization of the selected state parameters or directive changes of the ordered movement, performing the selected maneuvers, automatic realization of the object's complete movement along with all of its phases.

The proposed automatic control of the manipulating machine, according to the general concept show in the flowchart (Fig. 3), functions based on the previously calculated movement program and automatic stabilization utilizing the compiled control rights.

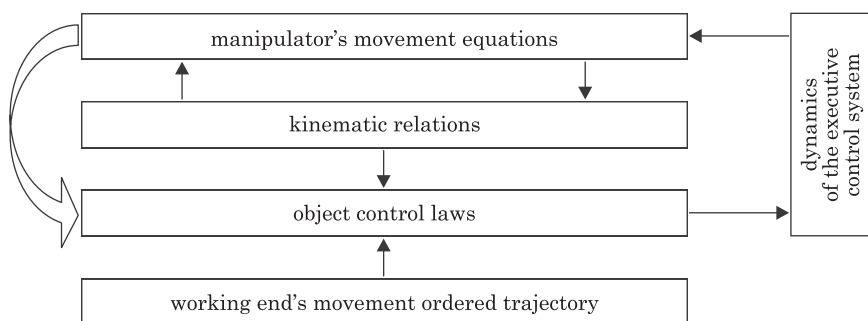


Fig. 3. Flowchart of the manipulator's control executive system



The control law were established in such a way that during movement of the manipulator deviations, which are the differences between the current state parameters ( $x, y, z, V_x, V_y, V_z, \Omega_x, \Omega_y, \Omega_z$ ) and the ordered parameters ( $x_z, y_z, z_z, V_x, V_y, V_z, \Omega_x, \Omega_y, \Omega_z$ ) are read. These deviations after proper amplification (with the use of  $K^i$  amplification coefficient) are transferred to the executive system of the control system, causing the ordered movements of the manipulator's arms.

$$T_1^{\phi_1} \dot{\phi}_1 + \phi_1 = K_{\Omega_z}^{\phi_1} (\Omega_z - \Omega_{zz}) + K_x^{\phi_1} (x - x_z) + K_y^{\phi_1} (y - y_z) + \phi_{10} \quad (9)$$

$$T_1^{\phi_2} \dot{\phi}_2 + \phi_2 = K_{\Omega_x}^{\phi_2} (\Omega_x - \Omega_{xz}) + K_{\Omega_y}^{\phi_2} (\Omega_y - \Omega_{yz}) + K_z^{\phi_2} (z - z_z) + \phi_{20} \quad (10)$$

$$T_1^{l_3} \dot{l}_3 + l_3 = K_{V_x}^{l_3} (V_x - V_{xz}) + K_{V_y}^{l_3} (V_y - V_{yz}) + K_{V_z}^{l_3} (V_z - V_{zz}) + l_{30} \quad (11)$$

where:

$T_1^i$  – time constants,

$K_j^i$  – control signals' amplification coefficients.

The set control laws are strongly non-linear functions of time. These are kinematic ties, non-integrable, not directly brought down to geometric ties, this is why they constitute non-holonomic ties imposed on the movement of the manipulator's arms (NEJMARK, FUFARJEV 1971). In order to verify such control laws the non-linear model of the manipulator's dynamics shall be adopted compiled with the use of analytical equations of movement for non-holonomic systems in generalized coordinates.

## Conclusions

The study presents the kinematics model and control laws describing non-holonomic constraints imposed on the movement of manipulator's joints. The resulting equations are kinematic ties of deviations between the realized and ordered parameters of movement of the grasping end of the manipulator. They determine the relations between the kinematic parameters of the grasping end, and the possible deviations of the individual manipulator's joints, which are time-determined thanks to  $T^i$  time constants. This way the control laws, along with movement equations, determine the behavior of the manipulator on the route during tracking, in order to enable its optimum control. They allow to introduce automatic control of the grasping end moving along a programmed route.

## References

- AJWAD S.A., IQBAL J., ULLAH M.I., MEHMOOD A. 2015. *A systematic review of current and emergent manipulator control approaches*. *Frontiers of Mechanical Engineering*, 10(2): 198-210.
- BERTONCELLI F., RUGGIERO F., SABATTINI L. 2020. *Linear time-varying MPC for nonprehensile object manipulation with a nonholonomic mobile robot*. In 2020 IEEE International Conference on Robotics and Automation (ICRA), p. 11032-11038.
- BI M. 2020. *Control of Robot Arm Motion Using Trapezoid Fuzzy Two-Degree-of-Freedom PID Algorithm*. *Symmetry*, 12(4): 665. doi: 10.3390/sym12040665.
- CAI J., DENG J., ZHANG W., ZHAO W. 2021. *Modeling Method of Autonomous Robot Manipulator Based on DH Algorithm*. *Mobile Information Systems*, 2021, Article ID 4448648, doi: 10.1155/2021/4448648.
- IVANOV S., ZUDILOVA T., VOITIUK T., IVANOVA L. 2020. *Mathematical Modeling of the Dynamics of 3-DOF Robot-Manipulator with Software Control*. *Procedia Computer Science*, 178: 311-319.
- JANKOWSKI K. 2005. *Inverse Dynamics Control in Robotics Applications*. Trafford Publishing: Bloomington, Canada.
- JARZEBOWSKA E., SANJUAN SZKLARZ P. 2017. *Model-based control of a third-order nonholonomic system*. *Mathematics and Mechanics of Solids*, 22(6): 1397-1406.
- KŁAK M., JARZEBOWSKA E. 2021. *Quaternion-Based Constrained Dynamics Modeling of a Space Manipulator with Flexible Arms for Servicing Tasks*. *Journal of Vibration Engineering & Technologies*, 9(3): 381-387.
- ŁADYŻYŃSKA-KOZDRAŚ E. 2009. *The control laws having a form of kinematic relations between deviations in the automatic control of a flying object*. *Journal of Theoretical and Applied Mechanics*, 47(2): 363-381.
- ŁADYŻYŃSKA-KOZDRAŚ E. 2012. *Modeling and numerical simulation of unmanned aircraft vehicle restricted by non-holonomic constraints*. *Journal of Theoretical and Applied Mechanics*, 50(1): 251-268.
- NEJMARK J., FUF AJEW N. 1971. *Dynamika układów nieholonomicznych*. Wydawnictwo Naukowe PWN, Wrocław.
- NIZIOŁ J. 2005. *Mechanika techniczna*. Tom II. *Dynamika układów mechanicznych*. Wyd. Komitet Mechaniki PAN, IPPT PAN, Warszawa.
- SIBILSKA-MROZIEWICZ A., ŁADYŻYŃSKA-KOZDRAŚ E. 2018. *Mathematical Model of Levitating Cart of Magnetic UAV Catapult*. *Journal of Theoretical and Applied Mechanics*, 56(3): 793-802.
- SINGH P.K., KRISHNA C.M. 2014. *Continuum arm robotic manipulator: A review*. *Universal Journal of Mechanical Engineering*, 2(6): 193-198.
- WEN Z., WANG Y., DI N., CHU G. 2015. *Fast recognition of cooperative target used for position and orientation measurement of space station's robot arm*. *Hangkong Xuebao/Acta Aeronautica et Astronautica Sinica*, 36(4): 1330-1338.



## ASSESSMENT OF WALL SALINITY IN THE SELECTION OF RENOVATION PLASTER SYSTEMS

*Arkadiusz Panuś*

ORCID: 0000-0002-9817-0192

Department of General Construction and Building Physics  
Faculty of Geoengineering  
University of Warmia and Mazury in Olsztyn

Received 21 September 2021, accepted 12 November 2021, available online 15 November 2021.

**Key words:** salinity analysis, colorimetry, salty wall, restoration plaster, ion chromatography.

### Abstract

This article presents issues related to assessing the degree of wall salinity to select plaster systems for renovations of damp building walls. The most commonly used salt concentration tests pose many difficulties. If used uncritically, they risk failing to select the right system or its incorrect make. The accuracy of the colorimetric method for testing chloride, nitrate, and sulphate content was analysed to exemplify the magnitude of the problem. Both multi-salt solutions of known concentrations and unknown composition extracted from drillings in the walls of a historical facility were examined. A comparative methodology using ion chromatography as a standard was employed in the research. The analytical methods and the selected modules of the „Statistica” software were used to analyse data and present the results. The colorimetric method has been shown to distort salt concentration values, posing a risk of unsuccessful repair work on high-salinity walls. A method for determining the correction reducing the measurement error has been proposed. The factors affecting the error were also mentioned. Attention has also been drawn to the resolution and application of a method with a correct concentration range intended to improve work efficiency and optimize the costs incurred in renovating the salty wall.

---

Correspondence: Arkadiusz Panuś, Katedra Budownictwa Ogólnego i Fizyki Budowli, Wydział Geoinżynierii, Uniwersytet Warmińsko-Mazurski, ul. Heweliusza 4, 10-724 Olsztyn, e-mail: [arkadiusz.panus@uwm.edu.pl](mailto:arkadiusz.panus@uwm.edu.pl).

## Introduction

When in operation, each facility is continuously exposed to adverse outdoor conditions. If the walls are not adequately protected, they may become wet and thus salty, as the transported water is, in fact, always a salt solution. Depending on the magnitude of the phenomenon, the salts cause relatively great damage to building materials due to crystallization. This problem has been known for years. In 420 B.C. HERODOTUS (420BC), an ancient Greek historian, said, "I observed... that salt exuded from the soil to such an extent as even to injure the pyramids". In modern times, information on this issue appeared already in 1895 (LUQUER 1895). Doehe estimated that in 2002, there were more than 1800 bibliographic entries in the scientific literature on the destruction of porous material caused by salts (DOEHNE 2002). Many of them have been cited in literature extensive review by DOEHNE (2002), GOUDIE, VILES (1997) and CHAROLA (2000).

The impact of the three salts (chlorides, nitrates and sulphates) is assumed to be the most significant for the building material (PAVLÍKOVÁ et al. 2011, PEŘINKOVÁ et al. 2021, WÓJCIK 2006). These are substances covered by instructions and recommendations from industry institutions and manufacturers. For example, the EUREKA EU-1270 programme proposed a salinity grade and damage classification based on the salt type and concentration (Tab. 1) (STILLHAMMEROVÁ 2006).

Table 1

EUREKA EU – 1270 salinity degree classification (% in mass)

Salt type	Class 0	Class 1	Class 2	Class 3	Class 4
Chlorides	0.00-0.01	0.01-0.03	0.03-0.09	0.09-0.28	>0.28
Nitrates	0.00-0.01	0.01-0.05	0.05-0.15	0.15-0.50	>0.50
Sulphates	0.00-0.02	0.02-0.08	0.08-0.24	0.24-0.77	>0.77

This classification uses five basic salinity degrees and identifies possible hazards and degradation degrees caused by these salts. According to Table 1 (STILLHAMMEROVÁ 2006), salinity classes are defined as follows:

- Class 0 – low salt concentration (trace amounts), no damage to the wall;
- Class 1 – very low salinity of the structure. Structures that are continuous moisture-borne engage in water capillary action (or other unfavourable phenomena) and may get damaged;
- Class 2 – average salinity of the structure. The life of the plasters and paintings is slightly reduced;
- Class 3 – high salinity of the structure. The life of plaster and paintings is reduced considerably. Despite the use of active vertical isolation, the wall is wet due to the hygroscopic nature of the salt;
- Class 4 – extra high salinity. The structure gets destroyed in a very short time.

In the context of damage, this classification is rather general because, in reality, the size of the damage is affected by the structure of the material under analysis. A small quantity of salt can cause extensive damage in material with small pore diameters, and conversely, high concentrations will not result in significant changes in materials with large pore diameters (BLÄUER BÖHM 2005). Such classifications only make sense if they refer to specific materials. Manufacturers of renovation plaster systems are well aware of this. Their products are designed to withstand the relevant concentration ranges. Depending on the substrate salinity, the contractor then selects appropriate materials to make the plaster resistant to harmful salts for up to 20 years. To simplify the wall renovation technology, manufacturers and contractors use a common classification language. The WTA Instructions 2-9-04, issued by the Technical and Scientific Association for Building Protection and Conservation of Monuments (WTA – Wissenschaftlich-Technische Arbeitsgemeinschaft für Bauwerkserhaltung und Denkmalpflege), serves as a reference (WÓJCIK 2010). Three salinity degrees for the three salts are defined in the WTA instructions (Tab. 2) (*WTA Merkblatt 2-9-04...* 2004). The plaster systems used are WTA-certified and are assigned to specific salinity concentration ranges. They are used to determine the number of system components and layer thicknesses (Tab. 3) (*WTA Merkblatt 2-9-04...* 2004).

Table 2

WTA salinity degree classification no. 2-9-04 (% in mass)

Salt type	Low	Medium	High
Chlorides	<0.2	0.2-0.5	>0.5
Nitrates	<0.1	0.1-0.3	>0.3
Sulphates	<0.5	0.5-1.5	>1.5
Total salts	0.1-0.4/ <sup>1</sup>	0.4-1.0/ <sup>1</sup>	>1.0

<sup>1</sup> If the nitrate content accounts for more than 50% of the total salinity, low and medium salinity shall be ranked one degree up

Table 3

Renovation plaster system components according to WTA no. 2-9-04

Salinity degree	Layer layout	Thickness [mm]
Low	Rendering	≤5
	Renovation plaster	≥20
Medium to high	Rendering	≤5
	Renovation plaster	10-20
	Renovation plaster	10-20
	Rendering	≤5
	Base plaster	≥10
	Renovation plaster	≥15

Knowledge of salt concentrations is of key importance here (PAVLÍKOVÁ et al. 2011, KONCA et al. 2016, GACZEK, FISZER 2014, KNOP 2016, NOCOŇ 2016). The pores of WTA restoration plasters are hydrophobic, which limits the deposition of salt in the plaster coating. If the substrate exhibits a medium to a high degree of salinity, double layer systems should be used, often with a base plaster storing salts (GACZEK, FISZER 2014) (Tab. 3). If the salinity of the substrate is incorrectly determined, mainly understated, the volume of the storage layer may be too small, which will cause premature saturation of the system and entail the necessity to rework, which involves significant costs. The situation is similar for the opposite. If concentrations get overestimated, the accepted (exaggerated) thickness of the storage layer puts the investor at risk of incurring unreasonable costs. Consequently, the investor questions the work effectiveness or states an abuse of material and thus refers the case to court. The judicial decisions are made based on the commissioned studies with the highest possible accuracy.

Contractors and architects typically use simple strip tests for salinity diagnostics. Some claim that they are estimates and do not give accurate results. There are no studies in the scientific literature describing the accuracy of these methods. Oberta used the colorimetric method (KOL) to research the capillary zone electrophoresis (CZE) method. The results showed deviations from the actual salt concentrations (Tabs. 4, 5) (OBERTA 2015).

Table 4

Comparison of test results for concentrations of water-soluble salt (Cl<sup>-</sup>) obtained using the CZE method

Type of material	Solution concentration real [%]	Solution concentration determined with CZE [%]	Deviation in the results [%]
Brick	1.57	2.17	38.22
Sandstone	0.61	0.83	36.07
Limestone	0.99	1.77	78.79

Table 5

Comparison of test results for concentrations of water-soluble salts obtained using the CZE and KOL method

Type of material	Concentration of solutions determined with KOL [%]			Concentration of the solution determined with CZE [%]		
	Cl <sup>-</sup>	NO <sub>3</sub> <sup>-</sup>	SO <sub>4</sub> <sup>2-</sup>	Cl <sup>-</sup>	NO <sub>3</sub> <sup>-</sup>	SO <sub>4</sub> <sup>2-</sup>
Brick	0.26 (0) <sup>1</sup>	0.30 (11) <sup>1</sup>	0.26 (-7) <sup>1</sup>	0.26 (0) <sup>2</sup>	0.27 (-11) <sup>2</sup>	0.28 (7) <sup>2</sup>
Sandstone	0.20 (-5) <sup>1</sup>	0.12 (-43) <sup>1</sup>	0.14 (-26) <sup>1</sup>	0.21 (5) <sup>2</sup>	0.21 (43) <sup>2</sup>	0.19 (26) <sup>2</sup>
Limestone	0.28 (0) <sup>1</sup>	0.32 (10) <sup>1</sup>	0.24 (-4) <sup>1</sup>	0.28 (0) <sup>2</sup>	0.29 (10) <sup>2</sup>	0.25 (4) <sup>2</sup>

<sup>1</sup> The value in brackets refers to the difference between the results obtained using the KOL and CZE methods

<sup>2</sup> The value in brackets refers to the difference between the results obtained using the CZE and KOL methods

The CZE method overstated the results by 36-79%. On the contrary, tests using the CZE and KOL methods (Tab. 5) gave similar values for chlorides. The difference in the results obtained using the KOL and CZE methods was -5-0%. It can thus be assumed that the deviation found in Table 4 for the CZE method is also applicable to the KOL method. For other salts, the differences in results obtained using CZE and KOL were more pronounced. For nitrates, they were -43-11% and -4-26% for sulphates. In both cases, the largest deviations applied to sandstone. Unfortunately, concerning nitrates and sulphates, it is difficult to make similar assumptions as for chlorides, as no comparison was made for CZE with the actual concentrations of these salts. Thus, we do not know what discrepancies (even hypothetical) can be expected when determining nitrate and sulphate concentrations using colorimetry. On the other hand, these parameters are very important for renovation works in salty facilities and should be carefully examined. In this work, the accuracy of colorimetric methods used in repair technology using renovation plasters was analysed for all of the above-mentioned salts.

## Materials and Methods

The following elements have been used for testing:

- Chloride titration test set in the range of 2-200 mg/L (0.0002-0.0200%)  $\text{Cl}^-$ ;
- Nitrate Test strips in the range 10-25-50-100-250-500 mg/L (0.0010-0.0025-0.0050-0.0100-0.0250-0.0500%)  $\text{NO}_3^-$ ;
- Sulphate Test strips in the range <200->400->800->1200->1600 mg/L (<0.02->0.04->0.08->0.12->0.16%)  $\text{SO}_4^{2-}$ .

Parallel, relevant concentrations were determined for the same solutions using ion chromatography (IC). Borelli described it as highly accurate (BORRELLI 1999). The authors' own studies confirmed this opinion. The accuracy of the chromatograph used proved very high. For the tests, a chromatograph equipped with a conductometric detector and UV-vis detector with a photodiode array and an ion-exchange column dedicated to separating anions such as chlorides, nitrates and sulphates was used. An external standard was used for determining the so-called calibration curve. It showed a correlation between the value measured by the apparatus and the test substance concentration. It was based on an analysis of several samples of known concentrations and integrals, the so-called peaks on the chromatogram (Fig. 1). The results of the studies exhibited a very high degree of correlation.

Model fit to the trial through the coefficient of determination  $R^2$  (the closer it is to unity, the better the fit). When determining calibration curves for chlorides, nitrates and sulphates, the  $R$ -square ( $R^2$ ) approximation value was always above 0.9998 (Tab. 6, Fig. 2). However, for comparing several populations of result,

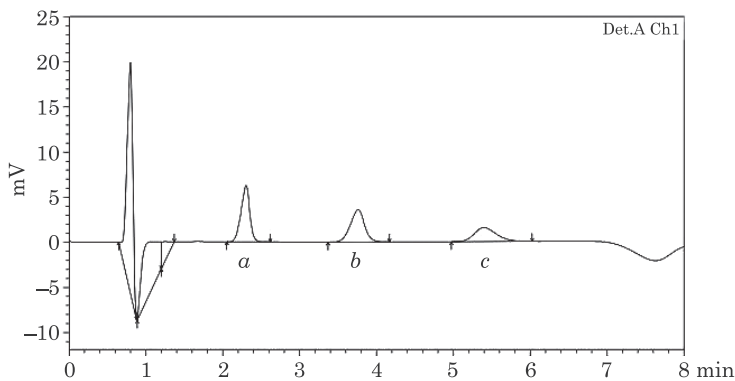


Fig. 1. Chromatogram with marked peaks for (a) chlorides, (b) nitrates, (c) sulphates

a coefficient of variation was used (RSD – relative statistical deviation) (if the resulting RSD is less than 25%, the results are assumed to be only slightly variable). For the calibration curves, the coefficient of variation of the RF response factor (RF %RSD) were 1-6% (Tab. 6, Fig. 2), where the RF response factor was defined as the quotient of the peak surface area and the concentration (or vice

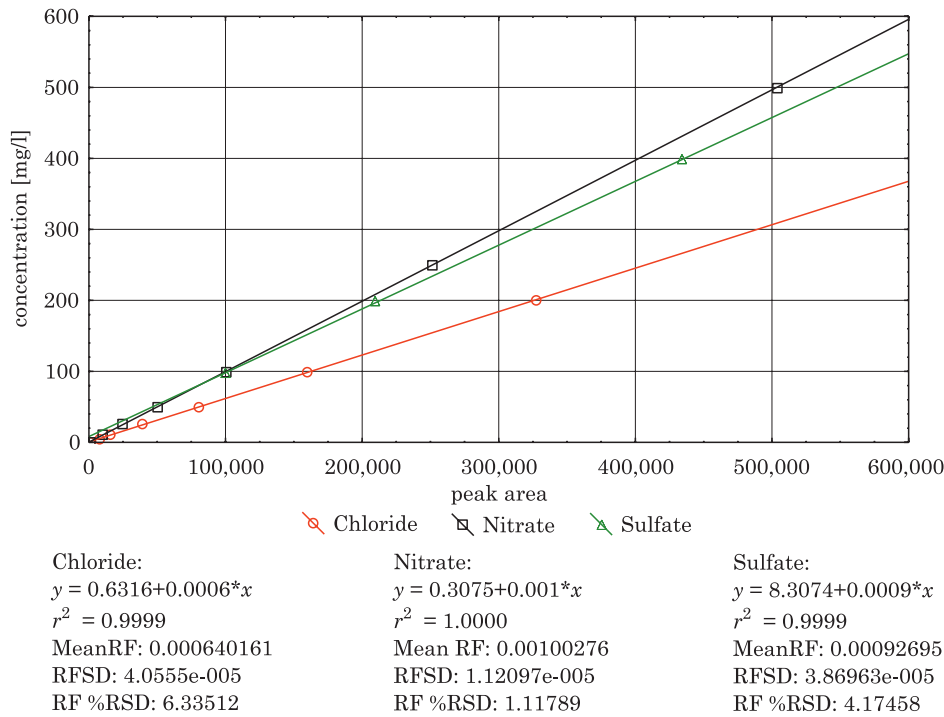


Fig. 2. Correlation curves of chlorides, nitrates, and sulphates



versa) of the standard solution. Therefore, the curve presented a very good fit to the results in the analysed range. Statistically, all values calculated from the correlation function obtained were subject to a minor error.

Table 6

Comparison of the obtained statistical calibration curves

Correlation curve	$R^2$	RF %RSD
Chlorides	0.999870	6.34
Nitrates	0.999997	1.12
Sulphates	0.999883	4.17

It was planned to run tests on two types of samples to determine the accuracy of the colorimetric method. In particular, measurements were performed for solutions of known and unknown concentrations. First, solutions with known concentrations were analysed in the ranges corresponding to the colorimetric method. Three multi-saline solutions were prepared: NaCl, NaNO<sub>3</sub> and NaSO<sub>4</sub> with (in mass) concentrations according to Cl<sup>-</sup> – NO<sub>3</sub><sup>-</sup> – SO<sub>4</sub><sup>2-</sup>, proportions as given below:

- solution no. 1: 0.0000-0.0000-0.0100%;
- solution no. 2: 0.0005-0.0010-0.0200%;
- solution no. 3: 0.0010-0.0025-0.0400%.

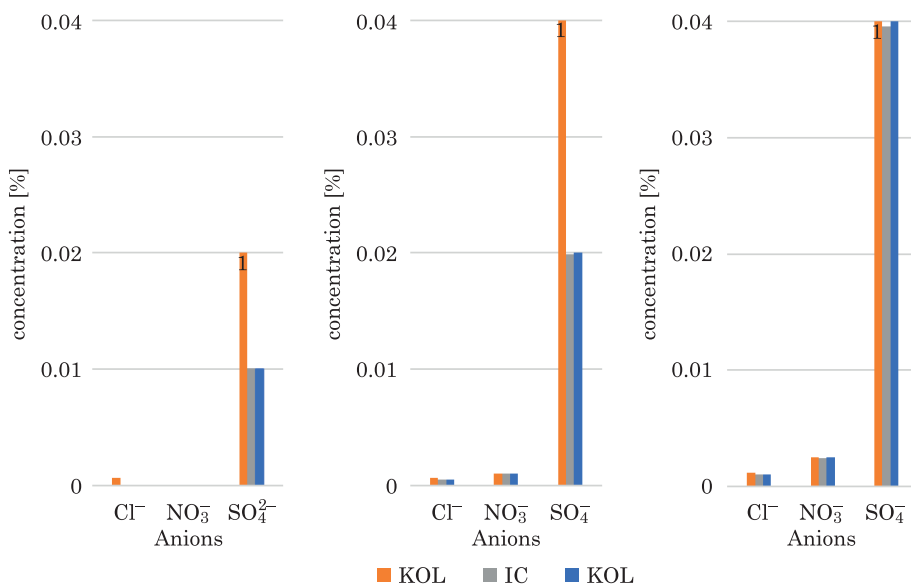
Tests on samples of unknown concentrations were then performed. The salt solutions were extracted from wall drillings of building facilities. 10 g of material was weighed, poured into 100 mL of demineralized water, stirred for 30 s, and filtered through quantitative hard filter papers (type 390, weight 84 g/m<sup>2</sup>). Individual samples (drillings) differed by colours, so they were grouped according to them. In this way, seven groups with three samples each were obtained, on average. An attempt was made to determine the discrepancy between the colorimetric method and ion chromatography results with such a population of results. To this end, the results obtained by the IC method were taken as a reference against which the results obtained in the KOL methods were compared. Deviations from the IC method were obtained.

## Results

### Solutions of Known Concentrations

When testing nitrate concentration, the colorimetric method determined the salt concentration without any error. The colours on the strips matched the standard colours for the individual concentrations (Fig. 3). However, when measuring chloride concentrations with the colorimetric method using titration,

errors have occurred. A so-called blind trial (solution free from the test substance) yielded a positive result. In a sample that did not contain any chlorides, the test detected a concentration of 0.0006%. This is a row of magnitude equal to the test resolution, as concentration is determined by adding drops with a volume equal to 6 mL of reagent (this corresponds to a concentration of 0.0006%). The other deviations resulted from the limitation resulting from constant volume (multiples of 6 mL) (Fig. 3). The greatest difficulties were encountered in the colorimetric sulphate test. Even though we prepared concentrations corresponding to the ranges indicated on the strips, the individual parts acquired imprecise colours. They overstated the values, which were difficult to determine precisely because the subsequent colour (indicative of higher concentrations) was only partially coloured (Fig. 3). To the contrary, the ion chromatography method determined the solutions with a high degree of precision within limits given to prepare the calibration solutions (Fig. 3).



<sup>1</sup>Concentration above the indicated value, slightly coloured towards the next concentration range (strip field)

Fig. 3. Comparison of test results for concentrations of water-soluble salts obtained using the IC and KOL method: *a* – solution no. 1, *b* – solution no. 2, *c* – solution no. 3

## Solutions of Unknown Concentrations

The results obtained for the reference concentration measurement method, IC, fell within the following ranges:

- 0.004-0.565% for chlorides (Appx 1);
- 0.002-1.225% for nitrates (Appx 1);
- 0.009-0.495% for sulphates (Appx 1).

The differences (deviations) in the KOL and IC results were in the range -65%÷50%. The discrepancies ranged from -100% to 100% for nitrates, and -60% to 2,122% for sulphates (Fig. 4, Appx 1). The deviation varied depending on the concentration of the test solution, inversely proportional. As the concentration decreased, the value of the deviation tended to increase. For nitrates and chlorides, this was accompanied by a tendency to increase range. The range of the deviation values for the nitrate test was still within the limit of low and medium salinity (according to WTA), and it was not noticeable at subsequent thresholds. The deviation values read from Figure 4 for each WTA threshold are given in Table 7.

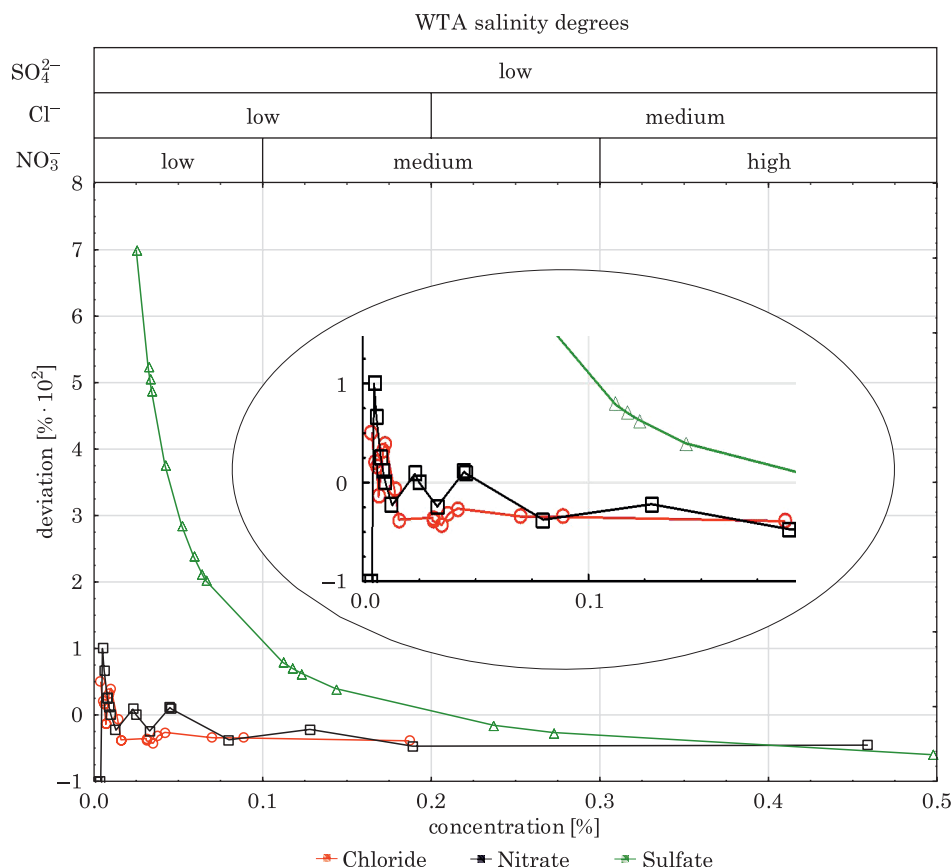


Fig. 4. Deviations in results obtained using colorimetry methods for concentrations of chlorides, nitrates, and sulphates from IC measurements

Table 7

Deviation values for WTA salinity degrees no. 2-9-04		
Salt type	Salinity threshold [%]	Deviation [%]
Chlorides	0.2	-40
Nitrates	0.1	-30
	0.3	-46
Sulphates	0.5	-60

No end of the decreasing trend was observed for chlorides and sulphates. Deviations (negative) may increase as the concentrations of chloride and sulphates increase. For the nitrate test, stabilization of the results was observed at  $-45\pm1\%$ . Nitrate tests posed much more problems in interpretation than in the previous test at known concentrations matching the test ranges. In this respect, there was no difference in the sulphate test.

### Discussion

In the case under analysis, high accuracy in nitrate and chloride measurements was achieved in the range of known concentrations (assigned to scale for colorimetric method tests). The situation significantly changed when solutions with a natural distribution of concentrations obtained from the facility were taken into account, and a significant deviation in the KOL-IC results was observed. A diminishing trend in changes in deviation values as a function of concentrations was observed for all tests. The sulphate test was particularly distinguishing, whereas the variation in deviations was similar for nitrates and chlorides. The scatter of the deviation values appeared similar. As the concentrations increased, the repeatability of the error value increased as well. At salinity thresholds (according to WTA), i.e. 0.2% for chlorides and 0.3%, it presented a high level. Less repeatability in error values was obtained at a salinity level of 0.1% for chlorides and 0.5% for sulphates. Thus, in Table 7, we precisely defined the value of deviations for specific salinity degrees in a way corresponding to error repeatability.

The results obtained using colorimetric methods varied from the conclusions drawn based on the Oberta study. The latter suggested positive deviations exceeding the actual chloride concentrations by more than 36%. However, in a direct study, negative deviations were obtained for WTA salinity thresholds. In the case of nitrates, the deviations were similar to the chloride test. The largest errors were obtained for the sulphate test. For this test, taking measurements proved problematic. The measurement was the most ambiguous because the

fields in the strips were partially coloured, and the resolution was the smallest of all methods.

Underestimated values obtained with the colorimetric method under investigation may be detrimental to the success of repair work on salty walls. A correction may be applied to the colorimetric test to reduce the measurement error, either using the deviations from Table 7 or by determining salt concentration using more accurate methods. Ion chromatography is a well-proven method. It requires a small amount of extract (approximately 1 cm<sup>3</sup>). For tests on historical sites (which require repairs most often), this becomes a major advantage since other methods require more material to be collected. The weighing method requires 50 cm<sup>3</sup> of extract obtained by pouring 1 to 5 g of the sample per 100 cm<sup>3</sup> (DOMASŁOWSKI et al. 2011). Machine price is the major disadvantage of the IC method. However, it is increasingly applicable to testing wall salinity (FRANZONI et al. 2011, FRANZONI et al. 2014, FRANZONI, BANDINI 2012, LUBELLI et al. 2018, LUBELLI 2006, GONÇALVES et al. 2006, CAMUFFO 2018, SARDELLA et al. 2018, SARDELLA et al. 2018, MARAVELAKI-KALAITZAKI et al. 2003, GONÇALVES 2007). However, these colorimetric tests may be a good complement to ion chromatography. Their advantage is that they are dedicated to a specific type of salt. An on-site exam can also be performed. However, when using such tests, attention should be paid to concentration ranges. The upper limit of the Chloride Test in question is 0.2% (200 mg/L). This is merely where mid-range concentrations start, according to WTA. Therefore, it will be impossible to distinguish between average and high salinity and select appropriate components of the renovation system for salty walls.

To be on the safe side, if we roughly assume a very high degree of salinity and it is average, then the costs of the materials used would be unjustifiably high. If, in turn, we attempt to determine salinity when the concentration is out of scale, we would need to keep repeating the test, iteratively approaching the scale through subsequent tests. Samples obtained from drillings taken from the same site must be diluted so that the test covers its range. This can consume large amounts of test material, time and accumulate measurement error due

Table 8

Comparison of salt concentration ranges in colorimetric tests  
with the wall salinity classification by WTA no. 2-9-04

Test	Concentration range
Nitrate Test	0.100-0.250-0.500% (after correction for dilution 1 g-10 dm <sup>3</sup> )
WTA no. 2-9-04	<0.1 (low); 0.1-0.3 (medium); >0.3% (high)
Sulphate Test	0.4->0.8->1.2->1.6% (after correction for dilution 1 g-10 dm <sup>3</sup> )
WTA no. 2-9-04	<0.5 (low); 0.5-1.5 (medium); >1.5% (high)

to successive dilutions of the solution. The same is true for matching the scale on the test strips against the salinity classification used by the WTA. In the case analysed, the scale did not match this classification (Tab. 8). This causes difficulties in accurately determining the salinity degree.

## Conclusions

The use of colorimetric methods for measuring salt concentrations for repairing salty walls using renovation plaster technology should be carefully evaluated in each case. Within certain concentration ranges colorimetric methods can produce results that differ significantly from the actual values. If the colorimetric method underestimates the salt concentration in the wall, there is a risk that the renovation of salty walls using the renovation plaster technology will fail. However, if the test overestimates the concentration, it exposes the investor to unreasonably high costs. This can entail severe financial consequences imposed on the test contractor.

Different colorimetric methods generate different measurement errors. To use a given measurement method, we should learn what the measurement error of the method is. Attention should be paid to the resolution of the test used and to the principles of measurement. Greater accuracy will be obtained if the measurement is performed with a test in which the individual concentration intervals get coloured differently. The more intervals and colours on a strip test, the higher the resolution and accuracy of the measurement. In a sense, one can calibrate a given test with the method presented above. The ion-exchange chromatography can be used as a reference in assessing the accuracy of salt concentration measurements in walls. Samples for testing should be taken from such locations to represent the concentration distribution in the tested facility. If the test results indicate that the test range is too narrow, economic considerations dictate that a test that can determine all salinity levels should be used.

What is important for the application of restoration plaster technology are the deviations of the result obtained by the colorimetric method, which is at the level of the WTA salinity degree thresholds, i.e. concentrations of 0.1; 0.2; 0.3; 0.5% (in mass). They may serve as a correction for the result obtained with a given colorimetric method provided that such deviation shows there is repeatability for successive concentrations. The accuracy of the correction in a given concentration range is obtained in direct proportion to the repeatability of the deviation.

Ion exchange chromatography may also be used as the main measurement method and the colorimetric method as a complementary method. It is especially applicable when dealing with a multi-anion solution with peaks overlapping

on the chromatogram. Assigning specific anions to the individual tests of the colorimetric method may help resolve doubts concerning the assignment of specific anions to peaks on the chromatogram and accelerate analytical work.

### Acknowledgments

I acknowledge any support given by Professor Robert Wójcik, especially for the donation of research materials (powder samples drilled from building wall).

### References


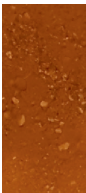
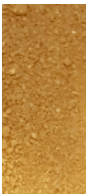
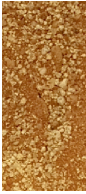
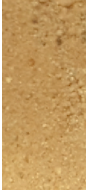
- BLÄUER BÖHM C. 2005. *Quantitative Salt Analysis in Conservation of Buildings*. Restoration of Buildings and Monuments, 11(6): 409-418. <https://doi.org/10.1515/rbm-2005-6001>.
- BORRELLI E. 1999. *Introduction, Salts*. In: *ARC Laboratory Handbook*. 1<sup>st</sup> ed. Eds. Ch. McDowall, C. Rockwell. ATEL S.p.A., 3: 3-24.
- CAMUFFO D. 2018. *Standardization Activity in the Evaluation of Moisture Content*. J. Cult. Herit., 31: S10-S14. <https://doi.org/10.1016/j.culher.2018.03.021>.
- CHAROLA A.E. 2000. *Salts in the Deterioration of Porous Materials: An Overview*. J. Am. Inst. Conserv., 39(3): 327-343. <https://doi.org/10.2307/3179977>.
- DOEHNE E. 2002. *Salt Weathering: A Selective Review*. Geol. Soc. Spec. Publ., 205: 51-64. <https://doi.org/10.1144/GSL.SP.2002.205.01.05>.
- DOMASŁOWSKI W. 2011. *Zabytki kamienne i metalowe, ich niszczenie i konserwacja profilaktyczna*. 1<sup>st</sup> ed. Wydawnictwo Naukowe Uniwersytetu Mikołaja Kopernika, Toruń, p. 1-565.
- FRANZONI E., BANDINI S. 2012. *Spontaneous Electrical Effects in Masonry Affected by Capillary Water Rise: The Role of Salts*. Constr. Build. Mater., 35: 642-646. <https://doi.org/10.1016/j.conbuildmat.2012.04.098>.
- FRANZONI E., BANDINI S., GRAZIANI G. 2014. *Rising Moisture, Salts and Electrokinetic Effects in Ancient Masonries: From Laboratory Testing to on-Site Monitoring*. J. Cult. Herit., 15(2): 112-120. <https://doi.org/10.1016/j.culher.2013.03.003>.
- FRANZONI E., SANDROLINI F., BANDINI S. 2011. *An Experimental Fixture for Continuous Monitoring of Electrical Effects in Moist Masonry Walls*. Constr. Build. Mater., 25(4): 2023-2029. <https://doi.org/10.1016/J.CONBUILDMAT.2010.11.047>.
- GACZEK M., FISZER S. 2014. *Tynki Specjalne*. Część 2. Builder, 6: 60-64.
- GONÇALVES T.D. 2007. *Salt Crystallization in Plastered or Rendered Walls*. Thesis for the degree of PhD, Technical University of Lisbon, Lisbon.
- GONÇALVES T.D., RODRIGUES J.D., ABREU M.M., ESTEVES A.M., SILVA A.S. 2006. *Causes of Salt Decay and Repair of Plasters and Renders of Five Historic Buildings in Portugal*. Proc. Int. Conf. Heritage, Weather. Conserv. HWC 2006, 1 (January): 273-284.
- GOUDIE A., VILES H. 1997. *Salt Weathering Hazard*. Wiley, Chichester, p. 1-256.
- HERODOTUS. 420BC. *Book 2*. The History of Herodotus, 2.
- KNOP K. 2016. *Wyprawy tynkarskie na bazie tynków renowacyjnych*. Renowacje i Zabyt., 4: 186-187.
- KONCA P., MAĆKOWIAK A., KONIARCZYK M. 2016. *Renovation plaster as a protection against salt crystallization induced damage*. J. Civ. Eng. Environ. Archit., 63(3): 177-184. <https://doi.org/10.7862/rb.2016.199>.
- LUBELLI B.A.A. 2006. *Sodium Chloride Damage to Porous Building Materials*. Thesis for the degree of PhD, Delft University of Technology, Delft.
- LUBELLI B., CNUDDÉ V., DIAZ-GONCALVES T., FRANZONI E., VAN HEES R.P.J., IOANNOU I., MENENDEZ B., NUNES C., SIEDEL H., STEFANIDOU M., VERGES-BELMIN V., VILES H. 2018. *Towards*

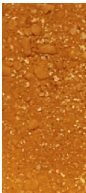
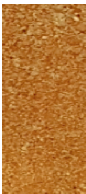
- a More Effective and Reliable Salt Crystallization Test for Porous Building Materials: State of the Art.* Mater. Struct., 51(2): 55. <https://doi.org/10.1617/s11527-018-1180-5>.
- LUQUER L.M. 1895. *The Relative Effects of Frost and the Sulphate of Soda Efflorescence Tests on Building Stones.* Trans. Am. Soc. Civ. Eng., 33(1): 235-247. <https://doi.org/10.1061/TACEAT.0001181>.
- MARAVELAKI-KALAITZAKI, P., BAKOLAS, A., MOROPOULOU, A. 2003. *Physico-Chemical Study of Cretan Ancient Mortars.* Cem. Concr. Res., 33 (5), 651-661. [https://doi.org/10.1016/S0008-8846\(02\)01030-X](https://doi.org/10.1016/S0008-8846(02)01030-X).
- NOCOŃ M. 2016. *System tynków renowacyjnych quick-mix.* Renowacje i Zabyt., 4: 176-179.
- OBERTA W., ŁUKASZEWICZ J.W. 2015. *Badania soli rozpuszczalnych w wodzie za pomocą strefowej elektroforezy kapilarnej.* Acta Univ. Nicolai Copernici, 46: 363-378. [https://doi.org/10.12775/AUNC\\_ZiK.2015.014](https://doi.org/10.12775/AUNC_ZiK.2015.014).
- PAVLÍKOVÁ M., PAVLÍK Z., KEPPERT M., ČERNÝ R. 2011. *Salt Transport and Storage Parameters of Renovation Plasters and Their Possible Effects on Restored Buildings' Walls.* Constr. Build. Mater., 25(3): 1205-1212. <https://doi.org/10.1016/j.conbuildmat.2010.09.034>.
- PEŘINKOVÁ M., DLÁBIKOVÁ I., POSPÍŠIL P., BÍLEK V. 2021. *Research into the Influence of Subsoil on Sulphates, Nitrates and Chlorides Accumulated in Renovation Plasters Used for Rehabilitation of Monuments in the Czech Republic.* J. Cult. Herit., 49: 197-210. <https://doi.org/10.1016/j.culher.2021.01.011>.
- SARDELLA A., DE NUNTIIS P., BONAZZA A. 2018a. *Efficiency Evaluation of Treatments against Rising Damp by Scale Models and Test in Situ.* J. Cult. Herit., 31: S30-S37. <https://doi.org/10.1016/J.CULHER.2018.03.020>.
- SARDELLA A., DE NUNTIIS P., RIZZO M., GIOSUÈ C., TITTARELLI F., BONAZZA A. 2018b. *In Situ Performance Evaluation of Chemical Injections against Rising Damp: A Case Study in Italy.* Measurement, 130: 128-136. <https://doi.org/10.1016/J.MEASUREMENT.2018.08.011>.
- STILLHAMMEROVÁ M. 2006. *Short Overview on Problems of Water Soluble Salts in Slovak Republic.* European Research on Cultural Heritage, 5: 119-123.
- WTA Merkblatt 2-9-04 Sanierputzsysteme. 2004. Wissenschaftlich-Technische Arbeitsgemeinschaft für Bauwerkserhaltung und Denkmalpflege, München.
- WÓJCIK R. 2006. *Anti-damp wall protection using the non-isothermal injection method.* Thesis for the degree of associate professor, University of Warmia and Mazury in Olsztyn, Olsztyn.
- WÓJCIK R. 2010. *Ochrona budynków przed wilgocią i wodą gruntową.* In: *Budownictwo ogólne. Fizyka budowli.* Vol. 2. 1<sup>st</sup> ed. Eds. J. Panas, M. Siarkiewicz. Arkady, Warszawa, p. 913-981.



## Appendix 1

Comparison of test results for concentrations (in mass) of water-soluble salts obtained using the IC and KOL method

Group		Sample	Concentration of chlorides [%]		Concentration of nitrates [%]		Concentration of sulphates [%]	
No.	Photo	No.	KOL	IC	KOL	IC	KOL	IC
1	2	3	4	5	6	7	8	9
1		15/100B/40-70	0.006 (-14) <sup>1</sup>	0.007	0.010 (25) <sup>1</sup>	0.008	0.200 (1900) <sup>1</sup>	0.010
		14/10A/40-160	0.007 (17) <sup>1</sup>	0.006	0.010 (0) <sup>1</sup>	0.010	0.200 (213) <sup>1</sup>	0.064
		1/100B/40-151	0.020 (-35) <sup>1</sup>	0.031	0.050 (11) <sup>1</sup>	0.045	0.200 (40) <sup>1</sup>	0.143
2		4/100B/10-130	0.058 (-35) <sup>1</sup>	0.089	0.100 (-47) <sup>1</sup>	0.189	0.200 (71) <sup>1</sup>	0.117
		14/10A/10-157	0.006 (50) <sup>1</sup>	0.004	0.000 (-100) <sup>1</sup>	0.002	0.200 (2122) <sup>1</sup>	0.009
		5/100B/40-34	0.006 (-14) <sup>1</sup>	0.007	0.010 (67) <sup>1</sup>	0.006	0.200 (2122) <sup>1</sup>	0.009
3		9/100B/10-103	0.200 (-65) <sup>1</sup>	0.565	0.500 (-59) <sup>1</sup>	1.225	0.200 (-60) <sup>1</sup>	0.497
		4/10A/80-135	0.010 (-38) <sup>1</sup>	0.016	0.010 (100) <sup>1</sup>	0.005	0.200 (700) <sup>1</sup>	0.025
		14/10A/80-163	0.012 (-33) <sup>1</sup>	0.009	0.010 (-23) <sup>1</sup>	0.013	0.200 (63) <sup>1</sup>	0.123
4		8/10A/40-114	0.026 (-32) <sup>1</sup>	0.038	0.050 (-38) <sup>1</sup>	0.080	0.200 (376) <sup>1</sup>	0.042
		15/100B/10-67	0.013 (-7) <sup>1</sup>	0.014	0.025 (-24) <sup>1</sup>	0.033	0.200 (506) <sup>1</sup>	0.033
		14/200C/10-159	0.007 (17) <sup>1</sup>	0.006	0.010 (11) <sup>1</sup>	0.009	0.200 (-26) <sup>1</sup>	0.272
5		11/100B/10-94	0.020 (-43) <sup>1</sup>	0.035	0.100 (-22) <sup>1</sup>	0.128	0.200 (203) <sup>1</sup>	0.066
		18/10A/40-42	0.031 (-26) <sup>1</sup>	0.042	0.250 (-46) <sup>1</sup>	0.459	0.200 (-16) <sup>1</sup>	0.237
		18/10A/1-39	0.046 (-34) <sup>1</sup>	0.070	0.500 (-41) <sup>1</sup>	0.842	0.200 (239) <sup>1</sup>	0.059

cont. Appendix 1								
1	2	3	4	5	6	7	8	9
6		8/10A/80-117	0.010 (-38) <sup>1</sup>	0.016	0.010 (25) <sup>1</sup>	0.008	0.200 (79) <sup>1</sup>	0.112
		10/10A/80-181	0.006 (20) <sup>1</sup>	0.005	0.000 (-100) <sup>1</sup>	0.004	0.200 (525) <sup>1</sup>	0.032
		4/200C/40-134	0.019 (-39) <sup>1</sup>	0.031	0.050 (9) <sup>1</sup>	0.046	0.200 (488) <sup>1</sup>	0.034
7		11/100B/40-97	0.014 (40) <sup>1</sup>	0.010	0.025 (0) <sup>1</sup>	0.025	0.200 (1011) <sup>1</sup>	0.018
		1/10A/10-147	0.114 (-39) <sup>1</sup>	0.187	0.025 (9) <sup>1</sup>	0.023	0.200 (285) <sup>1</sup>	0.052

<sup>1</sup> The value in brackets refers to the difference (deviation) between the results obtained using the KOL and IC methods

## TRIBOLOGICAL WEAR OF FE-AL COATINGS APPLIED BY GAS DETONATION SPRAYING

*Tomasz Chrostek*

ORCID: 0000-0002-6516-8192

Department of Materials and Machinery Technology  
University of Warmia and Mazury in Olsztyn

Received 21 September 2021, accepted 19 November 2021, available online 30 November 2021.

**Key words:** Gas Detonation Spraying, Coating, Fe-Al, intermetallic alloys, tribology.

### Abstract

Comparative tests of gas detonation (GDS) coatings were carried out in order to investigate the influence of spraying parameters on abrasive wear under dry friction conditions. The tests were carried out using the pin-on-disc (PoD) method at room temperature. The microstructure of the coatings was analysed by X-ray diffraction (XRD) and scanning electron microscopy (SEM/EDS) methods. The results showed that with certain parameters of the GDS process, the main phase of the produced coatings is the FeAl phase with the participation of thin oxide layers, mainly  $\text{Al}_2\text{O}_3$ . The tribological tests proved that the coatings sprayed with the shorter barrel of the GDS gun showed higher wear resistance. The coefficient of friction was slightly lower in the case of coatings sprayed with the longer barrel of the GDS gun. During dry friction, oxide layers form on the surface, which act as a solid lubricant. The load applied to the samples during the tests causes shear stresses, thus increasing the wear of the coatings. During friction, the surface of the coatings is subjected to alternating tensile and compressive stresses, which lead to delamination and is the main wear mechanism of the coatings.

## Introduction

Despite the low production costs, the industrial application of solid FeAl alloys is limited due to low ductility and resistance to cracking at room temperature. The research proved that Fe-Al coatings sprayed with supersonic methods solve the problems encountered in the production of these alloys using the traditional method (CHROSTEK 2020, SENDEROWSKI et al. 2016). In addition, the Fe-Al phase-matrix intermetals produced by the GDS method are a material with unique properties. They are resistant to high-temperature corrosion (heat resistance) in aggressive sulphide and chloride environments (SENDEROWSKI 2015). This creates potential opportunities for their use as heat-resistant construction materials (PANAS et al. 2019).

The reason for this is that the FeAl powder particles are subjected to strong oxidation in a hot stream of gaseous products of supersonic combustion detonation. This results in the formation of a multiphase coating structure with the participation of oxide phases formed at the grain boundaries in the form of thin films, due to the strong plastic deformation of the powder particles forming the coating. The grains of primary particles change their morphology from equiaxial to streaked during strong plastic deformation (CHROSTEK 2020, FIKUS et al. 2019, SENDEROWSKI et al. 2011).

Most of the research work focuses on the characteristics of the microstructure and thermophysical properties of the resulting coatings, forgetting about their functional properties. (BINSHI et al. 2004). However, from such coatings, above all, high wear resistance is expected (BOJAR et al. 2002), therefore the aim of this article is to investigate and compare the dry friction abrasive wear of GDS spray coatings with different spraying parameters.

## Materials and Method

The research was carried out on intermetallic protective coatings produced by the GDS method from alloy powder on a FeAl phase matrix with the composition Fe<sub>40</sub>Al<sub>10.05</sub>Zr % at. and 50 ppm B, produced by the company LERMPS-UTBM by the VIGA method (Vacuum Induction Melting and Inter Gas Atomization). The base material is 13CrMo4-5 (15HM) boiler steel with dimensions of 50×50×5 mm, which was blasted with electro corundum immediately before the spraying process. The surface roughness after sandblasting of the substrate was  $Ra = 18.98 \mu\text{m}$ . The coating in the form of a circular deposit (CHROSTEK 2020) was sprayed with the substrate stationary in relation to the barrel of the detonation gun operating at a frequency of 6.66 Hz. The barrel of the GDS gun was positioned at a distance  $L = 110 \text{ mm}$  of from the sprayed surface. Two barrel lengths were used, 590 and 1090 mm. All the GDS spraying parameters presented

above, together with the composition of the explosive detonation mixture and the flow of air transporting the powder, are presented in Table 1. The GDS spraying of the FeAl coating was performed by the Department of Protective Coatings – E.O. Paton Electric Welding Institute of the National Academy of Sciences of Ukraine, using the “Perun S” detonation gun.

Table 1

GDS spraying parameters				
Powder Fe40Al0,05Zr at.%+50 ppm B; particle size distribution (granulation) 5-40 $\mu\text{m}$				
Powder transporting gas – air			0.4 $\text{m}^3/\text{h}$	
Oxygen-fuel mixture			$\text{C}_3\text{H}_8$ – 0.45 $\text{m}^3/\text{h}$ $\text{O}_2$ – 1.52 $\text{m}^3/\text{h}$ air (as diluter gas) – 0.65 $\text{m}^3/\text{h}$	
Spraying frequency			$f = 6.66 \text{ Hz}$	
Coating	spraying distance $L$ [mm]	barrel length [mm]	PIP* [mm]	number of GDS shots
A	110	590	274.5	100
B		1,090	274.5	400
C		1,090	412.5	100
D		590	412.5	400

\* powder injection position – place of the introduction of the powder into the barrel at the time of detonation

The structural tests of the coatings were carried out using scanning electron microscopy with X-ray microanalysis (SEM/EDS) and X-ray diffraction (XRD). The point analysis and surface distributions of specific alloying elements were performed on a Quanta 3D FEG Dual Beam high-resolution scanning electron microscope with SE (secondary electron detector) and BSE (backscattered electron detector) detectors. SEM/EDS chemical composition studies in micro-areas were carried out using the EDAX Genesis Spectrum analyzer.

XRD tests were carried out using a Rigaku Ultima IV diffractometer with a  $\text{CoK}_\alpha$  monochromatic radiation focusing beam with a spectral wavelength  $\lambda = 0.178897 \text{ nm}$ . Filtering corresponding to the  $\text{CoK}_\alpha$  wave was used with the lamp operating conditions of 40 kV/40 mA. A record was made in the angular range from  $20^\circ$  to  $120^\circ$  with a scanning speed of  $1^\circ/\text{min}$ .

Microhardness measurements were made using the Vickers method using the Innovatest 400-DAT microhardness tester, at a load of 0.98 N (HV0.1) for 10 s, in accordance with the PN EN ISO 6507-1: 2007 standard. The research was carried out in a cross-section on polished metallographic specimens in a plane perpendicular to the applied Fe-Al coatings. The microhardness distribution

measurements were carried out with a step of 0.1 mm from the substrate towards the coating surface along three measurement paths spaced 0.1 mm apart.

Abrasive wear tests in dry friction conditions using the pin-on-disc method were performed on a Tribotester T-10 in dry sliding conditions at room temperature (20°C). The relative humidity of the ambient atmosphere was 50%. The sample was a pin with a diameter of  $\varnothing 7$  mm. Two samples were taken from each coating, which constituted a significant area of it (the diameter of the coating was  $\varnothing 25$  mm). EDM cutting was used. A pearlitic cast iron disc with a hardness of 33 HRC was used as a counter-sample. The radius of rotation was  $r = 18$  mm, which at the rotational speed of  $v_r = 48$  rpm gave the sliding speed  $v = 0.09$  m/s. The total friction path was 1,040 m, which each sample traveled during  $t = 11,500$  s (approx. 3 h). The pins were subjected to a load of  $F = 20$  N. The coefficient of friction was computer-monitored during the test by measuring the elastic deflection of the arm. The T-10 device is equipped with a measurement and control system, which includes: a set of measuring transducers, a computer with dedicated measurement and recording software (Fig. 1a, b). During the course of the test, the wear products from the friction junction were not removed in order to best reflect the actual conditions. Wear products always remain between the two materials during friction (Fig. 1c).

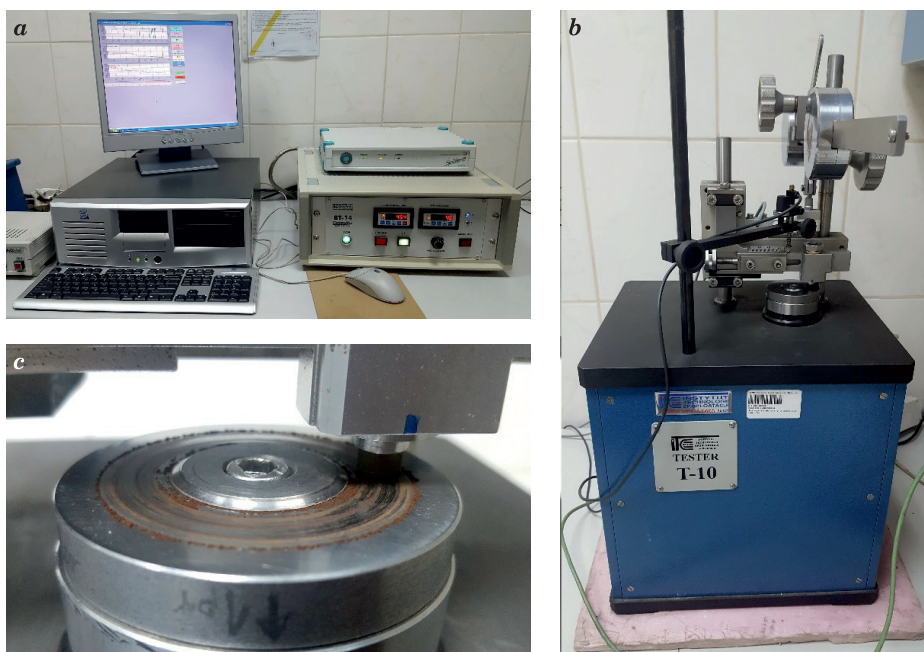


Fig. 1. Apparatus for abrasive wear tests using the pin-on-disc method: a – computer with a control controller, b – T-10 tester, c – visible oxidation of the surface layer of metal elements during the pin-on-disc measurement

## Results and Discussion

The XRD tests of the coatings (Fig. 2) indicate the presence of the FeAl phase as the basic component of the structure. At the same time, the share of  $\text{Fe}_3\text{Al}$  phase was confirmed. The presence of oxide phases FeO,  $\text{Fe}_3\text{O}_4$ ,  $\text{Al}_2\text{O}_3$  and spinel  $\text{Fe}(\text{Al}_2\text{O}_4)$  was also detected.

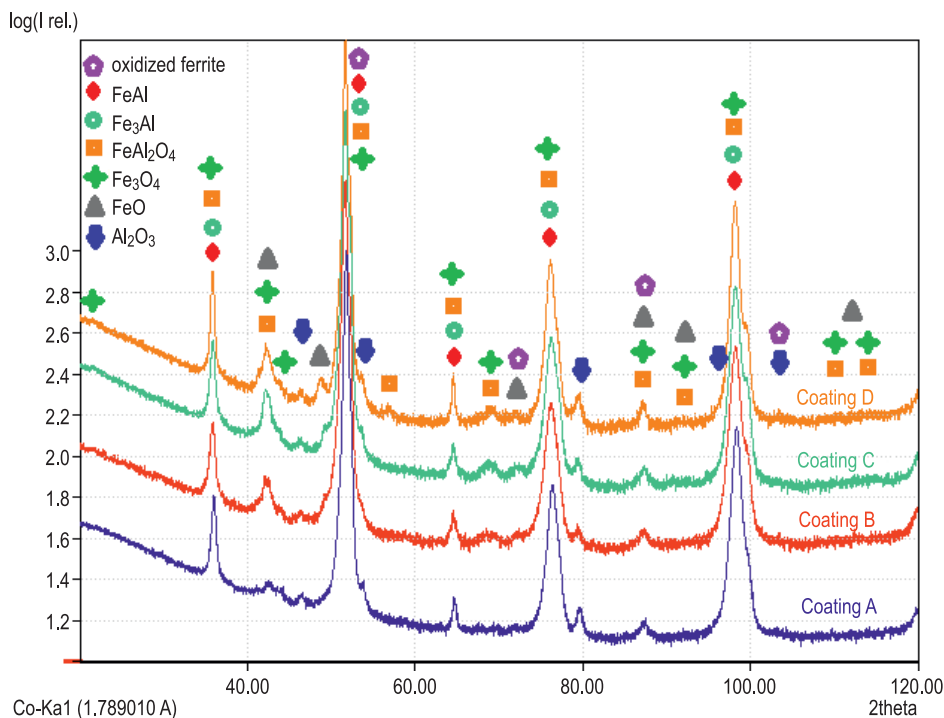


Fig. 2. XRD analysis of the phase composition of FeAl coatings produced by the GDS method

Figure 3a shows a photo of the SEM/EDS microanalysis that was performed on the surface of the coating. The powder particles melt or completely melt, resulting in a strong oxidation of the diffusing aluminum and the formation of FeO (1) and  $\text{Al}_2\text{O}_3$  (2) oxide phases on the surface of the molten particles. Structural studies carried out on the cross-section (Fig. 3b, c) show a typical lamellar structure with different (multi-phase) chemical composition, where we can distinguish the basic phase FeAl (3),  $\text{Al}_2\text{O}_3$  (6), oxidized ferrite (1),  $\text{Fe}_3\text{Al}$  (2), FeO,  $\text{Fe}_3\text{O}_4$  (4) and  $\text{Fe}(\text{Al}_2\text{O}_4)$ .

The content of alloy elements and oxygen mapped in the SEM/EDS microanalysis of chemical composition at the cross-section of FeAl coating (GDS) is presented in Table 2.



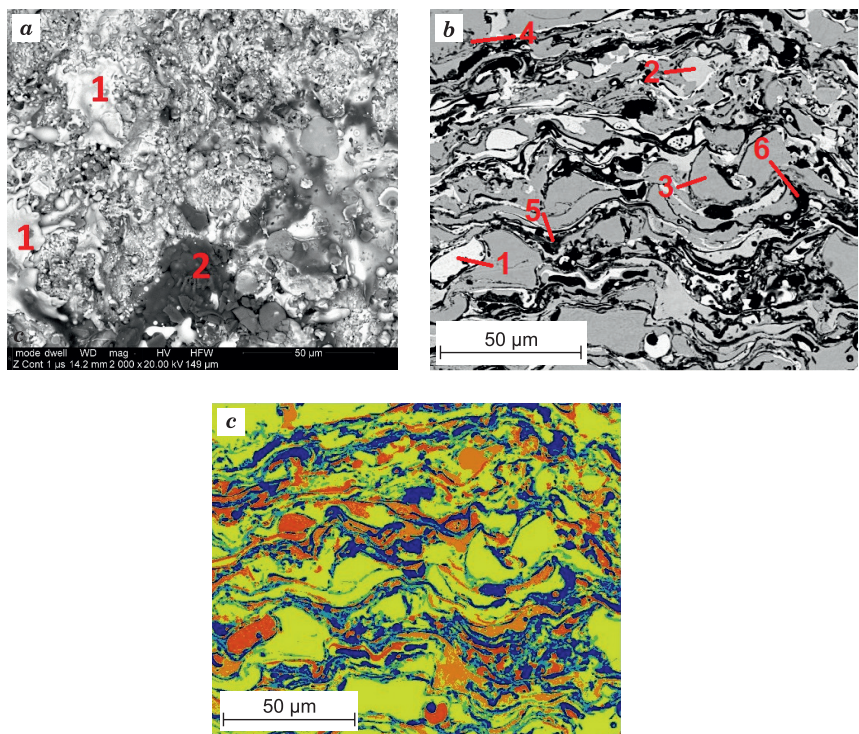


Fig. 3. SEM/EDS microanalysis of Fe-Al coatings formed in the GDS process:  
a – coating surface, b and c – coating cross-section

Table 2

Content of alloy elements and oxygen mapped in the SEM/EDS microanalysis of chemical composition at the cross-section of FeAl coating (GDS) (Fig. 3c)

Analyzed region on coating surface	Content of alloy elements [% at.]			Probable phase
	Fe	Al	O	
Blue	0.89	48.02	51.09	Al <sub>2</sub> O <sub>3</sub> phase
Light blue	22.10	35.12	42.78	Fe(Al <sub>2</sub> O <sub>4</sub> ) phase
Green	49.21	11.16	39.63	FeO, Fe <sub>3</sub> O <sub>4</sub> oxide phases
Yellow	55.88	40.59	3.53	weakly oxidized FeAl phase
Orange	76.86	18.79	4.35	weakly oxidized Fe <sub>3</sub> Al phase
Red	92.64	1.14	6.22	oxidized ferrite



The presence of very hard oxide phases in the coating structure has a significant impact on the degree of hardening of the produced coatings. For this purpose, the cross-sectional microhardness of the coatings was tested by making three measurement paths from the steel substrate to the top layer of the coating, at intervals of 0.1 mm (Fig. 4).

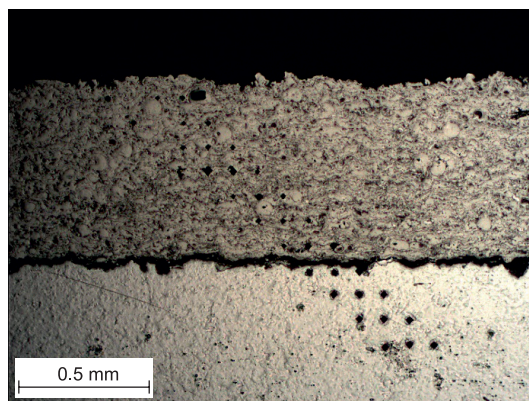


Fig. 4. Measurements of microhardness using the Vickers method on the cross-section of the coating A

The results obtained (Fig. 5) show a large difference in hardness in the multiphase coating structure from about 300 to 650 HV0,1 (ignoring the extremely low values caused by the porosity of the coating). The highest values are shown in strongly oxidized (dark) areas. The areas with phases with high iron content

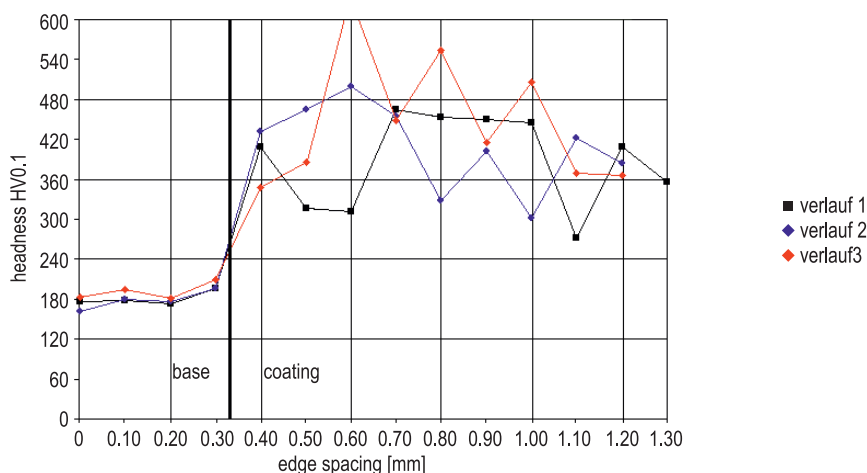


Fig. 5. Distribution of the microhardness HV0.1 of coating B along three parallel measuring paths

and low oxygen content show the lowest hardness. The average value of the microhardness of coatings made with a shorter barrel (590 mm) is 448 HV0.1, while the microhardness of coatings made with a longer barrel (1,090 mm) is 427 HV0.1. These values are much higher than the microhardness of the powder charge  $230 \pm 10$  HV0.1 (Fig. 6).

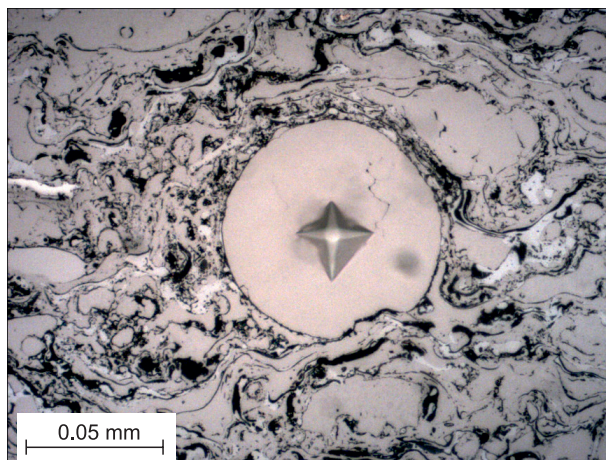


Fig. 6. An example of a microhardness measurement carried out using the Vickers method on the cross-section of an unfused powder particle, performed on coating A

The oxide phases  $\text{Al}_2\text{O}_3$ ,  $\text{FeO}$ ,  $\text{Fe}(\text{Al}_2\text{O}_4)$  occurring in the coating, also dispersed in micro-areas, are the main reason for the high hardness of intermetallic coatings produced by the GDS method.

The pin-on-disc (PoD) method is a commonly used technique to determine the friction coefficient  $\mu$  and wear under various tribological conditions. These studies allowed to determine the influence of the oxide phases on the functional properties of the cermet structure of the coating under conditions of abrasive wear during dry friction.

Figure 7 shows the evolution of the friction coefficient  $\mu$  as a function of the sliding distance. All tests showed a similar change in the coefficient of friction. In the first phase, an increase is visible up to about 15 minutes, followed by a second stabilization phase with slight fluctuations in value. The first phase is a typical run-in phenomenon where the surface topography changes until the system reaches steady state.

The high hardness of GDS coatings, determined by the structure with the participation of oxide ceramics, is also the direct cause of the high abrasive wear resistance of this type of coating under dry friction conditions. It can be assumed that the coefficient of friction  $\mu$  (Fig. 8) would be higher with

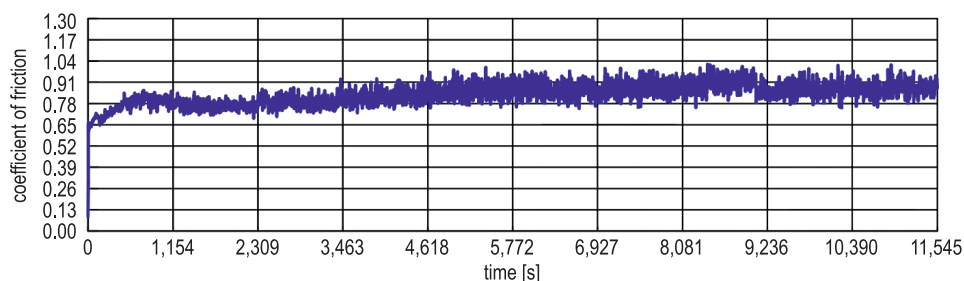


Fig. 7. Spindle sliding wear test on the disc: coefficient of friction as a function of the slip time of the coating *D* produced by the GDS method

the application of lower loads (the tests were carried out with a high unit load of the sample with the force  $F = 20$  N). As the load increases, the friction coefficient decreases slightly due to the increase in the friction contact temperature and the formation of larger surfaces of the oxide layer on the worn surface, which acts as a lubricant (Fig. 9) (BINSHI et al. 2004).

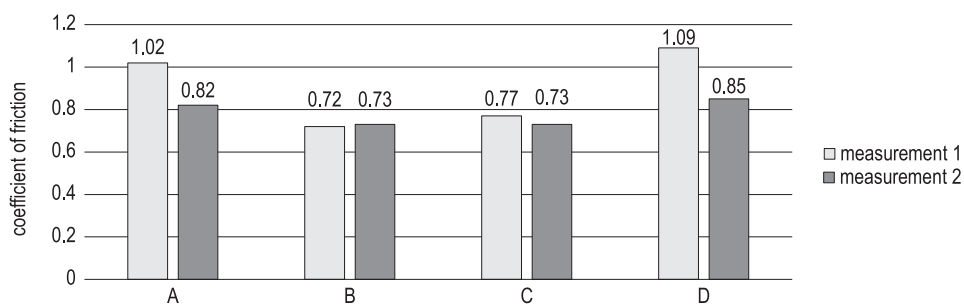


Fig. 8. Average coefficients of friction of the tested coatings at a constant load of  $F = 20$  N

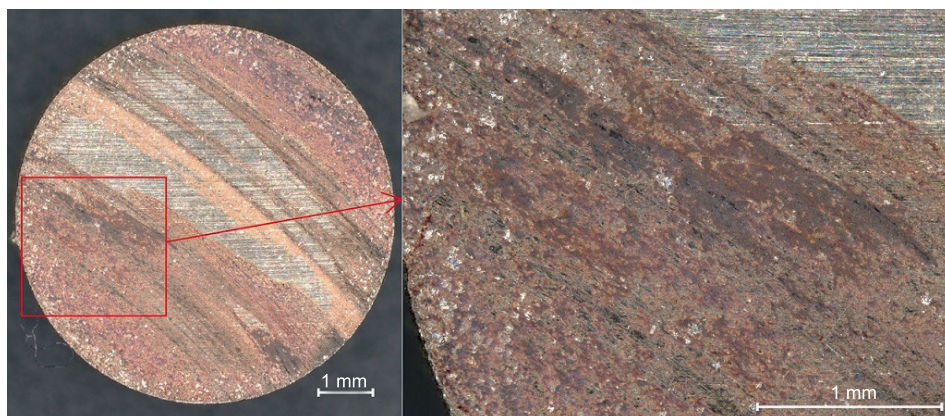


Fig. 9. Fe-Al coating of sample *B* after tribological tests with a visible oxide film on the surface

The sliding wear test shows changes in the wear rate of Fe-Al coatings under constant load. As shown in Figure 10, the greatest increase in wear occurs in the first stage of the test (up to about 10 minutes). Then the formation of a layer of oxides detaching from the surface of the sample slows down this process. The excess of accumulated powdered material (visible in the graph in the range from 2,309 s to 3,463 s) is pushed to the sides (Fig. 1c), which contributes to a further increase in consumption.

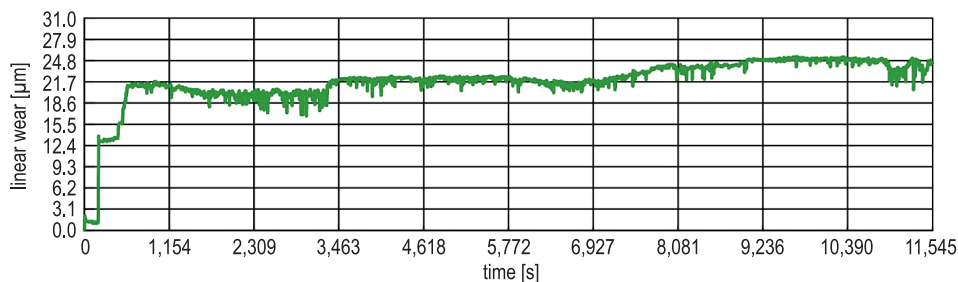


Fig. 10. Pin sliding wear test on the disc: linear wear as a function of the slip time of the coating C produced by the GDS method

The results of the research revealed that the length of the detonation gun barrel was of considerable importance for the strengthening of the structure. The coefficient of friction is clearly higher in the coatings sprayed with a shorter barrel (590 mm). This is also reflected in the wear of the coatings. The consumption of coatings A and D is much lower (Fig. 11). This shows that the use of a shorter barrel clearly increases the wear resistance of the GDS coating, despite the similar proportion of oxide phases in all tested coatings.

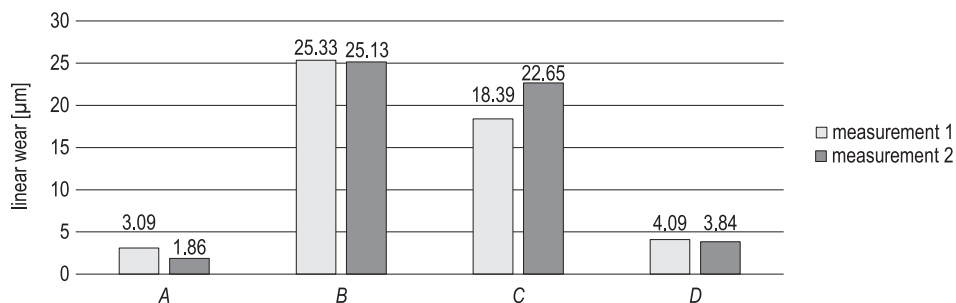


Fig. 11. Average rates of linear wear of the tested coatings at a constant load of  $F = 20$  N

Despite the low porosity (SENDEROWSKI 2015), individual grains are torn out of the matrix (Fig. 12). The reasons for this are: the high coefficient of friction ( $\mu = 0.72$ -1.09) (Fig. 8) and the brittleness of this type of coatings due to the high percentage of oxide ceramics. In addition, high loading causes maximum

shear stress, thereby increasing wear. During sliding, the surface of the coating is subjected to alternating tensile and compressive stresses, so delamination seems to be the dominant wear mechanism of the coatings.

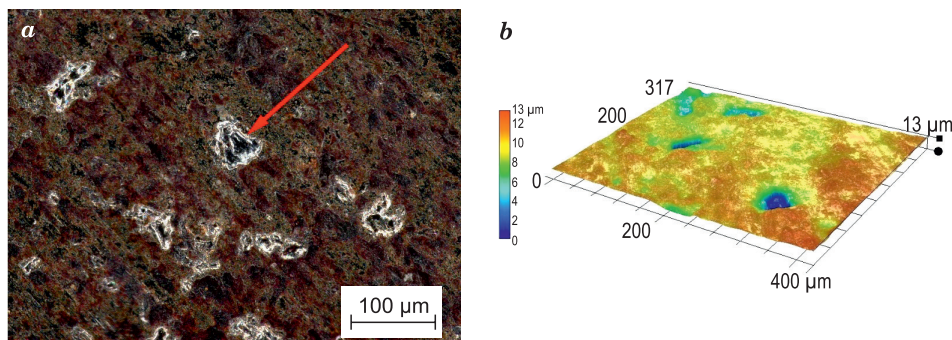


Fig. 12. Morphology of Fe-Al coatings of sample *B* produced by GDS method after wear tests: *a* – visible grains torn out from the matrix, *b* – 3D map of the area under study

## Conclusions

Tribological tests carried out on coatings produced with the gas detonation method (GDS) under dry friction conditions made it possible to compare the wear of the coatings with the use of various spraying parameters.

All tested coatings, regardless of the spraying parameters, have a lamellar structure, typical for coatings sprayed with supersonic methods. The basic structure is the FeAl phase. During the formation of the coating, changes occur with the participation of oxygen, during which oxide phases  $\text{Al}_2\text{O}_3$ ,  $\text{Fe}_3\text{O}_4$ , FeO,  $\text{Fe}(\text{Al}_2\text{O}_4)$  and phases poor in iron or aluminum are formed.

Coatings sprayed with a shorter barrel, 590 mm long, showed significantly higher wear resistance, despite the fact that the coefficient of friction was similar for both groups of materials.

Compressive and tensile stresses acting on the samples during the tests, as well as oxidized wear products in the friction area, led to material chipping, which is the main wear mechanism of the coatings. No cracks were observed in the coating structure.

The research proved that with properly selected spraying parameters, Fe-Al alloys in the form of protective coatings can have high abrasion resistance, also at room temperature.



## References

- BINSHI X., ZIXIN Z., SHINING M., WEI Z., WEIMIN L. 2004. *Silding wear behawior of Fe-Al and Fe-Al/WC coating prepared by high velocity arc spraying*. Wear, 257: 1089-1095.
- BOJAR Z., SENDEROWSKI C., DUREJKO T. 2002. *Structure and tribological properties of FeAl-based intermetallic coatings sprayed on steel substrate*. International Journal of Applied Mechanics and Engineering, 7: 335-340.
- CHROSTEK T. 2020. *Structural analysis of Fe-Al coating applied by gas detonation spraying*. Technical Sciences, 23(3): 221-232.
- FIKUS B., SENDEROWSKI C., PANAS A.J. 2019. *Modeling of Dynamics and Thermal History of Fe40Al Intermetallic Powder Particles Under Gas Detonation Spraying Using Propane-Air Mixture*. Journal of Thermal Spray Technology, 28(3): 346-358.
- PANAS A.J., SENDEROWSKI C., FIKUS B. 2019. *Thermophysical properties of multiphase Fe-Al intermetallic-oxide ceramic coatings deposited by gas detonation spraying*. Thermochemica Acta, 676: 164-171.
- SENDEROWSKI C. 2015. *Żelazowo-aluminiowe intermetaliczne systemy powłokowe uzyskiwane z naddźwiękowego strumienia metalicznego*. Bel Studio Sp. z o.o., Warszawa.
- SENDEROWSKI C., ASTRACHOV E., BOJAR Z., BORISOV Y. 2011. *Elementarne mechanizmy formowania powłoki intermetalicznej Fe-Al podczas natryskiwania gazodetonacyjnego*. Inżynieria materiałowa, 32(4): 719-723.
- SENDEROWSKI C., DUREJKO T., ZASADA D., NAPADLEK W., BOJAR Z. 2016. *Structure and properties of the FeAl (HVOF, HVOF, DGS) coating for power industry*. Inżynieria Materiałowa, 6(214): 283-288.



Yearbook peer-reviewed scientific journal

ISSN 1505-4675  
e-ISSN 2083-4527

**TECHNICAL SCIENCES**

Homepage: <https://czasopisma.uwm.edu.pl/index.php/ts/>



DOI: <https://doi.org/10.31648/ts.6804>

## INFLUENCE OF GEOMETRIC FEATURES ASSOCIATIVITY OF CAD CLASS MODELS ON THE PROCESS OF THEIR UPDATING – COMPARATIVE ANALYSIS

*Grzegorz Świaczny*

ORCID: 0000-0002-2966-9344

Department of Fundamentals of Machinery Design  
Silesian University of Technology in Gliwice

Received 12 June 2021, accepted 29 November 2021, available online 30 November 2021.

**Key words:** associativity, parametrization, 3D model, CAD.

### Abstract

This article deals with the topic of one of the most important features of modern CAX class systems – associativity. The term refers to the ability to form relations (links) between two or more objects (in terms of their selected features), and with the consequence creating an associative (linked) three-dimensional model. The author pays special attention to the very process of creating relations between objects, as it has a key impact on the structural stability of CAD class models, and thus on their susceptibility to possible modifications. To show that not all associativity brings a positive effect, the author presents two examples of its implementation. In order to emphasize the influence of the method of linking individual elements, both examples are based on the same 3D model – a thin-walled part with a positioning pin. That means the geometric form of the default part is the same, whereas only relations of the individual objects of the 3D model change. In the first scenario, correctly defined relations between objects make that the positioning pin offset does not affect the initial design conditions. The second scenario shows an incorrect implementation of associativity, as a result of which the same operation of positioning pin offset gives non-compliance with the initial design conditions and with the consequence an undesirable change in its geometry.

The article is an attempt to draw attention to the fact that the associative structure of 3D models is not always equal to the optimal solution. Only the well-thought-out nature of associativity allows to use all its advantages.

---

Correspondence: Grzegorz Świaczny, Katedra Podstaw Budowy Maszyn, Wydział Mechaniczny Technologiczny, Politechnika Śląska, ul. Konarskiego 18a, 44-100 Gliwice, email: [grzegorz.swiaczny@gmail.com](mailto:grzegorz.swiaczny@gmail.com).

## Introduction

The efficiency of application of CAx systems is a fundamental matter when considering on the topic of optimization of the design process. The choice of the right software and defining the methodology of work in this software can significantly contribute to accelerating the project implementation, reducing its costs, and increasing the quality of the final product. According to the author, it should be assumed that a modern CAx class system is an extensive tool that allows to create optimal engineering solutions. That means the sources of any difficulties and problems when creating 3D models and when implementing further changes to these models should not be attributed to the properties of the CAx system used. Moreover, the difficulties arising in the design process should not be excused by its limitations (WELYCZKO 2005). Assuming that the earlier mentioned selection of software was made in accordance with the nature of the designed products, the constructor of these models should be responsible for the cause of the vast majority of problems arising in working with CAD models. „The vast majority”, because it should be also assumed a certain minimum margin of error on the software side. On the other hand, the optimal structure of the 3D model creates a kind of synergy with the individual geometric features from which it is created, which in turn harmonizes with the architecture of the CAx system in which it was created. As a result, the occurrence of a possible error should be an indication to the constructor that there is a possibility to optimize the „3D model structure tree”.

At this point we begin to dive into more detailed construction terminology. Let us therefore focus on the most important issues from the point of view of the discussed topic.

## Materials and Methods

To better understand what an associativity is and why CAD class models use it in a better or worse way, it is worth to explain two additional terms.

The first of them is – already mentioned in the previous chapter – the **3D model structure tree**. Each 3D model in the CAD environment consists of hierarchically functions following one after another, which are saved in the form of a “tree” structure during its creation (Fig. 1).

The tree in its intent is supposed to record the history of this process, and with the consequence, to help constructor to identify the way of creating 3D model. What is important, that the 3D model structure tree created in this way allows to modify this model by editing, adding, or removing selected functions which create that tree (ŚWIACZNY, WYLEŻOŁ 2020a, 2020b). The modification



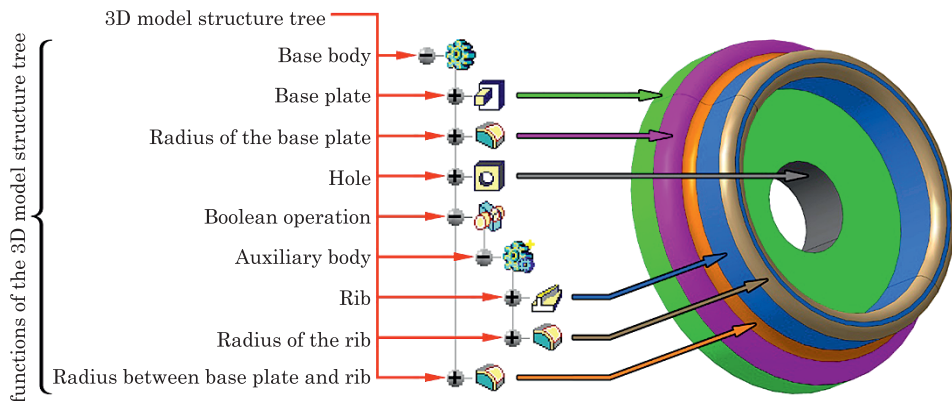


Fig. 1. An example of 3D model structure tree

process is laborious and error-prone because constructors have to repetitively edit and update CAD models. For example, the creation of cooling-holes/channels of injection mold entails several time-consuming and manual tasks, such as creating holes, maintaining the connections among them to form circuits. If these tasks can be partially automated, the design time can be reduced considerably and hence the productivity enhanced (MA, TONG 2003). The art of effective creation of CAD class models consists in preparing the structure tree in such a way that the modifications of these models, inevitable in the construction process, require a minimum involvement of the constructor (WELYCZKO 2005).

During adding further functions of the 3D model structure tree, the constructor uses the basic feature of the modern CAX class system – **parameterization** – to characterize them. Parameterization (which is the second term worth mentioning) is a feature of CAX systems that allows to define the created geometric objects by assigning them parameters such as dimension, logical value, material, or text. Modification of values of these parameters modifies the geometric objects to which they have been assigned. Moreover, by using these parameters, thanks to methodology implemented in modern CAX systems called Knowledge-Based Design (or Knowledge-Based Product Development), it is possible to create formulas, rules, checks, relations, and finally to create catalogs of 3D models (WYLEŻOŁ 2002). The term parametric design in engineering is a process of designing with parametric models in a virtual surrounding (a “parametric CAD system”) where geometrical and parameter variations are natural. In design a parameter is an entity that can hold a value to control geometrical components or relations between geometrical components. Parametric design implies the use of declared parameters to define a form (SALEHI, MCMAHON 2009).

The simplest example of using parameterization can be process of contour dimensioning. The rectangle shown in Figure 2 has a certain length and width. Their modification modifies the rectangle (Fig. 3).

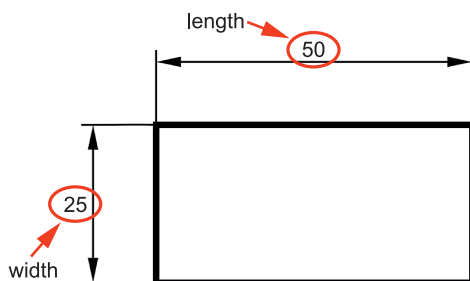


Fig. 2. Dimensioned rectangle as an example of using parameterization

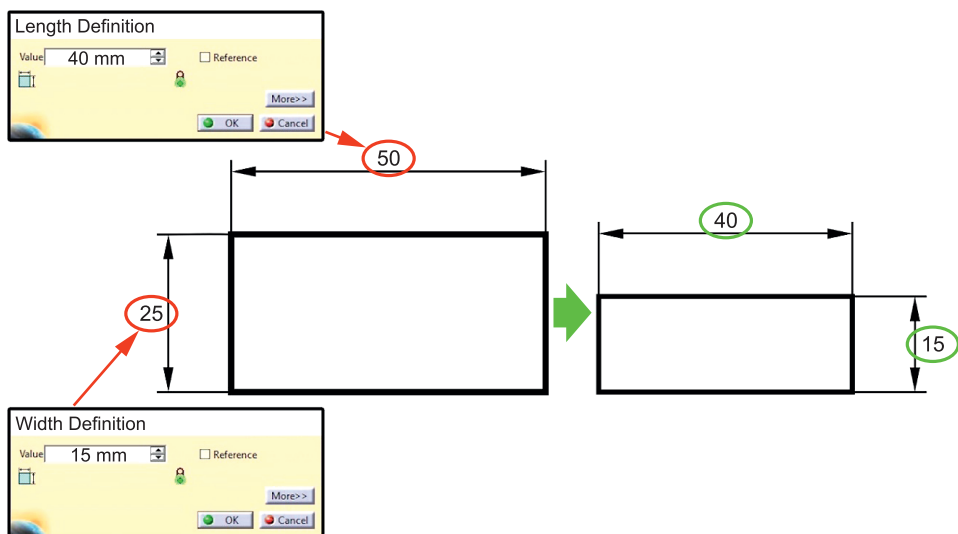


Fig. 3. Modification of rectangle parameters which causes the change of its geometry

What then is **associativity** itself? In most general, associativity connects the two functionalities described above and means the ability to create links between previously defined parameters, but also between individual geometric features, and even between individual 3D models or their assemblies. Related to the design process, associativity describes the fixed relationship between geometrical entities and objects (SALEHI, MCMAHON 2009). If, for example, the previously defined rectangle (Fig. 3) is used to create a cuboid, it will turn out that these two objects will be linked to each other in such a way that the rectangle will be superior to the cuboid, and the cuboid will be subordinate to

the rectangle (Fig. 4). In the environment of constructors such relation has been adopted to be called as „Parent – Child”, and the relation itself – as associativity. Associativity means that the modification of “Parent” causes the modification of his “Child (Children)” as well.

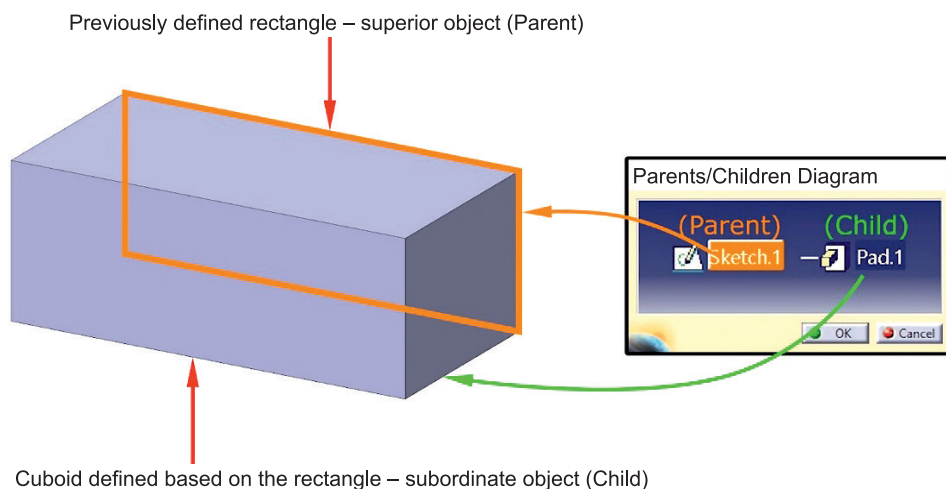


Fig. 4. Link between the superior rectangle (Parent) and the subordinate cuboid (Child)

Links can exist between two or more objects, which in the 3D model structure tree take the form of the previously mentioned functions. It causes, that with time they form a kind of net of connections (Fig. 5). It is important that the constructor is supposed to have full control over this net so that it forms a coherent and logical whole.

Thus, **parameterization** enables the characterization of the functions used to create the **3D model structure tree**, and **associativity** enables to assign relations between these functions and parameters by forming a net of connections. If the CAD system allowed only parametrization of single geometric elements without the hierarchical structure of 3D model and without „Parents/Children” links, propagation of construction changes from Parent elements to their dependent elements (Children) would not be possible. Therefore, subsequent geometric elements of the 3D model are created in relation to the elements defined earlier (WELYCZKO 2010). The availability of geometry associativities are a preliminary requirement for the effective support of the constructor (PÄTZOLD 1991). Let us see how two different nets of connections can affect the implementations of the same modification of an exemplary three-dimensional model.

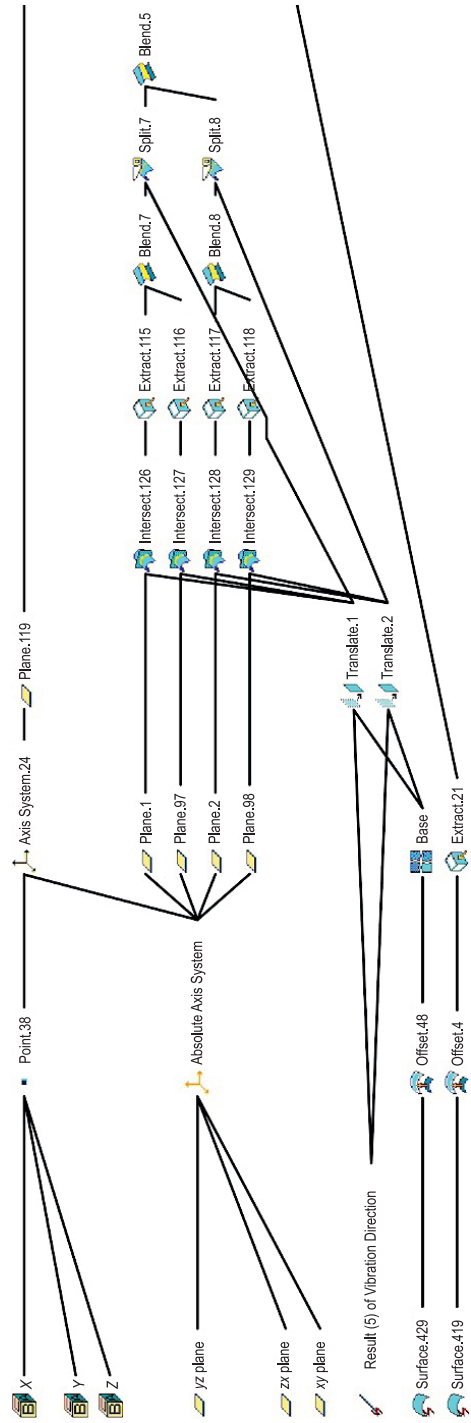


Fig. 5. The exemplary net of connections between functions of 3D model structure tree

## Results

Let us imagine a situation in which constructor has a task to design a positioning pin of a thin-walled element (Fig. 6).

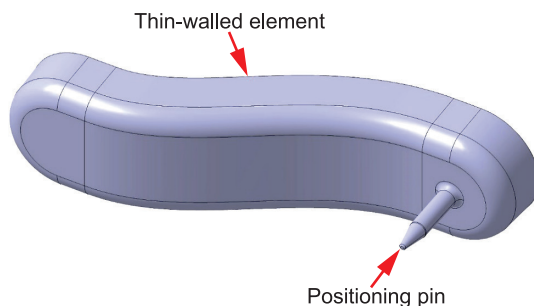


Fig. 6. 3D model of the thin-walled element with the positioning pin

The seemingly easy process requires a moment to think about how to connect the individual design features of the designed pin so that it meets the functional requirements, and its subsequent modification is as simple and short as possible.

The constructor defined the following initial **design conditions** (Fig. 7):

- the axis of the positioning pin is parallel to the mounting direction of its mating element;
- the height of the positioning pin (dimension  $A$ ) is between the intersection of its axis with the front face of the base body at point  $X$  and its vertex;
- the length of the tapered pin head (dimension  $B$ ) is measured from its top.

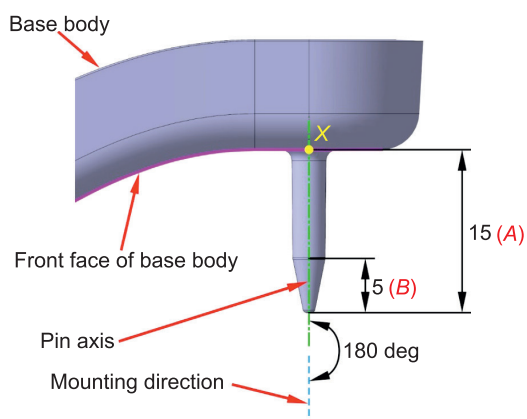


Fig. 7. The initial design conditions defined by the constructor

## Scenario I

In Scenario I, the fulfillment of design conditions was achieved by the following links of geometric features:

- in the definition of the pin axis, the mounting direction has been indicated – link with the line „Mounting direction” (Fig. 8);
- the surface defining the height of the positioning pin has been defined by offset from the surface perpendicular to its axis formed at the point *X* of intersection of this axis with the front face of the base body – link with the surface „Extrude.3” (Fig. 9);
- the surface defining the length of the tapered head has been defined by offset from the surface defining the height of the positioning pin – link with the surface „Offset.1” (Fig. 10).

After completion of the work, the constructor received a request from the customer to move the positioning pin to the center of the designed element. Additionally, due to problems with the assembly of the mating element, a decision was made to extend the pin by 5 mm. The previously assigned associativity

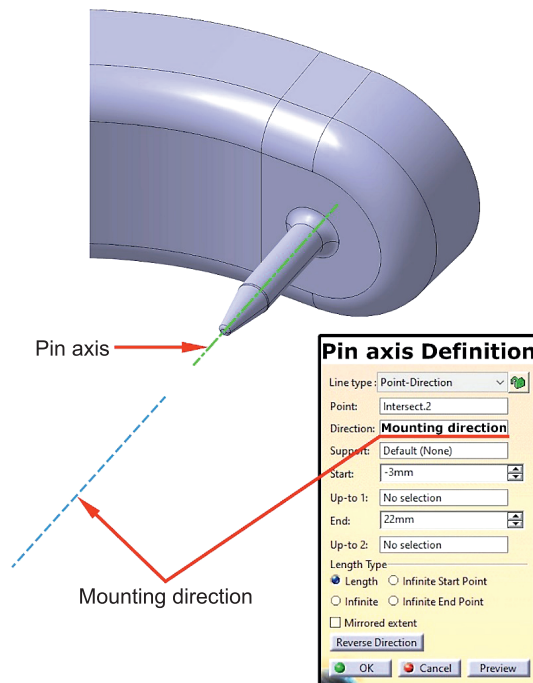


Fig. 8. Definition of the axis direction of the positioning pin

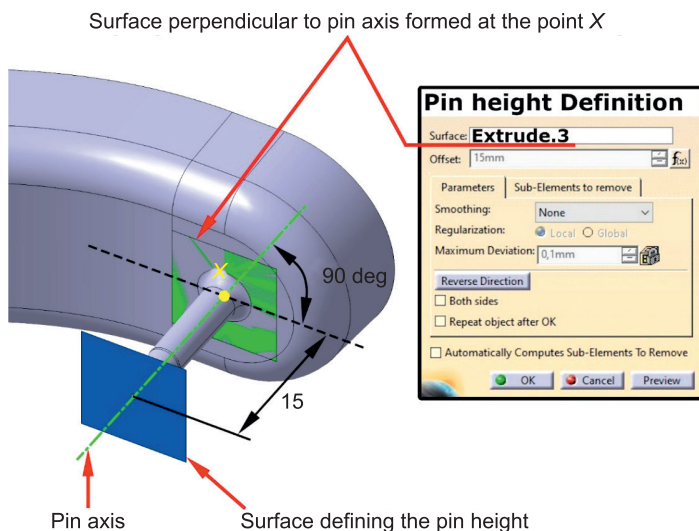


Fig. 9. Definition of the height of the positioning pin – Scenario I

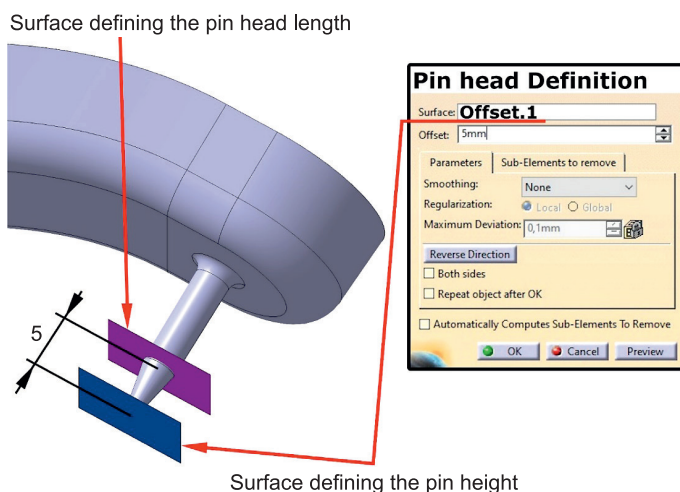


Fig. 10. Definition of the length of the tapered pin head – Scenario I

to the geometric features caused that the required modification came down to implementing new coordinates for the position of the pin and changing the parameter of its height. Properly created links ensured that the initial design conditions were maintained, and the time needed to implement the modifications was limited to a minimum (Fig. 11).

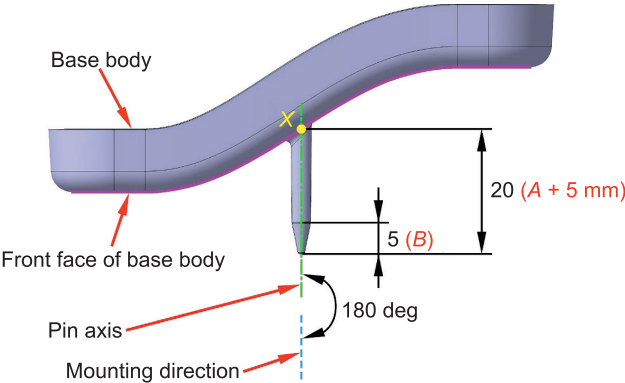


Fig. 11. Modification of the positioning pin that meets the initial design conditions due to properly created links – Scenario I

Scenario II

Now let us imagine an alternative scenario for the same task, in which the fulfillment of the last two design conditions was realized by assigning a different associativity to the geometric features:

- similar as before – in the definition of pin axis, the mounting direction has been indicated – link with the line „Mounting direction” (Fig. 8);
- the surface defining the height of the positioning pin has been defined this time by offset from the front face of the base body – link with the surface „Extrude.1” (Fig. 12);

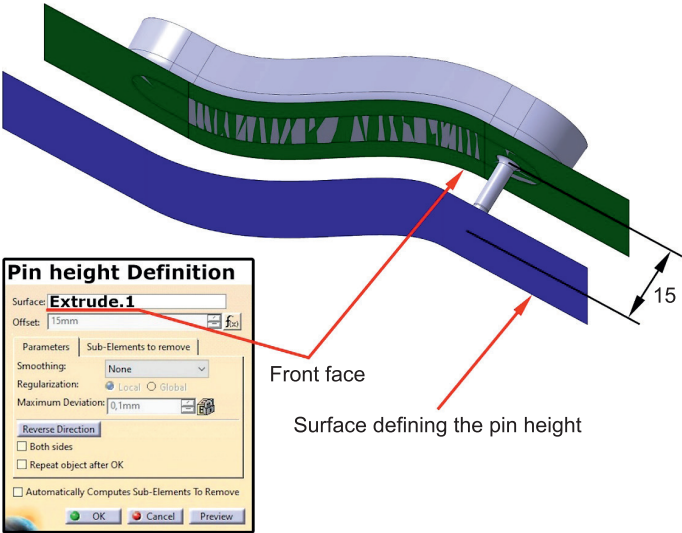


Fig. 12. Definition of the height of the positioning pin – Scenario II



– the surface defining the length of the tapered pin head has been defined this time by offset from the surface perpendicular to its axis formed at the point X of intersection of this axis with the front face of the base body – link with the surface „Extrude.3” (Fig. 13).

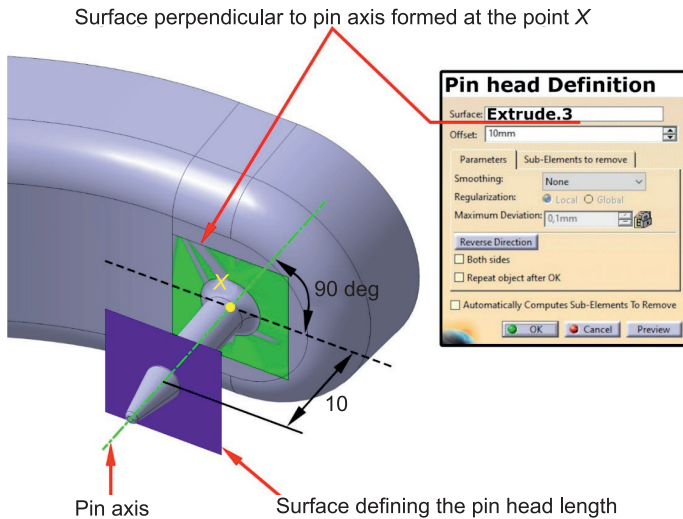


Fig. 13. Definition of the length of the tapered pin head – Scenario II

The positioning pin in the initial location maintains the same dimensions as in the original scenario, so it would have seemed that everything is fine, because the pin geometry meets the initial design conditions (Fig. 14).

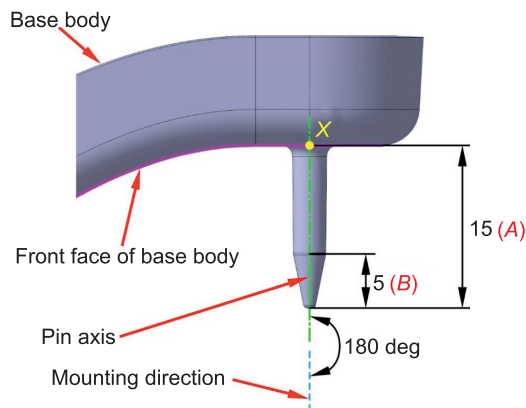


Fig. 14. The positioning pin built based on alternative links and meeting the initial design conditions – Scenario II

However, let us see what happens when the constructor receives the same request from the customer to move the pin to the center of the thin-walled element and to extend it by 5 mm.

After changing the coordinates for the position of the pin and its height, it turns out that:

- the pin axis is still in line with the mounting direction of the mating part – associativity correct (Fig. 15a);

- the pin height is different from its height in the original scenario. This is because of the link creating the height, which is based on the offset of the front face of the base body. This surface in the central region is not flat and is not perpendicular to the axis of the pin (which is parallel to the mounting direction). Although the Offset.1 is equal to the nominal height of the pin (15 mm), its curvature makes that the elongated pin (by 5 mm) is even longer – associativity incorrect (Fig. 15b);

- the length of the tapered pin head is different from its height in the original scenario. This is because of the link creating the length, which is based

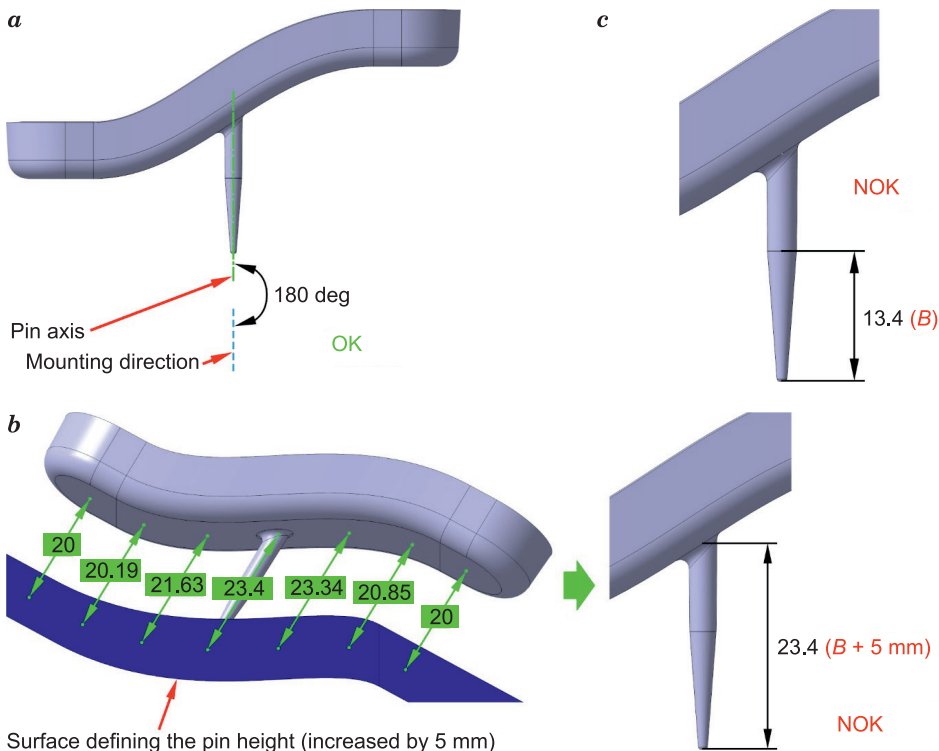


Fig. 15. The result of the positioning pin modification which does not meet all initial design conditions due to an incorrect selection of links – Scenario II: *a* – the pin axis is parallel to the mounting direction – associativity correct, *b* – wrong height of the positioning pin – associativity incorrect, *c* – wrong length of the tapered pin head – associativity incorrect

on a perpendicular surface created in point *X*. The link did not “react” to the elongation of the pin, the height of which was dependent on the other geometric feature – associativity incorrect (Fig. 15c).

As a result, the time needed to implement the customer’s requests will extend, because the constructor must either “manually” modify the values of the parameters of individual geometric features to meet the initial design conditions (which is not recommended) or consider the optimization of the links that he implemented to the 3D model structure tree.

## Discussion

The described scenarios revealed three guidelines that constructor should follow when creating associativity between elements:

- links should ensure the feasibility of the final product in terms of technology and assembly (**first design condition**);
- links should enable future design changes (**second design condition**);
- links should reflect the dimensions important from the technological and functional point of view (**third design condition**).

The capabilities of CAx systems in area of creating associativity between parameters, geometric features or individual three-dimensional models are very extensive. The links in the above example refer only to a few basic elements and certainly do not exhaust the possibilities of their further implementation. The net of connections of the same positioning pin could be defined in a number of other ways. Important is to choose the optimal one, considering the knowledge and experience of the constructor creating a given element.

According to the author, an apparently simple modification of the exemplary three-dimensional model shows the essence of the problem that may occur during the implementation of associativity in CAD class models. Interestingly, an experienced constructor, for example, by creating a complex 3D model structure tree of a car bumper, deals with issues related to correct or incorrect associativity, which are remarkably similar like those described above. It is obvious that as the structural complexity increases, the net of connections between the functions of such a tree also grows. However, contrary to appearances, the principles of its creation remain the same. Design intent captures the purpose of the modeling order and geometry chosen by the constructor. In modern parametric-based CAD systems, this is often stored within CAD features such as axis systems, planes, sketches, extrudes, revolves, and sweeps. It is also stored in the associations relating the CAD features together. By selecting features during the modeling process, an experienced constructor implicitly defines the important parameters of the model, which is extremely important to manufacturing and future updates to the design (STAVES et al. 2017). So, does an experienced constructor always

know the optimal system of links and relations, regardless of the complexity of the element he creates? The answer to this question is not as simple as might think. On the one hand, the design habits developed over the years of work significantly help to choose the most effective solutions. At a certain stage of his professional development, the constructor realizes that geometrical complexity of the designed element ceases to be relevant in the context of the difficulty of its creation. On the other hand, it should be remembered that 3D models in parametric systems are generated in a manner analogous to programming, in which we also have an ordered set of commands. Therefore, it can be said that the CAD system “triggers” a construction procedure that results in a geometric model (WELYCZKO 2011). That means there is almost always possibility of improving the “construction program”, and the “optimal solution”, in the case of the implementation of associativity, is a state to which the constructor should constantly strive.

## Conclusions

1. An associative model is the model which is built of parameters and geometric features linked to each other. Not all connections have a positive impact on the efficiency of creating 3D models, and in extreme cases, they may prevent further work in their creation and lead to the need to rebuild them.

2. Only a well-thought-out and logically coherent set of links between elements creates a structure susceptible to easy and quick modification of the 3D model, and with the consequence contributes to the greatest extent to the effectiveness of its creation.

3. When starting work on a 3D model, the constructor should take into account the implementation of well-thought associativity from the very beginning so as to avoid unwanted complications in the structure of this model. Lack of an initial analysis of the created object in terms of its functional requirements or possible future changes and relying only on CAD modeling habits may hinder the associativity implementation at a later time.

## References

- MA Y.-S., TONG T. 2003. *Associative feature modeling for concurrent engineering integration*. Computers in Industry, 51: 54.
- PÄTZOLD B. 1991. *Geometric-Associative modelling*. In: *Advanced modelling for CAD/CAM systems*. Eds. H. Grabowski, R. Anderl, M.J. Pratt. Research Reports ESPRIT, 7: 30.
- SALEHI V., MCMAHON CH. 2009. *Development of a generic integrated approach for parametric associative CAD systems*. International Conference on Engineering Design, ICED'09, 24-27 August 2009, Stanford University, Stanford, CA, p. 4, 6.
- STAVES D.R., SALMON J.L., RED W.E. 2017. *Associative CAD references in the neutral parametric canonical form*. Computer-Aided Design & Applications, 14(4): 409.

- ŚWIACZNY G., WYLEŻOŁ M. 2020a. *Improving the topology of CAD models in the context of their susceptibility to design changes – model preparation stage*. Part 1. *Mechanik*, 8(9).
- ŚWIACZNY G., WYLEŻOŁ M. 2020b. *Improving the topology of CAD models in the context of their susceptibility to design changes – phase of changes implementation*. Part 2. *Mechanik*, 10.
- WELYCZKO A. 2005. *CATIA v5. Examples of the effective use of the system in mechanical design*. Helion, Gliwice, p. 12, 27.
- WELYCZKO A. 2010. *CATIA v5. The art of surface modeling*. Helion, Gliwice, p. 148.
- WELYCZKO A. 2011. *Parametric or direct modeling?* *Projektowanie i Konstrukcje Inżynierskie*, 6.
- WYLEŻOŁ M. 2002. *Solid modeling in the CATIA system. Examples and exercises*. Helion, Gliwice, p. 10.



## INFLUENCE OF VARIOUS METHODS OF MODELLING THE WELDING PROCESS IN THE CAE ENVIRONMENT ON THE OBTAINED DEFORMATION RESULTS

*Tomasz Zadorożny<sup>1</sup>, Marcin Kalinowski<sup>2</sup>, Mirosław Szczepanik<sup>3</sup>*

<sup>1</sup>ORCID: 0000-0001-7216-1979

<sup>2</sup>ORCID: 0000-0002-2942-6537

Department of Mechanical Engineering  
PhD School, Silesian University of Technology in Gliwice

<sup>3</sup>ORCID: 0000-0001-7983-9463

Institute of Computational Mechanics and Engineering  
Faculty of Mechanical Engineering  
Silesian University of Technology in Gliwice

Received 06 July 2021, accepted 30 November 2021, available online 30 November 2021.

**Key words:** process simulation, FEM, welding, heat deformation, mesh type.

### Abstract

By simulating the welding process, potential non-conformities can be detected before serial production is launched, which can significantly reduce operation costs. There are many different possibilities for modeling the process, therefore it is very important to choose a method that will ensure high accuracy of the solution in a relatively short time. The article will present the influence of various methods of modeling the welding process in the CAE environment on the obtained deformation results. For the given geometry and type of weld, the thermal deformations have been simulated based on the Finite Element Method. Several analyzes were carried out using different process modeling approaches (mesh type). Finally, a comparison of the results for the discussed cases is presented to determine the influence of the parameters used on the deformation results obtained.

---

Correspondence: Tomasz Zadorożny, Katedra Mechaniki i Inżynierii Obliczeniowej, Wydział Mechaniczny Technologiczny, Wspólna Szkoła Doktorska, Politechnika Śląska, ul. Akademicka 2a, 44-100 Gliwice, e-mail: [zadorozny.tomasz@gmail.com](mailto:zadorozny.tomasz@gmail.com).

## Introduction

Simulations of technological processes are difficult and time-consuming due to many factors influencing their progress. Properly conducted simulation of the technological process can provide many valuable tips. They allow improving the manufacturing process, contributing to a significant reduction in costs related to technological time and potential repairs. The work aims to select an appropriate modeling method to determine the course of thermal deformation in the area of the welded component. The results of this type of simulation can help in the optimal selection of the fixing points of the components to be welded.

During the welding process, the weld area is intensively heated and then cooled. The temperature gradient causes uneven expansion and contraction of the weld and the surrounding area, which results in permanent deformations. The form and size of deformation are influenced by many factors, including mechanical limitations and the amount of heat supplied, which depends on the process parameters (welding current, welding speed, etc.). In most cases, the change of these parameters is limited by the quality requirements for the joint, therefore the method that does not directly affect the quality of the weld is to use appropriate constraints points. Based on the conducted review of the available literature, where the test and simulation results were present, can be clearly stated that ensuring appropriate process parameters (including adjustment of constraints points) significantly affects the form of geometric distortions. In the vast majority of works, 3D elements were used to model the problem, the comparison with real tests confirmed the high accuracy of this methodology. The use of 3D elements allowed to obtain high accuracy of the results of residual stresses and the course of deformation. The simulations and tests concerned small structures where the use of such methodology did not significantly extend the computation time. For these constructions, it was determined that the most effective geometric limitations work when they are as close as possible to the weld line. In industrial practice, it is not always possible to locate mechanical constraints in this way, so it is important to optimize their location.

There are many modeling methods, they assume some simplifications aimed at limiting the size of the numerical model and thus the computing time. Large numerical models (such as a train roof) consisting of 3D elements pose many problems with the calculation time or the visualization itself in the software, therefore a very important aspect is to select the appropriate modeling method at an early stage of the research. In engineering practice, 2D elements are most often used to limit the size of the numerical model. For such complex issues, it must be ensured that the use of 2D elements will ensure the correct response of the structure. One of the approaches is to carry out a series of analyzes on sample models and to compare the results to determine the appropriate modeling method. The following part of the article presents a comparison of three



different methods of modeling a welded joint in the simulation of a process aimed at determining thermal deformation. One of the commercial finite element method (FEM) HyperWorks program was used to solve the problem defined.

## Description of samples and boundary conditions

The considered welded sample consists of aluminum sheets joined together by a fillet weld (Fig. 1). Three different modeling methods are considered in this article. In order to accurately determine the impact of the modeling method on the time of solving the task, different lengths of the sheets joined together were analyzed for each described below methods (Tab. 1):

- the first model consists of shell elements without additional elements in the weld area (only quad elements);
- the second model is an expansion of the first one with additional surfaces to simulate a fillet weld (only quad elements);
- the third model consists of 3D elements that represent the weld geometry (hexa and penta elements).

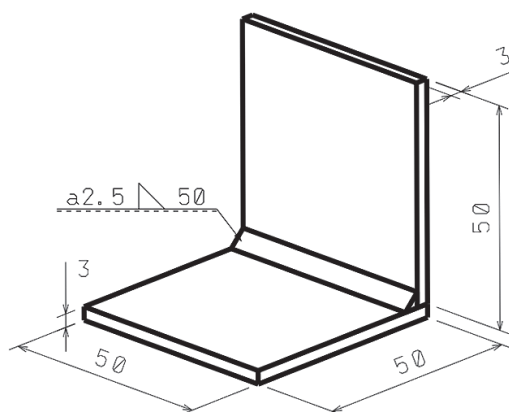


Fig. 1. Dimensions of samples

Table 1

Number of nodes and elements for different types of samples

Length	Sample I		Sample II		Sample III	
	nodes	elements	nodes	elements	nodes	elements
50 mm	2,278	2,178	2,482	2,475	6,902	4,488
200 mm	8,911	8,712	9,709	9,900	26,999	17,952
800 mm	35,443	34,848	38,617	3,960	107,387	71,808
3,200 mm	141,571	139,392	154,249	158,400	428,939	287,232
12,800 mm	566,083	557,568	616,777	633,600	1,715,147	1,148,928

The temperature value adopted in the analysis is 1,230°C, which corresponds to the real value during welding works. The temperature was applied to the point where the sheets were joined along the entire length using the first kind of boundary condition. The values shown were read after the sample had returned to ambient temperature which was set at 20°C. The heat transfer with the environment takes place over the entire surface, additional transfer through mechanical constraints points is not taken into account. Figure 2 shows a comparison of the weld modeling method for each of the samples and the applied constraints. An elastoplastic model of the material was used, Table 2 present the material data.

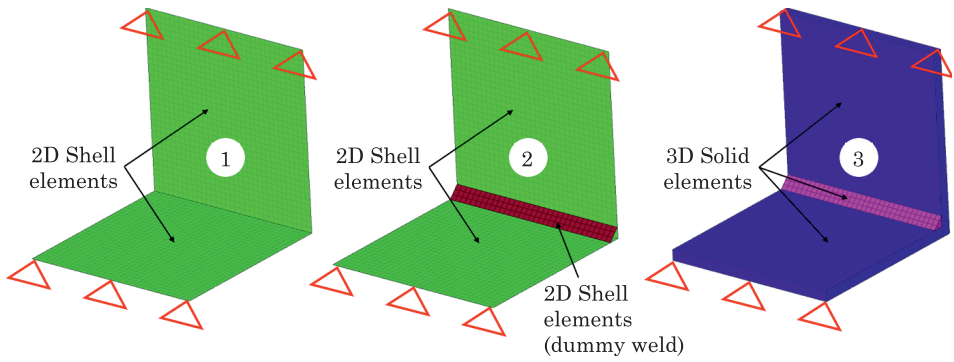


Fig. 2. Visualization of the modeling method and given boundary conditions

Table 2

Material properties	
Young's modulus [MPa]	7·10 <sup>4</sup>
Density [g/cm <sup>3</sup> ]	2.7
Poisson ratio	0.3
Thermal conductivity [W/(m·K)]	215
Heat transfer coefficient [W/(m <sup>2</sup> ·K)]	6.8
Thermal expansion coefficient [10 <sup>-6</sup> /K]	23.1

The Dirichlet boundary condition (the first kind of boundary condition) is based on the assumption that the function that solves a given problem takes predetermined values at the boundary of the domain.

For an ordinary differential equation of the 2<sup>nd</sup> order, the Dirichlet condition takes the following form:

$$y(a) = y_a, y(b) = y_b \tag{1}$$

where:

$y_a, y_b$  – defined.

A typical and the most common application is its implementation for the Laplace equation, and where for a given area:

$$\Omega \subset \mathbb{R}^n$$

a solution is sought:

$$u: \bar{\Omega} \rightarrow \mathbb{R}$$

which is continuous in  $\bar{\Omega}$  and fulfill the equation:

$$\Delta u = 0 \quad (2)$$

where:

$\Delta$  – a Laplace operator.

And the boundary condition takes the form:

$$u(x) = f(x) \quad \forall x \in \partial\Omega$$

where:

$f$  – a given function defined at the edge of the region,

$f: \partial\Omega \rightarrow \mathbb{R}$ .

When applying the first kind of condition, two relations should be fulfilled, the resulting system of equations can be written as:

$$\begin{cases} \Delta u = 0 & \text{on } \Omega \\ u = f & \text{in } \partial\Omega \end{cases}$$

This condition is used when describing the phenomenon of heat propagation (transport of internal energy), its adoption means that the temperature at the edge of the object is determined and fully controlled. This means that the area is in contact with the source of thermal energy and the object shows good conductivity properties.

## Results

Figure 3 shows the displacement distribution on the deformed model, the adopted scale of deformation is 5:1. Table 3 summarizes the deformation values obtained along with the difference expressed as a percentage in relation to the third sample. The third sample can be taken as representative, the numerical model consisting of 3D elements reflects the real geometry to the greatest extent. This modeling method was widely used in various research works and the numerical simulations of the process were compared with the results of real tests. The test results clearly show that the use of 3D elements guarantees high accuracy in terms of the obtained values of residual stresses and the course of deformation. For this reason, it is justified to consider this sample representative.

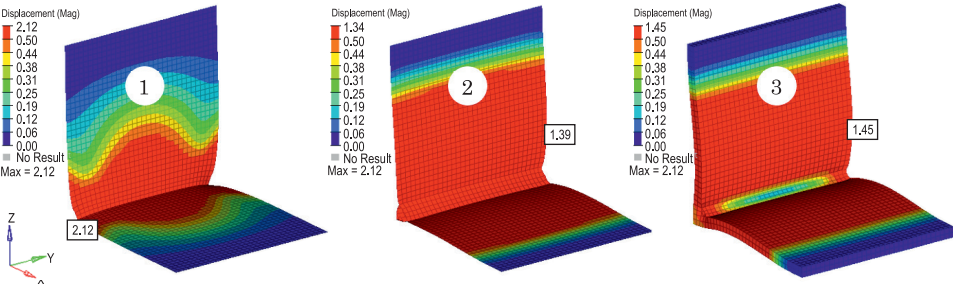


Fig. 3. Distribution of displacements on the deformed model, scale 5:1

Table 3

Maximum displacement values		
Sample	Maximum displacement [mm]	Difference [%]
I	2.12	31.6
II	1.39	4.3
III	1.45	0

The course of the deformations obtained for the second and third samples is similar, and the difference in the values of the obtained displacements is 4.3%. For the first sample, the deformation distribution and their maximum value differ significantly from the other two samples. It can therefore be concluded that the geometry of the weld has a big impact on the displacement distribution, which locally increases the stiffness of the structure and directly impacted the response of the system. The deformation distribution for the first sample indicates its unnatural deformation in the connection line where energy in the form of heat has been applied.

Detailed data on the time needed to simulate individual samples are presented in Table 4 and Figure 4. For the length of the joined sheets up to 200 mm, it can be noticed that the modeling method slightly affects the total calculation time. It is caused by a relatively small number of elements, so the time needed to create and solve the stiffness matrix for these cases is very similar. A clear difference in the computational time can be noticed for samples with a length of 3,200 mm, where the solution time of the model consisting of 3D elements (sample III) is significantly longer compared to other samples. With a further increase in the length of the sample, the disproportions increase, clearly indicating the third modeling method is the most time-consuming.

Table 4

Time to solve the task for different scenarios [s]					
Sample	50 mm	200 mm	800 mm	3,200 mm	12,800 mm
I	10	12	21	49	186
II	10	12	21	58	227
III	18	18	26	115	545

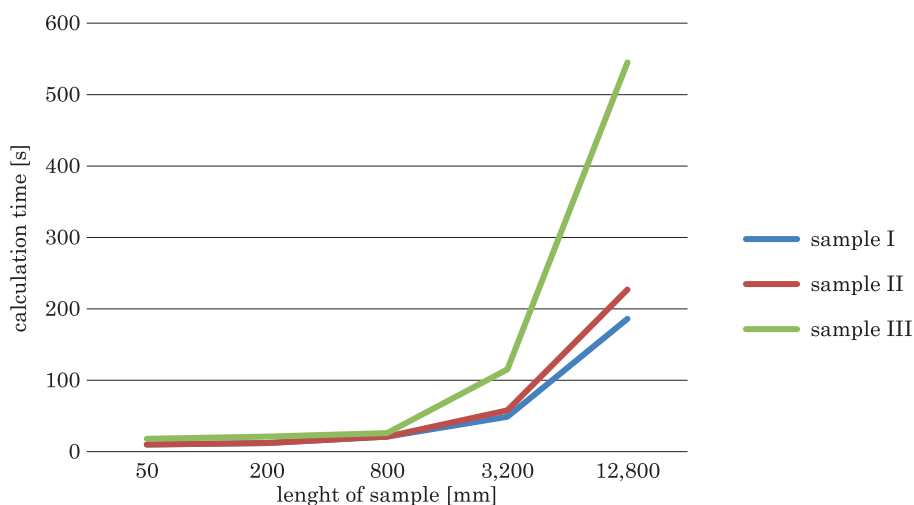


Fig. 4. Comparing the times of solving the task for different scenarios

## Conclusions

Thermal deformation of welded structures is a serious problem that entails costly repairs. Numerical calculations allow simulating the deformations with high accuracy. The introduction of this type of simulation into the design process in the case of low-series structures allows avoiding many problems already at the first assembly, where excessive deformations would occur without additional calculations.

Based on the obtained results, it can be seen that the modeling method has a clear impact on the time needed to simulate the process. The differences between the individual computational times increase with the increase in the number of elements of the numerical model, which is a natural phenomenon. Because welded structures are quite big and that simulation requires the creation of a numerical model that consists of a large number of finite elements, the selection of the appropriate modeling method is crucial. As can be observed, the course of deformation in the area of the sample created with the use of shell

elements together with the surface simulating the weld is similar to that obtained for a model consisting of 3D elements, the difference is 4.3%. It can therefore be considered that modeling with the use of shell elements is the appropriate approach provided that an additional plane simulating the weld is used. For the vast majority of structures, simulation of the process would not be possible using 3D element modeling, therefore such a simplification seems highly justified. An alternative modeling method using shell elements with additional surface significantly reduces the analysis solution time, which is equivalent to the possibility of simulating the process for large computational models. To optimize the production process, the deformations courses are relevant, and that for the above-mentioned methods are similar.

The deformation distribution obtained for the first sample, where the additional surface in the weld area is not taken into account, differs distinctly from the other results and does not coincide with the deformations obtained in practice. For these reasons, the use of such an approach in modeling seems to be unjustified for this kind of joints.

### Acknowledgements

This research was co-financed by the Ministry of Education and Science of Poland under grant No DWD/3/33/2019.

### References

- AALAMI-ALEAGHA M.E., ESLAMPANAH A. 2012. *Mechanical constraint effect on residual stress and distortion in T-fillet welds by three-dimensional finite element analysis*. Proceedings of the Institution of Mechanical Engineers - Part B, 227(2): 315-323.
- BARSOUM Z., LUNDBACK A. 2001. *Simplified FE welding simulation of fillet welds – 3D effects on the formation residual stresses*. Engineering Failure Analysis, 16(9): 2281-2289.
- COSIMO A., CARDONA A., IDELSOHN S.R. 2010. *General treatment of essential boundary conditions in reduced order models for non-linear problems*. Advanced Modeling and Simulation in Engineering Sciences, 3(1): 626-636.
- FRICKE S., KEIM E., SCHMIDT J. 2001. *Numerical weld modeling – a method for calculating weld-induced residual stresses*. Nuclear Engineering and Design, 206(2-3): 139-150.
- GIMENEZ G., ERRERA M., BAILLIS D., SMITH Y., PARDO F. 2015. *Analysis of Dirichlet-Robin interface condition in transient conjugate heat transfer problems. Application to a flat plate with convection*. European Conference on Turbomachinery Fluid Dynamics and Thermodynamics, Madrid.
- LIANG W., MURUKAWA H., DENG D. 2015. *Investigation of welding residual stress distribution in a thick-plate joint with an emphasis on the features near weld end-start*. Materials & Design, 67: 303-312.
- MAZUMDER S. 2016. *Numerical methods for partial differential equations. Finite difference and finite volume methods*. Elsevier, Amsterdam.

- ROSCA A.S., ROSCA D. 2006. *About using the Dirichlet boundary conditions in heat transfer equation solved by finite element method*. International Journal of Computers, Communications & Control, 1: 405-409.
- SZABO T. 2010. *On the Discretization Time-Step in the Finite Element Theta-Method of the Two-Dimensional Discrete Heat Equation*. Large-Scale Scientific Computing, 591: 626-636.
- VENKATKUMAR D., DURAIRAJ R. 2019. *Effect of Boundary Conditions on Residual Stresses and Distortion in 316 Stainless Steel Butt Welded Plate*. High Temperature Materials and Processes, 38: 827-836.
- WEN S.W., HILTON P., FARRUGIA D.C.J. 2009. *Finite element modelling of a submerged arc welding process*. Journal of Materials Processing Technology, 119(1-3): 203-209.
- ZADOROŻNY T., SZCZEPANIK M. 2020. *Numerical simulation of the welding process, the influence of constraint points locations on thermal deformations*. Scientific-Expert conference on railways RAILCON 2020, Nis, p. 145-148.
- ZIENKIEWICZ O.C., TAYLOR R.L., ZHU J.Z. 2013. *The Finite Element Method: Its Basis and Fundamentals*. Elsevier, Amsterdam.





## NUMERICAL SIMULATION OF FLOW THROUGH MICROCHANNELS WITH RANDOM ROUGHNESS

*Małgorzata Kmiotek<sup>1</sup>, Adrian Kordos<sup>2</sup>, Tomasz Iwan<sup>3</sup>*

<sup>1</sup> ORCID: 0000-0003-3229-0367

<sup>2</sup> ORCID: 0000-0003-3647-3283

Department of Aerospace Engineering  
Faculty of Mechanical Engineering and Aeronautics  
Rzeszow University of Technology

<sup>3</sup> ORCID: 0000-0001-5629-4165

Graduate Faculty of Mechanical Engineering and Aeronautics  
Rzeszow University of Technology

Received 12 November 2021, accepted 01 December 2021, available online 03 December 2021.

**Key words:** roughness, microchannels, microflows, mechanical engineering.

### Abstract

The aim of the study is to determine the effect of a randomly generated rough surface on the laminar flow of a fluid in a microchannel. Two-dimensional axially symmetric microchannels with a circular cross-section in the range of Reynolds number  $Re = 100-1700$  were considered. Flow numerical simulations were performed using the Ansys / Fluent software.

### Introduction

The rapid development of miniaturization observed in the last decade has provided new scientific problems and technological challenges. Microdevices and microcomponents are becoming increasingly widely used in numerous industrial applications from biomedicine to fuel cells. Most of these devices have microfluidic

---

Correspondence: Małgorzata Kmiotek, Katedra Inżynierii Lotniczej i Kosmicznej, Wydział Budowy Maszyn i Lotnictwa, Politechnika Rzeszowska, al. Powstańców Warszawy 8, 35-959 Rzeszów, e-mail: [kmimal@prz.edu.pl](mailto:kmimal@prz.edu.pl).

systems with various functionalities, from process to cooling (KMIOTEK, KUCABA-PIĘTAL 2018, KORDOS, KUCABA-PIĘTAL 2018, MARZEC 2021, ZAREMBA et al. 2018). Unfortunately, the direct translation of the flow models and heat transfer problems developed and tested for macrochannels is not justified for microchannels, because they do not take into account the phenomena significant in the microscale and the discrepancies increase with the reduction of the characteristic dimension and the surface treatment method. For example, as the channel size decreases, there is an increase in the effect of roughness on fluid flow.

While the flows in rough macrochannels are very well known, the micro scale has not been fully researched yet. Therefore, in recent decades, a lot of experimental research has been carried out on microchannels. Some of these studies indicate a change in the nature of the flow with a lower critical Reynolds number value than in the macro scale, as well as a greater roughness coefficient occurring in channels with a small hydraulic diameter. It is suggested by the increase of the roughness effect together with the decrease of the channel size (DAI et al. 2014, ZHANG et al. 2010).

The article presents how the flow in the microchannel is influenced by the occurrence of a randomly generated surface roughness, i.e., a set of unevenness (peaks and pits) on the real surface with relatively small spacing between vertices (KANDLIKAR 2006, WHITEHOUSE 2004),

In the macro scale, the material from which the element was made, the type of processing, and processing parameters undoubtedly have the greatest influence on the surface roughness. The surface can most often be characterized as a combination of two profiles – waviness and roughness (some surfaces also show a shape error). Waviness is measured over a much greater distance than roughness. The difference between the profiles is shown in Figure 1.

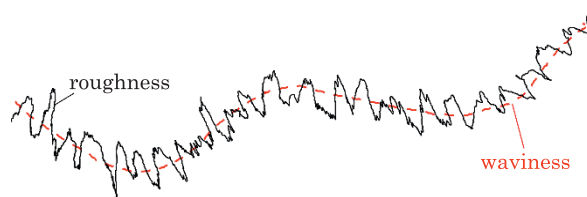


Fig. 1. Comparison of roughness and waviness

To describe the surface structure in the macroscale, various surface parameters are defined by means of numerical values. Many of them do not have a significant impact on the macroscale flow, however, they are particularly important in microchannels, because the considered inequalities are then larger. They can be divided into three groups (Fig. 2) describing the following features: amplitude, spacing, and slope, of which amplitude is of key importance in microflows.

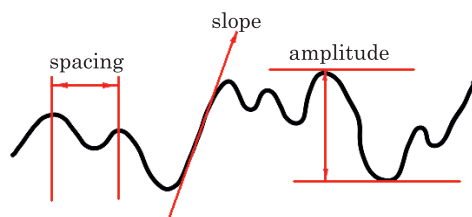


Fig. 2. Example parameters describing the surface

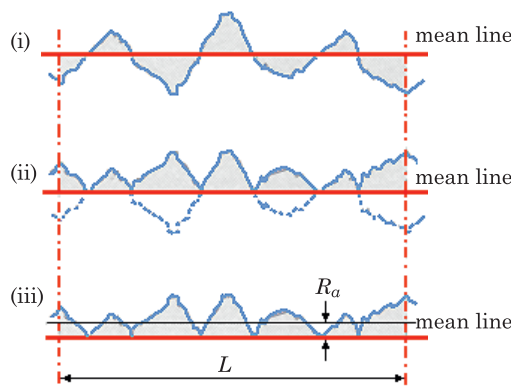
The most common and commonly used parameter describing the amplitude is the  $R_a$  parameter. Its value describes the arithmetic mean of the profile deviation from the mean. The calculation of this parameter is shown in Figure 3. The mean profile line (i) is determined by calculating the mean profile height along the sampling length. All negative deviations are converted to positive (ii). The mean line from the modified profile (iii) is then calculated. The  $R_a$  parameter alone is not sufficient to fully describe the surface roughness, but it is most commonly used in the case of microns. The  $R_a$  parameter is determined by the formula (WHITEHOUSE 2004):

$$R_a = \frac{1}{l_r} \int_0^{l_r} |z(x)| dx \quad (1)$$

where:

- $l_r$  – sampling length [m],
- $z(x)$  – profile height along the length  $x$  [m].

Surface roughness is the result of the simultaneous interaction of many independent factors, both random and determined, and as a result it has a very complex microgeometry. The size of the surface roughness depends on the type of material and, above all, on the type of its processing. Roughness is caused,


 Fig. 3.  $R_a$  parameter

among others, by the processes of decohesion, plastic deformation in the cutting zone and formation of chip segments, friction of the tool contact surface against the machined surface, and chip friction against the machined surface (WHITEHOUSE 2004).

When machining surfaces, even on a microscale, surface roughness is inevitable. There are many types of micro-machining methods with machining precision from  $10^{-2}$   $\mu\text{m}$  to 5  $\mu\text{m}$ , such as EDM (electrical discharge machining), ECM (electrochemical machining), pickling, micro-milling and so on (CHU et al. 2014). Depending on the production process, the microchannels can therefore even have a surface roughness in the order of the size of the channel. To properly design flow microdevices, it is necessary to determine the physical laws governing the fluid flow and heat transfer in the microchannel, taking into account the method of making the microdevice and the resulting roughness of the microchannel surface (KANDLIKAR 2006).

According to the knowledge of macrosystems, when the relative roughness is less than 5%, its influence on the coefficient of friction is negligible (KANDLIKAR 2006). For microscale channels, experimental and numerical results showed that surface roughness has a significant effect on heat transfer and heat transfer (ANSARI, ZHOU 2020, LU et al. 2020, MIRMANTO, KARAYIANNIS 2012). For example, the experiment of KANDLIKAR et al. (2005) indicated that for a 0.62 mm pipe with a relative roughness height of 0.355%, the influence of roughness on the coefficient of friction and heat conduction was significant.

In publication (DAI et al. 2014), the authors reviewed 33 scientific articles (a total of 5,569 data were collected) for flows in micro- and mini-channels with different wall roughness. The aim was to determine the effect of roughness on the friction coefficients. The authors concluded that if the relative roughness height is  $<1\%$ , it has little effect on the friction coefficient and the critical Reynolds number. A value of 1% has been suggested as the threshold for distinguishing between smooth and rough micro- and mini-channels.

Despite the availability of a large amount of experimental data, the flows in microscopes are still not fully investigated and described. Due to the scale of the phenomenon, numerical simulations seem to be a good tool. The data obtained through computational methods allows the analysis of many aspects difficult to grasp in an experiment, which will enable understanding of the basic physics of the problem.

Most often in the literature, the surface roughness is modeled with simple geometric shapes, e.g., triangles, rectangles, squares, ellipses, trapeziums (LALEGANI et al. 2018, ZHANG et al. 2010, CROCE 2016) and the fractal geometry method (JIA, SONG 2019) or Gaussian function (PELEVIĆ, VAN DER MEER 2016). However, due to the stochastic nature of roughness, a better approach seems to be to randomly generate surface irregularities, which will be described later in the article.

Literature analyzes show that roughness affects the streamline distribution. With a high roughness value, this can lead to the flow being detached near the wall and the formation of recirculation zones. Detachment of flow and recirculation areas are most likely the main causes of increased friction and the formation of a pressure gradient (ZHANG et al. 2010).

The aim of the study was to estimate the effect of roughness on the laminar flow of fluid in microchannels, as well as to select an appropriate method of roughness modeling to achieve the best compliance with the experimental data.

## Research methodology

Two-dimensional axially symmetrical microchannels with a circular cross-section were considered. On the wall of the microchannel there are elements simulating the roughness of the channel generated on the basis of the normal distribution, with the density function:

$$f_{\mu,\sigma}(x) = \frac{1}{\sigma\sqrt{2\pi}} \exp\left(\frac{-(x-\mu)^2}{2\sigma^2}\right) \quad (2)$$

where:

$\mu$  – expected value [–],

$\sigma$  – standard deviation [–],

$x$  – a random variable with the expected value  $\mu$  and variation  $\sigma^2$  [–].

The area was obtained by generating a random value from 0 to 1 as a random variable. The average was the radius of the channel (i.e., 25  $\mu\text{m}$ ), while the standard deviation was defined as the product of 1.25 and  $R_a$  (ZHANG et al. 2010). The radius  $r_i$  is randomly generated by the above-mentioned function. The variable  $x_i$  changed in the axial direction by a constant value equal to  $S_a$  ( $x_{i+1} = x_i + S_a$ ). Having these 2 parameters, it was possible to generate a random (one-dimensional) curve. To achieve the three-dimensional effect, further curves with  $S_\phi$  spacing are generated. The microchannel is modeled as axisymmetric, therefore the curves are averaged (i.e., rays having the same  $x$  variable are averaged).

As a result, we get  $i$  points with radius  $r_i$  and location on the  $x_i$  axis. This is visualized in Figure 4. Due to the randomness of the process,  $R_a$  of each surface is monitored, then the mean  $R_a$  of the generated surfaces is calculated. The final surface is accepted if the mean  $R_a$  (calculated from all surface components) does not differ by more than 0.3% from the target  $R_a$ .

The flow was assumed to be two-dimensional, axisymmetric, incompressible, and steady. The diameter of the channel was a characteristic dimension for the Reynolds number. The test fluid was water at room temperature (fluid density  $\rho = 998 \text{ kg/m}^3$ , dynamic viscosity  $\mu = 0.001 \text{ Pa}\cdot\text{s}$ ). The microchannel geometry is presented in Figure 5.

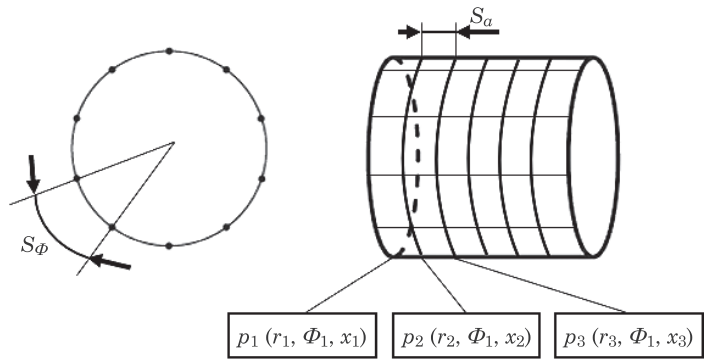


Fig. 4. The method of generating random points

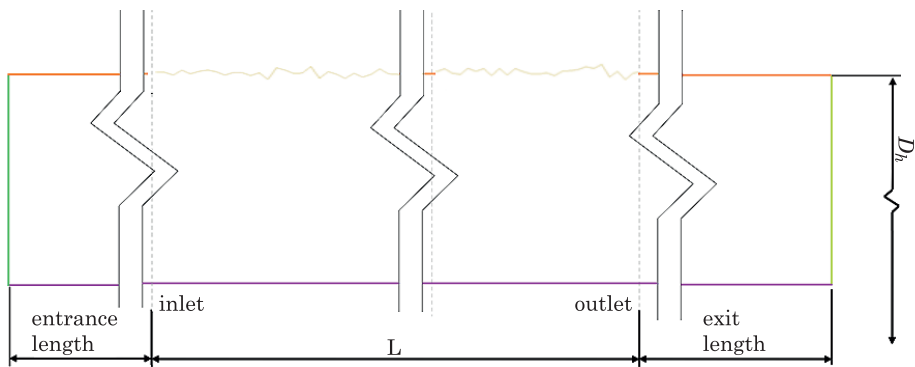


Fig. 5. Geometry of the microchannel

The parameters adopted for the calculations are presented in Table 1, while the parameter values used for the modeling of the random surface are presented in Table 2.

Table 1

Parameters used in the calculations			
Characteristic	Symbol	Value	Unit
Microchannel length	$L$	1	mm
Microchannel diameter	$D_h$	50	$\mu\text{m}$
Inlet velocity	$V_{in}$	2,01-42,12	m/s

Table 2

Parameters used in the modeling of a random surface

$S_\phi$	$S_a$
36°	1 $\mu\text{m}$

The flow in the microchannel results from the principles of fluid conservation (KANDLIKAR 2006):

1. Principles of conservation of mass:

$$\frac{\partial \rho}{\partial t} + \text{div}(\rho \bar{V}) = 0 \quad (3)$$

2. Principles of conservation of momentum:

$$\rho \frac{\partial \bar{V}}{\partial t} = \rho \bar{F} - \text{grad } p + \mu \Delta \bar{V} \quad (4)$$

where:

- $\bar{V}$  – velocity vector [m/s],
- $\rho$  – fluid density [kg/m<sup>3</sup>],
- $\bar{F}$  – vector of mass forces [N],
- $p$  – fluid pressure [Pa].

The system of equations adopted for modeling can be written in the form of equations:

– equation of continuity:

$$\frac{1}{r} \frac{\partial(r u_r)}{\partial r} + \frac{\partial(u_z)}{\partial z} = 0 \quad (5)$$

– momentum equations (Navier-Stokes):

$$\begin{aligned} \rho \left( V_r \frac{\partial V_r}{\partial r} + V_z \frac{\partial V_r}{\partial z} \right) &= -\frac{\partial p}{\partial r} + \mu \left[ \frac{1}{r} \frac{\partial}{\partial r} \left( r \frac{\partial V_r}{\partial r} \right) - \frac{V_r}{r^2} + \frac{\partial^2 V_r}{\partial z^2} \right] \\ \rho \left( V_r \frac{\partial V_z}{\partial r} + V_z \frac{\partial V_z}{\partial z} \right) &= -\frac{\partial p}{\partial z} + \mu \left[ \frac{1}{r} \frac{\partial}{\partial r} \left( r \frac{\partial V_z}{\partial r} \right) + \frac{\partial^2 V_z}{\partial z^2} \right] \end{aligned} \quad (6)$$

The commercial ANSYS Fluent software, using the finite volume method, was used to solve the equations.

The boundary conditions adopted for the analysis are:

- at the inlet to the duct, a profile was set up at the outlet of the reference pressure,
- zero tangential velocity on the channel wall (also impenetrability of the walls),
- axial symmetry.

The Reynolds number was determined from the formula (KANDLIKAR 2006):

$$\text{Re} = \frac{\rho V D_L}{\mu} \quad (7)$$

where:

- $D_L$  – characteristic dimension [m],
- $\mu$  – dynamic viscosity [kg/m·s],
- $V$  – flow velocity [m·s].

To determine the effect of roughness on the flow in the microchannel, the formulas used in macrochannels and milichannels were used. The dimensionless coefficient of friction (Fanning, Dracy) was determined (KANDLIKAR 2005). The Fanning friction coefficient ( $f_F$ ) is defined as:

$$f_F = \frac{\tau_w}{\frac{1}{2} \rho u_m^2} \quad (8)$$

where:

- $\tau_w$  – tangential stresses [Pa],
- $u_m$  – average velocity of the liquid in the channel [m/s].

The Darcy's coefficient of friction ( $f_D$ ), related to the Fanning's coefficient of friction, is expressed as:

$$f_D = 4f_F \quad (9)$$

Darcy's coefficient is also defined as the ratio of the Poiseuille number  $P_o$  to the number Re as in the formula (KANDLIKAR 2006):

$$f_D = \frac{P_o}{\text{Re}} \quad (10)$$

The Poiseuille number assumes a constant value, in the case of developed laminar flow, it differs depending on the shape of the channel cross-section. For a circular channel, the Poiseuille number is assumed to be constant at 64.

Formula for pressure drop taking into account friction losses:

$$\Delta p = \frac{2f_D \rho u_m^2 L}{D} \quad (11)$$

where:

- $D$  – channel diameter or hydraulic diameter if the channel cross-section is other than circular [m],
- $L$  – channel length [m].

The Dracy coefficient of friction depends on: the type of flow, wall roughness, pipe geometry (length, diameter) and is most often determined using the Moody diagram. Dracy's coefficient of friction for laminar flow can be determined based on the Hagen-Poiseuille law (KANDLIKAR 2005):



In macro and microscale in laminar flow, the coefficient of frictional loss depends on the Reynolds number and not on the roughness (KANDLIKAR 2005).

According to (DAI et al. 2014) after calculating the coefficient  $f_D$ , it is possible to calculate the corrected roughness coefficient matching the experimental data obtained in microchannel tests using, for example, the Gaussian distribution model, which assumes that the roughness behaves in accordance with the Gaussian normal distribution. The correlation was developed based on the standard deviation of the roughness profile. A correction factor has been introduced that modifies the friction coefficient  $f_D$ . The relative roughness of the discussed correlation is:

$$\frac{f_{D\text{corr}}}{f_D} = \begin{cases} 1 / \left[ 1 - 23 \left( \frac{2.5\varepsilon}{D} \right)^2 \right] & \text{for } \varepsilon/D \leq 0.04 \\ 1 / \left[ 1 - 50 \left( \frac{2.5\varepsilon}{D} \right)^{2.4} \right] & \text{for } 0.04 \leq \varepsilon/D \leq 0.06 \end{cases} \quad (12)$$

where:

$\varepsilon$  – the roughness height of the inner surface of the microchannel [m].

The construction of the microchannel geometry takes into account the entrance length. The entrance length was calculated from the formula (KANDLIKAR 2006):

$$h/D \cong 0.05 \text{ Re} \quad (13)$$

The entrance length of 6 mm was adopted for  $\text{Re} = 2,100$ . The value of the exit length was set at 0.5 mm.

Grid Convergence Index (GCI) relative to the average velocity in the section located in the middle of the channel length was determined to assess the correctness of the mesh compaction:

$$\text{CGI} = F_s \cdot \frac{\frac{|u_{h2} - u_{h1}|}{u_{h1}}}{a^p - 1} \cdot 100 \quad (14)$$

where:

$F_s$  – security factor [–],

$u_{h1}, u_{h2}$  – selected parameter (velocity is assumed) [m/s],

$h_1, h_2$  – number of finite elements [–],

$p = \frac{h_2}{h_1}$  – współczynnik zagęszczenia siatki [–],

$a$  – the approximation order of the calculations (the assumed value is 2) [–].

In order to optimize the mesh, a study of the GCI coefficient was performed. These studies have shown that with an element size of  $0.1 \mu\text{m}$ , the GCI coefficient is less than 0.4%.

The mesh was generated from elements of the prism and tetrahedron type.

## Research results

To investigate the effect of roughness on the flow in the microchannel, the following were analyzed:

- changing the shape of the roughness element – as a surface composed of points that meet the Gaussian distribution for the flow of fluid in a channel with a circular cross-section,
- a change in the Reynolds number from  $Re = 100$  to  $Re = 1,700$ .

Based on the calculations, the coefficients of linear loss, pressure loss were determined, and the current lines and velocity vector distributions were generated. Linear loss coefficients were compared to those derived from classical theory, Gaussian random distribution, and experimental data (MOHIUDDIN MALA, LI 1999).

The effect of the scatter of results resulting from the pseudo-random distribution of points from which the geometry is built was also investigated.

Due to the use of randomly generated geometry, it was required to create a statistical sample. For this purpose, 30 sample random surfaces of  $R_a = 1.75 \mu m$  (Fig. 6). The Darcy coefficient ( $f_{rand}$ ) was calculated from the formula (11), on the basis of the mean of these 30 models, for Reynolds numbers 100-1,700. Then, the standard deviation was calculated (Tab. 3).

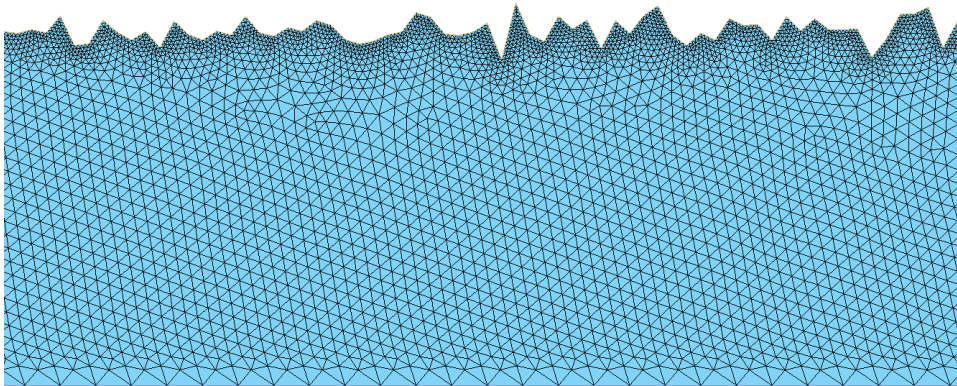


Fig. 6. An example of one of the generated geometries, together with the mesh

The results in Table 3 show that the greatest uncertainty concerns the higher values of Reynolds number, for  $Re = 1,700$ -99.8% of the results are within  $\pm 5.3\%$  of the mean value, while for  $Re = 100$  only within  $\pm 2.1\%$ .

Moreover, a comparison the Darcy roughness coefficient was made of the results from the random surface simulation ( $f_{rand}$ ), the coefficients resulting from the classical theory ( $f_{classic} = 64/Re$ ) and the results of the experimentally

Table 3

The influence of randomness on the results of the analyzes

Re	100	300	500	900	1,300	1,700
V	2.01	6.03	10.05	18.09	26.13	34.17
$f_{\text{rand}}$	0.704	0.241	0.149	0.090	0.068	0.056
$\sigma$	0.0051	0.0023	0.0018	0.0014	0.0013	0.0011
$f_{\text{rand}} + 3 \sigma$	0.719	0.248	0.155	0.094	0.072	0.059
$f_{\text{rand}} - 3 \sigma$	0.689	0.234	0.144	0.086	0.064	0.053

obtained coefficients ( $f_{\text{exp}}$ ) (MOHIUDDIN MALA, LI 1999), as well as those generated by the Gaussian random distribution formula ( $f_{\text{gaussian}}$ ) calculated from the formula (12). In the equation,  $f_D$  has been replaced by  $f_{\text{classic}}$ . All results were compared to the experimental data (Tab. 4).

Table 4

Comparison of Darcy roughness coefficients

Re	100	300	500	900	1,300	1,700
V	2.01	6.03	10.05	18.09	26.13	34.17
$f_{\text{exp}}$	0.720	0.242	0.146	0.088	0.068	0.058
$f_{\text{rand}}$	0.704	0.241	0.149	0.090	0.068	0.056
Absolute difference	-0.016	-0.001	0.003	0.002	0.000	-0.002
Relative difference	2.2	0.4	1.9	2.1	0.3	4.1
$f_{\text{classic}}$	0.640	0.213	0.128	0.071	0.049	0.038
Absolute difference	0.080	0.028	0.018	0.017	0.018	0.021
Relative difference	11.1	11.7	12.6	19.5	27.3	35.5
$f_{\text{gaussian}}$	0.777	0.259	0.155	0.086	0.060	0.046
Absolute difference	-0.057	-0.017	-0.009	0.002	0.008	0.013
Relative difference	7.9	7.2	6.1	2.3	11.7	21.7

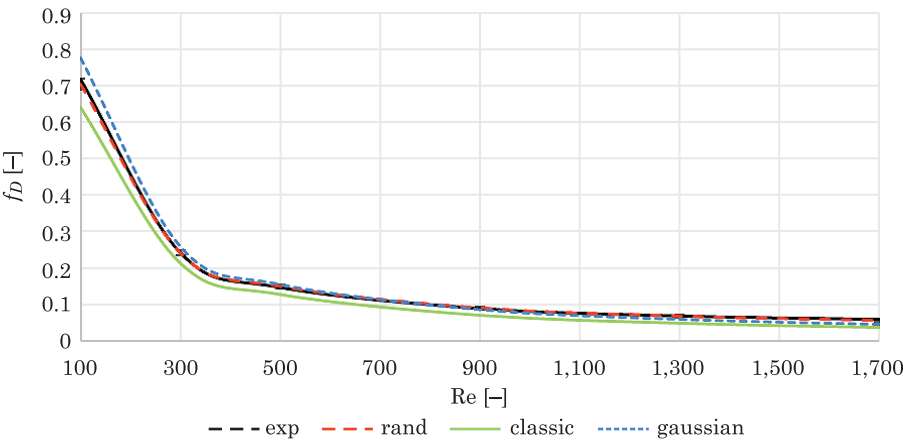


Fig. 7. Comparison of roughness coefficients

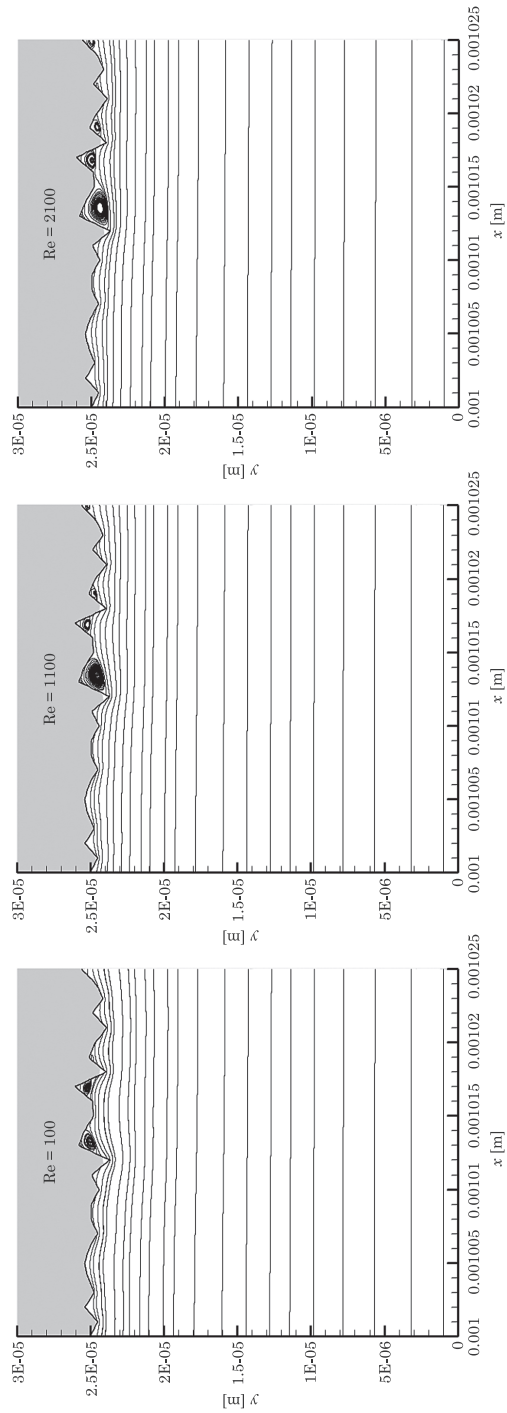


Fig. 8. Distribution of streamlines for a randomly generated surface

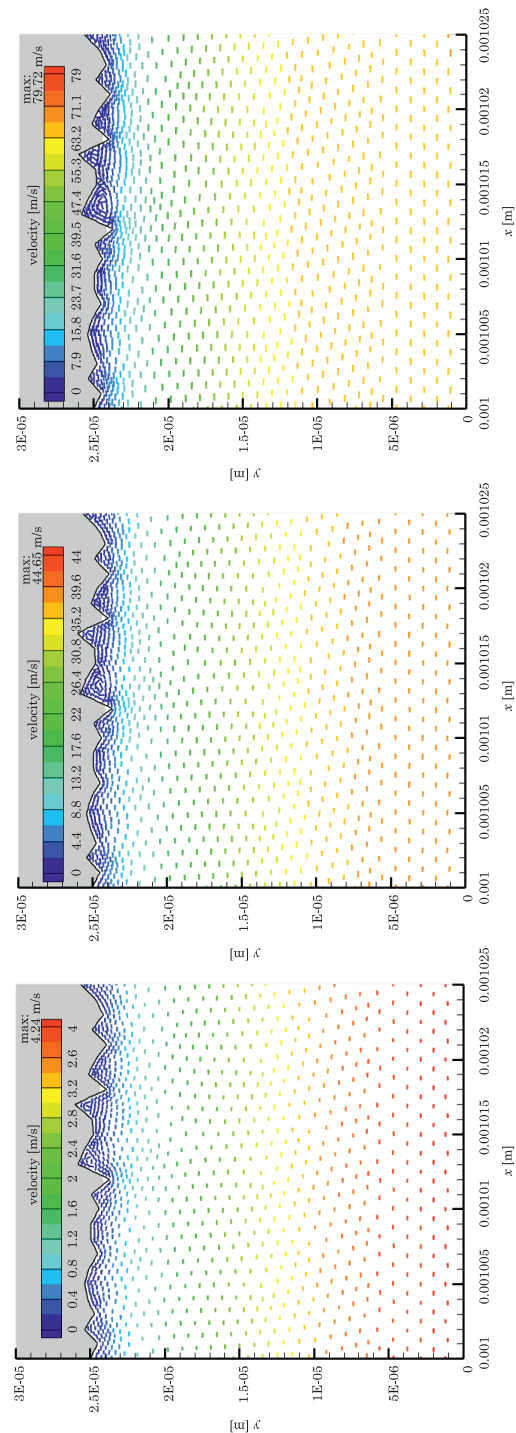


Fig. 9. Distribution of velocity vectors for a randomly generated geometry

Based on the results contained in Table 4 and Figure 5, it can be concluded that the randomly generated surface is very consistent with the experimental results. The maximum relative difference is about 4% for Reynolds number 1,700. For smaller Reynolds numbers the error does not exceed 2.2%. Using the data from the classical theory, it is possible to compute the corrected coefficients of a correlation using a random Gaussian distribution. It gives relatively good results not exceeding 8% error for Reynolds numbers from 0 to 1,100.

To visualize the flow and present the influence of the Reynolds number on the flow, the distributions of the streamlines and velocity vectors for the Reynolds numbers 100, 1,100 and 2,100 were generated for an exemplary configuration selected from 30 models (Fig. 6, 7).

The results of flows in microchannels with roughness  $w$  presented in Figures 8 and 9 show the deformation of the flow image. The analysis of the test results shows the formation of circulation zones in the cavities between the elements. With increasing speed, they increase their share in the considered cavity (the length of the vortex increases). The distribution of the vortices is irregular, depending on the depth of the pit and the Reynolds number.

To investigate the pressure drop in the microchannel, 26 measurement planes have been defined. The pressures were related to the cross section at the inlet to the channel. The inlet velocity is 2.01 m/s ( $Re = 100$ ) and 22.11 m/s ( $Re = 1,100$ ).  $R_a$  is  $1.75 \mu\text{m}$ . The results are presented for 3 exemplary models (surf\_1, surf\_2, surf\_3) selected from the group of 30 created (Fig. 8, 9).

The pressure drop for  $Re = 100$  is close to the linear function. However, when the flow velocity increases to  $Re = 1,100$ , pressure fluctuations along the channel axis become apparent. The nature of the curve is similar, but the larger scale (for  $Re = 1,100$ ) allows to see the nonlinearity of the phenomenon. Despite the fact that the pressure drop has a completely different character for different models, they all converge to one value for  $l = 0.001 \text{ m}$ .

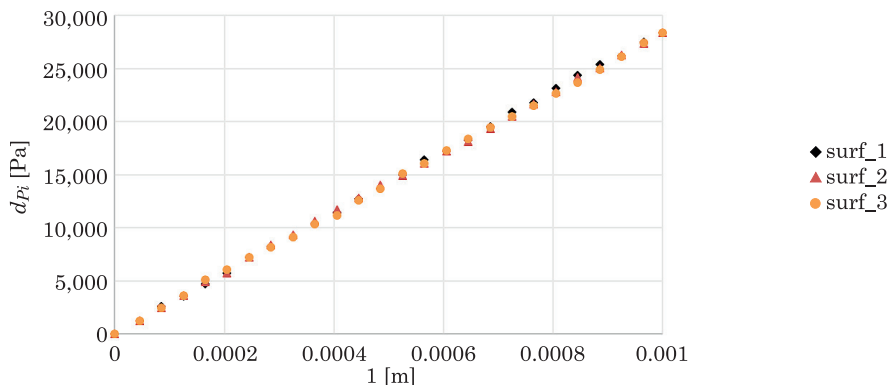


Fig. 10. Pressure drop for the number  $Re = 100$

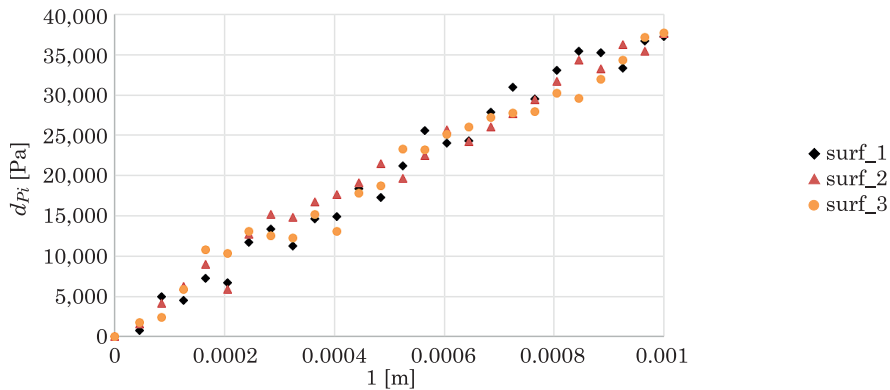


Fig. 11. Pressure drop for the number  $Re = 1,100$

## Conclusions

Along with the development of miniaturized technologies, microchannels have found wide application in microdevices, including in cooling systems of various technical devices, especially electronic devices. Hence, the need to research the influence of roughness on the flow in microchannels. The article presents the results of numerical tests of the influence of randomly modeled roughness on the flow and friction losses in microchannels. The analysis of the obtained results showed that the roughness has a significant influence on the flow in the microchannel.

The most important conclusions are as follows:

- Using the method of generating random geometry presented in the article, a very good agreement with the experimental data was obtained, especially in the range of lower Reynolds numbers, where the relative error was only 2.1%.
- The main reason of observed pressure drop is formation of recirculation zones in the roughness pits.
- The one of parameters influencing the length of the recirculation zones are the roughness height. As a result of increasing the speed, the vortices increase with the filling of a given cavity.
- Friction losses decreases as the Reynolds number increases.
- Comparing several methods of calculating the Darcy roughness coefficient, it was found that generating random geometry is the method whose results are closest to the data obtained by experiments. The coefficients resulting from the classical theory generate from 11.1 to 35.5% error (depending on the Reynolds number), therefore it is not the recommended method for calculating the linear loss factor in microchannels. On the other hand, the corrected coefficients using the formula obtained from the Gaussian distribution model achieve an amazingly

good result from 2.3 to 8% (for Reynolds numbers in the range 100-1,100). The discussed model works worst for Reynolds numbers in the range 1,100-1,700, reaching 22% of the relative error.

– The model created on the basis of pseudorandom numbers highlights the nonlinearity of the pressure drop along the channel axis (for higher Reynolds numbers – eg  $Re = 1,100$ ). This is expected on a micro scale where there are abrupt changes in parameters due to an increased proportion of roughness relative to the geometry dimension.

## References

- ANSARI M.Q., ZHOU G. 2020. *Influence of structured surface roughness peaks on flow and heat transfer performances of micro- and mini-channels*. International Communications in Heat and Mass Transfer, 110: 104428. <https://doi.org/10.1016/j.icheatmasstransfer.2019.104428>.
- CHU W.-S., KIM C.-S., LEE H.-T., CHOI J.-O., PARK J.-I., SONG J.-H., JANG K.-H., AHN S.-H. 2014. *Hybrid manufacturing in micro/nano scale: A Review*. International Journal of Precision Engineering and Manufacturing-Green Technology, 1(1): 75–92. <https://doi.org/10.1007/s40684-014-0012-5>.
- CROCE O.I.R.G. 2016. *Numerical simulation of gas flow in rough microchannels: hybrid kinetic – continuum approach versus Navier–Stokes*. Microfluidics and Nanofluidics, 20(5): 1–15. <https://doi.org/10.1007/s10404-016-1746-x>.
- DAI B., LI M., MA Y. 2014. *Effect of surface roughness on liquid friction and transition characteristics in micro- and mini-channels*. Applied Thermal Engineering, 67(1–2): 283–293. <https://doi.org/10.1016/j.applthermaleng.2014.03.028>.
- JIA J., SONG Q. 2019. *Effect of wall roughness on performance of microchannel applied in microfluidic device*. Microsystem Technologies, 25(6): 2385–2397. <https://doi.org/10.1007/s00542-018-4124-7>.
- KANDLIKAR S.G. 2005. *Roughness effects at microscale – Reassessing Nikuradse’s experiments on liquid flow in rough tubes*. Bulletin of the Polish Academy of Sciences: Technical Sciences, 53(4): 343–349.
- KANDLIKAR S.G. 2006. *Heat Transfer and Fluid Flow in Minichannels and Microchannels*. Elsevier, Amsterdam. <https://doi.org/10.1016/B978-0-08-044527-4.X5000-2>.
- KMIOTEK M., KUCABA-PIETAL A. 2018a. *Influence of slim obstacle geometry on the flow and heat transfer in microchannels*. Bulletin of the Polish Academy of Sciences: Technical Sciences, 66(2): 111–118. <https://doi.org/10.24425/119064>.
- KORDOS A., KUCABA-PIETAL A. 2018b. *Nanovortex evolution in entrance part of the 2D open type long nanocavity*. Bulletin of the Polish Academy of Sciences: Technical Sciences, 66(2): 119–125. <https://doi.org/10.24425/119065>.
- LALEGANI F., SAFFARIAN M.R., MORADI A., TAVOUSHI E. 2018. *Effects of different roughness elements on friction and pressure drop of laminar flow in microchannels*. International Journal of Numerical Methods for Heat & Fluid Flow, 28(7): 1664–1683. <https://doi.org/10.1108/HFF-04-2017-0140>.
- LU H., XU M., GONG L., DUAN X., CHAI J.C. 2020. *Effects of surface roughness in microchannel with passive heat transfer enhancement structures*. International Journal of Heat and Mass Transfer, 148: 119070. <https://doi.org/10.1016/j.ijheatmasstransfer.2019.119070>.
- MARZEC K. 2021. *Influence of Jet Position on Local Heat Transfer Distribution under an Array of Impinging Nozzles with Non-Planar Contour of the Cooled Surface*. Heat Transfer Engineering, 42(17): 1506–1521. <https://doi.org/10.1080/01457632.2020.1800280>.
- MIRMANTO M., KARAYIANNIS T. 2012. *Pressure drop and heat transfer characteristics for single-phase developing flow of water in rectangular microchannels*. Journal of Physics: Conference Series,



395. 6<sup>th</sup> European Thermal Sciences Conference (Eurotherm 2012) 4–7 September 2012, Poitiers, France. <https://doi.org/10.1088/1742-6596/395/1/012085>.
- MOHIUDDIN MALA G., LI D. 1999. *Flow characteristics of water in microtubes*. International Journal of Heat and Fluid Flow, 20(2): 142–148. [https://doi.org/10.1016/S0142-727X\(98\)10043-7](https://doi.org/10.1016/S0142-727X(98)10043-7).
- PELEVIĆ N., VAN DER MEER T.H. 2016. *Heat transfer and pressure drop in microchannels with random roughness*. International Journal of Thermal Sciences, 99: 125–135. <https://doi.org/10.1016/j.ijthermalsci.2015.08.012>.
- WHITEHOUSE D. 2004. *Surfaces and their Measurement*. Elsevier, Amsterdam.
- ZAREMBA D., BLONSKI S., JACHIMEK M., MARIJNISSEN M.J., JAKIELA S., KORCZYK P.M. 2018. *Investigations of modular microfluidic geometries for passive manipulations on droplets*. Bulletin of the Polish Academy of Sciences: Technical Sciences, 66(2): 139–149. <https://doi.org/10.24425/119068>.
- ZHANG C., CHEN Y., SHI M. 2010. *Effects of roughness elements on laminar flow and heat transfer in microchannels*. Chemical Engineering and Processing: Process Intensification, 49(11): 1188–1192. <https://doi.org/10.1016/j.cep.2010.08.022>.





## THE ADVANCED CAD MODEL OF A CARGO BIKE

*Sebastian Rzydzik<sup>1</sup>, Marcin Adamiec<sup>2</sup>*

<sup>1</sup> ORCID: 0000-0003-3352-3986

<sup>2</sup> ORCID: 0000-0002-3201-0276

Department of Fundamentals of Machinery Design  
Faculty of Mechanical Engineering  
Silesian University of Technology in Gliwice

Received 17 August, accepted 06 December, available online 07 December.

**Key words:** generative model, parametric model, mechanical design, CAD, bike, cargo bike.

### Abstract

This article describes a way to create a generative model using the example of a cargo bike model, which is a very simple object which can be used to present all important rules applied during creating generative models. Great attention was paid to the issue of model parameterization, which is an elementary thing in all modelling. Besides these aspects, it is also shown how to transform a parametric model into a generative model using programming languages. In the last part of the article, tests of correct working of model were included which also focused on the right position cyclist on the bike and shows how model of cargo bike could change its sizes thanks to correctly created generative model.

### Introduction

During the design process of a mechanical system, the most common problems include (KUANG-HUA 2014):

- frequent design changes, especially at the beginning of work;
  - an increase in the number and complexity of the required design changes,
- when the design process is carried out in large, distributed design groups implementing their subtasks in various engineering disciplines;

---

Correspondence: Sebastian Rzydzik, Katedra Podstaw Konstrukcji Maszyn, Wydział Mechaniczny Technologiczny, Politechnika Śląska, ul. Konarskiego 18a, 44-100 Gliwice, e-mail: [sebastian.rzydzik@polsl.pl](mailto:sebastian.rzydzik@polsl.pl).

– very often a simple change in one part causes an explosion of changes in related parts and assemblies, thus affecting assembly changes in the entire product;

– each time the changes made to the product model must meet the design constraints requirements.

In the 1960s, Ivan Sutherland developed a program called Sketchpad (SUTHERLAND 2003). Sutherland's idea for computer-aided drawing (later known as computer-aided design) was to first draw a sketch (a generic geometrical shape) and then add a set of dimensions. In fact, all current CAD systems use this concept. To increase the usability of the created geometric model, dimensions are divided into further dimensions with fixed values (fixed dimensions) and dimensions with floating values (open dimensions) (SHAH, MÄNTYLÄ 1995). It makes it easy to change the value of the selected dimensions depending on the respective needs. This model is called a parametric geometrical model (VUKAŠINOVIĆ, DUHOVNIK 2019, KALKAN et al. 2018). Parametric-based models allow for “reusable geometrical models” to be created. The creation process of parametric geometrical models requires experience and knowledge.

The advantages of parametric modelling include:

– the mechanical designer has the ability to define design variables by assigning dimensions to parts and creating geometric and form constraints between parts to build a parametric product model;

– in the case of a parametric product model, the designer can make changes to the model simply by modifying the values of the geometric dimensions. This allows, among others, to quickly identify potential collisions between elements in mechanisms;

– parametric product models allow designers to effectively search for alternative design solutions.

The next step in the development of CAD systems was the generative model. A generative model is intended to support the engineer in the course of routine activities (SKARKA 2006, 2011, COOPER et al. 1999, FOSTER 2019, BUONAMICI

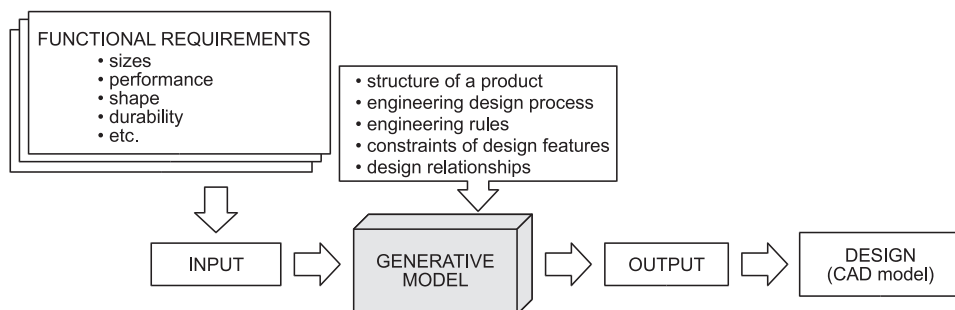


Fig. 1. Operation scheme for a generative model

Source: based on SKARKA (2006).

et al. 2020). To create such a model, a parametric geometrical model and the knowledge base associated with this model are needed. An applied parametric model is a generalized model, where the degree of generalization depends on the needs and use of such a model. Parametric models are used to create families of similar artefacts, while the generative model is a template of the engineering design process. It is a record of a certain class of artefacts, for which knowledge is acquired and stored in the form of relations between certain features and functional requirements (Fig. 1) (SKARKA 2006).

Creating generative models is a process related to such issues as: methodology of designing mechanical systems, computer science (practical knowledge of programming languages), CAX systems (including the ability to use an integrated programming language), and knowledge engineering. Due to the fact that the scope of issues is very wide, self-generating models should be created in interdisciplinary teams.

## **Methodology of creating generative models**

Our own observations allow us to conclude that the process of creating parametric models can be presented as a sequence of some stages. Below, it is proposed to create generative models in four stages:

STAGE 1: Standardization of the work environment. The purpose of this step is to determine the parameters of the working environment, i.e. to select the type of the CAD software and, if necessary, the software for numerical calculations and simulations; development of report templates and drawing documentation; selecting the type of software, storage location and repository structure for files with models and reports, etc.

STAGE 2: Analysis of the design of the mechanical system. The purpose of this stage is to analyse the structure of a mechanical system in the context of creating a parametric model of this system. To this end, it is necessary to analyse the individual components with regard to their use in an assembly or assemblies in relation to their use in a product. The parametric model is driven by the values of some of the highlighted parameters (main dimensions) that can affect the values of other parameters. For this purpose, an analysis of documentation from the element/assembly design process should be used. As a result of this analysis, the structure of the parametric model and the relational relations between elements and assemblies should be defined. Then sets of main dimensions and characteristic features will be created, as well as a set of constraints on the values assumed by these dimensions and features.

STAGE 3: Create a parametric model. At this stage, a parametric model should be created using the functions and tools available in the selected CAX system. The results of the analysis carried out in STAGE 2 are important here. Knowledge of the identified features and dimensions is crucial because at this

stage the computational models will be used to link the geometric, material, and dynamic features. The process of building parametric models can be presented as the following activities:

- analysis of the available parametric models and special tools available in the selected CAD program, intended for generating this class of models;
- in the case of using ready-made parametric models, adaptation of the obtained models to the adopted requirements and limitations;
- in case of the need to build own parametric models of parts – creating geometrical models of parts with a set of assigned parameter sets (main dimensions);
- if it is necessary to build own parametric models of assemblies, creating geometrical models of assemblies with a set of parameters sets assigned to them (main dimensions);
- development of calculation scripts for parametric models of assemblies and parts, with particular emphasis on the relations between dimensions belonging to these assemblies and parts, and development of calculation scripts for the adopted calculation models;
- if there is a need to use a dialog system for communication with the user – developing the form of graphical user interface dialog boxes with the use of built-in tools or programming libraries developed, e.g. in an external tool software.

The created parametric models can be the basis for the development of generative models. In this case, you can apply elements of knowledge-based design, ultimately integrating design knowledge into the CAD model.

STAGE 4: Verification of the model. This step is to verify the created parametric and/or generative model in relation to the adopted assumptions and constraints. The generated geometric form and the created program code for the adopted calculation model should be thoroughly checked. It is recommended to develop a test example to facilitate verification.

## **Cargo bike advanced CAD model**

The cargo bike model is a very good example of the utility of designing generative models. Every man and woman have different physiques and needs (RIGGS 2016). It is possible to design a generative model of cargo bike and provide the user with a form, where the user will be able to set information about his height, data about goods which he would like to transport, or the number of people who would be passengers of this bike, and based on these data algorithms, the model of cargo bike will be the most compatible with information which were set by the user in form.

Everyone has different body sizes, so it seems normal for not everyone to be comfortable riding on all sizes of bikes. Of course, there are parts that can be

regulated, such as seat height, but the first step in choosing a bike should be to fit the correct frame size. In practice, there is an important dimension that allows us to choose the right frame size. This is the height of the crotch, which is the dimension from the floor to the crotch. This value should be multiplied by a special coefficient which depends on the type of bike for which the frame is chosen. In this project, a frame for mountain bike (MTB) was created, so in this case the coefficient was 0.57. The received value is the ideal size of the seat tube, so due to this we can read the rest of the important dimensions from the table on the producer's website. Table 1 shows an example of this.

Table 1

Element	Frame sizes for MTB bike					
	Sizes [cm]					
	XS	S	M	L	XL	XXL
Seat tube	34.5	40	44	48	52	56
Frame tube	54.5	58.5	61	63.5	66	68.5
Head tube	9.5	10.5	11.5	12.5	13.5	14.5
Bottom tubes of rear triangle	44					
Seat tube angle	73					
Head tube angle	70					

Source: based on PRZECODZIEN (2020).

## Diagram of a generative CAD model

Figure 2 shows a diagram of the generative model developed. The source of parameters for frame sizes from each type of bike – Long John and Trike – is a part file named “GLOBAL PARAMETERS.ipt”. Then each type is shaped separately. Based on the three main dimensions of the cargo – width, length, and height – the dimensions of the cargo space are calculated. It was assumed that the method of fixing the wheels to the frame and the wheel sizes will be common for each type of bicycle. Depending on the bike type selected, the main assembly is made in “00\_cargobike\_longjohn\_iassembly.iam” or “00\_cargobike\_trike\_iassembly.iam” and then this assembly is read by the parent assembly model, a file named “#Generative model of cargo bike.iam”. This file has an attached script and a dialog form. The script contains the functions necessary to control the dialogue, as well as functions to calculate the dimensions of the frame, cargo space, and other parts. The form “Cargo bike frame selection” has been created to control the dialogue.

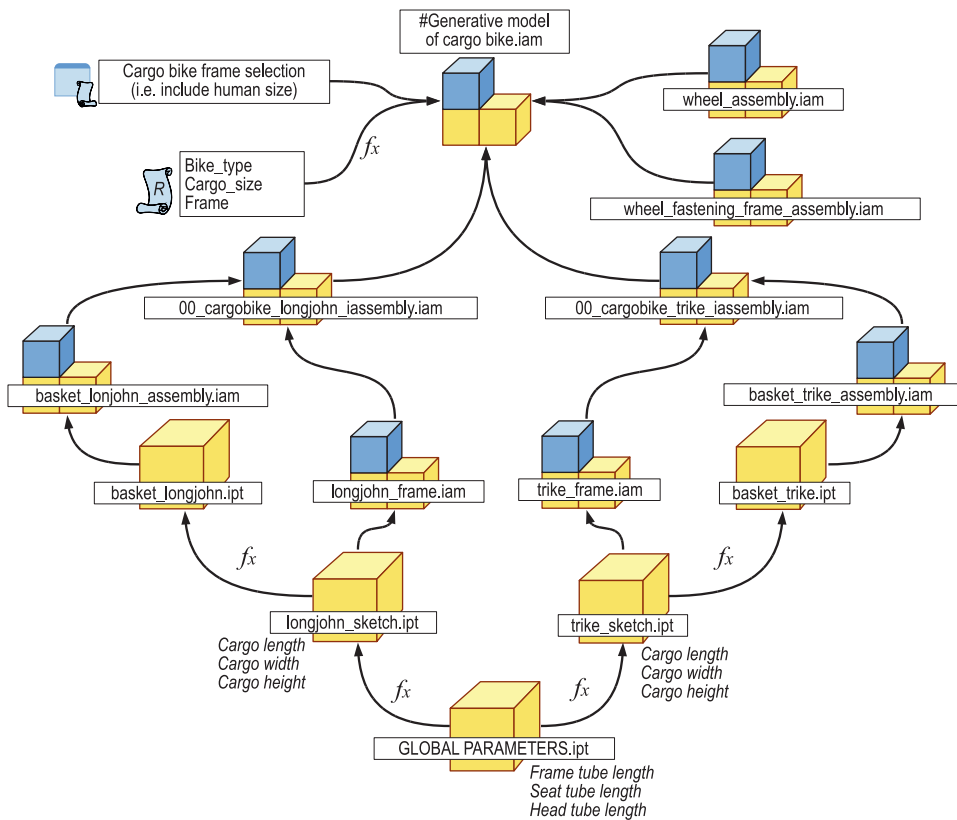


Fig. 2. Generative model diagram

## Generative model of a cargo bike

The first step in creating the right generative model is to prepare the correct parametric model (SHIH 2019, LANCASTER 2020). We can do it with a standard modelling method, which we use during our daily work. It is only important to find one or a few significant dimensions which will define other dimensions of the model. In case of creating cargo bike model this, the most important dimensions were length of seat tube, head tube and frame tube. So if there are only three control variables which will be responsible for all bicycle figure in part for cyclist, this is a good idea to put them into the separate model file and in the next steps of modelling relate to them. So, as we can see in Figure 3, a file with only three parameters in the list was created.



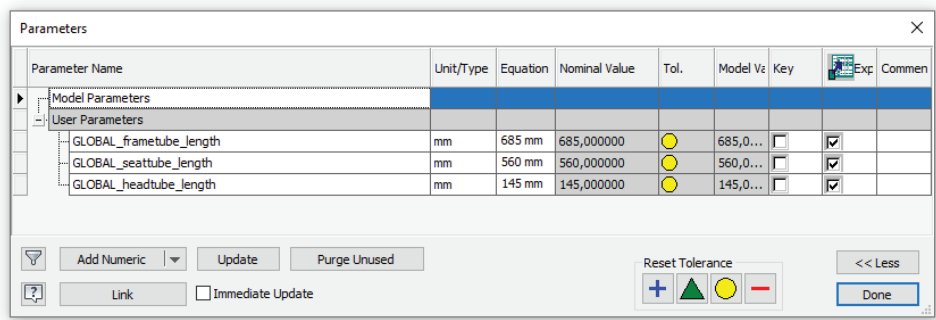


Fig. 3. Global parameters

Thanks to this simple operation, we obtained the possibility to import this parameter into any model file where it will be necessary. After this, I could create parameters in the file with a sketch of the bicycle. In the next steps, only these 3 variables were used to obtain any other tube figure of all the cargo bikes. The list of parameters and mathematical operations performed is shown in Figure 4.

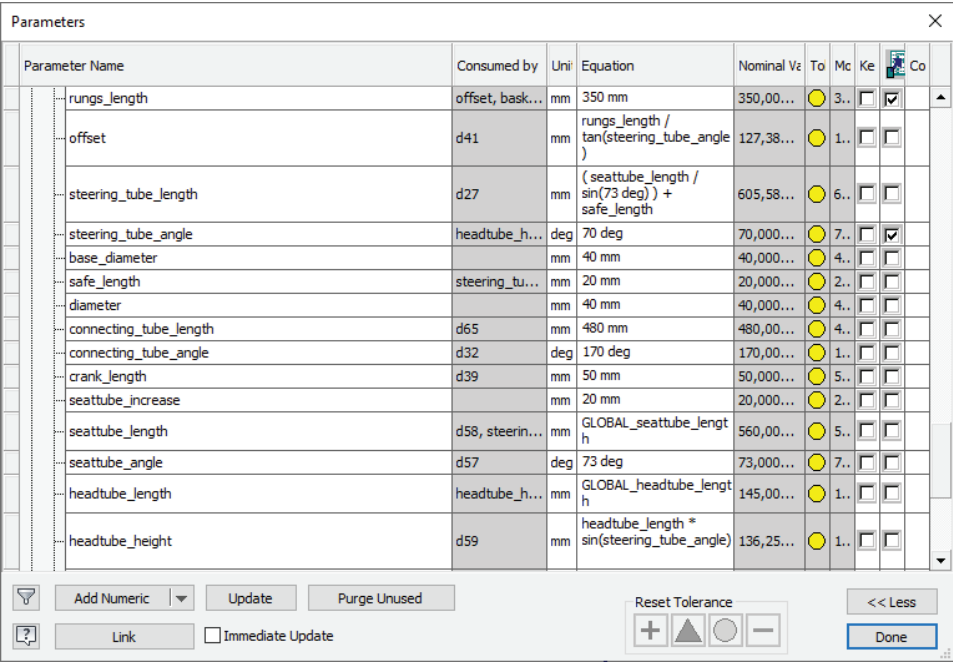


Fig. 4. List of parameters in the sketch file

In this project, the frame generator (Autodesk. 2020, MUNFORD 2016, SHIH 2019) was used. This is a tool offered by Autodesk Inventor that allows to replace the sketch with tubes models and create simple connections between these elements (LANCASTER 2020). Therefore, this is something which will be perfect to use in a bicycle model. The very important thing was also right and the full constraint of the sketch because during the model work all of these elements will be changing all the time. Thanks to the use of defined parameters and sketch constraints, a drawn model of a cargo bike could be built on a few planes in three-dimensional space. It is visible in Figure 5. After this, it was possible to create a frame assembly using the aforementioned tool.

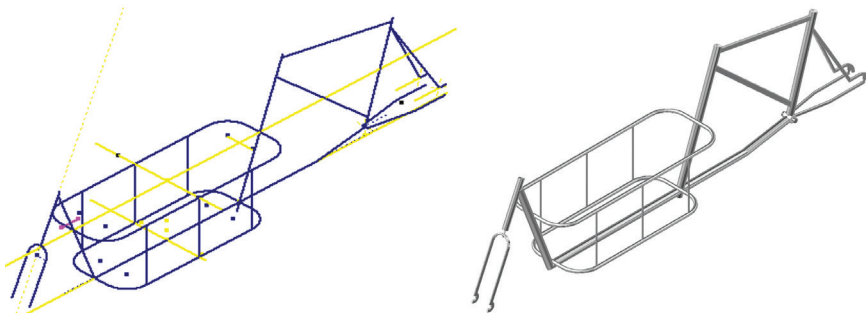


Fig. 5. Sketch and frame construction of a cargo bike

After the frames were fitted with the operations mentioned above, typical bicycle accessories and instruments such as wheels, saddle, steering wheel, and pedals were added. Normally, the Long-John bike also has a rod connecting the handlebar to the front wheel, which allows its turning, but this element was not included in the model as it is a less important accessory in the context of the main topic. So there were prepared in all 8 assemblies which differ from each other generally only in the form of a basket, but thanks to this and the option iAssembly in Autodesk Inventor it is simple to switch models between these which are actually required by the user. All of these assemblies are presented in Figure 6.

The very important item was the basket, which is used to transport goods and people. This is an accessory which has to cooperate with frame, so its dimension had to be correctly parametrized and addicted to dimensions of frame.

So, if we have prepared a parametric model now, we can focus on the most important part of generative models – the computer program and forms. The first step was to import all bicycle assemblies into one large assembly and turn off their visibility. In assumptions of the project program, the visibility between these models will be changed according to the information which will be put in the form of the user. The very good idea is also to create a list of control parameters that will cooperate with the script and will be used to store variable values. These things are visible in Figure 7.

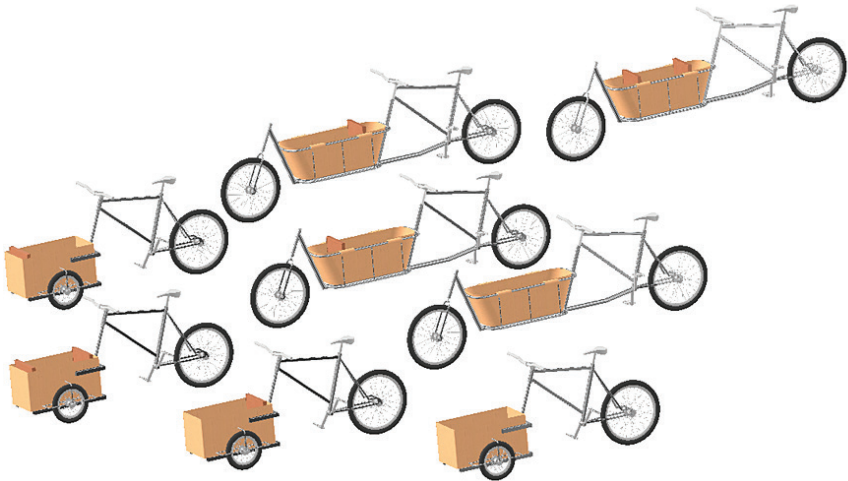


Fig. 6. All models of the cargo bike

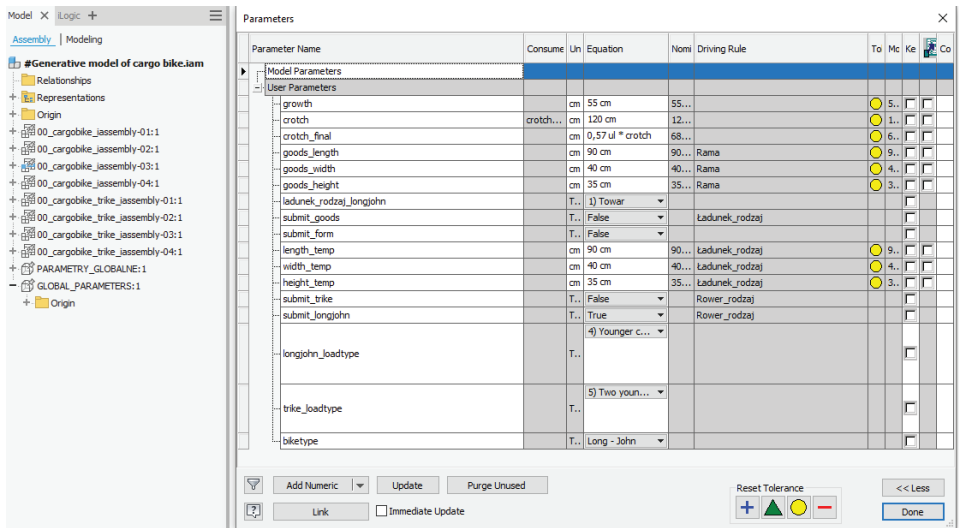
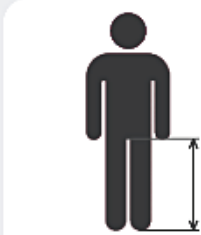


Fig. 7. Imported models and list of control parameters

After preparing the main model and parameters, it was possible to start programming all the generative parts. The first thing that was to be done was design the user form which will be responsible for the interaction between the user and the model. To implement these assumptions, the form was split into steps, and the first of them is selection of the type of cargo bike. There are only two options (for long john or trike) and each of them activates another section of form that is responsible for this type of cargo bike which the user has chosen. All this form was presented in Figure 8.

Cargo bike frame selection ✕

^ Frame size and bike type choosing



Bike type

☐ Long - John

☒ Trike

Crotch height

^ Type of cargo carried

Type of cargo carried by long-john

☒ 1) Goods

☐ 2) Adult or older child (over 12 y.o.)

☐ 3) Younger child (under 12 y.o.) front to the direction of journey

☐ 4) Younger child (under 12 y.o.) backwards to the direction of journey

☐ 5) Two younger children

Type of cargo carried by trike

☐ 1) Goods

☐ 2) Adult or older child (over 12 y.o.)

☐ 3) Younger child (under 12 y.o.) front to the direction of journey

☒ 4) Younger child (under 12 y.o.) backwards to the direction of journey

☐ 5) Two younger children sitting opposite each other

☐ 6) Two younger children sitting next to each other front to the direction of journey

☐ 7) Two younger children sitting next to each other backwards to the direction of journey

☐ 8) Four younger children

^ Dimensions of goods

The length of the goods

The width of the goods

The height of the goods

Fig. 8. Cargo bike selection form

Right working of this form and model was possible thanks to using rules which are written in Visual Basic of Applications language.

Rules *Goods\_type* and *Frame* are the most important rules in this model. They are responsible for switching bikes, assigning values to appropriate parameters, and generating the final version of the cargo bike. *Button\_active* is a rule that activates the 'OK' button in the form after entering the user's input data. Rule *Bike\_type* allows for dynamic switching between suitable fields in form according to chosen by user type of cargo bike. *Form\_open* is used as a trigger for opening the form at the moment when the model is opened.

## Verification tests

After creating all elements that were described above, it was necessary to check if the generative model fulfils its function. To show the differences in the position of the human body on a bicycle with different frame dimensions, a dummy model was used (Fig. 9).

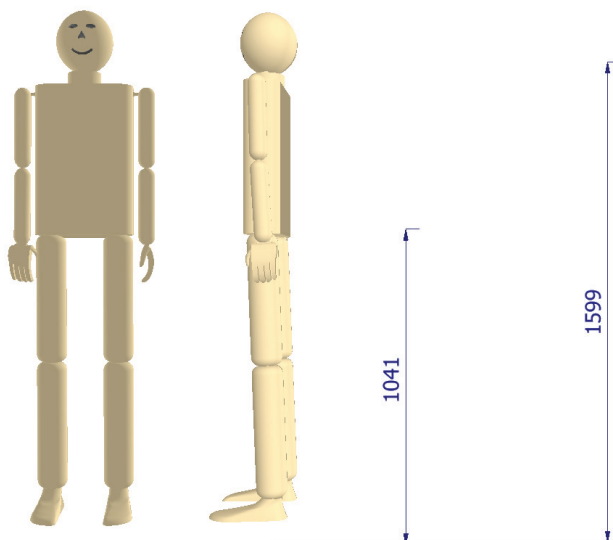


Fig. 9. Dummy model used to tests

In each of the tests, it had exactly the same dimensions, which was to show its current position. So, the dummy model was placed on the bike with the smallest frame. As you can see in Figure 10, the bike was too small for the person with a body similar to this dummy. It was not comfortable and ergonomic for cycling. After changing the crotch to a larger dimension, this situation was slightly better, but it was still not in the correct position (Fig. 11).

So, in the last test, the real value of the crotch dimension of the dummy was given. It was not surprising that in this case the frame size was acceptable for the body dimensions of the dummy (Fig. 12).

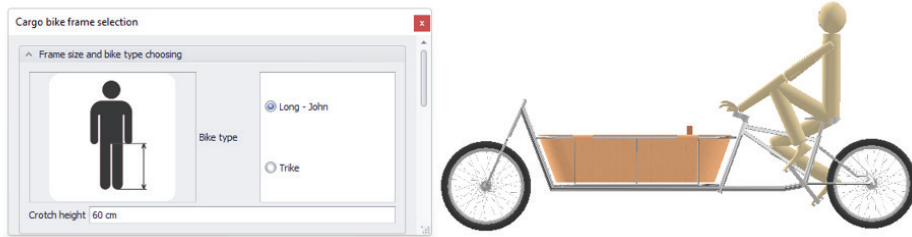


Fig. 10. Test with a dummy in the smallest frame

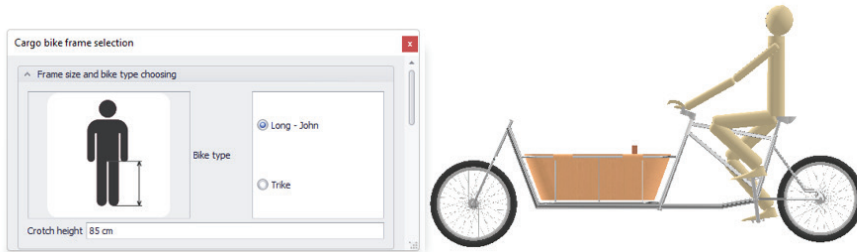


Fig. 11. Test with a dummy in the medium frame

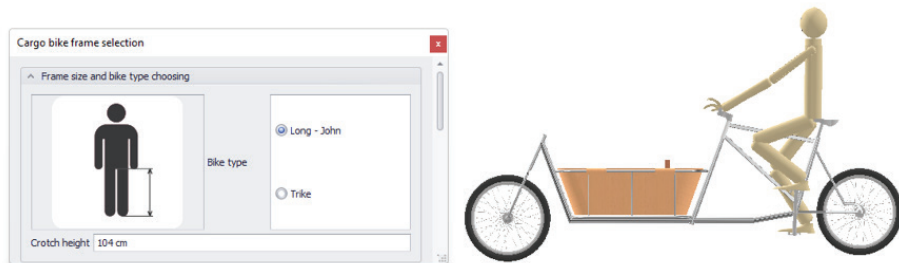


Fig. 12. Test with a dummy in the correct frame

Also, in the parameter lists there are changes which are submitted by the work of rules. In Figure 13 and Figure 14 the differences between the global parameters (which are the most important parameters in this model) were shown depending on the given height of the crotch. All operations and changes to parameter values take place in the background during the execution of the generative model functions, while the user entered only one piece of information in the form.

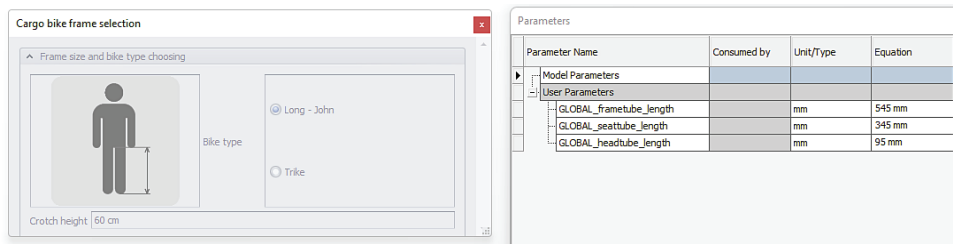


Fig. 13. Value of global parameters when a small crotch height value was given

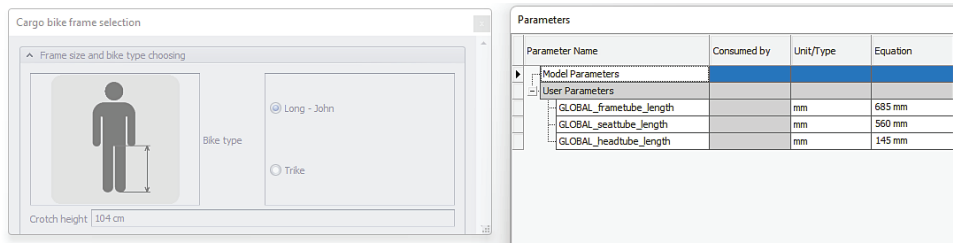


Fig. 14. Value of global parameters when a small crotch height value was given

Summary

Generative models are created using parametric models. Parameterization allows you to create reusable geometric models (SHAH, MÄNTYLÄ 1995) or structure families. The process of developing parametric models requires experience and knowledge about potentially other applications of the constructed system.

The input parametric model is a generalized model. The scope of the generalization depends on the needs and purpose of such a model. Parametric models are suitable for creating families of structures for a predetermined structural form. On the other hand, the auto-generating model is a construction template, a record of a class of technical objects, taking into account the design knowledge identified especially for their needs.

The main disadvantages of generative models are the following:

1. Their flexibility and use depend on the scope and quality of the integrated knowledge. In the case of newly created structures, the constructor, while selecting the design features, focuses solely on solving the current problem. At the same time, it does not deal with generalizing its actions, which should be treated as typical behavior. Only creating many similar solutions allows the constructor to refer to his experience and attempt to generalize the developed methods. This is a known issue and can only be mitigated; it cannot be eliminated. Therefore, autogenerating models are difficult to develop in innovative structures, although the knowledge contained therein may be the basis for the development of such structures.

2. The incorrect parameterized input geometric model (of parts and assemblies) causes many problems related to the resulting limitations in shaping geometrical features. Before the parameterization process of the geometric model, the basic parameters of the product, in particular the ranges of the main dimensions, should be clearly defined and then related to the design features. During the parameterization process, one should refer to experience (self or other constructors), because parameterization of geometric models is a complex creative process.

3. Although the methodologies for generating generative models are not related to specific CAX systems, their implementation must take into account the limitations imposed by a given CAX system. The most noticeable here is the lack of a format for recording geometric models, recognized by leading CAX software producers, along with the knowledge that was used to generate these models. The greatest hopes are associated with the STEP format, which according to the standard allows for the recording of information related to all phases of a product's existence.

## References

- Autodesk. 2020. *Frame Generator overview*. <https://knowledge.autodesk.com/support/inventor/learn-explore/caas/CloudHelp/cloudhelp/2020/ENU/Inventor-Help/files/GUID-953F560A-C2D3-4031-8348-762054C7C779-htm.html> (access: 09.11.2020).
- BUONAMICI F., CARFAGANI M., FURFERI R., VOLPE Y., GOVERNI L. 2020. *Generative Design: An Explorative Study*. Computer-Aided Design and Application, 18(1): 144-155.
- CAMBA J.D., CONTERO M., COMPANY P., HARTMAN N. 2020. *The Cost of Change in Parametric Modeling: A Roadmap*. Computer-Aided Design and Application, 18(3): 634-643.
- Cargocycles. 2020. *Long-John cargo bike photography*. <https://cargocycles.com.au/wp-content/uploads/2020/02/babboe-mini-vlt2020-2.jpg> (access: 09.11.2020).
- COOPER S., FAN I., LI G. 1999. *Achieving competitive advantage through knowledge-based engineering: a best practice guide*. Prepared for the Dept. of Trade and Industry by Dept. of Enterprise Integration, Cranfield University.
- FOSTER D. 2019. *Generative Deep Learning*. O'Reilly Media Inc., Sebastopol.
- ISO 10303: Industrial automation systems and integration – product data representation and exchange. Standard for the Exchange of Product model data (STEP). 2007. International Organization for Standardization. Mishra R.S., Mahoney M.W. Friction Stir Welding and Processing, 1<sup>st</sup> ed. ASM International, Materials Park, Ohio.
- KALKAN O.E., FATIH O., ALTUNİŞİK A. 2018. *Applications and usability of parametric modeling*. Journal of Construction Engineering, Management & Innovation, 1. <http://doi.org/10.31462/jcemi.2018.03139146>.
- KUANG-HUA C. 2014. *Product Design Modeling using CAD/CAE: The Computer Aided Engineering Design Series*. Elsevier, Amsterdam.
- LANCASTER M. (2016) *Inventor Frame Generator Skeleton and Model Structure*. SYNERGIS Engineering Desing Solutions. <https://synergis.com/2016/01/14/inventor-frame-generator-skeleton-and-model-structure> (access: 08.11.2020).
- MUNFORD P., NORMAND P. 2016. *Mastering Autodesk Inventor 2016 and Autodesk Inventor LT 2016*. Autodesk. Sybex Inc., Hoboken.
- PRZECHODZIEN Ł. 2020. *Rozmiar ramy rowerowej – jaki wybrać? Rowerowe porady*. <https://roweroweopady.pl/rozmiar-ramy-rowerowej> (access: 07.11.2020).



- RIGGS W.W. 2016. *Cargo Bikes as a Growth Area for Bicycle vs. Auto Trips: Exploring the Potential for Mode Substitution Behavior*. Transportation Research. Part F. Traffic Psychology and Behaviour, 43: 48-55. <http://doi.org/10.1016/j.trf.2016.09.017>.
- SHAH J.J., MÄNTYLÄ M. 1995. *Parametric and Feature-Based CAD/CAM: Concepts, Techniques and Applications*. A Wiley – Interscience publication, Hoboken, New Jersey.
- SHIH R. 2019. *Parametric Modeling with Autodesk Inventor 2020*. SDC Publications, Mission.
- SHIH R.H. 2019. *Learning Autodesk Inventor 2020: Modeling, Assembly and Analysis*. SDC Publications, Mission.
- SHKIH R.H. 2019. *Parametric Modeling with Autodesk Inventor 2020*. SDC Publications, Mission.
- SKARKA W. 2006. *Knowledge acquisition for generative model construction*. In: *Leading the Web in concurrent engineering: next generation concurrent engineering, Frontiers in Artificial Intelligence and Applications Series*. Eds. P.S. Ghodous, R. Dieng-Kuntz, G. Loureiro. IOS Press, Incorporated, p. 263–270.
- SKARKA W. 2011. *Ontology-based intelligent personal assistant*. In: *New World Situation: New Directions in Concurrent Engineering*. Eds. J. Pokojski, S. Fukuda, J. Salwianski. Proceedings of the 17<sup>th</sup> ISPE International Conference on Concurrent Engineering, Advanced Concurrent Engineering, Springer London, Limited, p. 267–274.
- SOBIESZCZANSKI-SOBIESKI J., MORRIS A., VAN TOOREN M. 2017. *Multidisciplinary Design Optimization Supported by Knowledge Based Engineering*. Wiley, Hoboken, New Jersey.
- SUTHERLAND I.E. 2003. *Sketchpad: A man-machine graphical communication system*. Tech. Rep. UCAMCL-TR-574, Computer Laboratory, University of Cambridge, Cambridge MA.
- Trike cargo bike photography*. 2020. Cargocycles. <https://cargocycles.com.au/wp-content/uploads/2018/02/babboe-big-01-65-1.jpg> (access: 09.11.2020).
- VUKAŠINOVIĆ N., DUHOVNIK J. 2019. *Advanced CAD Modeling. Explicit, Parametric, Free-Form CAD and Re-engineering*. Springer Nature, Switzerland AG.



## SIMULATION STUDY OF A COMPOSITE LANDIG GEAR OF ULTRALIGHT AND VERY LIGHT AIRCRAFT

*Paulina Zenowicz*

ORCID: 0000-0002-2778-2028

Faculty of Mechanical Engineering  
Silesian University of Technology in Gliwice

Received 09 August 2021, accepted 24 November 2021, available online 25 November 2021.

**Key words:** landing gear, aircraft vehicles design, knowledge-based design, drop test analysis, mechanical engineering, material engineering.

### Abstract

There is a need to design new, lighter aircraft structures, which has a direct impact on the safety and costs of aircraft maintenance. One of basic parts of an aircraft is its landing gear, whose main functions are to enable taxiing, safe landing, take-off, and to assist the remainder of ground operations. Landing gear failures are usually related to metallurgy, processing, environment, design, and causes of overload. These are conditions that can be prevented using modern methods to calculate the strength of such a landing gear in various conditions. The paper presents stages of a simulation study of the fixed three-wheeled spring landing gear for an ultralight aircraft. Analysis of forces acting on the landing gear during drop test and their implementation by numerical computer methods allowed for the creation of a model in the CAD (Computer-Aided Design) tool and its FEA (Finite Element Analysis). These results were compared between a modeled classic spring landing gear and the one made of composite materials. The further goal of the research will be to build a drop test stand for a small landing gear used in airplanes and drones. This method has a significant impact on simplifying the design of the landing gear, its modeling, and optimization.

## Introduction

The paper presents the stages of a simulation study of the fixed three-wheeled spring landing gear for an ultralight aircraft. The main assumptions of the paper are the type of landing gear mounting, the type of aircraft, and the layout of the landing gear, i.e. two rear wheels and the front one.

The limitations of the tested structures are the minimum load capacity, deflection, and thus the dissipation of the impact force during the drop test and landing, structure weight, and feasibility. The issues of attention are elaborated further in the text.

The landing gear analysis was performed based on mathematical equations developed based on applied mechanics. Shape optimization is an engineering problem, while the selected materials and their analysis are related to material engineering. Moreover, the analyzes were performed based on IT techniques. For the design purposes, the Zenith STOL CH701 aircraft was selected for which the landing gear was analyzed. This is a very popular aircraft in the world. It is well-known construction, but this model of an airplane is still produced (*Introducing the Zenith...* 2021).

For the aircraft to be admitted to air traffic, it must meet the requirements. Based on the CS-VLA and the general principles of designing the landing gear, calculations were made to determine the force acting on the landing gear during the drop test (*Easy Access Rules...* 2018). All the parameters adopted for the calculations were based on the data of the CH701 aircraft.

The landing gear is a very important structural element of an aircraft, as it is the only mechanical system in an aircraft that is adapted to contact with the ground, and its durability determines whether the aircraft lands safely. There are different types of landing gears in aviation. The article focuses on a three-wheeled beam-type landing gear. These landing gears are made of various materials such as steel and aluminum.

Due to the necessity to carry out a practical analysis, a design of a measuring stand is developed, the purpose of which is to compare the results obtained by mathematical analysis and by an analysis carried out in specialized software used in the aviation industry.

Figure 1 shows the scope of work needed to optimize the existing landing gear and use new material and shape for it. This work is focused on the steps marked with a red rectangle. These are the stages related to the initial design phases.

The next phases that will be carried out will present dynamic dependencies that should be met during dynamic analysis. The dynamic analysis will cover the entire landing gear, including wheels and tires. The first step is a static analysis of the chassis beam itself, which I focused on in this article. Landing gear failures account for many of all defects reported in general aviation. These errors are usually related to material properties, processing, environment, design,

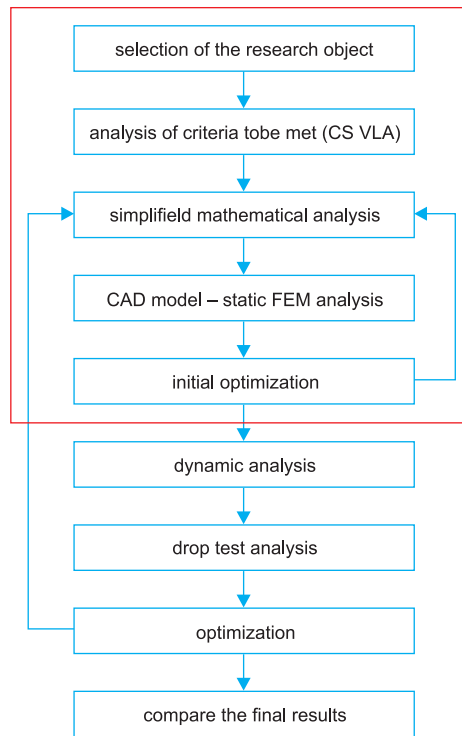


Fig. 1. Multidisciplinary approach to designing an airplane spring landing gear

and causes of overload. These are conditions that can be easily prevented by applying good engineering practices and maintenance practices that are usually well established in the aerospace industry (GUDMUNIDSSON 2013).

Landing gear efficiency depends on the damping system which is used in the landing devices. Highly effective rubber or hydraulic shock absorbers have high drag and weight. As a result, general aviation aircraft do not often use such damping devices. The most commonly used is the spring landing gear. Such a landing gear practically does not absorb impact energy and requires attention during landing. Of course, tires absorb some part of the energy, but it is a very small one and may not even be taken into account during the efficiency calculations. The shape and material of the spring used to have a direct impact on the performance of the selected landing gear (*Aircraft Landing Gear...* 2018).

The main approach reported in the paper is to perform FE (Finite Element Analysis) for the CAD (Computer-Aided Design) model of the Zenith STOL CH701 landing gear, using the calculations and recommendations contained in the CS-VLA.

This research aims to investigate ways of improving the efficiency of a general aviation airplane spring landing gear. The following tasks were solved to achieve

this goal: the laws of deformation of a standard metal spring and a similar composite spring were determined, the maximum load factor was compiled based on of values presented in the literature (RAYMER 1989) and an analysis of the landing gear mass change was made.

## Landing Gear of General Aviation Planes

The main functions of the landing gear are to enable taxiing, safe landing, and take-off, support for the remainder of the safe landing and ground operations. Currently, the most commonly used system is the “three-wheel” landing gear. With a three-wheeled landing gear e.g. in front of the main wheels, the airplane is stable on the ground and can land at a large angle of attack. Usually ultralight and very light airplanes use a fixed landing gear (RAYMER 1989).

Many general aviation aircraft use steel, aluminum, or composite spring to pick up and dampen the impact. Spring is popular because it is mechanically simple, usually light, and requires no maintenance.

The advantages of composite landing gear brackets are that they are lighter, more flexible, and non-corrosive. As the plane lands on the ground, the springs bend upward, dispersing and transferring the shock load to the airframe at a speed that will not deflect the plane.

## Requirements for landing gear of ultralight and very light planes

Requirements to the landing gear conditions for planes of little weight categories are described by special specifications (*Easy Access Rules...* 2018). Ultralight planes with MTOW (Maximum Take-off Weight) less than 450-600 kg must meet national documents of different countries. This class is regulated in the European Union Certifications Specifications for Very Light Aircraft (CS-VLA) (*Easy Access Rules...* 2018) and is limited to MTOW 750 kg. These requirements state that the calculated descent velocity, in meters per second, equals:

$$V_z = 0.51 \sqrt[4]{\frac{mg}{s}} \quad (1)$$

where

- $m$  – MTOW (Maximum Take-off Weight),
- $s$  – wing area,
- $g$  – gravitational acceleration.

The vertical landing loads determined as a result of such a landing also must be recalculated in accordance with CS-VLA for lateral and frontal landing loads. The effectiveness of the landing gear on the aircraft should also be verified by performing drop tests from a height:

$$h = 0.0132 \sqrt{\frac{mg}{s}} \quad (2)$$

According to CS-VLA, the height of the free drop test should be in the range from 0.235 m to 0.75 m. As a result, the drop test is often the main design case of landing gear loading.

Taking into account that the requirements for the landing gear of ultralight aircraft are simpler than very light ones, they were not considered in this research.

## Object of investigation

The considered STOL CH701 aircraft (Tab. 1) for which the landing gear was analyzed (Fig. 2) was selected for the analysis test. Designed for off-runway operations, the all-metal CH701 (Fig. 3), has many features that contribute to the aircraft's capabilities. The main difference of this aircraft is its ability to take off and land from very short distance.

For this, the wing of the aircraft has a very powerful aerodynamic devices: non-retractable slats and flaps.

Table 1

General characteristics and performance of CH701

General characteristics of CH 701
Wing area: 122.0 sq ft (11.33 m <sup>2</sup> )
Max takeoff weight: 1,100 lb (499 kg)
Fuel capacity: 20 US Gal (76 L)
Powerplant: 1 × Rotax 912 four-cylinder liquid-cooled piston engine, 80 hp (60 kW)

Source: based on *Introducing the Zenith...* (2021)

The main landing gear consists of wide wheels with hydraulic brakes (Fig. 2) attached to a leaf spring. The spring is made of aluminum alloy. There are recesses on the spring in the places where the spring is attached to the fuselage. Those are stress concentrators from the strength point of view. The wheels are covered with mudguard to prevent dirt from the wheels from getting onto the propeller during off-runway operations.



Fig. 2. CH-701 plane  
Source: courtesy V. Dudnik

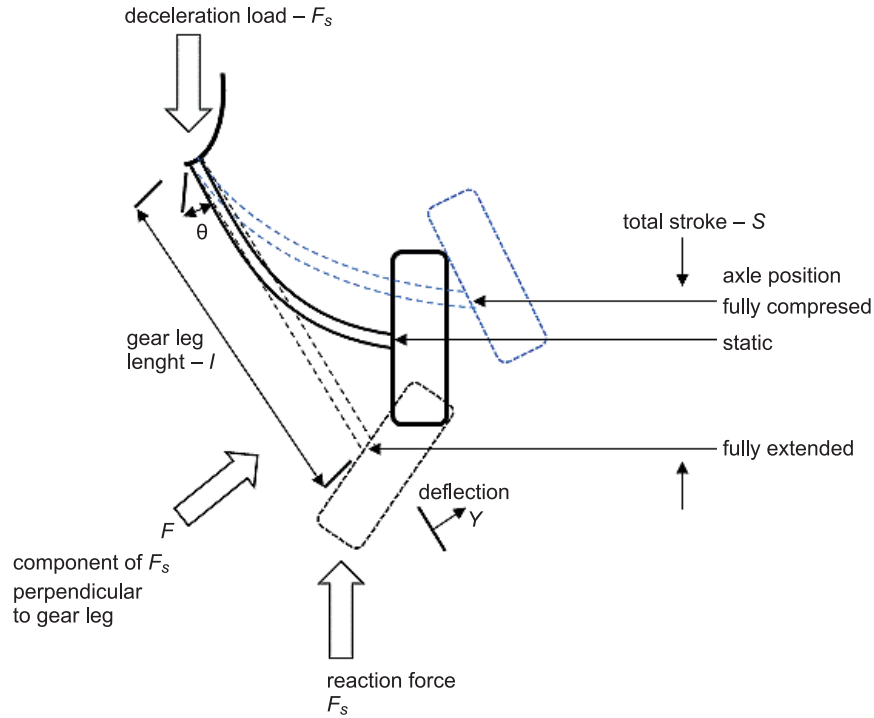


Fig. 3. Solid spring gear deflection  
Source: based on RAYMER (1989).



## Analysis based on simplified mathematical model and aircraft parameters

The shock absorber is represented by a leaf spring type, which depends on the elastic properties of the landing gear legs and normal force during contact with the ground. The diagram of the action of forces is presented in Figure 3.

For this example were calculated the reaction force  $F_s$  and a total stroke  $S$ .

$$F_s = \frac{W N_{\text{gear}}}{2} g \quad (3)$$

where:

$W$  – MTOW,  
 $N_{\text{gear}}$  – gear load factor,  
 $g$  – Earth's acceleration.

Gear load factor was taken from table data, for general aviation (RAYMER 1989):

$$N_{\text{gear}} = 3$$

The value of the force calculated from formula (3) is expressed as:

$$F_s = 7,342.8 \text{ N}$$

Then the total stroke is calculated for the aluminum and composite landing gear.

$$S = F_s (\sin^2 \theta) \frac{l^3}{3EI} \quad (4)$$

where;

$\theta$  – angle,  
 $l$  – length,  
 $E$  – Young modulus,  
 $I$  – moment of inertia.

It should be taken into account that different materials have different densities and Young's moduli. This has an impact on deflecting the landing gear leg during ground operations.

For the paper, a chassis made of 7075 T6 aluminum and Carbon Fiber Reinforced Polymer (CFRP) were considered. It should be emphasized that in this article CRFP was treated as an isotropic, homogeneous material, it is an introduction to the subsequent calculations, detailing the anisotropy of composite materials.

$$S_{\text{aluminium}} = 34.15 \text{ mm}$$

$$S_{\text{compostice (carbon fiber)}} = 16.42 \text{ mm}$$

### Analysis based on a detailed virtual 3D model

The analysis was performed in SolidWORKS® using the simulation static analysis module. In the beginning, supports have been added that are represented by the green arrows in Figure 4. They mark the places of supports – for both the landing gear cases, these are places where the landing gear connects to the plane. The landing gear is mounted in clamps at the fuselage. In the places where the clamps are to contact the beam, planes have been added, where the bindings have been added so that the beam also bends in the middle, which is in line with the actual deformations. Figure 5 presents mesh application.

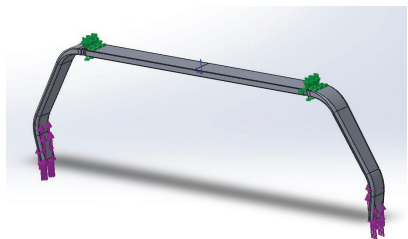


Fig. 4. Load and supports

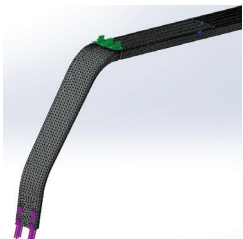


Fig. 5. Mesh application

Then loads were added. The force directions coincide with those in the plane, while the value was calculated using the analytical method. The purple arrows represent the force of  $F_s$ , calculated from formula (3), which is 7,342.8 N.

Then the material was selected, which is the aluminum alloy 7075 T6 and Carbon Fiber Reinforced Polymer. Again, to facilitate introductory calculations, isotropic properties of the composite material were assumed. Then the FEA mesh was selected, and the stress analysis was performed according to von Mises and deformation analysis.

For the analysis, a fine standard mesh was used with the size of one element: 8.5 mm and tolerance of 0.424 mm because it gives the most accurate results and the computation time is not significantly extended.

Table 2 shows a comparison of the analysis for an aluminum alloy beam for different mesh sizes.

Table 2

Dependence of the accuracy of the results on the size of the mesh

The global dimension of the mesh element [mm]	Mesh tolerance [mm]	Stress [MPa]	Displacement [mm]
33.95	1.69	208	22.72
18.25	0.91	227	23.02
8.48	0.42	216.5	23.17

## Comparison of results for landing gear analysis from different materials

The von Mises maximum stress criterion is based on the von Mises-Hencky theory, also known as shear energy or maximum strain energy theory. Concerning the principal stresses  $\sigma_1$ ,  $\sigma_2$ ,  $\sigma_3$  the von Mises stress in SolidWORKS® is expressed as (Dassault Systemes. 2019):

$$\sigma_{\text{Mises}} = \sqrt{\frac{[(\sigma_1 - \sigma_2)^2 + (\sigma_2 - \sigma_3)^2 + (\sigma_1 - \sigma_3)^2]}{2}} \quad (5)$$

The theory assumes that a plastic material starts to deflect at the point where the von Mises stress becomes equal to the stress limit. In most cases, the yield point is used as the stress limit. However, the SolidWorks® software allows using the maximum tensile strength or a user-defined stress limit.

$$\sigma_{\text{max.}} = \frac{\sigma_{\text{material}}}{k} \quad (6)$$

where

- $\sigma_{\text{max.}}$  – maximum allowable stress,
- $\sigma_{\text{material}}$  – ultimate tensile strength for each material,
- $k$  – safety factor, for landing gear  $k = 1.5$  (RAYMER 1989).

The paper assumes that the maximum stress is the limit for a given material. The maximum stress for each material was calculated according to formula (6). For the landing gear, the FEA simulation was used for two materials – aluminum alloy 7075-T6 and CRFP. Static analysis was performed for the previously modeled landing gear. The parameters of the considered materials are presented in Table 3.

Table 3

Parameters of the considered materials

Type of spring	Young's modulus [GPa]	Weight [kg]	Volume [m <sup>3</sup> ]	Density [kg <sup>3</sup> /m]	$\sigma_{\text{material}}$ [MPa]	$\sigma_{\text{max.}}$ [MPa]
Aluminium 7075 T6	71.7	13.7	0.00489	2,810	505	336.7
CFRP	150	7.8	0.00489	1,600	1,500	1,000

Source: based on INAGAKI (2000).

This analysis presents a static simulation of the landing gear deflection and von Mises stress under a given force  $F_s$ . The results in the form of reduced stresses and resultant displacements are presented in Table 4.

Table 4

Type of spring	Comeparison of results			
	von Mises reduced stress		Resultant displacement	
	min. [MPa]	max. [MPa]	min. [mm]	max. [mm]
Aluminium 7075 T6	0.005	208	0	22.72
CFRP	0.01	265	0	11.23

Figures below are von Mises stress static analysis (Fig. 7) and displacement (Fig. 8) figures for a beam made of 7075 T6 aluminum. The place of stress is concentrated under boundary conditions.

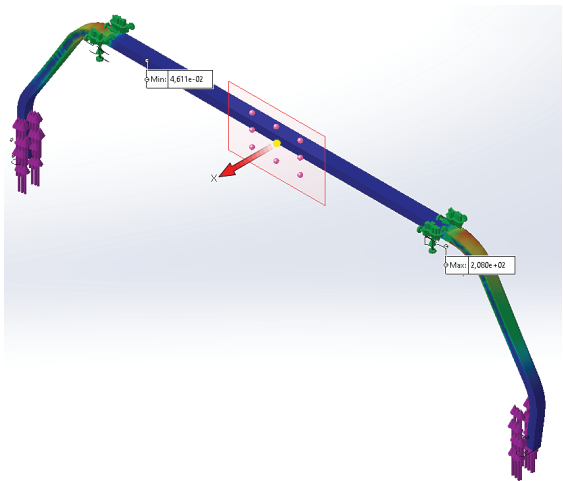


Fig. 6. Reduced stress according to von Mises – aluminum alloy

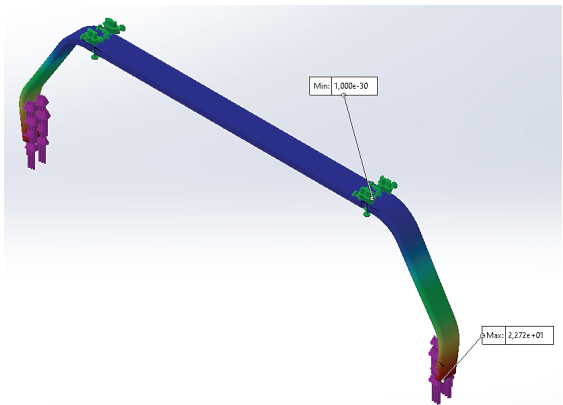


Fig. 7. Resultant displacement – aluminum alloy

The comparison of simulation results of the von Mises and displacement analysis are shown in Table 5.

Table 5

Type of spring	$\sigma$ [MPa]	von Mises reduced stress Max. [MPa]	Deformation of lowest point [mm] – calculated	Deformation of lowest point [mm] – from FEA
Aluminum 7074 T6	336.7	208	34.15	22.72
CFRP	1,000	265	16.32	11.23

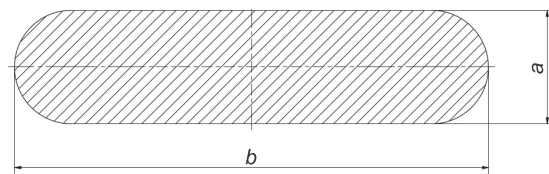


Fig. 8. Cross-section of the landing gear beam profile

Further analysis of the designed landing gear beam required interference with the shape of the profile used in the structure. Figure 8 shows the cross-section of the profile used in the analyzed beam. Its dimension is constant along its entire length and one of the main assumptions is to keep the  $b$  dimension constant. This assumption is required by the method of attaching the landing gear beam to the aircraft fuselage. The results of the analysis were obtained for the elements whose dimension was changed are presented in Table 6. The analysis shows the values of maximum deformations, displacements, and mass of the designed element.

Table 6

Profile thickness $a$ [mm]	Maximum Stress [MPa]	Maximum Displacement [mm]	Mass [kg]
25	268.6	11.24	13.94
20	354.8	20.4	11.06
18.5	401.4	24.5	10.37
17	491.6	30	9.51

## Conclusions

The presented transdisciplinary analysis concerns a simulation study of a composite landing gear of ultralight and very light aircraft. Limitations and rules that very light airplanes must meet were reviewed, and the object of investigation was selected. Based on the literature review, mathematical calculations of the aircraft parameters necessary for the drop test analysis were performed.

Computer-Aided Design (CAD) models were subjected to Finite Element Analysis (FEA) in the SolidWORKS® program, loading with previously calculated forces. At the same time, mathematical analysis was still carried out. The results of the mathematical analysis and FEA for the deformation of the landing gear were they are not identical due to the approximations used in the mathematical calculations. Some elements and factors important from the point of view of FEA, such as the fixing method, were omitted in the mathematical calculations. Based on the analysis presented above, comparative results of the landing gear for the two isotropic materials under consideration were obtained. The obtained results allowed for unequivocal determination of specific parameters for both types of the landing gear. The analysis showed that the landing gear made of CFRP showed less weight, greater resistance to reduced stress, and, as a result, less deflection of the beam. The results of the mathematical and computer analysis are presented in Table 3.

The maximum von Mises stresses for both the materials are less than the maximum calculated stresses. It should be noted that the SolidWORKS® program indicated the maximum reduced stresses in the places of the added supports, it is related to the problems of designing boundary conditions and results from measurement errors using the FEA method.

The highest stresses that occurred beyond the abovementioned points of support were respectively 137.7 MPa for the aluminum alloy 7075 T6 and 136.6 MPa for CFRP. It can be seen that the chassis made of CFRP is stiffer and lighter.

The next step in the analysis should be to analyze the CFRP material as a non-homogeneous anisotropic one, determining the orientation of the fibers. This will allow to improve the damping properties of the landing gear springs, to optimize its shape and further weight reduction.

The landing gear beam made of CRFP seems to be a better alternative for light aircraft, where the weight of all components is very important. Future research will be focused on improving the composite landing gear model and performing more advanced calculations taking into account the structure of this composite beam, the method of carbon fiber reinforcement, and the resulting anisotropy of local beam properties. In further studies, dynamic and simulation analysis for the drop test of a beam made of both materials will be carried out.

## References

- Aircraft Landing Gear Types and Arrangement*. 2018. Seronautics Guide. <https://www.aircraftsystemstech.com/> (access: 13.04.2021).
- DI LEO R., DE FENZA A., BARILE M., MOCCIA D., LECCE L. 2013. *Multi-body approach to the simulation of particular drop test for an aircraft landing gear*. Proceedings of the ECCOMAS Thematic Conference on Multibody Dynamics.
- Easy Access Rules for Very Light Aeroplanes (CS-VLA) (Amendment 1)*. 2018. European Aviation Safety Agency, EASA eRules.
- GUDMUNIDSSON S. 2013. *General Aviation Aircraft Design Applied Methods and Procedures*. Elsevier Science, Asterdam.
- INAGAKI M. 2000. *New Carbons – Control of Structure and Functions*. Elsevier Science, Amsterdam.
- Introducing the Zenith STOL CH701*. 2021. Zenith Aircraft Company. <https://www.zenithair.net/introduction-701> (access: 13.04.2021).
- KRUGER W.R. 1999. *Aircraft Landing Gear Dynamics: Simulation and Control*. Vehicle System Dynamics, 28.
- Kryterium maksymalnego naprężenia zredukowanego wg Misesa*. 2019. Dassault Systemes. <http://help.solidworks.com> (access: 13.04.2021).
- PRITCHARD J. 1999. *An Overview of Landing Gear Dynamics*. NASA Langley R.C.,/TM-1999- 209143, ARL-TR-1976, National Aeronautics and Space Administration Langley Research Center, Hampton, Virginia.
- RAYMER D.P. 1989. *Aircraft Design: A Conceptual Approach*, American Institute of Aeronautics and Astronautics. American Institute of Aeronautics and Astronautics, Inc. 370 L'Enfant Promenade, S.W., Washington, D.C. 20024, Washington D.C. 1989.







## **PSEUDO-RANDOM NUMBER GENERATOR BASED ON LINEAR CONGRUENCE AND DELAYED FIBONACCI METHODE**

*Radosław Cybulski*

ORCID: 0000-0003-1289-5318

Chair of Mathematical Method in Computer Science  
University of Warmia and Mazury in Olsztyn

Received 11 November 2021, accepted 04 December 2021, available online 06 December 2021.

**Key words:** Linear congruential method, Delayed Fibonacci technique, Hybrid pseudo-random number generator.

### **Abstract**

Pseudo-random number generation techniques are an essential tool to correctly test machine learning processes. The methodologies are many, but also the possibilities to combine them in a new way are plenty. Thus, there is a chance to create mechanisms potentially useful in new and better generators. In this paper, we present a new pseudo-random number generator based on a hybrid of two existing generators – a linear congruential method and a delayed Fibonacci technique. We demonstrate the implementation of the generator by checking its correctness and properties using chi-square, Kolmogorov and we apply the Monte Carlo Cross Validation method in classification context to test the performance of the generator in practice.

### **Introduction**

First question is what is it pseudo-random generator. It is generator which create a numbers in randomness method. To do that we need pseudo-random generator with good seed. But now is the question what is seed. The seed is the starting value on the basis of which the remaining numbers are generated.

---

Correspondence: Radosław Cybulski, Katedra Metod Matematycznych Informatyki, Wydział Matematyki i Informatyki, ul. Słoneczna 54, 10-710 Olsztyn, e-mail: [radoslaw.cybulski@uwm.edu.pl](mailto:radoslaw.cybulski@uwm.edu.pl)

Seed must have features two unpredictability, first in forward saying that other who's don't know seed can't create a good pseudo-random numbers. Second feature relies on that other can't create seed when knows created numbers. This features says why seed is that important in pseudo-random generators. When we looking on seeds in generators existing to create our method we can see different between, but it will be show in this introduction. Second question is how we can use pseudo-random generators. This generator can be used to Monte Carlo methods simulation, cryptography, and to create computer games when we need use randomness.

We will briefly introduce the algorithms on the basis of which we create our hybrid pseudo-random number generation method. Then, we will proceed with an overview of selected existing generators.

#### 1. Linear congruence generator (STALLINGS 2012)

The generation of pseudo-random numbers using a linear congruence generator is based on an iterative algorithm

$$X_{n+1} = (aX_n + c) \bmod m,$$

where individual parameters have the following meaning:

$m$  – module,  $m > 0$ ,

$a$  – multiplier,  $0 < a < m$ ,

$c$  – growth  $0 \leq c < m$ ,

$X_0$  – starting value (seed)  $0 \leq X_0 < m$ .

Each pseudo-random number being generated is from 0 to  $m - 1$  interval. It is worth noting here that only integers are used for the generator. For the quality of the generator functioning in this way it is critical to choose the values of  $a$ ,  $c$  and  $m$ . The main advantage of the linear congruence generator is the choice of two parameters, which are the multiplier ( $a$ ) and the modulus ( $m$ ), where it can happen that the generated sequence of numbers will be indistinguishable from the sequence of numbers that arise because of random drawing without returning numbers from the set  $\{1, 2, \dots, m - 1\}$ .

The disadvantage is that if the intruder knows our parameters, by using which the generation of pseudo-random numbers occurs, he can map the generated sequence himself. He will do it using the following equations:

$$X_1 = (aX_0 + c) \bmod m,$$

$$X_2 = (aX_1 + c) \bmod m,$$

$$X_3 = (aX_2 + c) \bmod m.$$

## 2. Delayed Fibonacci generator (Lagged Fibonacci Generator, online)

A pseudo-random number generator used to improve the linear congruence generator. Its origins date back to 1958, with contributions from GJ Mitchell and DP Moore. The algorithm is based on the following formula:

$$S_n = S_n - j * S_n - k \pmod{m}, 0 < j < k,$$

where the operator  $*$  can be any arithmetic operation or a bit operation. Depending on the operation used, the generator takes the appropriate name.

The operation of the generator starts with the selection of the  $j$  and  $k$  number values (they are the selected indices from the seed that take part in the creation of pseudo-random numbers). Then, the value of the number  $m$  is determined. The last parameter of the generator is the value  $val$ , which is considered as the seed. With this combination, our values will be drawn from the range of 0 to  $m - 1$ . It is also important to use the  $m$  value, which is a power of 2. The generator is delayed, because it remembers several values generated in the previous steps.

Let us discuss the content of the following sections. In the section 2 we have an overview of selected pseudo-random number generation methods. In the section 3 we present the idea of our algorithm. Then in section 4 we test our method using Chi-square and Kolmogorov's lambda consistency test. In the section 4.3 we conduct a critical discussion of our results. In section 5 we present the application of our method in practice. Finally, in section 6 we summarise the work.

We proceed to review what we consider to be the more important pseudo-random number generation techniques.

## Selected pseudo-random number generation techniques

In this section we will present a few pseudo-random generator with normal distribution.

### 1. Mersenne Twister (SULEWSKI 2019)

A popular pseudo-random number generator by Japanese scientists Matsumoto and Nishimura, generating pseudo-random numbers with a uniform distribution of massive period  $2^{19937} - 1$ . This algorithm provides a solution for generating pseudo-random numbers for many software systems. The generator was created to improve the quality of older generators.

### 2. Box-Muller (BM) generator (SULEWSKI 2019, BOX, MULLER 1958)

Let  $U_1, U_2$  be  $U(0, 1)$  pseudo-random numbers. The Box-Muller method generates a pair of independent pseudo-random numbers  $(Y_1, Y_2)$  from  $N(m, s)$ :

- $a = \sqrt{-2 \ln(U_1)}, b = 2\pi U_2$ ;
- $X_1 = a \sin(b), X_2 = a \cos(b)$ ;
- $Y_1 = sX_1 + m, Y_2 = sX_2 + m$ .

### 3. Polar Generator (SULEWSKI 2019, BELL 1968, KNOP 1969)

Let  $U_1, U_2$  be  $U(0, 1)$  pseudo-random numbers. A polar method generates a pair of independent pseudo-random numbers  $(Y_1, Y_2)$  from  $N(m, s)$ :

- $a = -1 + 2 * U_1, b = -1 + 2 * U_2$ ;
- $d = a^2 + b^2$ ;
- If  $d \geq 1$ , go to point 1;
- $e = \sqrt{\frac{-2 \ln(d)}{d}}$ ;
- $X_1 = ae, X_2 = be$ ;
- $Y_1 = s * X_1 + m, Y_2 = s * X_2 + m$ .

### 4. Quotient method (SULEWSKI 2019, KINDERMAN, MONAHAN 1977, WIECZOR-KOWSKI, ZIELINSKI 1997)

Let  $U_1, U_2$  be the pseudo-random numbers  $U(0, 1)$ . A quotient method generating a pseudo-random number  $Y$  from  $N(m, s)$ :

- $u = U_1, e = \exp(1), v = -\sqrt{2/e} + 2\sqrt{2/e}U_2$ ;
- $X = v/u$ ;
- If  $X^2 \leq 2(3 - u(4 + u))$ , go to point 6;
- If  $X^2 \leq 2/u - 2u$  and  $X^2 \leq -4 \ln(u)$ , go to point 6;
- Go to point 1;
- $Y = sX + m$ .

### 5. Ahrens-Dieter (AD) generator (SULEWSKI 2019, AHRENS, DIETER (1988))

Let  $U_1, U_2, U_3$  be  $U(0, 1)$  pseudo-random numbers. The Ahrens-Dieter method generates a pair of independent pseudo-random numbers  $(Y_1, Y_2)$  from  $N(m, s)$ :

- If  $U_1 < 0.5$  then  $a = 1$ . Go to point 3;
- $a = -1$ ;
- $b = -\ln(U_2)$ ;
- $c = \text{tg}[\pi(U_3 - 0.5)]$ ;
- $d = \sqrt{\frac{2b}{1 + c^2}}$ ;
- $X_1 = ad, X_2 = cd$ ;
- $Y_1 = s * X_1 + m, Y_2 = s * X_2 + m$ .

Now we turn to discuss the methodological details of our new pseudo-random number generation technique.

## Proposed Methodology

First, what we do, to create pseudo-random numbers, is the creation of generator seed. Seed is a message, whose input chars are changed into array ASCII codes. When we have seed, the next step to create pseudo-random numbers is to choose two numbers  $j$  and  $k$  (both numbers be in range between 0 and length seed, for example if our input message has 10 chars,  $j$  and  $k$  be in range between 0 and 9). These numbers are indexes from the array ASCII codes. Next we select number  $m$  that sets the generator range, if our  $m$  is 342, the biggest pseudo-random number will be equal 341. The last thing what we should do creates number  $n$ , that will determine how many sequences the generator will perform.

One sequence includes several operations:

Step 1

$$a = (S_j \text{ XOR } S_k) \bmod m,$$

$$b = (S_k * S_k) \bmod m;$$

Step 2

$$j = a \bmod S,$$

$$k = b \bmod S;$$

Step 3

$$S_j = a,$$

$$S_k = b.$$

Two pseudo-random numbers ( $a$  and  $b$ ) are created in one sequence. Next when we have created the numbers  $a$  and  $b$ , the numbers  $j$  and  $k$  are change based on actions described above. When we have new indexes  $j$  and  $k$ , old values on new indexes  $j$  and  $k$  are replaced by two pseudo-random numbers  $a$  and  $b$ .

Example of generator action

Input message: gerwok-nkl

Array ASCII codes from input message ( $S$ ): 103 101 114 119 111 107 45 110 107 108

$$j = 6$$

$$k = 8$$

$$m = 16452$$

$$n = 312$$

First sequence

$$a = (45 \text{ XOR } 107) \bmod 16452 = 70 \bmod 16452 = 70$$

$$b = (107 * 107) \bmod 16452 = 11449 \bmod 16452 = 11449$$

$$j = 70 \bmod 10 = 0$$

$$k = 11449 \bmod 10 = 9$$

$$S_j = 70$$

$$S_k = 11449$$

$$S = 70 \ 101 \ 114 \ 119 \ 111 \ 107 \ 45 \ 110 \ 107 \ 11449$$

Second sequence

$$a = (70 \text{ XOR } 11449) \bmod 16452 = 11519 \bmod 16452 = 11519$$

$$b = (11449 * 11449) \bmod 16452 = 131079601 \bmod 16452 = 6517$$

$$j = 11519 \bmod 10 = 9$$

$$k = 6517 \bmod 10 = 7$$

$$S_j = 11519$$

$$S_k = 6517$$

$$S = 70 \ 101 \ 114 \ 119 \ 111 \ 107 \ 45 \ 6517 \ 107 \ 11519$$

That will be created 624 pseudo-random numbers.

### 1. Illustration of examples of generated pseudo-random numbers

In this section, we shall present graphs of the distribution of pseudo-random numbers,  $A$  and  $B$ . The numbers generated using the three input sets will be presented. For each set two graphs will be presented, where one will show on the  $x$ -axis the number  $a$  and on the  $y$ -axis the number  $b$ . The second graph will be the inverse of the first one on the  $x$ -axis the number  $b$  and on the  $y$ -axis the number  $a$ . Additionally, we will show graphs presenting the numbers of generated pseudo-random numbers in intervals. The number of intervals, the size of the interval and the first upper limit of the interval is determined by:

$$k \approx \sqrt{n} + 1,$$

where:

$k$  – number of intervals,

$n$  – the number of pseudo-random numbers generated;

$$h \approx \frac{r}{k},$$

where:

$h$  – interval size,

$r$  – the difference between the largest and smallest pseudo-random numbers generated,

$k$  – number of intervals;

$$P_1 \approx n_{\min.} - \left(\frac{h}{2}\right) + h,$$

where:

$P_1$  – right limit of the first interval,

$n_{\min.}$  – the smallest pseudo-random number generated,

$h$  – size of the interval.

### 2. Example 1

Input message: gerwok-nkl

$$j = 6$$

$$k = 8$$

$$m = 16452$$

$$n = 84$$

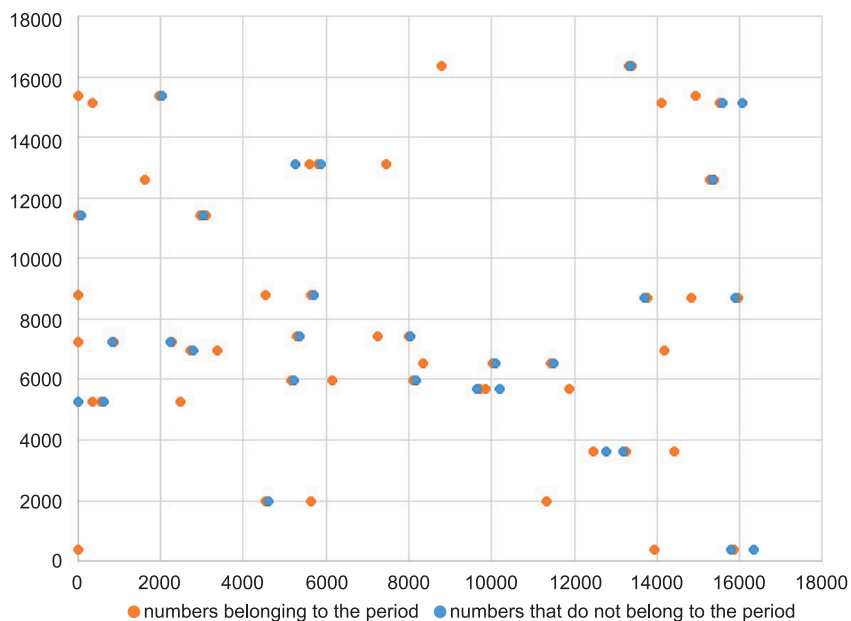


Fig. 1. Plot of distribution pseudo-random numbers  $A$  on the x-axis and pseudo-random numbers  $B$  on the y-axis

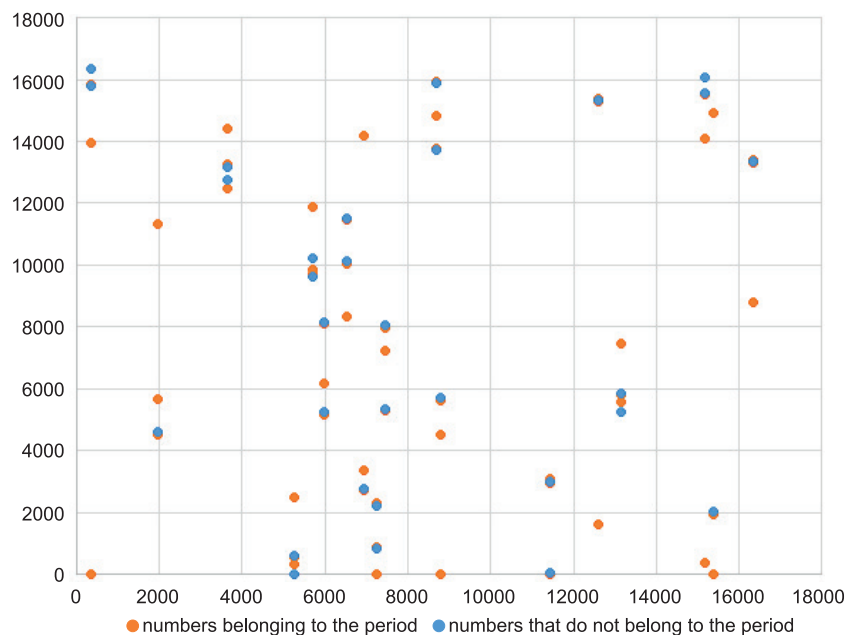


Fig. 2. Plot of distribution pseudo-random numbers  $B$  on the x-axis and pseudo-random numbers  $A$  on the y-axis

Looking at the graphs (Figs. 1, 2) it can be seen that not all points that were created during the generation of pseudo-random numbers were placed on the graph. The reason is that a generator period generates a repeating sequence of pseudo-random numbers from a certain point onward. In this example, the period starts with the 31<sup>st</sup> generator pass, up to this point points not belonging to the repeating sequence have been generated. While the length of the generator period for this example is 54. The distribution of the points itself shows a non-uniform distribution. If we analyze the generate pseudo-random numbers  $A$  and  $B$ , we can see that for the pseudo-random numbers  $B$  a repeating sequence of numbers has been formed, the length of which is 18.

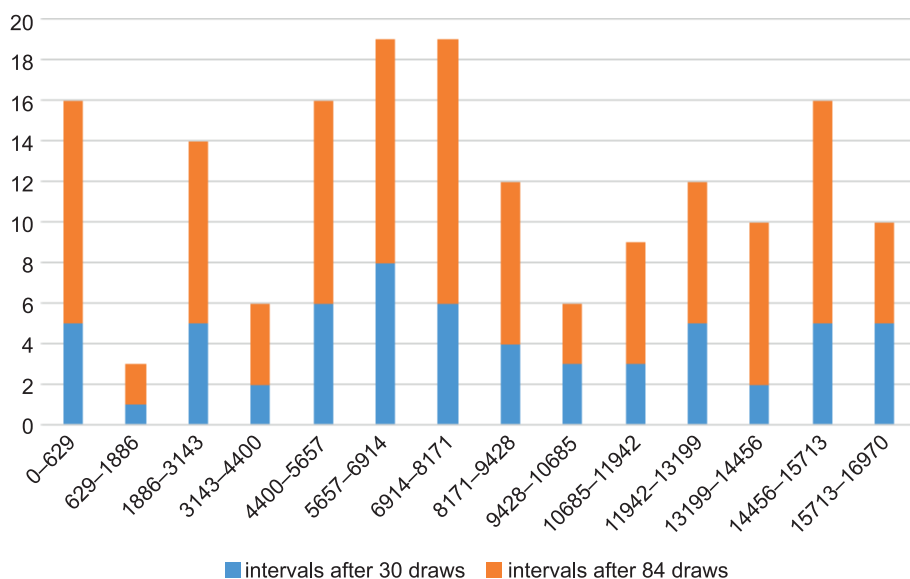


Fig. 3. Interval frequency histogram from generated numbers

The graph (Fig. 3) showing the distribution in numerical intervals shows the frequencies of pseudo-random numbers in each interval divided into two series. The first blue shows the distribution of numbers after 30 draws, and the second orange after 84 draws. The whole graph shows an uneven distribution of the intervals. Only after 30 draws we can observe small differences between the intervals. Although the generated unique points were used to build the counts (i.e. not repeating both values of  $A$  and  $B$  during the 84 draws, only after the next pass we will get the numbers  $A$  and  $B$  in the same configuration: the point created in the generation number 32 will be repeated in the generation number 85), we can see a large variation, which can be caused by the repeated values of the number  $B$  from time to time.



## 3. Example 2

Input message: &amp;\*&amp;06frD34&gt;";/[]234#^(&amp;

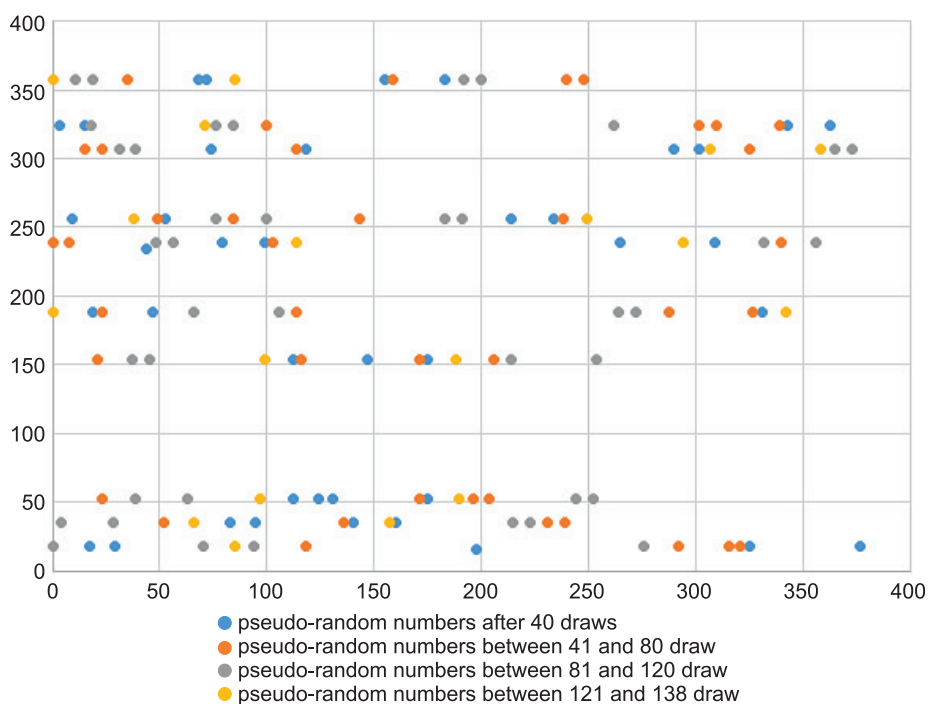
 $j = 6$  $k = 20$  $m = 391$  $n = 138$ 

Fig. 4. Plot of distribution pseudo-random numbers  $A$  on the  $x$ -axis and pseudo-random numbers  $B$  on the  $y$ -axis

The graphs (Figs. 4, 5) shown for the second example show a more true random distribution. The points marked with four colors show the distribution of pseudo-random numbers after a certain number of generations. For the second example, we also notice some distribution of points in intervals (the pseudo-random number  $B$  falls into a generator period of length 10), but the points themselves are unique, because after 138 steps of the generator, the first repetition of a point occurring will be recorded (20 points will be repeated). The generator period itself will start at 120 draws, thus if the parameter  $n$  is greater than 138 for the dataset, points from 120 draws will start to repeat.

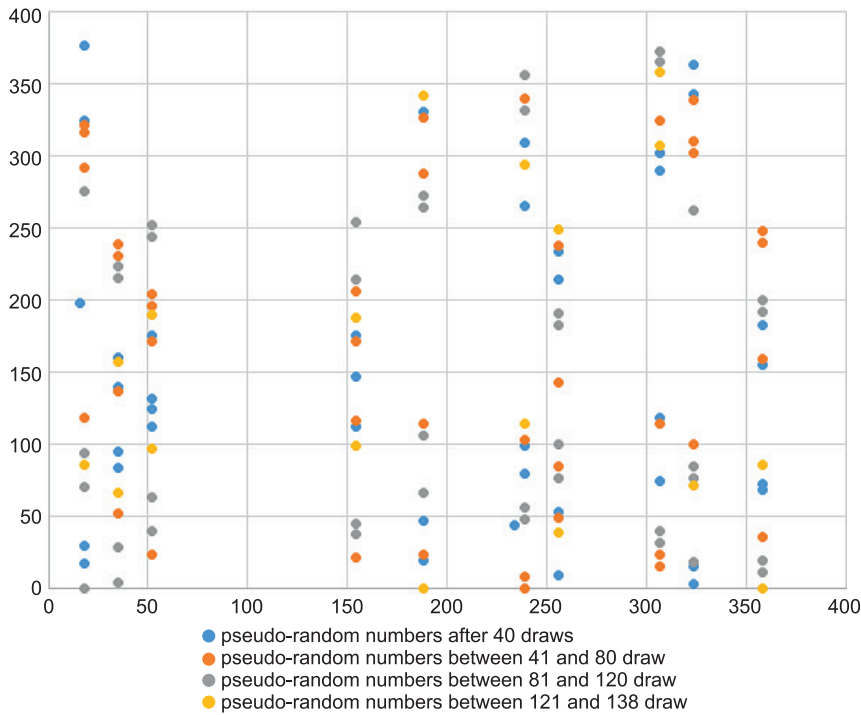


Fig. 5. Plot of distribution pseudo-random numbers  $B$  on the x-axis and pseudo-random numbers  $A$  on the y-axis

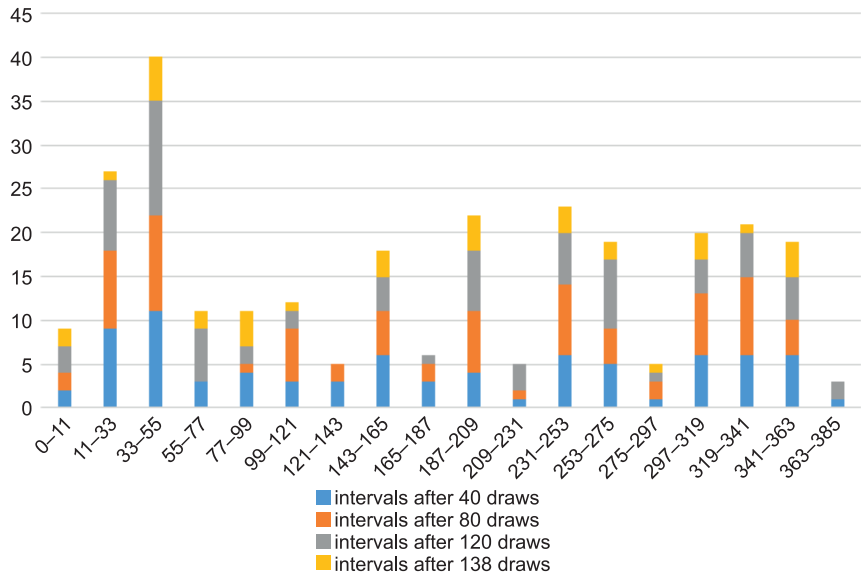


Fig. 6. Interval frequency histogram from generated numbers

As in the first example, we can observe a large variation between the counts of the given intervals (see Fig. 6). While presenting this graph lets us notice, some intervals have zero count after a given number of generator's passes. It can be seen, for example, in the range from 121 to 143 where only values after 40 and 80 generations appeared or in the last range where we can see occurrences after 40 and after 120 generations. The most even distribution between the intervals is in the case of the first series, where we can see small differences between the intervals.

#### 4. Example 3

Input message: GujRplS53

$j = 2$

$k = 5$

$m = 4213$

$n = 462$

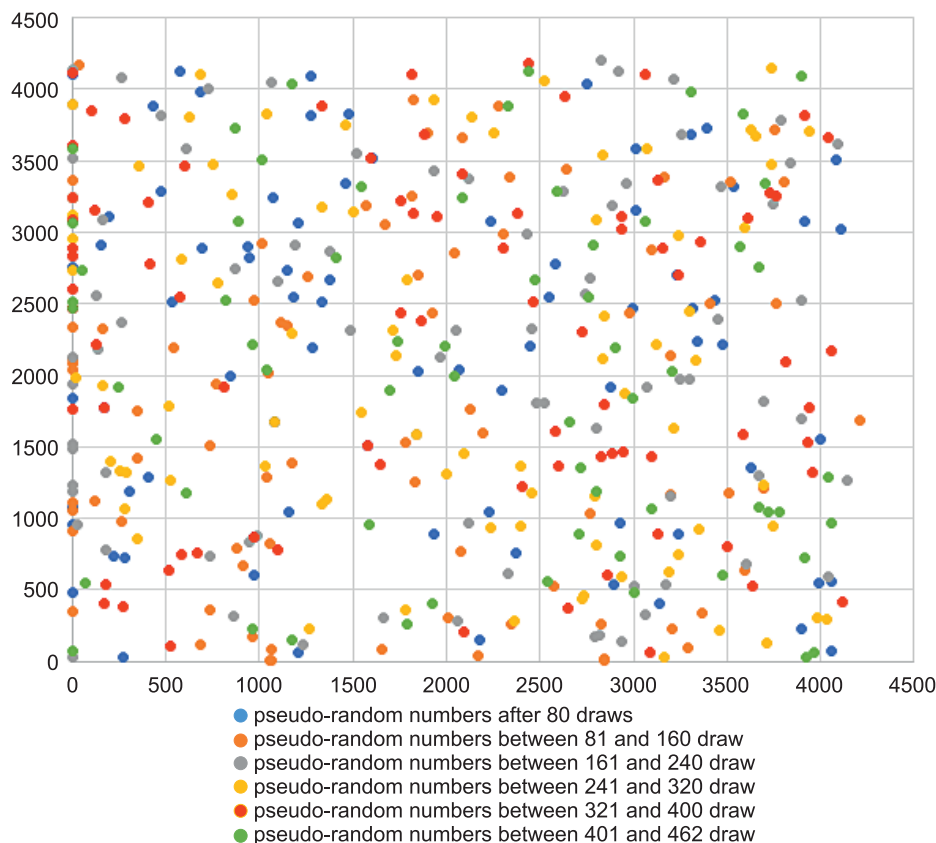


Fig. 7. Plot of distribution pseudo-random numbers  $A$  on the  $x$ -axis and pseudo-random numbers  $B$  on the  $y$ -axis

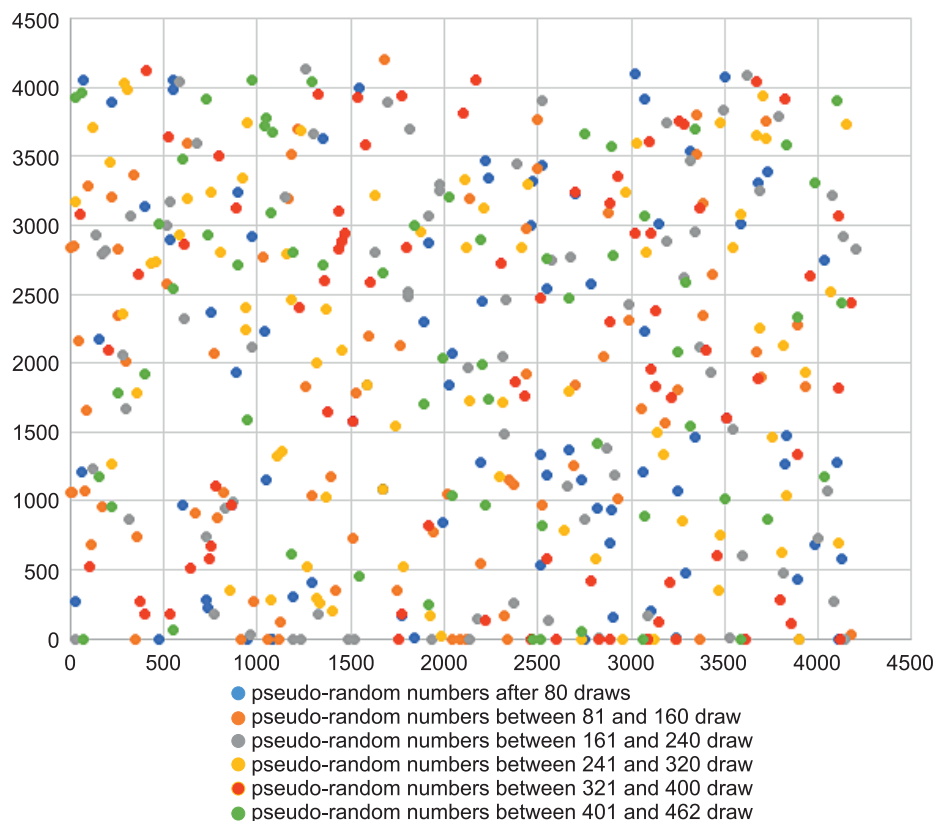


Fig. 8. Plot of distribution pseudo-random numbers  $B$  on the  $x$ -axis and pseudo-random numbers  $A$  on the  $y$ -axis

The graphs (see Figs. 7, 8) of the third example show the distribution of a large number of points, which have been divided into six insertion series, each series containing 80 points after the last. Here, we can see that the points are evenly distributed over the whole area of the graph. As in the previous examples, there is a generator period, but its size is much larger than in the other two examples. The generator period for this example starts at 83 generations and ends at 462 generations. This means that at 463 generations the values from the 83<sup>rd</sup> generation will be repeated.

The graph (see Fig. 9) showing the distribution of the numbers in the intervals shows a good distribution between the individual intervals. The exception is the first interval, in which, as we observe on the graphs of distribution, the value 0 is repeated, which overestimates the size of the first interval. As an exception to the equal abundance between compartments we can also consider the last allocation, in which the maximum values occur. An even distribution of the

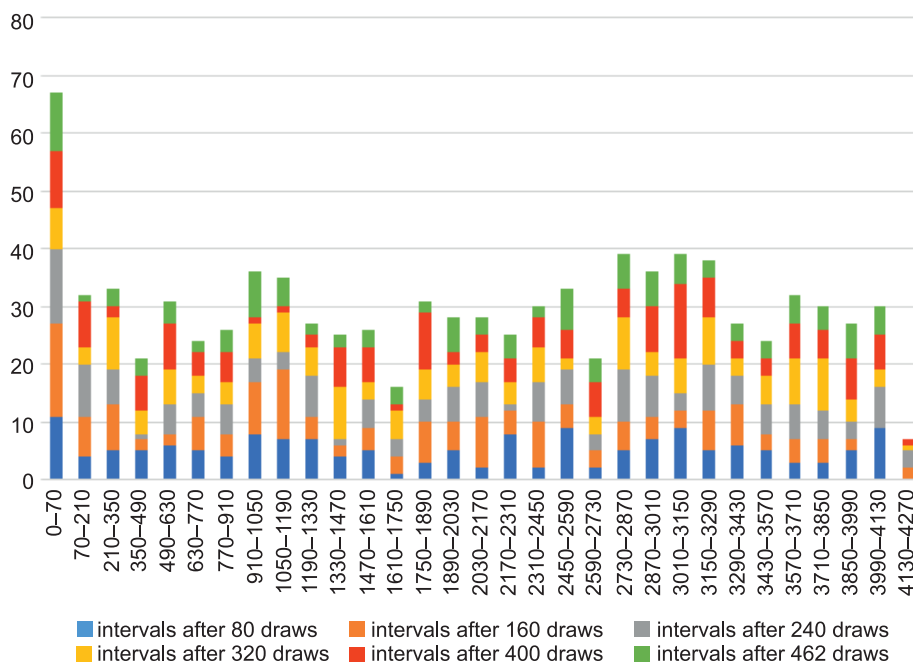


Fig. 9. Interval frequency histogram from generated numbers

abundance can also be observed if we look at the distribution between the series that was created when creating the graph.

### 5. Summary of examples

Summarizing the presented examples, we can observe that the values of pseudo-random numbers that will be created during the generation depend on the input parameters. During the generation we can get several generator periods. During the generation of numbers, there is a generator period only for the pseudo-random number  $B$ , which will cause that the points can be arranged in a certain characteristic way. Nevertheless, if there is no generator period for the number  $A$ , and we put the obtained numbers on the distribution graph we will get different points. It can be seen in the graphs of the first two examples. It also happens that the pseudo-random numbers  $A$  and  $B$  start to repeat after some time simultaneously, for example, as in the third example where there is a simultaneous generator period for both numbers.

Two parameters are of great importance when generating pseudo-random numbers: the seed and the parameter  $m$ . It is advisable that the parameter  $m$  is a large number, at most, it can be equal to 2147483646.

Let us now move on to testing the correctness of our technique.

Validation of our method

1. Chi-square test of compatibility (WOJTATOWICZ 1998)

It is one of the oldest statistical tests. Allowing us to test the hypothesis that a population has a certain type of distribution (described by a certain distribution in the form of a function), which be continuous or stepwise. The only limitation is that the sample be large, containing at least several dozen samples because the results be divided into certain classes of values. These classes should not be too few, at least 8 results should fall into each of them. In the case when there is a class smaller than 8 in the empirical distribution, this class should be combined with the neighboring one. For each class in the hypothetical distribution, theoretical counts are calculated, which are compared with the empirical counts using the appropriate chi-square statistic. When the discrepancies between the empirical and theoretical counts are too large, the hypothesis that the population has the assumed theoretical distribution be rejected.

The chi-square test formula:  $\chi^2 = \sum_{i=1}^k \frac{(n_i - np_i)^2}{np_i}$ .

The ranges were established in the same way as in the chart presentation. Results of the chi-square test for the examples shown.

Table 1

Chi-square test for the first example

For numbers	<i>K</i>	<i>R</i>	Degrees of freedom	Test statistic	Critical value
<i>A</i> and <i>B</i>	11	2	8	105.7046	15.5073
<i>A</i>	7	2	4	71.975	9.4877
<i>B</i>	6	2	3	8.3021	7.8147

Table 2

Chi-square for the second example

For numbers	<i>K</i>	<i>R</i>	Degrees of freedom	Test statistic	Critical value
<i>A</i> and <i>B</i>	13	2	10	172.5347	18.307
<i>A</i>	10	2	7	47.4164	14.0671
<i>B</i>	9	2	6	149.3395	12.5915

Table 3

Chi-square test for the third example

For numbers	$K$	$R$	Degrees of freedom	Test statistic	Critical value
$A$ and $B$	30	2	27	762.6274	40.1132
$A$	21	2	18	546.9795	28.8692
$B$	22	2	19	149.4899	30.1435

The null hypothesis for each test performed was rejected. It can be noted that the  $B$  numbers from the test for the first example were closest to the normal distribution. For each test, a probability of 0.05 was used to create the critical value.

In the tables, the parameter  $k$  is defined as the number of intervals taken for the test,  $r$  as the number of parameters taken to calculate the normal distribution (in this case the mean and standard deviation of the generated numbers).

## 2. Kolmogorov's lambda consistency test (WOJTATOWICZ 1998)

In the Kolmogorov's lambda consistency test, to verify the hypothesis that the population has a certain type of distribution, one does not, as in the chi-square test, consider the counts of the empirical series and compare them with the counts of the hypothetical series, but compares the empirical and hypothetical distributions. Because when the population has a distribution consistent with the hypothesis, the values of empirical and hypothetical distributions should be similar at all tested points. The test begins by analysing the differences between the two distributions. The largest of which will then be used to construct the lambda statistic, whose distribution does not depend on the form of the hypothetical distribution. This distribution determines the critical values in this test.

The formula for calculating the value of a statistic for a given interval:  
 $D = \sup|F_n(x) - F(x)|$

The formula for calculating the value of the test statistic:  $\lambda = \max(D\sqrt{n})$

For a fixed confidence level  $l$  we read the critical value from the limiting Kolmogorov distribution. The ranges were determined in the same way as in the presentation of the graphs.

Table 4

Kolmogorov test for the first example

For numbers	Alfa	Test statistic	Critical value
$A$ and $B$	0.05	1.2914	1.36
$A$	0.05	8.4866	1.36
$B$	0.05	1.3687	1.36

Table 5

Kolmogorov test for the second example

For numbers	Alfa	Test statistic	Critical value
<i>A</i> and <i>B</i>	0.05	2.3528	1.36
<i>A</i>	0.05	1.6761	1.36
<i>B</i>	0.05	2.3269	1.36

Table 6

Kolmogorov test for the third example

For numbers	Alfa	Test statistic	Critical value
<i>A</i> and <i>B</i>	0.05	2.5839	1.36
<i>A</i>	0.05	2.1126	1.36
<i>B</i>	0.05	1.8966	1.36

The Kolmogorov test values are more approximate as to the critical value. The null hypothesis was not rejected for the numbers *A* and *B* from the first example, so we can conclude that the generated numbers have a normal distribution with the parameters of the mean and standard deviation.

### 3. A critical analysis of our method

A problem associated with the hybrid pseudo-random generator is the creation of short-range pseudo-random numbers. It is mainly due to the setting of the parameter *m* (responsible for the upper range of the generated values), such an example would be the value 100 or 768. In some cases a small adjustment of the value of *m* is enough to get better quality-generated numbers. A superb choice of *m* values are prime numbers, in their case it is rare to generate pseudo-random values with a small period. It is also not advisable to create a seed where a character repeats several times.

In the next section we test our method in practice by applying the drawn objects to the classification process.

## Our method in action

The final part of verifying the performance of our technique was to perform classification using the kNN technique in the Monte Carlo Cross Validation model. We used an implementation in *R* language from the kNN library. Our goal was to check results of performed classification tests, in which objects



of training systems were generated by our method have distribution close to normal. The effect of the following test on the Statlog (Australian Credit Approval) Data Set (ICS-a. Online) and on the Statlog (Heart) Data Set (ICS-b. Online) is presented in the figures Interval frequency histogram from Australian Credit Approval Data Set and Interval frequency histogram from Heart Data Set.

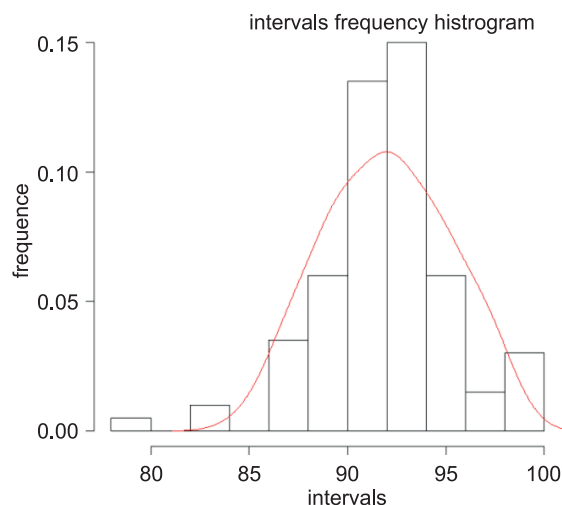


Fig. 10. Interval frequency histogram from Australian Credit Approval Data Set

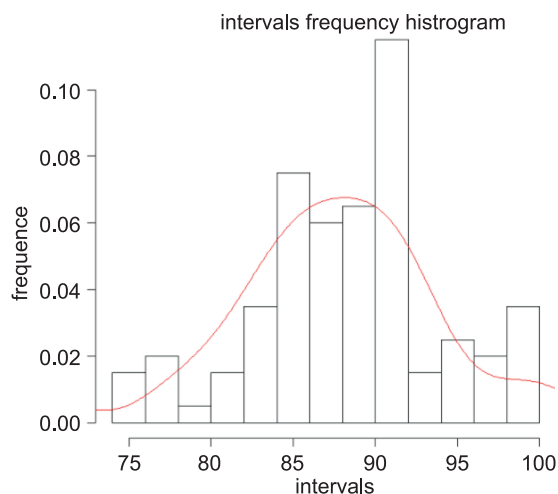


Fig. 11. Interval frequency histogram from Heart Data Set

## Test Purpose

The focus of the test is the proportion of zeroes and ones for the entire sequence. The purpose of this test is to determine whether the number of ones and zeros in a sequence are approximately the same as would be expected for a truly random sequence. The test assesses the closeness of the fraction of ones to  $\frac{1}{2}$ , that is, the number of ones and zeroes in a sequence should be about the same. All subsequent tests depend on the passing of this test (RUKHIN et al. 2010).

Test description:

- conversion pseudo-random numbers to binaries and create binary string;
- conversion to  $\pm 1$  (0 is converted to values -1, 1 is converted to values +1) and create sum  $S_n$  from binary string;

- compute the statistic:  $S_{\text{obs}} = \frac{|S_n|}{\sqrt{n}}$  where  $n$  is length of binary string;

- compute  $P\text{-value} = \text{erfc}\left(\frac{S_{\text{obs}}}{\sqrt{2}}\right)$ , where  $\text{erfc}$  is the complementary error function.

If  $P\text{-value}$  is  $> 0.01$ , then conclude that the sequence is random.

For our tests binary string was created with first twenty generation from our examples use in section Proposed Methodology.

1. Test purpose for first example

$n = 515$

$S_n = 107$

$S_{\text{obs}} = 4.7149$

$P\text{-value} = 2.4173\text{e-}06$

Sequence is non-random

2. Test purpose for second example

$n = 295$

$S_n = 17$

$S_{\text{obs}} = 0.9897$

$P\text{-value} = 0.3223$

Sequence random

3. Test purpose for third example

$n = 434$

$S_n = 24$

$S_{\text{obs}} = 1.1520$

$P\text{-value} = 0.2493$

Sequence random

## Conclusions

In this paper, we have presented a hybrid method of pseudo-random number generator, which is based on existing techniques for generating pseudo-random numbers. We have shown how to obtain pseudo-random numbers using the hybrid generator, examples with the distribution of numbers on graphs and graphs showing the counts of created values into intervals. In the presentation of the examples we showed its strengths and weaknesses, which include poor randomness in cases where we set a small value of the parameter  $m$ . As well as good points in the case of the third example where, despite the occurrence of a large period of the generator we see excellent randomness. The last stage that is presented is the tests of the correctness of the generator. If we looking on our examples in section test purpose we can see good quality of randomness in examples two and three. Only in first example created binary string is non-random.  $P$ -value for second example is 0.3223, for third example 0.2493 what can be mean that randomness for this generated numbers is very good quality. Only in first example created binary string is non-random.

## References

- AHRENS J.H., DIETER U. 1988. *Efficient table – free sampling methods for the exponential, Cauchy, and normal distributions*. Communication of the ACM, 31(11): 1330-1337.
- BELL J.R. 1968. *Algorithm 334: Normal random deviates*. Communication of the ACM, 11(7): 498.
- BOX G.E.P., MULLER M.E. 1958. *A note on the generation of random normal deviates*. Annals of Mathematical Statistics, 29(2): 610-611.
- ICS-a. Donald Bren School of Information and Computer Sciences. University of California, Irvine. <https://archive.ics.uci.edu/ml/machine-learning-databases/statlog/australian/australian.dat>.
- ICS-b. Donald Bren School of Information and Computer Sciences. University of California, Irvine. <https://archive.ics.uci.edu/ml/machine-learning-databases/statlog/heart/heart.dat>.
- KINDERMAN A.J., MONAHAN J.F. 1977. *Computer generation of random variables using the ratio of uniform deviates*. ACM Transactions on Mathematical Software, 3(3): 257-260.
- KNOP R. 1969. *Remark on Algorithm 334 [g5]: normal random deviates*. McGill University, Montreal.
- Lagged Fibonacci Generator. Security and So Many Things, Asecuritysite. <https://asecuritysite.com/encryption/fab>.
- RUKHIN A., SOTO J., NECHVATAL J., SMID M., BARKER E., LEIGH S., LEVENSON M., VANGEL M., BANKS D., HECKERT A., DRAY J., VO S. 2001. *A Statistical Test Suite for Random and Pseudorandom Number Generators for Cryptographic Applications*. Special Publication (NIST SP), National Institute of Standards and Technology, Gaithersburg, MD.
- STALLINGS W. 2012. *Kryptografia i bezpieczeństwo sieci komputerowych – matematyka szyfrów i techniki kryptologii*. Helion, Gliwice.
- SULEWSKI P. 2019. *Porównanie generatorów liczb pseudolosowych*. Wiadomości Statystyczne, 7: 5-31.
- WIECZORKOWSKI R., ZIELINSKI R. 1997. *Komputerowe generatory liczb losowych*. Wydawnictwo Naukowo-Techniczne, Warszawa.
- WOJTATOWICZ T.W. 1998. *Metody analizy danych doświadczalnych*. Wydawnictwo Politechniki Łódzkiej, Łódź.





## TEST RIG DEDICATED FOR HARDWARE USED IN WIND TUNNELS

*Aleksandra Ordon<sup>1</sup>, Paulina Kurnyta-Mazurek<sup>2</sup>*

<sup>1</sup>ORCID: 0000-0001-6935-0605

<sup>2</sup>ORCID: 0000-0002-0938-0113

Faculty of Mechatronics, Armament and Aerospace,  
Military University of Technology in Warsaw

Received 28 September 2021, accepted 12 December 2021, available online 12 December 2021.

**Key words:** wind tunnel measurement, servo-mechanism, LabVIEW software, myRIO controller.

### Abstract

The paper presents the results of work on measurement system dedicated to hardware used during wind tunnel tests, especially to servomechanisms. These devices could be applied to set specific position of control surface. Proposed system would ensure continuous monitoring of servo-rotor position and servo-motor temperature and would avoid uncontrolled change of control surface position.

The application designed to monitor the operating status of the servomechanism was prepared in the LabVIEW software and was implemented on the myRIO platform. Developed test rig allows to register time histories of servo-rotor position and temperature during test for different values of applied load. In the paper, studies plan were also presented.

Experimental studies show that before wind tunnel tests, selected servomechanism should be tested in terms of maintaining the parameters declared by the manufacturer, especially during continuous operation. Developed measurement system can be used during wind tunnel tests, as well as only for servo-mechanism parameter testing.

---

Correspondence: Paulina Kurnyta-Mazurek, Zakład Awioniki, Instytut Techniki Lotniczej, Wydział Mechatroniki, Uzbrojenia i Lotnictwa, Wojskowa Akademia Techniczna, 00-908 Warszawa, e-mail: paulina.mazurek@wat.edu.pl; aleksandra.ordon@student.wat.edu.pl.

## Introduction

Wind and water tunnel measurements play an important role in aircraft research programmes, due to the cost minimalization and time saving (BARLOW et al. 1999, Operations and Maintenance Manual 2012). These tests are one of the experimental method (LICHON et al. 2016), which allow to verify the characteristics obtained during computer studies performed in specialized software with use of numerical methods presented for example in (PANDYA et al. 2017, LI et al. 2018). Moreover, wind tunnel measurements provide the opportunity to studies of new solutions dedicated to aircrafts, before tests in flight, such as fault detection system described in (RUANGWISSET, SUWANTRAGUL 2008). Also in the paper (WIBOWO et al. 2019) comparison of aerodynamic characteristics of Sukhoi SU-33 aircraft and F-35 Lightning aircraft obtained in wind tunnels are presented.

Wind tunnel measurements allow to simulation of the aircraft real behavior in strictly defined conditions and with precisely set flight parameters. These tests enable to eliminate errors and improve of aircraft operating parameters at the design stage, as well as detect causes of failures that occurred in the air. In comparison with tests in flight, tunnel measurements possess several attractive advantages, such as reducing research time and costs.

For tunnel test, aircraft models in appropriate scale were made. These models were often prepared with use of method, which is very popular in engineering, namely 3D printing (MALEK et al. 2019, KINŃSKI, SOBIESKI 2020, RAZA et al. 2021). During tests, the control surfaces such as ailerons, elevator and rudder were locked in strictly defined position. Despite significant progress already reached in wind and water tunnel measurements, there remain numerous open challenges in this field. Sometimes, due to mounting errors or excessive load, the control surfaces change their position. For that reason, in the paper we proposed the use of servomechanism with dedicated measurement system to ensure continuous monitoring of servo-rotor position and servo-motor temperature. Designed system can be used during wind tunnel tests, as well as only for servo-mechanism parameter testing.

The contents of the paper are organized as follows. First section introduces servomechanism, considering their structures and operation principle. Second section reports on laboratory test stands, especially measurement system and developed algorithm. Afterwards, results in form of time histories of the measurement system are presented. Finally, some remarks are presented in Conclusion Section.

## Servomechanisms in aircraft models

Remote control servomechanism (RC servo) are devices designed specifically for pointerlike position-control applications. They are built of dc motor, feedback device and control circuit. An RC servo uses an outside pulse-width-modulated (PWM) signal to control the position of its shaft. To change the position of the shaft, the pulse width of the modulated signal is varied. To make the shaft go counterclockwise from neutral position, a pulse wider than 1.5 ms is applied to the control input. Conversely, to make the shaft go clockwise, a pulse narrower than 1.5 ms is applied. The shaft of the motor is usually limited to a rotation of  $180^\circ$  or  $210^\circ$ . The dependence between the servo arm position and the length of the supplied control impulse signal is shown in Figure 1.

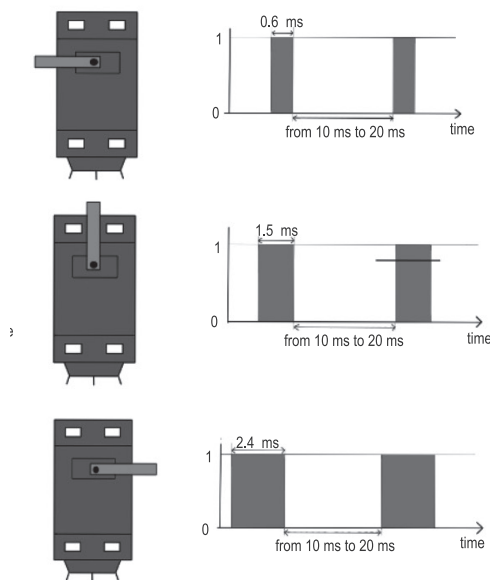


Fig. 1. The dependence between servo arm position and the length of the supplied control pulse signal

Servomechanisms in models airplanes are designed to precisely control the deflection of control surfaces, such as ailerons, flaps or rudder. Furthermore, they are used in landing gear extension mechanisms in unmanned aerial vehicles. They are also responsible for changes in the angle of attack of the rotor blades, as well as the pitch of the tail rotor in helicopter models (STEPHEN et al. 2011). Figure 2a shows a example of servomechanism and Figure 2b shows a fragment of the interior of the fuselage with marked servos in charge of controlling the rudder, elevator and throttle.

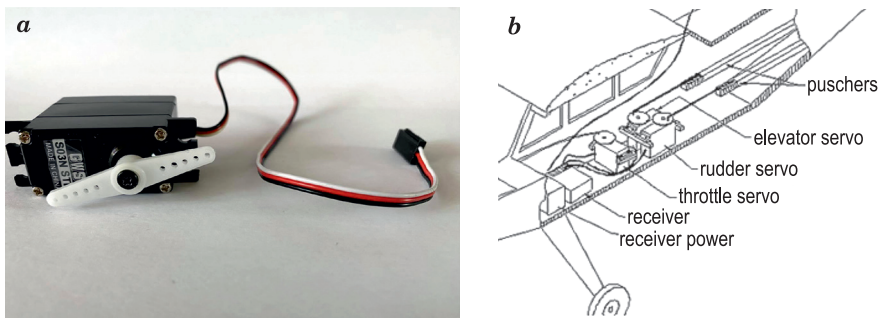


Fig. 2. Photo of the servomechanism GWS S0SN STD (a) and fragment of the interior of the fuselage (b)

In the Figure 3 servo control system was presented. When controlling servos within model airplanes, an initial control signal is first sent to a radiowave modulator circuit that encodes the control signal within a carrier wave. This carrier wave is then radiated off as a radiowave by an antenna and transmitted to the receiver circuit model. The receiver circuit recovers the initial control signal by demodulating the carrier. After that, the control signal is sent to the designated servo within the model and its arm is tilted by the specified angle.

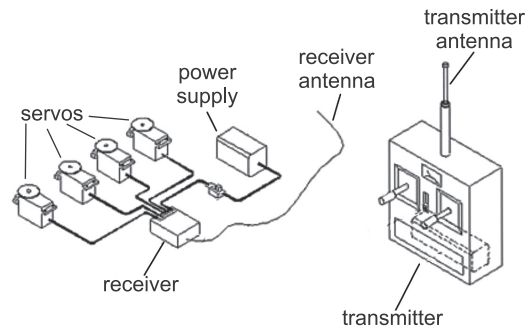


Fig. 3. Diagram of the four-channel control system of the flying model

If there is more than one servo per model, more channels are required. For example, most RC airplanes require a four-channel radio set. More complex models may use five or six channels to control additional features such as flaps and retractable landing gear. The main control channels of airplanes RC models include:

- throttle control channel;
- elevator control channel;
- aileron control channel;
- rudder control channel.



The first mentioned control channel comprises throttle position adjustment. It is responsible for controlling the number of engine revolutions per minute. It can be controlled using a single servo. In the case of internal combustion engines, the throttle regulates the amount of air-fuel mixture supplied to the combustion chamber. In the case of airplanes with an electric motor, it is not used because the engine speed is controlled by changing the value of the voltage supplied to the engine.

Another mentioned steering channel allows to adjust the position of the elevator. With its help, the pilot can change the flight path, angle of attack  $\alpha$  and side slip angle  $\beta$ .

The third control channel allows to control the deflection of the ailerons. These control surface make possible to change the roll angle  $\Theta$  of the plane, therefore they allow to make a turn, and even a rotation around the longitudinal axis of the plane ( $Ox$ ). Their position is changed by the movement of the control stick right-left or by the movement of the steering wheel in the appropriate direction. The aileron action changes the lifts on the wing.

The last mentioned control channel enables the control of the rudder position, which allows to initiate the rotation of the airplane about the vertical axis  $Oz$ . When its position is properly synchronized with the ailerons, it contributes to the correct execution of the turn.

## Test rig

The motivation for the implementation of this type of test rig is the need to verify the parameters of servomechanisms given by manufacturers in the catalog notes of devices that can be used in models used in tunnel tests. We additionally propose the use of the developed system in tunnel tests during the operation of the airframe surfaces of an airplane model. The observed and registered parameters of servomechanism are the angular position of the servo drive shaft and the temperature of the servo housing. To monitor the above-mentioned parameters, measurement system with potentiometer and temperature sensor were designed and manufactured (GÜNTER et al. 2006). The scheme of the rig stand is shown in Figure 4.

The myRIO device was used as a control unit in the designed test rig. In turn, the application managing the stand was made in the LabVIEW software due to the compatibility of this environment with the myRIO device. A potentiometer was used to perform the task related to the monitoring of the angular position of the servo shaft, while a resistance temperature sensor was used to measure the temperature, due to its high sensitivity even with small changes in temperature. An ammeter has been attached to the system, which gives information about the intensity of the current consumed by the servo. The stand base was designed in the SolidWorks program, and then printed with using a 3D printer.

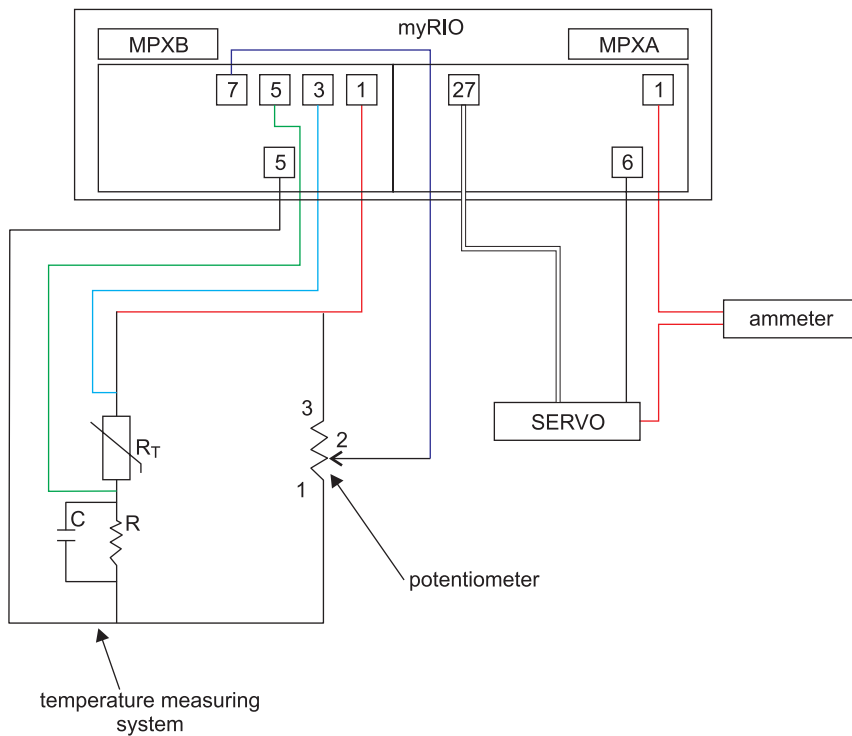


Fig. 4. Scheme of the test rig

The myRIO device in the designed laboratory stand acts as a control unit. It is a portable, configurable device that enables, among other things, the design of control systems and measurement applications. It is equipped with a powerful Cortex-A9 dual-core processor, Real Time System and FPGA (Field Programmable Gate Array). All elements of the system can be configured using applications prepared in the LabVIEW software. There are two expansion ports MPX A and MPX B at the user's disposal, led out to double-row 34-vertical connectors. The location of the connectors is identical in both ports, and their numbers along with the function performed are shown in Figure 4.

The test rig uses a temperature sensor, which is designed to monitor the temperature of the servo housing during operation with a load set by the user. It is a resistance sensor where the sensitive element is a thermistor with a negative temperature coefficient – NTC (Negative temperature coefficient). In this type of resistor, the resistance decreases with increasing temperature. The relationship between the resistance and the temperature in an NTC thermistor is described by the following equation which has been obtained from the datasheet:

$$T = \frac{1}{\frac{1}{T_0} + \frac{1}{\beta} \ln \left( \frac{R_T}{R_0} \right)} \quad (1)$$

where:

$R_T$  – the sensor resistance at a given temperature,

$R_0$  – the sensor resistance at the reference temperature,

$T$  – the sensor temperature at the time of measurement,

$T_0$  – the sensor reference temperature.

The symbol  $\beta$  means a constant that is provided by the manufacturer in the data sheet. In order to use the described sensor (thermistor) to measure the temperature of the servo, a specified measuring system should be built, which will consist of a resistor, sensor and a capacitor. Placing a thermistor in the upper branch of the voltage divider makes the voltage measurement more accurate. According to the catalog note of the NTC sensor, its accuracy of resistance measurement is 1% with increasing temperature. The temperature measuring system is shown in Figure 5.

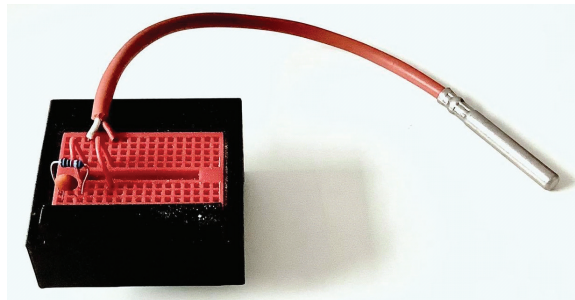


Fig. 5. Temperature measuring system

A potentiometer is a sensitive element in the system designed to monitor the position of the servo shaft, and thus also its horn. This measurement is especially important when testing the maximum time for which a given load is maintained as well as in monitoring the correctness of the control surfaces deflection of an airplane model during tunnel tests. In order to obtain greater accuracy of measuring the angular position of the towing bar and to facilitate the assembly at the stand, the potentiometer has a cap, designed and printed in a 3D printer. The potentiometer with the cap on is shown in Figure 6.

The potentiometer is connected to the servo shaft by means of a belt drive-like mechanism. All gear elements, i.e. potentiometer cover, servo shaft cover, as well as a rubber strip were designed in the SolidWorks program and printed in a 3D printer. With each movement of the servo shaft, the potentiometer knob sets in motion. The system for monitoring the position of the servo shaft is shown in Figure 7.

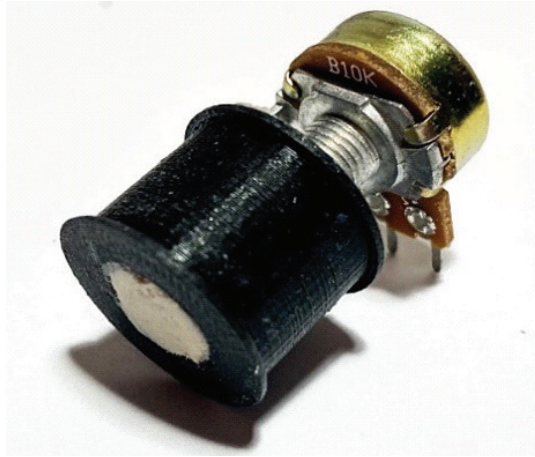


Fig. 6. Potentiometer with the cap

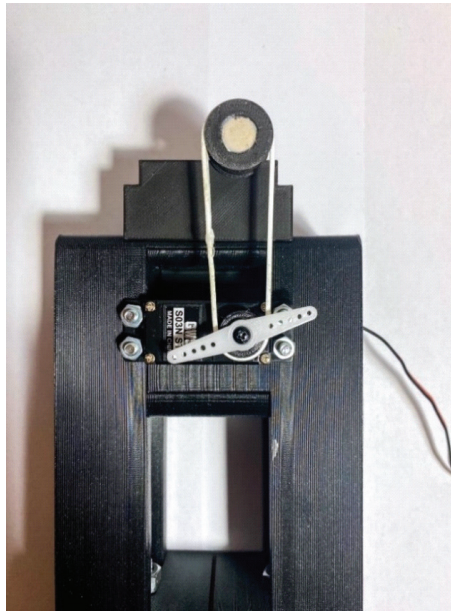


Fig. 7. Connection of a potentiometer with a servo

In order to enable the percentage assessment of the servo shaft position change, for each tested device, the difference in the potentiometer indications in its two extreme positions was calculated, which was divided into 100% of the range. When analysing the time courses, it should be assumed that a 1% change of the servo shaft position corresponds to a different value for each device.

For the servo GWS SO3N it is 0.03 V/°, for the Power HD 3001 HB it is 0.018 V/° and for the Power HD 6001 HB it is 0.027 V/°. The accuracy of reading the data from the potentiometer is 0.001 V. Due to the fact that the voltage change was converted into a percentage change of the shaft position, it was assumed that the measurements of the shaft position change were made with an accuracy of 0.1%.

The control and measurement application of the test rig was developed in the LabVIEW software. The prepared application is designed to control the angular position of the servo drive using the PWM signal, as well as receive data from the potentiometer and temperature sensor. The user interface of the developed application is presented in Figure 8.

The application has been divided into parts carrying out specific tasks. The servomechanism control section is marked by red line, the part showing the measurement results from the temperature sensor is blue. On the other hand, the fields on which the current voltage value from the potentiometer and the time history of the output voltage value from the potentiometer are displayed are marked by green line. Yellow is the color of the operating mode selection menu, by means of which the temperature sensor or potentiometer mode could be selected. Additionally, the user can stop the test (experiment) at any time and decide to save the data from the temperature sensor and potentiometer to a text file using the buttons in the menu (marked in purple). In the workstation selection section, it is possible to check status of individual systems, i.e., the position verification system and the temperature monitoring system. During operation in the “Measuring station” mode, it is possible to monitor the temperature, the position of the servo horn, control the servomechanism, and also save the measurement data to a text file. The application has protection against excessive heating of the housing of the tested servo. After exceeding the maximum operating temperature, the diode next to the thermometer starts to glow red.

The *Case* structure window that performs this task is shown in Figure 9. The part responsible for controlling the tested servo is marked in red, the measuring part responsible for reading the measurement parameters from the temperature sensor and potentiometer is marked in green, and the structure that records the measurement data to a file is marked by blue line. *While Loop*, in which the servo control task is performed, is executed every 10 ms. The tasks performed by the temperature sensor and the shaft position sensor of the servomotor are placed in the *While loop*. The *Wait* function is assigned a fixed value of 1 s. This means that the program waits a second between successive executions of the loop. Due to the fact that these components are placed in a separate structure, it is possible to disable their operation without interfering with the servo control. The sampling time values can be modified as needed. If we want to acquire data more frequently, we can reduce the value of the sampling time.

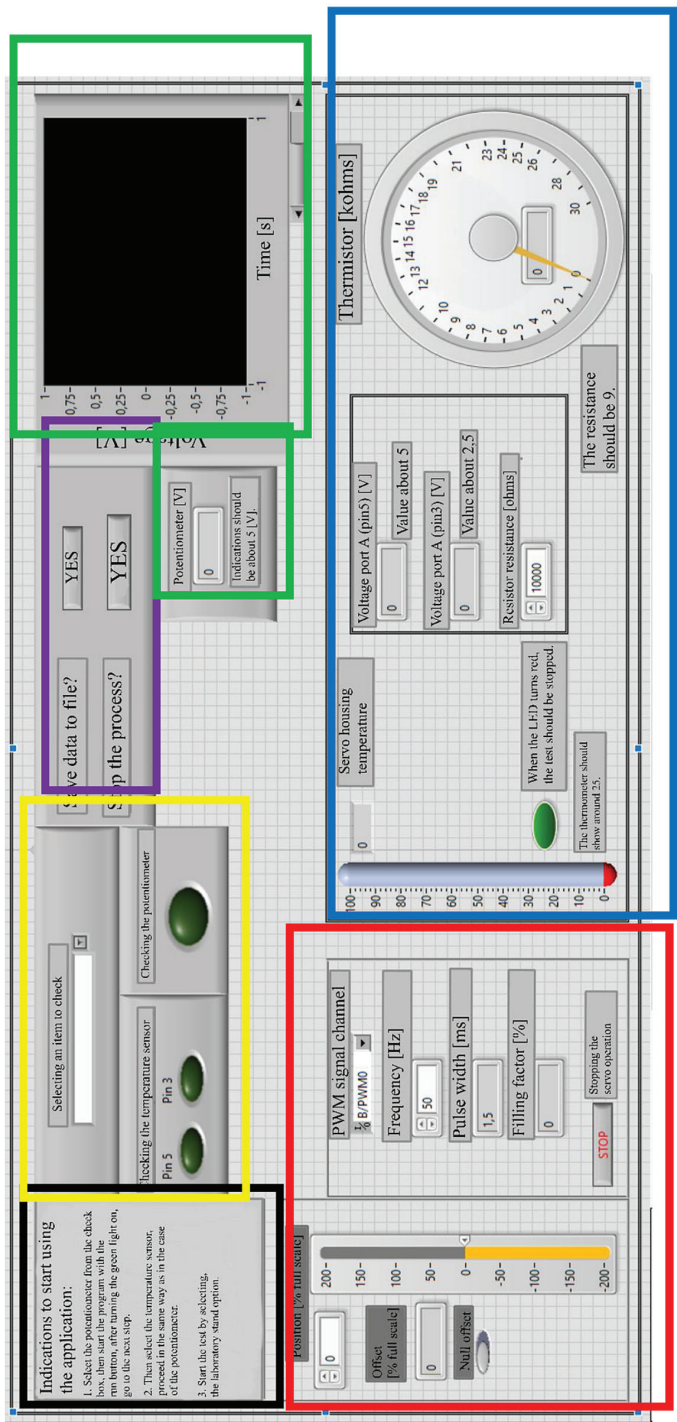


Fig. 8. Application interface





## Results and discussion

In order to verify the correct operation of the designed test stand, four measurement sessions were carried out for three different servos. The first one was a device dedicated to work with the myRIO platform (GWS S03N STD). Two another ones had designation Power HD 3001 HB and a Power HD 6001 HB, respectively. Their common feature is dimensions, they all belong to the standard category. For each research session, time history of the output voltage value from

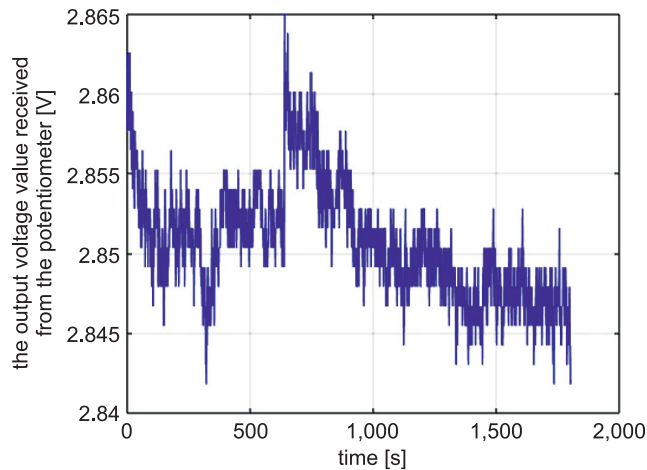


Fig. 10. Time history of the output voltage received from the potentiometer for 100% of the maximum load

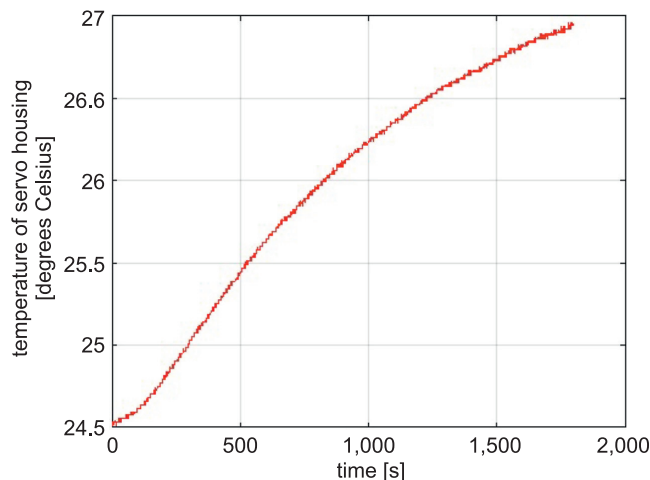


Fig. 11. The time history of the housing temperature of the tested servo, for 100% of the maximum load



the potentiometer were recorded, which determine the angular displacement of the actuator shaft and the time history of the device housing temperature were saved in text file too. Additionally, during the experiments, the intensity of the current consumed by the servo from the power source was examined. The duration of each experiment was 30 minutes, due to the fact that this is the maximum duration of the study in wind tunnels for a given position of the control surface. Each research experiment was divided into five stages, in which the load applied to the servo was 10, 30, 50, 70 and 100% of the maximum load, respectively. For each measurement, an appropriate mass in the form of a weight was suspended on the arm of the mechanism, 2 centimetres from the shaft center of the device. The values of individual loads for all devices are presented in Table 1.

Table 1

	Values of servo loads		
	GWS S03 STD [kg]	POWER HD 3001 HD [kg]	POWER HD 6001 HD [kg]
10% of maximum load	0.170	0.175	0.290
30% of maximum load	0.510	0.525	0.870
50% of maximum load	0.850	0.875	1.450
70% of maximum load	1.190	1.225	2.030
100% of maximum load	1.700	1.750	2.900

Time histories were recorded for each servo. Time histories of potentiometer output voltage and temperature of the GWS S03N STD servo for 100% load are shown in Figures 10 and 11.

Figure 12 shows the percentage change in the angular position of all tested servos depending on the load. The best operating parameters have a servo-mechanism dedicated to myRIO with the designation GWS S03N STD, which

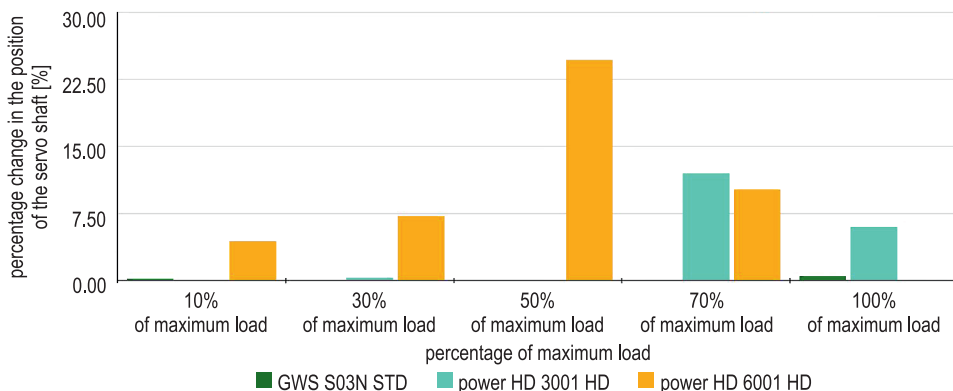


Fig. 12. Comparison of the percentage change in the angular position of the servo shaft during operation

maintained a given position during operation under each given load. The servomechanism with similar operating parameters, designated as POWER HD 3001 HB, did not maintain its position at the load equal to 70 and 100% of the maximum load. The last tested servo POWER HD 6001 HD did not maintain the set position under any load.

Analysing the above graph, it can be concluded that in the last stage of the tests, it should not be assumed that the device will maintain the set load, because it may have a manufacturing defect, similar to the most likely recently tested device, which did not meet its operating parameters.

## Conclusion

In the paper, we proposed measurement system dedicated to hardware used during wind tunnel tests, especially to servomechanisms. These measurements are a one of experimental methods in the aircraft research programme, which let to obtaining the full range of data needed to guide detailed design decisions for many practical engineering problems.

In order to reduce the costs of the design and research of the aircraft system, in our work, we propose the use of servos both in tunnel tests and in flight test. In that case, detailed servomechanism test should be performed, especially its data sheet parameters should be studied. For that reason, test rig were designed and made.

The test rig is very universal and its operation is very intuitive, therefore it enables the testing of operating parameters and monitor of the servomechanisms operation. This is especially useful in tunnel tests where the control surfaces of the model are deflected and the servo shafts are loaded throughout the test. Hence, it is justified to perform tests of servomechanisms before using them in tunnel tests. Thanks to them, it is possible to eliminate the error related to the servo not maintaining the set position or excessive heating of the housing. The data presented in the previous chapter show that not all devices maintain the load declared by the manufacturer. The servo was tested and it probably had a manufacturing defect. Conducting the tests on the prepared stand made it possible to quickly identify it and reject it for later use in tunnel tests.

## References

- BARLOW J.B., RAE W.H., POPE A. 1999. *Low-Speed Wind Tunnel Testing*. 3<sup>rd</sup> Ed., Wiley, Hoboken.
- HOMMEL G., HUANYE S. 2006. *Embedded Systems – Modeling, Technology, and Applications*. Springer Netherlands, Amsterdam.
- KIŃSKI W., SOBIESKI W. 2020. *Geometry extraction from GCODE files destined for 3D printers*. Technical Science, 23(2): 1-16. <https://doi.org/https://doi.org/10.31648/ts.5644>.

- LI S., NIU X., HUANG X. 2018. *Study on the correlation between the dynamic test of airfoil wind tunnel and CFD calculation*. CSAA/IET International Conference on Aircraft Utility Systems (AUS 2018), p. 62-66. <https://doi.org/10.1049/cp.2018.0263>.
- LICHOŃ D., MIKOŁAJCZYK A., KISZKOWIAK Ł., ŁĄCKI T. 2016. *Identification of UAV static aerodynamic characteristics in the water tunnel balance research*. Zeszyty Naukowe Politechniki Rzeszowskiej, 293, Mechanika 88RUTMech., XXXIII, 88 (2): 127-140.
- MAŁEK E., MIEDZIŃSKA D., POPLAWSKI A., SZYMCZYK W. 2019. *Application of 3d printing technology for mechanical properties study of the photopolymer resin used to print porous structures*. Technical Science, 22(2): 183-194.
- Operations and Maintenance Manual. 2012. Model 2436 Flow Visualization Water Tunnel, Rolling Hills Research Corporation. References.
- PANDYA Y., SREEVANSU Y.G., SHARMA A., JAIN K., JENA S., PAWAR A.A., RANJAN K.S., SAHA S. 2017. *Aerodynamic characterization of a model aircraft using wind-tunnel testing and numerical simulations*. First International Conference on Recent Advances in Aerospace Engineering (ICRAAE), p. 1-6. <https://doi.org/10.1109/ICRAAE.2017.8297239>.
- RAZA A., FARHAN S., NASIR S., SALAMAT S. 2021. *Applicability of 3D Printed Fighter Aircraft Model for Subsonic Wind Tunnel*. International Bhurban Conference on Applied Sciences and Technologies (IBCAST), p. 730-735. <https://doi.org/10.1109/IBCAST51254.2021.9393214>.
- RUANGWISET A., SUWANTRAGUL B. 2008. *Wind tunnel test of UAV fault detection using principal component based aerodynamic model*. IEEE International Conference on Mechatronics and Automation, p. 150-154. <https://doi.org/10.1109/ICMA.2008.4798742>.
- TOBIN S.M. 2010. *DC Servos: Application and Design with MATLAB*. CRC Press Inc., Boca Raton.
- WIBOWO S.B., FAJAR M., NAUFAL W.F., SINURAT D.F., SUTRISNO I., BASUKI B. 2019. *Comparison of Aerodynamic Characteristics on Sukhoi SU-33-like and F-35 Lightning II-like Models using Water Tunnel Flow Visualization Technique*. 5<sup>th</sup> International Conference on Science and Technology (ICST), p. 1-6. <https://doi.org/10.1109/ICST47872.2019.9166275>.

## Reviewers of Years – book 2021

Rafał Anyszka (Poland)	Jerzy Napiórkowski (Poland)
Radosław Bielawski (Poland)	Maciej Neugebauer (Poland)
Grzegorz Chomka (Poland)	Sabrina Nilufar (United States)
Jerzy Chudy (Poland)	Paweł Obstawski (Poland)
Fernando David Cúñez (Brazil)	Krzysztof Pancerz (Poland)
Robertas Damasevicius (Lithuania)	Zbigniew Pater (Poland)
Adam Deptuła (Poland)	Paweł Pawlik (Poland)
Roy Dibyendu (India)	Rafał Perz (Poland)
Jerzy Domański (Poland)	Antonin Pistek (Czech Republic)
Szymon Glowacki (Poland)	Krzysztof Ropiak (Poland)
Monika Gwoździk (Poland)	Tomasz Rydzkowski (Poland)
Daniel Janecki (Poland)	Witold Rządkowski (Poland)
Małgorzata Jaros (Poland)	Adam Sajek (Poland)
Stanisław Józwiak (Poland)	Ewelina Sendek-Matysiak (Poland)
Magdalena Lemecha (Poland)	Wojciech Sobieski (Poland)
Peter Lisý (Slovakia)	Mariusz Sobol (Poland)
Luka Boban (Croatia)	Patrik Šťastný (Slovakia)
Sergiy Luniov (Ukraine)	Maciej Sydor (Poland)
Edyta Ładyżyńska-Kozdraś (Poland)	Zenon Syroka (Poland)
Abhishek Madduri (United States)	Jože Tavčar (Slovenia)
Andrzej Majka (Poland)	Yuliia Udovytska (Ukraine)
Oto Makýš (Slovakia)	Ryszard Woźniak (Poland)
Łukasz Miazio (Poland)	Ireneusz Wróbel (Poland)
Danuta Miedzińska (Poland)	Aleksejs Zacepins (Latvia)
Tomasz Muszyński (Poland)	Konrad Zajkowski (Poland)
Ryszard Myhan (Poland)	Penka Zlateva (Bulgaria)
Catalin Nae (Romania)	

## **Guide for Authors**

### **Introduction**

Technical Sciences is a peer-reviewed research Journal published in English by the Publishing House of the University of Warmia and Mazury in Olsztyn (Poland). Journal is published continually since 1998. Until 2010 Journal was published as a yearbook, in 2011 and 2012 it was published semiyearly. From 2013, the Journal is published quarterly in the spring, summer, fall, and winter.

The Journal covers basic and applied researches in the field of engineering and the physical sciences that represent advances in understanding or modeling of the performance of technical and/or biological systems. The Journal covers most branches of engineering science including biosystems engineering, civil engineering, environmental engineering, food engineering, geodesy and cartography, information technology, mechanical engineering, materials science, production engineering etc.

Papers may report the results of experiments, theoretical analyses, design of machines and mechanization systems, processes or processing methods, new materials, new measurements methods or new ideas in information technology.

The submitted manuscripts should have clear science content in methodology, results and discussion. Appropriate scientific and statistically sound experimental designs must be included in methodology and statistics must be employed in analyzing data to discuss the impact of test variables. Moreover there should be clear evidence provided on how the given results advance the area of engineering science. Mere confirmation of existing published data is not acceptable. Manuscripts should present results of completed works.

There are three types of papers: a) research papers (full length articles); b) short communications; c) review papers.

The Journal is published in the printed and electronic version. The electronic version is published on the website ahead of printed version of Technical Sciences.

**Technical Sciences does not charge submission or page fees.**

### **Types of paper**

The following articles are accepted for publication:

### **Reviews**

Reviews should present a focused aspect on a topic of current interest in the area of biosystems engineering, civil engineering, environmental engineering, food engineering, geodesy and cartography, information technology, mechanical engineering, materials science, production engineering etc. They should include all major findings and bring together reports from a number of sources. These critical reviews should draw out comparisons and conflicts between work, and provide an overview of the 'state of the art'. They should give objective assessments of the topic by citing relevant published work, and not merely present the opinions of individual authors or summarize only work carried out by the authors or by those with whom the authors agree. Undue speculations should also be avoided. Reviews generally should not exceed 6,000 words.

### **Research Papers**

Research Papers are reports of complete, scientifically sound, original research which contributes new knowledge to its field. Papers should not exceed 5,000 words, including figures and tables.

### **Short Communications**

Short Communications are research papers constituting a concise description of a limited investigation. They should be completely documented, both by reference list, and description of the experimental procedures. Short Communications should not occupy more than 2,000 words, including figures and tables.

### **Letters to the Editor**

Letters to the Editor should concern with issues raised by articles recently published in scientific journals or by recent developments in the engineering area.

### **Contact details for submission**

The paper should be sent to the Editorial Office, as a Microsoft Word file, by e-mail: techsci@uwm.edu.pl

### **Referees**

Author/authors should suggest, the names, addresses and e-mail addresses of at least three potential referees. The editor retains the sole right to decide whether or not the suggested reviewers are used.

### **Submission declaration**

After final acceptance of the manuscript, the corresponding author should send to the Editorial Office the author's declaration. Submission of an article implies that the work has not been published previously (except in the form of an abstract or as part of a published lecture or academic thesis or as an electronic preprint), that it is not under consideration for publication elsewhere, that publication is approved by all authors and tacitly or explicitly by the responsible authorities where the work was carried out, and that, if accepted, it will not be published elsewhere in the same form, in English or in any other language.

To prevent cases of ghostwriting and guest authorship, the author/authors of manuscripts is/are obliged to: (i) disclose the input of each author to the text (specifying their affiliations and contributions, i.e. who is the author of the concept, assumptions, methods, protocol, etc. used during the preparation of the text); (ii) disclose information about the funding sources for the article, the contribution of research institutions, associations and other entities.

### **Language**

Authors should prepare the full manuscript i.e. title, abstract and the main text in English (American or British usage is accepted). Polish version of the manuscript is not required.

### **The file type**

Text should be prepared in a word processor and saved in doc or docx file (MS Office).

### **Article structure**

Suggested structure of the manuscript is as follows:

Title

Authors and affiliations

Corresponding author

Abstract

Keywords

Introduction

Material and Methods

Results and Discussion

Conclusions

Acknowledgements (optional)  
References  
Tables  
Figures

### **Subdivision – numbered sections**

Text should be organized into clearly defined and numbered sections and subsections (optionally). Sections and subsections should be numbered as 1. 2. 3. then 1.1 1.2 1.3 (then 1.1.1, 1.1.2, ...). The abstract should not be included in numbering section. A brief heading may be given to any subsection. Each heading should appear on its own separate line. A single line should separate paragraphs. Indentation should be used in each paragraph.

Font guidelines are as follows:

- Title: 14 pt. Times New Roman, bold, centered, with caps
- Author names and affiliations: 12 pt. Times New Roman, bold, centered, italic, two blank line above
- Abstract: 10 pt. Times New Roman, full justified, one and a half space. Abstract should begin with the word Abstract immediately following the title block with one blank line in between. The word Abstract: 10 pt. Times New Roman, centered, indentation should be used
- Section Headings: Not numbered, 12 pt. Times New Roman, bold, centered; one blank line above
- Section Sub-headings: Numbered, 12 pt. Times New Roman, bold, italic, centered; one blank line above
- Regular text: 12 pt. Times New Roman, one and a half space, full justified, indentation should be used in each paragraph

### **Title page information**

The following information should be placed at the first page:

#### **Title**

Concise and informative. If possible, authors should not use abbreviations and formulae.

#### **Authors and affiliations**

Author/authors' names should be presented below the title. The authors' affiliation addresses (department or college; university or company; city, state and zip code, country) should be placed below the names. Authors with the same affiliation must be grouped together on the same line with affiliation information following in a single block. Authors should indicate all affiliations with a lower-case superscript letter immediately after the author's name and in front of the appropriate address.

#### **Corresponding author**

It should be clearly indicated who will handle correspondence at all stages of refereeing and publication, also post-publication process. The e-mail address should be provided (footer, first page). Contact details must be kept up to date by the corresponding author.

#### **Abstract**

The abstract should have up to 100-150 words in length. A concise abstract is required. The abstract should state briefly the aim of the research, the principal results and major conclusions. Abstract must be able to stand alone. Only abbreviations firmly established in the field may be eligible. Non-standard or uncommon abbreviations should be avoided, but if essential they must be defined at their first mention in the abstract itself.

**Keywords**

Immediately after the abstract, author/authors should provide a maximum of 6 keywords avoiding general, plural terms and multiple concepts (avoid, for example, 'and', 'of'). Author/authors should be sparing with abbreviations: only abbreviations firmly established in the field may be eligible.

**Abbreviations**

Author/authors should define abbreviations that are not standard in this field. Abbreviations must be defined at their first mention there. Author/authors should ensure consistency of abbreviations throughout the article.

**Units**

All units used in the paper should be consistent with the SI system of measurement. If other units are mentioned, author/authors should give their equivalent in SI.

**Introduction**

Literature sources should be appropriately selected and cited. A literature review should discuss published information in a particular subject area. Introduction should identify, describe and analyze related research that has already been done and summarize the state of art in the topic area. Author/authors should state clearly the objectives of the work and provide an adequate background.

**Material and Methods**

Author/authors should provide sufficient details to allow the work to be reproduced by other researchers. Methods already published should be indicated by a reference. A theory should extend, not repeat, the background to the article already dealt within the Introduction and lay the foundation for further work. Calculations should represent a practical development from a theoretical basis.

**Results and Discussion**

Results should be clear and concise. Discussion should explore the significance of the results of the work, not repeat them. A combined Results and Discussion section is often appropriate.

**Conclusions**

The main conclusions of the study may be presented in a Conclusions section, which may stand alone or form a subsection of a Results and Discussion section.

**Acknowledgements**

Author/authors should include acknowledgements in a separate section at the end of the manuscript before the references. Author/authors should not include them on the title page, as a footnote to the title or otherwise. Individuals who provided help during the research study should be listed in this section.

**Artwork****General points**

- Make sure you use uniform lettering and sizing of your original artwork
- Embed the used fonts if the application provides that option
- Aim to use the following fonts in your illustrations: Arial, Courier, Times New Roman, Symbol
- Number equations, tables and figures according to their sequence in the text
- Size the illustrations close to the desired dimensions of the printed version



## **Formats**

If your electronic artwork is created in a Microsoft Office application (Word, PowerPoint, Excel) then please supply 'as is' in the native document format

Regardless of the application used other than Microsoft Office, when your electronic artwork is finalized, please 'Save as' or convert the images to one of the following formats (note the resolution requirements given below):

EPS (or PDF): Vector drawings, embed all used fonts

JPEG: Color or grayscale photographs (halftones), keep to a minimum of 300 dpi

JPEG: Bitmapped (pure black & white pixels) line drawings, keep to a minimum of 1000 dpi or combinations bitmapped line/half-tone (color or grayscale), keep to a minimum of 500 dpi

## **Please do not:**

- Supply files that are optimized for screen use (e.g., GIF, BMP, PICT, WPG); these typically have a low number of pixels and limited set of colors
- Supply files that are too low in resolution
- Submit graphics that are disproportionately large for the content

## **Color artwork**

Author/authors should make sure that artwork files are in an acceptable format (JPEG, EPS PDF, or MS Office files) and with the correct resolution. If, together with manuscript, author/authors submit color figures then Technical Sciences will ensure that these figures will appear in color on the web as well as in the printed version at no additional charge.

## **Tables, figures, and equations**

Tables, figures, and equations/formulae should be identified and numbered consecutively in accordance with their appearance in the text.

Equations/mathematical and physical formulae should be presented in the main text, while tables and figures should be presented at the end of file (after References section). Mathematical and physical formulae should be presented in the MS Word formula editor.

All types of figures can be black/white or color. Author/authors should ensure that each figure is numbered and has a caption. A caption should be placed below the figure. Figure must be able to stand alone (explanation of all symbols and abbreviations used in figure is required). Units must be always included. It is noted that figure and table numbering should be independent.

Tables should be numbered consecutively in accordance with their appearance in the text. Table caption should be placed above the table. Footnotes to tables should be placed below the table body and indicated with superscript lowercase letters. Vertical rules should be avoided. Author/authors should ensure that the data presented in tables do not duplicate results described in figures, diagrams, schemes, etc. Table must be able to stand alone (explanation of all symbols and abbreviations used in table is required). Units must be always included. As above, figure and table numbering should be independent.

## **References**

References: All publications cited in the text should be presented in a list of references following the text of the manuscript. The manuscript should be carefully checked to ensure that the spelling of authors' names and dates of publications are exactly the same in the text as in the reference list. Authors should ensure that each reference cited in the text is also present in the reference list (and vice versa).

Citations may be made directly (or parenthetically). All citations in the text should refer to:

1. Single author

The author's name (without initials, with caps, unless there is ambiguity) and the year of publication should appear in the text

2. Two authors

Both authors' names (without initials, with caps) and the year of publication should appear in the text

3. Three or more authors

First author's name followed by et al. and the year of publication should appear in the text

Groups of references should be listed first alphabetically, then chronologically.

*Examples:*

"... have been reported recently (ALLAN, 1996a, 1996b, 1999; ALLAN and JONES, 1995). KRAMER et al. (2000) have recently shown..."

The list of references should be arranged alphabetically by authors' names, then further sorted chronologically if necessary. More than once reference from the same author(s) in the same year must be identified by the letters "a", "b", "c" etc., placed after the year of publication.

References should be given in the following form:

KUMBHAR B.K., AGARVAL R.S., DAS K. 1981. Thermal properties of fresh and frozen fish. *International Journal of Refrigeration*, 4(3), 143–146.

MACHADO M.F., OLIVEIRA F.A.R., GEKAS V. 1997. Modelling water uptake and soluble solids losses by puffed breakfast cereal immersed in water or milk. In *Proceedings of the Seventh International Congress on Engineering and Food*, Brighton, UK.

NETER J., KUTNER M.H., NACHTSCHEIM C.J., WASSERMAN W. 1966. *Applied linear statistical models* (4th ed., pp. 1289–1293). Irwin, Chicago.

THOMSON F.M. 1984. Storage of particulate solids. In M. E. Fayed, L. Otten (Eds.), *Handbook of Powder Science and Technology* (pp. 365–463). Van Nostrand Reinhold, New York.

Citation of a reference as 'in press' implies that the item has been accepted for publication.

Note that the full names of Journals should appear in reference list.

### **Submission checklist**

The following list will be useful during the final checking of an article prior to the submission. Before sending the manuscript to the Journal for review, author/authors should ensure that the following items are present:

- Text is prepared with a word processor and saved in DOC or DOCX file (MS Office).
- One author has been designated as the corresponding author with contact details: e-mail address
- Manuscript has been 'spell-checked' and 'grammar-checked'
- References are in the correct format for this Journal
- All references mentioned in the Reference list are cited in the text, and vice versa
- Author/authors does/do not supply files that are too low in resolution
- Author/authors does/do not submit graphics that are disproportionately large for the content